NASA CR-72703
R-8361

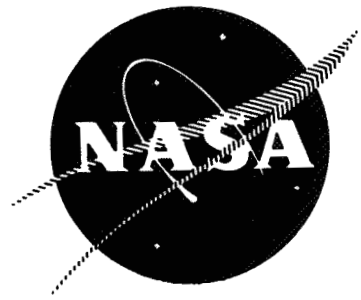

INVESTIGATION OF GAS-AUGMENTED INJECTORS

prepared for

NATIONAL AERONAUTICS AND SPACE ADMINISTRATION

CONTRACT NAS3-12001

Rocketdyne
North American Rockwell

Requests for copies of this report should be referred to

National Aeronautics and Space Administration
Scientific and Technical Information Facility
P.O. Box 33
College Park, Md. 20740

NASA CR-72703
R-8361

FINAL REPORT

INVESTIGATION OF GAS-AUGMENTED INJECTORS

by

P. F. Mehegan
D. T. Campbell
C. H. Scheuerman

prepared for

NATIONAL AERONAUTICS AND SPACE ADMINISTRATION

September 1970

CONTRACT NAS3-12001

Technical Management
NASA Lewis Research Center
Cleveland, Ohio
Liquid Rocket Technology Branch
T. Male

ROCKETDYNE
A Division of North American Rockwell Corporation
Canoga Park, California

FOREWORD

This final report documents a 26-month program to investigate the gas-augmented injector concept. The program was conducted under Contract NAS3-12001, by NASA Lewis Research Center under the direction of T. Male, Technical Program Manager. This report was prepared under Rocketdyne G.O. 09100 in compliance with Paragraph C of Exhibit B, Contract NAS3-12001.

ABSTRACT

The gas-augmented injector program was initiated to investigate the use of high-energy gas to enhance atomization and mixing and to generally improve gas-liquid injector concepts. Performance analyses, cold-flow experiments, and hot-firing tests were systematically conducted to produce stable operation with combustion efficiencies to 99 percent using large thrust-per-element injectors; i.e., 20,000-lb (88,900 N)-thrust per element with LOX/H_2 propellants and 5000-lb (22,200 N)- thrust per element with FLOX/CH_4 propellants. Also, promising analytical/cold-flow/hot-fire performance correlation techniques were developed that may be used to guide future injector designs.

CONTENTS

ILLUSTRATIONS

TABLES

INTRODUCTION

The basic approach underlying the gas augmented rocket engine injector program was to utilize high-energy gas to improve the atomization and mixing of gas-liquid propellants with subsequent high performance and stability. Other potential benefits included reduced fabrication and development costs, increased throttling capability without performance loss, and reduced injector and system pressure losses.

Under Contract NAS3-7962, an investigation was conducted to determine the performance and stability of large-thrust-per-element oxygen/hydrogen injector concepts which utilized hot gas in combination with commonly used injection systems to improve atomization, vaporization, and mixing of the propellants. Analyses and cold-flow experiments were used to guide the selection of injector concepts for hot-firing evaluations. The hot-firing results of this program proved feasibility of the hot gas injection (gas augmentation) principle and also demonstrated that high combustion efficiencies and stable operation were possible with 20,000-pound (88,960 newtons)-thrust-per-element injectors.

Under Contract NAS3-7962, a high-pressure gas generator or preburner was considered to be the source of hot gas to be used for augmentation. Other sources of hot gas might be heated fuel, tapped from the main pump discharge flow and passed through a separate heat exchanger section of the chamber, or possibly only the main fuel through the normal coolant cycle.

The subject program, Investigation of Gas Augmented Injectors, was intended to extend the knowledge of gas augmentation and generally to improve gas-liquid propellant injectors. Analysis, design, and experimental test efforts are employed to accomplish these improvements, particularly in the areas of larger thrust per element, higher performance, improved combustion stability, and throttling capability. Four tasks were used to describe the program: Hydrogen Gas Augmentation Tests (Task I), Evaluation of Gas-Liquid Injection Characteristics (Task II), Application to Space Storable Propellants (Task III), and Space Storable Tests (Task IV).

The main objective of Task I was to determine design criteria for high performance and to evaluate stability with large-thrust-per-element, gas augmented injectors. Gaseous hydrogen was used for augmenting the atomization and mixing processes of the liquid oxygen/gaseous hydrogen main propellants. Performance analyses, cold-flow tests and hot-firing tests were used to determine the injection-augmentation characteristics required relative to high performance. Stability trends were evaluated through bomb pulsing.

The objective of Task II was to determine the important parameters that affect atomization and mixing of gas-liquid propellant combinations and to derive a correlation from the parameters useful in prediction of c* efficiency. Cold-flow tests using propellant simulant fluids were conducted to determine the propellant droplet sizes, the dropsize distribution, and the mass and mixture ratio distribution for various types of gas-liquid coaxial and impinging jet injector elements generally suitable for propellants such as oxygen-hydrogen, fluorine-hydrogen, and FLOX-methane. Propellant atomization investigations were conducted using the molten wax method. Propellant mass and mixture ratio distributions were determined by collecting simulated liquid propellants in collection vessels and by gaseous stagnation pressure measurements with an impact probe.

The objective of Task III was to determine, through analysis and cold-flow experiments, the applicability of the gas augmentation principle to relatively large-thrust-per-element, FLOX-methane injectors. The analysis was used to predict the injection characteristics required for high performance. The cold-flow experiments were used to screen the atomization, mass, and mixture ratio distribution characteristics of the candidate injector concepts and consequently to support the performance analysis.

Task IV was a space storable hot-firing test program to investigate performance, stability, and throttleability of injector concepts which evolved from the analysis and cold-flow test results of Task II and III. The main propellants for this task were FLOX-methane with heated methane as the augmenting gas. The primary goals were to obtain a high performing, stable injector concept and to determine performance controlling design and operating criteria.

The interrelationship of the various program tasks is shown by the block diagram presented in Fig. 1. The reporting categories or subtasks are shown that were used to describe the major areas of work. As shown under Task I, the hydrogen gas augmentation analysis was followed by hardware fabrication and then hot-firing tests. The analysis phase of Task I was also used to prescribe the type of hot-fire tests which were the most meaningful. Information gained during the Task I analysis and hot-fire testing was used to improve the analytical techniques under Task II and III. Analyses and cold-flow experiments were used during Task II to characterize the performance controlling injection parameters, applicable to gas-liquid systems in general. This information was then applied to analysis, hardware design, fabrication, and cold-flow testing relative to the FLOX-methane propellant system under Task III. Finally, the Task III analysis and cold-flow testing were used to guide the selection and hot-fire testing of injector concepts under Task IV.

Details of the work performed under each of the four tasks are presented in this final report. Materials presented herein were accomplished during a 26-month period beginning 30 June 1968.

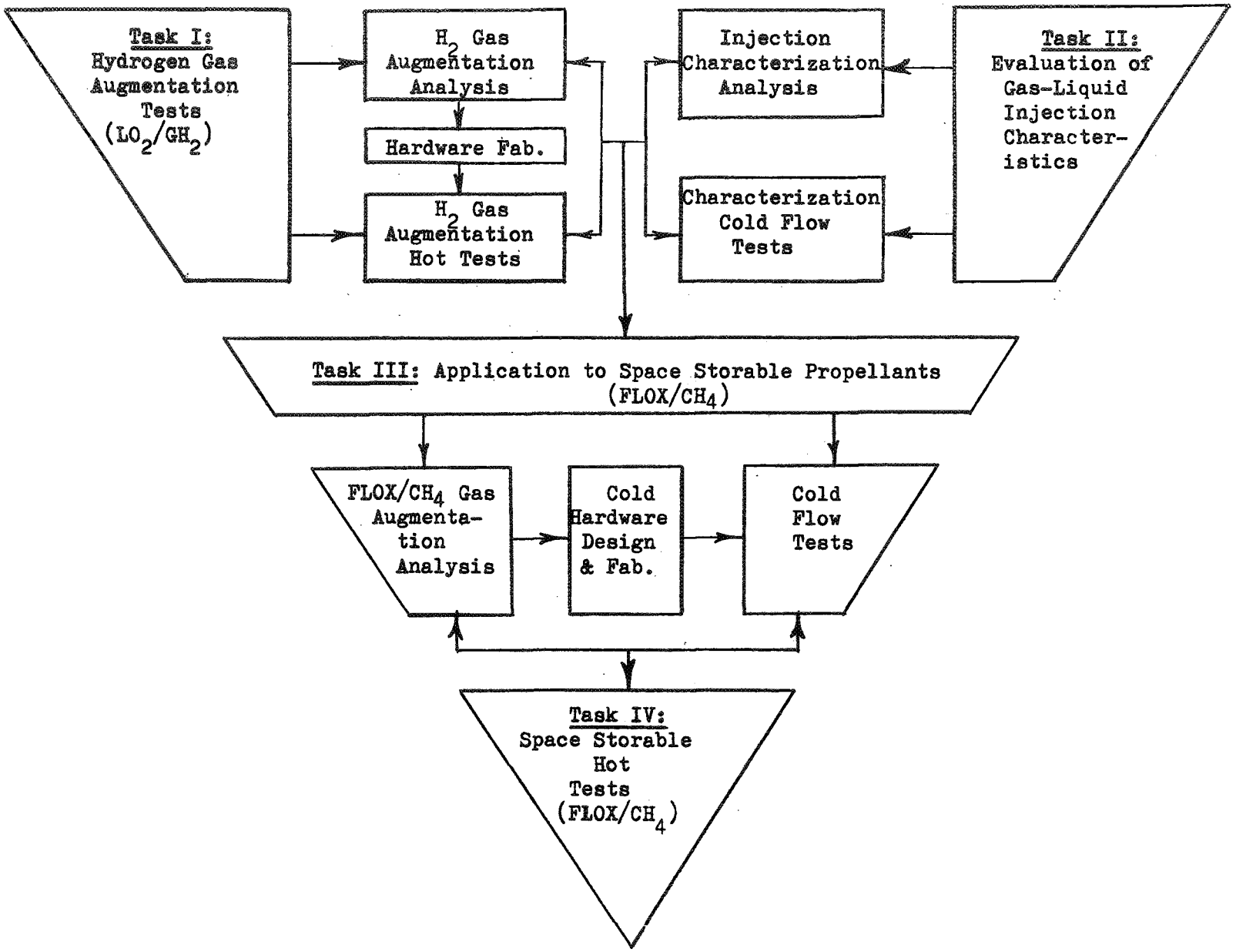

Figure 1. Program Flow Diagram, Investigation of Gas Augmented Injectors (NAS3-12001)

SUMMARY

The gas-augmented injector program was designed to investigate the use of high-energy gas to enhance the atomization and mixing processes for large thrust per element injectors and generally to improve the performance and stability of injector concepts using gas-liquid propellant combinations. Performance analyses, cold-flow tests, and hot-firing tests were employed to accomodate the investigations. The program was divided into four tasks: Task I--Hydrogen Gas Augmentation Tests, Task II--Evaluation of Gas-Liquid Injection Characteristics, Task III--Application to Space Storable Propellants, and Task IV--Space Storable Tests.

The Task I phase of the program was established to determine design criteria for high performance and to evaluate stability of large thrust per element, gas-augmented injectors. Liquid oxygen/gaseous hydrogen were the main propellants, with additional gaseous hydrogen used for augmenting the atomization and mixing processes. Performance analyses and approximately 34 cold-flow tests were conducted with the results used to guide the injector and hot-fire test selections. Inert fluids were used and liquid mass distributions were determined during the cold-flow tests simulating the hot-fire propellants and injection parameters. After the analysis and cold-flow tests, nine hot-firing tests were conducted to evaluate performance and stability of a single 20,000-lb (88,900 N)-thrust per element injector (recessed 4 on 1). Mixture ratios, chamber pressures, and hydrogen gas temperatures were varied over a relatively wide range to establish useful performance correlating parameters and design criteria. Performance (c* efficiency) during these tests ranged from 91 to 99 percent and dynamic stability was demonstrated through artificially induced pressure disturbances. Feasibility of the gas-augmentation principle was evident and useful design criteria emerged from the data.

The Task II phase of the program was generated to evaluate and characterize the performance controlling design and operating parameters of gas-liquid injector elements suitable for application to the LOX/GH_2, FLOX/CH_4, and LF_2/GH_2 propellant combinations. Elements investigated were the basic

impinging, basic concentric tube, concentric tube with swirler, impinging concentric, and tricentric with centerbody types. Cold-flow tests were conducted using propellant simulants to determine the propellant droplet sizes, the dropsize distribution, and the mass and mixture ratio distribution for the various injector elements, sized to match hot-firing designs from about 50- to 2000-lb (222 to 22,200 N)-thrust per element. Propellant atomization investigations were accomplished using the molten wax technique. Propellant mass and mixture ratio distributions were determined by collecting simulated liquid propellants in collection vessels and by gaseous stagnation pressure measurements with an impact probe developed for two-phase flowfield application. The key feature of the probe was to measure the gas stagnation pressure at a point in the probe where gas-liquid interactions were at a minimum.

Approximately 120 cold-flow atomization and mass distribution tests were conducted on the five basic element injector models. Nearly the same sets of design and operating variables were investigated during both atomization and distribution tests. Data from each of the atomization tests provided a distribution of dropsizes around a median size as well as a single mass median dropsize. These dropsize data were used to predict individual injector vaporization efficiencies under hot-firing conditions using the FLOX/CH_4 propellant system as a baseline.

Liquid and gas mass distributions were combined to determine mixing uniformity and mixing efficiencies based on the FLOX/CH_4 system. For the concentric element types (i.e., basic concentric, concentric with swirler, and tricentric with centerbody), the measured gas and liquid mass distributions were combined directly to determine the mixing efficiencies. The measured mass distributions for the impinging element types (i.e., basic impinging and impinging concentric) were somewhat complicated because, under certain conditions, a significant amount of the liquid mass was collected in a zone outside of the measured gas distribution. Therefore, a simple empirical recirculation model was developed to approximate the hot-firing results and thereby supply a quantity of gas to the outer liquid-rich zone. This model was used with the mass distribution data to determine the mixing efficiencies for the impinging element concepts.

Each Task II injector concept was rated independently with respect to atomization and mixing potential. The results indicated the impinging concentric, the tricentric with centerbody, and the recessed basic concentric to be the most promising concepts for use in Task III.

During Task III performance and analyses and cold-flow experiments were accomplished to determine if the large thrust per element gas-augmented injector concept was applicable to the FLOX/CH_4 propellant systems. Under this task, cold-flow experiments with inert fluids were used to simulate the atomization and mixing characteristics of the most promising injector concepts that evolved from Task II. As in Task II, the atomization experiments were conducted using the molten wax technique and the mixing data were obtained through the use of liquid and gas mass distribution measurements. Also, the experimental techniques and data reduction procedures were essentially the same as used under Task II. However, the Task III testing and hardware geometry were oriented toward the FLOX/CH_4 propellant combination as opposed to a more universal gas-liquid propellant system application under Task II.

Insufficient Task II cold-flow data somewhat limited the confidence level in predicting the combustion efficiency for the FLOX/CH_4 propellant system. In addition, several potentially important design variables for the selected concepts were yet to be evaluated. Thus, the Task III testing was directed toward further optimization of the individual injector concepts and toward improved capability for predicting their hot-firing performances.

A series of 42 cold-flow tests, 23 atomization and 19 mixing tests was conducted using single-element injector models of the impinging concentric, tricentric with centerbody, and the recessed basic concentric concepts sized for a maximum of 5000 lb (22,200 N) thrust with the FLOX/CH_4 propellant combination. Data from the resultant atomization and mixing tests and from the Task II tests were subsequently used to predict vaporization and mixing efficiencies that were in turn used to guide injector concept selections for the Task IV hot-fire testing. Two single 5000-lb (22,200 N)-thrust per element concepts were selected--the tricentric with centerbody and the impinging concentric concepts.

The objective of the Task IV hot-firing tests was to investigate performance, stability, and throttleability of the two injector concepts at a nominal 500-psia (345 x 10^4 N/m^2) chamber pressure and 5000-lb (22,200 N)-thrust level. The propellant combination used for these tests was FLOX/$CH_{4(g)}$ with a performance goal of 96-percent c* efficiency. The test series was formulated to investigate the effects of fuel (CH_4) injection velocity and temperature, liquid injection velocity, ratio of "secondary" fuel to total fuel flowrate, chamber pressure (throttle tests), and orifice geometry.

A total of 40 tests was conducted with the two injector concepts. A combustion efficiency of 97 percent was achieved with the tricentric with centerbody injector at a nominal 5.25 MR and 30-in. (0.76 m) L* chamber; increasing to 98 percent at mixture ratios around 4.75. The impinging concentric injector achieved a combustion efficiency of 96 percent at 4.75 mixture ratio in a 30-in. (0.76 m) L* chamber, increasing to 99 percent with a 57.6-in (1.46 m) L* chamber. The stability characteristics of the injectors were generally stable with no acoustic type instabilities observed. Dynamic stability was demonstrated during one test through artificially generated disturbances by pulse guns. Feasibility of the gas-augmentation principle and large thrust per element injectors was again demonstated with FLOX/CH_4.

Performance data for each Task IV injector were obtained under widely ranging design and operating parameters, thereby providing a good test of the cold-flow/analytical prediction methods. In addition, the analysis applied both to the LOX/H_2 and FLOX/CH_4 test data permitted further understanding of the performance controlling parameters. As a result, very promising analytical/cold-flow performance correlation techniques were formulated that may be used to guide future injector designs.

CONCLUSIONS AND RECOMMENDATIONS

GAS-AUGMENTED FLOX/CH_4 INJECTORS

High-performance (i.e., 97-percent η_{c*}) and stability were demonstrated with FLOX/$CH_{4(g)}$ at a MR of 5.25 and nominal chamber pressure of 500 psia (345 x 10^4 N/m^2) using the gas-augmented, 5000-lb (22,200 N)-thrust, single-element tricentric with centerbody injector in a 30-in. (0.76 m) L* chamber. This exceeded the target performance of 96 percent.

Performance analysis indicates that further design optimization of the tricentric injector can raise performances to about 99 percent under similar operating conditions and further, may permit a reduction in the high injection pressure (ΔP) used with this injector.

FLOX/$CH_{4(g)}$ performance with a 5000 lbf/element impinging concentric concept, was slightly lower (e.g., 96-percent η_{c*}) than those of the tricentric type in the same (30 in.; 0.76 m) L* chamber. However, analysis indicates similar combustion efficiency can be achieved with some design modification. Dynamic stability was demonstrated with this concept.

The tricentric with centerbody injector concept was recommended for further testing to maximize its performance, determine its throttle capability, and qualify it for application as a single-element injector for FLOX/CH_4 engine systems with 5000 lbf (22,200 N) or lower (and possibly higher) thrust requirements. Although slightly lower performing in its present version, the impinging concentric injector concept also shows promise for this type of application and merits further development.

GAS-AUGMENTED LOX/H_2 INJECTORS

High performance (η_{c*} = 98 to 99 percent) and dynamic stability were demonstrated with LOX/$H_{2(g)}$ using a gas-augmented impinging concentric injector at the 20,000-lb (88,900 N)-thrust per element level.

Analysis based on both cold-flow and hot-firing data indicates that the tricentric with centerbody injector would be applicable to O_2/H_2 systems at moderate thrust levels. Performance capability is expected to be in the 99- to 100-percent η_{c^*} range. The dynamic stability of these large, thrust per element injectors may permit unbaffled operation which is generally unacceptable with conventional thrust per element injectors.

ANALYSIS/COLD-FLOW/HOT-FIRE CORRECTIONS

The performance analysis approach, which utilizes cold-flow injector characterization to indicate atomization and propellant mixing capabilities, has been extended successfully for application to gas-liquid injectors. The necessary technology, apparatus, and instrumentation for cold-flow measurement of both spray and gas flow distribution have been developed and checked out. This included development of a special two-phase flow impact probe.

Empirical verification of the cold-flow/analytical method, using Task IV hot-firing data predictions, was very good relative to the tricentric injector data. Impinging concentric injector performances were underestimated by several percent, primarily as a result of imprecise interpolation between and extrapolation from test conditions simulated in cold flow. Nevertheless, trends and approximate levels of performance were predicted consistently and effectively.

The following steps are recommended for improving accuracy and range of applicability of the cold-flow/analytical performance analysis procedure developed under the subject contract:

1. Hot-Fire Test Verification With Other Injector Concepts. The basic recessed post concentric element is attractive for possible large thrust per element application.

2. Hot-Firing Test Verification With Different Contraction Ratio Chambers. All tests in Task IV were in an $\varepsilon_c = 2.0$ chamber. Tests with different ε_c are needed to determine what influence combustion gas velocity might have on $\overline{D}$ for gas-liquid injectors. With liquid-liquid systems, this has been found to be a very important factor in determining $(\eta_{c^*})_{vap}$.

3. Additional Cold-Flow Testing. The previously discussed problems, resulting from the extensive need to interpolate or extrapolate between existing cold-flow data, could be greatly alleviated by further cold-flow testing. Since this contract was conducted, pressurized cold-flow mixing and atomization facilities have been developed which permit gas density variations and would allow, for instance, testing at hot-firing levels of $\rho_g V_g^2$.

COLD-FLOW/HOT-FIRE TESTING AT LOWER THRUST LEVELS

Results of the subject program were primarily directed toward application at high thrust per element (e.g., 2000-to 20,000-lbf (8890 to 88,900 N)-thrust per element, whereas most gas-liquid injectors employ elements in the thrust range of 20 to 500 lbf (89 to 2200 N). The cold-flow/analytical techniques developed under this program, should be extended by selected cold-flow and hot-fire testing to smaller scale injection elements to provide the same type of analytical capability to the more typical gas-liquid injectors.

The extended (low- and high-thrust levels) parametric performance correlations, supported and substantiated by the selected hot-fire testing should be applied to develop a gas-liquid version of the LISP (Liquid Injector Spray Patterns) computer program. Such a program would: (1) serve as a catalog for all available single injector element atomization and mixing data, and (2) would be able to analytically describe the gas-spray flowfield of multiple element injectors for any specified arrangement and orientation of elements over the injector face.

TASK I, HYDROGEN GAS AUGMENTATION TESTS

The Task I phase of the program was primarily directed toward evaluating the use of relatively high-energy hydrogen gas to augment the atomization and mixing processes of large-thrust-per-element injectors. Performance analyses and a series of cold-flow tests were conducted to predict the injection characteristics required to attain high performance and to guide the hot-fire test selections. Based on these studies, existing hardware from Contract NAS3-7962 was modified, as required, and subjected to experimental hot-firing tests to determine performance and stability.

HYDROGEN GAS AUGMENTATION ANALYSIS

Analytical Approach

The performance analysis approach used requires evaluation of two principal modes of performance losses: incomplete propellant spray vaporization in the (subsonic) combustion chamber and imperfect mixing of fuel and oxidizer. Overall c* efficiency is predicted by the product of the vaporization-limited and the mixing-limited combustion efficiencies, $(\eta_{c^*})_{vap}$ and $(\eta_{c^*})_{mix}$, respectively. This approach was developed and substantiated first in application to liquid/liquid propellant systems and is discussed in some detail in Ref. 1 and 2. It is described briefly in the following paragraph.

A one-dimensional, vaporization-limited spray combustion model provides $(\eta_{c^*})_{vap}$, the c* efficiency obtainable with perfect distribution, as a function of the following input parameters:

1. Propellant combination and overall mixture ratio
2. Mean dropsize (e.g., $\bar{D}$, the mass median diameter) of fuel and/or oxidizer
3. Spray size distribution functions (e.g., Nukiyama-Tanisawa)
4. Injection velocities

5. Injector end chamber pressure

6. Chamber geometry

A stream tube (mixing-limited) model is used to obtain $(\eta_{c^*})_{mix}$ using cold-flow propellant distribution data as input. This model assumes complete vaporization (in the combustion chamber) of all propellant in each stream tube. The stream tube combustion gases are considered to expand isentropically through the nozzle. Another basic assumption is that static pressure at any transverse station of the nozzle is uniform. The procedure for predicting hot-fire performance efficiencies is depicted in Fig. 2.

Injector Concept Selection

The 20,000-lb (88,960 N)-thrust-per-element recessed impinging jet injector was selected for primary consideration during the hydrogen gas augmentation analysis phase of the program. This injector concept was selected because of its previously demonstrated high performance under Contract NAS3-7962 (Ref. 3). The concept consists of a central fuel jet surrounded by and impinging with four equally spaced oxidizer/fuel coaxial jets. All the orifices are inside a shallow recessed cup with the centerline impingement point of the coaxial jets just downstream of the injector face. A sketch illustrating this injector concept is presented in Fig. 3.

Specific injector design criteria for the hot-fire LOX/GH_2 tests were determined by performance analysis utilizing correlations developed from the previous hot-fire data with this injector type and from cold-flow spray distribution test data obtained under the subject task. The correlations developed and their use in the hot-fire injector design are discussed below in the appropriate sections.

Correlation of Previous Gas Augmented Injector Test Data

The hot-firing data obtained with the impinging coaxial injector using hot gas augmentation (Contract NAS3-7962) was empirically correlated with the ratio of total injected gas momentum to liquid (oxidizer) flowrate, $M_g/\dot{w}_o$. This index

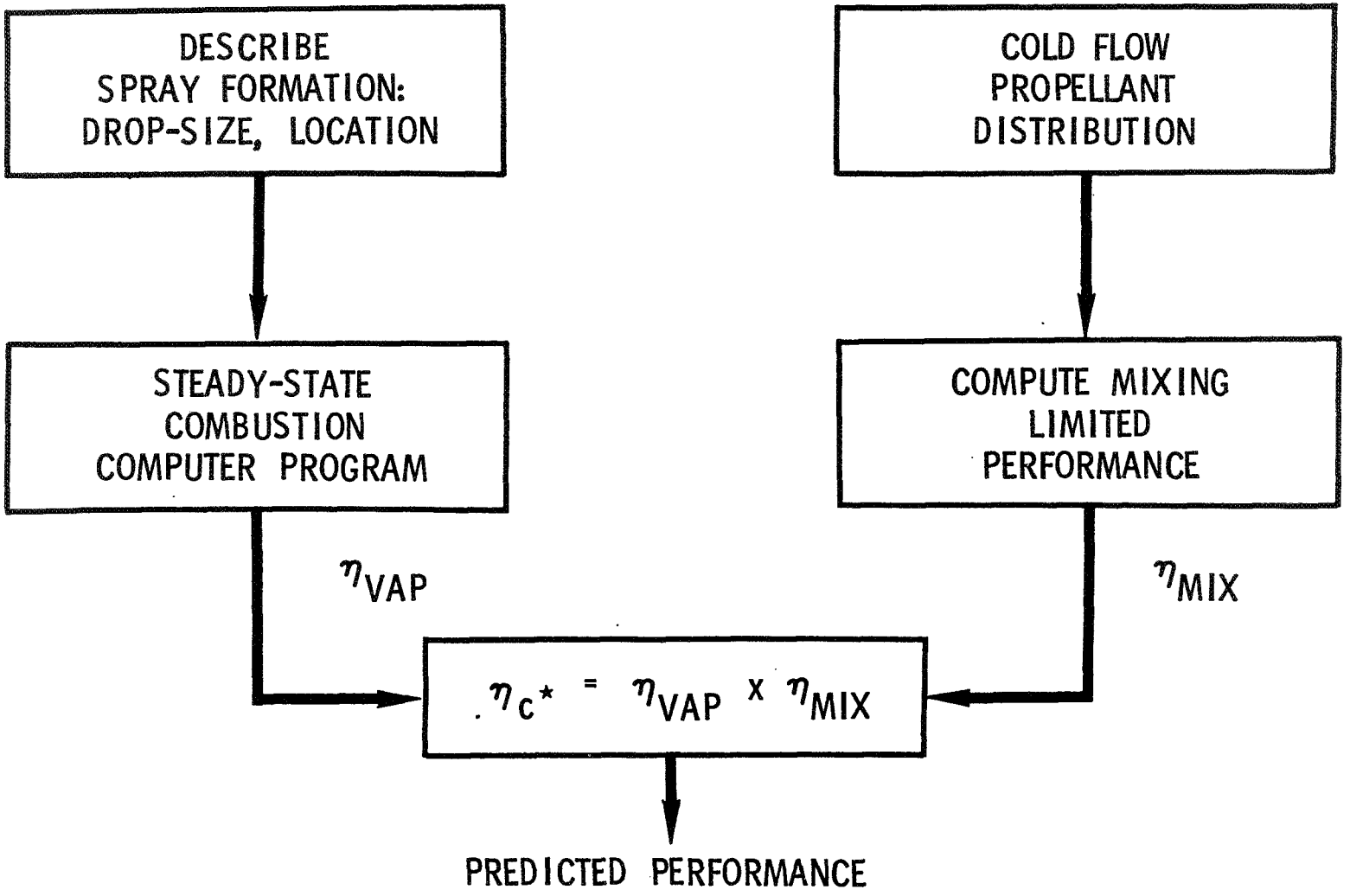

Figure 2. Semi-Analytical Performance Prediction

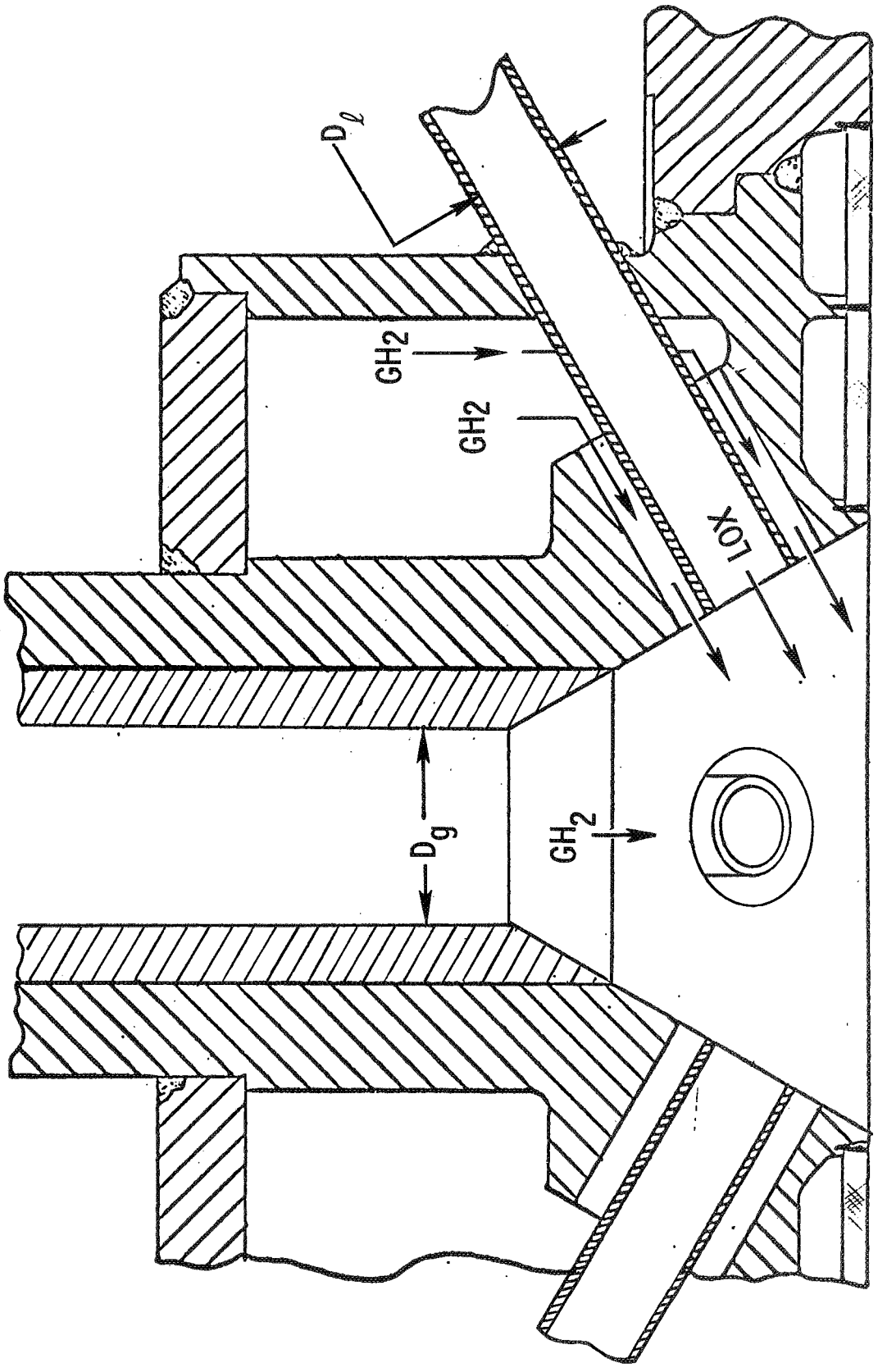

Figure 3. Recessed Impinging Jet Injector

was considered to be an indicator of the potential capability of the gas (fuel as well as augmenting gas) to atomize and mix with the liquid oxidizer (LOX). The correlation is illustrated in Fig. 4. The trend with $M_g/\dot{w}_o$ appeared to be quite significant and suggested that the Task I injectors should be designed with this parameter in excess of 600 ft/sec (183 m/sec).

Examination of the effect of chamber L*, also seen in Fig. 4, permitted a more definitive analysis of the performance data. By crossplotting η_{c*} vs L* at constant operating conditions, and extrapolating the hot-firing η_{c*} to long chamber lengths, the mixing-limited combustion efficiency, $(\eta_{c*})_{mix}$, was obtained (i.e., Fig. 5). Analysis of liquid rocket engine performance data has indicated that, with increasing chamber length, spray vaporization will approach 100 percent, but the degree of propellant mixing changes relatively slowly from that established near the injector. Thus, extrapolation of hot-firing performance data to increasing chamber length asymptotically approaches the limit set by mixing. As indicated by Fig. 5, the long (70-in., 1.778 m) L* data was completely mixing-limited, i.e., $(\eta_{c*})_{vap}$ = 100 percent, and thus provided $(\eta_{c*})_{mix}$ directly.

Previous experience with gas-liquid impinging jet injectors had indicated a significant correlation between the degree of liquid stream penetration into a gas stream and the propellant mixing or distribution uniformity. This penetration is indexed by an analytical "penetration parameter" defined by the following equation:

$$\frac{X_p}{D_g} = 2.5\left[\frac{M_\ell}{M_g}\cos^2\theta\right]^{1/2} \qquad (1)$$

where

M_ℓ = liquid jet momentum (individual jet)

M_g = gas jet momentum (through central showerhead gas orifice)

θ = complement of the impingement angle between the liquid and gas jets

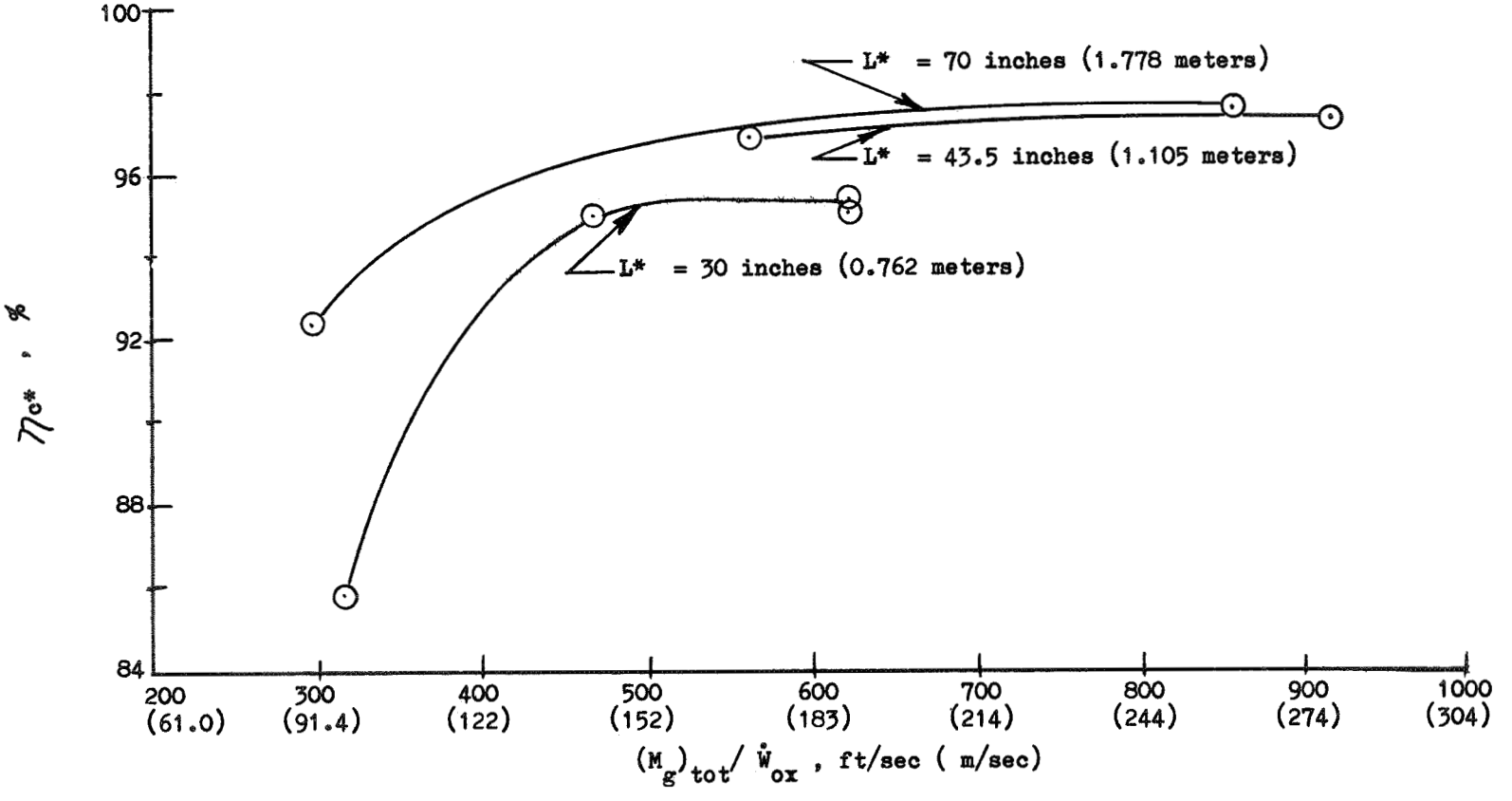

Figure 4. Gas Momentum Effects on Injector Performance: Recessed Impinging Jet Injector (Contract NAS3-7962)

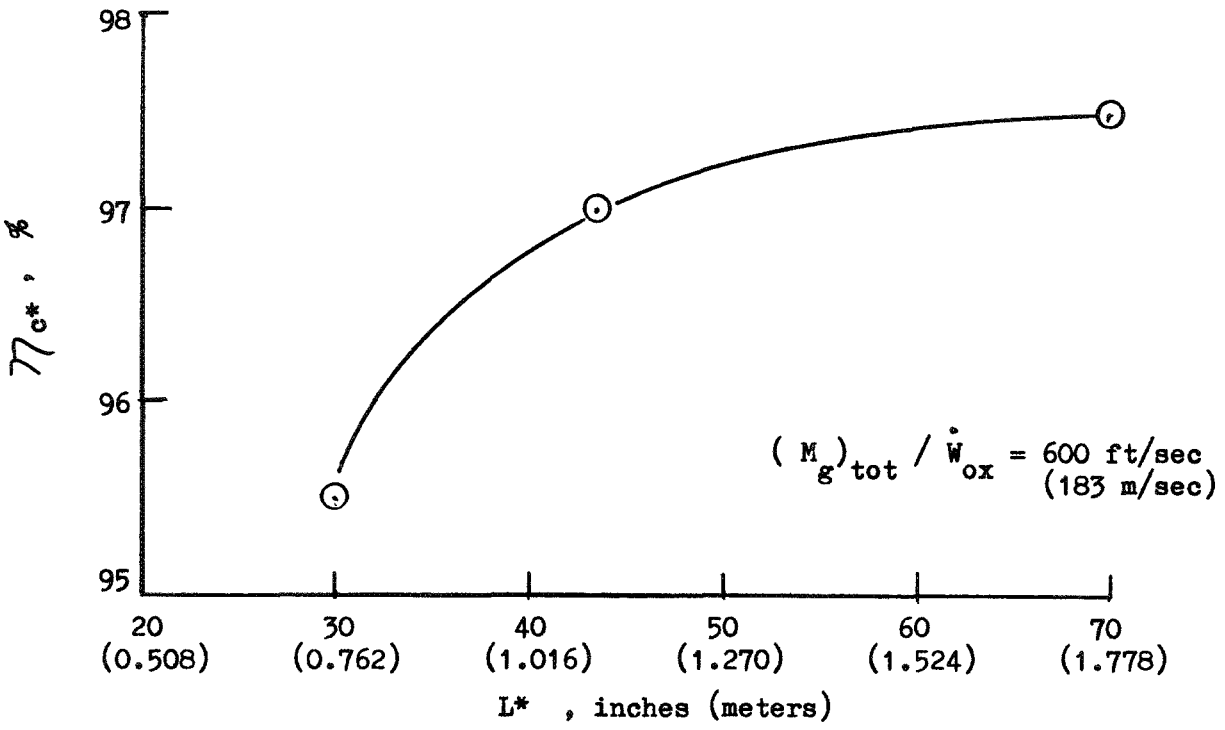

Figure 5. Characteristic Length Effect on Injector Performance: Recessed Impinging Jet Injector (Contract NAS3-7962)

The liquid penetration parameter was calculated for the long L* (mixing-limited) hot-fire tests made under Contract NAS3-7962 and the experimental $(\eta_{c^*})_{mix}$ values were plotted against X_p/D_g as shown in Fig. 6. An optimum value of the penetration parameter was indicated to lie between 0.5 and 0.8, although this optimum was relatively weak. The mixing potential of the recessed impinging injector was subsequently investigated further by tests using simulated "cold-flow" propellants. These tests are described in the next subsection.

By comparing the Contract NAS3-7962 hot-firing performance data with appropriate mixing-limited combustion efficiencies, losses caused by incomplete vaporization were found to be on the order of 2 percent (i.e., $(\eta_{c^*})_{vap}$ was $\approx$ 98 percent) with a 30-in. (0.762 m) L* chamber and $M_g/\dot{w}_o \approx 600$ ft/sec (183 m/s). A vaporization-limited combustion model (Ref. 1 and 2) was then run at the hot-firing operating conditions to calculate $(\eta_{c^*})_{vap}$ for various oxidizer mean dropsizes, D_{30}. Comparison of these parametric curves with the empirical values of $(\eta_{c^*})_{vap}$ indicated the hot-firing mean dropsizes to be approximately 120 microns (120×10^{-6} m).

Cold-Flow Studies

Analysis of the NAS3-7962 performance data indicated that propellant mixing played a role at least as important as that of spray vaporization. Furthermore, performance losses associated with $(\eta_{c^*})_{mix}$ cannot readily be reduced by increasing the chamber size. Previous success in characterizing propellant mixing of liquid-liquid injectors by use of cold-flow simulation techniques led to experimental cold-flow testing of contemplated Task I injector designs as described below. It should be kept in mind that in this initial testing only the liquid flow distribution was measured.

Test Facility. A series of cold-flow liquid mass flux distribution tests was conducted to support the hydrogen gas augmentation analysis. A liquid mass collection system (Fig. 7) was designed and fabricated primarily for these tests and the following Task II and Task III cold-flow studies. The collection system grid is comprised of 100 collection tubes, 1 in. (0.0254 m) in diameter.

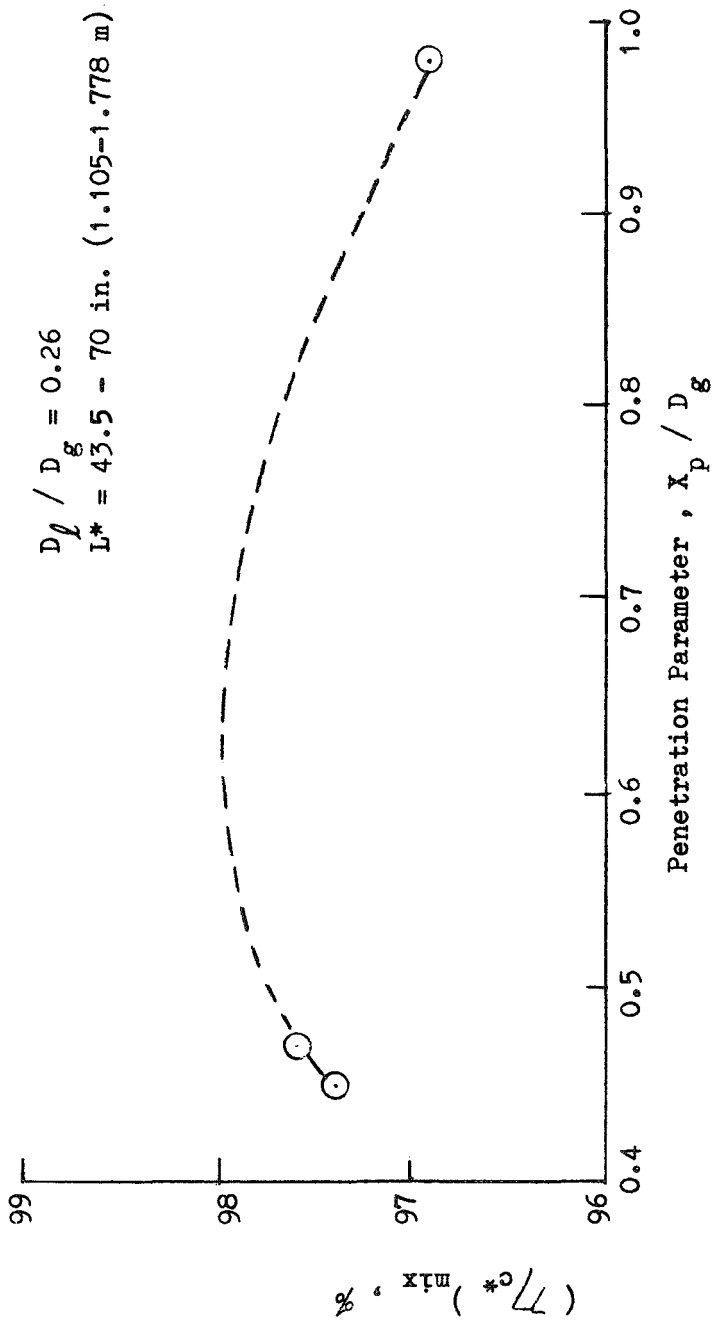

Figure 6. Mixing Efficiency vs Penetration Parameter: Recessed Impinging Jet Injector (Contract NAS3-7962)

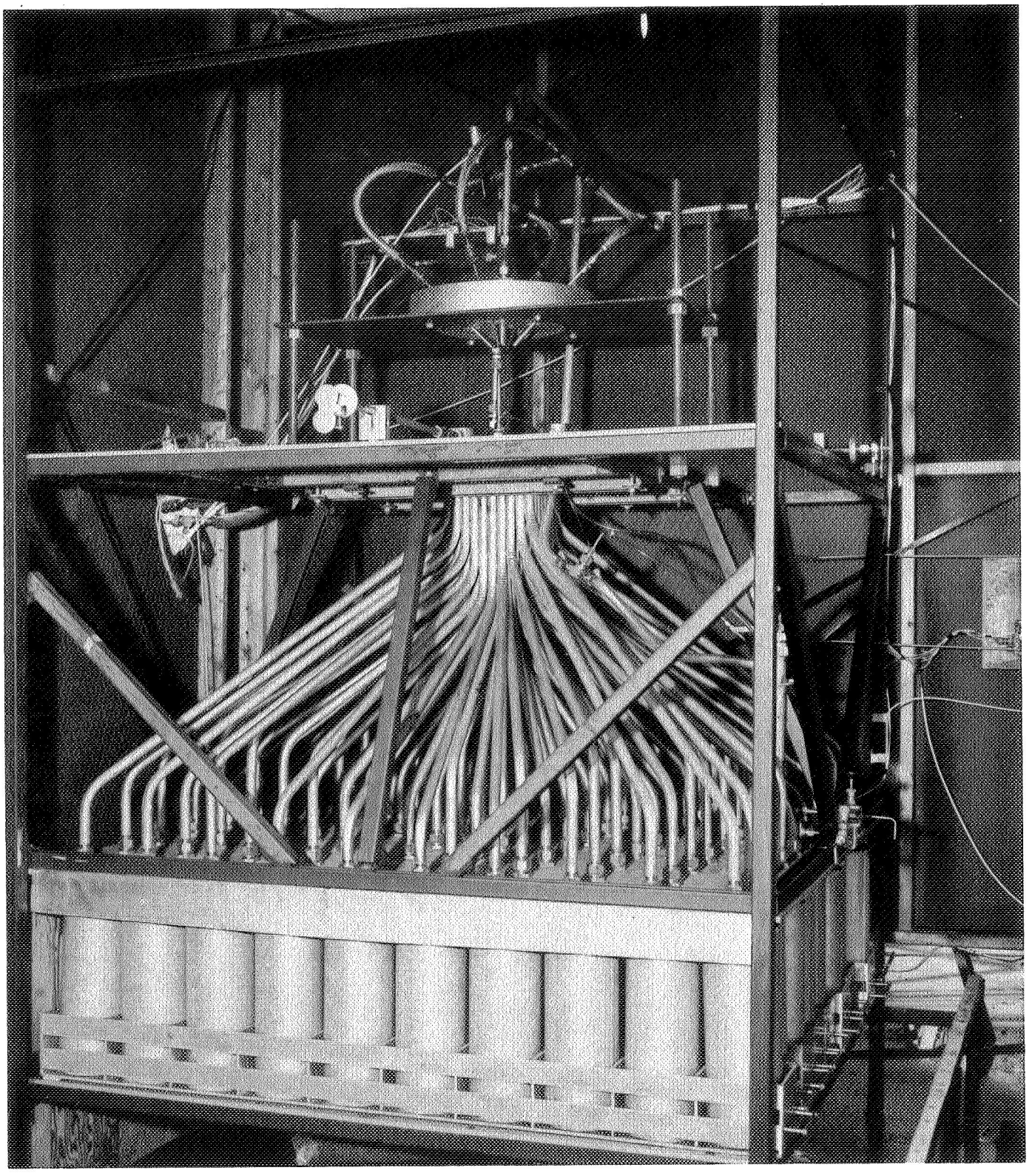

5AJ31-9/29/69-SIB

Figure 7. Mixing Facility Test Stand

The overall size of the tube matrix is 10 by 10 in. (0.254 m). Each of the collection tubes is squared at the end, 1 by 1 in. (0.0254 m), to maximize the collection grid sampling area. The collection tubes diverge from the collection plane to a 7 by 7 ft (2.134 m) base. The base is 1/2-in. (0.0127 m) aluminum plate and separates the upper portion of the assembly from the collection vessels. Beneath the aluminum plate are 10 racks which house the collection vessels. The open area between the plate and collection vessel is sufficient to allow the gas to escape. The collection vessels are 6-3/8-in. (0.162 m) diameter galvanized closed-end cylinders 18 in. (0.457 m) in length. Critical details of this design are based on experiments described in the following paragraphs.

Two potential problem areas arise in attempting to characterize a liquid-high velocity gas injection system by cold-flow spray collection. The first concerns possible distortion of the flow field caused by blockage by the collection grid. Preliminary calculations, utilizing droplet drag equations, indicated that a droplet initiating at the very edge of the injector element would be deflected, at most, only about one tube diameter (1 in. or 0.0254 m) if the entire gas flow were blocked. Since 84 percent of the collection grid is open area, the majority of the gas would not be blocked. A short experimental study was conducted utilizing one typical collection tube to quantitatively establish the maximum degree of flow distortion which might be encountered. Results revealed a maximum of 4-percent variation in collected flow because of simulated blockage by the collection system. This percentage variation decreased rapidly to less than 1 percent as the tube was placed nearer to the center of the injected stream. To evaluate the influence of this deviation from the undisturbed liquid flow distribution on predicted mixing efficiency*, two typical flow distribution profiles were assumed and a mixing efficiency was calculated for each case. In both cases, the difference in the actual (undisturbed) mixing

*It should be noted that at this point in the program gas flow distribution measurements were not possible. Thus, the "mixing efficiencies" referred to during this phase of Task I were calculated using cold-flow liquid distribution measurements with assumed uniform gas flow profiles.

efficiency and the mixing efficiency which would be predicted from the liquid flow collection system results was less than 0.3 percent, i.e., negligible.

The second potential cold-flow facility problem area could occur as the collected propellant simulant passes from the collection tubes into the storage vessels. The gas must escape through the open area between the collection tube and the storage vessel. This creates the possibility of entrained liquid being carried out of the vessels by the gas. A series of tests was conducted to determine the magnitude of this problem. Test results indicated that large diameter (6-3/8 in., 0.162 m) storage vessels were necessary. Experiments using this size storage vessel with a single collection tube indicated negligible losses of liquid caused by entrainment. This was qualitatively confirmed by high-speed photography.

Cold-Flow Tests. Thirty-four tests were made utilizing the simulated 5000-lb (22,240 N) thrust model (available from Contract NAS3-7962) of the recessed impinging jet injector. The listed thrust level of cold-flow model injectors corresponds to the nominal thrust level of the simulated hot-firing injectors using the same orifice dimensions. A 5000 lbf (22,240 N) thrust model injector was used because a 20,000 lbf (88,960 N) injector was considered to be too large for the cold-flow facility. This injector model contains four coaxial gas-liquid jets (annulus gas) impinging with a single central gas jet within a recessed cup. A photograph of the injector is shown in Fig. 8. Water and gaseous nitrogen were used to simulate the hot-fire propellants (liquid oxygen and gaseous hydrogen, respectively). To fully simulate both the hot-firing atomization and mixing characteristics in the cold-flow tests, it was desirable to match such hot-firing parameters as the liquid/gas penetration parameter (X_p/D_g), liquid-gas orifice diameter ratio (D_ℓ/D_g), the gas momentum parameter ($M_g/\dot{w}_\ell$), and mixture ratio. Unfortunately, it is not possible at atmospheric pressure to match all these hot-firing parameters in a single test. However, each of these parameters was varied individually, while the other parameters were maintained as nearly as possible within their respective hot-firing ranges.

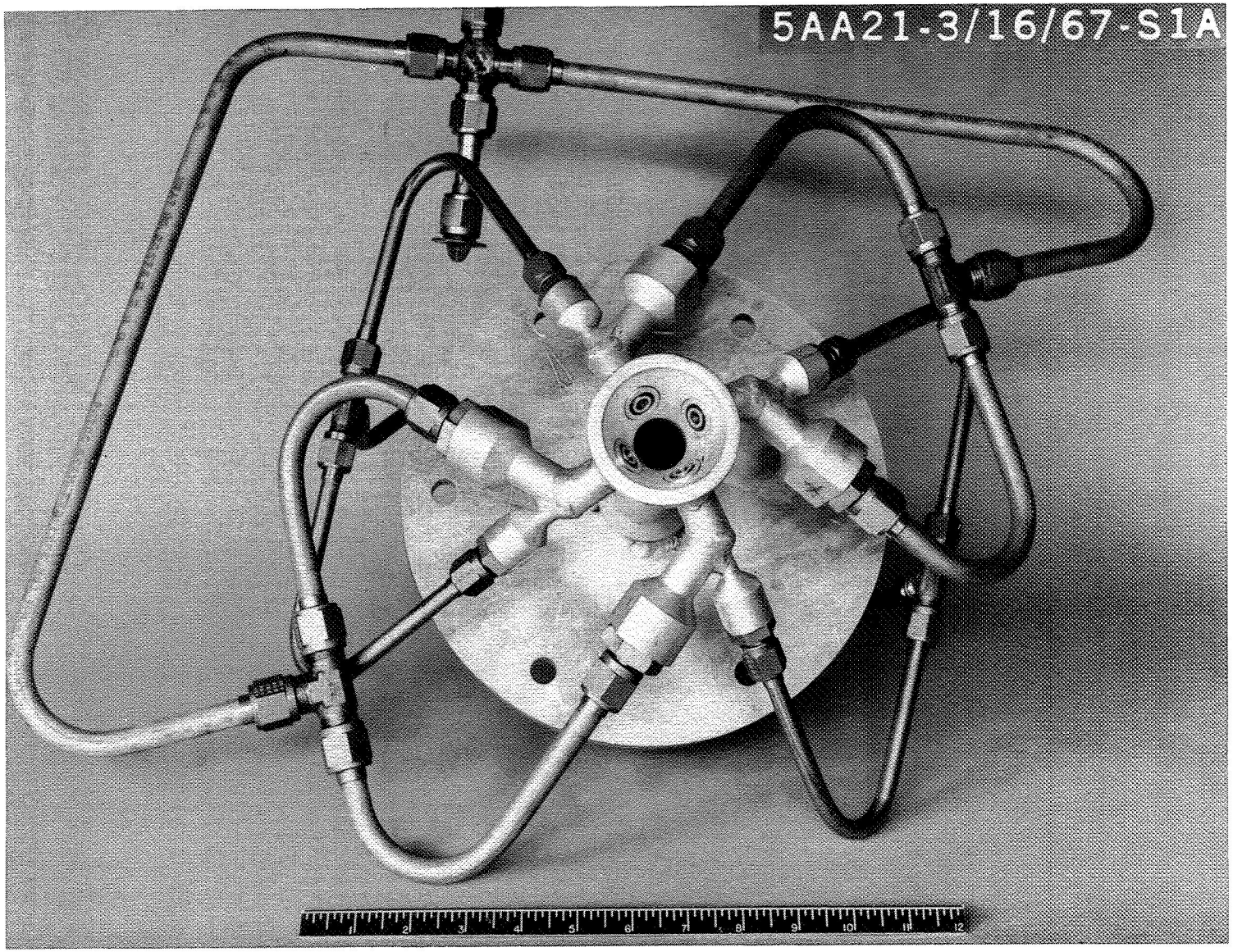

Figure 8. Recessed Impinging Jet Injector Model Used in Cold-Flow Tests

To see the interaction of some of the simulated hot-fire parameters, Eq. 1 was reduced to the following form:

$$\frac{X_p}{D_g} = 2.5 \cos\theta \left(\frac{\dot{w}_\ell}{4\dot{w}_{g,c}}\right)\left(\frac{D_g}{D_\ell}\right)\left(\frac{\rho_g}{\rho_\ell}\right)^{1/2} \quad (2)$$

where

$\dot{w}_\ell$ = total liquid flowrate ($\dot{w}_\ell/4$ = liquid flowrate per liquid orifice)

$\dot{w}_{g,c}$ = gaseous flowrate through the central gas orifice

D = orifice diameter

ρ = density

g = gaseous

ℓ = liquid

θ = complement of the impingement angle between the liquid and gas jets

Four basic methods were used in the cold-flow tests to vary this penetration parameter (X_p/D_g), including variation of: (1) the overall mixture ratio ($\dot{w}_\ell/\dot{w}_g$) with no annulus gas, i.e., $\dot{w}_{g,c} = \dot{w}_g$, (2) gas orifice diameter (D_g), (3) liquid orifice diameter (D_ℓ), and (4) gas flowrate through the central gas orifice ($\dot{w}_{g,c}$) at constant overall mixture ratio. The mixture ratio was varied from 4.3 to 11.4, gas orifice diameter from 0.437 to 0.964 in. (1.11 to 2.45 x 10^{-2} m). The fourth method above involved operating at a constant overall mixture ratio, by injecting a percentage of the simulated gaseous propellant through annular orifices surrounding each of the liquid orifices. This percentage varied from 6.5 to 25 percent of the gas flowrate. One test was also run using helium gas and water to see the effect of the gas density in Eq. 2. The orifice diameter ratio, D_ℓ/D_g, was varied by use of various combinations of insert tubes in the gas and liquid orifices. The diameter ratio ranged from 0.133 to 0.374 in these tests.

To obtain cold-flow spray distribution data which is relevant to hot-firing tests, careful consideration must be given to the selection of the distance downstream from the injector to the collection grid. A series of four tests was performed varying this collection distance from 2 to 7 in. (5.1 to 17.8 x 10^{-2} m) while holding all other operating conditions constant. The intent of this test series was primarily to gain an indication of the sensitivity of liquid spray uniformity to collection distance. A secondary objective was to obtain another indication of the possible spray field distortion caused by the presence of the collector in the gas flow path. All other tests were conducted with a collection distance of 5 in. (12.7 x 10^{-2} m), which was selected as a result of observed cold-flow spray formations.

Cold-Flow Test Results. The Task I cold-flow liquid distribution measurements data were reduced using the assumption that the gaseous fuel simulant would be equally distributed in each of the collection tubes. Thus, the calculated "mixing efficiency" was essentially a relative distribution efficiency for the liquid only. It was recognized that the mixing efficiency calculated in this manner could not be expected to quantitatively predict hot-firing performances. However, it was considered that the ability to uniformly distribute the oxidizer spray was a desirable feature and the mixing efficiency should provide a useful index of this ability.

The cold-flow test results, along with the test operating conditions, are shown in Table 1. The results for a 5 in. (0.127 m) injector-to-collector distance and no annulus gas flow are shown graphically in Fig. 9 and 10. Figure 9 illustrates the effect of the penetration distance parameter on mixing efficiency for fixed ranges of D_ℓ/D_g. The mixing efficiency rises from about 85 to 96 percent as X_p/D_g is increased from 0.12 to 0.58. The optimum value of X_p/D_g, according to Fig. 9, would be between 0.5 and 0.8 which is consistent with the Contract NAS3-7962 hot-firing correlations. The suggested downturn of $(\eta_{c^*})_{mix}$ with X_p/D_g approaching 0.8 is quite tenuous, however, being based on a single point.

TABLE 1

TASK I COLD-FLOW TEST DATA

Run No.	D_ℓ		D_g		% Annulus gas*	MR	$\frac{D_\ell}{D_g}$	$\frac{X_p}{D_g}$	E_m, %	$(\eta_{c^*})_{mix}$, %
	in.	m	in.	m						
1	0.258	0.656×10^{-2}	0.964	2.45×10^{-2}	0.0	6.50	0.268	0.45	67.6	91.9
2	↓	↓	↓	↓	↓	4.72	↓	0.32	66.4	91.4
3						7.58		0.52	67.2	92.3
4						11.40		0.76	61.2	89.0
5			0.798	2.03×10^{-2}		5.07	0.324	0.29	60.0	87.9
6			↓	↓		7.65	↓	0.43	68.4	92.9
6A						7.52		0.42	65.9	91.4
7						10.50		0.58	72.5	96.3
8			0.892	2.26×10^{-2}		4.85	0.289	0.30	61.9	89.1
9			0.892	2.26×10^{-2}		7.58	0.289	0.47	72.9	93.8
10			0.691	1.76×10^{-2}		4.47	0.374	0.22	60.4	88.6
11			↓	↓		7.66	0.374	0.37	67.6	92.0
12						4.66	0.374	0.22	61.2	88.9
13	↓	↓	0.964	2.45×10^{-2}		4.95	0.268	0.12	53.5	85.8
16	0.078	0.198×10^{-2}	↓	↓		4.65	0.081	1.00	36.1	46.9
17	0.129	0.328×10^{-2}				4.85	0.133	0.62	42.6	63.6
18	0.258	0.656×10^{-2}			↓	4.92	0.268	0.33	67.1	91.6
19	0.259	0.659×10^{-2}			13.9	4.90	↓	0.39	64.8	90.4
20	↓	↓			24.7	4.94		0.45	59.3	87.4
21			↓	↓	6.8	5.02	↓	0.37	65.8	91.1
22			0.891	2.26×10^{-2}	6.5	4.97	0.289	0.34	66.8	91.4
23	↓	↓	0.798	2.03×10^{-2}	6.5	4.81	0.324	0.29	63.8	89.9
24	0.169	0.429×10^{-2}	0.964	2.45×10^{-2}	0.0	5.08	0.176	0.52	51.5	82.8
25	0.129	0.328×10^{-2}	↓	↓	6.5	4.93	0.133	0.72	41.4	60.0
26**	0.258	0.656×10^{-2}			0.0	4.30	0.268	0.29	34.5	70.2
27**	0.258	0.656×10^{-2}	↓	↓	0.0	4.29	0.268	0.29	53.6	85.8

TABLE 1

(Concluded)

Run No.	D_ℓ		D_g		% Annulus gas*	MR	$\frac{D_\ell}{D_g}$	$\frac{X_p}{D_g}$	E_m, %	$(\eta_{c^*})_{mix}$, %
	in.	m	in.	m						
28**	0.258	0.656×10^{-2}	0.964	2.45×10^{-2}	0.0	4.31	0.268	0.29	79.3	96.7
29	0.258	0.656×10^{-2}	0.964	2.45×10^{-2}	↓	4.37	0.268	0.29	63.9	90.6
30	0.129	0.328×10^{-2}	0.691	1.76×10^{-2}		4.57	0.186	0.45	50.6	80.3
31	0.129	0.328×10^{-2}	0.437	1.11×10^{-2}		5.16	0.294	0.32	64.3	88.4
32	0.169	0.429×10^{-2}	0.691	1.76×10^{-2}		5.17	0.245	0.38	61.7	87.8
33	0.258	0.656×10^{-2}	0.691	1.76×10^{-2}		10.50	0.374	0.49	69.3	94.9
34	0.258	0.656×10^{-2}	0.437	1.11×10^{-2}		10.50	0.590	0.32	55.2	73.2

*Percent of all gas injected

**Injector-to-collector distance was 2 in. (0.051 m) for test 26, 4 in. (0.102 m) for test 27, and 7 in. (0.178 m) for test 28. The distance for all other tests was 5 in. (0.127 m).

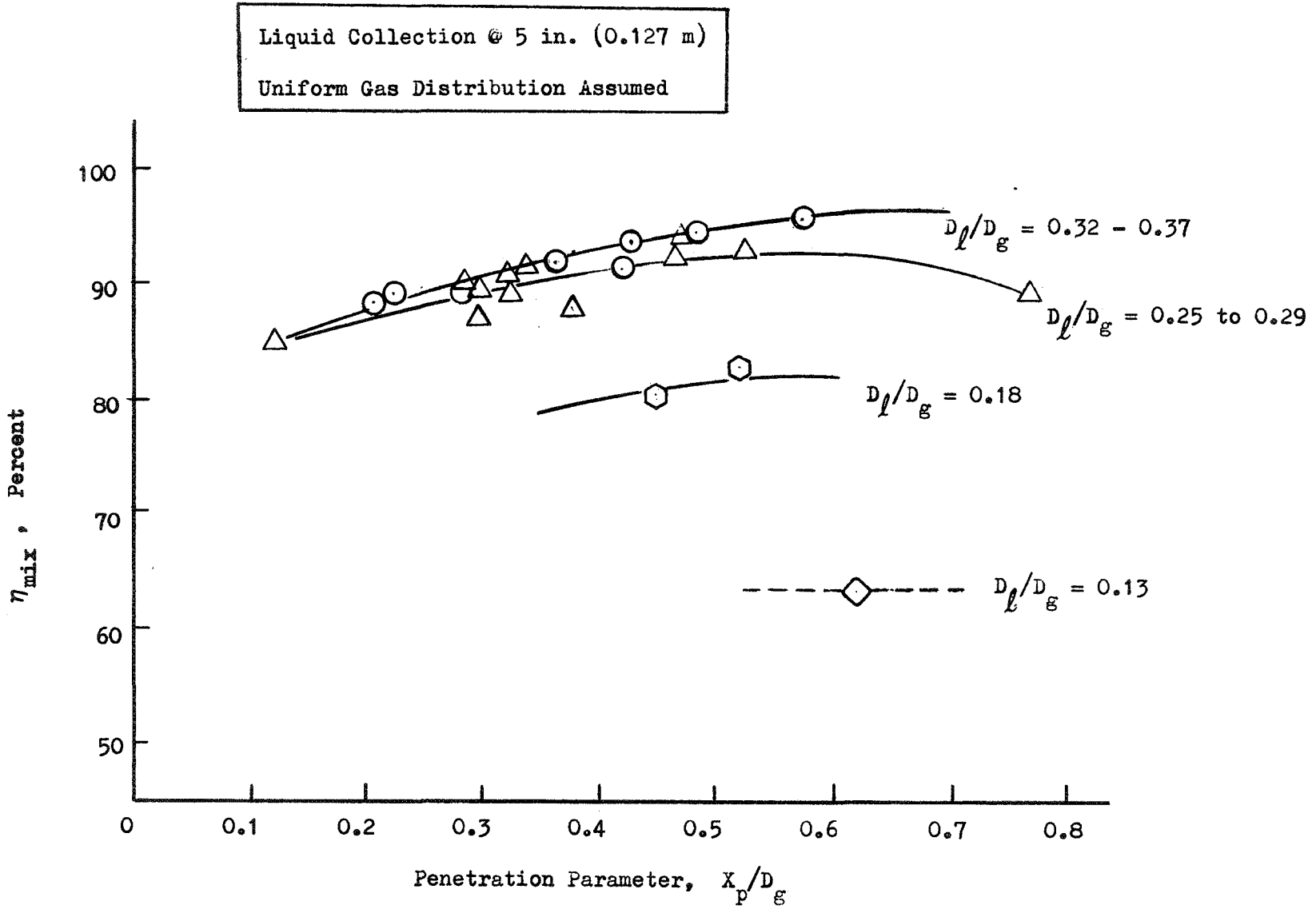

Figure 9. Penetration Distance Influence on Mixing Efficiency

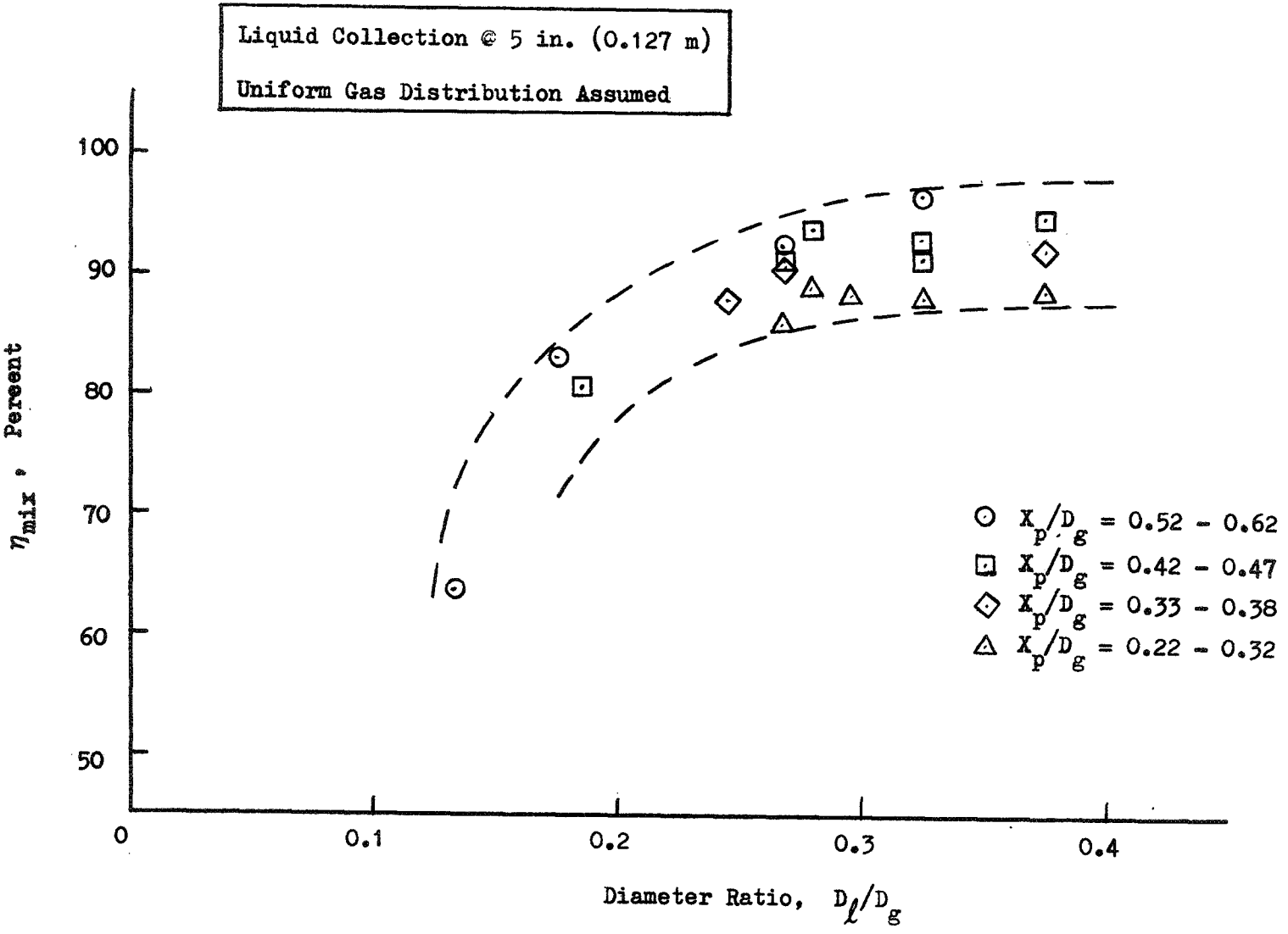

Figure 10. Diameter Ratio Influence on Mixing Efficiency

Liquid mass flux plots, such as that illustrated in Fig. 11 and 12, provided more detailed insight into the influences of X_p/D_g. As X_p/D_g was increased from the value (0.43) shown in Fig. 11, the four "humps", associated with spray stripped off the incoming liquid jets, moved radially inward and combined into one central hump (Fig. 12). Qualitatively, the overall spray uniformity could be seen to improve as X_p/D_g was increased.

The most surprising result of these cold-flow tests was that the liquid-gas orifice diameter ratio, D_ℓ/D_g, has a very strong influence on spray distribution uniformity, independent of X_p/D_g. This is seen in Fig. 9 and again, more explicitly, in Fig. 10. In the range of D_ℓ/D_g = 0.3 to 0.4, spray uniformity is relatively constant and the mixing efficiency is high, e.g., 90 to 96 percent depending on X_p/D_g. When D_ℓ/D_g was decreased below about 0.3, however, $(\eta_{c^*})_{mix}$ fell off abruptly (e.g., to 60 percent at D_ℓ/D_g = 0.133).

Test results obtained from the variable annulus gas (around each liquid jet) flow tests are shown in Fig. 13. For these data, the mixture ratio and orifice diameters were held constant, although the penetration parameter was allowed to increase from 0.32 to 0.45 as the annulus gas percentage increased from 0.0 to 25 percent. These tests indicate that injection of a portion of the fuel through the annulus orifices has little influence on spray uniformity up to about 10-percent annulus gas. However, further increase in annulus flow to 25 percent results in a decrease in mixing efficiency of about 4 percent. Referring to Fig. 9, the change in X_p/D_g from 0.32 to 0.45 should have resulted in about a 1-percent increase in mixing efficiency, so the decline caused by annulus gas flow alone would be slightly greater than suggested in Fig. 13.

In the test series in which the injector-to-collector distance was varied, 2 to 7 in. (5.1 to 17.8 x 10^{-2} m) collection distances were utilized while all other operating conditions remained constant (X_p/D_g = 0.29, D_ℓ/D_g = 0.27, no annulus gas). Assuming a uniform fuel (gas) distribution, the liquid relative mixing efficiency was calculated and is plotted along with the percentage of the injected liquid caught by the collection vessels in Fig. 14. Note that the percentage collected curve peaks at 4 to 5 in. (10.2 to 12.7 x 10^{-2} m). Apparently, with the collection grid as close as 2 in. (5.1 x 10^{-2} m), some spray is lost

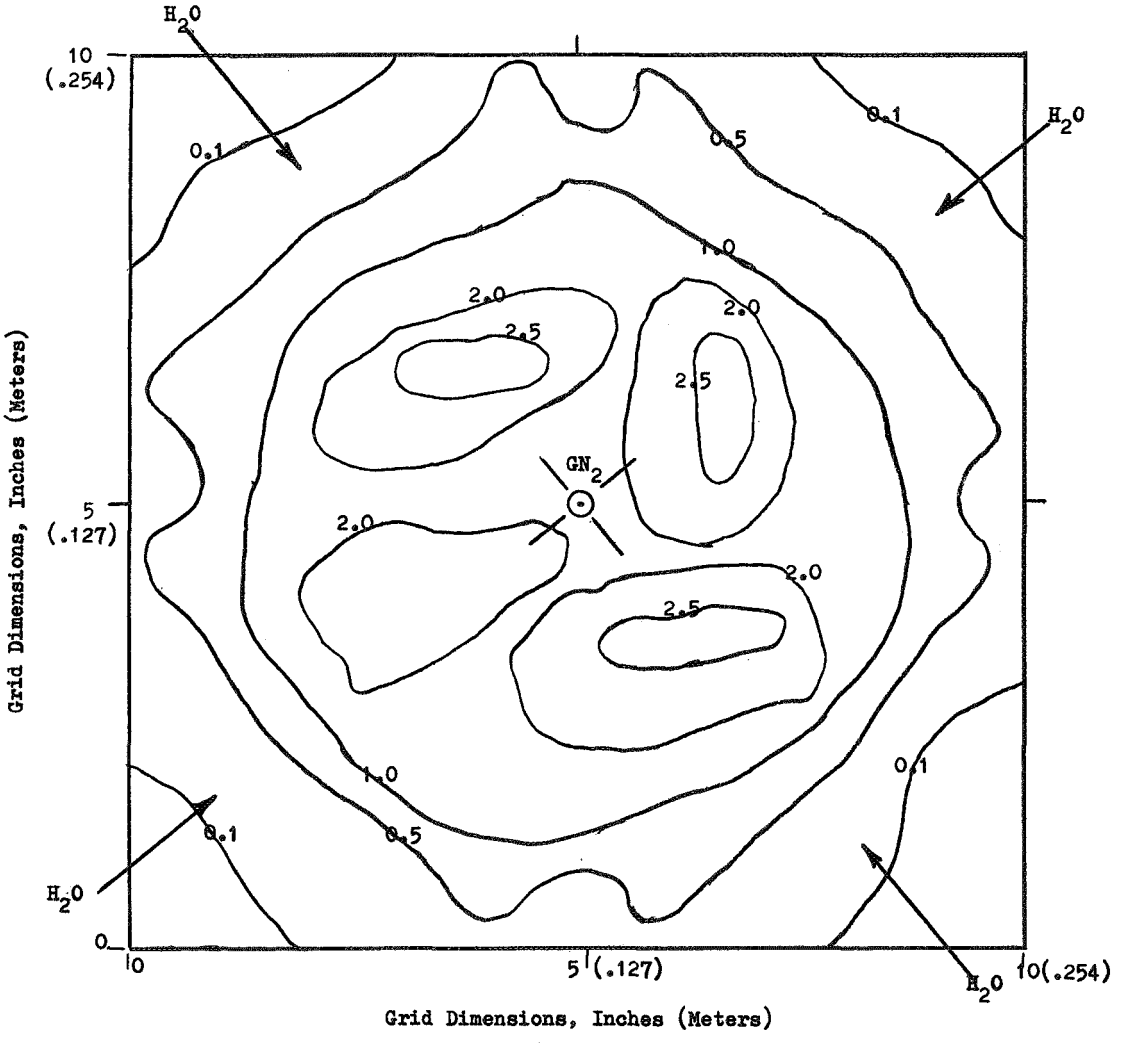

Figure 11. Liquid Mass Distribution for Test No. 6, X_p/D_g = 0.43 (Contours are in Mass Fractions for a 100 Tube Collection Matrix)

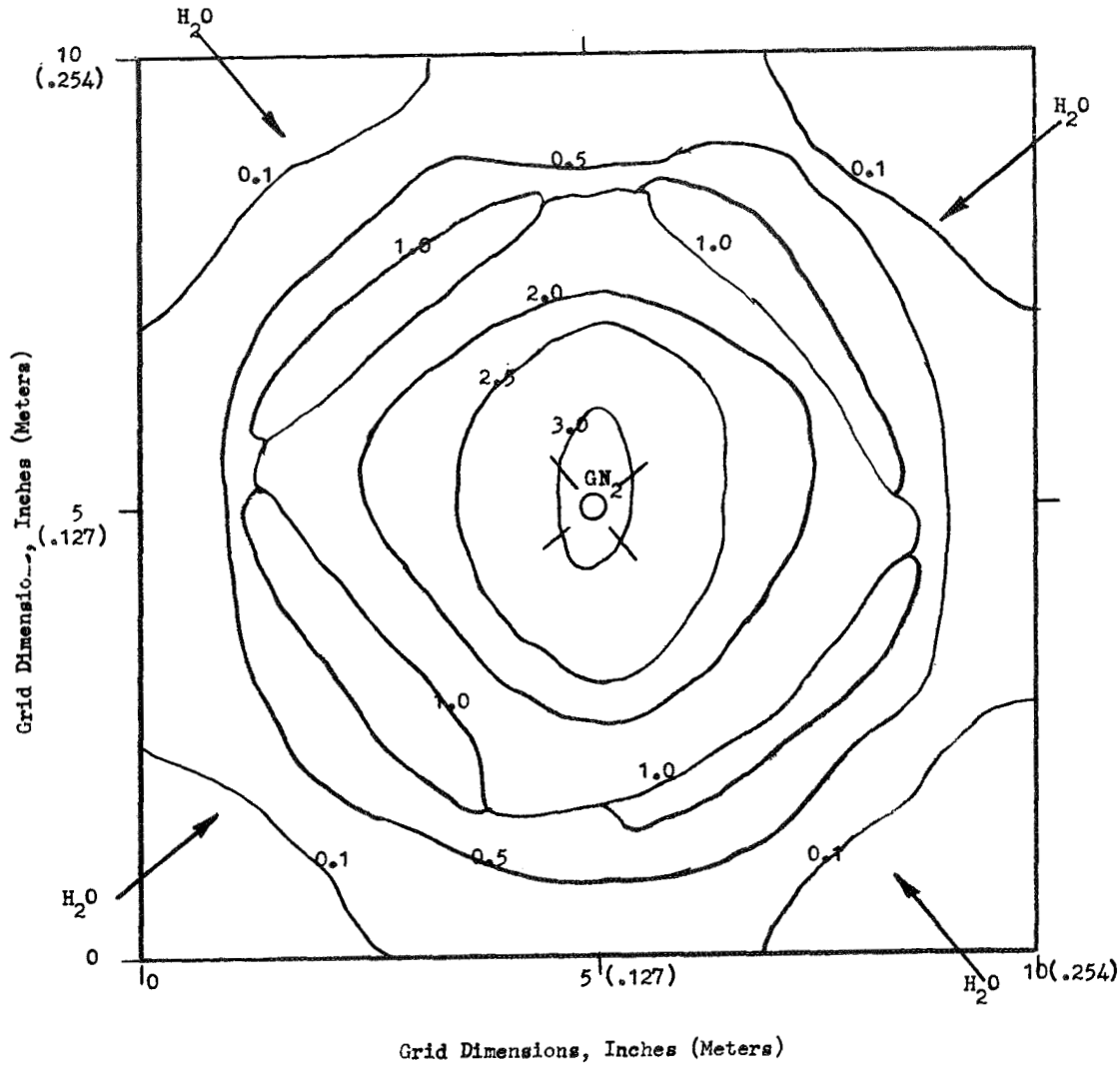

Figure 12. Liquid Mass Distribution for Test No. 4, X_p/D_g = 0.78 (Contours are in Mass Fractions for a 100 Tube Collection Matrix)

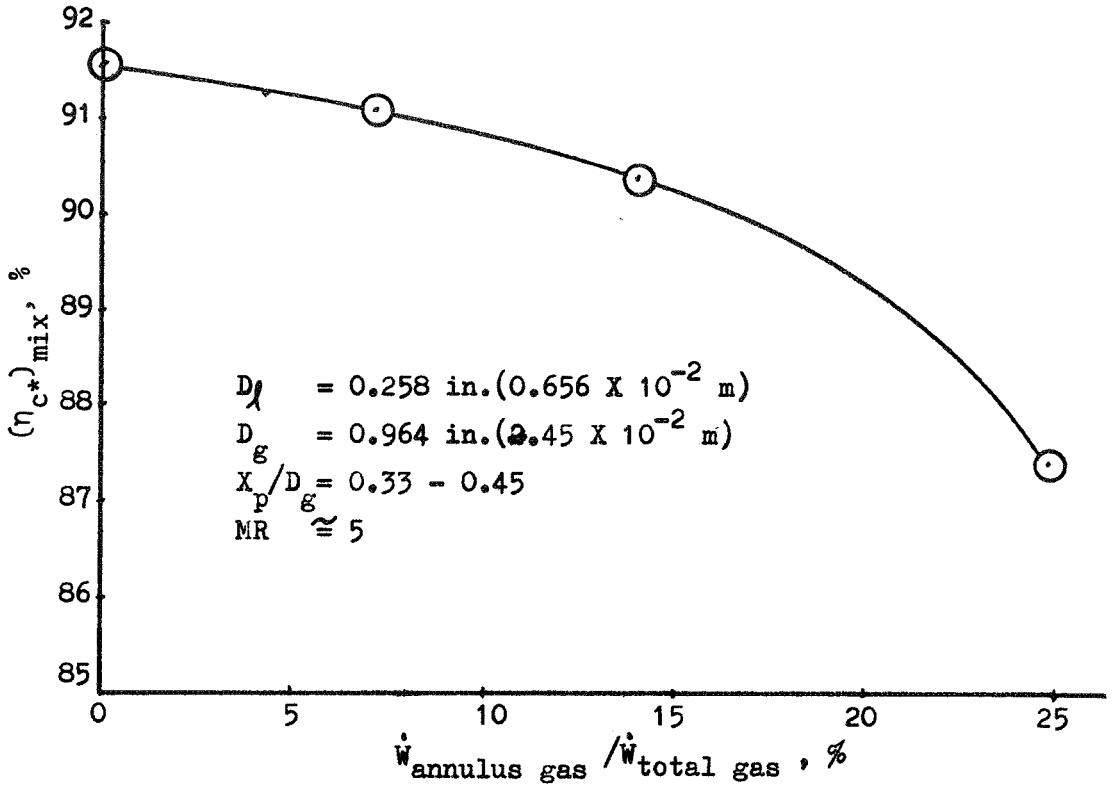

Figure 13. Annulus Gas Effect on Liquid Mixing Efficiency

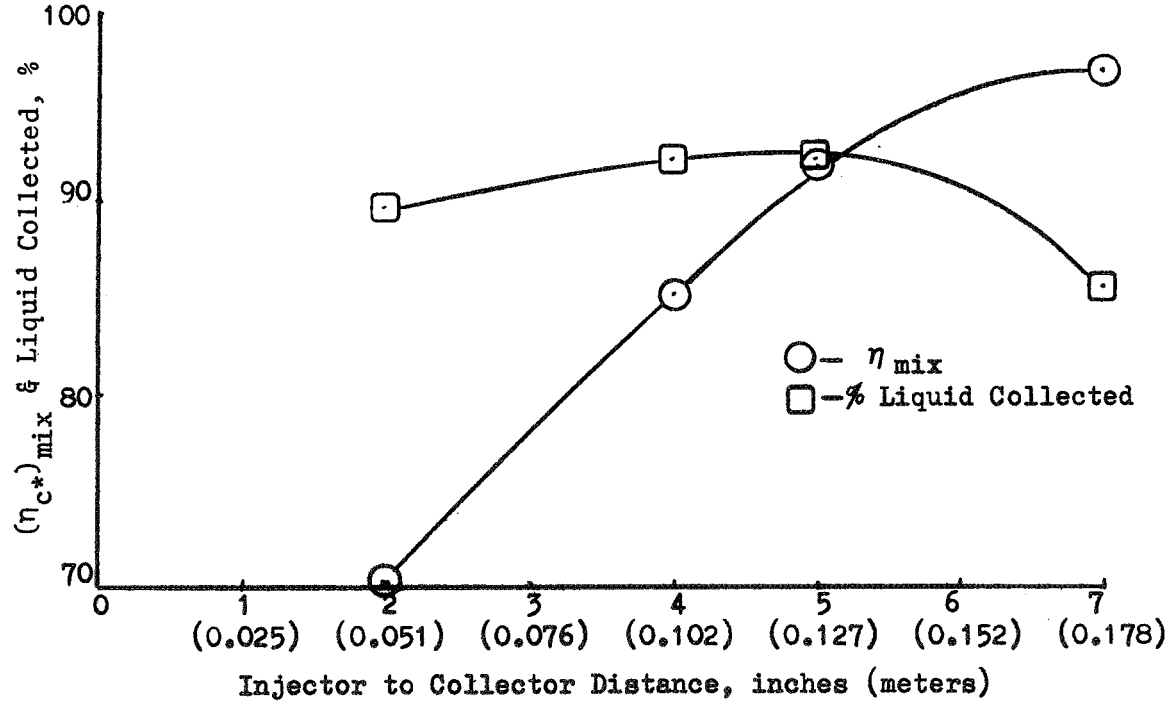

Figure 14. Injector-to-Collector Distance Effect on Liquid Mixing Efficiency

because of disruption of the spray/gas flowfield, while at 7 in. (17.8×10^{-2} m) or beyond, spray begins to spread beyond the collection grid. The relative mixing efficiency continued to climb as the collection distance was increased. The reason for the latter result is that the liquid was quite concentrated at the 2-in. (5.1×10^{-2} m) collection distance, but spread as the collection distance was increased, therefore covering the collection grid more uniformly. A 5-in. (12.7×10^{-2} m) collection distance was used in all other Task I cold-flow tests, to remain near the highest percentages of collected liquid and to closely approximate the performance observed in previous hot-fire studies with this injector.

Cold-Flow Test Summary. As described, the five variables investigated in cold-flow tests and the ranges over which they were changed were as follows:

Mixture Ratio	4.3 to 11.4
Gas Orifice Diameter, D_g	0.437 to 0.964 in. (1.11 to 2.45×10^{-2} m)
Liquid Orifice Diameter, D_ℓ	0.078 to 0.258 in. (0.198 to 0.656×10^{-2} m)
Annulus Gas Flow	0 to 25 percent
Density of gas, ρ_g	0.01 to 0.07 lb/ft^3 (0.16 to 1.12 kg/m^3)

From the data presented in the previous section, it was concluded that the uniformity of liquid distribution is governed by two-dimensionless correlating parameters, the ratio of liquid orifice diameter to gas orifice diameter (D_ℓ/D_g) and the penetration distance ratio (X_p/D_g). These controlling parameters were varied over the ranges 0.133 to 0.374 and 0.12 to 1.0, respectively. To obtain the most uniform liquid distribution, cold-flow results indicate the diameter ratio should be 0.3 or higher while the penetration distance ratio should be about 0.5 to 0.8. It was also concluded that a small percentage ($\leq$ 10 percent) of annulus gas could be used without significantly decreasing the uniformity of the liquid distribution.

Application of Performance Correlations

The purpose of the empirical/analytical study performed in Task I was to predict the injection characteristics required to attain high performance and to guide the hot-fire investigation of the single element, 20,000-lb (88,960 N)-thrust recessed impinging jet injector. To accomplish this, the parametric data generated in this study for vaporization and mixing efficiencies were used to guide the hot-fire injector design and to predict overall c* efficiency levels for the contemplated hot-fire injector. The overall efficiency levels were determined by taking the product of the predicted vaporization and mixing efficiencies evaluated at specific operating conditions. Plans for a hot-fire test series were then created to provide the maximum amount of design information for the number of scheduled tests.

Injector Conceptual Design. Nominal LOX/GH_2 mixture ratio, chamber pressure, and thrust per element were contractually specified as 5.0, 500 psi (345 x 10^4 N/m^2), and 20,000 lbf (88,960 N), respectively, for the hot-fire tests. In addition, it was decided to define conceptual design values for two cases: one with no annular fuel and the other with about 30 percent of the fuel injected through the annular orifices. Within these constraints, the performance criteria developed in the preceding analysis were used to develop conceptual design values.

As previously stated, the total injected gas momentum to liquid oxidizer flowrate ratio was used as an index of the performance potential for the recessed impinging concentric injector. Figure 15 illustrates the ratios attainable for the subject LOX/GH_2 system as a function of the hydrogen injection area and temperature for 100 percent of the fuel injected from the central orifice. For 70 percent (i.e., the annulus gas design), the curves are similar except that the central fuel orifice area would be 70 percent of that shown in Fig. 15. For maximum performance it was expected that the injector should operate at ratios of gas momentum to oxidizer flowrate up to about 600 ft/sec (183 m/s). Nominal fuel injection areas for the two hot-fire designs mentioned above were

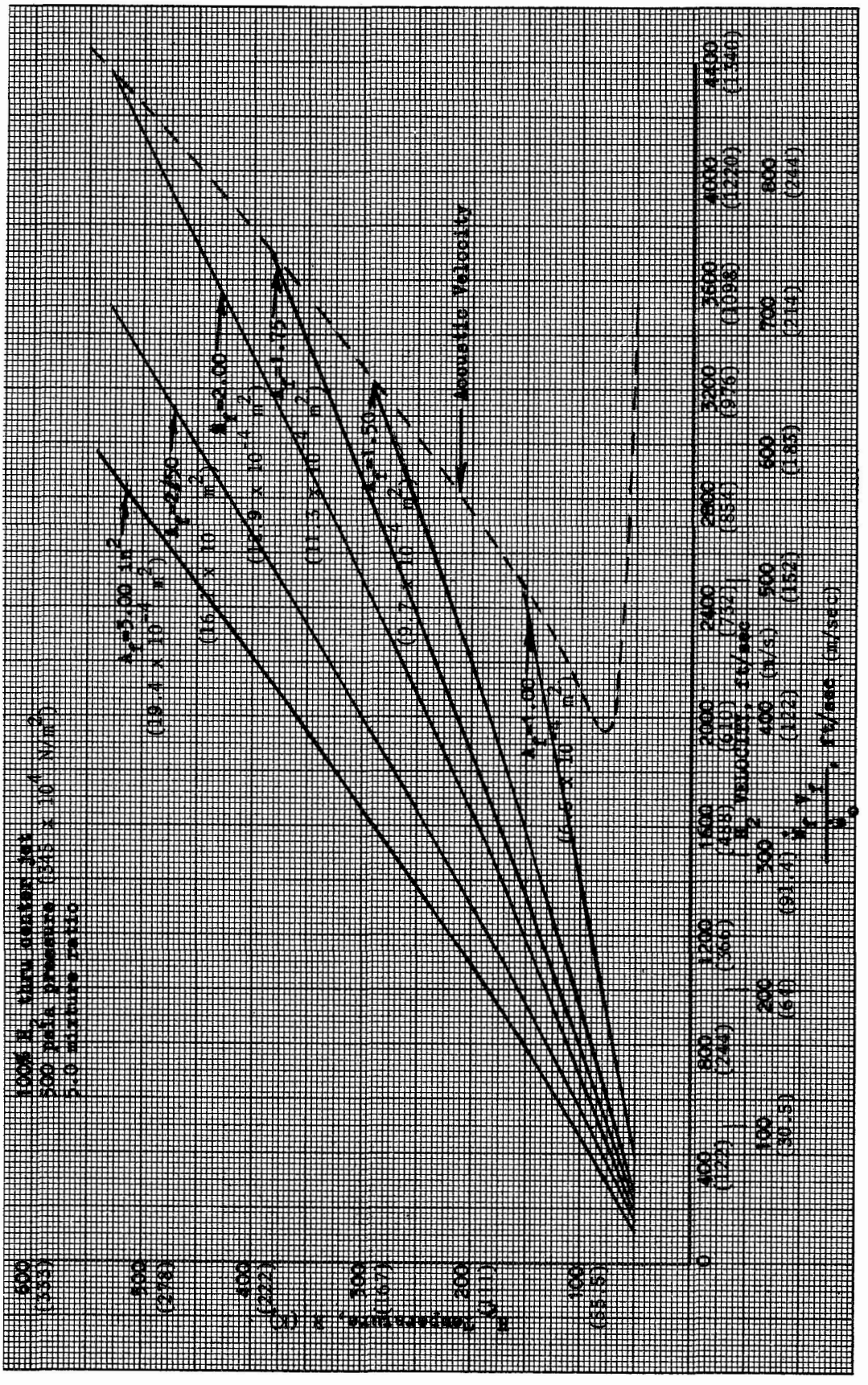

Figure 15. Recessed Cup Injector H_2 Temperature Effects

selected to be 2.0 and 1.27 in.^{2} (1.29 and 0.82 x 10^{-3} m^2), respectively. This allowed testing over a wide range of $M_g/\dot{w}_o$ (up to and including 600 ft/sec, 183 m/s) by variation of the fuel injection temperature.

The optimum penetration parameter (X_p/D_g) appeared to be between 0.5 and 0.8 from the cold-flow (spray distribution) study results. Also, it was determined that the diameter ratio, D_ℓ/D_g, should be maintained in the range of 0.3 or above. Orifice diameter ratios were selected to be 0.32 and 0.4 for the 100 and 70 percent center fuel flowrate injectors, respectively, so (1) the diameter ratio criterion was satisfied, (2) the penetration parameter was kept in the optimum range, and (3) the same liquid orifice diameter could be used for both of the injector configurations.

Performance Prediction. Analytical prediction of the characteristic velocity efficiency for the planned LOX/GH_2 injector/thrust chamber combination required assessment of the vaporization and propellant mixing efficiencies. To predict $(\eta_{c^*})_{vap}$, a series of vaporization-limited performance curves was generated at the planned nominal chamber pressure, mixture ratio, etc., with the combustion model described in Ref. 1 and 2. These parametric curves describe $(\eta_{c^*})_{vap}$ as a function of L* and D_{30} (Fig. 16 and 17). For the planned 30-in. (0.762 m) L* chamber, it remained only to estimate D_{30}. To do so, an empirical equation of Ingebo was used; not directly, but rather to extrapolate the empirical value of 120 μ (120 x 10^{-6}m) from NAS3-7962 operating conditions. This equation is:

$$D_{30} = \frac{1}{2.64\sqrt{\frac{V_j}{D_j}} + 0.97\,(\Delta V)} \qquad (3)$$

where

V_j = liquid injection velocity

D_j = liquid orifice diameter

ΔV = gas-to-liquid velocity difference

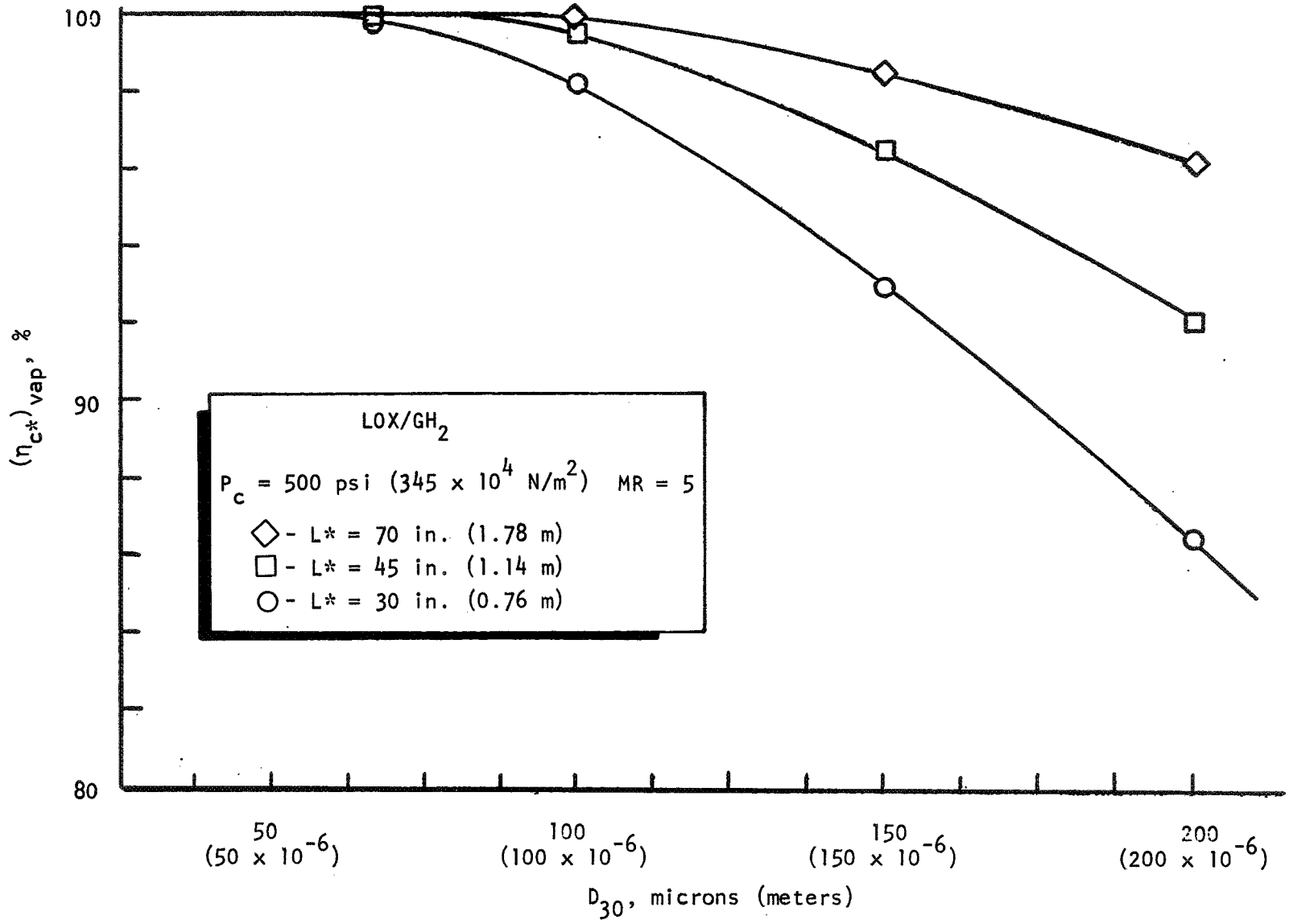

Figure 16. Predicted Vaporization Efficiency vs D_{30}

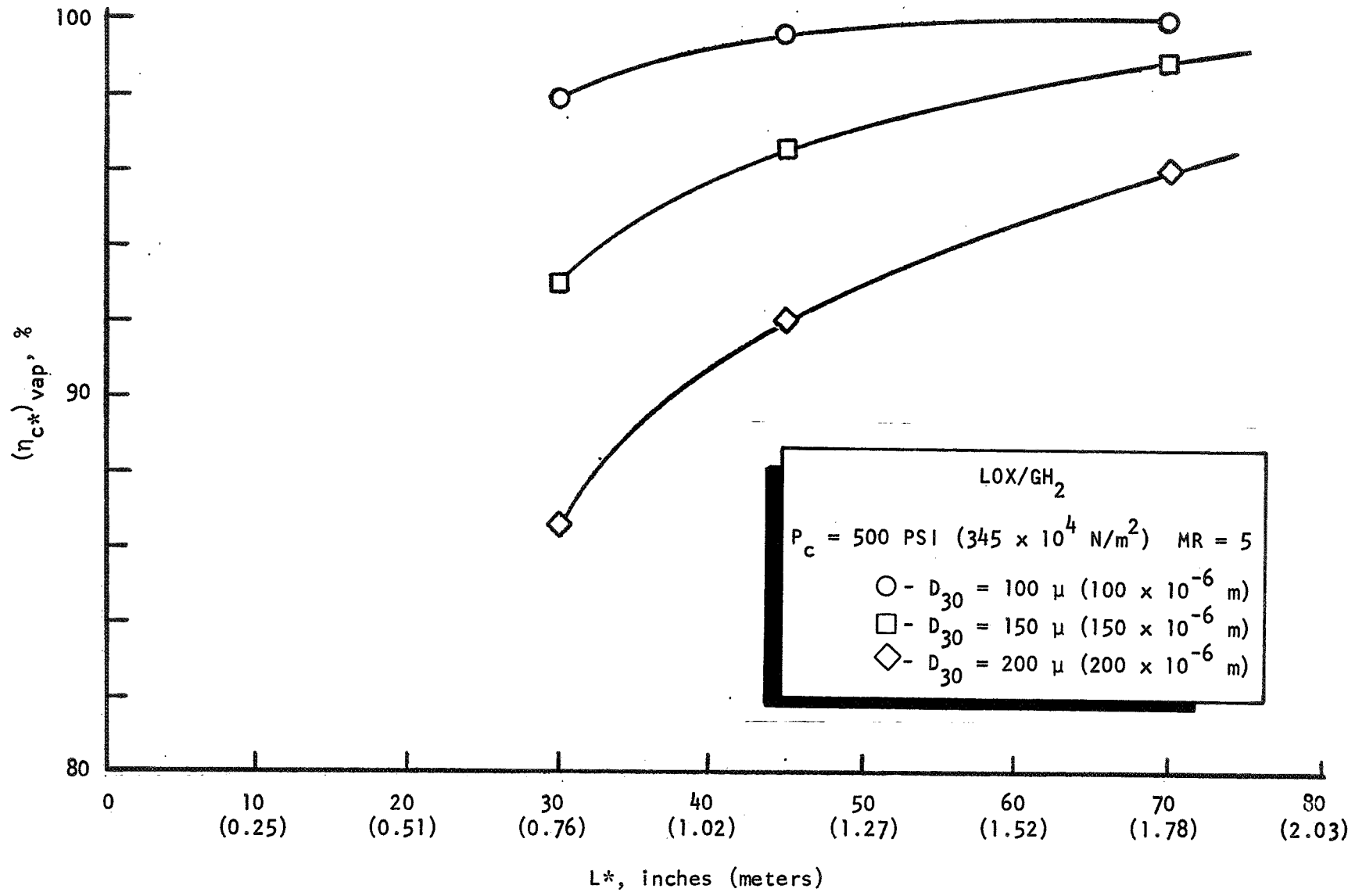

Figure 17. Predicted Vaporization Efficiency vs L*

The parameters used in Eq. 3 are listed in Table 2 for (1) the previous test conditions under which an apparent D_{30} of 120 μ (120 x 10^{-6} m) was calculated, and (2) nominal planned Task I hot-firing conditions.

TABLE 2

DROPSIZE PARAMETERS FOR TASK I PERFORMANCE PREDICTIONS

	V_j, ft/sec (m/s)	D_j, in. (m x 10^{-1})	$V_g - V_\ell$, ft/sec (m/s)	D_{30}, μ (m x 10^{-6})
NAS3-7962 Test	120 (36.6)	0.509 (0.129)	1800 (549)	120
Task I Hot-Firing Nominal Condition (No Annulus Fuel)	150 (45.8)	0.509 (0.129)	3600 (1098)	61
Task I Hot-Firing Nominal Condition (30% Annulus Fuel)	150 (45.8)	0.509 (0.129)	3400 (1037)	64

Note that a dropsize of approximately 60 μ (60 x 10^{-6} m) was predicted for the nominal Task I hot-firing tests both with and without annulus fuel flowrate. Referring to the combustion model parametric curves in Fig. 16 and 17, the predicted dropsize of approximately 65 μ (65 x 10^{-6} m) or less indicated that essentially 100-percent $(\eta_{c*})_{vap}$ could be expected.

The predicted mixing efficiency was based on the relative mixing efficiencies obtained in the cold-flow spray studies. For liquid-to-gas diameter ratios greater than 0.3 and liquid penetration parameters in the 0.5 to 0.8 range, the relative mixing efficiency was on the order of 96 percent for zero annulus fuel and 91 percent for 30 percent annulus fuel. It was recognized that these efficiencies might not be directly equivalent to a hot-fire mixing efficiency because the true gas flux distribution would not be uniform as was assumed in the cold-flow analysis. However, mixing efficiencies in this range were obtained with this injector in the previous program (NAS3-7962), which lend credence to the values. In summation, the analysis predicted that η_{c*} on the order of 96 percent would be attainable in the hot-firing tests.

Selection of Test Parameters. As mentioned above, the operating parameters which appeared to influence the atomization and mixing characteristics of this injector concept were the injected gas momentum to oxidizer flowrate ratio ($M_g/\dot{w}_o$), the liquid penetration parameter (X_p/D_g), the liquid-to-gas diameter ratio (D_ℓ/D_g), and the percent annulus flowrate.

Within the available number of tests, X_p/D_g and $M_g/\dot{w}_o$ were selected as the primary test parameters. The liquid-to-gas diameter ratio (D_ℓ/D_g) was not parametrically varied, but set in its optimum range (according to cold flow) on the order of 0.3 to 0.4. From a performance standpoint most of the tests were to be run without annulus gas. It was recognized, however, that this annulus gas might be needed from an injector cooling standpoint and so alternate tests were planned with annulus gas (about 30 percent of the fuel injection rate).

Ranges of the two primary test parameters were determined to be: X_p/D_g = 0.40 to 1.0 and $M_g/\dot{w}_o$ = 100 to 600 ft/sec (30.5 to 183 m/s). Off-nominal chamber pressure and mixture ratio operations were necessary to accomplish this range of variation with minimal changes of hardware. Specifically, necessary mixture ratio variations were in the 3.0 to 5.5 range and necessary chamber pressure variations were from about 300 to 520 psi (207 to 358 x 10^4 N/m^2). The penetration parameter, X_p/D_g, was expected to primarily affect mixing while $M_g/\dot{w}_o$ was expected to primarily influence atomization (and therefore vaporization). To clearly distinguish between these two principle modes of c* performance losses, the X_p/D_g influence was initially evaluated in long chamber (L*) tests where complete vaporization would be assured, with subsequent short chamber tests used to investigate $M_g/\dot{w}_o$ and the vaporization efficiency.

HYDROGEN GAS AUGMENTATION HARDWARE FABRICATION

Hardware for the hydrogen gas augmented hot-firing tests consisted mainly of a 20,000-lb (88,960 N)-thrust-per-element, single element, recessed impinging jet injector and a workhorse thrust chamber. In addition, a bomb (pulse gun) ring and pulse guns were used for stability evaluations.

Injector

The 20,000-lb (88,960 N)-thrust-per-element recessed impinging jet injector was selected for hydrogen gas augmentation because of previously demonstrated high performance under Contract NAS3-7962. This injector consisted of a central fuel jet surrounded by and impinging with four equally spaced coaxial oxidizer/fuel jets. All the jets or injector orifices were inside a shallow recessed cup, thus the centerline impingement point of the jets was 0.130 in. (0.330×10^{-2} m) downstream from the plane of the injector face. The included angle of the coaxial impinging jets was 120 deg (2.094 rad).

Gaseous fuel was supplied to the central injector orifice through a straight line from directly behind the injector. The oxidizer was manifolded into the recessed cup through four 0.509 in. ID (0.0129 m) by 0.058 in. (0.147×10^{-2} m) wall tubes which served as the impinging oxidizer orifices. The four tubes were symmetrically manifolded together from a common point at one side and to the back of the injector. Additional gaseous fuel supply was available to enter the recessed cup through a 0.172 in. (0.437×10^{-2} m) wide annulus around each of the oxidizer tubes. These four annular fuel passages were supplied from an annular manifold which, like the oxidizer, was supplied from behind and to one side of the injector element.

The 20,000-lb (88,960 N) element was mounted in the center of a flat, circular injector faceplate which was protected by hydrogen (fuel) transpiration cooling through Rigimesh. Type 347 CRES material was used to construct the injector components. A photo of the injector face is shown in Fig. 18.

To accomplish the selected parametric variations, it was necessary to provide for modification of the central gas orifice size. Three different inserts were fabricated to reduce the central gas jet orifice size from the original 1.953 in. diam to 1.595, 1.382, or 1.270 in. (0.0496 m to 0.0405, 0.0351, or 0.0323 m). The central insert installation is shown in Fig. 19.

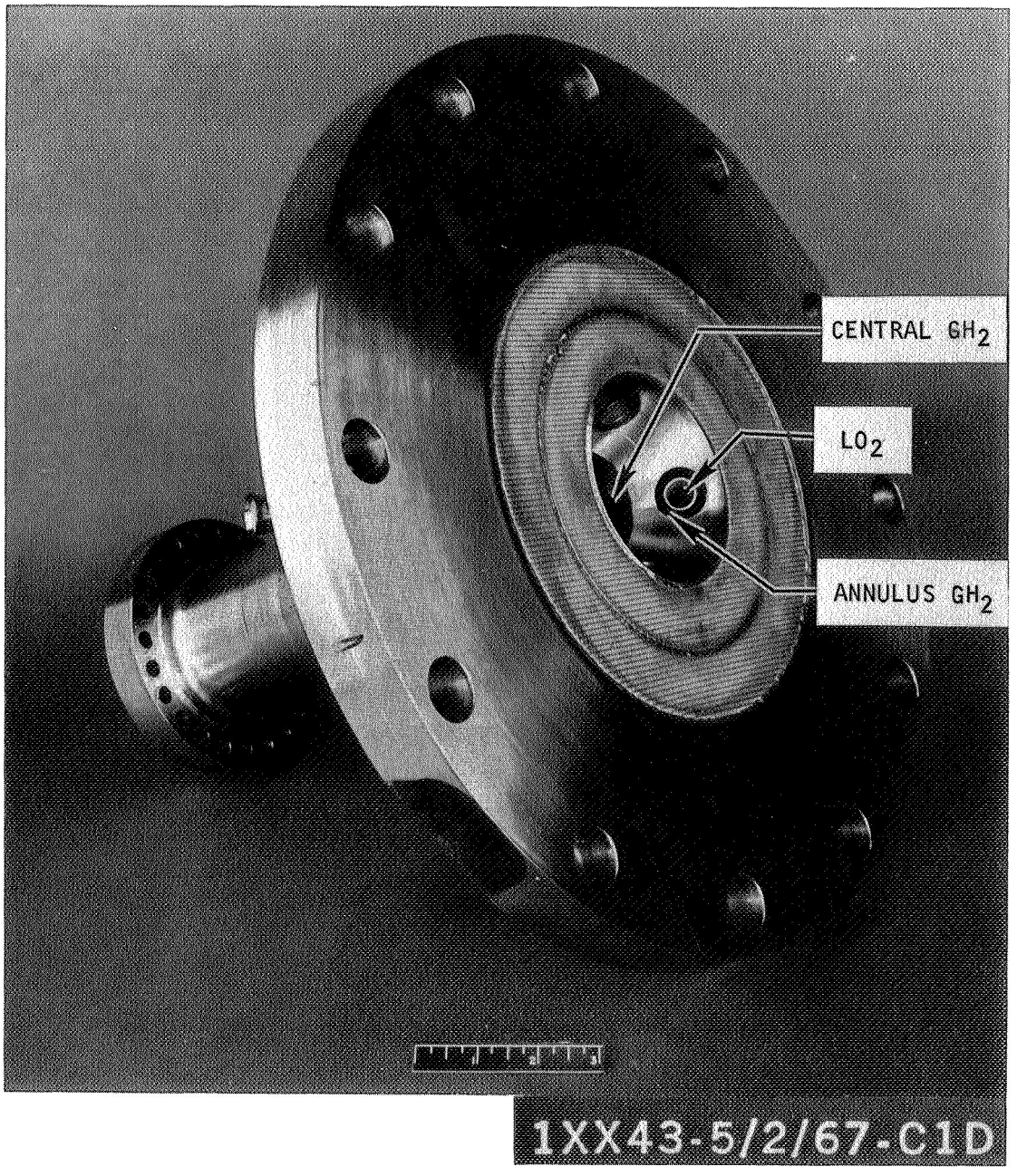

Figure 18. Recessed Impinging Jet Injector Configuration: 20,000-lb (89,000 N) Thrust

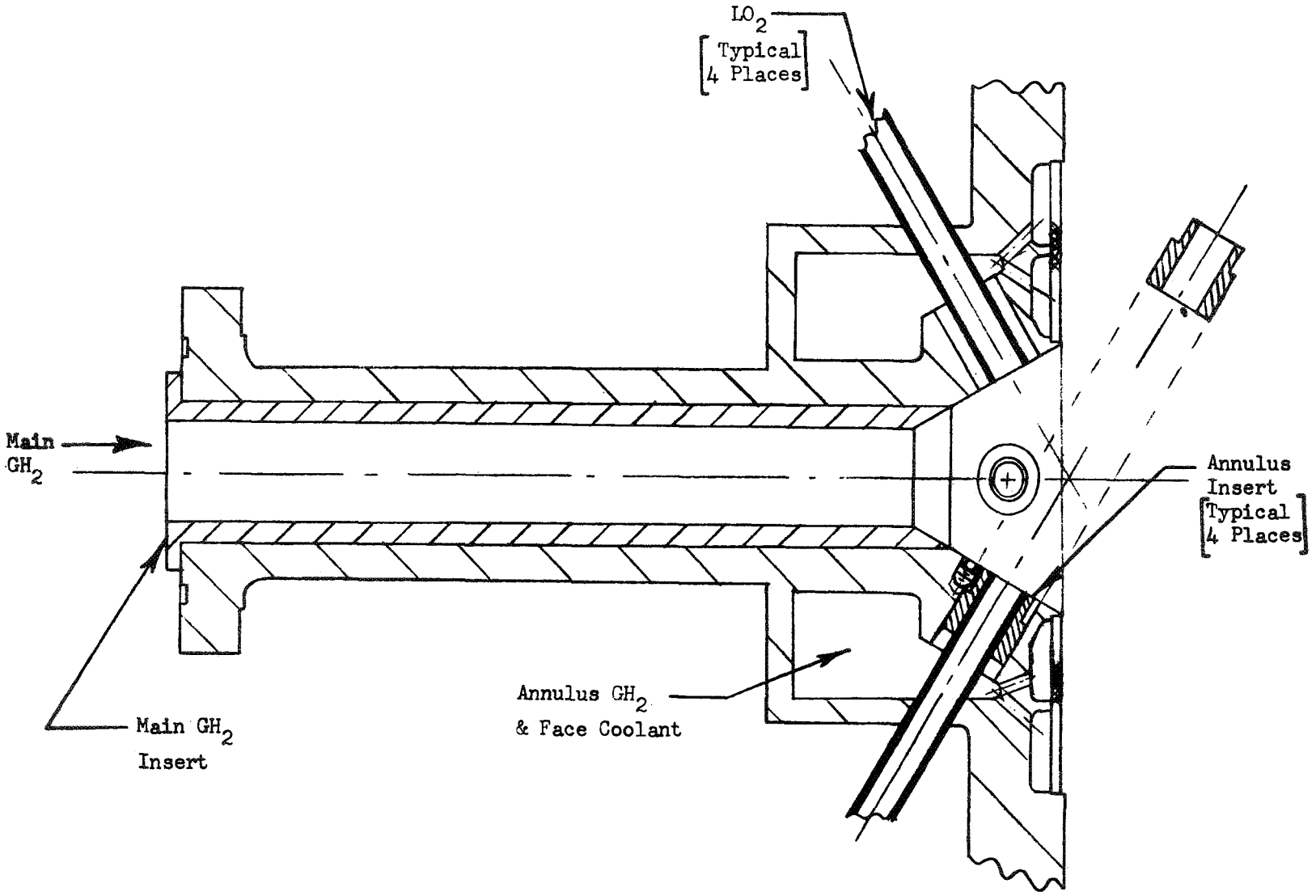

Figure 19. 20,000-Pound-Thrust Recessed Impinging Jet Injector Modification

The annulus orifice area of the basic injector was about 35 percent of the total fuel orifice area*. Because it was desired to vary the relative amount of gas injection through the annulii around the four oxidizer orifices, two sets (4 each) of inserts were fabricated; one set to restrict the annulus gas orifice area to about 15 percent of the total fuel orifice area, and one set to completely close off the annulus gas flow. The annulus insert installation is shown in Fig. 19.

Thrust Chamber

A workhorse thrust chamber (Fig. 20) was designed and fabricated under Contract NAS3-7962, and this chamber was used as the injector test bed during the hydrogen gas augmentation hot-fire testing phase of the program. The chamber design consisted of an uncooled copper combustion zone and a water-cooled copper nozzle. The combustion zone section of the chamber was a 1-in. (2.54×10^{-2} m) thick copper liner inside a 3/8-in. (0.953×10^{-2} m) thick steel jacket. A transient heat transfer analysis (see Appendix E) was used to predict wall temperature data for the combustion zone. The maximum allowable duration was approximately 3 seconds before melting of the wall would occur at the hot gas surface. Longer acceptable durations were predicted if a thermally insulating combustion zone coating was used. Thus, a 0.010 in. (2.54×10^{-4} m) graduated inconel-zirconium oxide coating was applied to the hot gas side wall of the uncooled combustion zone. The coating composition was as follows:

Thickness, in. (m)	Coating Composition
0.0015 (3.81×10^{-5})	100% inconel
0.0025 (6.35×10^{-5})	70% inconel-30% zirconium oxide
0.0035 (8.89×10^{-5})	30% inconel-70% zirconium oxide
0.0025 (6.35×10^{-5})	100% zirconium oxide

*Because annulus fuel was injected at ambient temperature and the center fuel temperature was a variable, no attempt was made to keep the center and annulus fuel velocities constant.

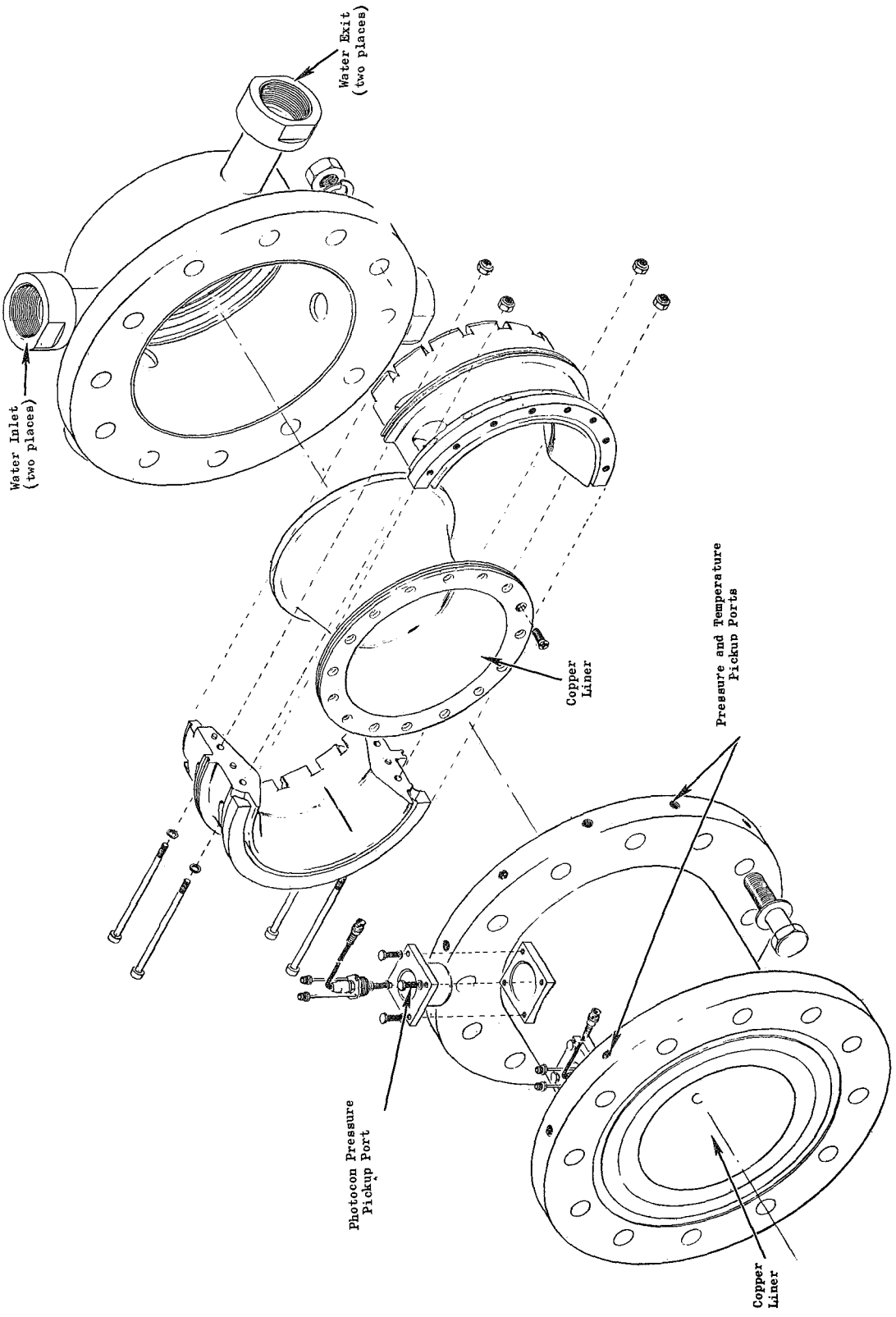

Figure 20. Isometric View of Workhorse Thrust Chamber Used for Hot-Firing Tests

Two combustion zone sections (spools) were used; one was 13.23 in. (0.336 m) long, giving an L* of 30 in. (0.762 m), and one was 20 in. (0.508 m) long to increase the L* to 70 in. (1.778 m) when both spools were used.

The heat fluxes in the nozzle throat and the converging and expansion sections (Appendix E) required water cooling to allow for a reasonable test duration. The necessary wall thickness at the throat was determined by considering the heat flux capability of the wall and the material strength. The nozzle section was supplied with coolant from two inlet lines located 180 deg (3.141 rad) apart. From the inlets, the water coolant was distributed into a common manifold cavity inside a carbon-steel nozzle shell. The coolant then passed from the manifold through a single, constant-width 0.1-in. (2.54×10^{-3} m) passage behind the nozzle-contoured wall, into a common exit manifold at the nozzle exit, and then out through two exit passages 180 deg (3.141 rad) apart and 90 deg (1.571 rad) from the inlet passages. An isometric drawing of the nozzle and related cooling passages is shown in Fig. 20.

Pertinent thrust chamber design geometry is as follows:

Combustion chamber diameter, in. (m)	8.55 (0.217)
Nozzle throat diameter, in. (m)	6.05 (0.154)
Nozzle throat area, $in.^2$ (m^2)	28.75 (0.0185)
Contraction area ratio (ε_c)	2
Expansion area ratio (ε_e)	2
Nozzle convergence angles, deg (rad)	60 (1.047)
Nozzle divergence angle, deg (rad)	30 (0.524)
Injector-to-throat length; 30-inch L*, in. (m)	15.77 (0.401)
Injector-to-throat length; 70-inch L*, in. (m)	35.77 (0.909)

Temperature and pressure instrumentation ports were located at selected positions in the combustion zone as shown in Fig. 20. Provisions were made for installing chamber-wall heat flux probes at six axial and circumferential locations within the combustion chamber. Two of the six ports for the probes were in the flange adjacent to the injector, and the remaining four ports were in

the flange just upstream of the nozzle converging section. Three pressure-pickup ports were also located in the chamber flanges, one at the injector end and two adjacent to the nozzle. Four Photocon pressure transducer ports were positioned in the thrust chamber combustion zone. Three of these ports were located 3 in. (0.0762 m) downstream from the injector end of the chamber at 0, 120, and 225 deg (0, 2.094, and 3.926 rad) from the top centerline looking aft. The fourth Photocon port was 3 in. (0.0762 m) upstream from the nozzle converging section on the top centerline (0 deg). After the first hot-firing test, the Photocons were relocated to the bomb ring at 30, 120, and 330 deg (0.523, 2.094, and 5.752 rad) from the top centerline. These Photocon pressure pickup ports were for fast-responding and wide-frequency range instrumentation used for stability evaluation.

Under Contract NAS3-7962, erosion had been experienced around the Photocon instrumentation ports during several of the hot-firing tests. Because of this prior erosion history, the Photocon installation for the subject program was modified so that the pickup was recessed away from the hot gas wall as shown in Fig. 21. First, they were mounted on the chamber wall and later on the bomb ring. The resonant frequency of the recessed cavities was approximated from the following equation:

$$f = \frac{C_a}{2\pi} \frac{d}{D} \frac{12}{\sqrt{\ell\, L}} \tag{4}$$

where C_a is the sound speed in the cavity, assumed to be 2500 ft/sec (762 m/s) and L, D, ℓ, and d are the cavity dimensions as shown below:

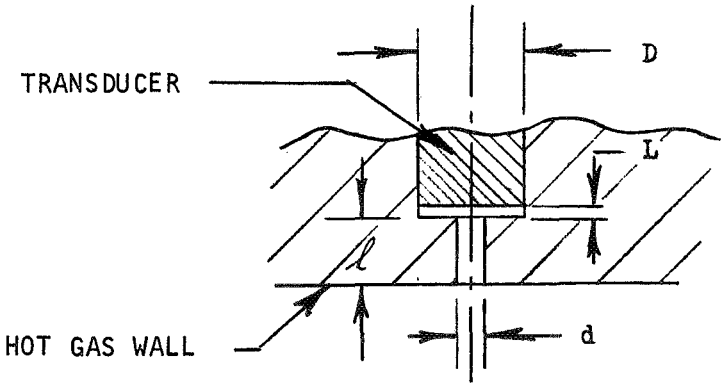

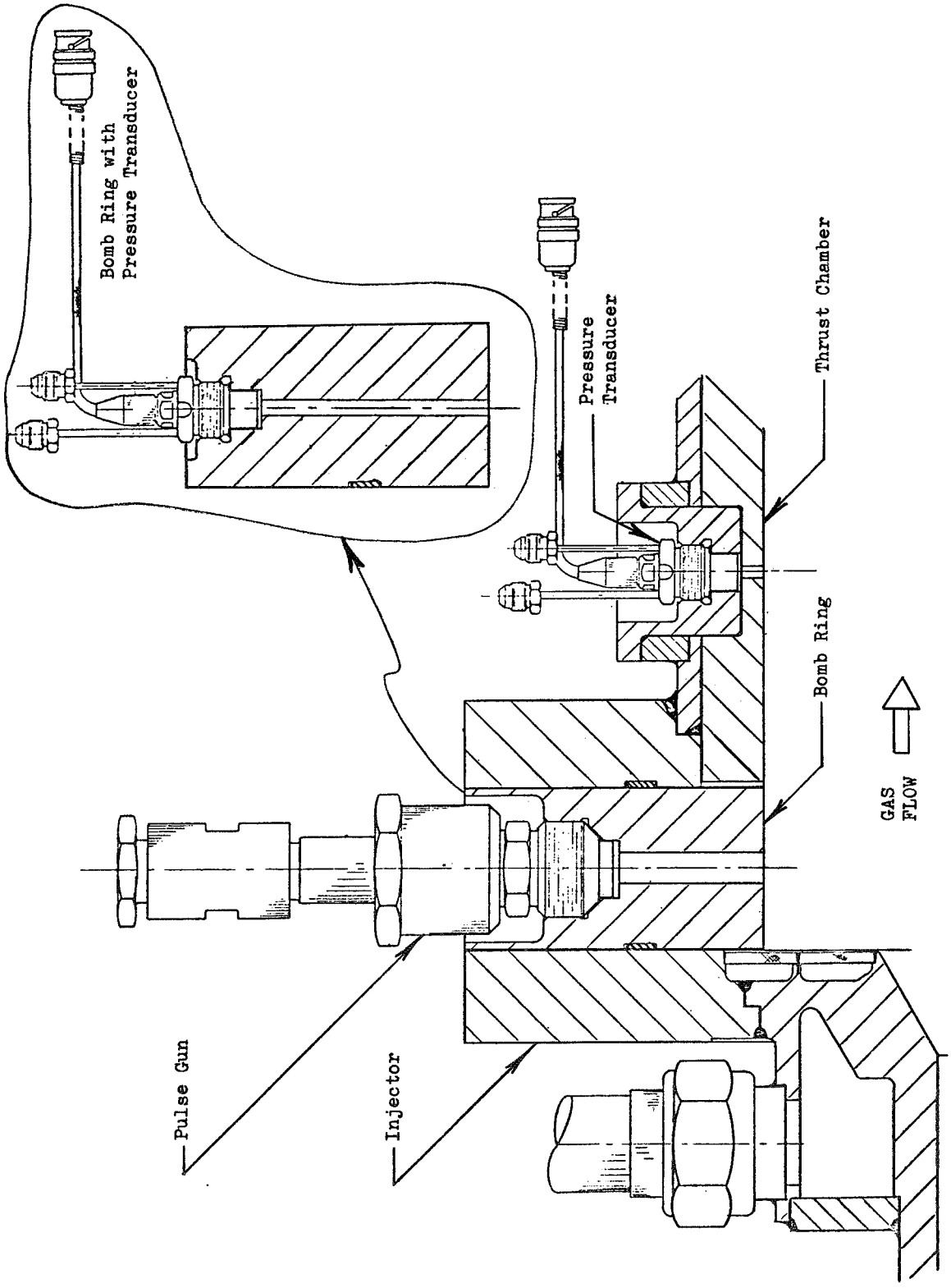

Figure 21. Pulse Gun and Photocon Installation

The cavity resonant frequencies (f) were calculated to be about 14,000 and 5900 Hz for the chamber and bomb ring installations, respectively; outside the most common chamber acoustic frequencies (first tangential ~4500 Hz, second tangential ~7500 Hz, first radial ~9400 Hz). Therefore, if these chamber acoustic frequencies were to occur, the recorded amplitudes would be close to their actual values. The biggest unknown here was the effective speed of sound in the cavity. If the speed of sound were greater than the assumed 2500 ft/sec (762 m/s), the cavity resonant frequencies would also be greater.

Bomb Ring/Pulse Gun

During the hot-firing phase of the program, bomb (pulse gun) tests were conducted to determine the stability characteristics of the injector. A bomb ring was designed and fabricated to house three pulse guns which were used to generate finite amplitude disturbances for artificial instability initiation. The bomb ring was sandwiched between the chamber and injector as shown in Fig. 21. The bomb ring was 2.50 in. (0.0635 m) thick which, when used with the existing thrust chamber, increased the L* by 5 in. (0.127 m).

Three pulse guns were mounted in bosses machined in the ring. All of the gun axes were in a single plane normal to the combustor axis and approximately 1.25 in. (0.0318 m) below the injector face. The pulse guns were oriented to give tangential, radial, and chordal disturbances as shown in Fig. 22. This orientation was tailored mainly for the single element (centrally located) injector configuration.

Existing gunpowder pulse guns (Fig. 22) were used which were designed for pulsing the XRL booster engine. The pulse gun/bomb ring barrels were examined as possible quarterwave dampers for any induced instability. The simplified approach taken was to assume that the total length of the pulse gun, and its connecting tube through the chamber wall (bomb ring), formed a quarterwave resonator. The corresponding frequency was then compared with expected instability frequencies. This approach required knowledge (or assumption) of the effective sound speed in the gun barrel. Six cases were considered, two each

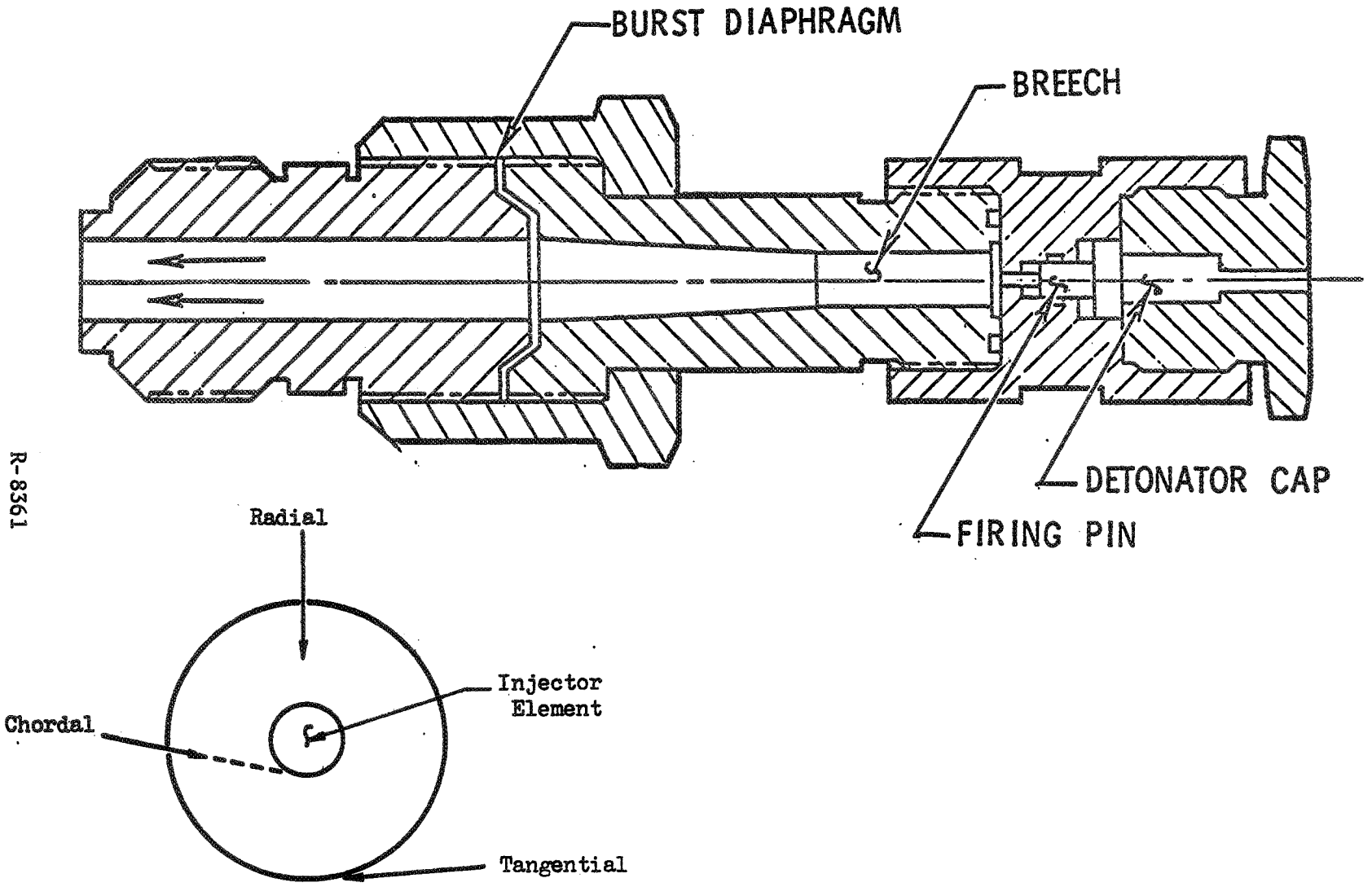

Figure 22. Pulse Gun and Gun Orientation

for radial, chordal, and tangential gun orientations: (1) unfired guns with C_b = 2500 ft/sec (762 m/s) sound speed and (2) just-fired guns with 4000 ft/sec (1219 m/s) sound speed.

Assumed effective barrel lengths, L_b, were:

	Unfired	Fired
Radial Gun, in. (m)	5.35 (0.136)	7.35 (0.187)
Chordal Gun, in. (m)	5.85 (0.149)	7.85 (0.199)
Tangential Gun, in. (m)	7.60 (0.193)	9.60 (0.244)

with $L_b = \lambda/4 = C_b/4f$, the corresponding frequencies were:

	Unfired	Fired
Radial Gun, Hz	1402	1633
Chordal Gun, Hz	1282	1529
Tangential Gun, Hz	987	1250

These frequencies were considerably lower than those of the most likely chamber cross-sectional acoustic resonances (first tangential, second tangential, and first radial) so that damping of these instabilities by pulse gun cavities appeared unlikely. These pulse gun barrel frequencies were comparable to those of the possible first longitudinal modes, however.

HYDROGEN GAS AUGMENTATION HOT-FIRING TESTS

The Task I hot-fire testing phase of the program was conducted primarily to demonstrate performance and stability of the large thrust-per-element impinging concentric injector and to aid in establishing design criteria for high performance. Liquid oxygen/gaseous hydrogen were used as the main propellants with the gaseous hydrogen injection especially designed to augment the atomization and mixing processes. The 20,000-lb (88,960 N)-thrust-per-element, recessed, impinging jet injector concept was selected for the hot-firing demonstrations because of promising results under Contract NAS3-7962. The injector design was modified to accommodate the change of "augmenting gas" from the hot

O_2/H_2 combustion gas to hydrogen and to permit the desired parametric performance evaluation. A workhorse thrust chamber was used as the test bed for the hot firing.

The test series was formulated to evaluate first*, the parameters which control mixing and subsequently to evaluate vaporization controlling parameters at a relatively constant mixing efficiency. A long L* chamber was used for the mixing limited tests, to assure complete vaporization. A relatively short L* chamber was used for the vaporization-limited performance tests. Mixture ratio, chamber pressure, hydrogen gas temperatures, and gas orifice sizes were changed to explore performance correlating parameters such as the penetration parameter (X_p/D_g), the injected gas momentum to oxidizer flowrate ratio ($M_g/\dot{w}_o$), and the percent annulus gas. Dynamic stability of the hardware was evaluated during selected tests, aided by artificially induced pulse gun disturbances.

Facilities and Equipment

The LOX/hydrogen gas augmented injector performance and stability tests were conducted at CTL-3, cell 18B, of the Rocketdyne Santa Susana Propulsion Field Laboratory. CTL-3 is a multiposition test complex containing four multicell test modules with a central control and recording center, and is the facility utilized for the hot-fire testing under Contract NAS3-7962. A schematic of the test system is presented in Fig. 23 showing the valves, flowmeters, and the primary control orifices relative to the main propellants and coolant. Also shown are some of the basic chamber assembly temperature and pressure measurements recorded during the testing.

The test facility consisted of a thrust mount attached to a concrete bed, plumbing for the main propellants, plumbing for water coolant, and the electrical and control systems. A 20,000-lb (88,960 N)-thrust load cell was used to measure the main thrust component from the chamber firing in a horizontal

*Because of the injector face erosion encountered in the first test (with no annulus gas), these goals were redefined to first establish the minimum amount of annulus fuel flow required for face cooling and then investigate mixing and vaporization independently.

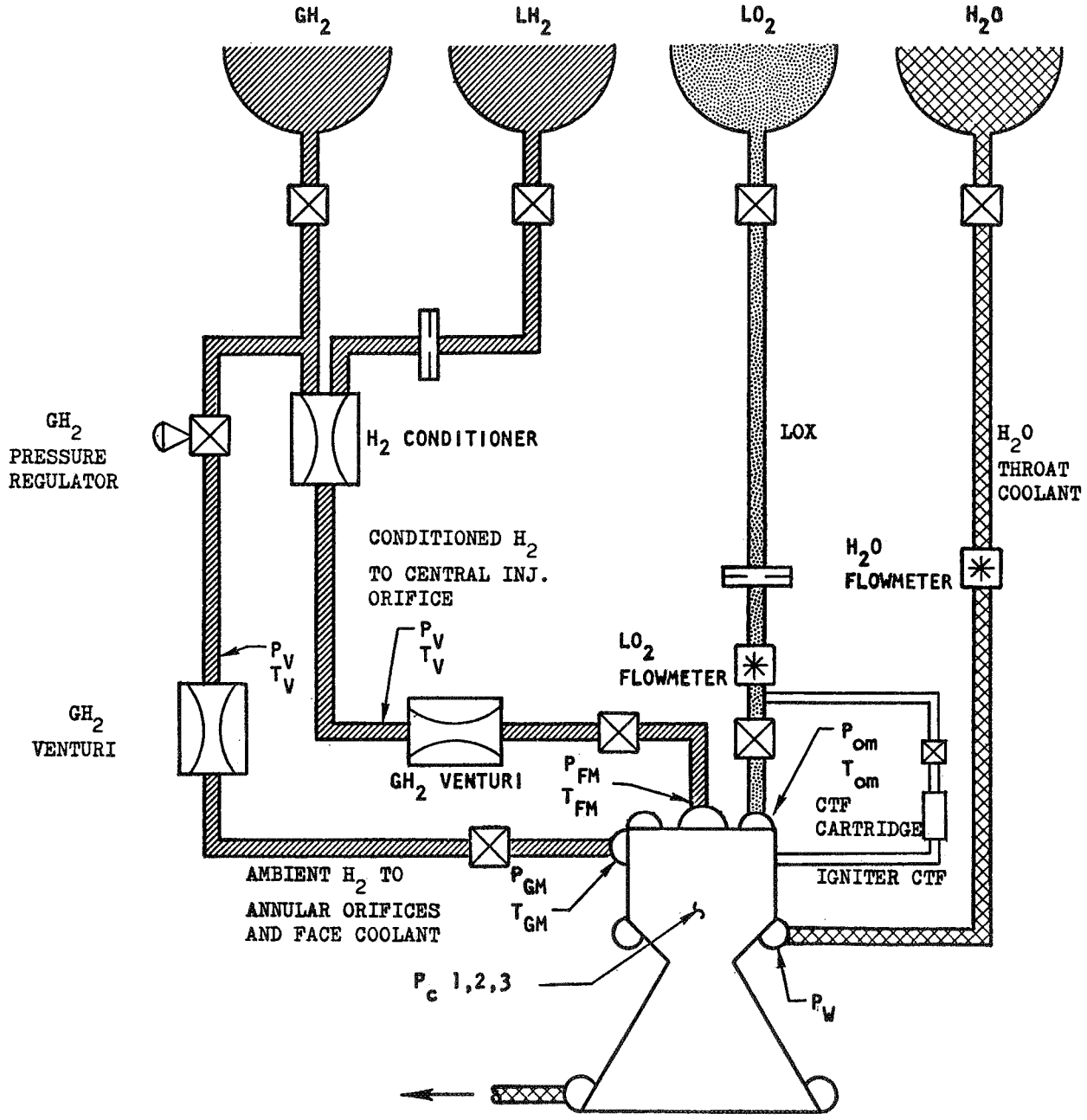

Figure 23. CTL-3, 18B System Schematic (Task I)

position. The main propellant lines and water coolant lines tied into the plumbing for adjacent test cell 18A. Therefore, the tanks, many of the valves, control, and much of the instrumentation were common to both test positions. High-pressure helium, GN_2, and GH_2 systems were used for pressurizing the propellant tanks, purging, and for valve operation.

A single LOX run tank supplied oxidizer to the injector with a turbine-type flowmeter used to measure the total LOX flow from the tank. Tank pressure variations and a venturi were used to orifice and to control the flow in the main LOX line. The "main" hydrogen system was designed to deliver hydrogen gas or liquid over the desired range of temperatures, pressures, and flowrates to the central showerhead gas orifice in the injectors. A temperature servocontrolled LH_2/GH_2 mixer system was used to obtain the required conditioned hydrogen potentially ranging from ambient temperature down to about 50 R (28 K) hydrogen. Sonic venturii were used to meter the main hydrogen and provide mass flowrate control independently of the operating chamber pressure. An ambient temperature hydrogen gas system was utilized to supply the injector annulus and face coolant flow. A 2800-psig (1930×10^4 N/m^2) hydrogen source was employed for this gas, metered and controlled by a sonic venturi. A dome-loaded pressure regulator was also used upstream of the sonic venturi to control the mass flowrate.

A CTF system was used for igniting the main propellants. The CTF was housed in a replaceable cartridge containing a burst diaphragm on each end. CTF was propelled into the chamber by igniter GOX which continued to flow and sustain ignition after the CTF slug was expelled. CTF and GH_2 reaction generated the initial ignition.

Water was used as the coolant for the thrust chamber nozzle section. A turbine-type flowmeter and orifices (upstream and downstream of the nozzle) were used to measure and control the flow.

A wide variety of measuring devices and control systems were used throughout the test program. Table 3 shows the main parameters recorded during the bulk

TABLE 3

BASIC INSTRUMENTATION FOR HOT-FIRE TESTS

Parameter	Range	Recorder
Oxidizer System		
Hypergol Upstream Pressure, psig (N/m^2)	0/2000 (0/1379 x 10^4)	DIGR
Hypergol Downstream Pressure, psig (N/m^2)	0/2000 (0/1379 x 10^4)	DIGR and Oscillograph
LOX Tank Pressure, psig (N/m^2)	0/3000 (0/2068 x 10^4)	DIGR
LOX Temperature at Flowmeter, F (K)	-300/-200 (89/144)	DIGR and Oscillograph
Upstream LOX Flowmeter Pressure, psig (N/m^2)	0/3000 (0/2068 x 10^4)	DIGR
LOX Injection Pressure, psig (N/m^2)	0/2000 (0/1379 x 10^4)	DIGR and Oscillograph
LOX Injection Temperature, F (K)	-325/+175 (75/353)	DIGR and Oscillograph
LOX Injection Pressure (Photocon), psig (N/m^2)	0/2000 (0/1379 x 10^4)	Tape
LOX Flowrate, lb/sec (N/s)	0/65 (0/289)	DIGR and Oscillograph
Fuel Systems		
LH_2 Tank Pressure, psig (N/m^2)	0/3000 (0/2068 x 10^4)	DIGR
Main Injector Venturi Upstream Pressure, psig (N/m^2)	0/2000 (0/1379 x 10^4)	DIGR
Main Injector Venturi ΔP, psi (N/m^2)	0/1000 (0/689 x 10^4)	DIGR
Main Injector Venturi Upstream Temperature, F (K)	-425/+100 (19/311)	DIGR and Oscillograph
Augmenting Gas Venturi Upstream Pressure, psig (N/m^2)	0/3000 (0/2068 x 10^4)	DIGR
Augmenting Gas Venturi Upstream Temperature, F (K)	0/100 (256/311)	DIGR
GH_2 Regulator Pressure, psig (N/m^2)	0/3000 (0/2068 x 10^4)	DIGR
Fuel Injection Pressure, psig (N/m^2)	0/2000 (0/1379 x 10^4)	DIGR and Oscillograph
Fuel Injection Temperature, F (K)	-425/+100 (19/311)	DIGR and Oscillograph
Augmenting Gas Injection Pressure, psig (N/m^2)	0/2000 (0/1379 x 10^4)	DIGR and Oscillograph
Augmenting Gas Injection Temperature, F (K)	-325/+175 (75/353)	DIGR

TABLE 3

(Concluded)

Parameter	Range	Recorder
Water Coolant System		
Flowrate, lb/sec (N/s)	0/80 (0/356)	DIGR and Oscillograph
Inlet Pressure (2 required), psig (N/m^2)	0/1000 (0/689 x 10^4)	DIGR
Inlet Temperature, F (K)	0/400 (256/478)	DIGR
Outlet Pressure (2 required), psig (N/m^2)	0/1000 (0/689 x 10^4)	DIGR
Outlet Temperature (2 required), F (K)	0/400 (256/478)	DIGR
Tank Pressure, psig (N/m^2)	0/2000 (0/1379 x 10^4)	DIGR
Hot Gas System		
Chamber Pressure (2 required), psig (N/m^2)	0/1000 (0/689 x 10^4)	DIGR and Oscillograph
Chamber Pressure (Photocon) (3 required), psig (N/m^2)	0/1000 (0/689 x 10^4)	Tape
Chamber Temperature, Nanmac (4 required), F (K)	0/2000 (256/1367)	Oscillograph
Accelerometer* (axial), g	0/300	Tape
Thrust (axial), lb (N)	0/22,000 (0/97,900)	DIGR and Oscillograph

*Accelerometer used in conjunction with VSC device

of the testing, the type of recording used, and the range of the pickups used. Chamber pressures, thrust, injection pressures, injection temperatures, and the main propellant flowrate parameters were recorded on an oscillograph (for transient response) and also on direct-inking graphic recorders (DIGR's). Other DIGR parameters included tank pressures, CTF ignition system pressures, water coolant pressures and temperatures, and in general all parameters where response time was not critical. Chamber wall temperatures were recorded on the oscillograph to achieve rapid response. Response from high-frequency instrumentation, consisting of three chamber pressure Photocons, one oxidizer injection pressure Photocon, and an axial accelerometer, was recorded on tape. This high-frequency instrumentation was primarily for monitoring and analysis of combustion stability. The accelerometer was monitored by a vibration safety circuit device with a variable delay time and "g" cutoff loading.

Event recorders, sequence timers, etc., were employed throughout the program for proper test setup and control. Motion picture coverage of all firings was used to aid test analysis and provide test documentation. One Fastax ($\sim$2000 frames/sec), two Milliken ($\sim$400 frames/sec), and two Bell and Howell ($\sim$64 frames/sec) cameras were employed to photographically cover each test.

Test Procedures

Basically, both the start and cutoff sequences for all tests were fuel rich. Specifically, the tests began with purges "on" in the main propellant lines. These purges were checked and/or sequenced off as the propellants entered. Next, the water coolant for the chamber nozzle was switched on, followed by GH_2 for injector face cooling. At about the same time, the main GH_2 entered through the central injector orifice. The fuel lead continued for about 12 seconds, long enough for the temperature to stabilize, and then ignition was achieved by a CTF hypergol slug entering the chamber. Igniter oxidizer (GOX) followed the CTF and sustained ignition. Approximately 2 seconds after ignition, the main oxidizer (LOX) flow entered the chamber with subsequent pressure buildup and mainstage. The cutoff sequence was basically the reverse of

the start sequence; i.e., oxidizer off first, then fuel off about 4.5 seconds later followed by water coolant off and line purges on as the propellant flows decayed. A typical operating sequence is depicted by Fig. 24.

Testing

Test Plan. The test plan for the hydrogen gas augmentation hot-firing phase of the program was formulated to demonstrate performance and stability of the selected large thrust/element injector and to establish design criteria for the gas augmented injector concept. An initial test (described later) was conducted, with no annulus gas, resulting in injector face erosion. To avoid this problem and to achieve the test objectives, the approach used thereafter was (1) to establish the minimum amount of annulus fuel flow required for heat transfer (cooling) purposes, (2) to evaluate (at a constant percentage of annulus gas) the parameters which control mixing by testing in a long L* chamber where complete spray vaporization would be expected, and (3) to evaluate the vaporization controlling factors at the best mixing condition and at a constant percentage of annulus gas.

Basically, the first six tests were designed so that performance would be mixing limited; i.e., the L* was sufficiently long enough, 75 in. (1.905 m)*, so that atomization and vaporization were essentially completed and the mixing processes controlled performance. The penetration distance parameter, X_p/D_g, was to be explored relative to the mixing limited performance. The orifice diameter ratio (D_ℓ/D_g) was set, as a result of the preceding analysis, at 0.32 for the first test (no annulus gas) and at 0.4 for the remaining tests. The last three tests were to be conducted under conditions where the mixing efficiencies were known and relatively high and the L* was low, 35 in. (0.889 m)**. Thus, the vaporization influences on performance were expected to be predominant. The main vaporization correlating parameter to be explored was the

The chamber L was 70 in. (1.778 m), but the addition of the bomb ring, which was present for all tests, lengthened the L* to 75 in. (1.905 m).
**The chamber L* was 30 in. (0.762 m), but the addition of the bomb ring, which was present for all tests, lengthened the L* to 35 in. (0.889 m).

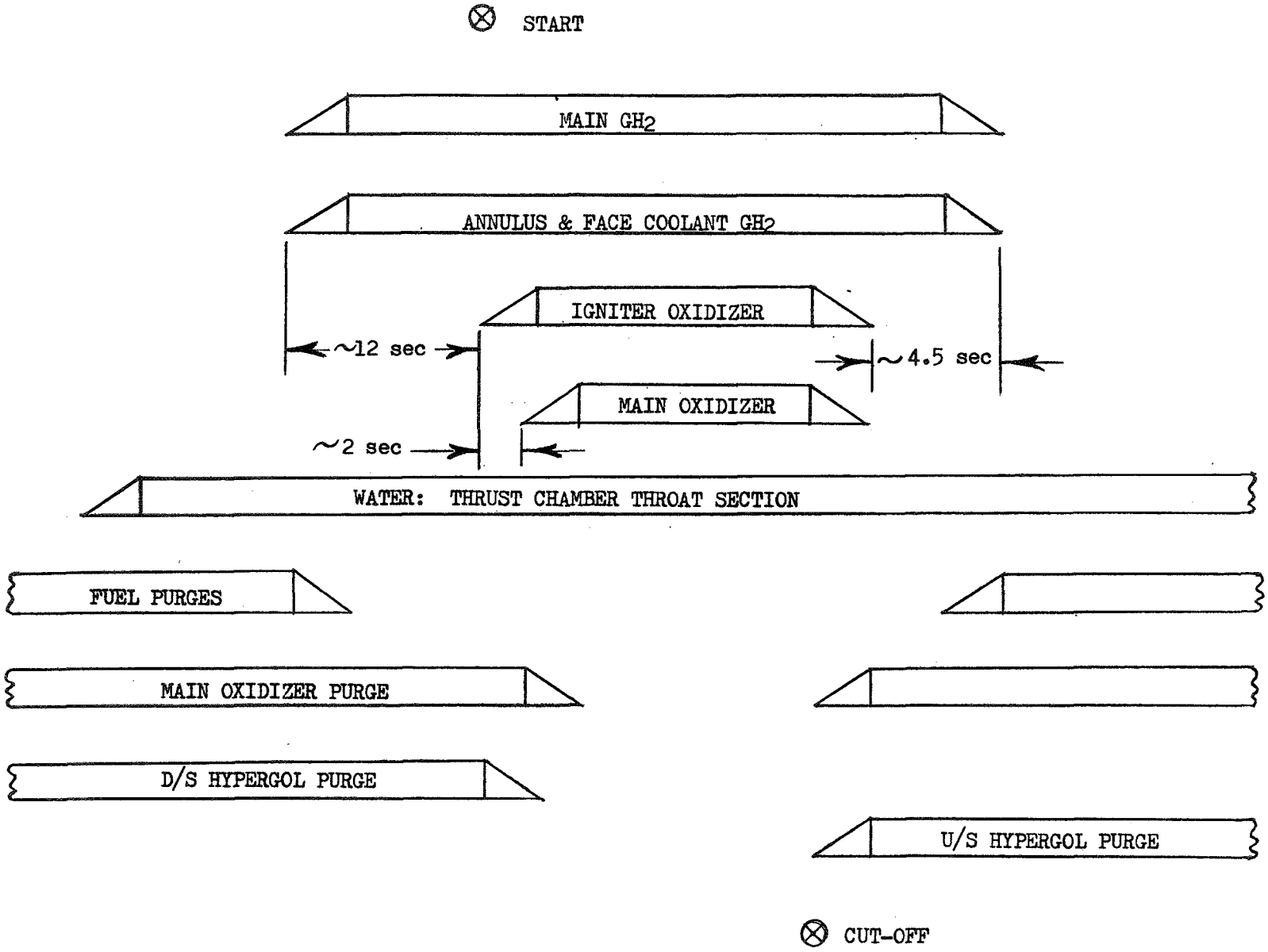

Figure 24. Test Operational Sequence

center gas momentum/oxidizer flowrate ($M_g/\dot{w}_o$) ratio. Off-nominal chamber pressure and mixture ratio operations were planned in conjunction with some of the tests to sufficiently establish the correlating parameter influence and at the same time minimize hardware changes. Description of the individual tests follows.

Test No. 1. The first LOX/GH_2 hot-firing test was conducted using the 20,000-lb (88,960 N)-thrust-per-element (single element) recessed impinging jet injector containing a 1.595-in. (0.0405 m)-diameter central GH_2 jet impinging with four 0.509-in. (0.0129 m)-diameter oxidizer jets (4-on-1). The annulus gas orifices (annular orifices around each oxidizer orifice) were plugged as shown in Fig. 19. Approximately 10 percent of the fuel was used as coolant for the injector Rigimesh. The thrust chamber for this test contained a two-piece uncooled copper combustion zone, a water-cooled copper nozzle and a steel bomb (pulse gun) ring mounted at the injector end. The injector-to-throat length was 38.27 in. (0.976 m) and the resultant L* was 75 in. (1.905 m). The test was programmed for 2 seconds of mainstage at 450 psia (310 x 10^4 N/m^2) chamber pressure and 4.75 mixture ratio with a main fuel (GH_2 through the center jet) temperature of 400 to 425 R (222 to 236 K). During the test, the actual LOX flowrate was somewhat lower than planned resulting in a chamber pressure of 385 psia (265 x 10^4 N/m^2) and a mixture ratio of 3.81. The actual mainstage portion of the test lasted for 1.98 seconds. Pertinent operating conditions and performance numbers for this test and all subsequent tests are listed in Table 4.

Posttest inspection of the hardware revealed considerable damage to the recessed cup portion of the injector, to the bomb ring, and to thrust chamber walls. This damage appeared to be caused by recirculating gases adjacent to the walls of the injector cup and adjacent to the chamber wall near the injector face. A photograph of the injector damage is shown in Fig. 25. This photograph shows the cup erosion around the oxidizer orifices. The erosion is about 1/4-in. (6.35 x 10^{-3} m) deep, maximum, and it occurs upstream as well as downstream and between the oxidizer orifices. Figure 26 shows the worst of the chamber wall erosion in the area near the injector face. Eroded

TABLE 4

TASK I, HOT-FIRE TEST RESULTS (O_2/H_2)

Test No.	Duration, seconds	Characteristic Length (L*)		Throat Area		Vacuum Thrust		Nozzle Chamber Pressure		Oxidizer Flowrate		Central Fuel Flowrate		Central Fuel Temperature		Annulus[a] and FC Fuel Flowrate		Mixture Ratio	Vacuum I_s, seconds	I_s Efficiency, percent	c*		X_p/D_g[b]	Total $M_g/\dot{W}_o$	η_{c^*} From F, percent	η_{c^*} From P_c percent
		in.	m	$in.^2$	$m^2 \times 10^{-3}$	lb	N	psi	$N/m^2 \times 10^4$	lb/sec	N/s	lb/sec	N/s	R	K	lb/sec	N/s				ft/sec	m/s				
1	1.98	75	1.91	29.20	18.84	15,545	69,150	385.0	265.4	35.63	158.5	8.40	37.4	428	238	0.94	4.2	3.81	345.7	93.3	8096	2468	0.36	9.92	96.8	99.3
2	0.52	75	1.91	29.16	18.81	20,830	92,660	510.2	344.9	52.84	235.0	4.09	18.2	448	249	5.51	24.5	5.50	333.7	94.0	7715	2352	0.97	2.52	97.6	99.2
3	0.51	75	1.91	29.22	18.85	21,127	93,980	511.3	352.5	52.36	232.9	7.22	32.1	398	221	3.34	14.9	4.96	335.8	93.1	7688	2343	0.58	3.98	96.5	97.1
4	1.98	75	1.91	29.36	18.94	21,193	94,270	519.0	350.9	52.85	235.1	7.32	32.6	390	217	3.46	15.4	4.90	333.1	92.2	7753	2363	0.57	4.10	95.6	97.8
5[c]	1.60	75	1.91	29.37	18.95	21,092	93,820	515.1	355.1	51.20	227.7	7.57	33.7	194	108	3.43	15.3	4.65	339.2	93.6	7871	2399	0.77	2.56	97.0	98.9
6[c]	1.54	75	1.91	29.36	18.94	12,011	53,430	291.7	201.1	28.31	125.9	6.52	29.0	197	109	1.93	8.6	3.35	326.7	88.5	7549	2301	0.38	9.18	91.9	92.9
7[c]	1.66	35	0.89	29.42	18.98	20,442	90,930	503.4	347.1	52.63	234.1	7.50	33.7	197	109	3.23	14.4	4.90	322.6	89.7	7509	2289	0.81	2.31	91.9	95.1
8[c]	1.59	35	0.89	29.45	19.00	20,270	90,170	501.1	345.5	53.36	237.4	7.11	31.6	250	139	3.29	14.6	5.13	317.9	89.0	7435	2266	0.76	2.55	91.2	94.8
9	2.63	35	0.89	29.41	18.98	13,806	61,410	341.9	235.7	29.56	131.5	4.80	21.4	147	82	5.30	23.6	2.93	348.1	93.5	8145	2483	0.69	8.70	95.9	99.4

[a] Face coolant (FC) is 100 percent of this fuel flowrate for test No. 1 and ~ 15 percent for tests 2 through 9. Ambient temperature annulus and FC fuel used.

[b] Annulus and FC flowrate not used for these computations, $X_p/D_g = 2.5\left[\frac{M_\ell}{M_g}\cos^2\theta\right]^{1/2}$

[c] Bomb tests

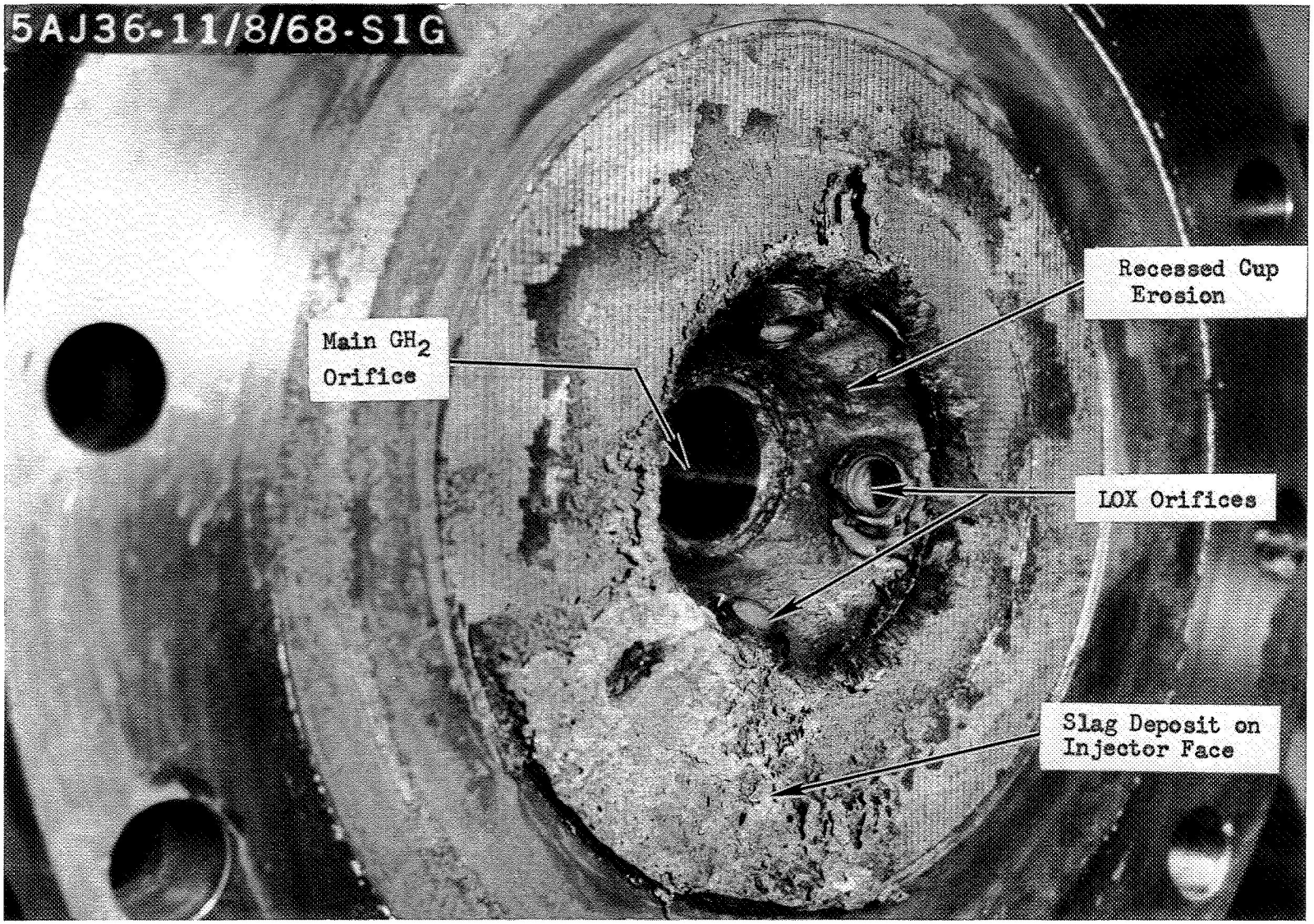

Figure 25. Recessed Impinging Jet Injector, Posttest No. 1

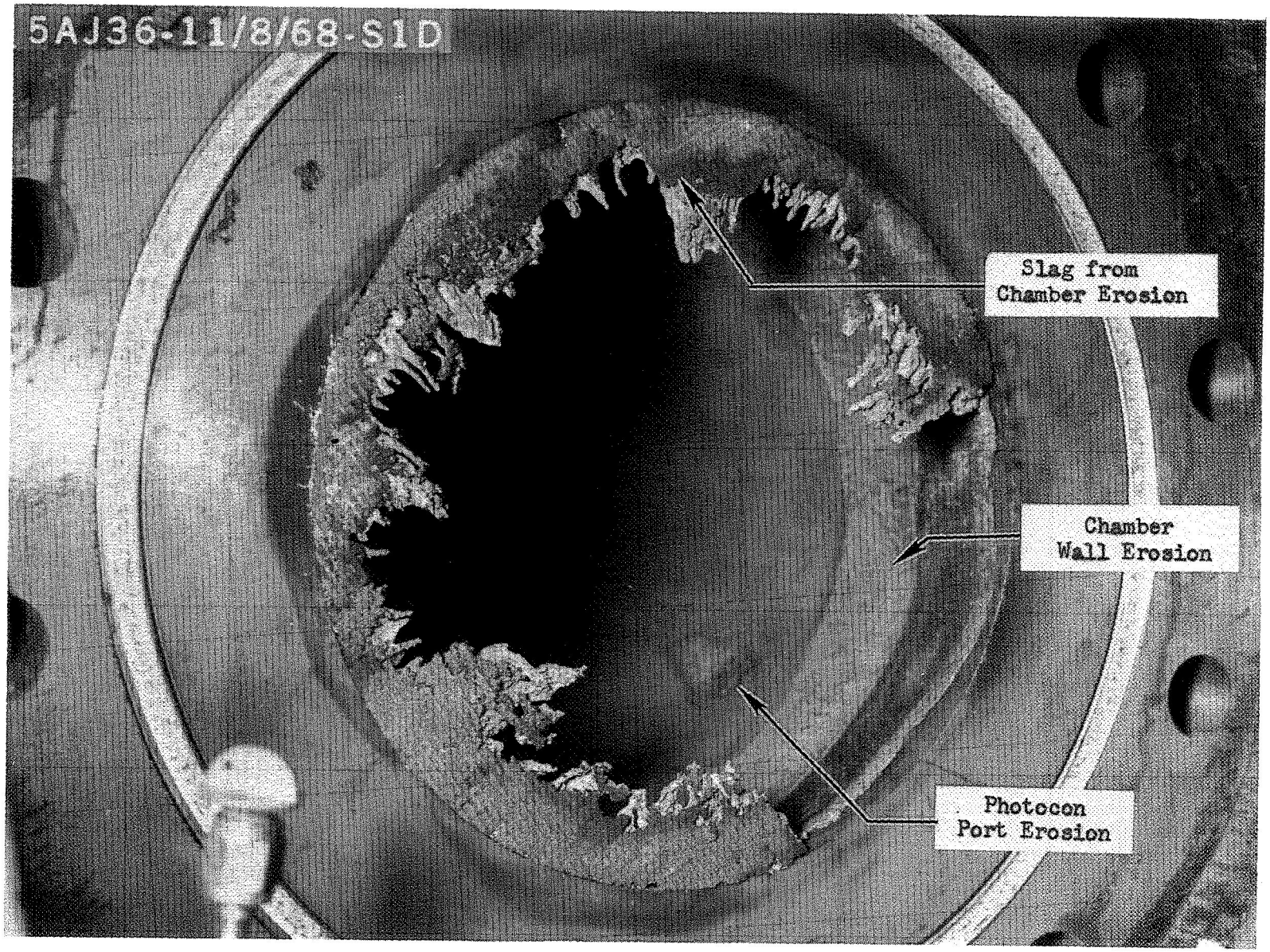

Figure 26. Thrust Chamber Injector End, Posttest No. 1

areas in Fig. 26 include: (1) the copper chamber wall adjacent to the bomb ring, (2) the bomb ring, and (3) the Photocon pressure transducer ports. Some erosion was also experienced at the joint between the two uncooled copper combustion chamber sections (copper liner inside a steel shell) and at the leading edge (start of convergence) of the water-cooled copper nozzle liner. The deepest chamber erosions occurred in zones radially outward from the four oxidizer orifices, thereby suggesting that the oxidizer streams did not penetrate significantly into ("bounded off") the high velocity ~3550 ft/sec (~1080 m/s) central gas jet.

Injector repair procedures included: (1) to remove the four oxidizer tubes, the Rigimesh face and the damaged portion of the cup wall, and (2) insert new material to build up the cup wall, weld the cup insert in place, machine and drill the new cup, install a new Rigimesh face, and install four new oxidizer tubes (orifices). This repair essentially returned the injector to its original condition. The combustion chamber section adjacent to the injector was repaired by installing a new uncooled copper liner inside the steel jacket and by plugging the damaged Photocon pressure transducer ports (three new Photocon ports were added to the bomb ring). The second (downstream) copper combustion chamber section and the water-cooled copper nozzle liner were repaired by building up the eroded areas with copper weld material and machining to the original contour. Bomb ring repair procedures were to remove the damaged surface and replace the lost material with a sleeve which was welded in place.

Under Contract NAS3-7962, the above mentioned 20,000-lb (88,960 N) recessed impinging jet injector had been fired several times (Ref. 3) with no evidence of injector or chamber erosion when GH_2 was flowing through the four annular orifices around the oxidizer orifices. This annulus gas was omitted for the first test where the above-mentioned damage occurred. Thus, it was concluded that the annulus gas significantly influences the hardware erosion susceptibility; therefore, ambient temperature annulus gas was included in all subsequent tests.

Tests No. 2 and 3. Tests 2 and 3 were relatively short (~ 1/2 second)-duration tests designed to determine whether annulus gas (GH_2) would prevent injector erosion and, if so, how much was required. The 20,000-lb (88,960 N) recessed impinging jet injector was again used, but modified slightly to provide a 1.27-in. (0.0323 m)-diameter central GH_2 jet impinging with the four oxidizer jets, each surrounded by an annular flow of ambient temperature GH_2. Ambient GH_2, ~15 percent of the total annulus-face coolant flow, was also used to cool the Rigimesh face. The thrust chamber for these tests was essentially the same as used during test No. 1 (75 in. (1.905 m) L*). During test No. 2, the combined annulus gas and face coolant flow was about 57 percent of the total fuel flowrate, and during test No. 3 this flow was cut to about 30 percent. In addition, during these tests the penetration distance (X_p/D_g) parameter was varied to determine its effect on the mixing limited performance. Tests results were satisfactory and no hardware damage was sustained.

Test No. 4. Test No. 4 was essentially a repeat of test No. 3 except for increasing the duration to ~2 seconds. Test results were satisfactory except for some minor thrust chamber erosion at the downstream edge of the bomb ring, in the joint between the bomb ring and upper combustion zone spool section and in the joint between the upper and lower combustion zone spools. These erosions were most likely perpetrated by discontinuities in the chamber walls at these joints. Most of the erosions were midway between, 45 deg (0.785 rad) from, the LOX jets.

Tests No. 5 and 6. Tests No. 5 and 6 were conducted to further evaluate the penetration distance parameter, X_p/D_g, and the mixing limited combustion efficiency. The annulus gas-face coolant flow was about 30 and 23 percent, respectively*, of the total fuel flow. The hardware remained the same as

*This percentage varied somewhat because of a difference in injected mixture ratio. The annulus gas face coolant flow was maintained constant at about 5 percent of the total propellant flowrate for these tests.

used for the previous tests. The test duration for tests No. 5 and 6 was set for about 1.5 seconds to minimize chamber erosion. Test results were satisfactory and very little chamber erosion occurred.

Test No. 7. Test No. 7 was essentially a repeat of test No. 5 except the chamber L* was reduced to 35 in. (0.889 m) to evaluate the vaporization effects. Test results were satisfactory.

Tests No. 8 and 9. Tests No. 8 and 9 with the 35-in. (0.889 m) L* chamber were satisfactory except that the $M_g/\dot{w}_o$ ratio was somewhat lower than desired during test No. 8, and during test No. 9 the quantity of annulus gas-face coolant flow was excessive; i.e., 52.8 percent compared to the targeted 30 percent. The excessive annulus gas flow was caused by a facility pressure regulator failure. Results from tests No. 8 and 9 are listed in Table 4 along with results from the previous tests.

In addition to performance, dynamic stability evaluation was pursued during tests No. 5 through 8. Three pulse guns were triggered during each of these tests and the pulse gun charge sizes varied from 10 to 80 grains (6.5 to 51.8 x 10^{-4} kilograms). Sketches depicting the pulse gun and the three different orientations used are shown in Fig. 22.

Test Results

Performance. The index of injector performance for the experimental program is corrected c* efficiency. This parameter was calculated by two independent methods, one based on measurement of chamber pressure, and the other on measurement of thrust. Correlation of these two methods can allow an independent check on the data measurement accuracy. The procedures for computing the performance were similar to those used under Contract NAS3-7962 (Ref. 3) and are summarized in Appendix B. Efficiencies based on thrust averaged about 2.2 percent (0.6 to 3.6 percent) less than those based on chamber pressure, although the observed trends were always the same. Techniques for obtaining

the chamber pressure and thrust parameters used are described in Appendix C along with some factors which may explain the thrust and chamber pressure efficiency differences.

As previously described, the first six tests were designed to characterize mixing-limited combustion efficiency. The performance obtained during these tests are shown in Fig. 27. In this figure, the c* efficiency is plotted against the penetration parameter, X_p/D_g. These data actually represent the mixing limited combustion efficiency because the chamber L* was relatively long [75 in. (1.905 m)] and vaporization was essentially complete, i.e., $(\eta_{c^*})_{vap} \cong 100$ percent. Also included in the figure is one data point (run 023) from the NAS3-7962 program, which used the hot gas augmented version of the same injector concept. With the percent annulus plus face coolant (Rigimesh) gas between about 23 and 57 percent of the total fuel flow (4.4 to 7.6 percent of total flow as annulus gas), a smooth correlation exists with the penetration parameter. As X_p/D_g increases from about 0.4 the performance, $(\eta_{c^*})_{mix}$ rises sharply at first, and then levels out. Between X_p/D_g of 0.7 to 1.0 it reaches a value of 97 or 99 percent, according to thrust or chamber pressure, respectively. Only the performance of test No. 1 with 0-percent annulus gas injection (about 10 percent of the total fuel was supplied as injector face coolant through the Rigimesh) fell off of this curve. If this test No. 1 data are valid (in spite of the injector erosion encountered) the indication is that overall propellant mixing was less degraded at these conditions when there was no annular fuel injection. Similar results were observed in the Task I cold-flow study.

The vaporization-limited performance data from tests No. 7 through 9 are plotted in Fig. 28, together with the previously discussed 75-in. (1.905 m) L* test data (runs 2 and 5) and several data points from the "Two-Stage Program" (NAS3-7962). Tests No. 2, 5, and 7 through 9 were selected with an X_p/D_g value between 0.69 and 0.98 and D_ℓ/D_g of 0.4 so that the propellant mixing efficiency would remain virtually constant and differences in vaporization efficiency would be evident. As expected, the figures show that (η_{c^*}) levels increase with chamber L*. For a fixed chamber size, the performance

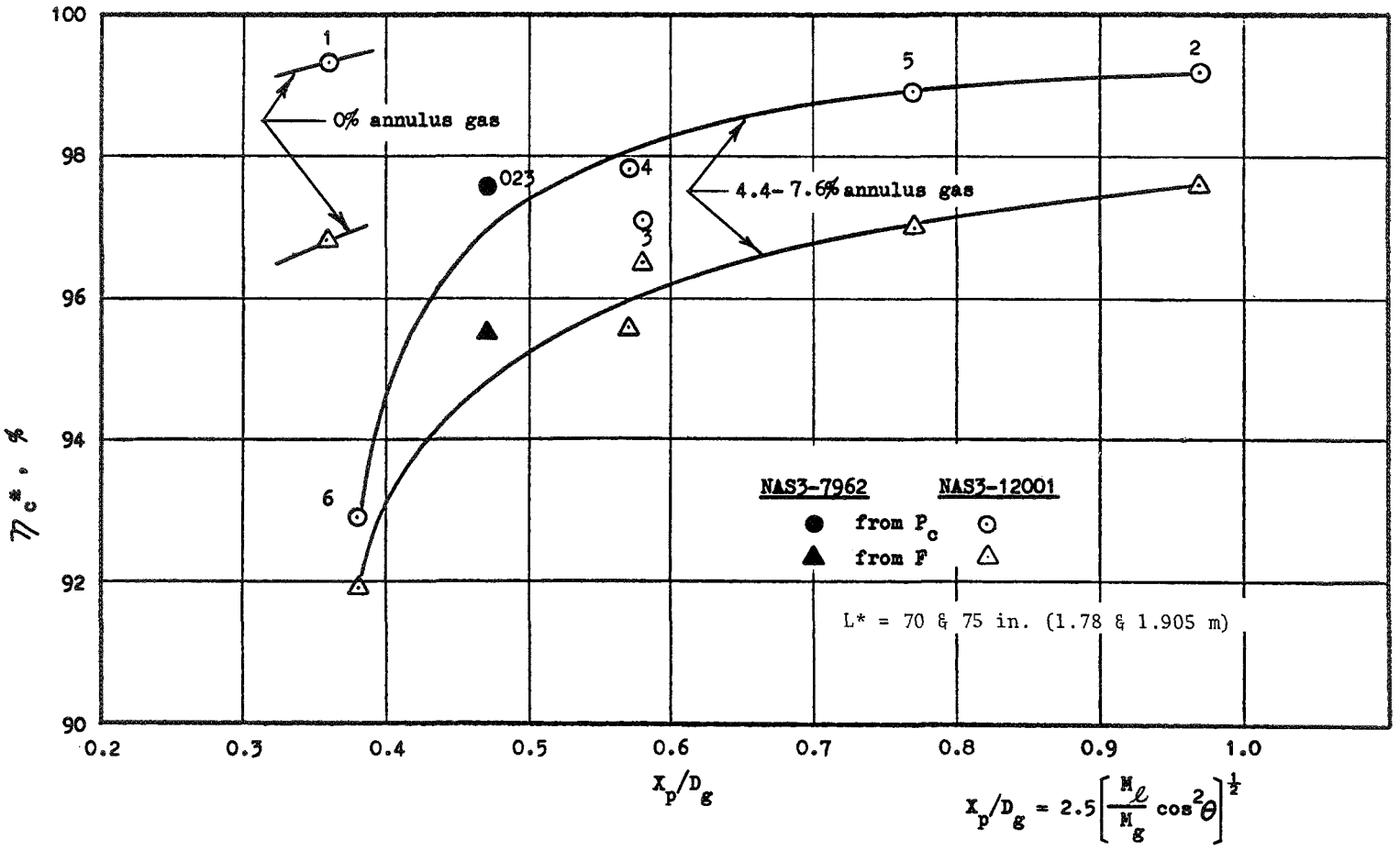

Figure 27. Mixing Limited Performance, Recessed Impinging Jet Injector

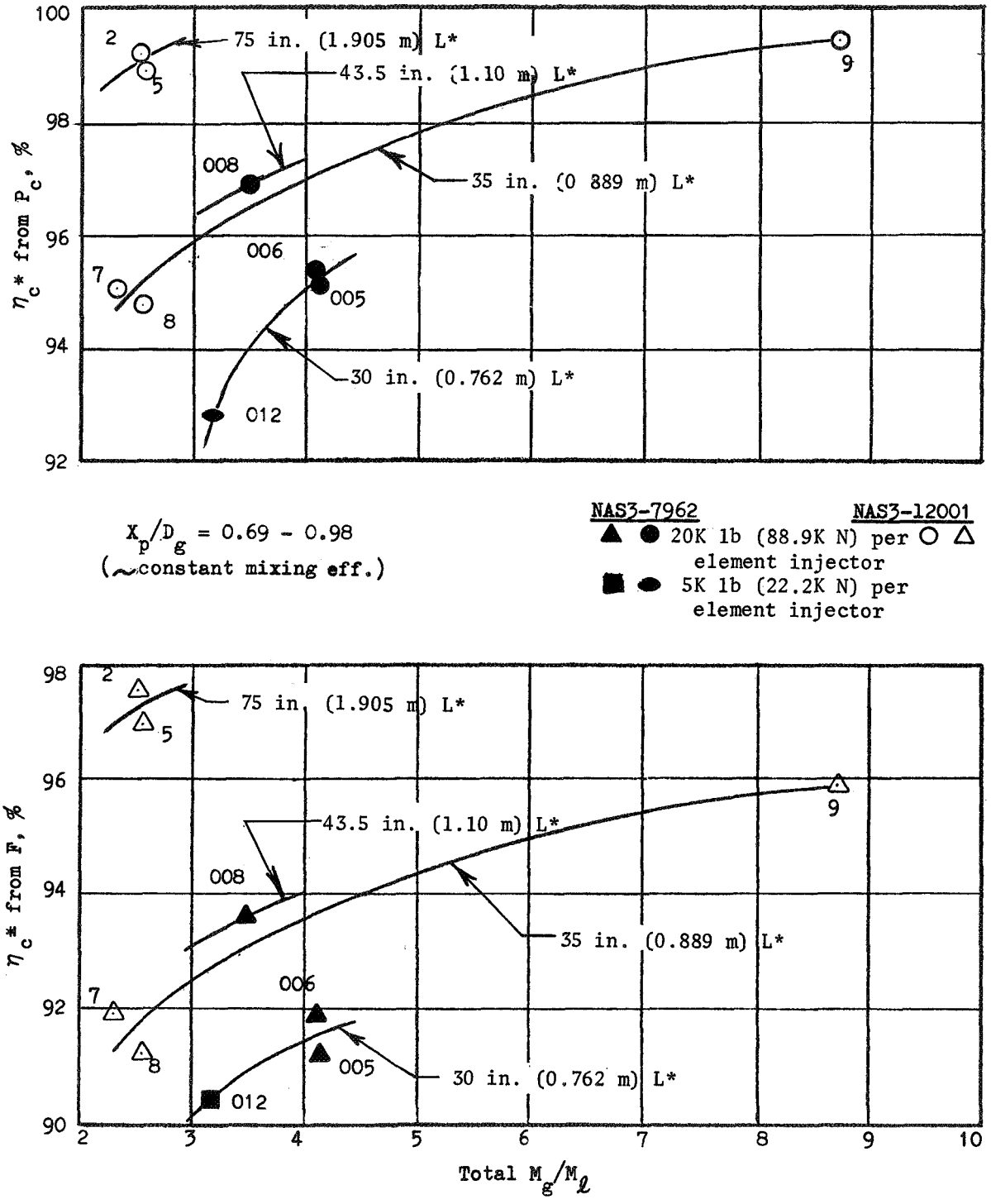

Figure 28. Vaporization-Limited Performance, Recessed Impinging Jet Injector

plotted against $(M_g)_{tot}/M_\ell$ seems to correlate well. Originally, the data were plotted against $(M_g)/\dot{w}_\ell$ but there was appreciable scatter so the momentum ratio was selected as a better empirical parameter for correlating vaporization efficiency. It should be noted that M_g represents the total injected gas momentum, i.e., the sum of the center and annulus gas momentum. The test data do not correlate when only the center gas or only the annulus gas momentums are used, thereby implying that both gas streams contribute to the vaporization processes.

The vaporization effects on performance indicated in Fig. 28 can be shown more explicitly by applying the $(\eta_{c^*})_{mix}$ information (Fig. 27) to the measured performance data (Fig. 28) to obtain $(\eta_{c^*})_{vap}$ directly, i.e.:

$$(\eta_{c^*})_{vap} = \frac{\eta_{c^*}}{(\eta_{c^*})_{mix}} \tag{5}$$

The results are shown in Fig. 29 where $(\eta_{c^*})_{vap}$ is plotted against $(M_g)_{tot}/M_\ell$ for constant values of L*. Essentially, the trends shown in Fig. 29 are a repeat of those described in Fig. 28, except that $(\eta_{c^*})_{vap}$ is shown quantitatively.

One of the program objectives is to establish design criteria which can be used to generate future high-performing gas augmented injector concepts. Figures 27 and 29 were established with this end in mind. Further work was needed, however, to refine the correlating parameters used, namely the X_p/D_g and M_g/M_ℓ parameters, and to determine whether additional parameters were necessary to define performance characteristics.

Stability. A major program objective was to evaluate the stability characteristics of the hardware, particularly the injector. Wide frequency range, fast responding instrumentation was used during each test to monitor the stability characteristics. The instrumentation consisted of one axial accelerometer, one oxidizer injection pressure Photocon and three chamber pressure Photocons. During the first test, two of the chamber pressure Photocons were

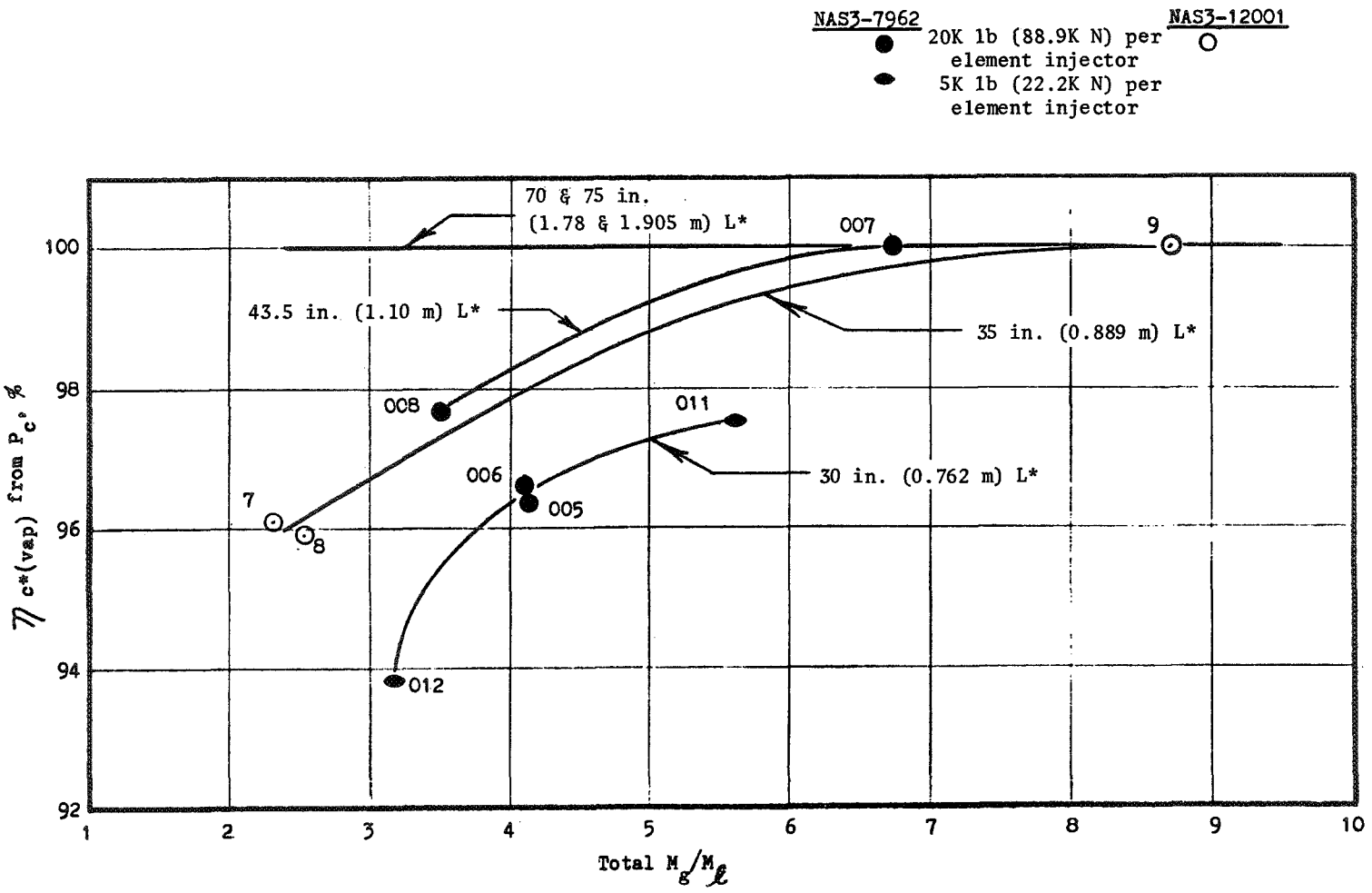

Figure 29. Vaporization Efficiency, Recessed Impinging Jet Injector

5-1/2 in. (0.14 m) downstream of the injector face and the third chamber pressure Photocon was 12-3/4 in. (0.32 m) downstream of the face. Each of these three Photocons was recessed about 0.38 in. (0.0097 m) away from the hot gas wall. During subsequent tests No. 2 through 9, the three chamber pressure Photocons were installed in the bomb ring 1-1/4 in. (0.032 m) downstream of the injector face and recessed about 3-1/2 in. (0.089 m) from the hot gas wall. Output from this instrumentation was recorded on tape, transcribed on oscillogram-type records and for some tests transcribed on expanded scale Brush records.

Dynamic stability characteristics were observed during tests No. 5 through 8. For each of these tests three pulse guns were fired, each with different size charges. The charge sizes and the gun orientations are listed in Table 5.

TABLE 5

PULSE GUN CHARGE SIZE AND ORIENTATION

Test No.	Charge Size, grains (kilograms)			Maximum P_c Overpressure, psi (N/m^2)
	Radial	Chordal	Tangential	
5	10 (6.5×10^{-4})	40 (25.9×10^{-4})	80 (51.8×10^{-4})	320 (220×10^4)
6	20 (13.0×10^{-4})	80 (51.8×10^{-4})	40 (25.9×10^{-4})	700 (480×10^4)
7	40 (25.9×10^{-4})	20 (13.0×10^{-4})	10 (6.5×10^{-4})	300 (210×10^4)
8	80 (51.8×10^{-4})	10 (6.5×10^{-4})	20 (13.0×10^{-4})	460 (320×10^4)

During each test, the charges were sequenced to fire in order of ascending weight; thus in a test firing using charge weights of 10, 80, and 40 grains (6.48×10^{-4}, 51.84×10^{-4}, and 25.92×10^{-4} kilograms) the order of firing would be 10 grains, 40 grains, and lastly the 80-grain charge. About 250 milliseconds were allowed between the pulse gun firings, which were sequenced after approximately 0.75, 1.00, and 1.25 seconds of mainstage. A vibration safety cutoff (VSC) device was set for 40 milliseconds of sustained instability at 300 g rms before possible shutdown.

Table 5 also shows the maximum P_c overpressure recorded by the Photocons. This maximum overpressure generally occurred in conjunction with the largest charge size and, as anticipated, it appeared to be a function of the Photocon location relative to the gun orientation. The absolute magnitude of the P_c overpressures are inconclusive and serve only to show that the disturbances were significant. The pulse gun pulses did not produce a LOX injection pressure overpressure.

A typical expanded Brush record is presented in Fig. 30 showing the 80-grain (51.8×10^{-4} kilograms) charge disturbance from the radial pulse gun during test No. 8. The trace from the P_c Photocon No. 3 shows an overpressure of 460 psi (320×10^4 N/m^2) above the nominal. This pickup was 120 deg (2.094 rad) away from the radial pulse gun barrel (P_c No. 1 and 2 were both 30 deg, 0.523 rad, from the gun barrel) and it was in the same plane. All of the traces indicate that the disturbance damps in less than 5 milliseconds.

Analysis of Results

Mixing Efficiency Analysis. One of the main objectives of the hydrogen gas augmentation hot-firing phase of the program was to experimentally evaluate the parameters which control propellant mixing, thereby permitting empirical improvement of the cold-flow mixing limited performance correlations. Thus the Task I cold-flow results were compared with the mixing hot-fire results. These data (from Fig. 9 and 27) are replotted in Fig. 31 as a function of the liquid/gas penetration parameter (X_p/D_g) and the liquid-to-gas orifice diameter ratio. It is recognized that there is a difference in scale* between hot fire and cold flow as well as the percent annulus fuel flowrate**. However, with these qualifications an excellent correlation was obtained. Thus, cold-flow mixing tests in which the uniform gas assumption was used for data

*Hot-fire scale was 20,000-lbf (88,960 N)-thrust-per-element compared to cold flow 5000-lbf (22,200 N)-thrust-per-element.

**Hot-fire percent annulus fuel was approximately 26 percent of the total propellant flow in Fig. 31 while cold flow was without annulus gas.

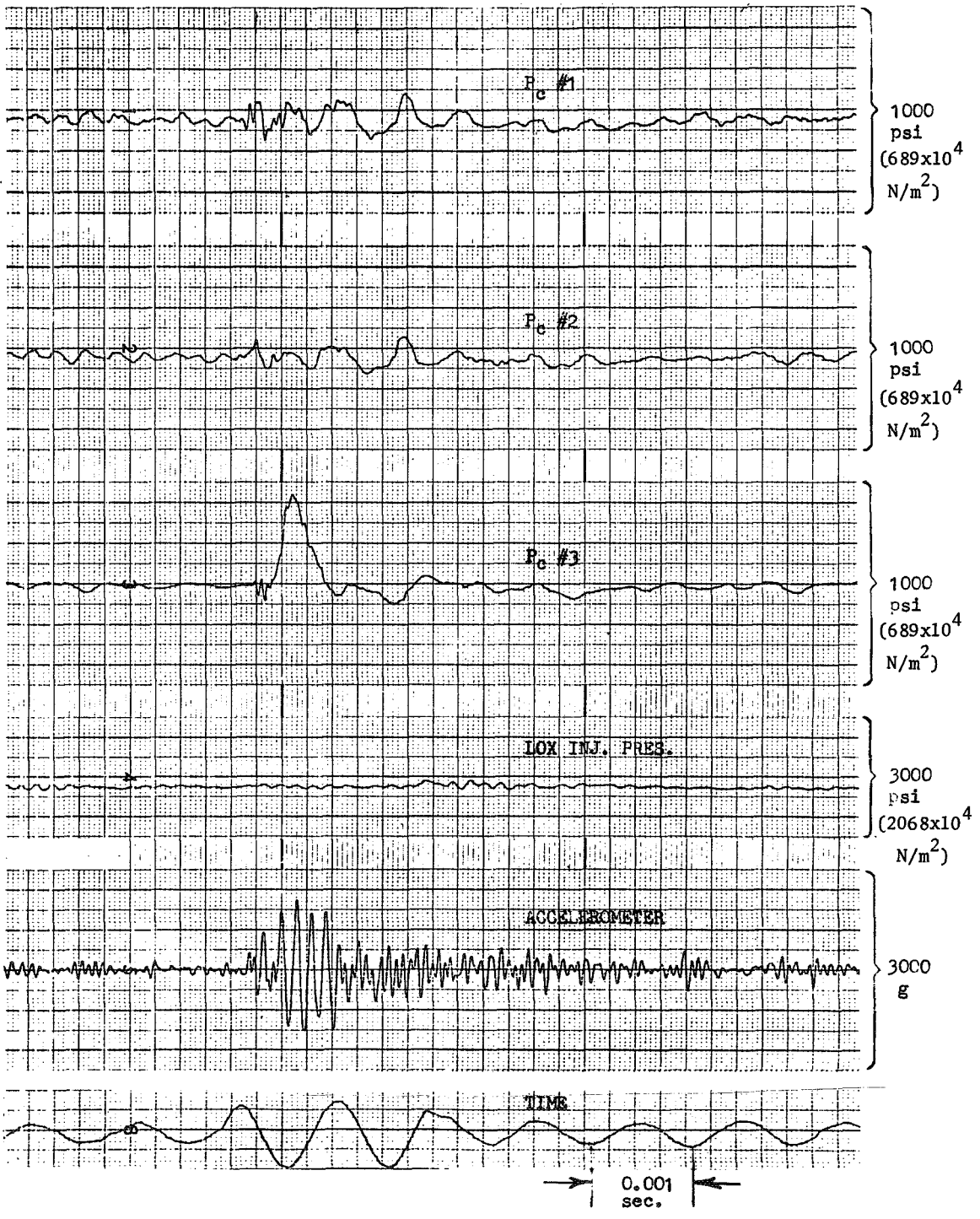

Figure 30. Brush Record of 80-Grain (51.8×10^{-4} kg) Pulse Gun Disturbance, Test No. 8

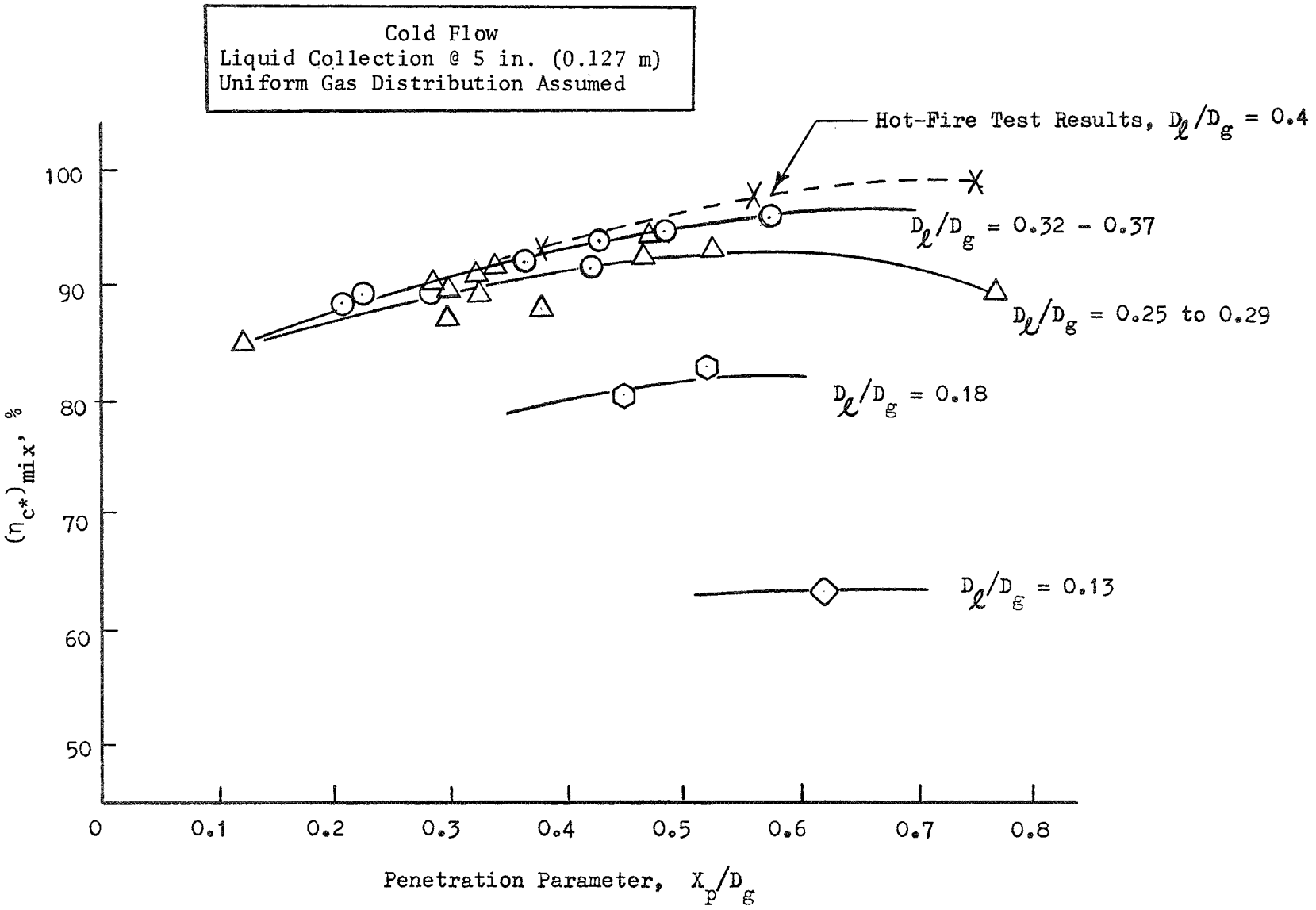

Figure 31. Penetration Distance Influence on Mixing Efficiency

reduction purposes, effectively predicted mixing efficiencies for the 20,000-lb (88,960 N) recessed impinging jet injector with LOX/GH_2 propellants. Whether or not the uniform gas flow assumption was acceptable for other element sizes, types, or flow conditions remained to be seen. This will be further discussed under the Task II portion of this report.

Vaporization Efficiency Analysis. The vaporization-limited performance results from a previous hot gas augmented program (Contract NAS3-7962) and from the current LOX/hydrogen testing, each using the recessed impinging (coaxial) injector, were empirically correlated with the gas-to-liquid momentum ratio (Fig. 29).

As previously described, vaporization-limited combustion model performance data, $(\eta_{c*})_{vap}$, were also generated for the hot-firing injector/thrust chamber conditions as a parametric function of LOX dropsize (D_{30}) and chamber L* (see Fig. 16 and 17). The hot-fire data and the combustion model data may be directly compared to yield vaporization efficiency vs chamber characteristic length at several constant values of momentum ratio. Because of the very close similarity between the experimental and analytical families of curves, it was possible to infer direct correspondence between the analytical mean droplet size and the hot-firing momentum ratio. The volumetric mean dropsize so predicted is plotted against the hot-fire momentum ratio for each value of L* in Fig. 32. Note that this yields one curve which is independent of chamber characteristic length, as expected. Thus, the volume mean dropsize may be predicted from the momentum ratio (Fig. 32). This dropsize and the chamber characteristic length can then be used to obtain the predicted vaporization efficiency as is illustrated by the dashed curves in Fig. 33. Note the correspondence between these calculated curves and the solid line hot-firing data curves repeated from Fig. 29. At no point do the analytical and experimental efficiencies differ by more than 1 percent.

Stability. All of the stability records suggest that the injector/thrust chamber hardware is dynamically stable under each of the conditions tested.

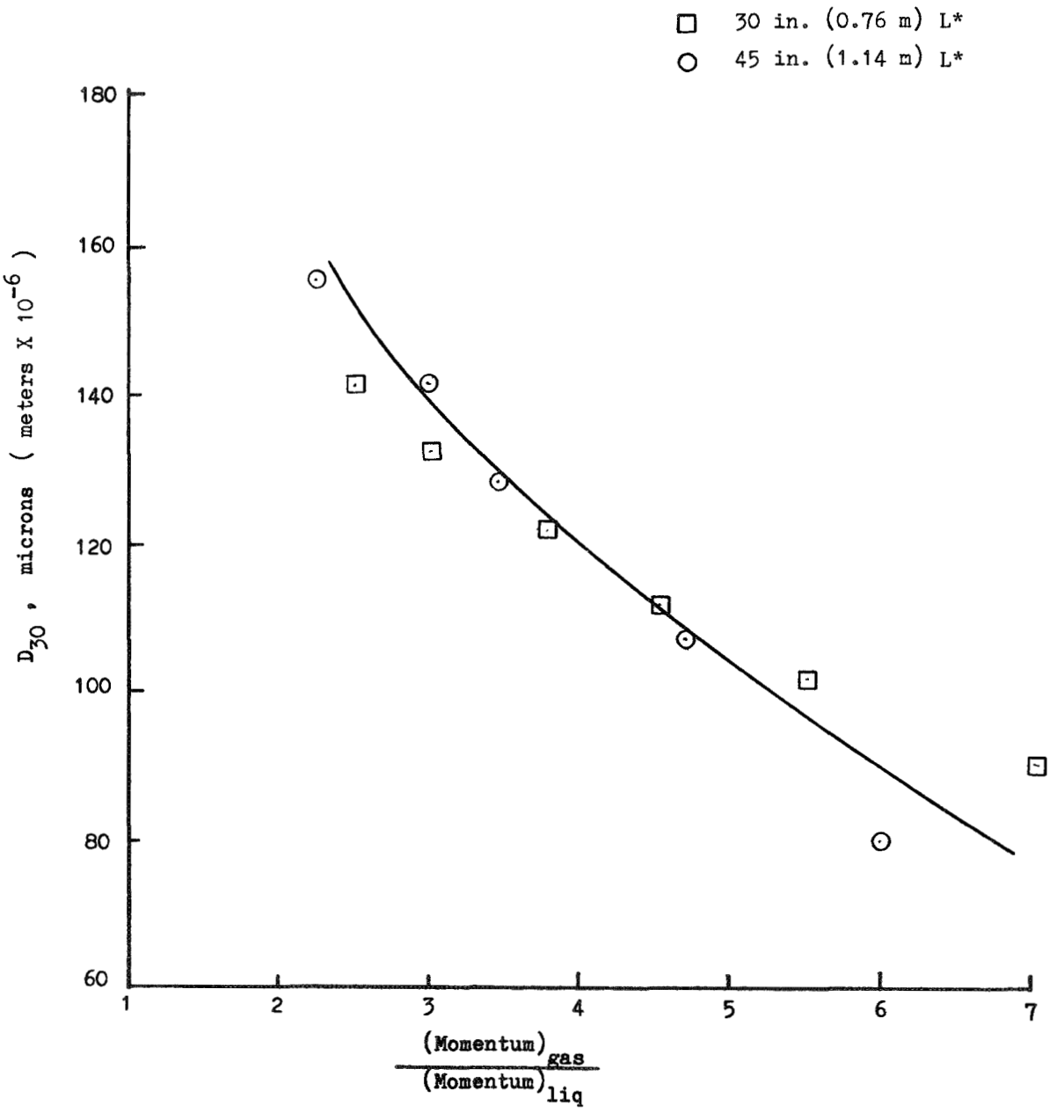

Figure 32. Predicted Volume Mean Dropsize vs Momentum Ratio

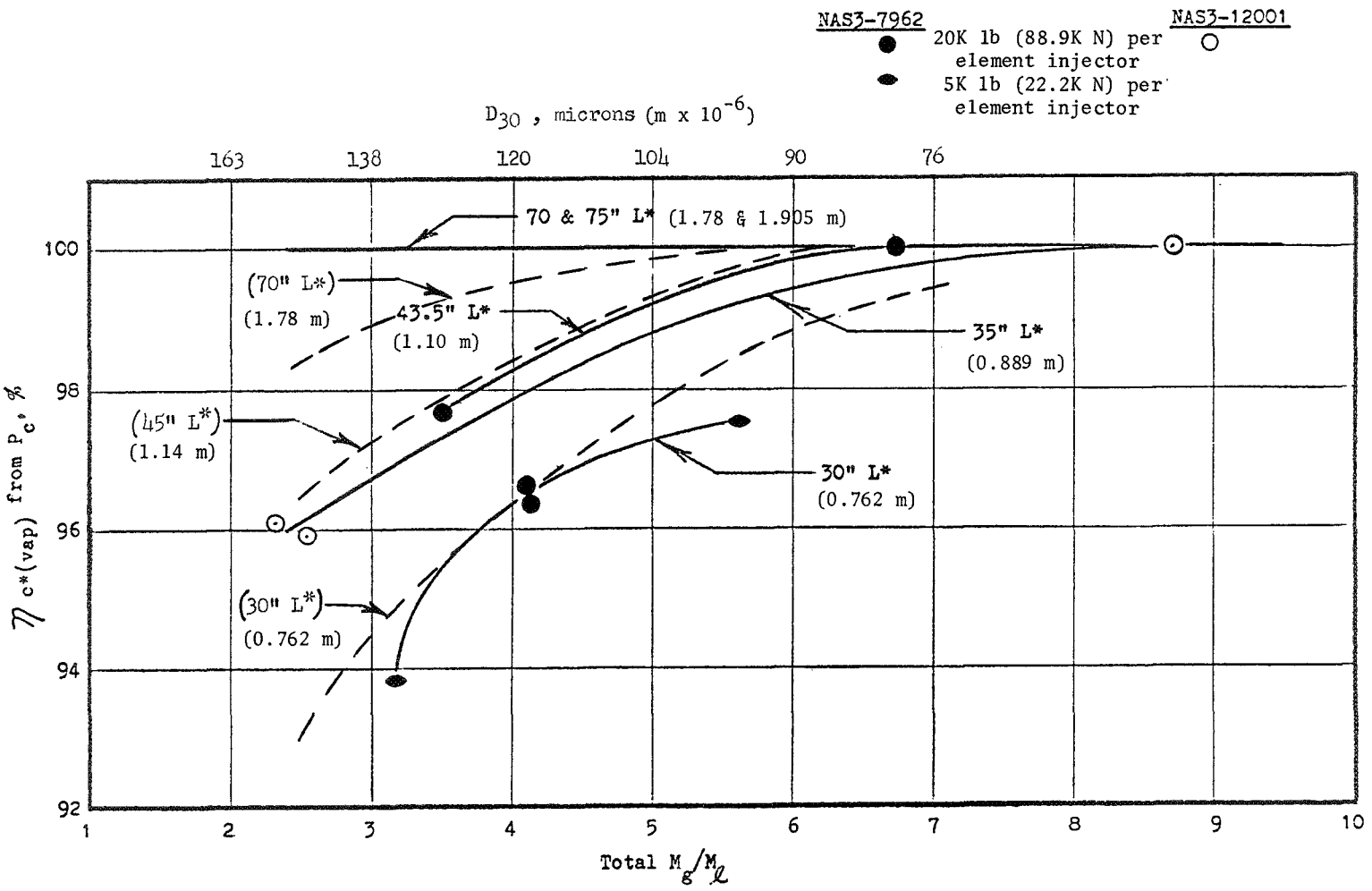

Figure 33. Vaporization Efficiency, Recessed Impinging Jet Injector

Traces of low amplitude "noises" were observed at several different frequencies, although none were specifically singled out. Some general observations are listed below regarding the stability results:

1. The composite (compound) steady-state noise levels recorded by the chamber pressure and LOX injection pressure Photocons were nominally about ±5 percent (peak-to-peak) of the operating pressures, independent of the pulsing. The true amplitudes recorded may be effected by the cavities leading to the recessed pressure pickups.

2. A predominant frequency could not be singled out during any of the tests although traces of several different frequencies were observed, namely those around the 1200, 2000, and 4000 Hz ranges. The latter is near the chamber first tangential acoustic mode frequency of ~4500 Hz.

3. The observed frequencies were not clearly defined, but could be feed-system coupled, acoustic type and/or related to the recessed pressure pickup cavities.

4. All of the pulse gun disturbances damped completely in less than 5 milliseconds.

5. No disturbance was recorded by the pressure pickups or accelerometer when the 10-grain (6.5×10^{-4} kilograms) charge was fired; the 20- and 40-grain (13.0×10^{-4} and 25.9×10^{-4} kilograms) charge disturbances were recorded some of the times and the 80-grain (51.8×10^{-4} kilograms) charge disturbance was recorded all of the time by the P_c pickups and accelerometer.

TASK II, EVALUATION OF GAS-LIQUID INJECTION CHARACTERISTICS

The objective of Task II was to evaluate and characterize the performance controlling design and operating parameters of gas/liquid impinging jet and coaxial injector elements suitable for application to the LOX/GH_2, $FLOX/CH_4$, and LF_2/GH_2 propellant combinations. In accord with the performance analysis concepts presented in the Task I discussion, the injectors' influence on performance was deemed to be a function of their ability to atomize and uniformly mix the propellants. Elements investigated include basic impinging, basic concentric tube, concentric tube with swirler, impinging concentric, and tricentric with centerbody types.

Injector characterization was accomplished primarily by means of tests using nonreactive propellant simulants. These cold-flow tests were conducted to determine the propellant droplet sizes, the dropsize distribution, and the mass and mixture ratio distribution for the various injector elements, sized to match hot-firing designs from about 50-to 5000-lbf (222 to 22,200 N) thrust/element.

It should be noted that throughout Task II the emphasis was placed on breadth in lieu of intensity of the investigation. This is appropriate in lieu of the fact that this work represents the first application of the subject cold-flow injector characterization techniques to simulate gas/liquid injector. The inclusion of diverse types of injector concepts together with the many design and operating variables and the desired broad scope of application presented a very large potential test matrix. To span these conditions with a limited allocation of tests, emphasis was placed upon (1) defining key or controlling parameters, and (2) determining trends in atomization and mixing with these variables. Thus, in many cases, "two-point curves" were generated and extensive use was made of cross-plots and interpolation.

DESIGN OF COLD-FLOW INJECTORS

A mathematical analysis was performed to determine the requirements for cold-flow modeling of a hot-firing gas/liquid rocket engine injector. This analysis was

supported by another program; however, results are directly applicable and are briefly summarized here. The approach was to (1) set up the physical equations applicable to gas/liquid flow processes and gas/liquid interactions, (2) nondimensionalize the equations, and (3) determine a minimum set of parameters or groups of parameters necessary to describe the resultant two-phase flow field.

To obtain information of general applicability and to maintain simplicity, two zones were considered. The first, Zone I, was characterized by interaction between a gas stream and a single liquid jet. Zone II, on the other hand, involved interaction between the gas and liquid spray of a two-phase flow field. It was concluded that the Zone II-type, ambient-pressure cold-flow simulation should be avoided. In other words, cold-flow measurements should be made fairly close to the injector, near the axial region where spray formation is completed. This requirement is in accord with existing combustion analysis at Rocketdyne whereby analytical models are relied upon to describe the downstream flow processes and combustion phenomena.

The dominant parameters for Zone I were indicated to be the injected gas/liquid momentum ratio, the dynamic pressure of the injected gas $\left(\rho_g V_g^2\right)$ and a geometric scale factor, e.g., the gas jet diameter $\left(D_g\right)$. Relative dimensions of other orifices and their spacing and impingement angles should also match those of the injector being simulated.

The cold-flow injectors were designed to have the same range of orifice dimensions as the hot-firing elements they model. It was desirable to produce correlations applicable to gas/liquid propellant combinations normally employed at mixture ratios from 5.0 to 15.0; furthermore, the range of interest for (hot firing) gas densities and velocities was broad. Thus, even for a given thrust/element level the simulated hot firing oxidizer and fuel injection areas cover a wide range, e.g., at 5000 lbf (22,200 N) thrust/element liquid injection areas of interest vary from 0.16 to 0.41 $in.^2$ $\left(1.03 \text{ to } 2.64 \times 10^{-4} \ m^2\right)$ while those of the gas vary from 0.12 to 1.08 $in.^2$ $\left(0.77 \text{ to } 6.97 \times 10^{-4} \ m^2\right)$. Variations in simulated thrust per element call for further proportionate changes in orifice flow areas. Design of a nominal or baseline model injector was generated for each element type and

average values were selected for the orifice sizes. Parametric changes in these dimensions during the cold-flow testing were designed to permit interpolation or extrapolation of the results for application to specific propellant systems at specific operating conditions. Because of the importance of varying orifice sizes, each type of model injector was designed to permit maximum use of inserts and sleeves.

Impinging Stream Injector Model

As a result of the planned sequence of testing, the first injectors to be designed were the basic impinging stream types. Simple impinging gas/liquid elements, in general, involve the spacing of a number (e.g., one for a doublet, two for a triplet, etc.) of liquid jets about a central showerhead gas jet. Three configurations of impinging jet injectors were used for the subject (Task II) tests: (1) pentad, (2) triplet, and (3) unlike doublet. The pentad type was selected as the baseline impinging jet pattern. The impinging jet injector was designed to facilitate changing the number of liquid jets in addition to varying orifice diameters. Removable orifice tubes of various sizes were held in the injector block with collet chucks. This enabled simple variation of orifice diameters while maintaining the rigidity required. In addition, the actual orifice tubes were designed to protrude from the injector block making it possible to maintain the free stream length-to-diameter ratio (L/D) approximately constant for both the gas and the liquid jets. The gas free stream L/D was kept at approximately 2 and the liquid free stream L/D's were as close as possible to 6. The orifices contained rounded entrances and an L/D of approximately 10 to obtain repeatable turbulent flow characteristics. These requirements were included to prevent extraneous effects caused by varying injector hydraulics. A sketch of the impinging injector block assembly and a collet chuck is presented in Fig. 34.

The atomization test model simulated orifice areas of approximately 50-to 2500-lbf (222 to 11,100 N) thrust/element injectors, while mixing test model areas corresponded to 500 to 5000 lbf (2220 to 22,200 N) thrust/element. The baseline model for the atomization tests had a nominal gas-side injection area of 0.27 in.^{2} (1.74×10^{-4} m^2) at the 2500-lbf (11,100 N) thrust/element level. The baseline mixing

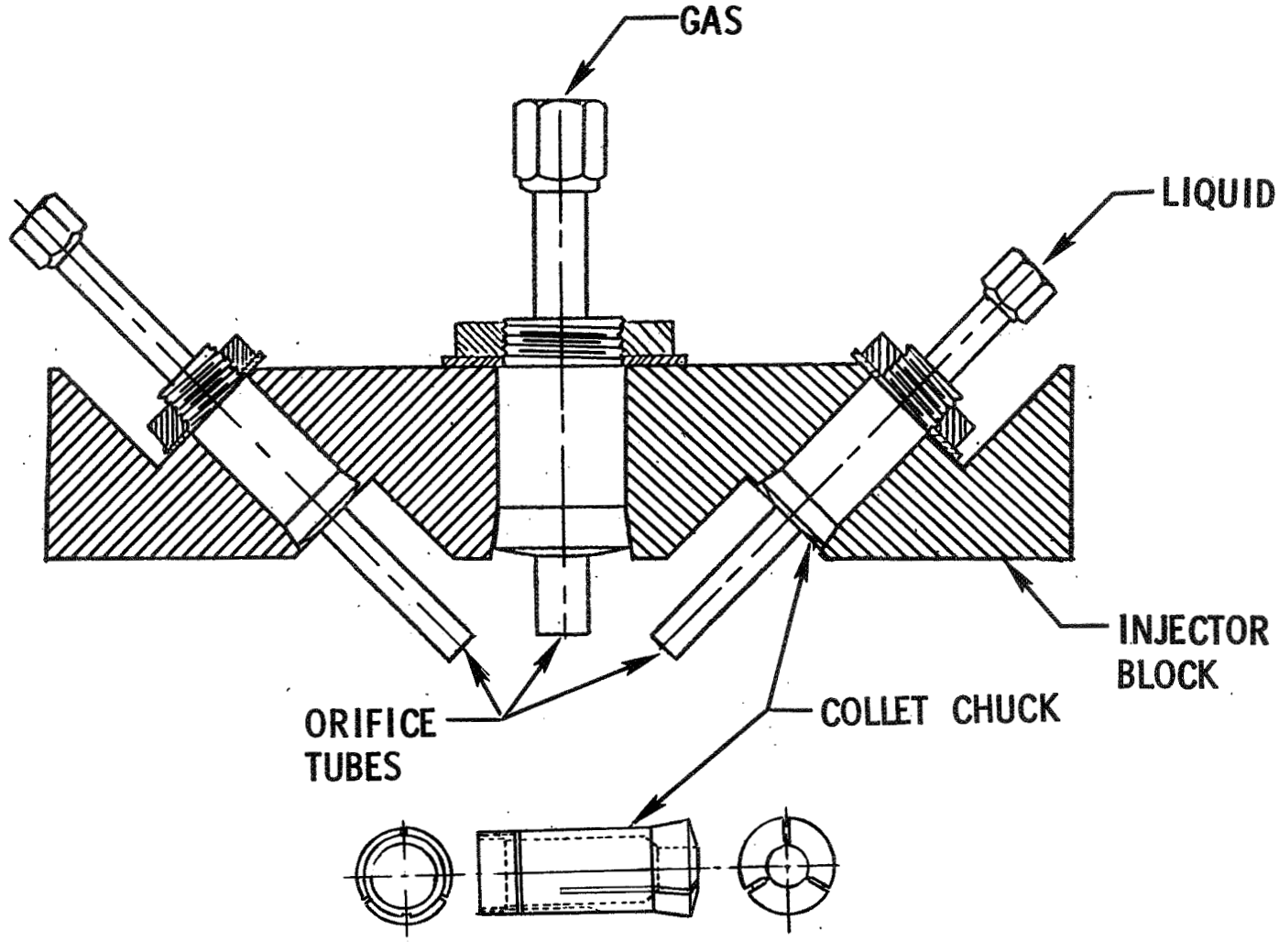

Figure 34. Basic Impinging Stream Injector

test model was designed with a gas-side injection area of 0.5 in.^{2} $\left(3.23 \times 10^{-4}\ m^2\right)$ at the 5000-lbf (22,200 N) thrust/element level. Selected orifice dimensions are listed in Table 6 . For each case the included angle between impinging gas and liquid stream was 45 deg (0.79 rad).

TABLE 6

BASIC IMPINGING STREAM INJECTOR ORIFICE DIMENSIONS

Atomization Model					Mixing Model			
Gas Orifice Size (D_g)		Liquid Orifice Size (D_ℓ)			Gas Orifice Size (D_g)		Liquid Orifice Size (D_ℓ)	
in.	m x 10^{-2}	in.	m x 10^{-2}	Element Type	in.	m x 10^{-2}	in.	m x 10^{-2}
0.259 to 0.810	0.658 to 2.057	0.067 to 0.206	0.170 to 0.523	Pentad	0.277 to 0.810	0.704 to 2.057	0.084 to 0.435	0.213 to 1.105
0.584	1.483	0.206	0.523	Triplet	0.810	2.057	0.334	0.848
0.584	1.483	0.206	0.523	Unlike Doublet	0.810	2.057	0.334	0.848

Concentric Tube Injector Model

The basic concentric tube configuration permitted variation of liquid orifice diameter, gas annulus gap, and post recess. A sketch of the injector assembly, Fig. 35, illustrates how this was accomplished. The two removable sleeves plus the liquid post permitted variation of the gas and liquid injection areas, either separately or together. Hot-firing experience indicated the oxidizer center post should have as thin a wall as feasible. The post wall thickness was selected to be 0.065 in. $\left(0.165 \times 10^{-2}\ m\right)$ for a 5000-lbf (22,200 N) thrust/element injector $\left(0.620\right.$ in. or $\left.1.575 \times 10^{-2}\ m\right.$ post ID$)$ and was reduced in proportion to the post ID for smaller injector elements. Post recess was varied by adjustment of the post location within its sleeve. Two gas-side inlets were used to minimize flow

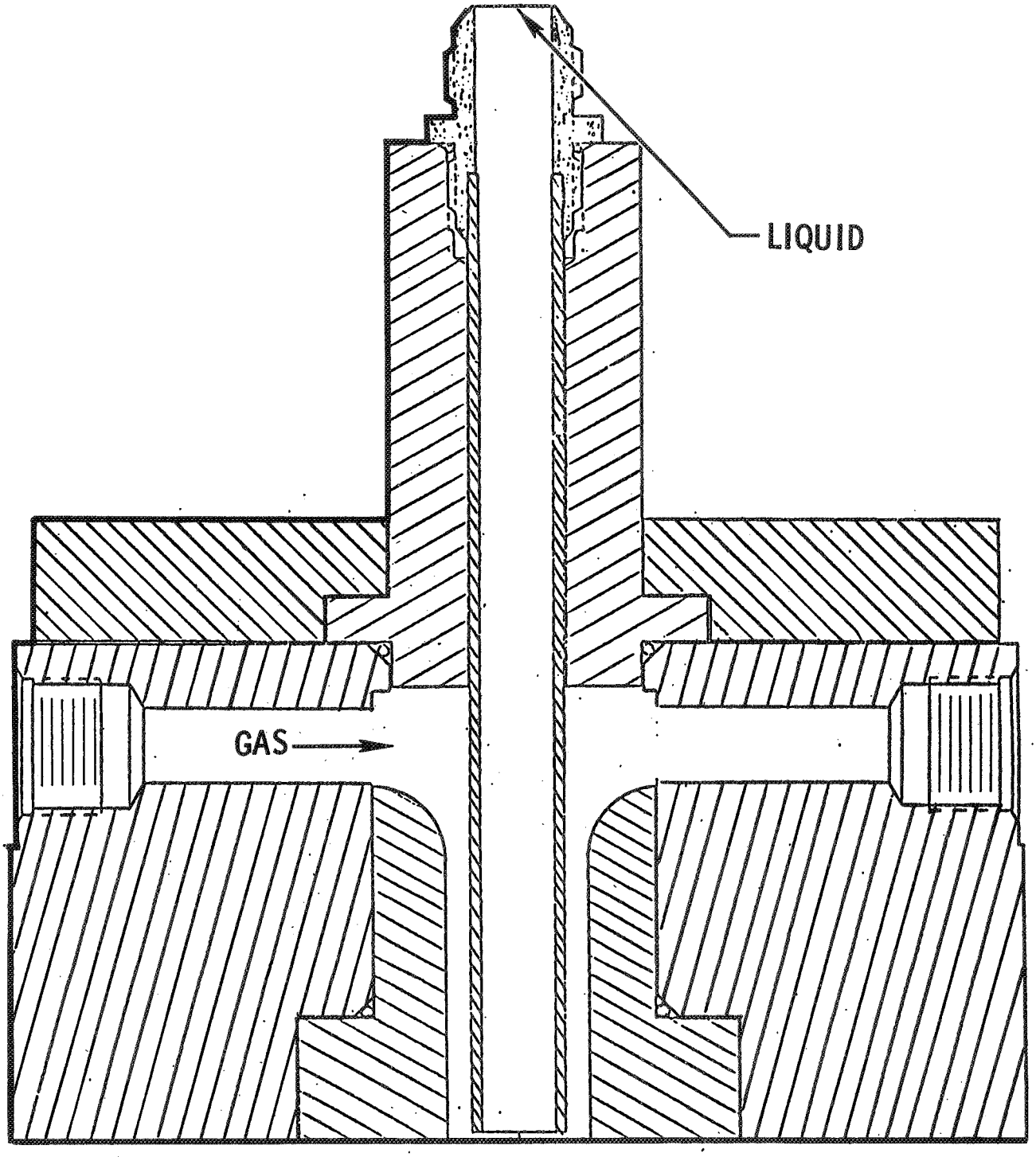

Figure 35. Basic Concentric Tube Injector

maldistribution in the annular gas injection orifice. In addition, all orifices contained rounded entrances and an L/D of approximately 15 to obtain repeatable turbulent flow characteristics.

Specific model orifice dimensions for the basic concentric tube mixing and atomization tests are listed in Table 7. For the mixing tests, the nominal area for a 5000-lbf (22,200 N) thrust/element injector was taken as the baseline area, i.e., 0.302 in.^{2} $\left(1.95 \times 10^{-4}\ m^2\right)$ for the liquid orifice area. This area was then reduced by a factor of 10 (500-lbf or 2220 N thrust/element) for the scaling tests. The post thickness was set at 0.065 in. $\left(0.165 \times 10^{-2}\ m\right)$ for the baseline injector model and scaled to 0.022 in. $\left(0.056 \times 10^{-2}\ m\right)$ for the 500-lbf (2220 N) thrust/element model. For the atomization tests, the baseline model areas were selected based on 1000-lbf (4450 N) thrust/element and also reduced by a factor of 10 for scale effects tests. The baseline and scaled injectors for the atomization tests were at a somewhat lower thrust level than the mixing tests, because of anticipated atomization (wax) facility limitations.

TABLE 7

BASIC CONCENTRIC TUBE INJECTOR ORIFICE DIMENSIONS

	Liquid Orifice Size (D_ℓ)		Post Thickness		Gas Annulus Gap		Post Recess	
	in.	m x 10^{-2}	in.	m x 10^{-2}	in.	m x 10^{-2}	in.	m x 10^{-2}
Mixing Model	0.620	1.575	0.065	0.165	0.225	0.572	1.20 0.60 0.0	3.05 1.52 0.0
	0.206	0.523	0.022	0.056	0.067	0.170	0.38 0.19 0.0	0.97 0.48 0.0
Atomization Model	0.277	0.704	0.029	0.074	0.102	0.259	0.54 0.27 0.0	1.37 0.69 0.0
	0.077	0.196	0.008	0.020	0.031	0.079	0.15 0.08 0.0	0.38 0.19 0.0

The concentricity of the gas annulus was maintained by two sets of three fins spaced 120 deg (2.09 rad) apart, protruding from the liquid posts at approximately 20 and 60 gap widths from the injector face. In addition, the concentricity of each injector model was maintained (as measured with drill blanks) to within an approximate 5-percent tolerance.

Concentric Tube With Swirler Injector Model

The concentric tube with swirler injector concept was designed with swirl developed by two tangential-entry liquid passages into the base of the liquid orifice. This (hydraulic swirl) design permitted use of most of the basic concentric tube hardware, requiring modification only of the inlet manifold to the oxidizer post. This design had an additional advantage in that a direct comparison could be made between the basic concentric tube and the concentric tube with swirler injector concepts at constant orifice diameters and simulated propellant flowrates. An assembly sketch of the concentric tube with swirler design is presented in Fig. 36. The primary dimensions for the mixing and atomization tests are given in Table 8.

TABLE 8

CONCENTRIC TUBE WITH SWIRLER INJECTOR DIMENSIONS

	Liquid Orifice Size (D_ℓ)		Post Thickness		Gas Annulus Gap (Y_g)		Swirl Inlet Diameter,* (D_s)	
	in.	m x 10^{-2}	in.	m x 10^{-2}	in.	m x 10^{-2}	in.	m x 10^{-2}
Mixing Model	0.206	0.523	0.022	0.056	0.067	0.170	0.136	0.346
	0.206	0.523	0.022	0.056	0.067	0.170	0.086	0.218
	0.206	0.523	0.022	0.056	0.067	0.170	0.070	0.178
Atomization Model	0.277	0.704	0.029	0.074	0.102	0.259	0.194	0.493
	0.277	0.704	0.029	0.074	0.102	0.259	0.136	0.346
	0.277	0.704	0.029	0.074	0.102	0.259	0.096	0.244
	0.277	0.704	0.029	0.074	0.102	0.259	0.070	0.178
	0.277	0.704	0.029	0.074	0.102	0.259	0.055	0.140

*Two inlets used

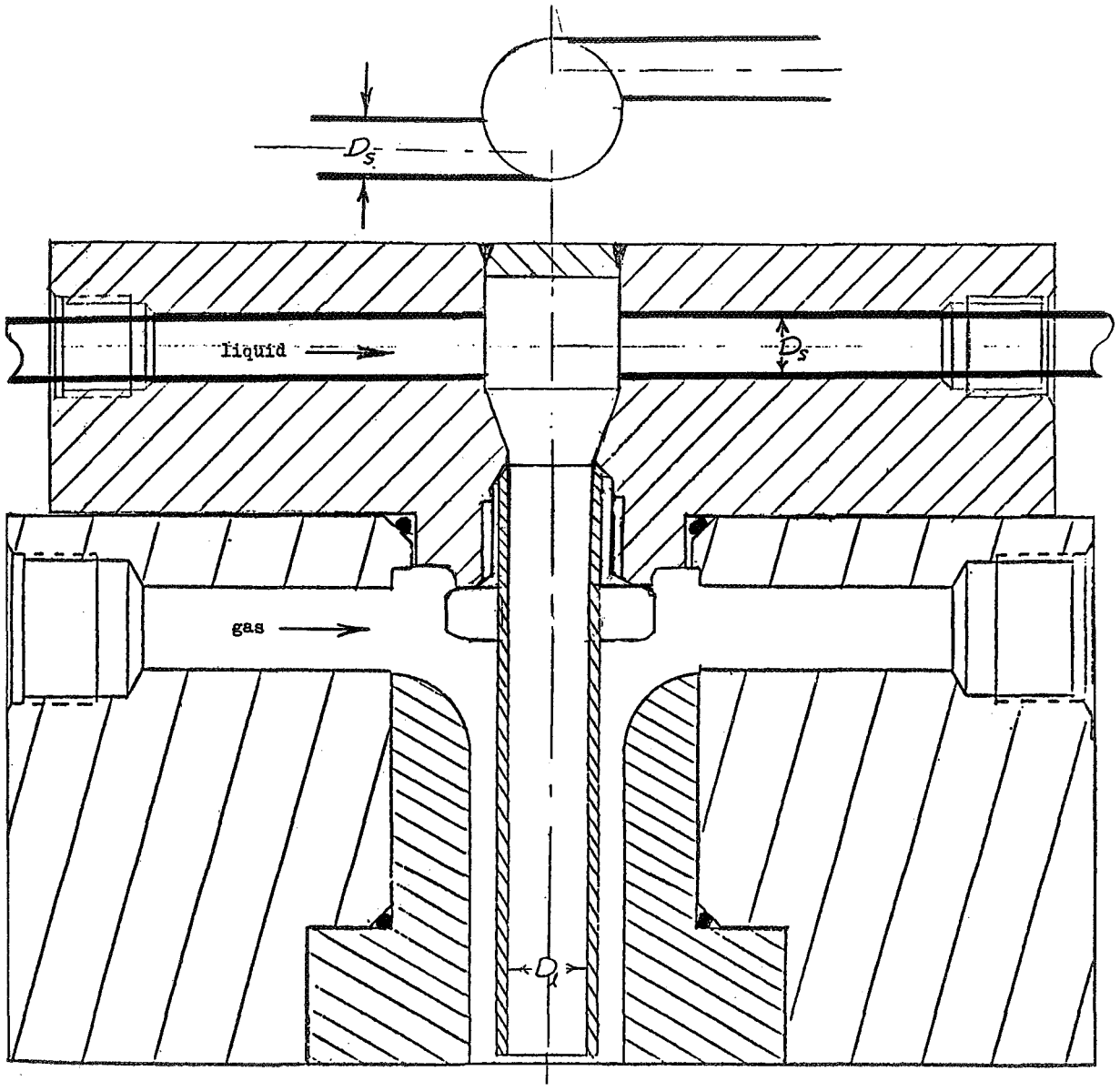

Figure 36. Concentric Tube Injector With Swirler

The 5000-lbf (22,200 N) thrust/element size was selected as maximum for the mixing test model as was the 1000-lbf (4450 N) thrust/element size for the atomization tests. All tests were conducted with the zero recess configurations. Annulus concentricity was maintained as described for the basic concentric configuration.

Primary variables for the concentric tube with swirl tests were the liquid swirl velocity and the gas injection velocity. The former was varied by insertion of variable size swirl tubes, which were held in by Swagelok fittings, while the latter was to be varied by simultaneously throttling both the gas and the liquid flowrates.

Impinging Concentric Tube Injector Model

This configuration consisted of four liquid/gas concentric elements (liquid in the center) impinging on a central showerhead gas stream. The injector pattern was similar to the impinging concentric injector used under Contract NAS3-7962 and used in the cold-flow and hot-fire injector study conducted under Task I of the subject contract. The main difference was the absence of the recessed cup, which was utilized in these previous studies, and in the change in the included angle between opposing liquid/gas coaxial tubes.

The impinging concentric design incorporated portions of the basic impinging stream and basic concentric tube injector designs. The injector block and collet chuck-type assembly was used for the impinging concentric elements to facilitate size changes in the liquid/gas coaxial and the central gas injection tubes. In addition, this made it possible to hold the free stream length-to-diameter ratio approximately constant for both the gas and liquid jets by allowing the orifice tubes to protrude from the injection block. The gas and liquid free stream L/D's were kept at approximately 2 and 6, respectively, while the orifice L/D's was maintained at approximately 10. The gas/liquid coaxial tubes were manifolded with a Swagelok tee and Swagelok reducer combination. The degree of concentricity of the coaxial tubes was again maintained by the methods used with the basic concentric concept. Adjustable

supports were added to the injector block to hold the manifolds. An assembly sketch of the impinging concentric design is presented in Fig. 37. The primary dimensions for the mixing and atomization tests are given in Table 9.

TABLE 9

IMPINGING CONCENTRIC TUBE INJECTOR DIMENSIONS

	Gas Orifice Diameter (D_g)		Liquid Orifice* Diameter (D_ℓ)		Gas Annulus* Gap (Y_g)		Post Thickness	
	in.	m x10^{-2}	in.	m x10^{-2}	in.	m x10^{-2}	in.	m x10^{-2}
Atomization Model	0.460	1.170	0.152	0.386	0.034	0.086	0.020	0.051
	0.745	1.892	0.152	0.386	0.034	0.086	0.020	0.051
	0.319	0.810	0.105	0.267	0.011	0.028	0.010	0.025
Mixing Model	0.620	1.575	0.194	0.493	0.060	0.153	0.028	0.071
	0.930	2.362	0.194	0.493	0.060	0.153	0.028	0.071
	0.319	0.810	0.105	0.267	0.011	0.028	0.010	0.025

*Four orifices used

The element sizes for this injector configuration corresponded to about 5000 to 1000 lbf (22,200 to 4450 N) thrust/element for the mixing tests and 2500 to 1000 lbf (11,100 to 4450 N) thrust/element for the atomization tests. In all cases, the impinging concentric tube elements contained zero recess.

Tricentric With Centerbody Injector Model

Details for the design of the tricentric-with-centerbody injector concept were planned so both the annulus gaps and centerbody diameters could be varied. A sketch of the hardware is presented in Fig. 38 and the primary dimensions for the three mixing and atomization test models are given in

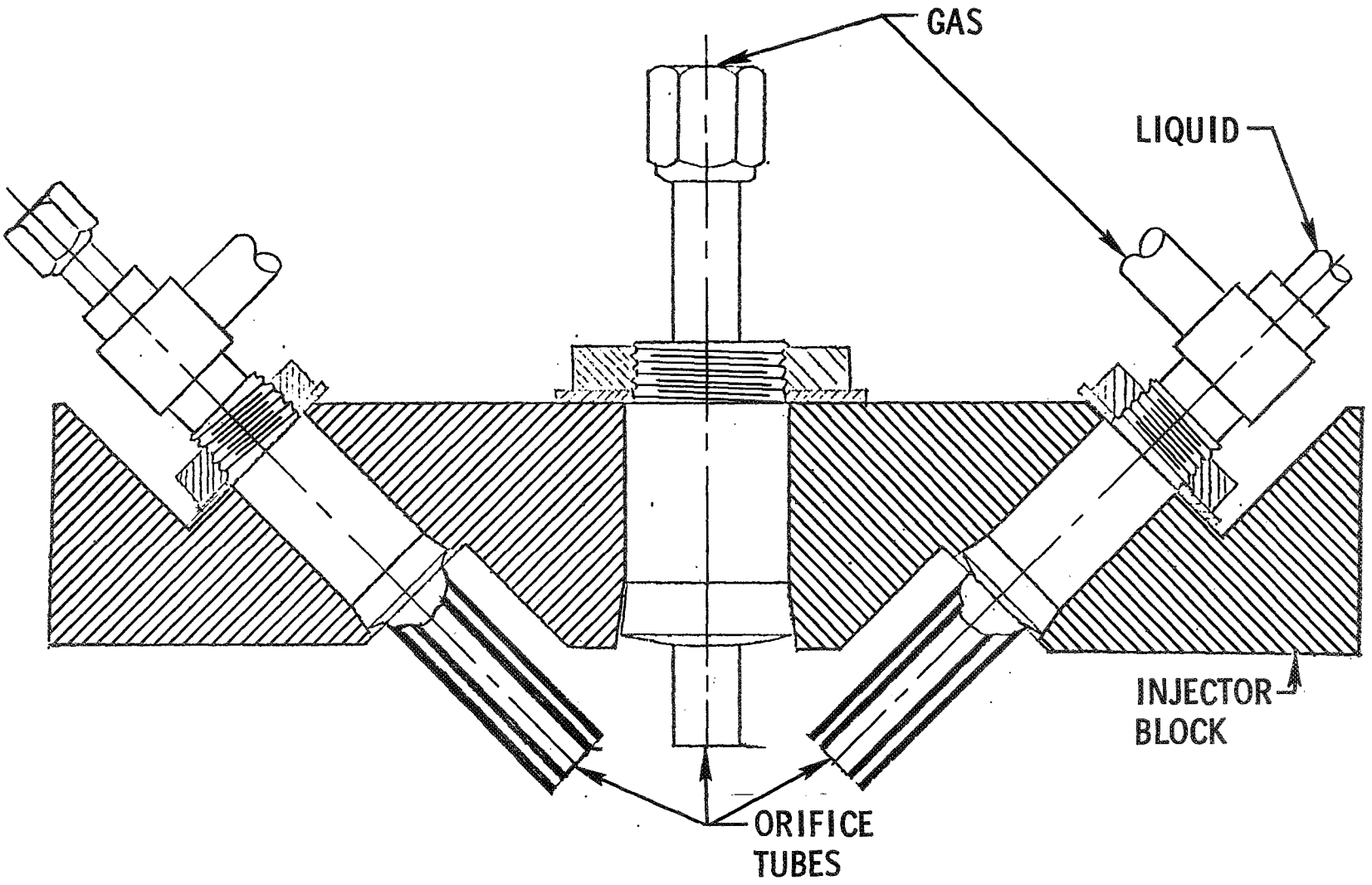

Figure 37. Impinging Concentric Tube Injector

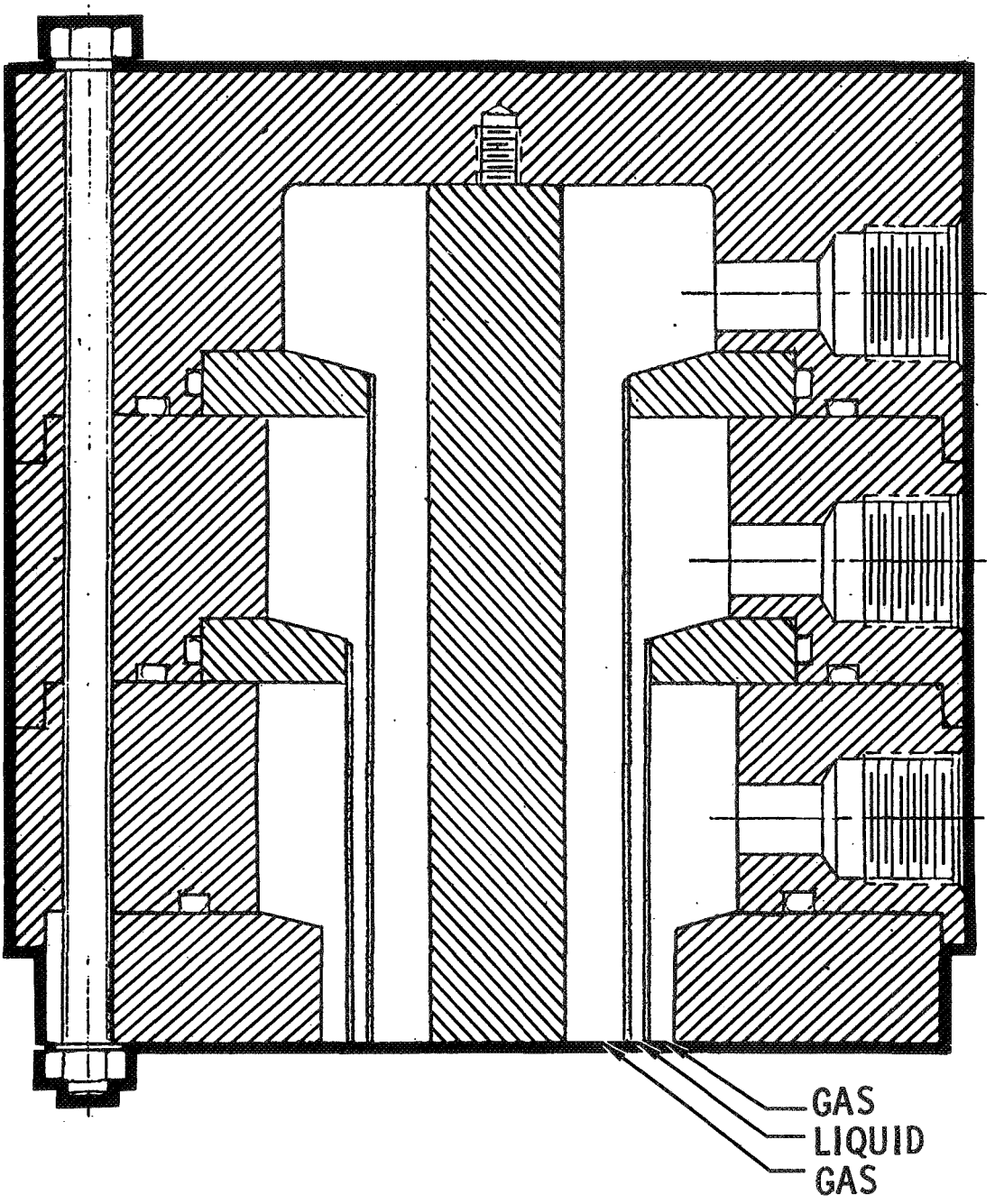

Figure 38. Tricentric Injector With Centerbody

Table 10. The same model sizes were used for both mixing and atomization tests, corresponding to approximately 2500 to 5000 lbf (11,100 to 22,200 N) thrust/element.

Wall thicknesses between annular passages were maintained constant at 0.035 in. $\left(0.089 \times 10^{-2} \text{ m}\right)$ for all configurations tested. Also, a zero recess was used for all configurations. Each of the annular passages was supplied through three inlet ports, thereby ensuring a more uniform flow distribution in each annulus. The degree of concentricity was again kept approximately uniform by the protruding fin arrangement described in the basic concentric section of this report. A photo of the baseline model with the 0.25-in. $\left(0.64 \times 10^{-2} \text{ m}\right)$ diameter centerbody is shown in Fig. 39.

TABLE 10

TRICENTRIC WITH CENTERBODY INJECTOR DIMENSIONS

Inner Gas Annulus			Liquid Annulus			Outer Gas Annulus		
ID, in. $(m \times 10^{-2})$	OD, in. $(m \times 10^{-2})$	$Y_{g'}$ in. $(m \times 10^{-2})$	ID, in. $(m \times 10^{-2})$	OD, in. $(m \times 10^{-2})$	$Y_{\ell'}$ in. $(m \times 10^{-2})$	ID, in. $(m \times 10^{-2})$	OD, in. $(m \times 10^{-2})$	Y_{g}, in. $(m \times 10^{-2})$
0.250 (0.635)	0.493 (1.252)	0.121 (0.307)	0.563 (1.430)	0.680 (1.728)	0.059 (0.150)	0.750 (1.905)	0.861 (2.185)	0.056 (0.142)
0.750 (1.905)	0.860 (2.183)	0.055 (0.140)	0.930 (2.360)	1.000 (2.540)	0.035 (0.089)	1.070 (2.720)	1.150 (2.920)	0.040 (0.102)
0.750 (1.905)	0.995 (2.525)	0.122 (0.310)	1.065 (2.705)	1.180 (3.000)	0.058 (0.147)	1.250 (3.175)	1.368 (3.475)	0.059 (0.150)

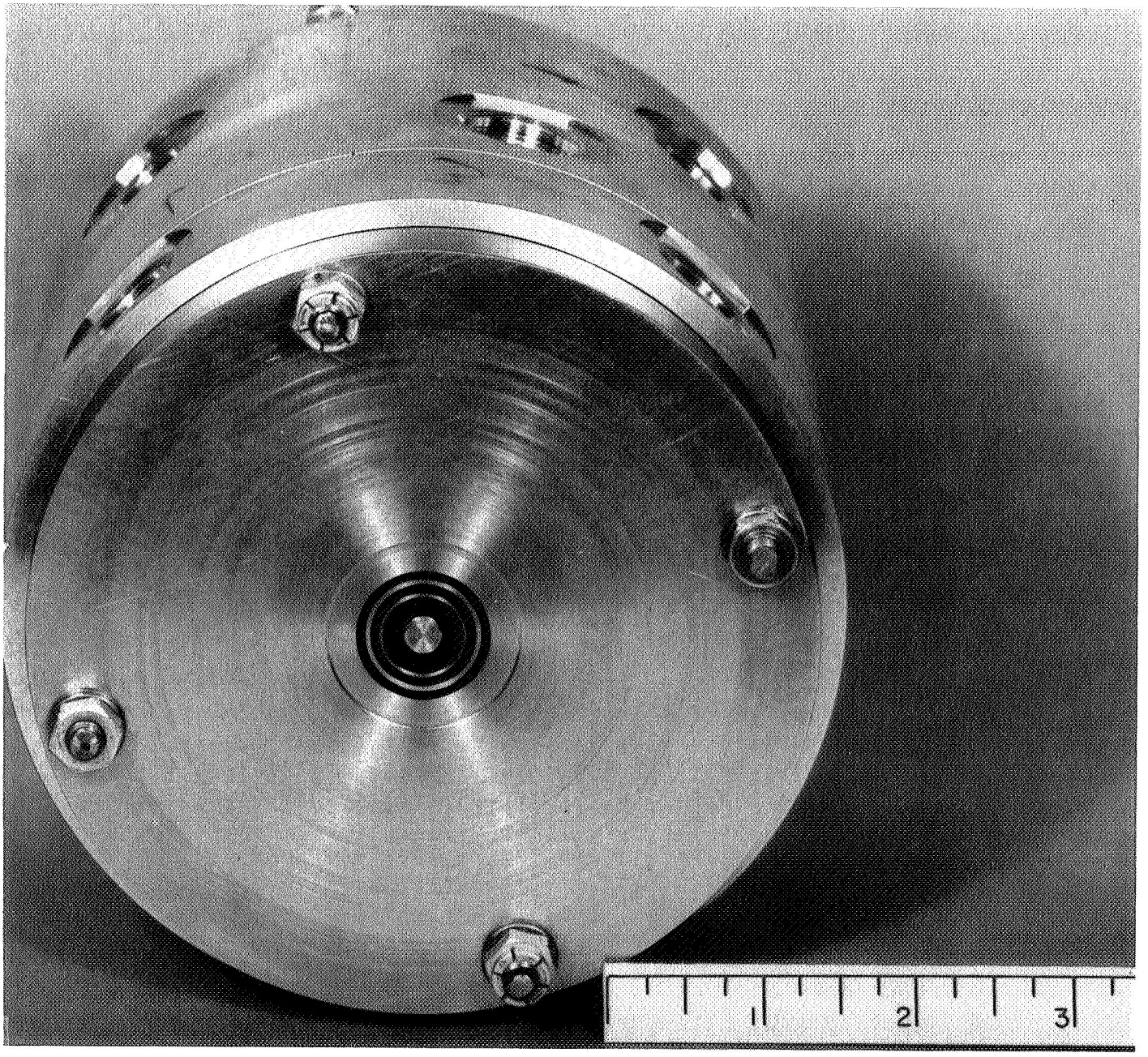

5AA31-12/10/69-S1

Figure 39. Tricentric With Centerbody Baseline Cold-Flow Injector

EXPERIMENTAL APPARATUS AND TEST PROCEDURES

The cold-flow distribution tests were conducted in the Propulsion Research Area (PRA) and the molten wax atomization (dropsize) tests were made at the Combustion and Heat Transfer Laboratory (CHTL) at Rocketdyne's Santa Susana Field Laboratory. Existing facilities were employed; however, a certain amount of facility preparation was necessary to accomplish the Task II objectives. A brief description of the existing facilities and the facility buildup is presented below, along with the test procedures for the respective flow distribution and atomization test systems.

Mass Flux and Mixture Ratio Distribution Test Facility

Facility Description. The cold-flow facility used for the Task II propellant mixing tests includes two 43-gal $\left(0.163\ m^3\right)$, 1440-psi $\left(9930 \times 10^3\ N/m^2\right)$ vessels and complete utility and high-pressure gas systems. The vessels are suitable for either water or trichloroethylene use as the liquid flow media. The testing at this facility is monitored from an adjacent control center.

The facility has a variety of mass flux and mixture ratio distribution collection and measuring equipment available for cold-flow injector characterization. The mass and mixture ratio measuring system is capable of sampling injectors producing sprays up to 10 in. (0.254 m) in diameter. The liquid sampling system, described under Task I, consists of a 10 by 10 matrix of 100 individual 1-in. $\left(2.54 \times 10^{-2}\ m\right)$ square-ended tubes. The gaseous mass flux distribution is measured by means of a specially designed impact probe* described in Appendix A. Gas total pressure profiles are taken along horizontal paths over an area corresponding to the liquid flowfield. In addition, the liquid mass distribution can be measured with the impact probe. Local valleys and peaks in mass flux and mixture ratio distribution can be readily ascertained within the flowfield.

*This probe also permits collection and measurement of liquid (spray) flows over a much finer mesh of locations than the 1-in. by 1-in. $\left(2.54 \times 10^{-2}\ m\right)$ square-ended tube matrix.

Flow system instrumentation consists of five Taber "Teledyne" series-bonded strain gage pressure transducers, two iron-constantan type J thermocouples, a Fischer-Porter turbine-type volumetric flowmeter, and a Flowdyne venturi. Measurements of water tank pressure, venturi upstream and throat pressures, propellant injection pressures, and gas temperature at the venturi and injector were made. These measurements were recorded on Dynalog direct-inking graphic recorders. The volumetric flowmeter signals were recorded on a CEC multichannel oscillograph.

A computer program permits machine calculation of the local mass flux and mixture ratio characteristics of a specific element or a multiple-element injector from the raw measurement data. Graphical presentation of the distribution profiles can be made by hand or by employment of cathode-ray, three-dimensional, machine plotting techniques.

To accomplish the test objectives in the most effective manner, several items were added to the existing facility. The gas/liquid distribution facility preparation consisted of four subtasks as follows:

1. Improvement of the two-phase impact probe design
2. Design, fabrication, and application of two-phase flow measurement calibration equipment for the impact probe
3. Fabrication of a two-dimensional traversing mechanism to accurately position the impact probe for the injector gas flow distribution measurements
4. Design, fabrication, and checkout of an oxygen sampling system to determine the amount of air ingestion at any point in the two-phase flowfield

The first two subtasks, although conducted under Task II, are described in Appendix A. The latter are described below.

Two-Dimensional Traversing Mechanism. A two-dimensional traversing mechanism was designed and fabricated to accurately and reproducibly position the impact probe in the flowfield generated by cold-flow injectors. A schematic and photograph of the traversing mechanisms are presented in Fig. 40 and 41, respectively. The impact probe was attached to the traversing block which is positioned by manual rotation of the two threaded shafts. The mechanism is capable of reproducibly positioning the impact probe to within 0.020 in. $\left(5.08 \times 10^{-4} \text{ m}\right)$.

The traversing mechanism was fabricated from stainless steel and bronze to prevent rusting in the moist flow environment. Teflon insert bearings were employed in each of the four guides which slide over the guide bars.

Oxygen Sampling System. During Task I of the subject contract, it was found that if gas mass flux distribution measurements were made at ambient conditions, the mass of ingested air may be quite significant. Consequently, a measurement of the ingested air at the measurement plane was necessary to define the distribution of the injected gas. The oxygen concentration was determined at each measurement point to determine the amount of air ingested. A schematic of the subject system was shown in Fig. 42.

The gas sample to be analyzed for oxygen concentration was drawn through the impact probe as illustrated in Fig. 42. The system was designed so that the previous gas sample would be purged with a vacuum pump from the system before a new gas sample was drawn into the sample chamber. The oxygen concentration in the sample chamber was measured by a commercially available Beckman Model 715 oxygen monitor. Because the instrument measured the partial pressure of the oxygen in the gas sample, it was necessary to measure the total pressure of the gas sample to determine the oxygen concentration. The pressure in the sample chamber was measured by a MKS Baratron pressure meter whose output was recorded by direct readout.

Checkout tests on the oxygen sampling system revealed operating procedure problems in measuring the concentrations of entrained air. It was found that

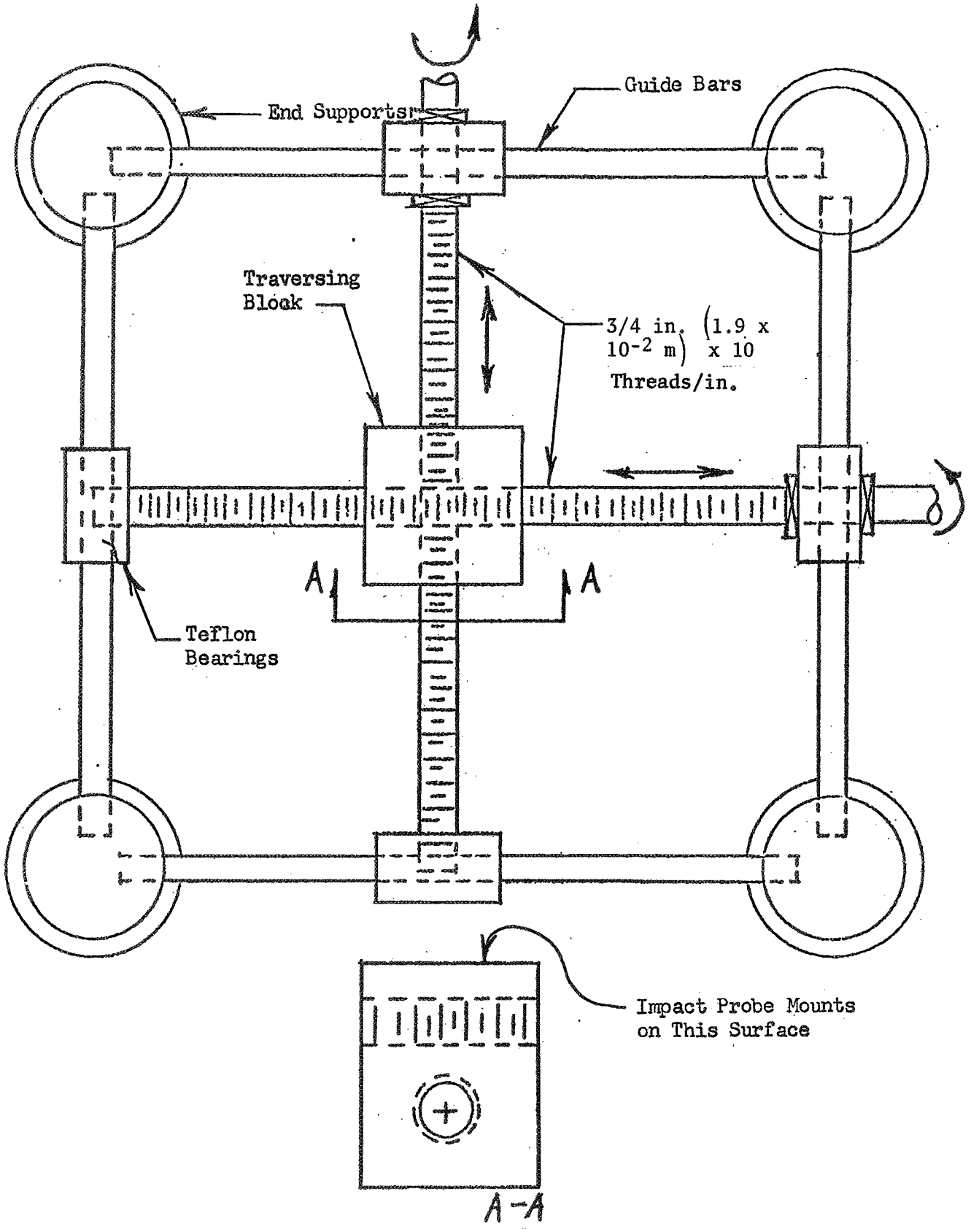

Figure 40. Two-Dimensional Traversing Mechanism

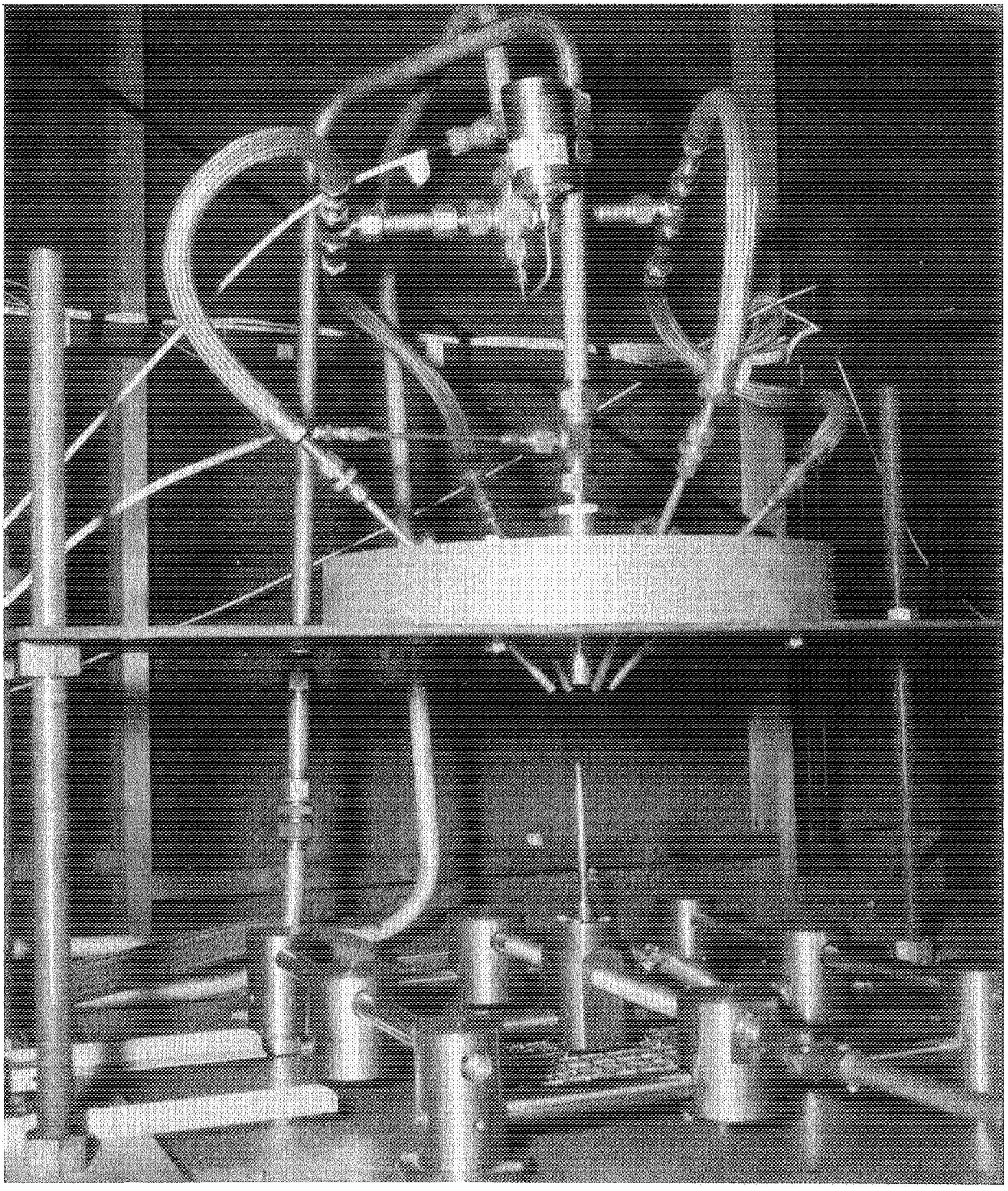

5AJ31-9/29/69-SIC

Figure 41. Basic Impinging Injector, Mixing Facility Traversing Mechanism and Impact Probe

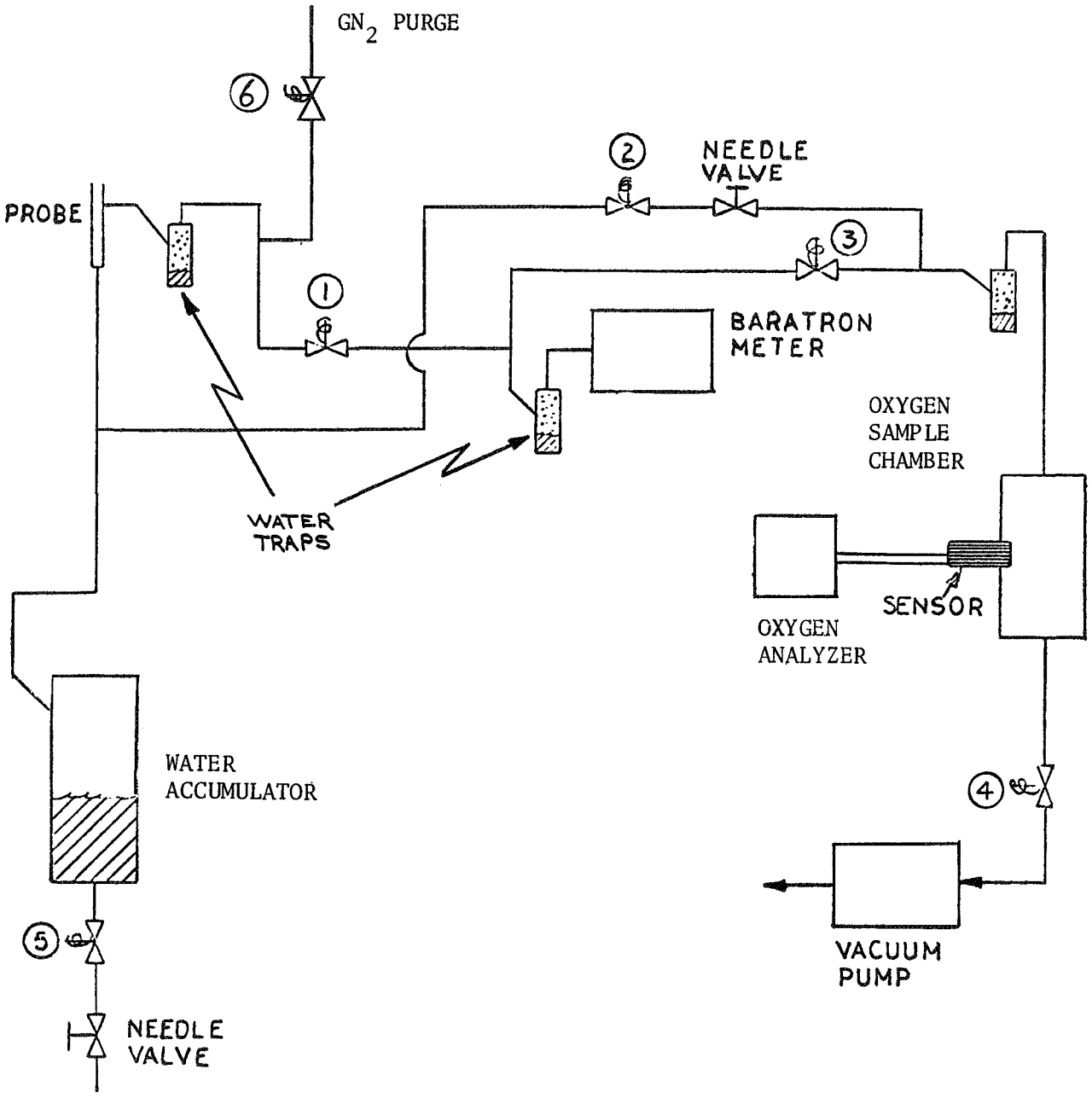

Figure 42. Mixing Facility Gas Sampling System

excessive moisture in the sample chamber affected the instrument's readings. In addition, the Baratron pressure meter was affected by moisture contamination. These problems were solved by the addition of water condensation traps upstream of the oxygen sampler and pressure meter (Fig. 42).

Mixing Test Procedure. For all tests, gas flow distributions were measured over the maximum area where measurable dynamic pressure readings could be obtained. Simultaneous liquid flow collections were acquired at each of these (closely spaced) points. When the injected gas and liquid flowfields coincided, no other measurements were necessary. In other cases, the liquid spray fields expanded enough to require additonal liquid flow measurements outside the gas flowfield, which were obtained with the 10-in. by 10-in. (0.254 x 0.254 m) collection grid. Both methods of data acquisition are described below.

Gas and liquid measurements made with the impact probe were accomplished as follows:

1. The liquid tank and gas venturi were pressurized to give the desired flowrates.
2. The impact probe was positioned in the two-phase flowfield with all valves closed.
3. The probe purge valve (No. 6) was opened to allow a GN_2 purge through the probe.*
4. The vacuum pump was turned on (valve No. 4 closed).
5. The injector liquid and gas main valves were opened.
6. After flowfield stabilization, the probe purge valve was closed, turning on a timer which was slaved to the probe purge valve.
7. Valve No. 1 was opened allowing the gas stagnation pressure to be measured.

*The GN_2 purge going through the probe allowed the overall flowfield to stabilize with no probe spray collection

8. Valve No. 1 was closed and valves No. 2, 3, and 4 were opened allowing the vacuum pump to purge the oxygen sampling system.

9. Valve No. 4 was closed and the injected gas sample was allowed to fill the oxygen sample chamber.

10. Upon reaching steady-state conditions in the oxygen sample chamber, valve No. 2 was closed and the chamber pressure and oxygen content were recorded from the Baratron and oxygen analyzer, respectively.

11. Valve No. 3 was closed and the probe purge valve was opened, thus turning off the timer.

12. The liquid and gas main valves were closed.

13. Valve No. 5 was opened and the liquid from the water accumulator was drained into a graduated cylinder. The volume of liquid and the flow duration were recorded.

14. The probe was moved to a new position.

The probe positioning was somewhat different with the impinging vs the concentric-type injectors. The initial probe position for both concepts was the geometric center of the injection area. The symmetry of the concentric element flowfield permitted a less extensive array of measurement locations; i.e., the grid for the concentric elements consisted of one ray with a 0.1- or 0.2-in. $\left(2.54 \text{ or } 5.08 \times 10^{-3} \text{ m}\right)$ spacing between probe positions, depending on the flowfield size. Some symmetry is retained with the impinging-type injector concepts; e.g., each quadrant with a pentad (each half with an unlike doublet) should be symmetrical about the appropriate centerlines. Therefore, the collection grid for the impinging pentad* injectors consisted of one quadrant with 0.2-in. $\left(5.08 \times 10^{-3} \text{ m}\right)$ spacing between probe positions. These data were then analytically mirrored into the other three quadrants. For both the concentric and impinging-type injectors, spot measurements were made to verify the assumptions of symmetry.

*The sample grid for the unlike doublet covered two quadrants.

Different collection distances were also used for the concentric and impinging injector investigations: 5-in. (0.127 m) collection distance with impinging and 3-in. (0.076 m) with concentric. These distances were chosen because prior analytical experience and photography indicated that they represented a good approximation of the primary propellant mixing region during combustion.

When the 1-in. $\left(2.54 \times 10^{-2}\ \text{m}\right)$ grid liquid collection measurements were made, the following procedure was used. The liquid and the gas systems were pressurized to give the desired flowrates. The main valves were opened and after injection pressures had become steady, a pneumatically actuated shutter was opened over the grid for a selected time interval and then closed. The main valves were then closed to conclude the test run. Time intervals were between 15 and 30 seconds for all injectors tested. The data recorded for each test included oxidizer and fuel simulant flowrates, injection pressures, flow duration, and the volume of oxidizer simulants collected in each of the 100 collection tubes. Volumetric measurements were obtained by use of graduated cylinders.

Atomization Test Facility

Facility Description. A previously existing wax flow facility (Fig. 43) was used, developed primarily for liquid/liquid injector dropsize measurements. The overall system consisted of two molten wax tanks, one hot water tank, pneumatic control valves, and a thermostatically controlled oil bath vessel in which the wax and water tanks are immersed. Associated flow and collection equipment included Taber injection pressure transducers, turbine (liquid) flowmeters, a particle collector, and a particle catch basin into which the wax particles were washed from the particle collector. The hot oil bath is electrically heated by means of a 30-kw $\left(30 \times 10^{3}\ \text{watts}\right)$ thermostatically controlled heater and an electrically operated pump which circulates the oil from the oil bath container through the heater and back again to ensure uniform temperature. In addition, hot oil is forced through the jacketed run

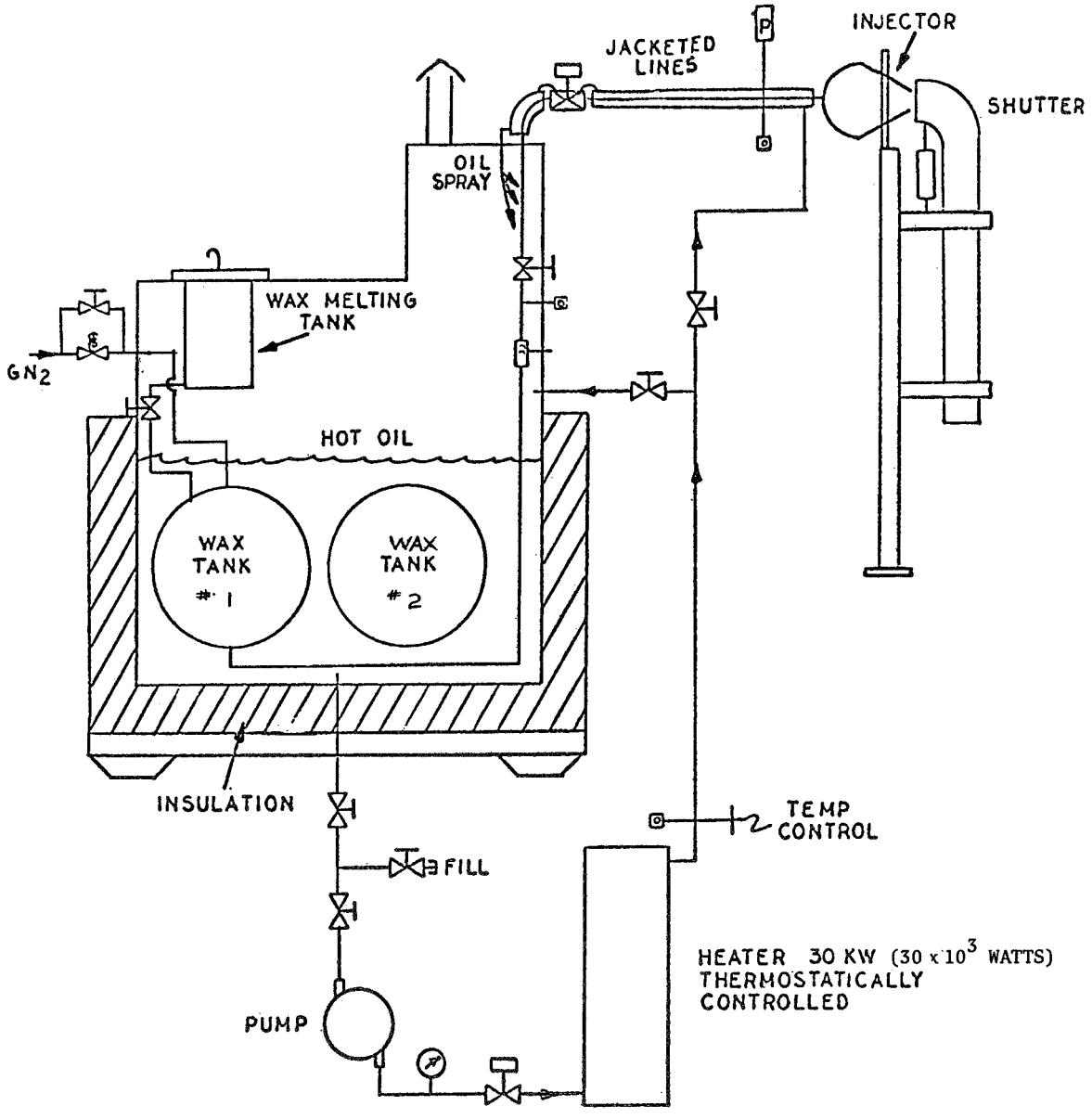

Figure 43. Schematic of Hot Oil Bath and Wax System for Molten Wax Facility

lines and valve to ensure that the wax does not freeze prior to injection. Each wax flow line (one from each tank) has three parallel line sections; each containing a flowmeter, a thermocouple, and a hand shutoff valve. A wide range of flowrates can be obtained by opening the hand shutoff valve leading to the flowmeter spanning the correct flowrate range.

A deflector tube (shutter) is used between the injector and the particle collector, which ducts the injected streams away from the collector until steady-state injector flow conditions are established. The deflector tube is moved by the use of a high-speed pneumatic actuator for the duration of the run and is replaced prior to simulant cutoff, thus eliminating wax particle collection during start and cutoff transients.

The particle collector is an 18-by 50-ft (5.5 x 15.3 m) epoxy-coated wooden platform which slopes gradually toward the center of the platform and away from the injector. The entire platform is located under a semi-enclosed structure which shields the collection area from wind currents which might cause the smaller particles to be blown away. The slope of the particle collector causes the wax droplets to be directed into a relatively small particle catch basin when the impact surface is washed down with water. The catch basin has several baffles to ensure that none of the wax particles are washed overboard.

To accommodate the testing of gas/liquid injector elements, a gas simulant system was installed as shown in Fig. 44. The gas simulant was heated to a temperature above the wax melting point to prevent freezing of the molten wax streams before atomization was completed. Gas heating was accomplished using a 30-kw $\left(30 \times 10^3 \text{ watts}\right)$ Chromalox circulation heater.

Gas could be supplied and regulated from two separate sources to provide flexibility in the choice of simulant gas. The temperature and pressure were measured upstream of the venturi flowmeter and the static pressure at the venturi throat was monitored to ensure that sonic flow was established. Gas injection pressure and temperature were also measured.

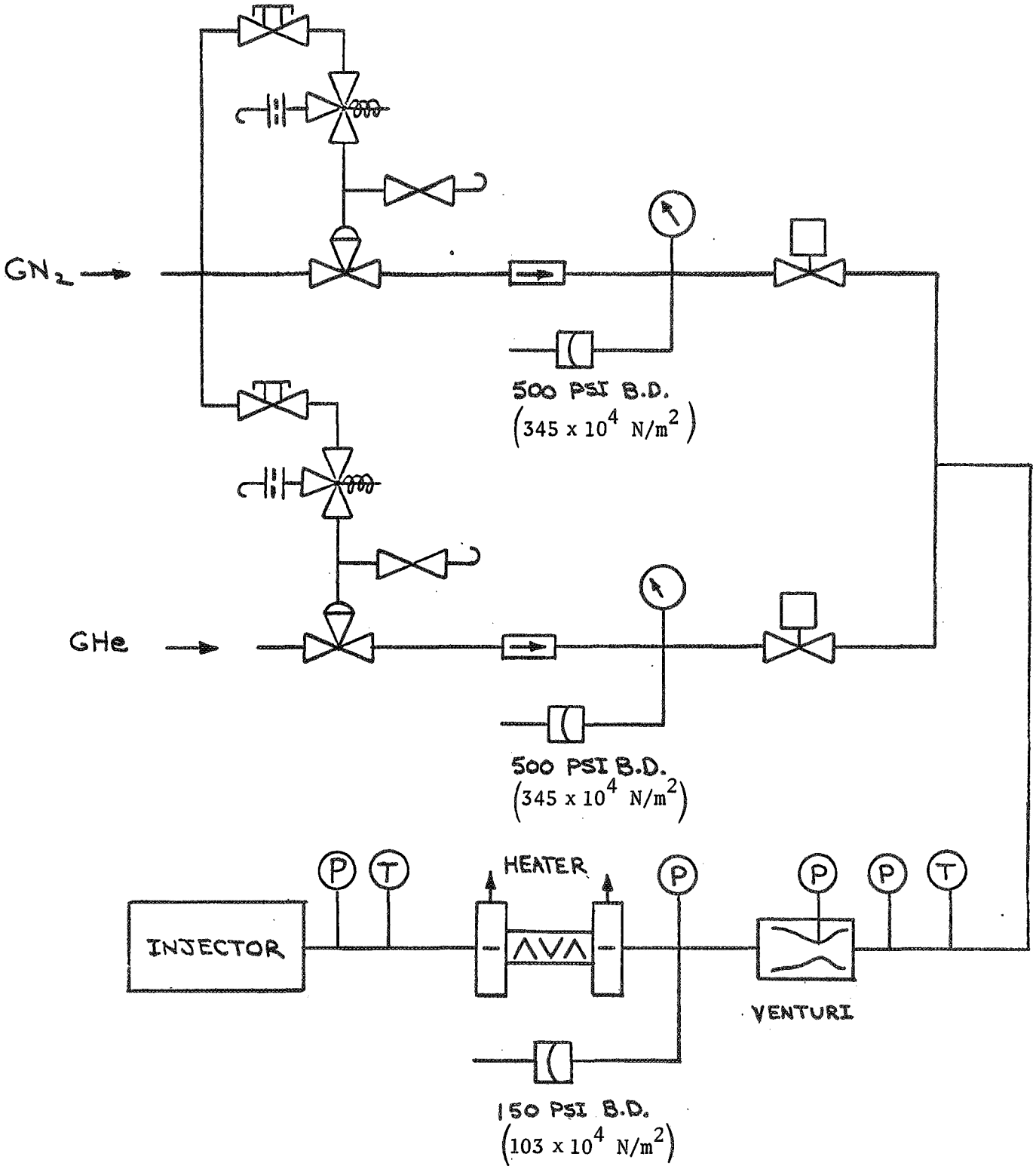

Figure 44. Schematic of Atomization Hot-Gas Supply System

Atomization Test Procedure. The procedure followed for the atomization tests was as follows:

1. The oil heater, used to heat the wax tanks and lines, was turned up to normal operating temperature and the entire wax flow system was heated above the melting temperature of the test wax.
2. The injector element was installed on the wax flow facility and oriented so that the wax spray created by the injector would enter the deflection shutter (up position).
3. After installing the required gas venturi, the heated GN_2 flow was established to heat the gas lines and injector manifold passages.
4. If the test gas was other than GN_2, the appropriate gas bottle bank was readied and short-duration flowrate checks were made.
5. The wax particle collection platform was cleaned by washing it down with water and a water sheet was established over 1/3 of the platform where the particles were expected to impact (to prevent sticking).
6. After selecting the required flowmeter, the wax tanks were pressurized and short-duration wax/gas flows were made into the shutter to determine the wax tank pressure and hand valve settings required for the desired wax flowrate.
7. The gas main valve was opened after which the wax main valve allowed both simulated propellant to flow into the deflection shutter.
8. The pneumatically actuated deflection was dropped after both flowrates were established and the wax particles were injected over the collection platform for from 3 to 20 seconds.
9. The deflection shutter was raised and the wax and gas main valves were closed.
10. The tanks were depressurized.
11. The particles were then washed with water from the particle impact surface into the particle collection vessel.

12. The particles were scooped from the surface of the water in the particle collection vessel and placed in a large plastic bag for temporary storage.

13. A 50-g $\left(50 \times 10^{-3} \text{ kg}\right)$ sample of particles was placed in a Buchner funnel and subjected to suction for removal of water which has adhered to the particles during the particle impact surface washdown.

14. After the particles had been partly dried by suction, they were removed from the Buchner funnel and placed in a vacuum chamber for a period of at least 48 hr $\left(173 \times 10^{3} \text{ sec}\right)$ to ensure that the particles were completely free of water.

15. After drying, the particle sample was sieved. A series of 23 standard testing sieves ranging in size from 53 to 2380 μ $\left(53 \text{ to } 2380 \times 10^{-6} \text{ m}\right)$ was available. For any particular sample, only 12 of the sieves were used, the particular sieve sizes used depending upon the anticipated size range. The particular sample of wax $\left(\text{usually 10 g or } 10 \times 10^{-3} \text{ kg}\right)$ was placed on the largest screen of the selected set of twelve sieves. The sieves were shaken on a RO-TAP automatic sieve shaker for 30 min (1800 sec), during which time the shaking was stopped once every 6 min (360 sec) to release any particles which became wedged in the sieve screens.

16. After the sieving operation was completed, the mass of particles retained on each sieve was weighed on an electric balance. A total recovery of 95 to 98 percent of the mass originally introduced into the sieves was possible.

Because of the high gas velocities involved, the testing of large thrust per element gas/liquid injectors raised concern about the ability of the wax collection platform to capture a sufficient percent of the injected wax particles. To investigate this problem, a check was made on the percent of

injected wax that was retained on the collection platform and subsequently recovered. The test results showed that over 96.5 percent of the wax sample was collected.

Normally only a portion of the collected wax particles were sieve-analyzed. To validate this procedure, multiple samples were obtained for the same test. Dropsize analysis showed differences of less than 2 percent in the entire dropsize distribution curves from these multiple samples.

Atomization Facility Checkout Tests

Under the subject program, the molten wax technique of modeling the atomization characteristics of rocket injectors was applied for the first time to gas/liquid injectors. A brief test series was run to evaluate the facility capabilities with regard to modeling moderately large thrust, gas/liquid impinging jet elements. Analysis of the data generated in these tests also provided some preliminary indication of the parametric influence of gas velocity and density. Four tests were conducted using a gas/liquid impinging doublet; three with a triplet, and two with a coaxial element. Table 11 summarizes the more significant operating conditions and the measured mass median dropsizes for these nine tests. Results indicated the limits of the facility capabilities to be a function of the wax flowrate and the dropsize distributions attained by the individual injector. No problems were encountered with the thrust-per-element sizes in the 2500-lbf (11,100 N) range for the impinging jet injectors and the 1000-lbf (4,450 N) range for the coaxial injectors. Still larger elements can be accommodated if they are relatively good atomizers and provide droplets small enough (e.g., $\overline{D} \sim 1000\ \mu$ or 10^{-3} m) to freeze prior to contact with the collection surface.

As a secondary result of these checkout tests, some initial indication of dropsize effects to be expected with various injectors was obtained and served to aid the planning of the Task II test matrices. The gas velocity influence on liquid dropsize observed in these checkout tests was similar for all three injector element types. The influence of gas density is

TABLE 11

PRELIMINARY COLD-FLOW ATOMIZATION TEST RESULTS

Run	Injector	Simulant Gas	V_g		$\rho_g V_g^2$		$\dot{w}_g$		$\dot{w}_\ell$		Measured $\overline{D}$,
			ft/sec	m/s	$lb/in.^2$	$N/m^2 \times 10^4$	lb/sec	N/s	lb/sec	N/s	μ or m x 10^{-6}
1	Unlike Doublet	N_2	1060	323	16.81	11.60	0.032	0.143	0.160	0.716	163
2		N_2	577	176	4.38	3.02	0.015	0.067	0.075	0.336	250
3		H_e	1120	342	2.35	1.62	0.004	0.018	0.057	0.255	310
4		H_e	2820	860	17.47	12.05	0.012	0.053	0.160	0.716	160
5	Triplet	N_2	1150	355	20.27	13.98	0.270	1.210	1.500	6.710	250
6		N_2	1150	355	20.27	13.98	0.270	1.210	1.500	6.710	240
7		N_2	530	162	3.68	2.54	0.120	0.537	1.500	6.710	375
8	Coaxial	N_2	650	198	5.56	3.83	0.130	0.582	0.580	2.600	540
9		N_2	465	142	2.84	1.96	0.100	0.448	0.580	2.600	680

illustrated in Fig. 45, in which $\overline{D}$, obtained from the impinging gas/liquid unlike doublet tests, is plotted against gas velocity for both nitrogen and helium gas tests. As expected, poorer atomization was obtained with the lighter gas at a given gas velocity. Another method of presentation was suggested by a consideration of the general differential equations governing interaction between a gas stream and a single liquid jet. A characteristic parameter obtained in this manner was the gas momentum flux $\left(\rho_g V_g^2\right)$. In Fig. 46 the helium and nitrogen test data for the unlike doublet element are correlated by a single straight line when the median dropsize is expressed as a function of $\rho_g V_g^2$. For this injector, median dropsize is proportional to $\left(\rho_g V_g^2\right)^{-1/3}$.

DATA REDUCTION PROCEDURE

As mentioned in the Task I analysis, the performance analysis approach used requires evaluation of two principal modes of performance losses: (1) incomplete propellant spray vaporization and (2) imperfect mixing of fuel and oxidizer. The cold-flow tests simulating each of these modes will be described in a subsequent section. The reduction of these data into a form from which quantitative comparisons may be made of both vaporization and mixing losses is described in the following sections.

Propellant Atomization Test Data

The raw data obtained in an atomization test included the sieved dropsizes and the mass of wax particles retained on each of the 12 sieves used. These data were then converted into terms of the total (cumulative) fraction of mass. An examples of the results from this operation are shown in the characteristic "S" curve presented in Fig. 47. This cumulative weight fraction versus particle diameter was curve fit by an IBM-360 computer program into a simple fourth-order polynomial. Then a particle size mass mean dropsize can be calculated with a cumulative weight fraction equal to 0.5. This mass median particle diameter ($\overline{D}$) was used to nondimensionalize the array of particle diameters, thereby yielding a curve of the cumulative weight fraction

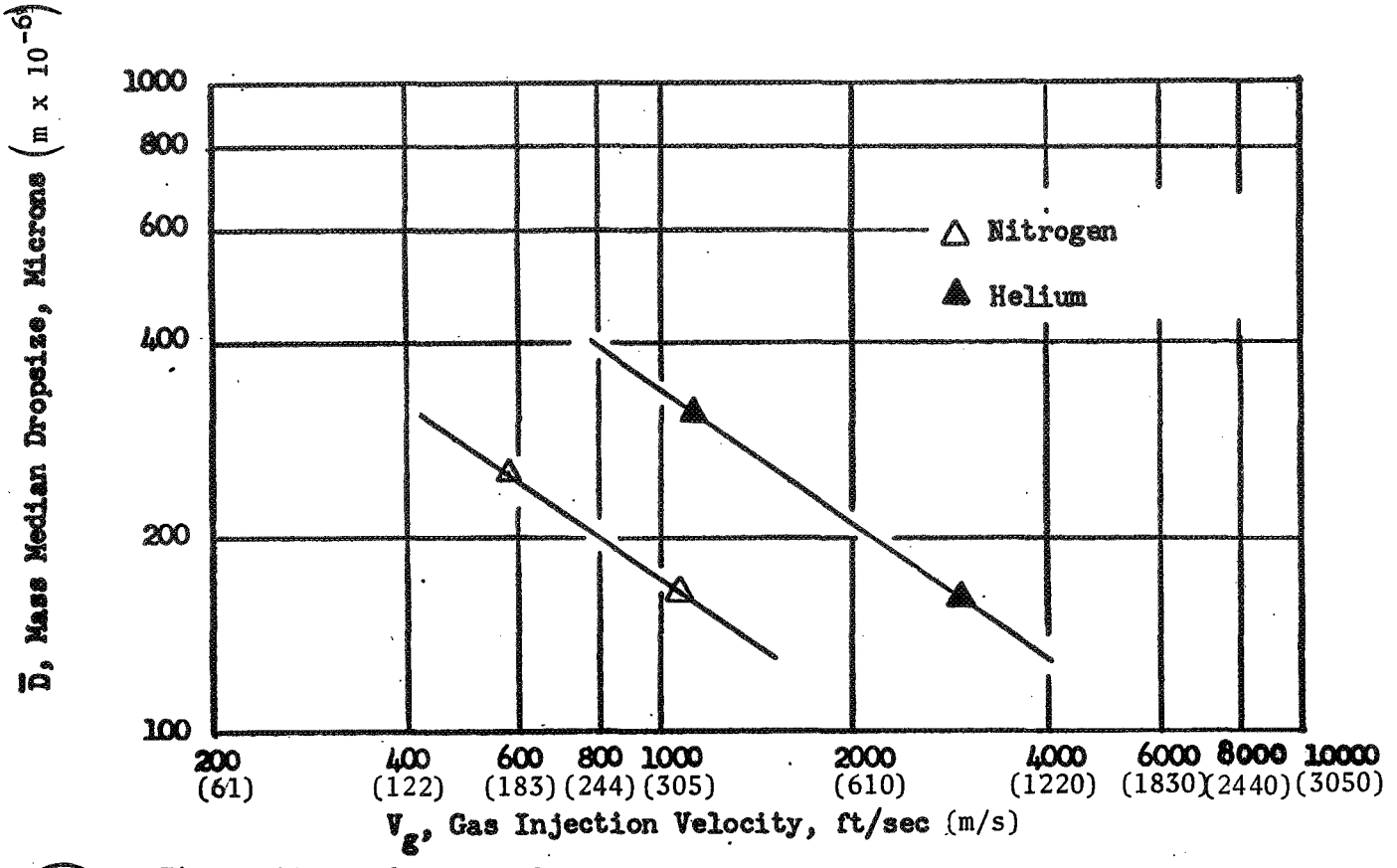

Figure 45. Influence of Gas Density on Unlike Doublet Element Dropsize

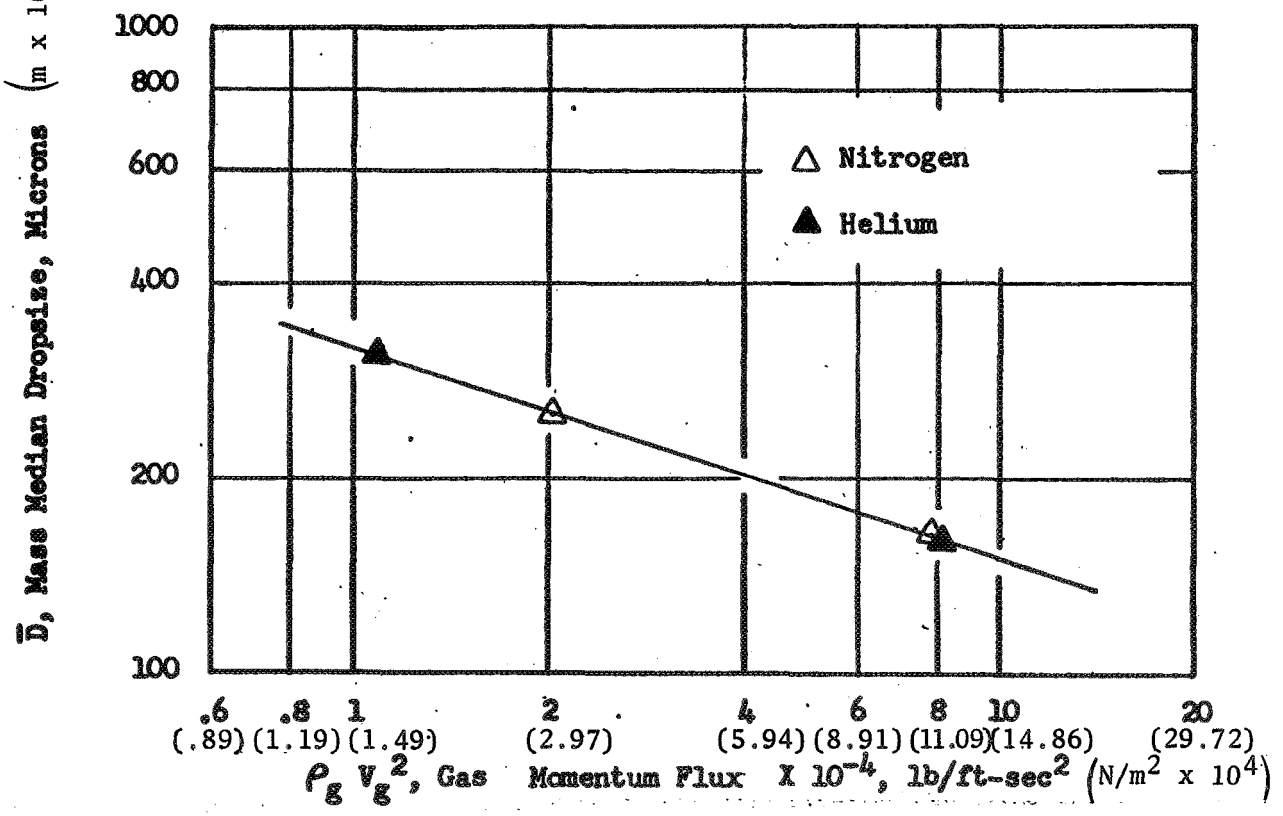

Figure 46. Dependence of Unlike Doublet Element Dropsize on Gas Dynamic Pressure

versus $D/\overline{D}$, i.e., the spray distribution function. The spray distribution function and the mass median dropsize were directly input, along with appropriate thrust chamber design and operating parameters, to the vaporization limited combustion model described in Ref. 1 and 2, and subsequently a predicted vaporization efficiency was obtained.

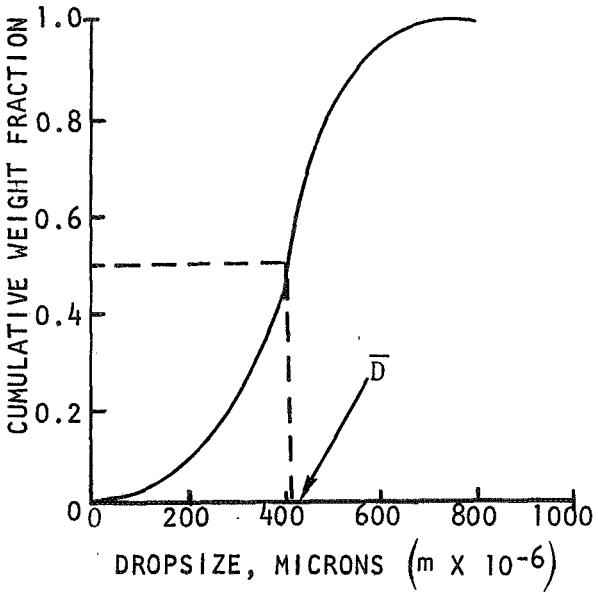

Figure 47. Typical "S" Curve for Dropsize vs Cumulative Weight Fraction

Propellant Distribution (Mixing) Test Data

Direct experimental cold-flow mixing data consisted of (1) the volume of oxidizer simulant (liquid) collected in each collection area, (2) the test duration, (3) the gas stagnation pressure in each collection area, and (4) the oxygen (ingested air) content of the collected gas in each collection area. These data were processed by an IBM-360 computer to produce the following output: total mass flux of oxidizer, total mass flux of fuel, collection efficiency for both oxidizer and fuel, mixture ratio and mass flux for each measurement location, the mixing factor $\left(E_m\right)$, and the predicted c* efficiency, η_{c^*mix}. (The latter was based on a selected propellant combination, overall mixture ratio and chamber pressure.) The following sections describe the process by which these outputs were calculated.

Oxidizer (Liquid) Mass Flux Calculation. Liquid collection measurements were made by (1) the impact probe, which could be positioned anywhere in the 10- by 10-in. (0.254 x 0.254 m) collection surface, and (2) the 10 x 10 matrix of 1-in. $\left(2.54 \times 10^{-2}\ \text{m}\right)$ square collection tubes. The local liquid flowrates were calculated by dividing each local measured mass of liquid collected by the flow duration.

For all concentric type injectors, the flowfield was considered symmetrical* about the geometric center of the injector, and the liquid flux measured by the probe $\left(\dot{w}_\ell / A_{probe}\right)$ was assumed to be constant in the annular zone determined by the radial position of the probe. For each concentric injector element test, the measured liquid mass was integrated over the flowfield and divided by the total mass injected to determine a liquid collection efficiency. This ranged from approximately 70 percent to 130 percent. The local liquid flowrates were then corrected by the necessary factor to make the total integrated flow equal to the injected flowrate (as measured by the turbine flowmeter).

For the impinging-type injectors, the liquid was collected by the probe and by the 1-in. $\left(2.54 \times 10^{-2}\ \text{m}\right)$ grid. The 1-in. $\left(2.54 \times 10^{-2}\text{m}\right)$ grid liquid collection efficiencies were all approximately 90 to 100 percent so no normalization to the injected flowrate was made. A grid spacing smaller than 1 in. $\left(2.54 \times 10^{-2}\ \text{m}\right)$ was required for data reduction in areas encompassed by the two-phase flowfield. Therefore, in these areas, the liquid mass collected by the probe was measured over a nominal 0.2-in. $\left(0.508 \times 10^{-2}\ \text{m}\right)$ grid spacing, which is the same as used for the gas stagnation pressure. Again the local liquid flowrates were determined by dividing the collected mass by the flow duration, integrating over the flowfield and correcting for the collection efficiency.

Fuel (Gas) Mass Flux Calculation. A gas stagnation pressure probe was used to measure the gas impact pressure and thereby determine the gas flow distribution in the two-phase flowfield produced by an injector. The development

*This assumption was verified by spot checks in each test.

of this probe is described in some detail in Appendix A of this report. The technique required measurement of the gas total pressure profiles over the selected matrix of positions in the collection plane. The collection "grid" consisted of annular zones for the concentric injectors and a 0.2-in. (0.5×10^{-2} m) square grid spacing for each of the impinging injectors. Since the measured total pressures included some variable (e.g., 5 to 10 percent) "overpressure," depending on the local mixture ratio, an iterative method of data reduction was necessary. This method is described as follows:

Assuming that the static pressure across the flowfield was constant and equal to the atmospheric pressure, each local Mach number was determined utilizing the following equation:

$$M = \left\{ \left[\left(\frac{P_{oi}}{P} \right)^{\gamma-1/\gamma} - 1 \right] \left[\frac{2}{\gamma-1} \right] \right\}^{1/2} \tag{6}$$

where

P_{oi} = measured total pressure at location i

P = static pressure

γ = specific heat ratio

The local gas density and velocity was then calculated by use of the gas injected stagnation temperature (measured just upstream of the injector) and the following equations:

$$T = T_o / \left(1 - \frac{\gamma-1}{2} M^2 \right) \tag{7}$$

$$\rho = P/RT \tag{8}$$

$$V = M \sqrt{g_c \gamma RT} \tag{9}$$

where

T = static temperature

T_o = stagnation temperature

R = universal gas constant divided by the gas molecular weight

V = gas velocity

ρ = gas density

The gas flowrate can then be determined with the corresponding gas flow area. Since the total volume of the liquid was small compared to the gas volume (e.g., at a mixture ratio of 10 this ratio is approximately 0.01), the area taken up by the liquid was ignored and the flow area for the gas was equated to the probe inlet cross-sectional area. This resultant flow was assumed constant over the small grid area $\left(\text{nominal } 0.2 \text{ in. or } 0.508 \times 10^{-2} \text{ m}\right)$.

The gas flowrate in each grid tube was then combined with the local liquid flowrate in that tube to obtain the local mixture ratio. An overpressure ratio was then calculated from the experimental calibration curve presented in Appendix A. This yielded a new corrected gas stagnation pressure and gas flowrate. The process of calculating the gas flowrate was repeated until less than a 1-percent change in the calculated gas flowrates occurred. This computation was accomplished with a simple computer program and the iteration converged rapidly.

A two-phase stream expanding in ambient air will ingest significant quantities of the surrounding medium. Thus the local gas flowrates determined according to the preceding paragraph were comprised of both the injected fuel simulant $\left(GN_2\right)$ and air. To distinguish between them, the oxygen content of the collected gas was measured at every collection point. Assuming standard air as the ingested medium, the oxygen content allowed the fuel simulant flowrate to be determined in each measurement location. These local gas flowrates were then integrated over the collection plane to determine the gas collection efficiency $\left(\dot{w}_{\text{collected}}\right)/\left(\dot{w}_{\text{injected}}\right)$, where $\dot{w}_{\text{injected}}$ was measured by the venturi flowmeter in the feed line. Fuel (gas) collection efficiencies ranged

from approximately 50 to 180 percent. The local fuel simulant flowrates were then corrected by the necessary factor so that the integrated sum across the flowfield equaled the injected flowrate.

An effort was made to improve the variance in gas collection efficiencies, but this was not achieved within the limited available expenditure of time and effort.* Upon repeat tests, however, measured mixing efficiencies and flow profile shapes were repeatable. Also, as described in the following section, consistent and physically reasonable parametric trends in gas/liquid flow distribution and mixing were observed. These results indicate that the measurements provided an accurate assessment of relative gas flow distribution, in spite of the variance from the overall injected flowrate.

Mass Flux and Mixture Ratio Distribution. As described above, for each test the local oxidizer and fuel simulant flowrates were determined over a matrix of locations covering the measured flowfield. These measured flowrates were then input to a simple computer program where they were converted to the simulated hot-fire propellant flowrates and subsequently prepared for several modes of display. For concentric injectors the cold-flow injected mixture ratio matched the simulated hot-firing mixture ratio; however, for impinging type injectors the liquid penetration parameter was simulated instead $\left[\left(X_p/D_g\right)_{\text{cold-flow}} = \left(X_p/D_g\right)_{\text{hot-fire}}\right]$.

The computer printout includes a tabulated matrix of the experimental data (converted to actual propellant flowrates) which specifies the local mass

*Gas-phase-only tests provided a successful mass balance. With two-phase flow, some improvement was achieved by measuring the flowfield at 5 in. (0.127 m) rather than 3 in. (0.076 m) from the injector and, partially for this reason, the Task II mixing test matrix was run with a 5-in. (0.127 m) collection distance. Possible reasons for the imbalance include (1) recirculation and ingestion of GN_2-rich air, (2) low-velocity gas flow outside the measurement zone, and (3) intermittent, partial probe flooding under high mixture ratio, low gas velocity flow conditions. The latter was the most probable cause of "overcollection." Indication was that a small bleed flow through the probe may substantially alleviate the flooding problem and permit more accurate gas-phase mass balances.

flux of each propellant, the local mixture ratios, and the total propellant mass fraction over each measurement area. The resultant propellant mass and mixture ratio distributions can be graphically displayed in several ways. With the concentric type injectors, a convenient form of graphical display is the mass flux (fuel, oxidizer, or total) plotted against the radius along a selected ray passing through the center of the flowfield (Fig. 48). A second method of graphical data presentation suitable for any injector type is the contour plot. These were obtained for each impinging injector test. An example of this plot is presented in Fig. 49. Individual grid lines represent contours of constant variable (i.e., mass flux, mixture ratio, etc.) magnitude such as do elevation grid lines on a topography map. Tables are provided on the side of each such plot to indicate the quantitative value of the contour lines. A key number located on each contour of the matrix coordinate defines the range of values represented by that contour.

Mixing Factor and Predicted Mixing Efficiency Calculation. The flow profile and contour displays provided detailed qualitative information regarding the fuel gas and liquid oxidizer (spray) flow distribution. For quantitative measure of how well the injectors mix the propellants, a data reduction computer program was designed to calculate a mixing factor $\left(E_m\right)$ which is an index that defines the mass weighted deviation of local mixture ratio from the initially injected overall mixture ratio. The index $\left(E_m\right)$ was developed by Rupe (Ref. 4) and is defined below.

$$E_m = \left[1 - \sum_i^N MF_i \frac{\left(R - r_i\right)}{R} - \sum_i^N MF_i \frac{\left(R - \bar{r}_i\right)}{R - 1} \right] 100 \qquad (10)$$

where

E_m = mixing index

MF_i = mass fraction in the streamtube* (summation of streamtube covers the area's flowfield)

*Refer to preceding section to illustrate the method of obtaining streamtube mass fractions from measured data

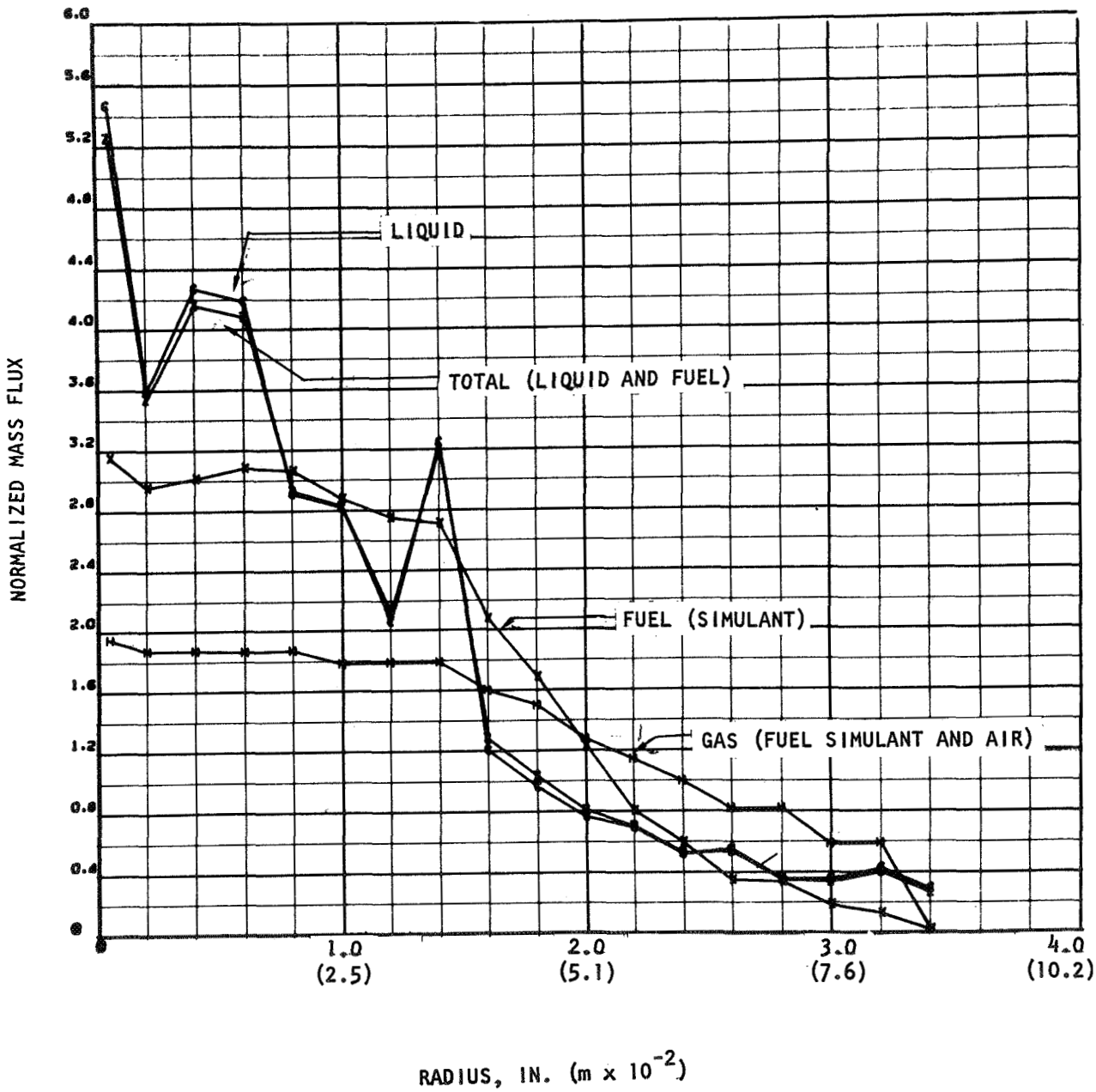

Figure 48. Mass Flux Distribution: Tricentric With Centerbody Injector

X_p/D_g = 0.71

D_ℓ/D_g = 0.31

$P_g V_g^2$ = 14.3 psi (9.9×10^4 N/m^2)

D_g = 0.62 inch (1.57×10^{-2} m)

IDENTIFICATION (lbm/sec)

0--0.002203	7--0.005008
1--0.002604	8--0.005408
2--0.003005	9--0.005809
3--0.003405	
4--0.003806	
5--0.004206	
6--0.004607	

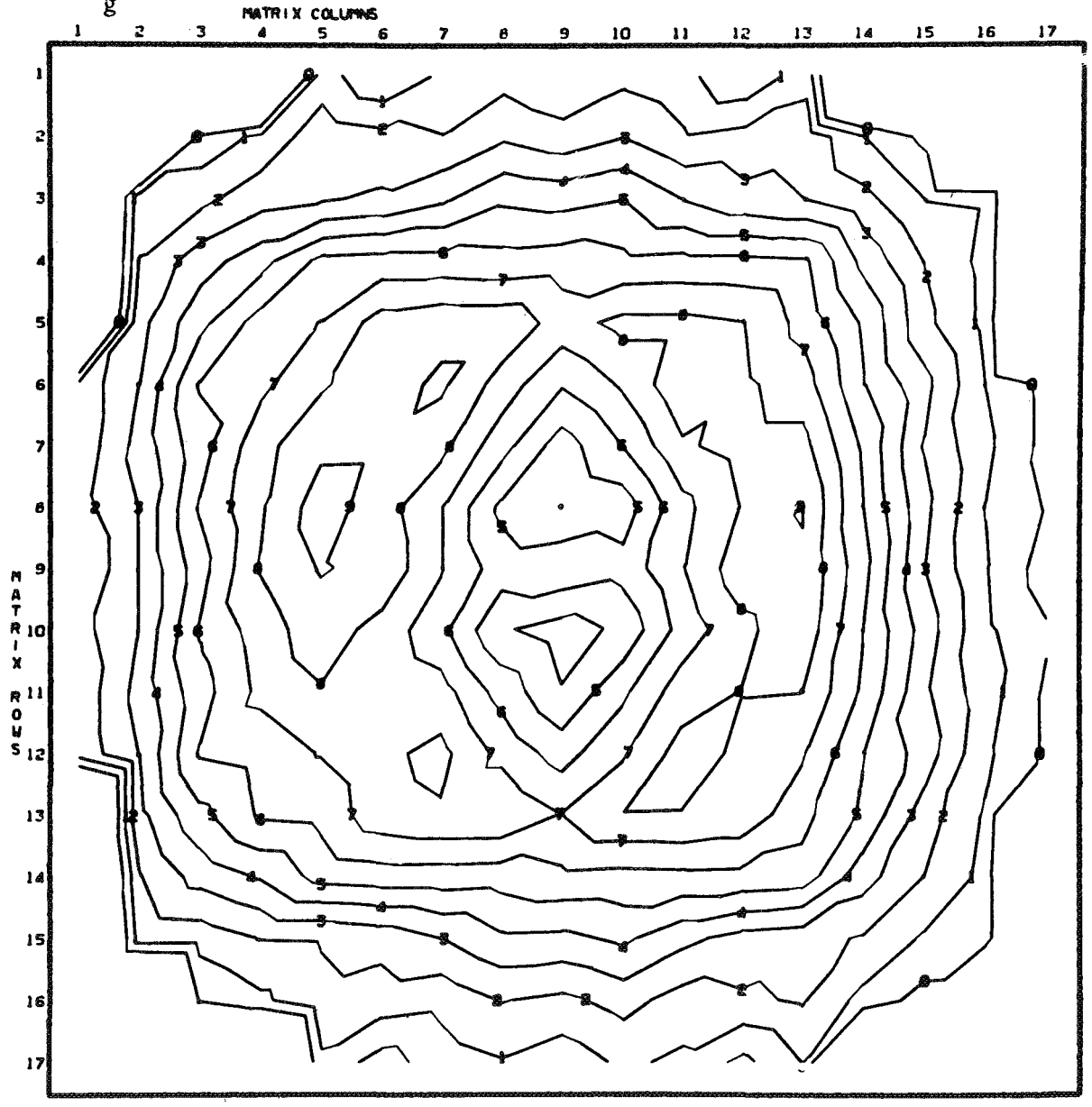

Figure 49. Liquid Mass Flux Distribution, Impinging Concentric Injector (Test M-29)

R = ratio of total oxidizer mass to total oxidizer and fuel mass

r_i = ratio of oxidizer mass to total oxidizer and fuel mass in an individual streamtube for $r_i < R$

$\overline{r}_i$ = ratio of oxidizer mass to total oxidizer and fuel mass in an individual streamtube for $r_i > R$

A mixing-limited combustion efficiency $\left(\left(\eta_{c^*}\right)_{mix}\right)$ was also calculated for each test using a simple streamtube "mixing model." The mixing model considers an idealized rocket engine containing a number of individual streamtubes. Each streamtube at its own mass and mixture ratio is allowed to expand isentropically through the chamber and nozzle without heat or mass transfer to adjacent streamtubes. The c* efficiency due to mixing $\left(\left(\eta_{c^*}\right)_{mix}\right)$ is determined by summation of individual mass weighted c* contributions of each individual streamtube and comparing the total to that theoretically attainable at the injected mixture ratio.

Correction factors for changes in specific heat ratio as a function of mixture ratio may be applied. However, if the effect of γ variation on the sonic point for each individual station can be neglected, the mixing η_{c^*} can be expressed simply as

$$\left(\eta_{c^*}\right)_{mix} = \frac{\sum_{i}^{N} MF_i c^*_i}{c^*_{theo}} \tag{11}$$

where

MF_i = the mass fraction in the individual stream being considered

c^*_i = theoretical c* corresponding to the mixture ratio of the local stream

c^*_{theo} = theoretical c* corresponding to the overall mixture ratio

Unlike the E_m computation, evaluation of $\left(\eta_{c^*}\right)_{mix}$ requires specification of the simulated hot-firing propellant combination, the overall mixture ratio, and the chamber pressure. This information is essential to evaluate the theoretical characteristic velocities and makes the calculated values applicable only to the specified propellants. Of course, the raw experimental mixing data may be subsequently reused with alternate propellant systems to provide appropriate $\left(\eta_{c^*}\right)_{mix}$.

For tests utilizing the concentric injector elements, the mixing factor and predicted mixing efficiencies were calculated directly from the measured oxidizer and fuel simulant local flowrates. In contrast with the concentric injectors, large gas/liquid impinging elements in open-air cold-flow tests normally produced liquid spray fields which expand beyond the accompanying gas flow patterns. Based on such flow behavior, relatively low values of E_m and mixing efficiency would be predicted. Hot-firing tests, however (e.g., those under Task I of the subject contract), have shown large-scale impinging and impinging coaxial injectors capable of producing good propellant mixing with $\left(\eta_{c^*}\right)_{mix}$ as high as 95 to 99 percent. The principal reason for this improvement in mixing under hot-firing conditions is believed to be recirculation of fuel-rich gases out of central low-mixture-ratio zones of high gas flowrates and into the outer spray-rich zones. Other previous evidence of recirculation in hot-firing tests is discussed in Appendix D. As a result, a simple recirculation model was formulated to partially redistribute the flows measured in cold-flow tests of impinging-type injectors, permitting a calculation of E_m and $\left(\eta_{c^*}\right)_{mix}$. The model is described in detail in Appendix D. All Task II impinging injector mixing data were reduced using this recirculation model prior to calculation of the corresponding E_m and $\left(\eta_{c^*}\right)_{mix}$.

COLD-FLOW CHARACTERIZATION TESTS AND RESULTS

Cold-flow testing, using propellant simulant fluids, was conducted to determine the propellant dropsizes and the mass and mixture ratio distributions for various single element gas-liquid injector concepts. The element types tested included basic impinging, basic concentric tube, concentric tube with swirler, impinging concentric tube, and the tricentric with centerbody concepts described earlier in this report. Mixing of the propellant simulants was measured by direct collection of the liquid spray and by use of a two-phase impact probe to measure gas velocity profiles. The molten wax technique was applied to determine atomization characteristics.

Approximately 120 cold-flow tests were conducted, about equally divided between the atomization tests and propellant mixing tests. Essentially the same sets of variables were investigated in both propellant mixing and atomization tests. The principal design and operating variables included the liquid-gas penetration parameter (X_p/D_g), the gas momentum flux ($\rho_g V_g^2$), geometric scale (indexed, for example, by D_g), relative gas-liquid orifice size ratios, gas-liquid velocity differences ($V_g - V_\ell$), mixture ratio, and several parameters specific for particular element types such as the number of liquid jets surrounding (and impinging with) the central gas jet, coaxial element post recess and swirl velocity.

The results of these tests are presented in the following subsections. It should be noted that these Task II experimental tests cover numerous injection element types and a large number of variables. As a result, this first extensive cold-flow evaluation of gas-liquid injectors was, by nature, exploratory with the prime consideration being prediction of the relative significance and trends associated with various design and operating parameters. In order of presentation the test series and experimental parametric correlations of mass median dropsizes ($\bar{D}$) and Rupe mixing factor (E_m) are first described sequentially for each kind of injection element. These two parameters are convenient single indices of atomization and mixing quality, respectively. They do not tell the entire story, however, because dropsize

distribution (about $\bar{D}$) and detailed mass and mixture ratio (spatial) distribution must also be known to fully evaluate an injector. These latter data are discussed in subsequent subsections.

Cold-Flow Median Dropsizes and Mixing Factors

Basic Impinging Stream Cold-Flow Tests. Seventeen atomization and seventeen mixing cold-flow tests were conducted with this injector concept. These tests and the results are described below.

Atomization Tests. Seventeen cold-flow atomization tests were conducted with the basic impinging stream injector. A summary of the test operating conditions and resultant median dropsizes is given in Table 12. Primary variables for these tests were initially expected to be the number (N) of liquid orifices impinging on the central gas orifice, the element size (D_g), gas momentum flux ($\rho_g V_g^2$), and the liquid-gas penetration parameter (X_p/D_g). To vary X_p/D_g with a fixed gas density it was necessary to change either mixture ratio or D_ℓ/D_g. Accordingly, the first six tests were designed to investigate the possible independent influence of mixture ratio (MR) and/or liquid-to-gas orifice diameter ratio (D_ℓ/D_g) on the dropsize distribution. Thus, the primary variables mentioned above were held constant in these tests. These data are presented in Fig. 50 a and b. The mass median dropsize appeared to be strongly affected by the liquid-to-gas diameter ratio (D_ℓ/D_g) in these curves, but influenced weakly, if at all, by mixture ratio.

Based on these results, D_ℓ/D_g was added to the list of controlling parameters and subsequent tests were conducted to obtain parametric effects of the penetration parameter, X_p/D_g, by varying mixture ratio at constant D_ℓ/D_g. Results of these tests with a pentad (N = 4), triplet (N = 2), and unlike doublet (N = 1) injector are illustrated in Fig. 50c. For the pentad injector the mass median dropsize is seen to be independent of X_p/D_g in the 0.3 to 0.8 range. The apparent liquid-liquid interaction resulted in appreciably larger dropsizes for $X_p/D_g > 1$; however, although only two points were obtained with

TABLE 12

SUMMARY OF BASIC IMPINGING STREAM ATOMIZATION TESTS

Test No.	Number of Liquid Orifices	Liquid Orifice Diameter (D_ℓ)		Gas Orifice Diameter (D_g)		D_ℓ/D_g	$\rho_g V_g^2$		X_p/D_g	MR	Measured $\bar{D}$, μ or
		in.	m x 10^{-2}	in.	m x 10^{-2}		lb/in.^{2}	N/m^2 x 10^4			m x 10^{-6}
A-1	4	0.094	0.239	0.584	1.485	0.161	15.80	10.90	0.596	5.81	165
A-2	↓	0.094	0.239	↓	↓	0.161	17.97	12.38	0.565	14.12	132
A-3	↓	0.185	0.470	↓	↓	0.317	17.65	12.17	0.293	14.21	283
A-4	↓	0.185	0.470	↓	↓	0.317	14.99	10.33	0.313	5.96	281
A-5	↓	0.152	0.386	↓	↓	0.260	15.70	10.82	0.590	9.25	233
A-6	↓	0.206	0.523	↓	↓	0.353	15.52	10.70	0.605	12.87	298
A-8	↓	0.152	0.386	↓	↓	0.260	8.32	5.73	0.581	9.71	302
A-9	↓	0.152	0.386	↓	↓	0.260	2.35	1.62	0.577	9.90	384
A-10	↓	0.152	0.386	↓	↓	0.260	15.71	10.83	0.305	4.90	248
A-11	↓	0.152	0.386	↓	↓	0.260	15.91	10.98	0.908	14.61	282
A-12	1	0.206	0.523	↓	↓	0.353	15.94	11.00	0.690	3.77	185
A-13	1	0.206	0.523	↓	↓	0.353	15.88	10.95	1.168	6.37	193
A-14	4	0.067	0.170	0.259	0.658	0.260	8.65	5.96	0.639	10.69	175
A-15	4	0.206	0.523	0.810	2.060	0.255	8.31	5.73	0.607	9.75	290
A-16	2	0.206	0.523	0.584	1.485	0.353	15.92	10.98	0.493	5.39	214
A-17	2	0.206	0.523	0.584	1.485	0.353	15.98	11.02	0.892	9.74	246
A-18	4	0.152	0.386	0.584	1.485	0.260	16.23	11.20	1.139	18.43	402

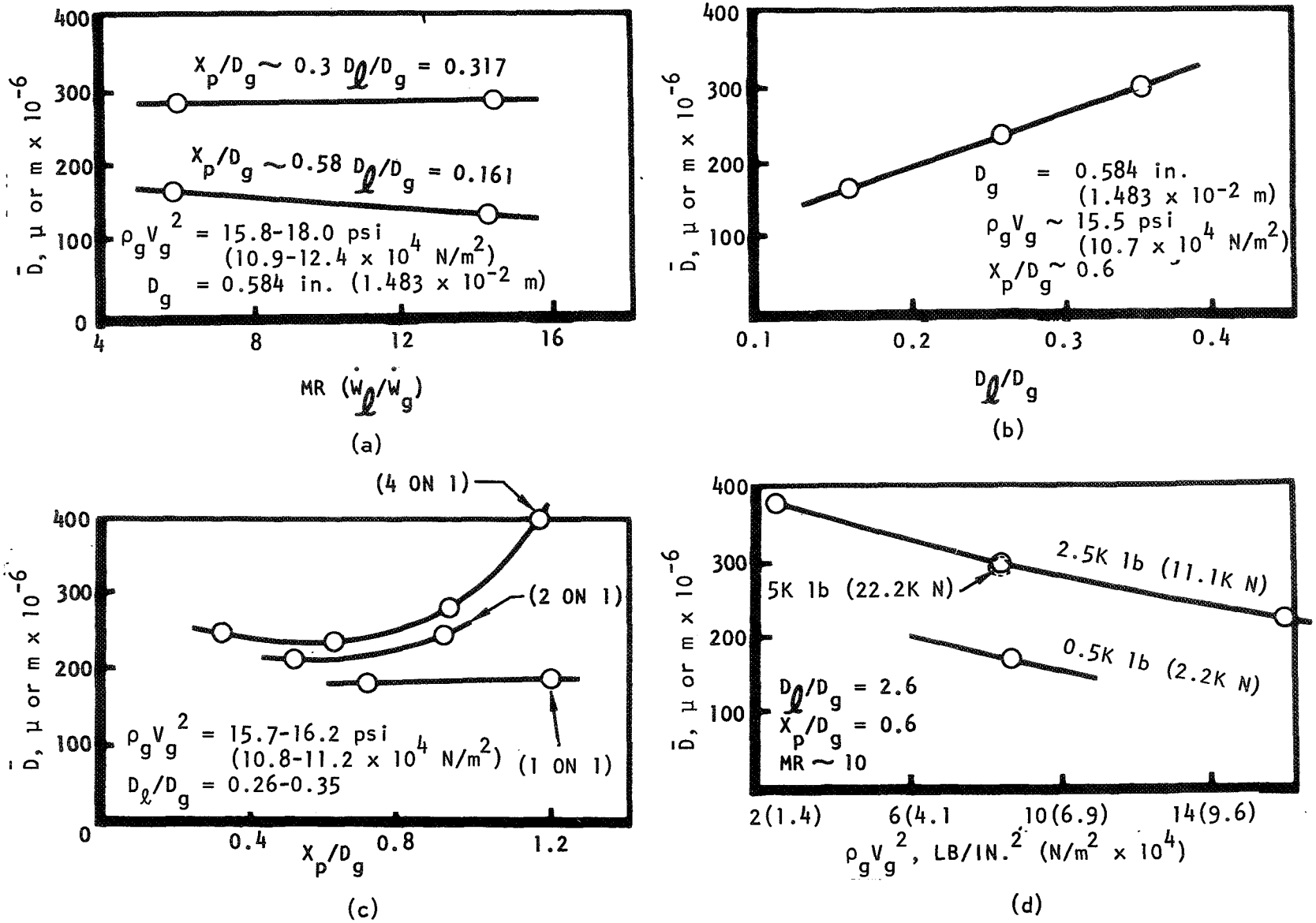

Figure 50. Basic Impinging Stream Injector Atomization Test Results

the triplet injector, a behavior similar to the pentad atomization characteristics is suggested. To the contrary, the unlike doublet results exhibited little or no variance with liquid penetration parameter. This was as expected since it cannot have any liquid-liquid impingement. It should be noted that the gas dynamic pressure ($\rho_g V_g^2$) was held nearly constant in these tests, so, for a constant penetration parameter and constant gas flowrates, less liquid flow was injected with the unlike doublet than the triplet and less with the triplet than with the pentad injectors. Thus, the Fig. 50c curves do not necessarily imply superior atomization levels with the unlike doublet injector under usual design requirements where the liquid-gas flowrates are specified.

The influence of $\rho_g V_g^2$ on mean dropsize is shown in Fig. 50d for constant D_ℓ/D_g, X_p/D_g, and element size. For the pentad injector and for the applicable range of operating conditions, the mass mean dropsize is proportional* to $(\rho_g V_g^2)^{-1/4}$. A photograph (Fig. 51) visually illustrates the spray field of the highest gas momentum flux used.

The influence of scale, or element size, on mass mean dropsize for the pentad element is also shown in Fig. 50d for constant diameter ratio, penetration parameter, gas momentum flux, and mixture ratio. Note that as the thrust per element decreased from on the order of 5K to 0.5K lb (22,200 to 2220 m) the mass median dropsize attained was decreased by a factor of two. However, the limited data available indicated this influence of scale to be nonlinear as can be seen in the figure.

The overall effect of geometry (fuel and oxidizer orifices sizes) on D is seen most readily in Fig. 52. In this figure, $\rho_g V_g^2$ is constant for all data points and X_p/D_g was within a range (see Fig. 50c) where it did not affect $\bar{D}$.

*This must be qualified in that ρ_g was not varied independently. This tentative conclusion is based on the previously discussed tests with a gas-liquid doublet whereby $\rho_g V_g^2$ effectively correlated $\bar{D}$ dependence upon both ρ_g and V_g.

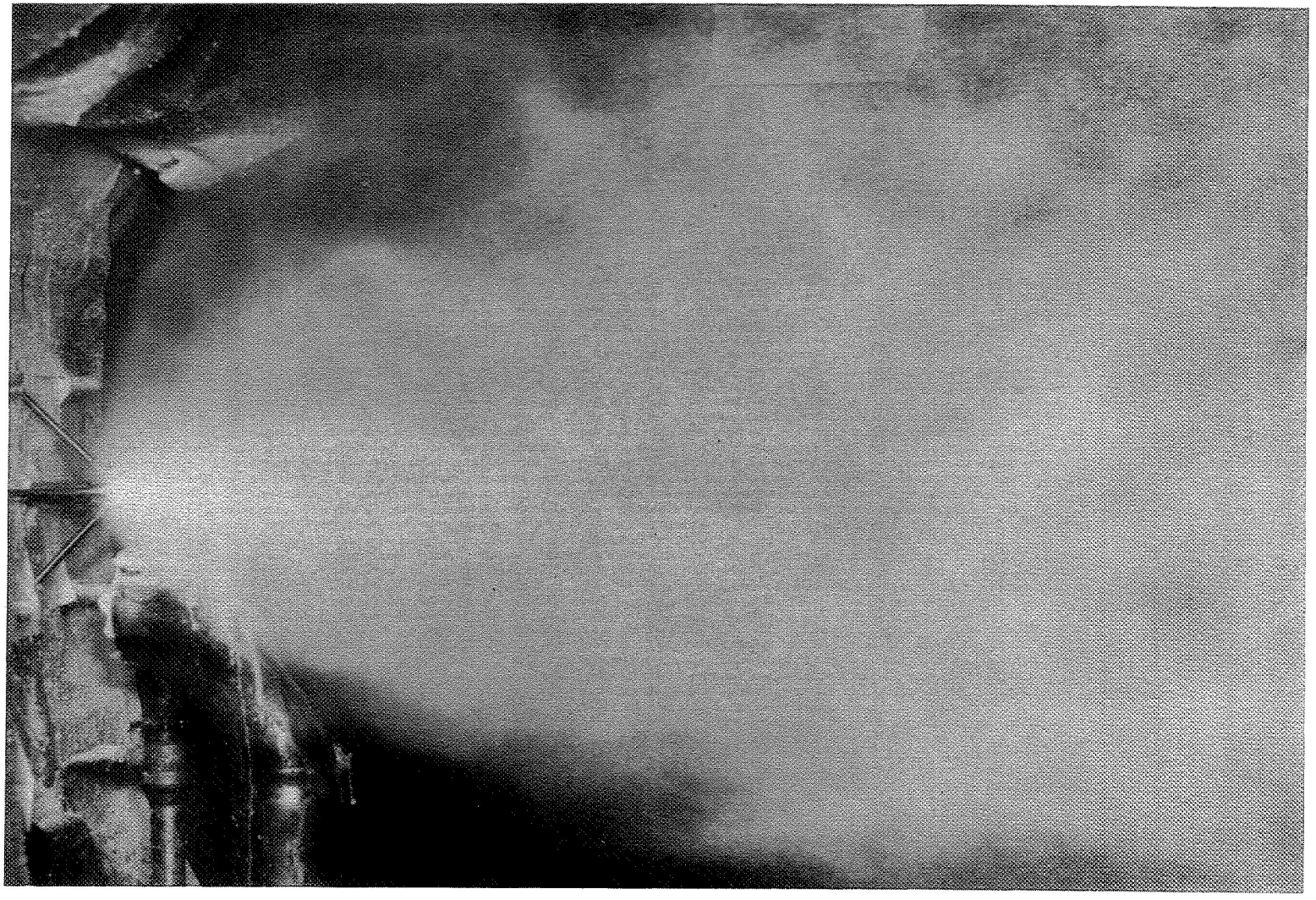

Figure 51. Wax Spray Flowfield From Basic Impinging Stream Injector (Test No. 5 $\rho_g V_g^2 = 15.7$)

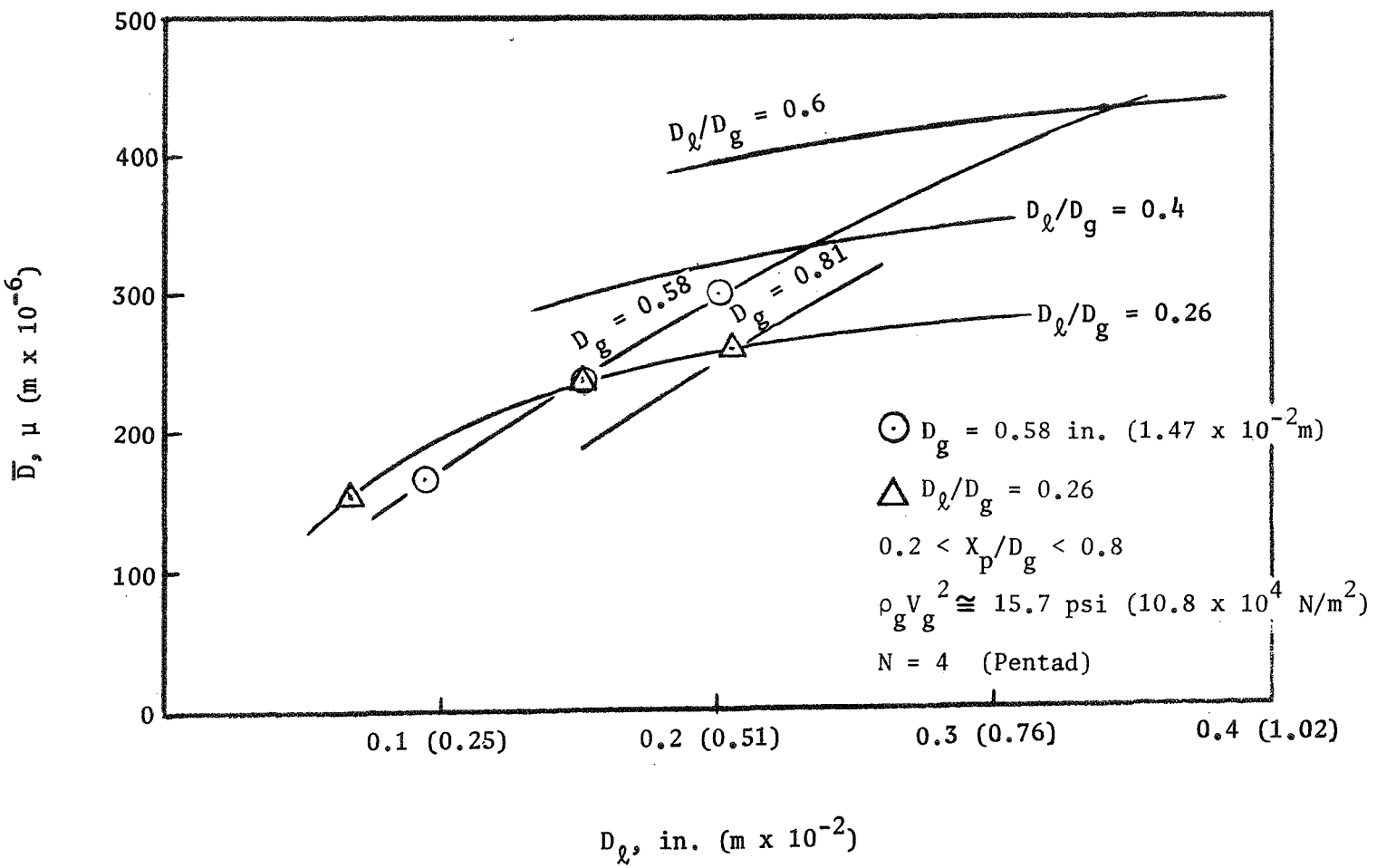

Figure 52. Mass Median Dropsize vs Orifice Geometry: Basic Impinging Stream Injector

These curves were obtained by combining and cross-plotting the D_ℓ/D_g and the scale (D_g) parametric data. Specification of any two of the indicated parameters (D_ℓ, D_ℓ/D_g, D_g) is, of course, sufficient. In order of geometry parameter influence $D_\ell > D_\ell/D_g > D_g$ so D_ℓ with D_ℓ/D_g is probably the most suitable pair.

Mixing Tests. Operating conditions for the 17 propellant mixing tests which were conducted with basic impinging elements are given in Table 13. The first five tests were conducted using a collection distance of 3 in. (7.6×10^{-2} m). In attempting a mass balance on each of these runs, significantly more gas flowrate was measured than was injected (see Appendix A). Because of the somewhat better gas mass balances at a 5-in. (12.7×10^{-2} m) collection distance, the subsequent mixing tests with all impinging injectors were conducted at this distance.

The results of the basic impinging element mixing tests are presented below in terms of the mixing factor, E_m. As described in the Data Reduction section, the experimental gas and liquid flow distribution data were input to the simple recirculation model (Appendix D) to obtain these values of E_m.

Six tests were conducted to investigate the two parameters D_ℓ/D_g and X_p/D_g for the pentad injector at constant scale (D_g) and gas momentum flux. D_ℓ/D_g effects are best seen in Fig. 53a, where E_m is seen to decrease gradually (with constant X_p/D_g) in the range of $D_\ell/D_g = 0.17$ to 0.4, and then rapidly as the diameter ratio is further increased. Figure 53b illustrates the dependence of E_m on X_p/D_g. A continual E_m rise is seen up to about $X_p/D_g = 1.0$. Two data points for the gas-liquid doublet (N = 1) suggest a similar trend although at $X_p/D_g = 0.7$ and $D_\ell/D_g = 0.41$ the doublet E_m is somewhat higher (85 percent) than that of the pentad (77 percent). The remaining parameters investigated were the gas momentum flux and scale. Results from varying each of these parameters individually at constant X_p/D_g, D_ℓ/D_g, and mixture ratio are presented in Fig. 53c and 53d.

TABLE 13

SUMMARY OF BASIC IMPINGING STREAM MIXING TESTS

Test No.	Number of Liquid Orifices	Collection Distance		Liquid Orifice Diameter (D_ℓ)		Gas Orifice Diameter (D_g)		D_ℓ/D_g	MR	X_p/D_g	$\rho_g V_g^2$		E_m, percent
		in.	m x 10^{-2}	in.	m x 10^{-2}	in.	m x 10^{-2}				psi	N/m^2 x 10^4	
M-1	4	3	7.6	0.245	0.622	0.810	2.057	0.302	6.4	0.36	14.3	9.9	—
M-2	↓	↓	↓	0.245	0.622	↓	↓	0.302	12.8	0.71	14.9	10.3	—
M-3				0.435	1.105			0.537	11.7	0.35	14.0	9.7	—
M-4				0.435	1.105			0.537	11.7	0.35	14.0	9.7	—
M-5		↓	↓	0.135	0.343			0.167	0.8	0.08	13.8	9.5	—
M-6		5	12.7	0.245	0.622			0.302	6.9	0.36	14.3	9.9	64.4
M-7		↓	↓	0.245	0.622			0.302	13.2	0.71	14.7	10.1	80.6
M-8				0.435	1.105			0.537	11.6	0.35	14.9	10.3	45.2
M-9				0.334	0.849			0.412	18.0	0.70	14.6	10.1	77.3
M-10				0.135	0.343			0.167	7.3	0.71	14.5	10.0	82.3
M-11	↓			0.209	0.531			0.258	15.7	0.96	14.4	9.9	91.1
M-12	1			0.334	0.849			0.412	4.5	0.70	14.8	10.2	84.8
M-13	1			0.334	0.849			0.412	7.4	1.15	13.1	9.0	91.8
M-14	4			0.245	0.622			0.302	12.5	0.66	6.0	4.1	93.2
M-15	↓			0.245	0.622	↓	↓	0.302	14.3	0.72	1.6	1.1	63.8
M-16		↓	↓	0.084	0.213	0.277	0.704	0.303	12.7	0.63	14.8	10.2	73.8
M-17	↓	↓	↓	0.185	0.470	0.620	1.573	0.298	12.9	0.67	15.4	10.6	90.1

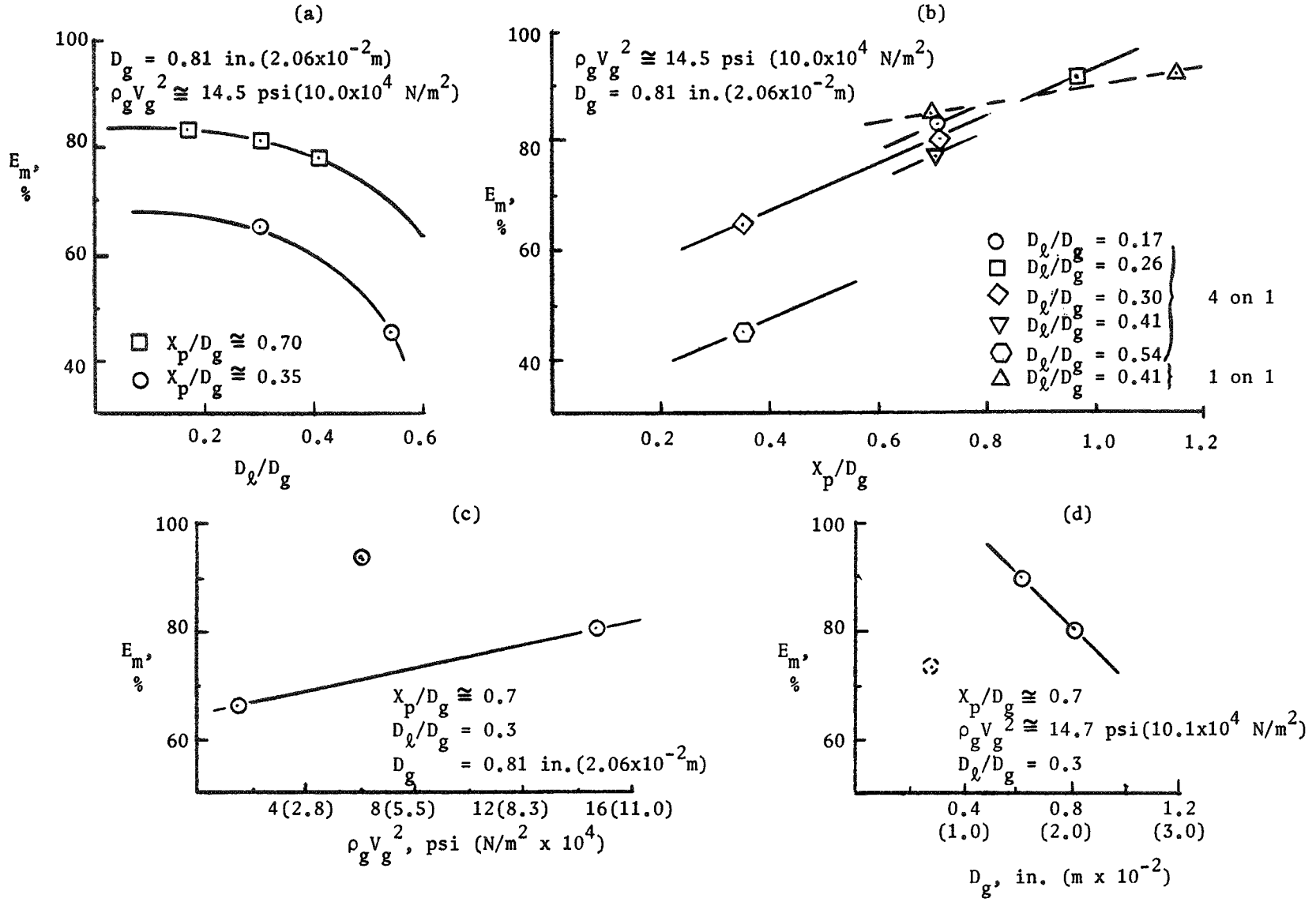

Figure 53. Summary of Cold-Flow Mixing Results: Basic Impinging Injector

All 17 mixing tests except for two of the points (runs 14 and 15) presented in Fig. 53 c were conducted with an injected gas momentum flux of approximately 14.8 psi (10.2×10^4 N/m^2). However, as the injected gas momentum flux was decreased from this range to 6.0 and to 1.6 psi (4.1 and to 1.1×10^4 N/m^2) the ratio of the measured-to-injected fuel (gas) flowrates increased substantially beyond the tolerable limits. This was attributed to local probe flooding and was alleviated in later tests by producing a small positive bleed through the probe. However, data from runs 14 and 15 are highly questionable and no curve can be drawn through the points in Fig. 53c.

An additional point which is subject to question is plotted with a dashed symbol in Fig. 53d. This figure illustrates the effect of scale on mixing factor. The low value of E_m at the smallest scale cannot be easily explained. One possibility, however, is that the impact probe was too large to adequately investigate the flowfield resulting from the smallest scale tested (D_g = 0.277 in. or 0.704×10^{-2} m) and thus the corresponding data point may be invalid. It should be noted that this was the only test made with this small injector element.

In a manner similar to that used with dropsize correlations (Fig. 52), E_m is shown in Fig. 54 as a function of both geometric parameters (scale and diameter ratio) using data from Fig. 53a and 53d and with constant $\rho_g V_g^2$ and X_p/D_g for the pentad element.

Basic Concentric Tube Cold-Flow Tests. Twenty atomization and twelve mixing experiments were made with the basic concentric tube injector concept (Fig. 35). Variables which were investigated included gas velocity, mixture ratio, the ratio of post recess to the central (liquid) orifice diameter, and scale (element size).

Atomization Tests. Operating conditions for the atomization tests are given in Table 14 along with the median dropsizes attained. The initial tests were conducted at constant scale and at a constant mixture ratio of approximately 10.0. The post recess was varied by changing the length of the liquid

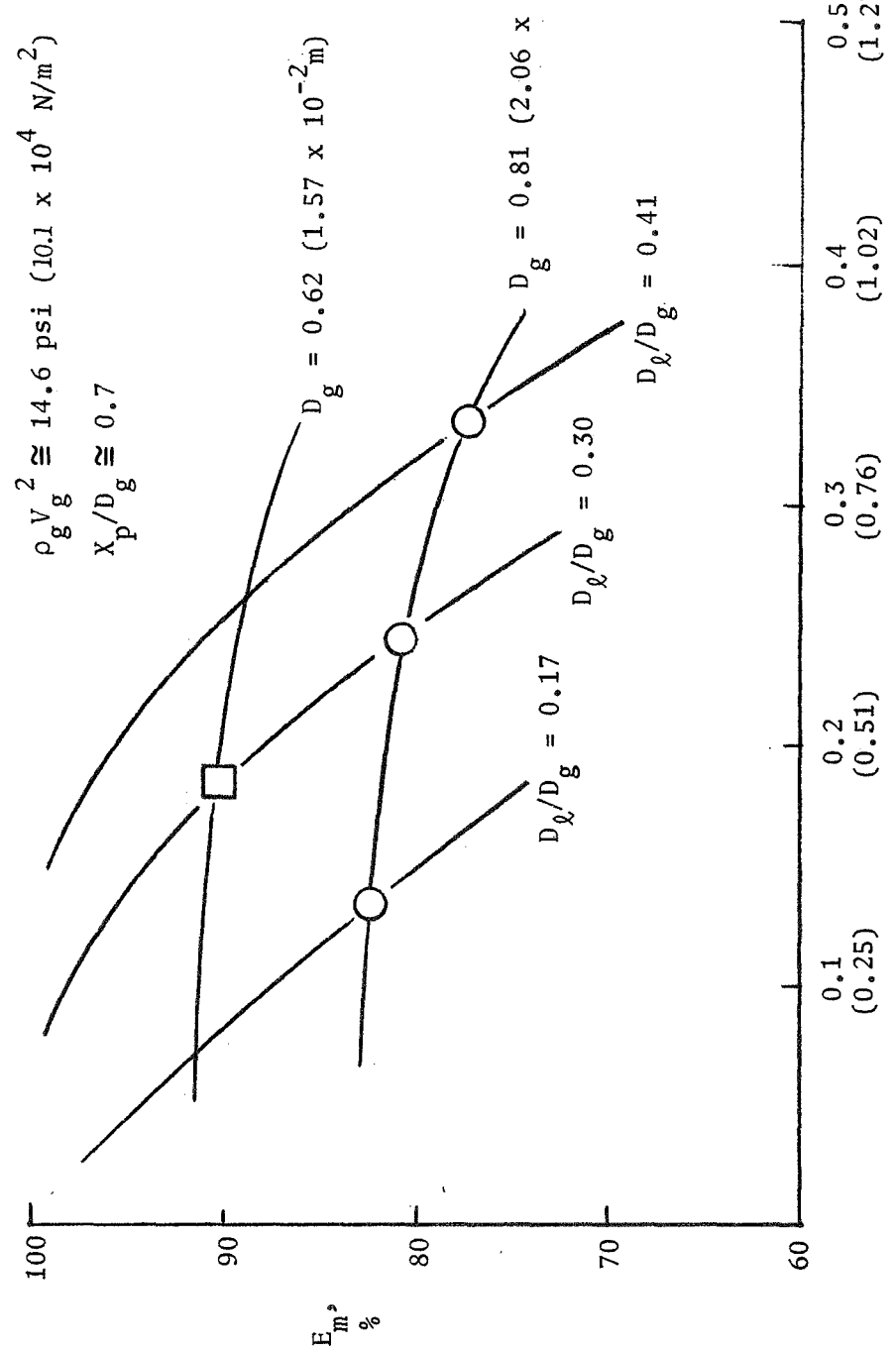

Figure 54. Mixing Factor vs Orifice Geometry: Basic Impinging Injector

TABLE 14

SUMMARY OF BASIC CONCENTRIC TUBE ATOMIZATION TESTS

Test No.	Central Orifice Diameter (D_ℓ)		Annulus Gap (Y_g)		Post Recess (ID)	MR	Gas Velocity (V_g)		Liquid Velocity (V_ℓ)		Measured $\bar{D}$, μ or
	in.	m x 10^{-2}	in.	m x 10^{-2}			ft/sec	m/s	ft/sec	m/s	m x 10^{-6}
A-21	0.277	0.704	0.102	0.259	2.04	10.7	370	113	9.5	2.9	390
A-22	↓	↓	↓	↓	2.04	10.0	1112	339	31.0	9.5	252
A-23					1.03	10.0	369	113	8.9	2.7	818
A-24					1.03	9.8	740	226	18.6	5.7	595
A-25					1.03	10.2	1109	338	31.4	9.6	611
A-26					0.08	10.7	366	112	9.5	2.9	1140
A-27					0.08	10.3	1115	340	31.8	9.7	797
A-28	0.077	0.196	0.031	0.079	2.00	9.9	688	210	21.2	6.5	173
A-29	↓	↓	↓	↓	1.02	10.3	343	145	10.4	3.2	655
A-30					1.02	10.3	1017	310	35.6	10.9	675
A-31					0.00	10.0	695	212	21.2	6.5	286
A-32	0.277	0.704	0.102	0.259	2.04	13.2	743	226	25.0	7.6	681
A-33	↓	↓	↓	↓	1.03	13.4	366	112	11.9	3.6	1154
A-34					1.03	13.8	1109	338	40.9	12.5	846
A-35					0.08	13.4	741	226	25.4	7.7	1209
A-36					2.04	5.7	738	225	10.8	3.3	154
A-37					1.03	5.9	366	112	5.3	1.6	440
A-38					1.03	6.0	1108	338	18.5	5.6	215
A-39					0.08	5.7	735	224	10.7	3.3	523
A-40*	↓	↓	↓	↓	1.03	13.7	2582	787	13.6	4.1	183

*Helium gas simulant used. GN_2 used for all other tests

orifice post, while the gas-to-liquid velocity difference was varied by pressure throttling. The results of these experiments are presented in Fig. 55b, where the mass median dropsize is plotted as a function of the post recess-to-liquid orifice diameter ratio and the gas-to-liquid velocity difference. Results show, as expected, the dropsize to be a strong function of post recess-to-liquid orifice diameter, with the dropsize decreasing when the recess ratio is increased from 0.0 to 2.0 liquid diameters. The gas-to-liquid velocity difference exerted a similar effect over the range tested, with the higher gas velocities resulting in smaller mean dropsizes.

Tests were subsequently conducted similar to those mentioned above, but at a lower and higher constant mixture ratio. Results from these are presented in Fig. 55c for mixture ratios of 5.85 and 13.3, respectively. The effects of varying post recess and velocity difference were similar to those described in Fig. 55b. Note, however, that in Fig. 55c the velocity difference was varied over a wider range (370 to 2570 ft/sec; 113 to 783 m/s) which decreased the mass median dropsize by approximately 90 percent*. Thus, mean dropsize appeared to be extremely sensitive to both post recess and gas-to-liquid velocity difference. This concurred with results derived from previous experiments and from the analytical stripping models presently used to predict vaporization performance. The above results are cross-plotted in Fig. 56 to describe the effect of mixture ratio on mass median dropsize. Note that decreasing mixture ratio markedly decreased the mass mean dropsize attainable. By decreasing the mixture ratio over the range tested, the mass mean dropsize was decreased by 50 percent or greater at post recess-to-liquid diameter ratios of 1.0 and less. A flattening effect was seen at the larger post recess when the mixture ratio was less than 10.

*To obtain subsonic gas velocities in the 2570 ft/sec (783 m/s) range, it was necessary to use helium as the simulant gas. The effect of this density change was not accounted for in Fig. 55c. However, multiplying the results by the density ratio to the 1/3 or 1/4 power (previous correlations and/or stripping models) will not significantly alter the slope of the curve presented.

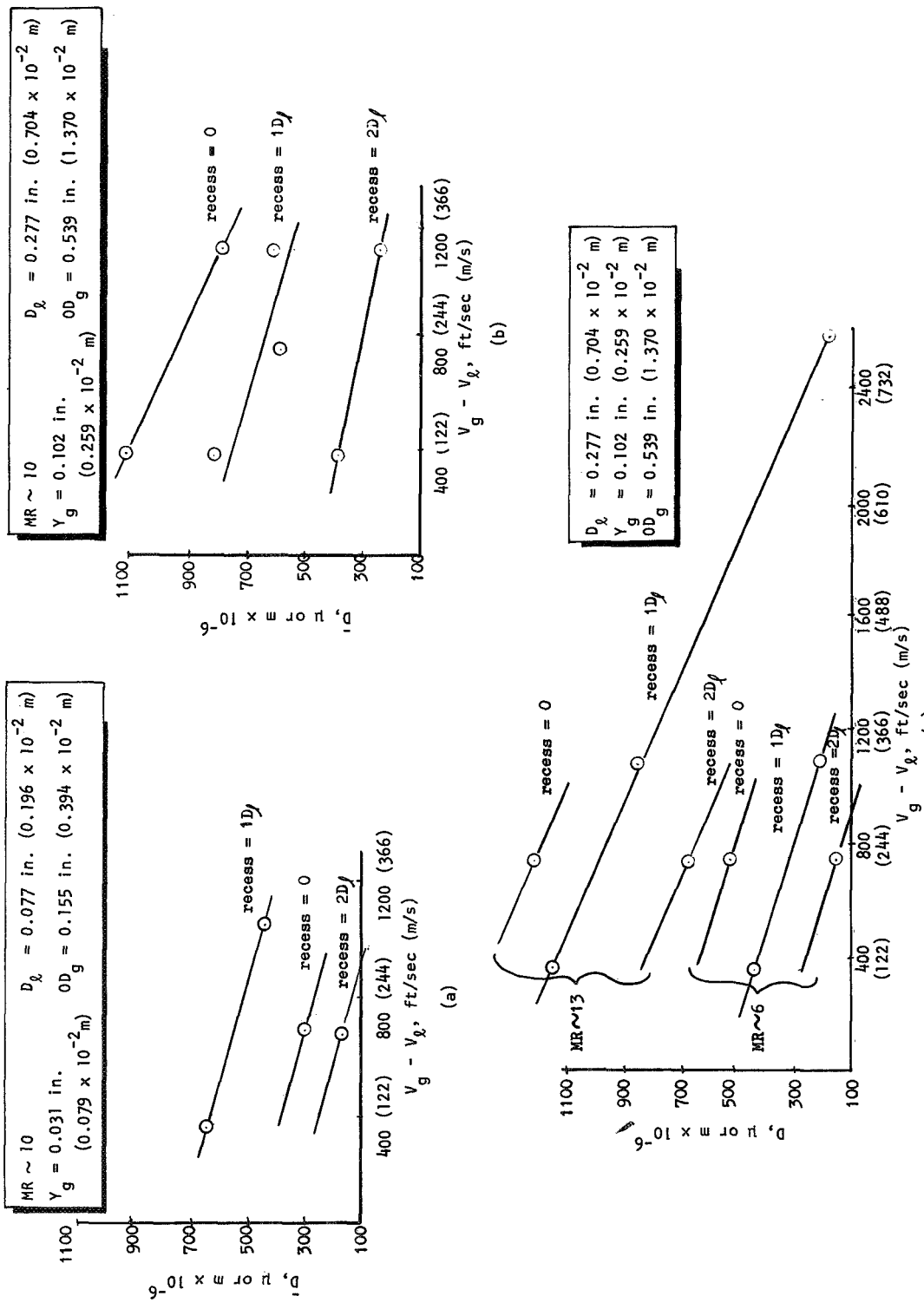

Figure 55. Basic Concentric Tube Injector Atomization Test Results

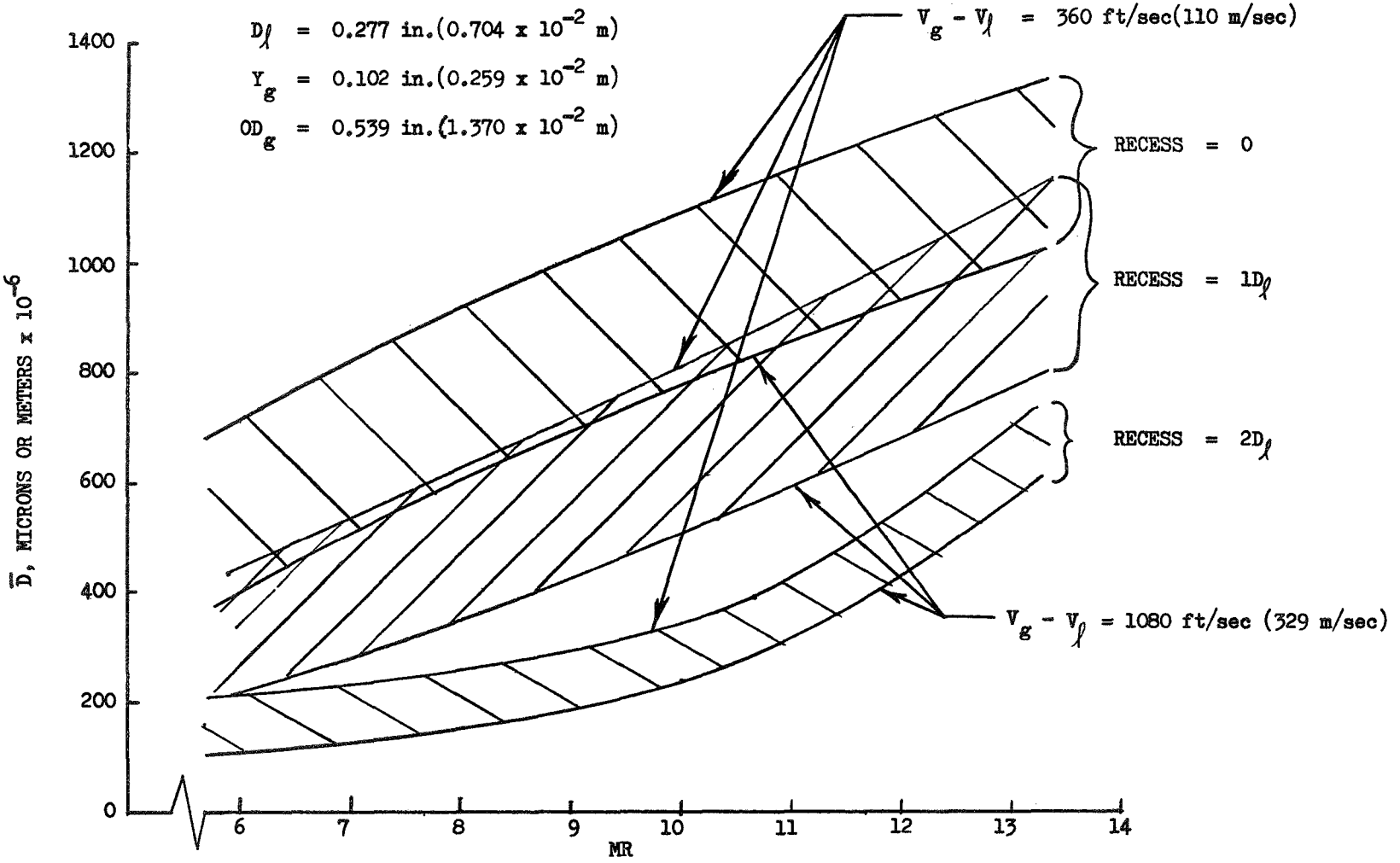

Figure 56. Mixture Ratio Influence on Dropsize for the Basic Concentric Tube Injector

Four tests were conducted with a 10:1 scale reduction (100 lb; 445 N thrust/element) injector. Due to relatively low simulated propellant flowrates, however, some difficulty was encountered in heating the gas to the wax boiling point and in maintaining steady gas flowrates to the injector manifold. The mass median dropsizes attained in these tests are plotted in Fig. 55a. Note that a significantly smaller dropsize was obtained for the zero recess test than for the tests with post recess equal to one liquid diameter. This is in direct contradiction to all the larger scale data and several reported experimental investigations. It was concluded that some of these tests should be repeated to conclusively determine the effect of scale on atomization.

To summarize, the mass median dropsize attainable with the basic concentric element was seen to be extremely sensitive, over the range tested, to post recess, gas-liquid velocity difference, and mixture ratio. As expected, the mean dropsize was decreased with increasing velocity difference, post recess, and with decreasing mixture ratio (less liquid to strip and/or lower liquid velocities per unit gas flowrate). The median dropsizes attained were quite large (500 μ; 500 x 10^{-6} m and greater) for a majority of these tests. Practically, these values would be too high for applicable to hot-fire studies; thus, from the atomization point of view, relatively large concentric hot-fire injector elements would be designed with as much post recess as possible (limited by injector heat transfer and/or cup pressure drop) and with gas velocities as high as feasible.

Mixing Tests. Twelve propellant mixing experiments were conducted with the basic concentric tube injector concept; operating conditions for these tests are summarized in Table 15. Nine of the originally planned tests were dropped from the test matrix due to the extremely high mass median dropsizes attained in the atomization experiments with some hardware configurations and operating conditions. The changes in this matrix included running the majority of the tests with the smaller, approximately 500 lbf (2220 N) thrust/element, of the two available cold-flow injectors. In addition, all planned tests at a mixture ratio of 13 ($\bar{D}$ = 600 to 1300 μ; 600 to 1300 x 10^{-6} m) and

TABLE 15

SUMMARY OF BASIC CONCENTRIC TUBE MIXING TESTS

Test No.	Central Orifice Diameter (D_ℓ)		Annulus Gap (Y_g)		Post Recess $\frac{}{(ID)_\ell}$	MR	Gas Velocity (V_g)		Liquid Velocity (V_ℓ)		E_m, percent
	in.	m x 10^{-2}	in.	m x 10^{-2}			ft/sec	m/s	ft/sec	m/s	
M-18	0.206	0.523	0.067	0.170	1.06	6.0	897	274	14.1	4.3	74.0
M-19	↓	↓	↓	↓	↓	5.6	703	214	10.0	3.0	71.4
M-20	↓	↓	↓	↓	↓	6.3	380	116	5.6	1.7	80.6
M-21	↓	↓	↓	↓	↓	10.3	908	277	23.9	7.3	54.6
M-22	↓	↓	↓	↓	↓	10.0	362	110	8.6	2.6	41.5
M-23	↓	↓	↓	↓	1.95	9.9	691	211	16.5	5.0	33.1
M-24*	↓	↓	↓	↓	1.06	6.1	2325	709	5.6	1.7	--
M-25	↓	↓	↓	↓	1.95	4.9	698	213	8.3	2.5	74.8
M-26	↓	↓	↓	↓	0.02	5.8	672	205	9.5	2.9	53.2
M-27	0.620	1.575	0.225	0.572	1.97	6.1	390	119	6.2	1.9	76.5
M-28	↓	↓	↓	↓	1.97	6.0	961	293	18.2	5.5	81.3
M-29	↓	↓	↓	↓	1.16	6.0	664	202	11.2	3.4	58.2

*Helium gas simulant used. GN_2 used for all other tests.

all but one test with zero post recess ($\bar{D}$ = 500 to 1300 μ; 500 to 1300 x 10^{-6} m) were deleted.

Several general trends were seen in the raw data. In the center of the flowfield, large quantities of liquid were observed, decreasing as the flowfield radius increased. The gas mass flux was oriented in the opposite manner; lower in center and increasing with radius until a maximum was obtained. In addition, the oxygen content in the measured gas was seen to increase with increasing radius, showing an increase in the ratio of entrained air to injected nitrogen. Thus, the raw data trends were as expected.

The mixing factors, E_m, were calculated for each test directly from the cold-flow local flowrates measured. Results are reported below.

The effect of varying post recess at constant mixture ratio (6.0) is shown in Fig. 57 a for constant $V_g - V_\ell$. Note the 20 percent increase in the mixing factor as post recess increases from 0 to 2 liquid diameters. Thus, the amount of post recess exerts considerable influence on mixing. This parameter was seen to improve atomization in the same manner (i.e., increased post recess decreased $\bar{D}$). As observed from Fig. 57a, raising $V_g - V_\ell$ at a fixed degree of post recess showed a lesser, but still significant, enhancement of mixing efficiency.

The post recess and the injection velocity difference were also varied at a constant mixture ratio of 10. Predicted mixing factors for these cold-flow tests are shown in Fig. 57b. The data point associated with the greatest post recess appears to represent an anomaly in that it exhibits the lowest mixing efficiency. This data point has a relative velocity, $V_g - V_\ell$, approximately halfway in between the $V_g - V_\ell$ of the other two points. Although no evidence has been found to disregard this test, the post recess trend observed at a mixture ratio of 6.0 (Fig. 57a) is regarded with a much higher confidence level because it represents more data and because it is more consistent with other experimental results.

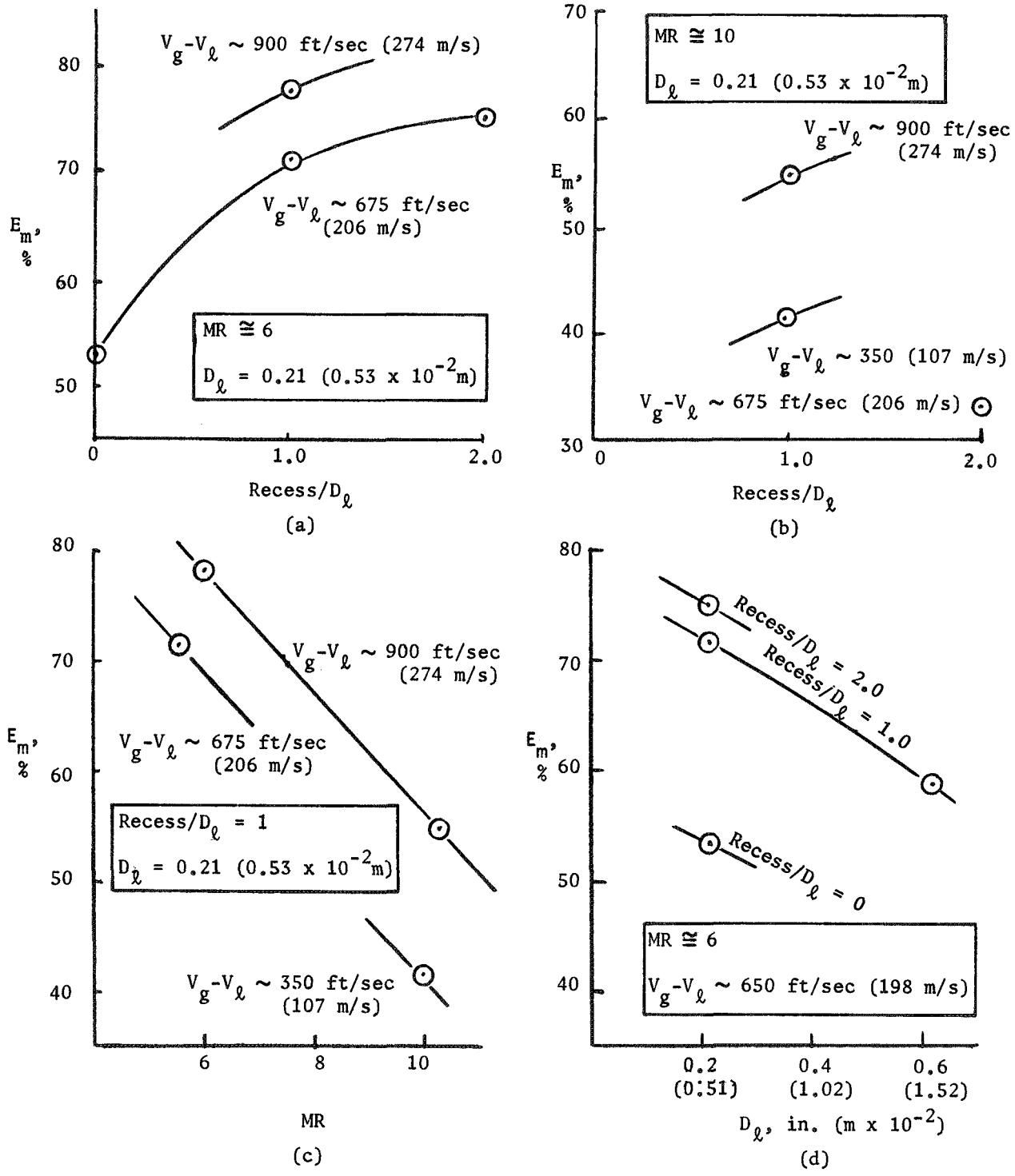

Figure 57. Summary of Cold-Flow Mixing Results: Basic Concentric Tube Injector

The data in Fig. 57a and 57b are cross-plotted in Fig. 57c to illustrate the effect of mixture ratio at constant recess and $V_g - V_\ell$. The effect of scaling the basic concentric tube is shown in Fig. 57d for a mixture ratio of 6.0. As the liquid orifice diameter was increased from 0.2 in. (0.5×10^{-2} m) to 0.6 in. (1.6×10^{-2} m), a mixing factor decrease of approximately 13 percent was observed.

Concentric Tube With Swirler Cold-Flow Tests. Six atomization and three mixing cold-flow tests made with this injector concept as described below.

Atomization tests. Six concentric tube with swirler injector atomization tests were conducted; the operating conditions for these tests, along with the median dropsizes measured, are summaried in Table 16. The swirl was developed by tangential liquid entry into the base (upstream section) of the liquid orifice (Fig. 36). The swirl entrance area was varied for constant gas and liquid flowrates, permitting variation of the swirl velocity at constant liquid flowrates. Results are presented in Fig. 58 where mass median dropsize is plotted against swirl velocity (swirl entering velocity) for two constant injection velocity differences ($V_g - V_\ell$). Note that the addition of swirl velocities of only 33 ft/sec (10.1 m/s) decreased the mass median dropsize by more than 50 percent at $V_g - V_\ell$ = 1080 ft/sec (330 m/s). As with the basic concentric element, increasing gas velocity markedly decreased the dropsize attained. The mass median dropsize passed through a minimum value and again increased with increasing swirl velocity at the lower gas velocities, $V_g - V_\ell$ = 360 ft/sec (110 m/s), which might be an indication that the liquid swirl velocity was high enough to drive the liquid through the gas stream before complete stripping could occur.

The trends with this concept indicate that relatively large thrust per element injectors may be plausible with respect to atomization if a liquid swirl is added and high gas velocities are employed. The combined effects of post recess and liquid swirl cannot be ascertained since only the 0.0 recess condition was tested in combination with the swirl. Further testing would be required to examine such combined effects.

TABLE 16

SUMMARY OF CONCENTRIC TUBE WITH SWIRLER TESTS

Test No.	Central Orifice Diameter (D_ℓ)		Annulus Gap (Y_g)		Central Orifice Area (A_ℓ)		Annulus Area (A_g)		MR	Annulus Gas Velocity (V_g)		Inlet Swirl Diameter (D_s)		Inlet Swirl Velocity (V_s)		Measured $\bar{D}$, μ or	E_m,
	in.	m x 10^{-2}	in.	m x 10^{-2}	$in.^2$	m^2 x 10^{-4}	$in.^2$	m^2 x 10^{-4}		ft/sec	m/s	in.	m x 10^{-2}	ft/sec	m/s	m x 10^{-6}	Percent
Atomization Tests																	
A-41	0.277	0.704	0.102	0.259	0.060	0.387	0.140	0.903	10.2	1108	338	0.194	0.493	32.6	9.9	359	
A-42	↓	↓	↓	↓	↓	↓	↓	↓	10.0	1122	342	0.136	0.346	65.5	20.0	321	
A-43									10.4	1118	340	0.096	0.244	134.8	41.0	276	
A-44									10.1	365	111	0.096	0.244	37.8	11.5	686	
A-45									10.2	371	113	0.070	0.178	72.1	22.0	789	
A-46									10.4	365	111	0.055	0.140	118.3	36.1	916	
Mixing Tests																	
M-25	0.206	0.523	0.067	0.170	0.033	0.213	0.067	0.432	9.9	910	278	0.070	0.178	101.0	30.8		84.1
M-26	↓	↓	↓	↓	↓	↓	↓	↓	9.8	923	282	0.136	0.346	26.3	8.0		--
M-27									9.9	918	280	0.086	0.218	66.0	20.1		86.0

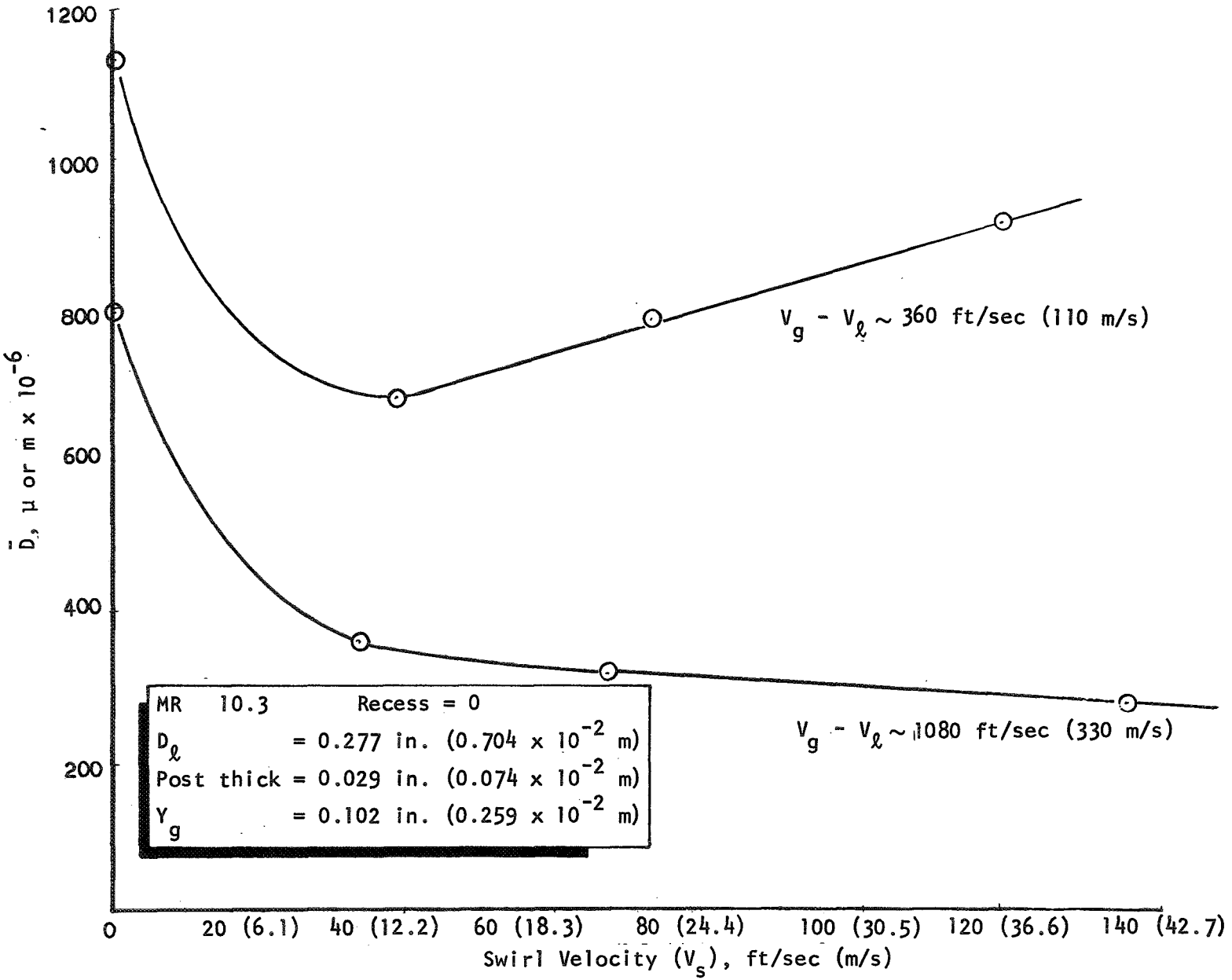

Figure 58. Concentric Tube With Swirl Injector Atomization Test Results

Mixing Tests. Three propellant mixing experiments were conducted with the concentric tube with swirler injector concept. Operating conditions for these tests are summarized in Table 16. The only test variable was the liquid swirl velocity. Three additional mixing tests were originally planned; however, these mixing tests were dropped from the test matrix due to the relatively large mass median dropsizes attained in the atomization experiments employing relatively low gas velocities (i.e., under 400 ft/sec; 122 m/s).

Several interesting qualitative trends were seen from the mixing test data. The maximum liquid flux point did not occur in the center as with the basic concentric experiments. Instead, this zone of maximum liquid flux moved radially outward, as expected, with increasing swirl velocity. The gas stagnation pressures were somewhat more uniform with the concentric with swirl element than with the basic concentric injector tests. The oxygen content (from ingested air) was again seen to increase with increasing radius from the center of the flowfield as was observed in the basic concentric tube element tests.

In Fig. 59, E_m for the concentric with swirl element is plotted against (inlet) swirl velocity for a constant mixture ratio (10), scale (D_ℓ = 0.206 in.; 0.523 x 10^{-2} m), ($V_g - V_\ell$ = 875 ft/sec; 267 m/s) and zero recess. Also included is a zero swirl point interpolated to the appropriate MR, $V_g - V_\ell$, and zero recess from the basic concentric E_m data (Fig. 57). Evidently the addition of swirl markedly enhances E_m; however, an optimum value of swirl is suggested by the decrease in E_m between V_s = 66 and 101 ft/sec (20.1 and 30.8 m/s).

Impinging Concentric Tube Cold-Flow Tests. Eight mixing and nine atomization tests were conducted with the impinging concentric tube injector concept (Fig. 37). Primary variables include scale, the liquid-gas penetration parameter, the liquid-to-gas diameter ratio, the ratio of annulus to central orifice fuel (gas) simulant flowrates, and the fuel momentum flux level.

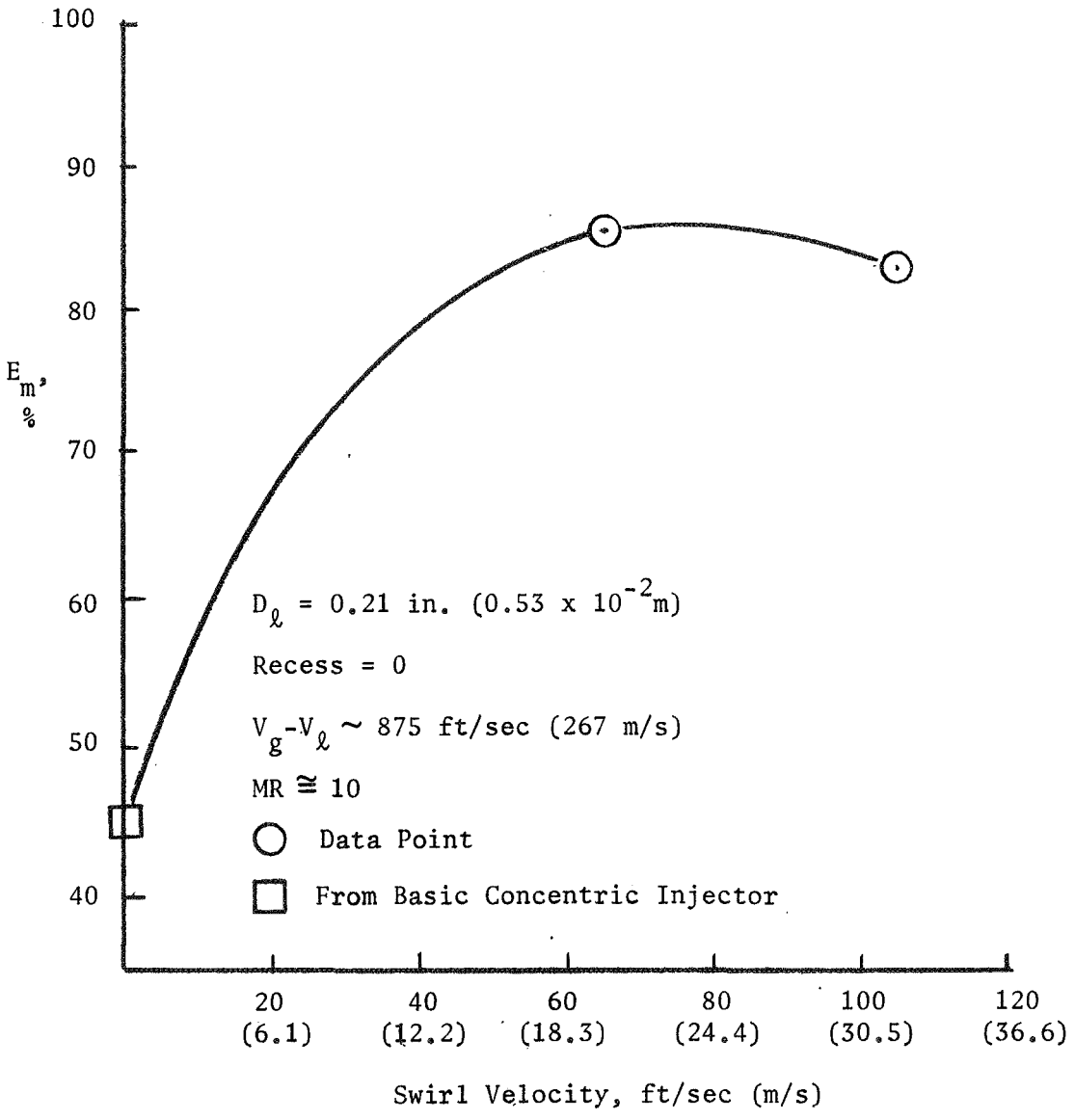

Figure 59. Summary of Cold-Flow Mixing Results: Concentric Tube With Swirler Injector

With the exception of the annulus to central fuel flowrate ratio, these are the same variables examined for the basic impinging injector concept. Data from these tests are described in the following sections.

Atomization Tests. Operating condition and mass median dropsizes attained for all tests with this injector concept are summarized in Table 17. The mass median dropsize is plotted as a function of each of the test variables in Fig. 60. The dependence of the mass median dropsize on the liquid penetration parameter in the 0.3 to 0.9 range is illustrated in Fig. 60a. The curve is similar to the results observed in the basic impinging stream test series over the X_p/D_g range tested.

The influence of liquid-to-gas orifice diameter on mass median dropsize is illustrated in Fig. 60d for tests in which the other primary variables were held constant. As illustrated, the dropsize is seen to be strongly affected by D_ℓ/D_g. As D_ℓ/D_g varies from 0.2 to 0.33, the mass median dropsize increases by approximately 40 percent. This slope also coincides with data taken in the basic impinging stream test series. It should be noted, however, that a decrease in annulus gas velocity was accompanied by the D_ℓ/D_g increase and may have contributed to the rise in $\bar{D}$.

The effect of varying the center orifice gas momentum flux on dropsize is shown in Fig. 60b. Again, the other primary variables mentioned above were held constant during these tests. Dropsize decreases only slightly (approximately 9 percent) with increasing momentum flux in this range, which was quite surprising.

The influence of scale on mass mean dropsize is shown in Fig. 60b for constant D_ℓ/D_g, X_p/D_g, $\rho_g V_g^2$, and the ratio of annulus to total gas flowrates. As the simulated thrust per element decreased from about 2500 to 1000 lb (11,100 to 4450 N), the mass median dropsize attained was decreased by approximately 23 percent.

TABLE 17

SUMMARY OF IMPINGING CONCENTRIC TUBE TESTS

Test No.	Liquid Orifice Diameter (D_ℓ)		Central Gas Orifice Diameter (D_g)		Annulus Gap (Y_g)		MR	D_ℓ/D_g	X_p/D_g	$(\rho_g V_g^2)_{center}$		$(\dot{w}_{ann}/\dot{w}_{tot})_{gas}$	Measured $\bar{D}$, μ or	E_m,
	in.	m x 10^{-2}	in.	m x 10^{-2}	in.	m x 10^{-2}				psi	N/m^2 x 10^4		m x 10^{-6}	percent
Atomization Tests														
A-51	0.152	0.386	0.460	1.170	0.034	0.086	4.8	0.33	0.30	16.8	11.6	0.2	250	
A-52	↓	↓	↓	↓	↓	↓	9.7	↓	0.59	16.6	11.4	0.2	260	
A-53	↓	↓	↓	↓	↓	↓	14.5	↓	0.89	16.7	11.5	0.2	276	
A-54	↓	↓	↓	↓	↓	↓	7.1	↓	0.58	16.2	11.2	0.4	187	
A-55	↓	↓	↓	↓	↓	↓	10.3	↓	0.60	6.6	4.6	0.2	280	
A-56	↓	↓	↓	↓	↓	↓	10.1	↓	0.60	11.3	7.8	↓	276	
A-57	↓	↓	0.745	1.890	↓	↓	6.5	0.20	0.68	13.7	9.5	↓	185	
A-58	0.105	0.266	0.319	0.810	0.011	0.028	11.3	0.33	0.70	16.0	11.0	↓	201	
A-59	0.152	0.386	0.460	1.170	0.034	0.086	24.8	0.33	0.57	4.0	2.8	↓	250	
Mixing Tests														
M-28	0.194	0.493	0.620	1.570	0.060	0.152	15.0	0.31	0.96	14.5	10.0	0.2		89.7
M-29	↓	↓	↓	↓	↓	↓	11.0	↓	0.71	14.3	9.9	↓		72.2
M-30	↓	↓	↓	↓	↓	↓	6.3	↓	0.40	14.5	10.0	↓		65.1
M-31	↓	↓	↓	↓	↓	↓	8.1	↓	0.68	15.7	10.8	0.4		60.1
M-32	↓	↓	↓	↓	↓	↓	10.9	↓	0.68	9.2	6.3	0.2		66.3
M-33	↓	↓	↓	↓	↓	↓	11.2	↓	0.68	4.4	3.0	↓		69.1
M-34	↓	↓	0.930	2.360	↓	↓	7.4	0.21	0.67	16.8	11.6	↓		71.7
M-35	0.105	0.266	0.319	0.810	0.011	0.028	11.6	0.33	0.70	14.8	10.2	↓		87.4

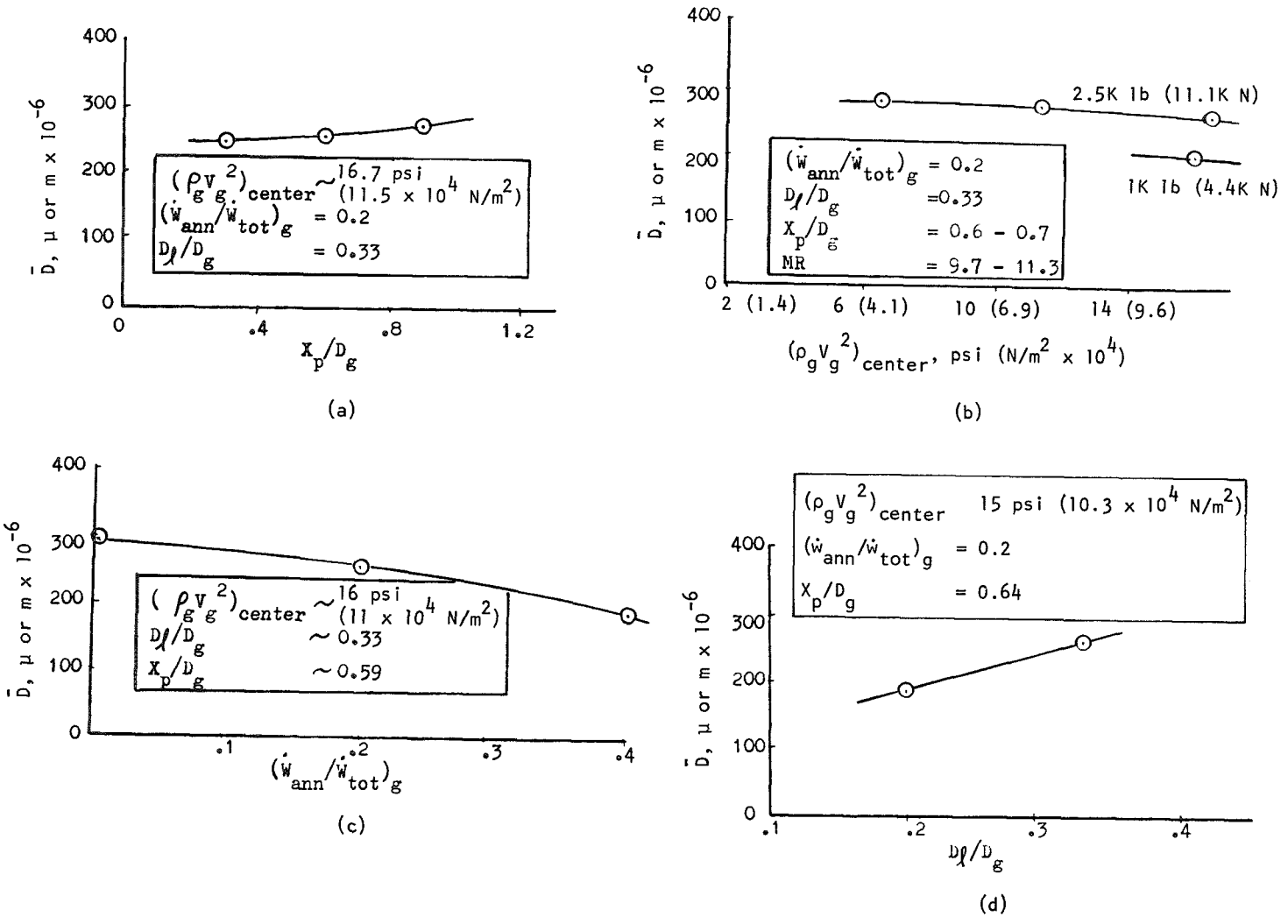

Figure 60. Impinging Concentric Tube Injector Atomization Test Results

The remaining variable investigated was the ratio of annulus gas flowrate to total gas flowrate. The effect of varying this parameter while holding the other four primary variables constant is illustrated in Fig. 60c, which includes zero annulus gas flowrate point from the basic impinging stream series, corrected for the constant operating conditions. This curve indicates a dropsize decrease of approximately 34 percent (282 to 188 μ; 282 to 188 x 10^{-6} m) as this flowrate ratio increases from 0.0 to 0.4; however, this must be interpreted with caution since the percent annulus gas increase was effected by an increase in annular gas velocity rather than by a reduction in the center gas flow as would occur in a hot-firing case.

Mixing Tests. Operating conditions for the mixing tests with the impinging concentric concept are summarized in Table 17. Several qualitative trends were seen from the raw data. Higher gas stagnation pressures were observed in the center of the flowfield,, decreasing with increasing radius. As the penetration parameter increased, the maximum level of the gas stagnation pressure decreased significantly; i.e., 75 to 9 mm Hg (100 to 12 x 10^2 N/m^2) as X_p/D_g varied from 0.4 to 0.96. This indicated a substantial increase as expected, in spray/gas interaction at high X_p/D_g, whereby much of the gas momentum was transferred to the spray. The oxygen content of the flowfield varied approximately inversely with the stagnation pressure. The relative minimum oxygen content occurred in the center and amounted to on the order of 4 percent, which corresponds to about 20 percent ingested air by volume. Liquid mass fluxes exhibited four peaks at the liquid penetration parameters less than 0.7 and a centralized peak at higher X_p/D_g. The gas and spray flow distributions are further discussed in a following subsection.

Quantitative results of the propellant mixing tests are presented below in terms of the mixing factor, E_m. The initial tests were designed to investigate the influence of the liquid penetration parameter on mixing. In these tests the liquid flowrate was increased, at constant center and annulus gas flowrates, to increase X_p/D_g. Results are plotted in Fig. 61a. These three tests were the same tests used to develop the recirculation model (with LOX/GH_2 simulation) using empirical correlation with the Task I hot-firing data

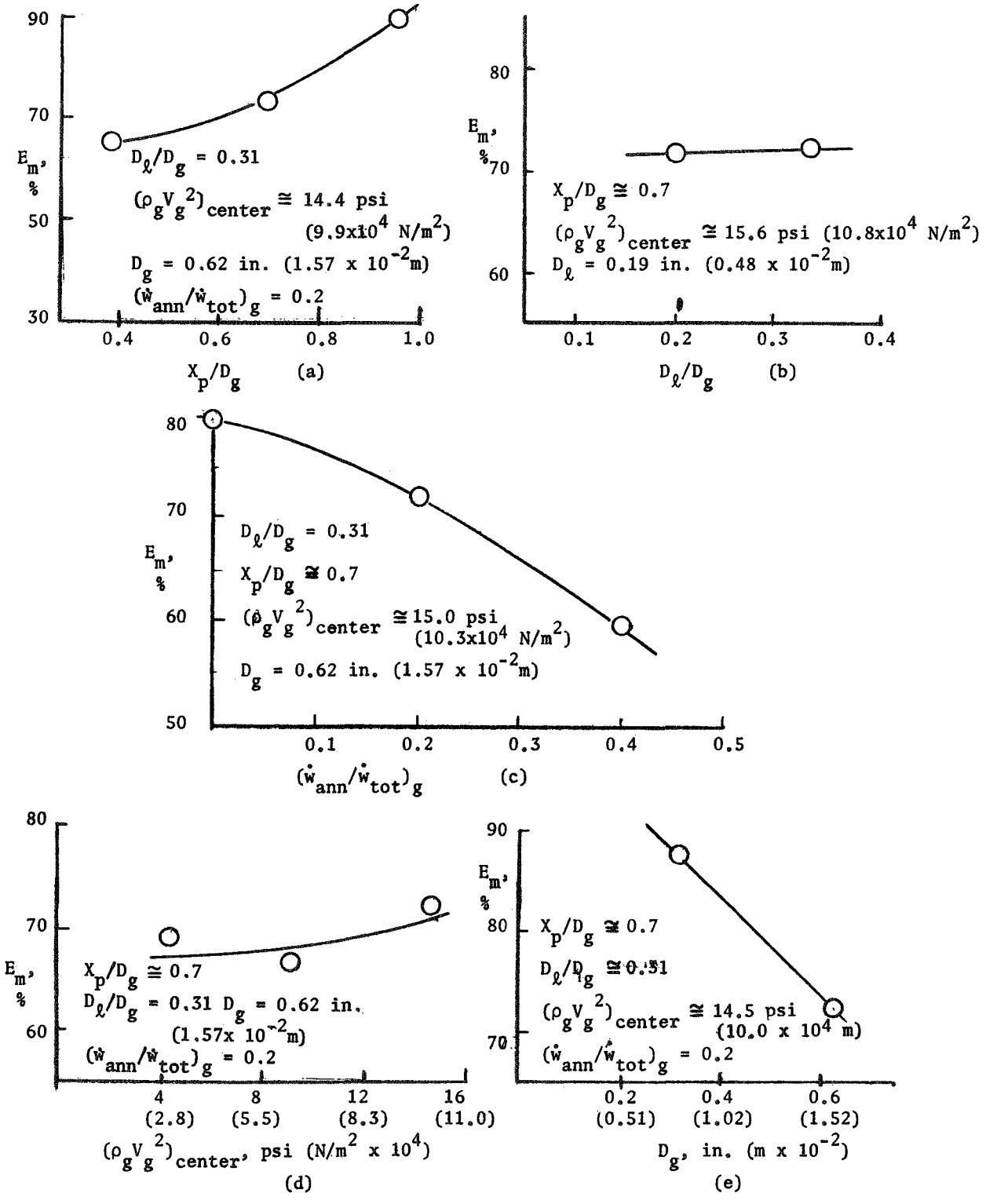

Figure 61. Summary of Cold-Flow Mixing Results: Impinging Concentric Injector

as described in Appendix D. The impinging concentric element curve of E_m versus X_p/D_g (Fig. 61a), wherein D_ℓ/D_g was 0.31, corresponds quite closely in both level and trend with that observed with the basic impinging element (Fig. 53) for $0.17 \leq D_\ell/D_g \leq 0.4$. The only significant difference is at the mid-point ($X_p/D_g = 0.7$) where E_m was lower for the impinging concentric element, resulting in a curve of increasing upward slope. The curve appeared to be linear for the basic impinging element. The upward trend of mixing with X_p/D_g is also in accord with the hot firing $(\eta_{c^*})_{mix}$ obtained in Task I LOX/GH_2 tests for the impinging concentric injector with $D_\ell/D_g = 0.4$. Over the range $0.4 \leq X_p/D_g \leq 0.80$ the hot firing $(\eta_{c^*})_{mix}$ increased from 93 to 99 percent.

The effect of the liquid-to-gas diameter ratio is illustrated in Fig. 61b. The penetration parameter was held constant in these tests by varying the overall mixture ratio along with D_ℓ/D_g. Note that mixing factor remains nearly constant for these two tests. Similar results were obtained with the basic impinging concept over this limited D_ℓ/D_g range, i.e., $0.21 \leq D_\ell/D_g \leq 0.31$. However, a continued increase of D_ℓ/D_g beyond 0.3 resulted in a decline in mixing for the basic impinging injector. On the other hand, Task I cold-flow work (which assumed uniform gas distribution) indicated that mixing level to decline sharply with D_ℓ/D_g, less than 0.2. The conservative approach then would be to maintain D_ℓ/D_g between 0.2 and 0.3 or perhaps 0.2 and 0.4.

The influence of increasing the annulus gas flowrate is presented in Fig. 61c, holding the center gas and liquid flowrates constant. In effect, this increases the gas-liquid concentric tube $V_g - V_\ell$ and decreases the concentric tube mixture ratio. In light of the basic concentric element cold-flow results this would be expected to increase the concentric streams' potential. However, the overall element mixing factor is seen to decrease substantially as the annulus gas flowrate is increased. In Task I cold-flow tests a similar effect was observed as the percent annulus gas was increased, although in that case this was accomplished at constant mixture ratio by simultaneously decreasing the center gas injection rate and increasing that of the

annulus gas. (Again it is to be remembered that gas flow distributions were not actually measured in Task I.)

The remaining parameters investigated were the center gas momentum flux and scale. All other operating conditions were held constant for these tests. Resultant mixing factors are plotted in Fig. 61d and 61e. Although there is some data scatter, the influence of $\rho_g V_g^2$ on mixing appears to be weak in the range tested (Fig. 61d). If these data are plotted together with the basic impinging E_m versus $\rho_g V_g^2$ data, Fig. 53c, an upward trend with increasing $\rho_g V_g^2$ is suggested. The effect of scale on mixing, plotted in Fig. 61e, was as expected: decreasing scale by a factor of four increased the mixing factor from 72.5 to 87.5 percent.

Tricentric With Centerbody Cold-Flow Tests. Six atomization and five mixing tests were conducted with the tricentric with centerbody injector concept. Primary variables for these tests included the gas injection velocities, mixture ratio, thickness of the liquid and gas streams, and scale.

Atomization Tests. Operating conditions and the mass median dropsizes attained in each of the atomization tests are summarized in Table 18. The first three tests were designed to investigate the effect of gas injection velocities on mass median dropsize. The baseline injector hardware pictured in Fig. 39 was utilized for these tests, and the mixture ratio was held constant. The results of these tests are plotted in Fig. 62a. As expected, the mass median dropsize decreased with increasing gas injection velocities. Over the V_g (gas velocity) range of 330 to 1050 ft/sec (101 to 320 m/s) the median dropsize decreased by approximately 32 percent.

The centerbody diameter for the first three tests was 0.25 in. (0.64×10^{-2} m). This diameter was increased to 0.75 in. (1.91×10^{-2} m) for the next test while maintaining constant inner fuel, oxidizer, and outer fuel injection areas. Thus, because of the increased perimeter of each annular orifice, the annulus gaps were decreased substantially. A photograph of this injector is presented in Fig. 63, and the test results are plotted in Fig. 62b.

TABLE 18

SUMMARY OF TRICENTRIC WITH CENTERBODY TESTS

Test No.	Inner Gap		Liquid Gap		Outer Gap		Total Gas Area		Liquid Area		MR	Gas Velocity (V_g)		$\rho_g V_g^2$		Measured D, μ or	E_m,
	in.	m x 10^{-2}	in.	m x 10^{-2}	in.	m x 10^{-2}	$in.^2$	m^2 x 10^{-3}	$in.^2$	m^2 x 10^{-3}		ft/sec	m/s	psi	N/m^2 x 10^4	m x 10^{-6}	percent
Atomization Tests																	
A-61	0.121	0.307	0.059	0.150	0.056	0.142	0.282	0.182	0.115	0.074	9.9	1054	322	15.0	10.7	286	
A-62	0.121	0.307	0.059	0.150	0.056	0.142	0.282	0.182	0.115	0.074	10.3	663	202	5.4	3.7	335	
A-63	0.121	0.307	0.059	0.150	0.056	0.142	0.282	0.182	0.115	0.074	10.1	330	101	1.3	0.9	421	
A-64	0.055	0.140	0.035	0.089	0.040	0.102	0.279	0.180	0.106	0.068	10.2	655	200	5.3	3.7	633	
A-65	0.122	0.310	0.058	0.147	0.059	0.150	0.583	0.376	0.203	0.131	10.0	666	203	5.5	3.8	356	
A-66	0.122	0.310	0.058	0.147	0.059	0.150	0.583	0.376	0.203	0.131	5.0	668	204	5.5	3.8	249	
Mixing Tests																	
M-36	0.121	0.307	0.059	0.150	0.056	0.142	0.282	0.182	0.115	0.074	9.8	954	291	16.4	11.3		73.8
M-37	0.121	0.307	0.059	0.150	0.056	0.142	0.282	0.182	0.115	0.074	9.6	629	192	6.5	4.5		74.8
M-38	0.121	0.307	0.059	0.150	0.056	0.142	0.282	0.182	0.115	0.074	9.9	271	83	1.1	0.7		60.3
M-39	0.122	0.310	0.058	0.147	0.059	0.150	0.583	0.376	0.203	0.131	10.1	624	190	6.1	4.2		83.3
M-40	0.055	0.140	0.035	0.089	0.044	0.102	0.279	0.180	0.106	0.068	10.0	619	189	6.1	4.2		64.3

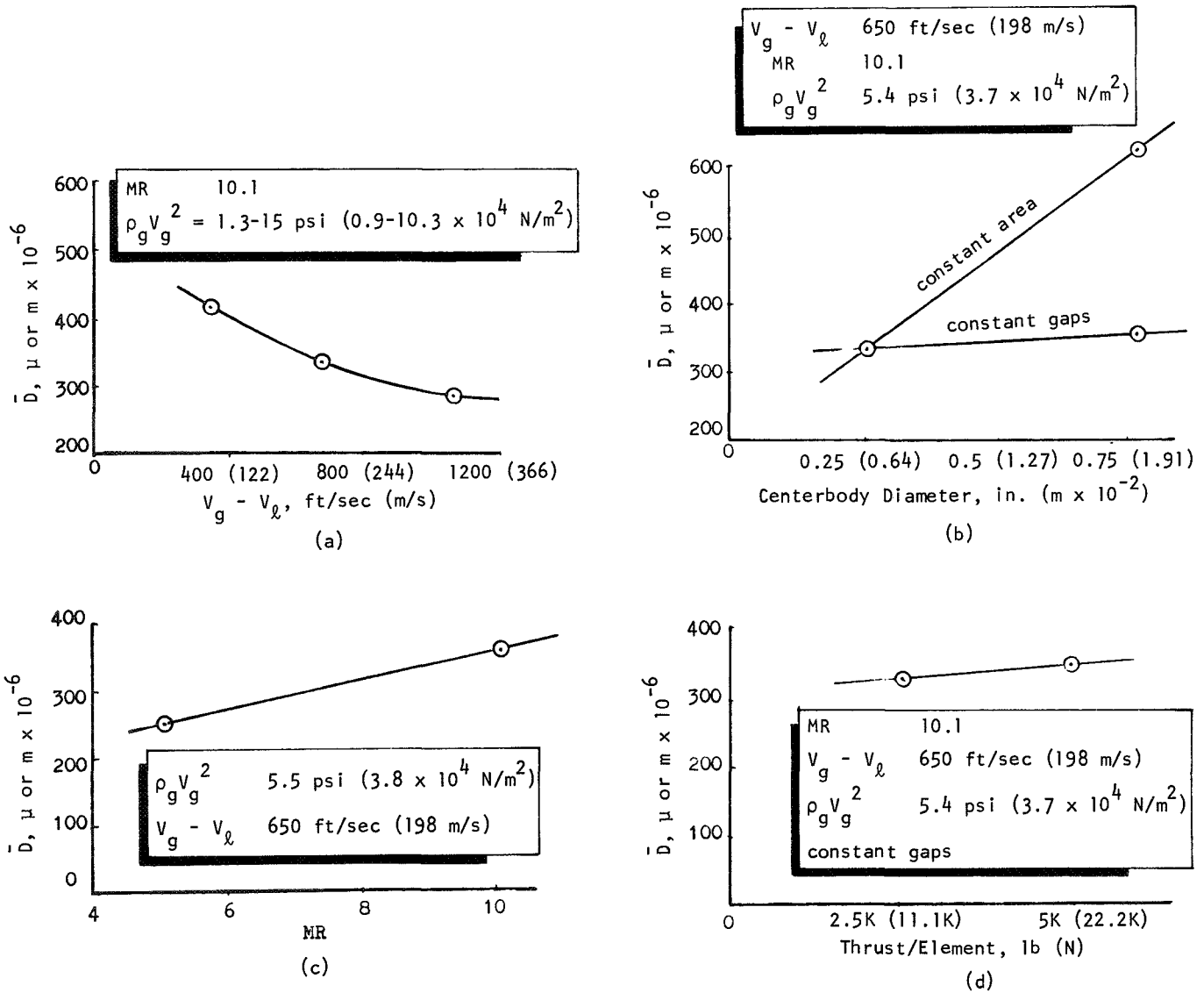

Figure 62. Tricentric With Centerbody Injector Atomization Test Results

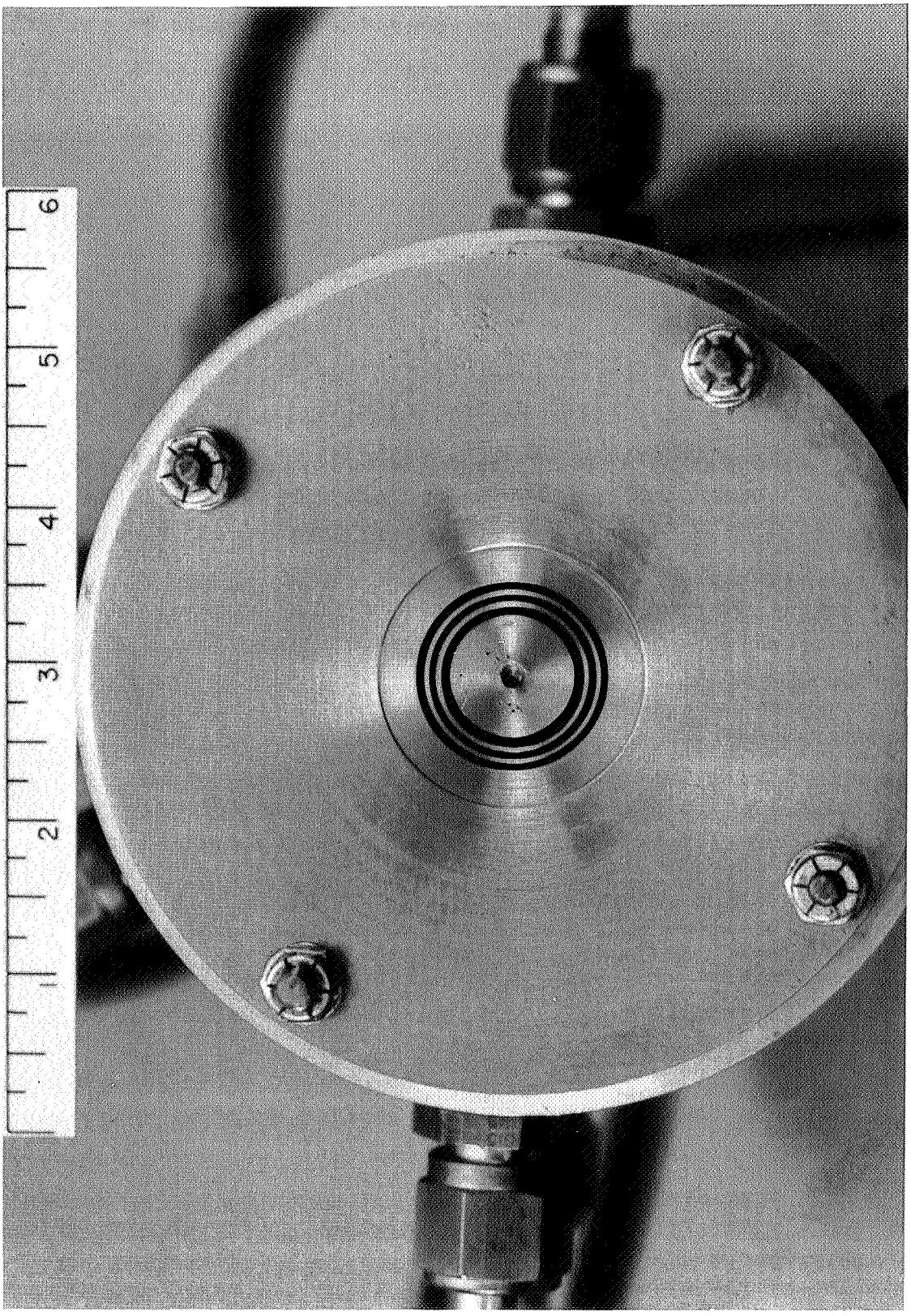

Figure 63. Tricentric With Centerbody Cold-Flow Injector (Injector Area Same as Baseline Injector)

Note that the mass median dropsize increased approximately 90 percent as the centerbody diameter increased and the annulus gaps were decreased. Contrary to expectation, this means that larger dropsizes were obtained with this injector when the liquid annulus gap decreased (while maintaining constant liquid and gas injection areas). Possibly the effectiveness of the augmenting gas was reduced by the reduced size of the gas annulus gaps.

The third hardware variation involved changing the centerbody diameter from the baseline value of 0.25 in. (0.64×10^{-2} m) to 0.75 in. (1.91×10^{-2} m), while maintaining the same annulus gaps as the baseline injector. This resulted in a significantly greater injection area. Two tests were conducted with this injector. In the first, the mixture ratio and injection velocities were held the same as those of the baseline injector tests. A very small dropsize change, approximately 7 percent, was observed in this test as illustrated in Fig. 62b and 62d. This verifies the expection that this type of element can be changed in size (increased flowrate) with little effect on atomization, provided the annular gap dimensions are not varied. In the second test, the mixture ratio was decreased by a factor of 2 (from 10 to 5) while holding the gas injection velocity constant. This test was added to the test matrix because of the strong trends observed with mixture ratio in the basic concentric tube cold-flow tests. Test results, plotted in Fig. 62c, for the tricentric with centerbody concept also illustrate a strong influence of mixture ratio with the mass median dropsize decreasing by approximately 30 percent as the mixture ratio was changed from 10 to 5.

Mixing Tests. The tricentric with centerbody injector cold-flow mixing experiments were conducted employing the same hardware and basically the same test series as utilized in the atomization tests described in the preceding section. Operating conditions for the mixing tests are summarized in Table 18.

Several qualitative trends were seen in the raw data. Gas stagnation pressures were relatively constant in the middle of the flowfield and decreased at its edge. Also, the dynamic pressures were reduced by an order of magnitude as the injected gas velocity dropped from 950 to 270 ft/sec (290 to 82 m/s).

The oxygen content from ingested air increased with radius as expected. In general, with the larger centerbody diameters, the oxygen content in the center was somewhat lower, indicating a slower ingestion of air. Liquid mass flux maximized near the center of the flowfield and decreased with radius.

Mixing factors (E_m) were calculated for each test directly from the cold-flow local flowrates measured. The effect of varying $V_g - V_\ell$ at constant mixture ratio is shown in Fig. 64a. Note the expected increase in the mixing factor as $V_g - V_\ell$ increased. The results of varying scale (i.e., injection area) and annulus gaps are presented in Fig. 64b. Since these two parameters were both varied by changing the centerbody diameter, the mixing factor is plotted against centerbody diameter for convenience. A significant mixing factor is seen with increasing scale, but fixed annulus gaps. This is somewhat surprising since the mean dropsize found in the atomization tests was not altered by a change in total injection area. However, when scale (total injection area) was held constant and the annulus gaps were decreased, a significant decrease in the mixing factor was observed, which is in accord with the reduction in atomization effectiveness under the same conditions.

Dropsize Distribution About the Median Dropsize

Hot-fire vaporization efficiencies are determined by the distribution of dropsizes around a median dropsize value as well as the absolute magnitude of that median. Dropsize distributions about the mean were investigated for each injector type. These distributions were obtained by plotting each of the experimental cumulative weight fractions versus a nondimensional dropsize ($D/\bar{D}$), with the data for each individual injector concept plotted on one graph. Curves were then drawn (for each injector type) through the least, the average, and the most monodispersed distributions as shown in Fig. 65. The difference between the least and most monodispersed curve for the basic concentric was significantly greater than that for any of the other concepts. Comparing the median dropsize data and the dropsize distribution data for this concept indicates that the tests which produced the more nearly monodispersed spray were those which resulted in the smaller values of $\bar{D}$. Thus optimization

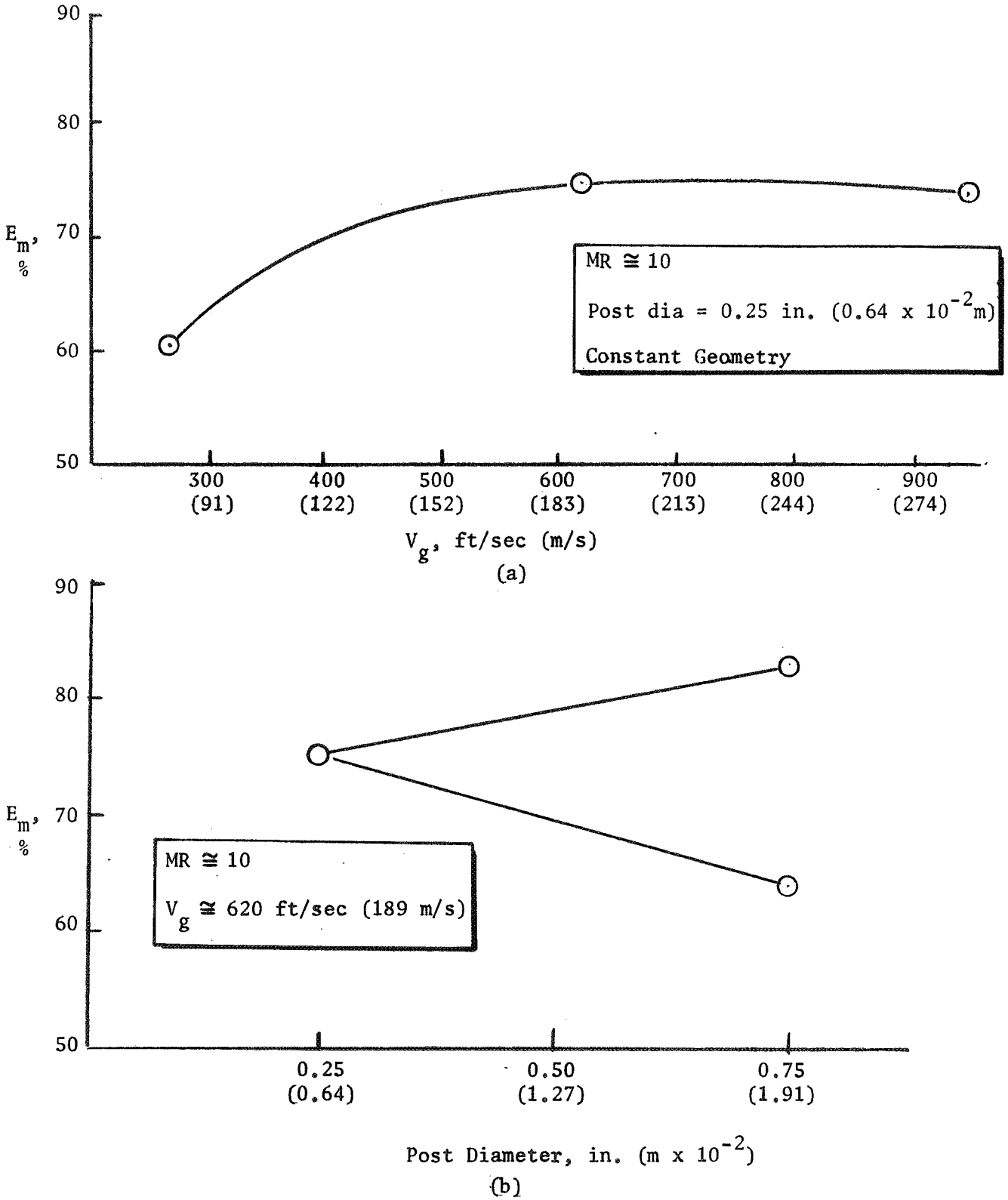

Figure 64. Summary of Cold-Flow Results: Tricentric with Centerbody Injector

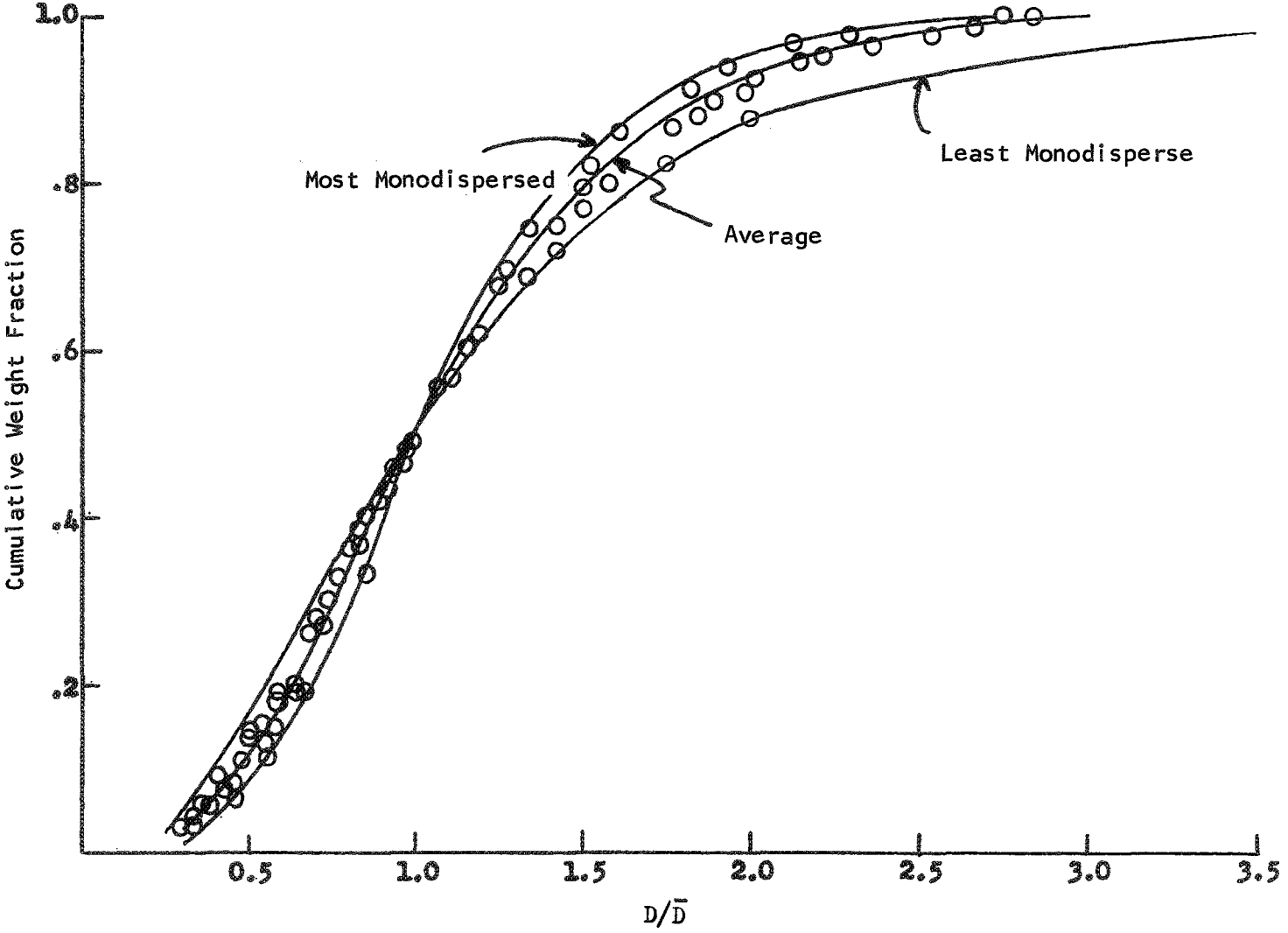

Figure 65. Impinging Coaxial Experimental Dropsize Distribution

of the mass median dropsize improved the dropsize distribution as well. The range from minimum to maximum experimental median dropsizes was not wide enough with the other concepts to distinguish this trend.

Figure 66 provides a direct comparison of the average dropsize distribution curves produced by the various types of injector elements. Also shown is a standard Nukiyama-Tanasawa distribution (Ref. 5) which has frequently been used to describe polydisperse sprays in combustion model analysis. Clearly, the experimental data are relatively less monodisperse than the "N-T" curve.

In a subsequent section, "Performance Effects," combustion model calculations were applied to quantitatively evaluate the effects of dropsize distribution about $\bar{D}$ in terms of $(\eta_{c^*})_{vap}$ for a reference combustion system ($FLOX/CH_4$ at 500 psia (345×10^4 N/m^2) in a 30-in. (0.762 m) L* chamber). The maximum spread in $(\eta_{c^*})_{vap}$ from the least monodispersed (concentric element) test to the most monodispersed (impinging concentric element) test corresponded to about ±2.5 percent. It was concluded that the appropriate dropsize distribution curves should be used to predict exact values of vaporization efficiencies; however, the dropsize distribution is clearly a secondary parameter to $\bar{D}$ itself. Thus parametric analysis of atomization potential in terms of $\bar{D}$ is justified.

Mass Flux and Mixture Ratio Profile Investigation

Mass and mixture ratio profiles from each type of injection element were analyzed to better understand the effect of varying design parameters. Several examples are shown in the following sections. For the concentric type injector concepts, two types of curves are used: one to show the mixture ratio profile versus radius, and the other to show total (gas and liquid) mass flowrate per inch of radius normalized by the injected flowrates and plotted as a function of radius. The symmetry of the concentric-type (this also includes the swirl and tricentric elements) element flowfield lends itself to this one-dimensional profile, which is impractical with the impinging concepts.

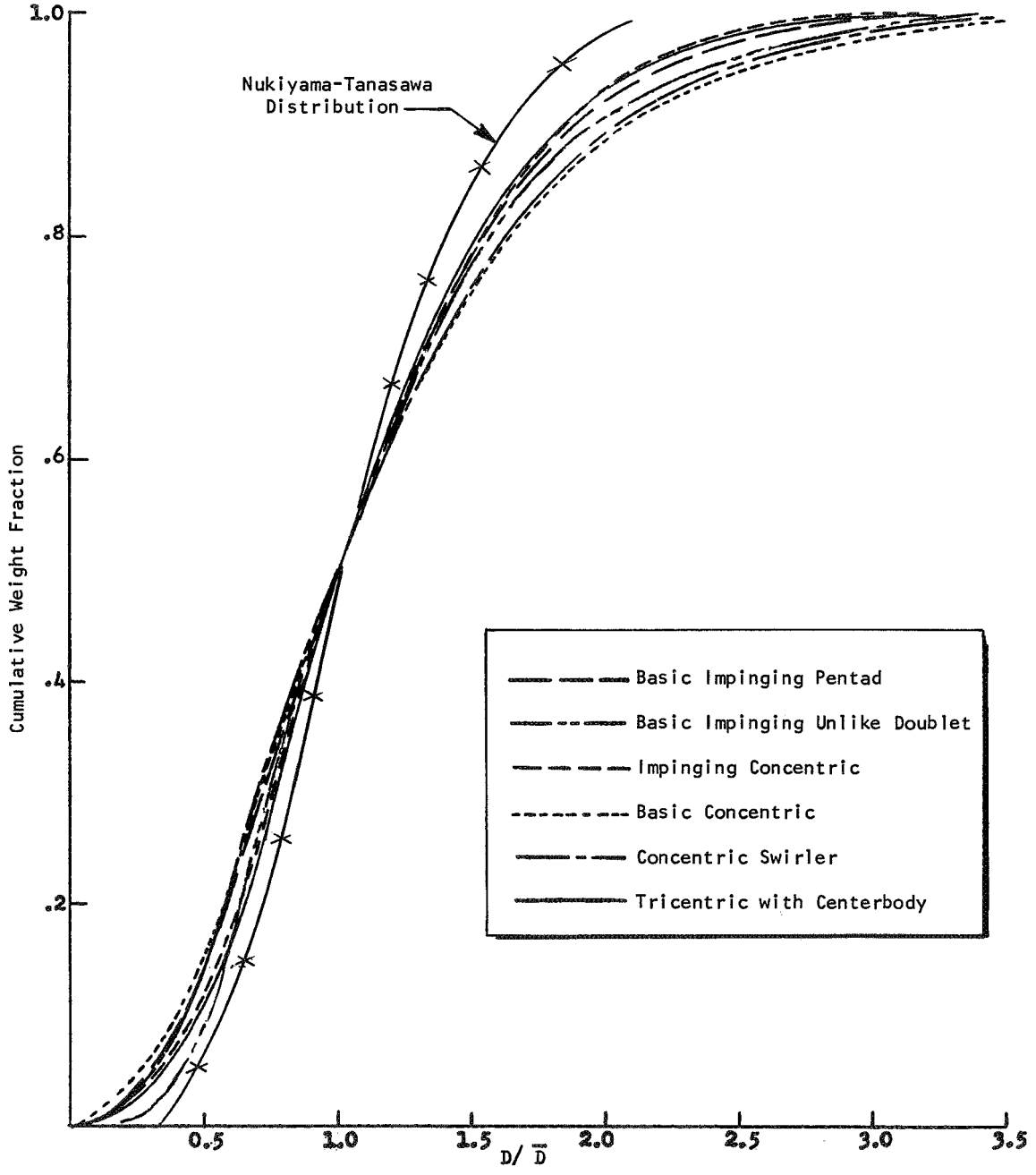

Figure 66. Average Experimental Dropsize Distribution for Task II Injector Concepts

Thus, the concentric element results are reported together, after which the impinging element results are reported in terms of two-dimensional contour plots of the measured flowfields.

Basic Concentric. The principal variables investigated experimentally with this concept are the amount of post recess, $V_g - V_\ell$, and mixture ratio. Each mixture ratio profile decreases, in general, with radius from a central maximum to a minimum at the edges. In contrast, the mass fraction profiles generally go through a maximum as the radius increases from zero and then declines with larger radius.

Mass and mixture ratio profiles are shown in Fig. 67 for tests investigating the amount of post recess with the small-scale concentric tubes. Note the pronounced drop in centerline mixture ratio as the recess is increased. In addition, the mixture ratio at larger radial distances from the element centerline is increased with increasing post recess. Both changes reflect the enhanced gas-liquid stripping and momentum exchange which results from post recessing. The net effect of increasing the post recess is greater mixture ratio uniformity. Similar results can be seen with the mass profile with the region of maximum mass flux moving radially outward with increasing post recess. This flattening of both mass and mixture ratio profiles as the amount of post recess increases yields a rather large increase in mixing efficiency. Similar results can be seen with the larger-scale injector model.

The effects of increasing $V_g - V_\ell$ are plotted in Fig. 68 again for the small-scale concentric element. The most noticeable effect is a large reduction of the centerline mixture ratio as $V_g - V_\ell$ is increased. The mixture ratio at $r \geq 0.4$ in. (1.02×10^{-2} m) is raised by the higher $V_g - V_\ell$. The mass flux profiles for different $V_g - V_\ell$ reflect an outward movement under the influence of increased shear by the gas.

Decreasing the injected mixture ratio has a profound effect on both the mass and the mixture ratio profiles. This is illustrated in Fig. 69. The centerline mixture ratio is decreased by 67 percent as the injected mixture ratio

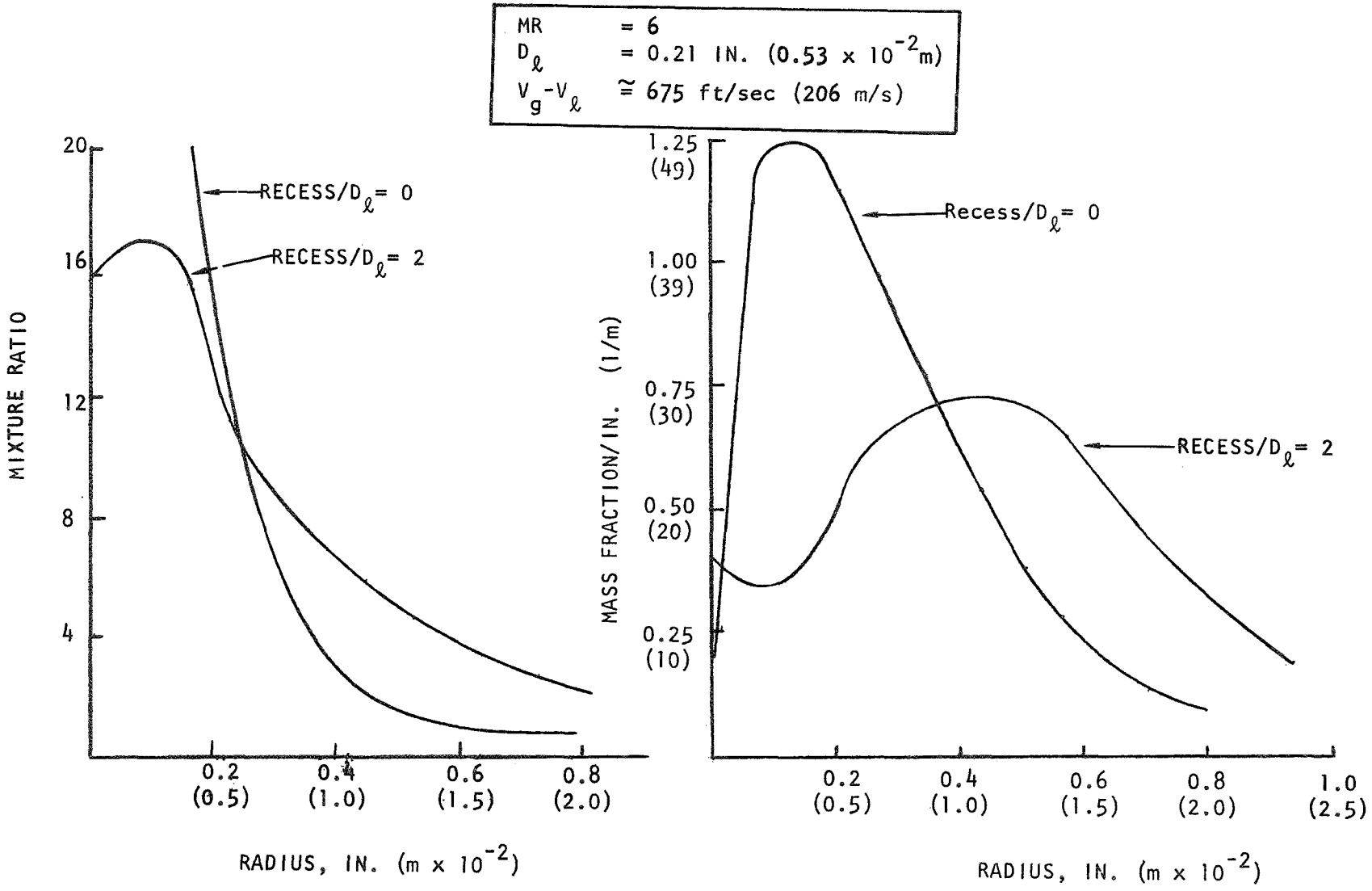

Figure 67. Mass and Mixture Ratio Profiles Versus Post Recess: Basic Concentric Injector

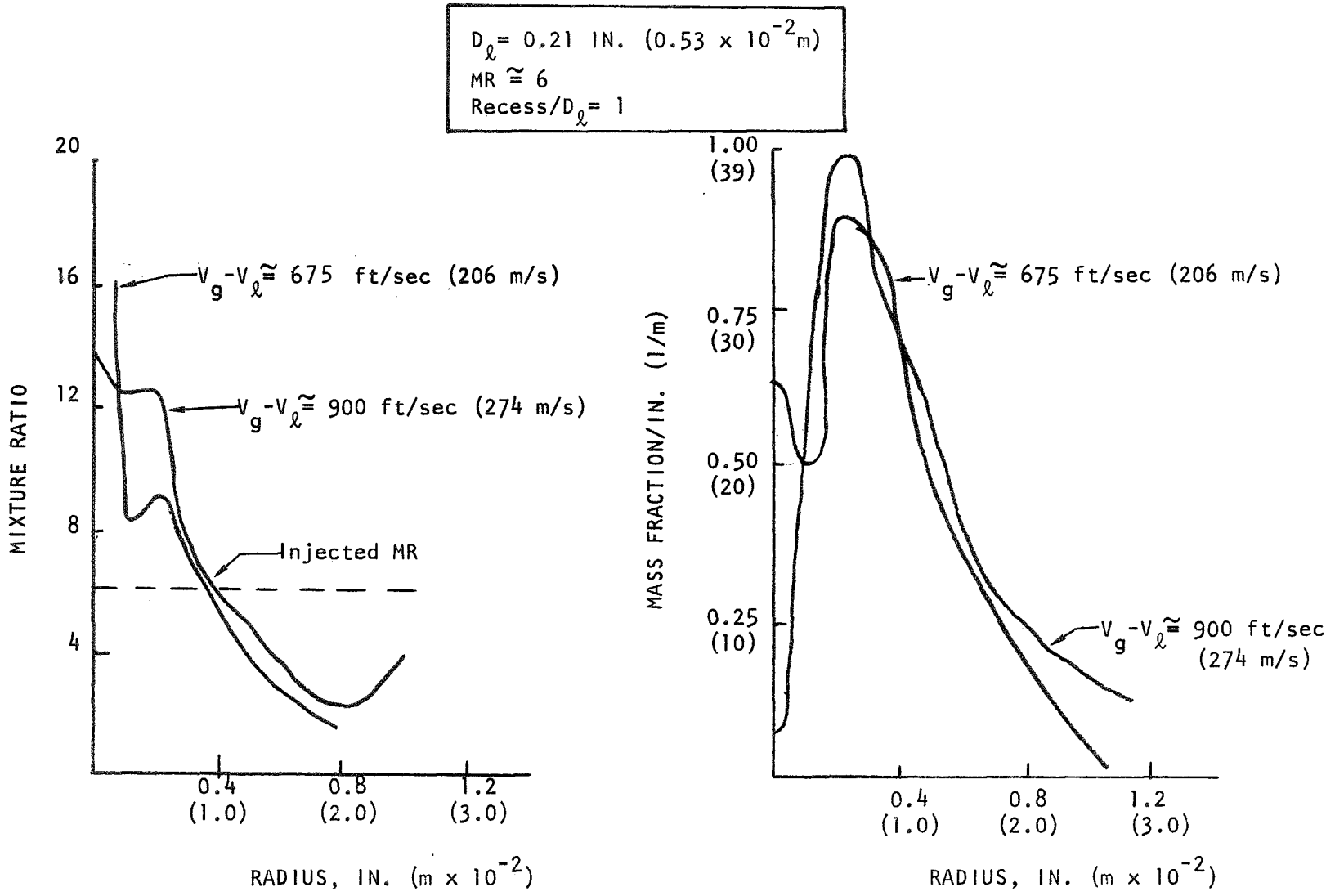

Figure 68. Mass and Mixture Ratio Profiles Versus V_g-V_ℓ: Basic Concentric Injector

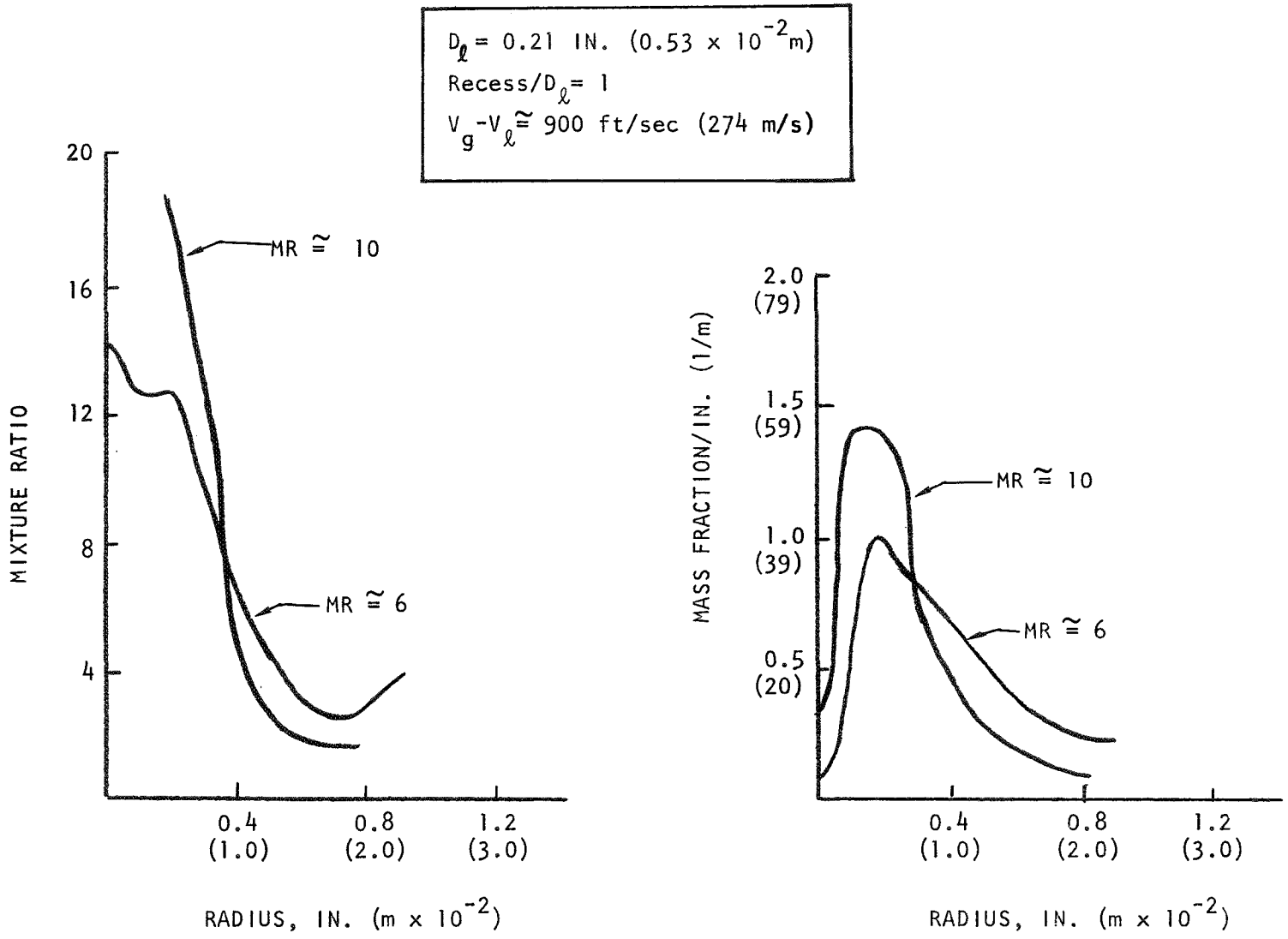

Figure 69. Mass and Mixture Ratio Profiles Versus Mixture Ratio: Basic Concentric Injector

decreases from 10 to 6. As radius increases, the local mixture ratio decreases in both cases until the local mixture ratios are equal at a radius of approximately 0.4 in. (1.02×10^{-2} m). The mass flux profile is also flattened as the injected mixture ratio is decreased, reflecting a better capability of the gas to atomize and disperse the relatively smaller amount of liquid.

Concentric With Swirler. The only parameter investigated in mixing tests with this concept was the liquid swirl velocity. As previously reported, the variance of this parameter covers a fairly narrow range (65 to 100 ft/sec; 19.8 to 30.5 m/s). Thus, the mass and mixture ratio profiles were relatively similar for these two tests. However, comparing the swirler type element to the basic concentric (at zero swirl velocity) gives a significant indication of the effect of swirl on mixing. Representative flow profiles for the basic concentric (swirl velocity = 0) and concentric with swirl (swirl velocity = 65 ft/sec; 19.8 m/s) are shown together in Fig. 70. Other parameters such as $V_g - V_\ell$, mixture ratio, and element size were the same for both tests. The introduction of swirl dramatically shifted the mixture ratio profile so that the high mixture ratios occurred at large radii, rather than near the injection element's axis. The mass flux profile also reflects the substantial outward motion of spray due to the hydraulic swirl.

Tricentric With Centerbody. The primary parameters investigated with the tricentric with centerbody concept include $V_g - V_\ell$ and annulus gap dimensions. Mass and mixture ratio profiles for these tests are plotted in Fig. 71 and 72. It is of interest that the existence of two gas-liquid interfaces with this element results in two annular maxima in total mass flux per inch of radius. The liquid is apparently drawn inward and outward from its zone of initial injection by these two gas streams, to the extent that a mixture ratio minimum is produced at an intermediate radius. The extremely high mixture ratio approached at radii near zero and again at radii of about 1.5 inches result from the fact that some spray traverses each of the two annular gas streams. However, the amount of mass so involved is small and the importance of these high mixture ratios may be minimal.

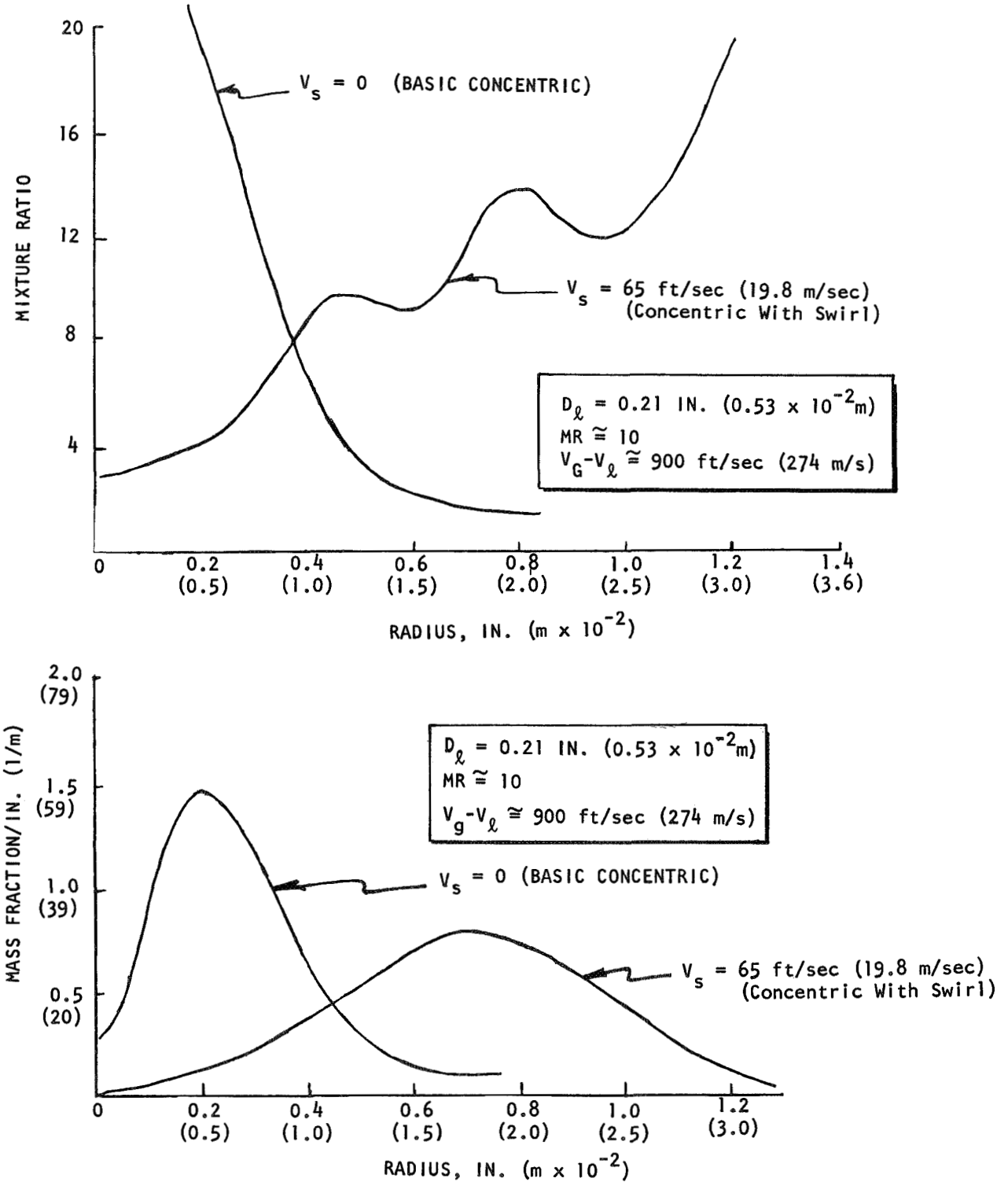

Figure 70. Mass and Mixture Ratio Profiles for Basic Concentric and Concentric With Swiler Element

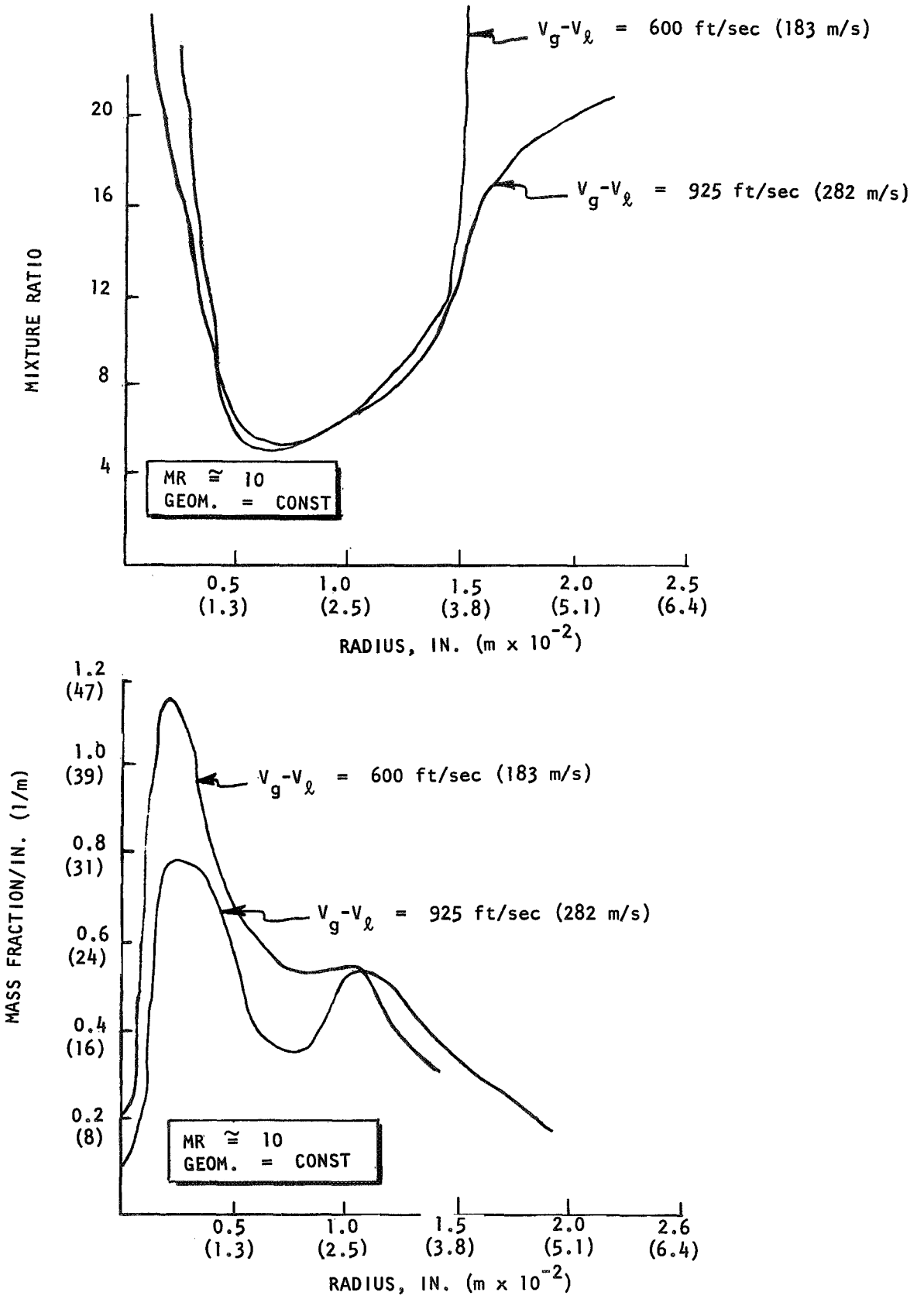

Figure 71. Experimental Mass and Mixture Ratio Profiles for the Tricentric With Centerbody Element

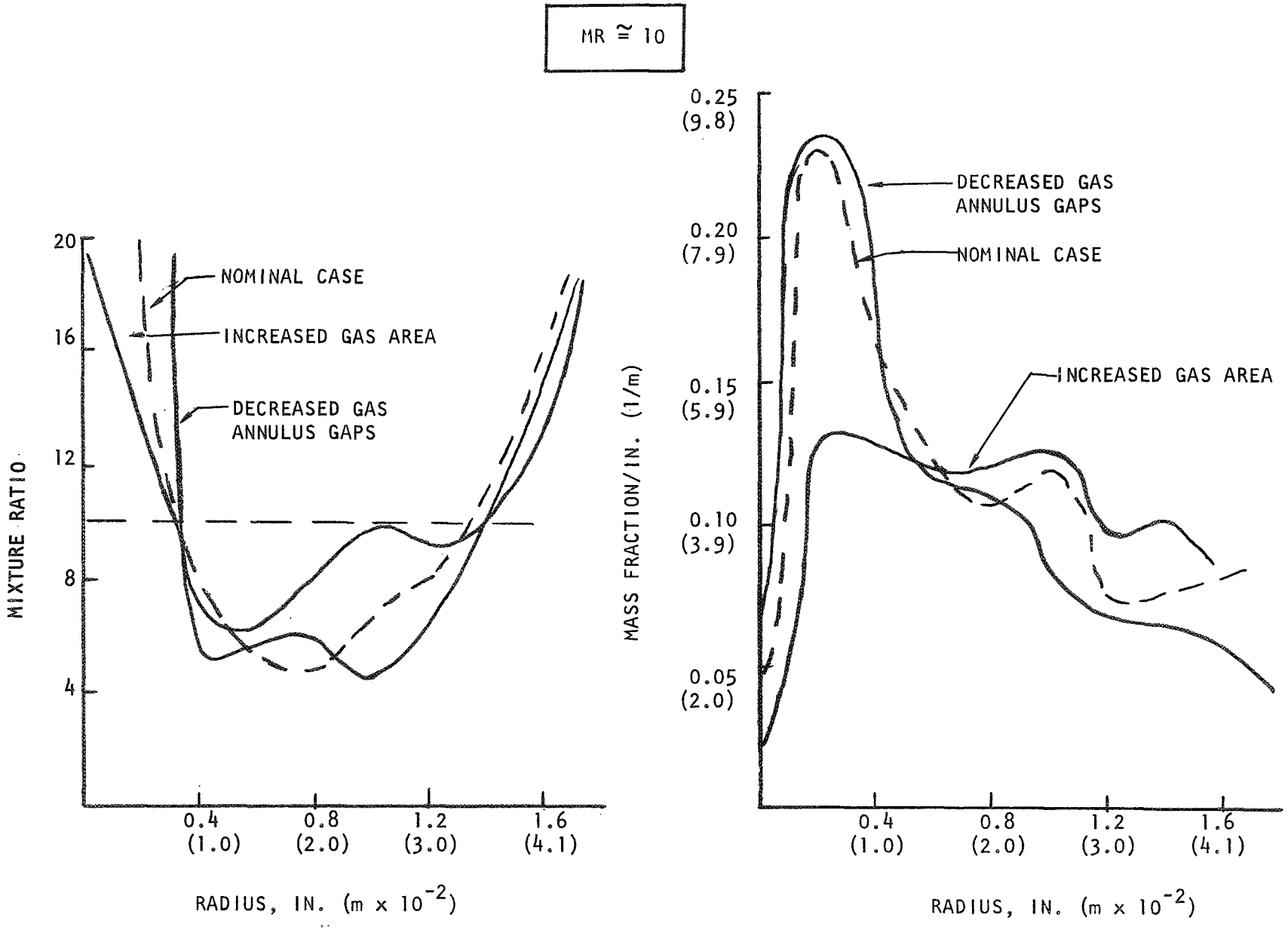

Figure 72. Mass and Mixture Ratio Profiles Versus Gas Annulus Geometry: Tricentric With Centerbody Injector

The effect of $V_g - V_\ell$ on the mass and mixture ratio profiles for this injector is illustrated in Fig. 71. Increasing $V_g - V_\ell$ is seen to reduce the liquid penetration across the outer gas annulus, as seen in the lowered mixture ratio at large radii. The mass flux profiles indicate increased $V_g - V_\ell$ causes an increase in two-phase flow at the outer radius at the expense of the flux at the inner maximum flow radius, i.e., there is a net outward shift in the flowfield.

Two perturbations were made experimentally with gap dimensions. In one case, the injection area was held constant while the annulus gaps were decreased, resulting in a mixing efficiency decrease (previously discussed). In the second case, the orifice injection area was increased while holding all three annulus gaps constant, resulting in slight increase in mixing efficiency. The mass flux and mixture ratio profiles are presented in Fig. 72. Decreasing the annulus gaps (constant injection areas) did not appreciably alter the total mass flux profile; however, it did result in a shift to very high mixture ratio at small radius ($r \leq 0.4$ in.; 1.02×10^{-2} m). Both effects contributed to a reduction of E_m (poorer mixing). On the other hand, the increase in injection areas (constant gap sizes) tended to smooth both mass flux and mixture ratio as was reflected in the relatively improved mixing.

Basic Impinging. The primary variables investigated with this concept include liquid penetration parameter (X_p/D_{g_2}), liquid-to-gas orifice diameter ratio (D_ℓ/D_g), gas dynamic pressure ($\rho_g V_g^2$), scale (D_g), and the number of liquid orifices. Because of the two-dimensionality of the flowfields that result from this injector type, mass flux distributions cannot in general be represented by a single curve. One method used to display these flowfields is by use of contour plots of liquid and gas mass flux. Both gas and liquid contour plots must be examined to evaluate a given run condition. Figure 73 presents a typical gas mass flux contour*. This particular diagram, at a

*The gas mass flux contours and profile included in this section are based on measured gas flux and are not corrected for ingested gas or altered by using the gas recirculation model.

X_p/D_g = 0.71

D_ℓ/D_g = 0.30

$\rho_g V_g^2$ = 14.7 psi ($10.1 \times 10^4 N/m^2$)

D_g = 0.81 IN. ($2.1 \times 10^{-2} m$)

IDENTIFICATION

0 -- 0.570
1 -- 0.817
2 -- 1.065
3 -- 1.310
4 -- 1.560
5 -- 1.805
6 -- 2.055
7 -- 2.295
8 -- 2.550
9 -- 2.795

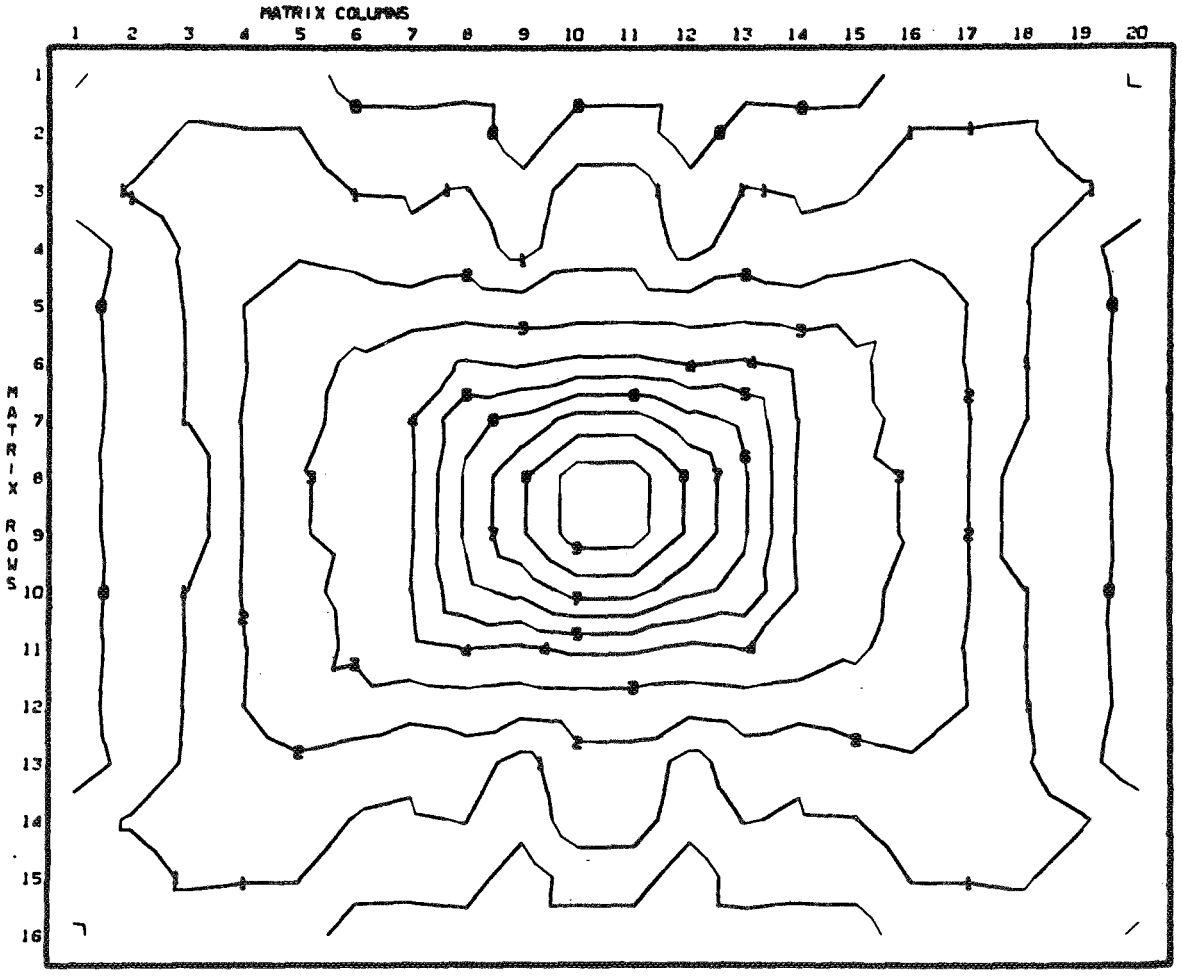

Figure 73. Normalized Gas Mass Flux Distribution: Basic Impinging (4 on 1) Injector Test M-2

nominal test condition, shows a mass flux maximum (high contour line numbers) in the center, and monotonic decreasing flux with increasing distance from the center. Note that the flowfield exhibits a relatively square pattern as a result of gas being "squeezed" between the four incoming liquid jets.

The liquid penetration (X_p/D_g) has a pronounced effect on both the gas and the liquid normalized mass flux pattern. Liquid mass flux contours for low and high X_p/D_g (0.35 and 0.96) are presented in Fig. 74 and 75 for the pentad injector case. The four high liquid concentration points which are in line with the liquid orifices in Fig. 74 graphically illustrate the limited penetration of the bulk of the liquid into the gas stream at $X_p/D_g = 0.35$. For this test, the liquid flux in the geometric center of the flowfield is at a relative minimum. As the penetration parameter is increased, the four high liquid flux zones combine into a single peak at the center (see Fig. 75; $X_p/D_g = 0.96$). Figure 76 illustrates the liquid flow pattern for an intermediate value of X_p/D_g (0.71), where the flowfield is intermediate between the extremes shown in the two preceding figures. In this case, which is typical of the "nominal" penetration parameter, the relative maximum liquid flux appears as a broad annular ring. This liquid flowfield transition can also be shown in normalized mass flux profiles. Figure 77 presents profiles corresponding to the contours of Fig. 74, 75, and 76 for the case in which the ray chosen for presentation is in the plane defined by two opposing liquid orifices (vertical in Fig. 74). Again, for low penetration, the liquid mass flux maximum occurs away from the geometric center (0.75 in.; 0.019 m). Medium penetration is characterized by a relatively uniform mass flux distribution. Finally, liquid mass flux concentration at the center coincides with a high value of the penetration parameter. Note that this profile (normalized flowrate per square inch) cannot be directly compared to the profiles presented for the concentric injector concept in which flowrate per inch of radius was plotted. The present method was chosen for impinging-type injectors because the flowfields are not axisymmetric.

Profile curves can be used in a similar fashion to illustrate the change in normalized gas mass flux distribution with changes in penetration parameter.

X_p/D_g = 0.36

D_ℓ/D_g = 0.30

$\rho_g V_g^2$ = 14.3 psi ($9.9 \times 10^4 N/m^2$)

D_g = 0.81 IN. ($2.1 \times 10^{-2} m$)

IDENTIFICATION

0 -- 0.474
1 -- 0.674
2 -- 0.875
3 -- 1.074
4 -- 1.273
5 -- 1.472
6 -- 1.674
7 -- 1.872
8 -- 2.080
9 -- 2.270

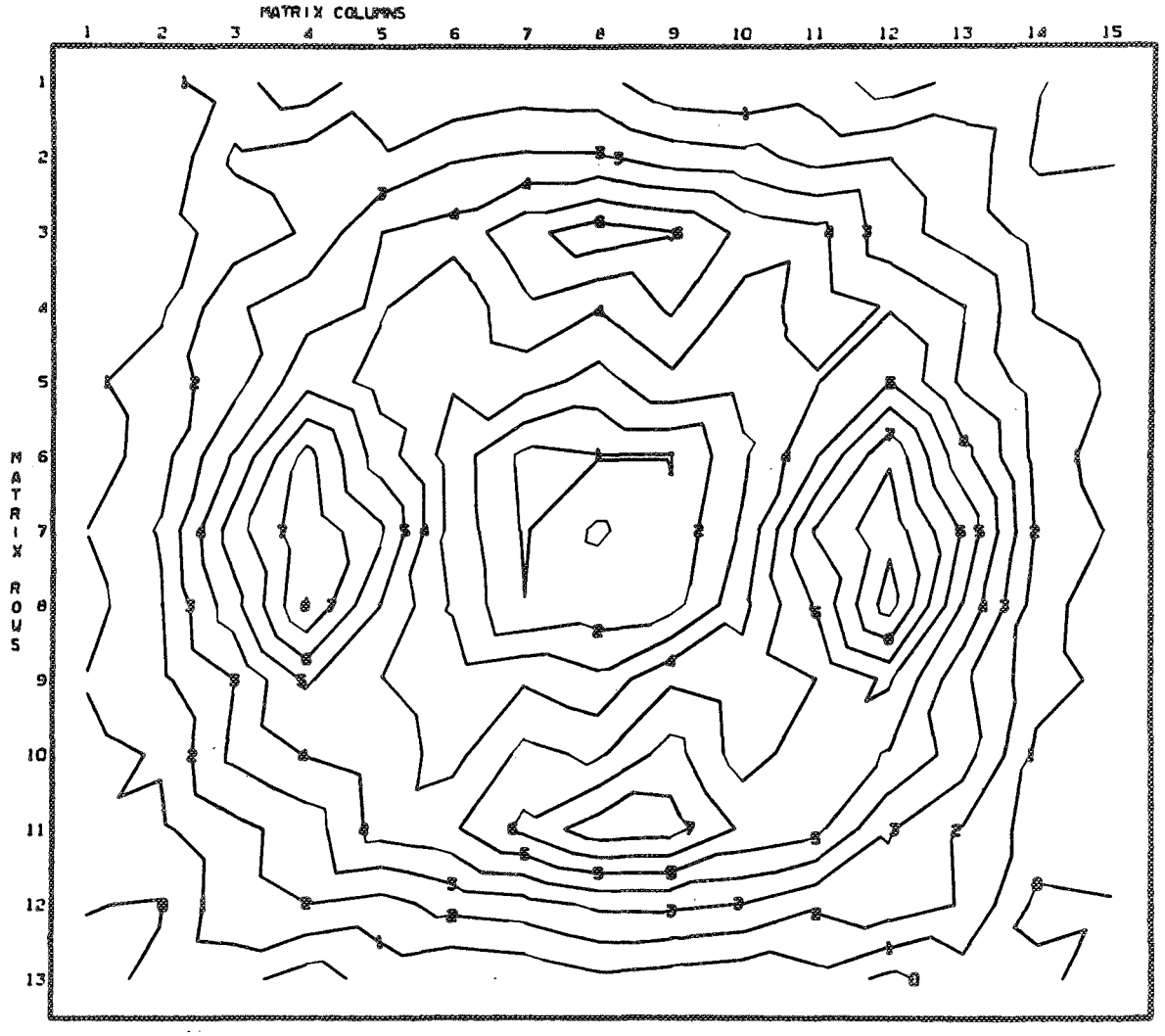

Figure 74. Normalized Liquid Mass Flux Distribution: Basic Impinging (4 on 1) Injector Test M-1

X_p/D_g = 0.96

D_ℓ/D_g = 0.26

$\rho_g V_g^2$ = 14.4 psi ($9.9 \times 10^4 N/m^2$)

D_g = 0.81 IN. ($2.1 \times 10^{-2} m$)

IDENTIFICATION

0 -- 0.421
1 -- 1.065
2 -- 1.700
3 -- 2.340
4 -- 2.980
5 -- 3.620
6 -- 4.270
7 -- 4.910
8 -- 5.550
9 -- 6.200

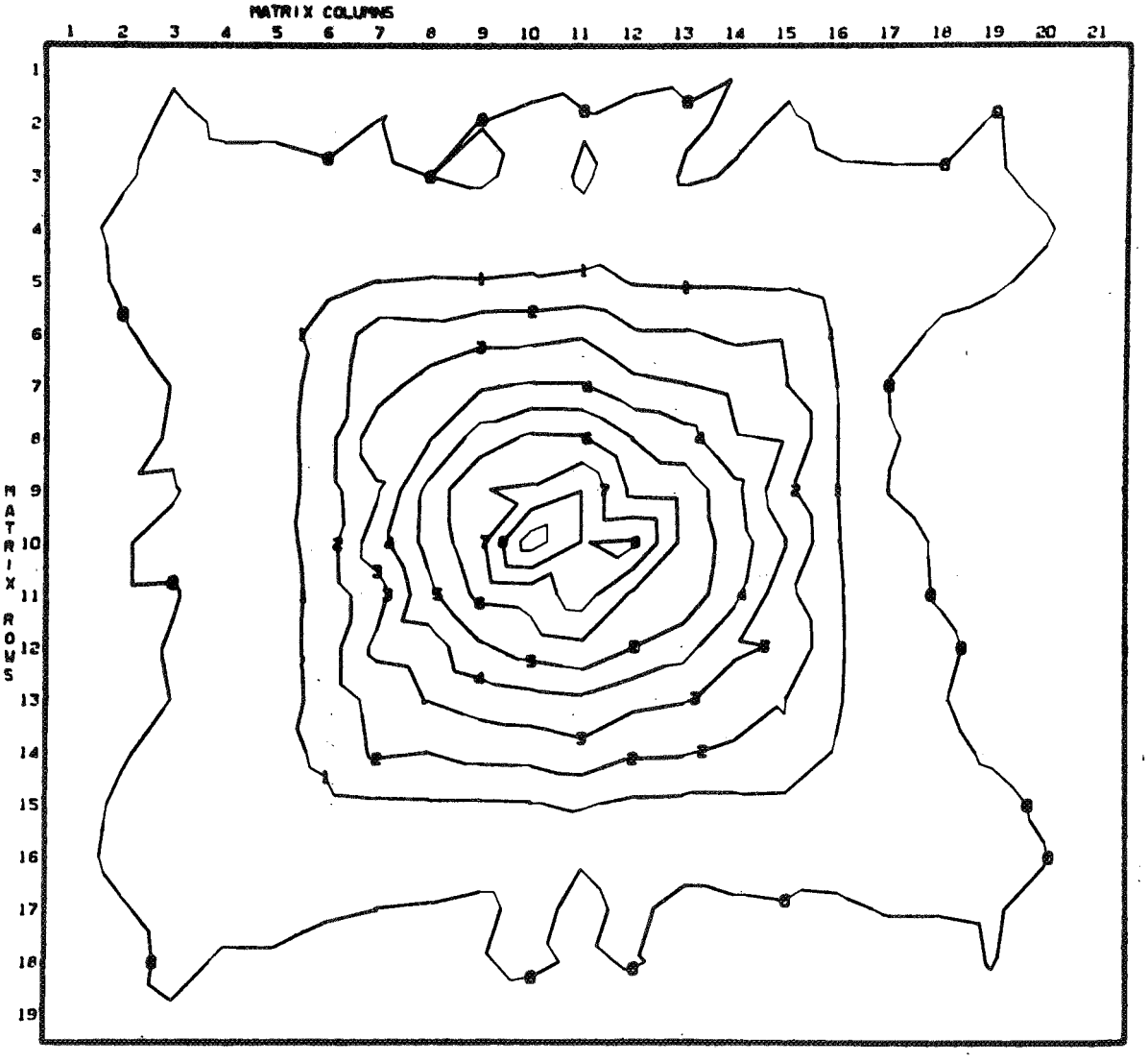

Figure 75. Normalized Liquid Mass Flux Distribution: Basic Impinging (4 on 1) Injector Test M-6

X_p/D_g = 0.71

D_ℓ/D_g = 0.30

$\rho_g V_g^2$ = 14.7 psi ($10.1 \times 10^4 N/m^2$)

D_g = 0.81 IN. ($2.1 \times 10^{-2} m$)

IDENTIFICATION

0 -- 0.293
1 -- 0.522
2 -- 0.751
3 -- 0.980
4 -- 1.205
5 -- 1.435
6 -- 1.665
7 -- 1.895
8 -- 2.120
9 -- 2.350

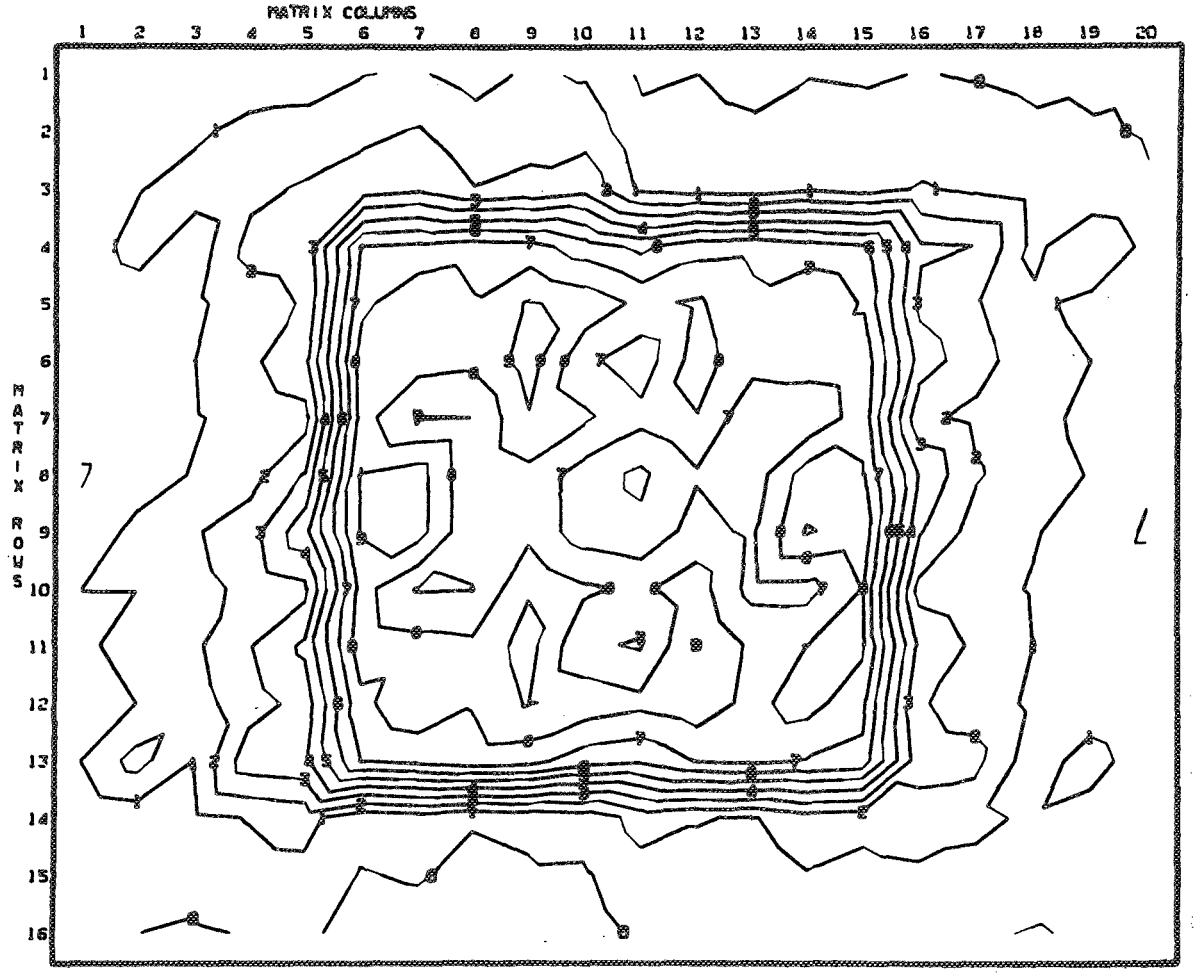

Figure 76. Normalized Liquid Mass Flux Distribution: Basic Impinging (4 on 1) Injector Test M-2

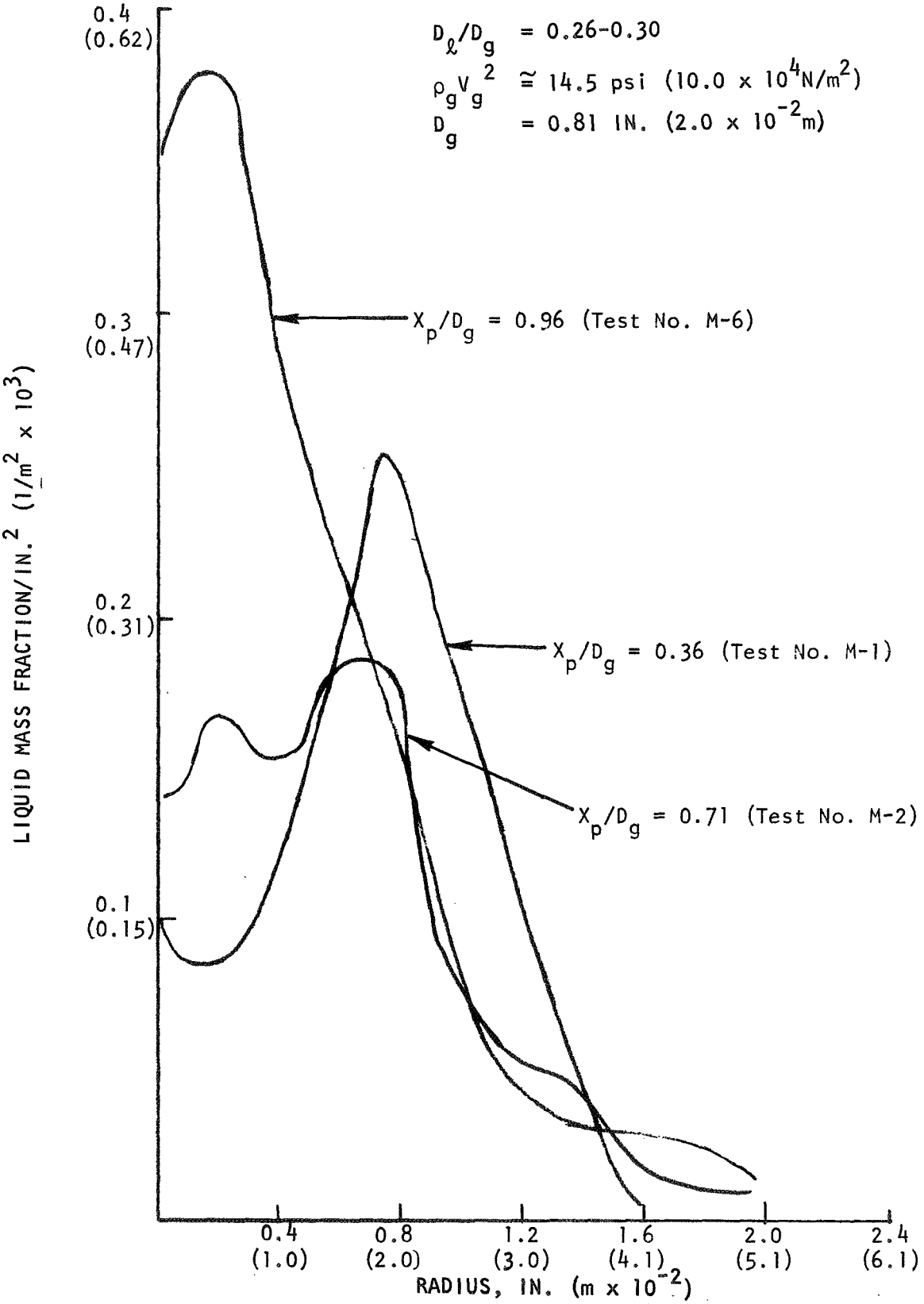

Figure 77. Liquid Mass Distribution Profiles vs X_p/D_g: Basic Impinging (4 on 1) Injector

Refer to Fig.78 in which a ray similar to that used in Fig.77 was chosen. The trend with increasing X_p/D_g is obvious. The gas flux relative maximum remains at the center, but decreases in magnitude with increasing X_p/D_g, reflecting greater interaction of gas-liquid momenta. Additional profiles taken at other locations through the flowfield indicate the same flowfield trends.

Another key mixing parameter was the liquid-gas diameter ratio. For the basic impinging injector, D_ℓ/D_g was varied by changing the liquid orifice diameter, D_ℓ (constant D_g). To change D_ℓ/D_g in this manner at constant X_p/D_g, ρ_g, and $\rho_g V_g^2$, the liquid jet velocity changes inversely proportional to D_ℓ/D_g while mixture ratio increases proportionally with D_ℓ/D_g. The effects of diameter ratio are best shown by the liquid and gas mass flux profiles* of Fig.79 and 80 . The trend is the same for both liquid and gas distributions: when D_ℓ/D_g increases, the relatively high mass flux near the center is markedly diminished as the flows are shifted radially outward. Basically, then, the trend is toward more uniform gas and liquid mass flux as D_ℓ/D_g rises.

The primary influence of the gas dynamic pressure parameter ($\rho_g V_g^2$) is on the distribution of the gas mass flux. As shown in flux profiles of Fig. 81, decreasing $\rho_g V_g^2$ tends to make the gas mass flux more evenly distributed. This trend reflects the fact that the gas velocity gradients are lower for lower values of $\rho_g V_g^2$. On the other hand, variation of the normalized liquid mass flux profile with gas dynamic pressure ratio is not pronounced.

Scale (D_g) changes did not have significant visual effect on the mass flux distributions of either the gas or the liquid.

The final parameter investigated with the impinging concept was the number of liquid orifices. Two tests were made with an unlike-doublet configuration,

*The contour plots for tests with variable D_ℓ/D_g at $X_p/D_g \cong 0.7$ are qualitatively similar and, in appearance, are much like Fig.76. Only by examination of the profiles was the effect of D_ℓ/D_g clearly apparent.

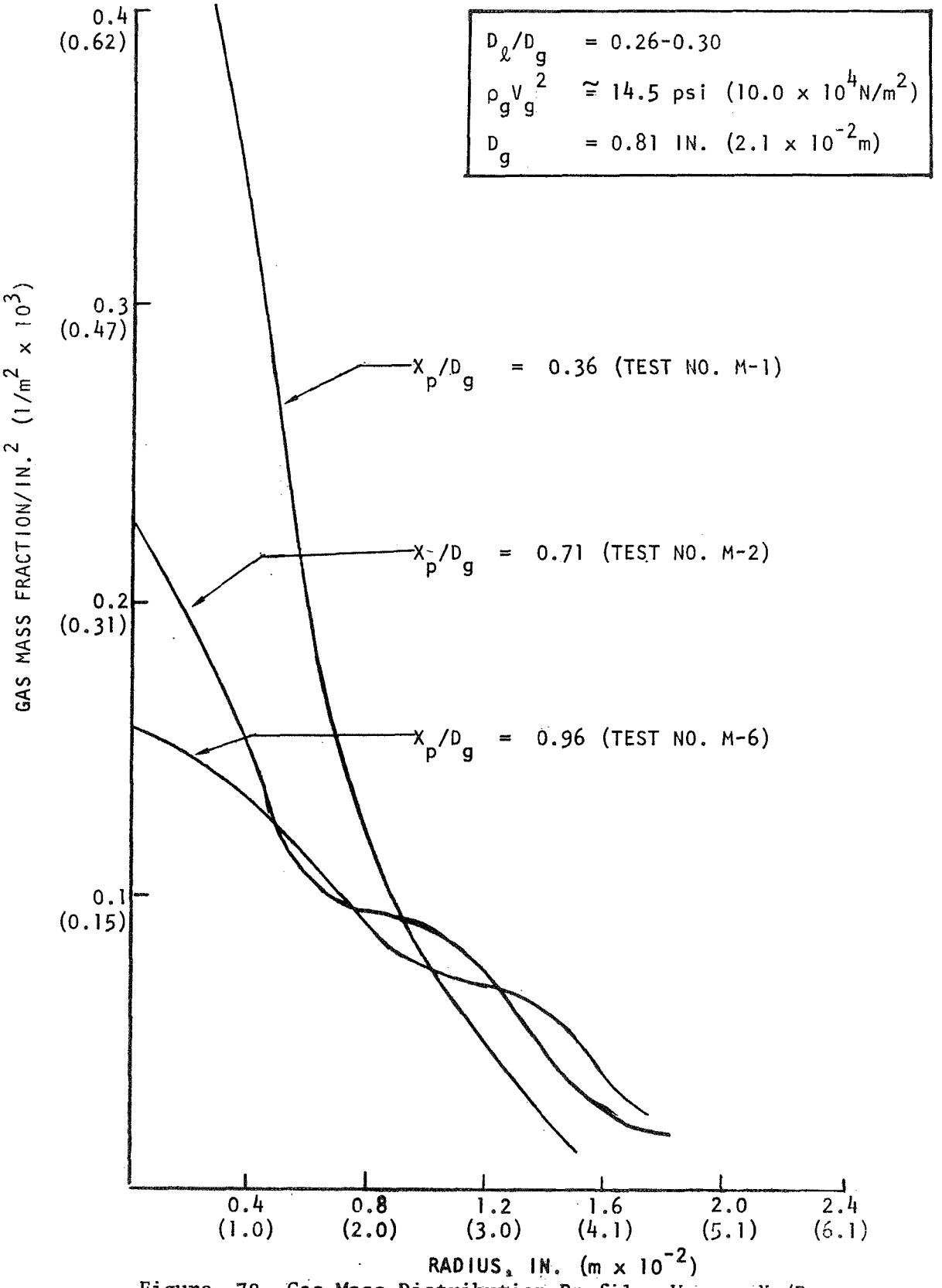

Figure 78. Gas Mass Distribution Profiles Versus X_p/D_g: Basic Impinging (4 on 1) Injector

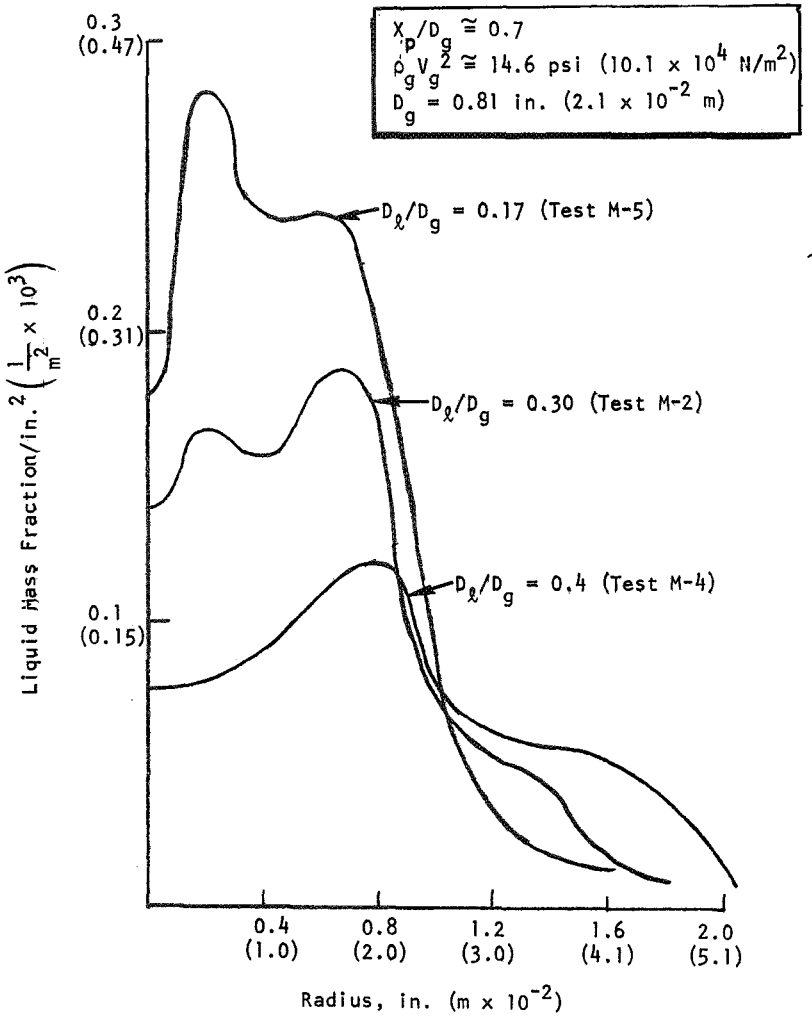

Figure 79. Liquid Mass Distribution Profiles vs D_ℓ/D_g: Impinging (4 on 1) Injector

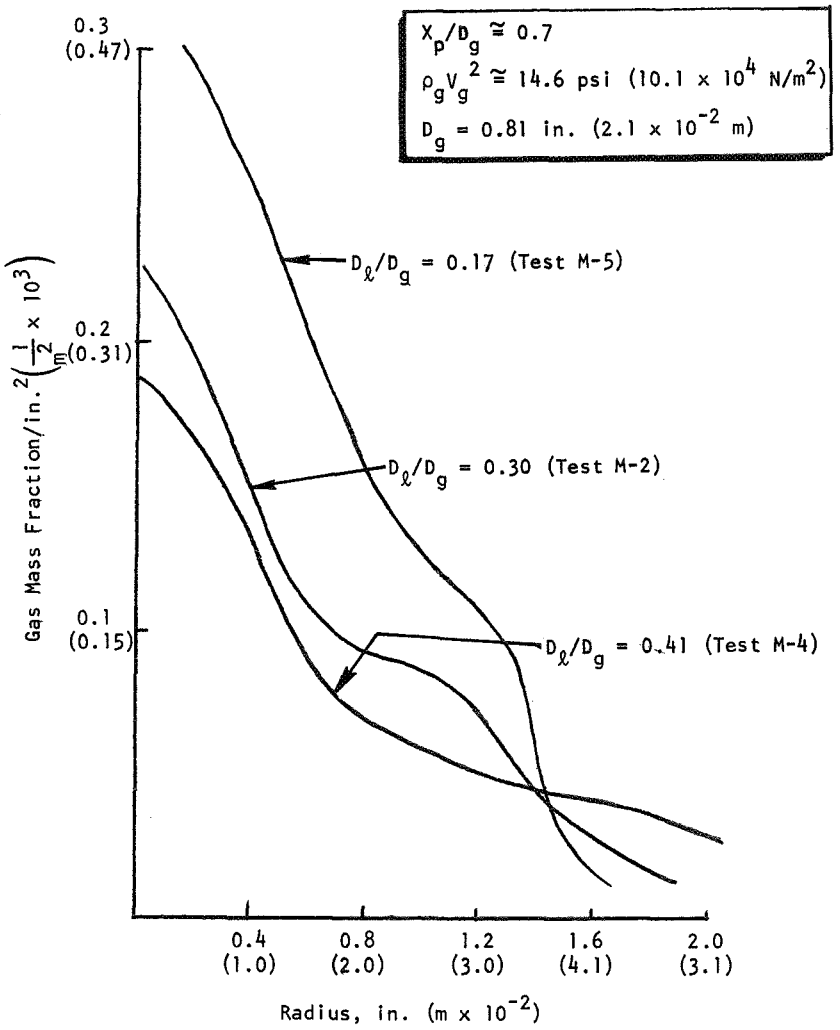

Figure 80. Gas Mass Distribution Profiles vs D_ℓ/D_g: Impinging (4 on 1) Injector

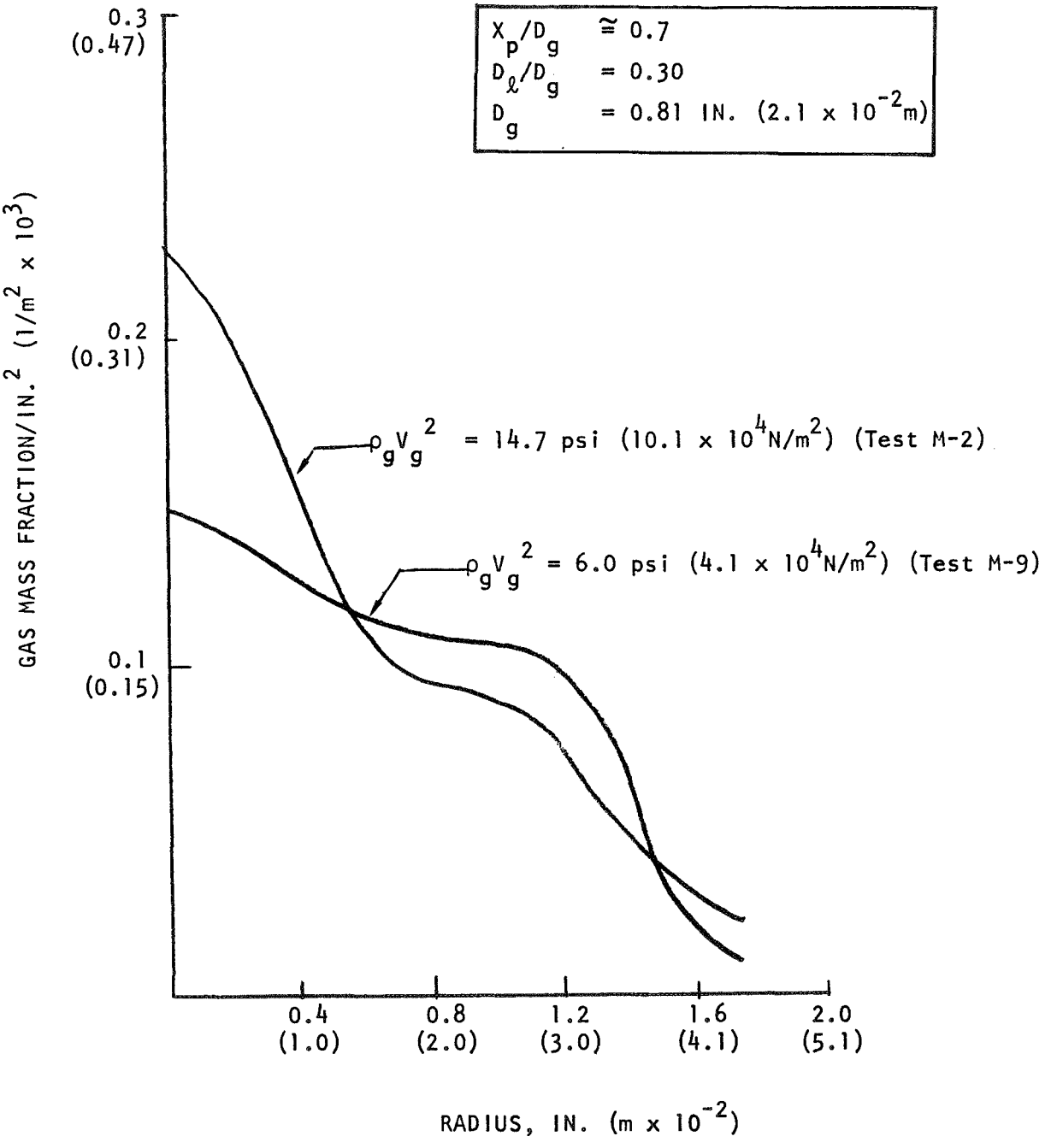

Figure 81. Gas Mass Distribution Profiles Versus $\rho_g V_g^2$: Impinging (4 on 1) Injector

with the variable being the liquid penetration. Gas mass flux contours are presented in Fig. 82 and 83 for $X_p/D_g = 0.7$ and $X_p/D_g = 1.15$, respectively. Note that the general shape of the contour plots is similar in nature to those of liquid-liquid unlike-doublet injectors. The effect of increasing liquid penetration is clearly shown in Fig. 83 in which the gas flowfield begins to form two primary zones separated by the liquid jet. Liquid flux contours are presented in Fig. 84 and 85 for the same two test conditions. For the liquid case, increasing X_p/D_g reduces the ability of the gas to spread out the liquid, thus resulting in a more concentrated liquid zone. A more important conclusion is reached by comparing the relative position of the gas and liquid maxima for a particular test condition. At low penetrations (Fig. 82 and 84), the gas and liquid maxima are separated, whereas for $X_p/D_g = 1.15$ (Fig. 83 and 85) the liquid penetrated has increased to the point where the two mass flux maxima coincides, resulting in good mixing. Further increases in X_p/D_g might be expected to result in decreased mixing.

Impinging Concentric. Many of the variables and results for the impinging concentric injector concept are similar to the basic impinging concept. Liquid penetration, orifice diameter ratio, and gas dynamic pressure were varied in addition to the percent annulus gas. Again the two-dimensionality of the flowfield requires mass flux contours for a full display.

The results of varying the liquid penetration parameter are similar to the corresponding results from the basic impinging element. The liquid mass flux contour plots for the impinging concentric concept correspond closely to Fig. 74 through 76 (basic impinging). The contour pattern changes of these two injector types are quite analogous. Also, the gas mass flux profiles for the impinging concentric element indicate penetration parameter effects similar to those of Fig. 78.

For the impinging concentric element, the liquid-gas diameter ratio was varied by changing the gas diameter (instead of changing D_ℓ as was done for the basic impinging element). While the range of variation ($D_\ell/D_g = 0.21$ to 0.31) was not as great as for the basic impinging element (0.17 to 0.41), the same trends

X_p/D_g = 0.70

D_ℓ/D_g = 0.41

$\rho_g V_g^2$ = 14.8 psi ($10.2 \times 10^4 N/m^2$)

D_g = 0.81 IN. ($2.1 \times 10^{-2} m$)

IDENTIFICATION

0 -- 0.567
1 -- 0.988
2 -- 1.410
3 -- 1.830
4 -- 2.250
5 -- 2.670
6 -- 3.090
7 -- 3.510
8 -- 3.920
9 -- 4.330

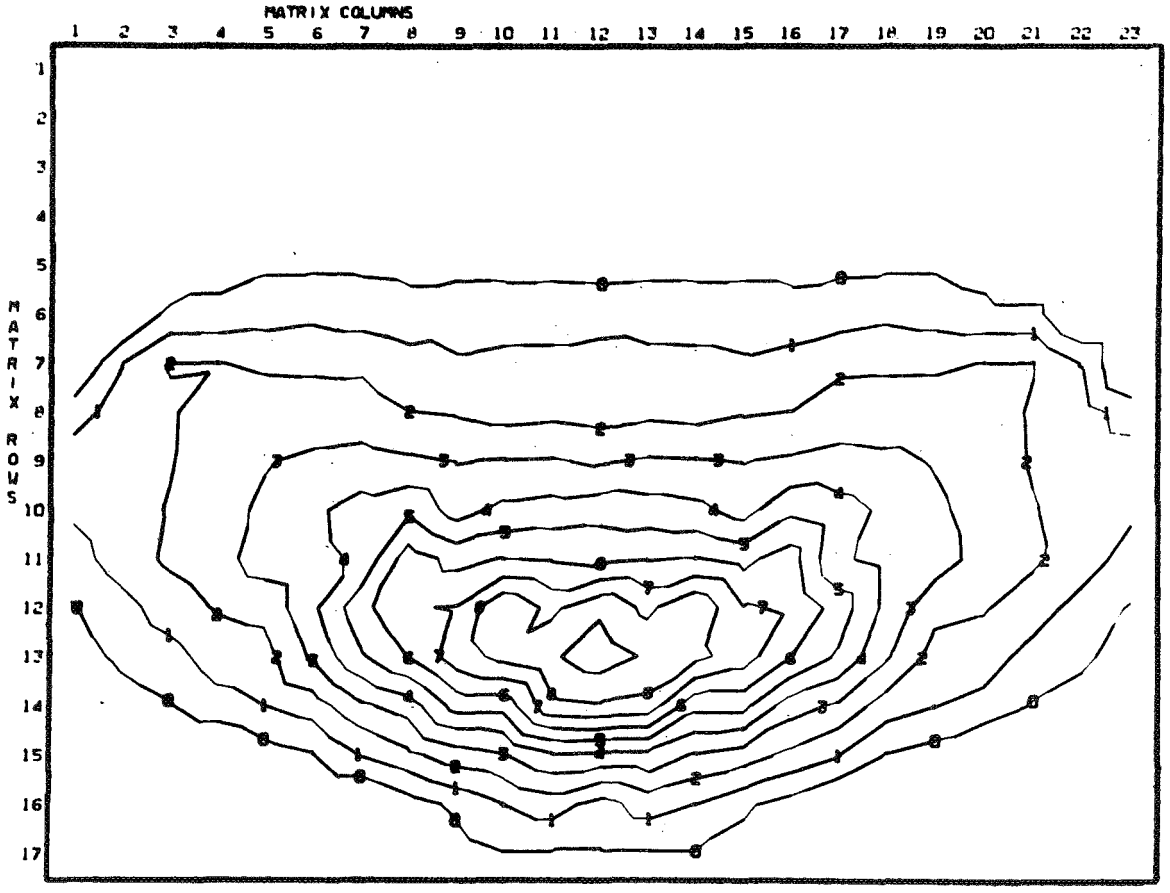

Figure 82. Normalized Gas Mass Flux Distribution: Impinging (1 on 1) Injector Test M-7

X_p/D_g = 1.15

D_ℓ/D_g = 0.41

$\rho_g V_g^2$ = 13.1 psi ($9.0 \times 10^4 N/m^2$)

D_g = 0.81 IN. ($2.1 \times 10^{-2} m$)

IDENTIFICATION

0 -- 0.462
1 -- 0.682
2 -- 0.903
3 -- 1.121
4 -- 1.345
5 -- 1.560
6 -- 1.790
7 -- 2.010
8 -- 2.230
9 -- 2.450

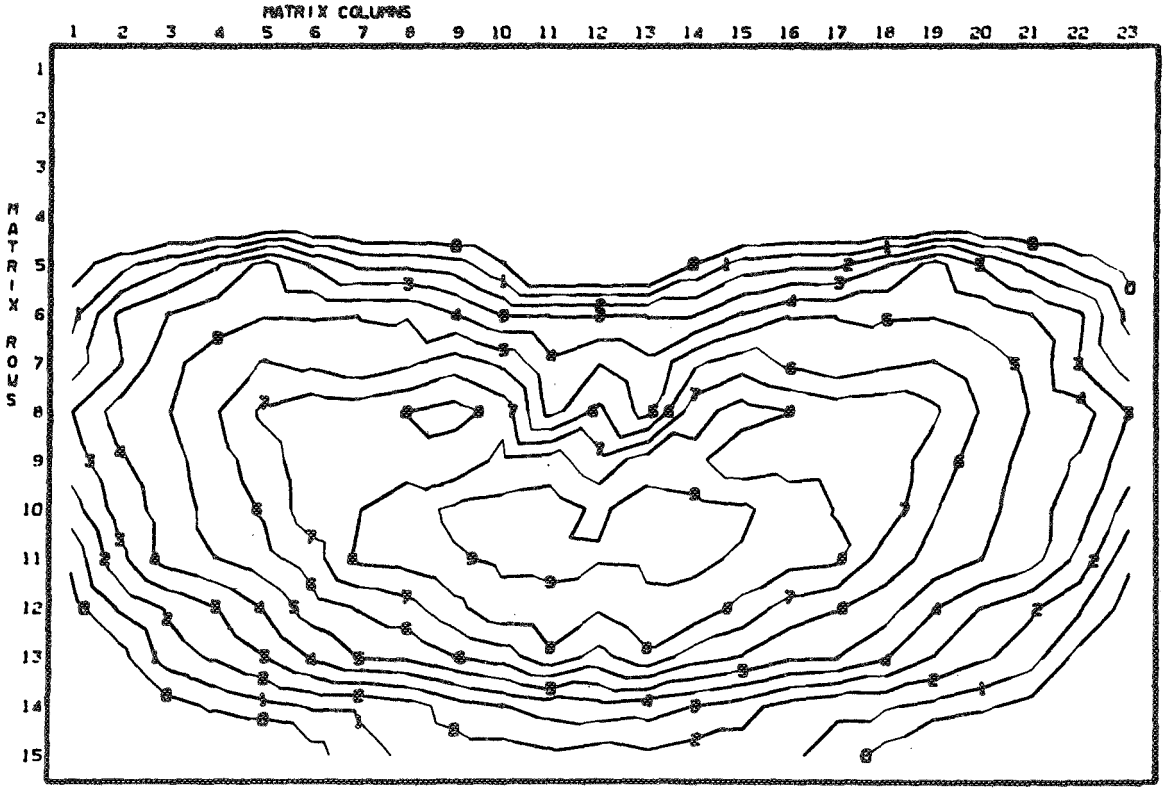

Figure 83. Normalized Gas Mass Flux Distribution: Impinging (1 on 1) Injector Test M-8

X_p/D_g = 0.70

D_ℓ/D_g = 0.41

$\rho_g V_g^2$ = 14.8 psi ($10.2 \times 10^4 N/m^2$)

D_g = 0.81 IN. ($2.1 \times 10^{-2} m$)

IDENTIFICATION

0 -- 0.537
1 -- 1.600
2 -- 2.670
3 -- 3.740
4 -- 4.800
5 -- 5.870
6 -- 6.920
7 -- 8.000
8 -- 9.080
9 -- 10.100

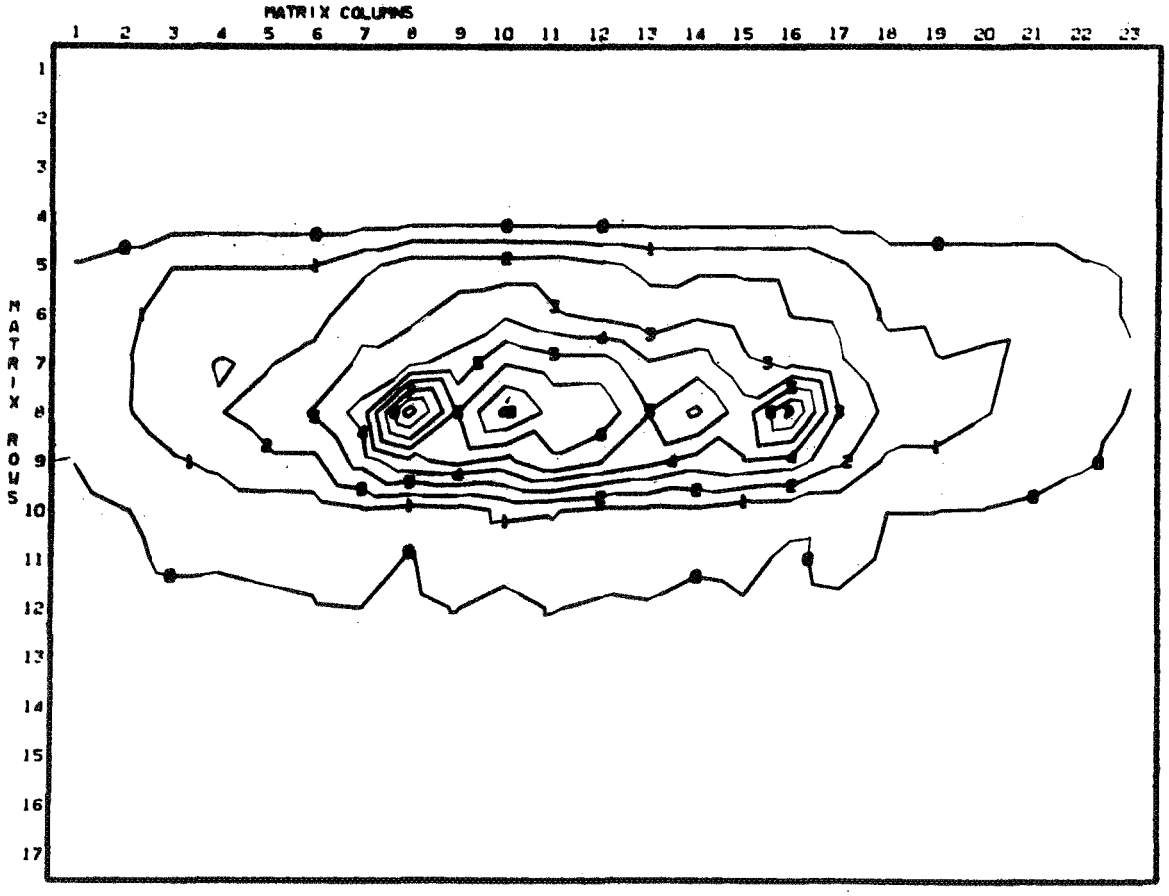

Figure 84. Normalized Liquid Mass Flux Distribution: Impinging (1 on 1) Injector Test M-7

X_p/D_g = 1.15

D_ℓ/D_g = 0.41

$\rho_g V_g^2$ = 13.1 psi ($9.0 \times 10^4 N/m^2$)

D_g = 0.81 IN. ($2.1 \times 10^{-2} m$)

IDENTIFICATION

0 -- 0.517
1 -- 1.535
2 -- 2.560
3 -- 3.570
4 -- 4.600
5 -- 5.630
6 -- 6.660
7 -- 7.680
8 -- 8.700
9 -- 9.710

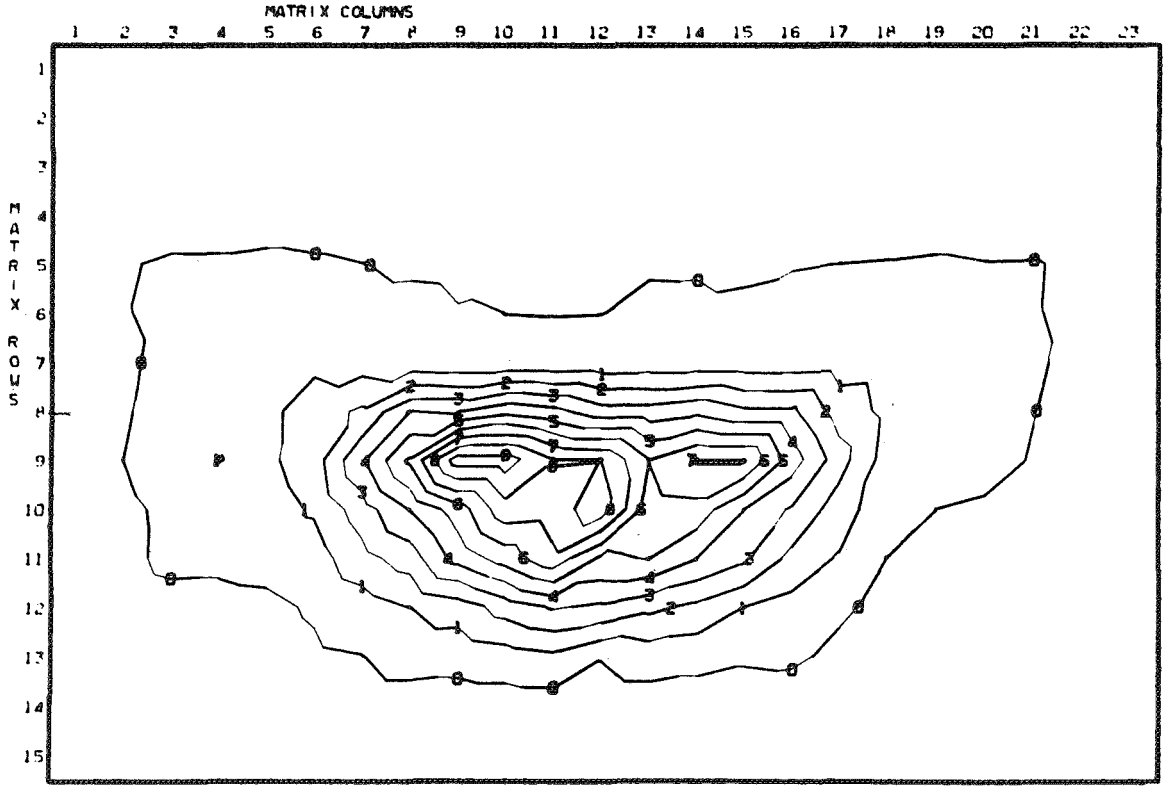

Figure 85. Normalized Liquid Mass Flux Distribution: Impinging (1 on 1) Injector Test M-8

were observed. Namely, both the gas and liquid mass flux distribution become more uniform as D_ℓ/D_g increases. As with the basic impinging injectors, it should be noted that increasing mass flux uniformity did not imply improved mixing as D_ℓ/D_g is increased.

The percent annulus gas parameter is defined as $100X\ (\dot{w}_{annulus}/\dot{w}_{total})_{gas}$. It is obvious from the mass flux profiles presented in Fig. 86 and 87 that this parameter has an effect on both gas and liquid distributions. In these tests, the percent annulus gas was increased from 0.2 to 0.4 by raising the annulus gas velocity. Clearly most of the additional annulus gas accumulates near the center of the flowfield (Fig. 86).

For the liquid distribution (Fig. 87), the result of increasing the percent annulus gas from 0 to 20 percent is increasing liquid uniformity. This reflects the fact that the annulus gas is mixing with some of the liquid in the region outside of the center gas jet. However, as the annulus gas velocity was further increased (20- to 40-percent annulus gas), this trend apparently reverses with a strong maximum spray flux forming at a radius of about 0.6 in. (0.015 m), i.e., just outside the strong gas flux zone along the axis.

Variations in the center gas jet dynamic pressure ($\rho_g V_g^2$) did not have a strong effect on the shape of gas or liquid mass flux profiles. Whereas relatively uniform gas flux occurred at low values of gas dynamic pressure for the basic impinging element, the impinging concentric data suggested a slight trend in the opposite direction.

Scale or D_g changes from 0.32 to 0.62 in. (0.81 to 1.57×10^{-2} m), at constant D_ℓ/D_g (for the impinging concentric element) did not have any obvious effect on either the gas or liquid mass flux distribution; i.e., consistent with the basic impinging element trends.

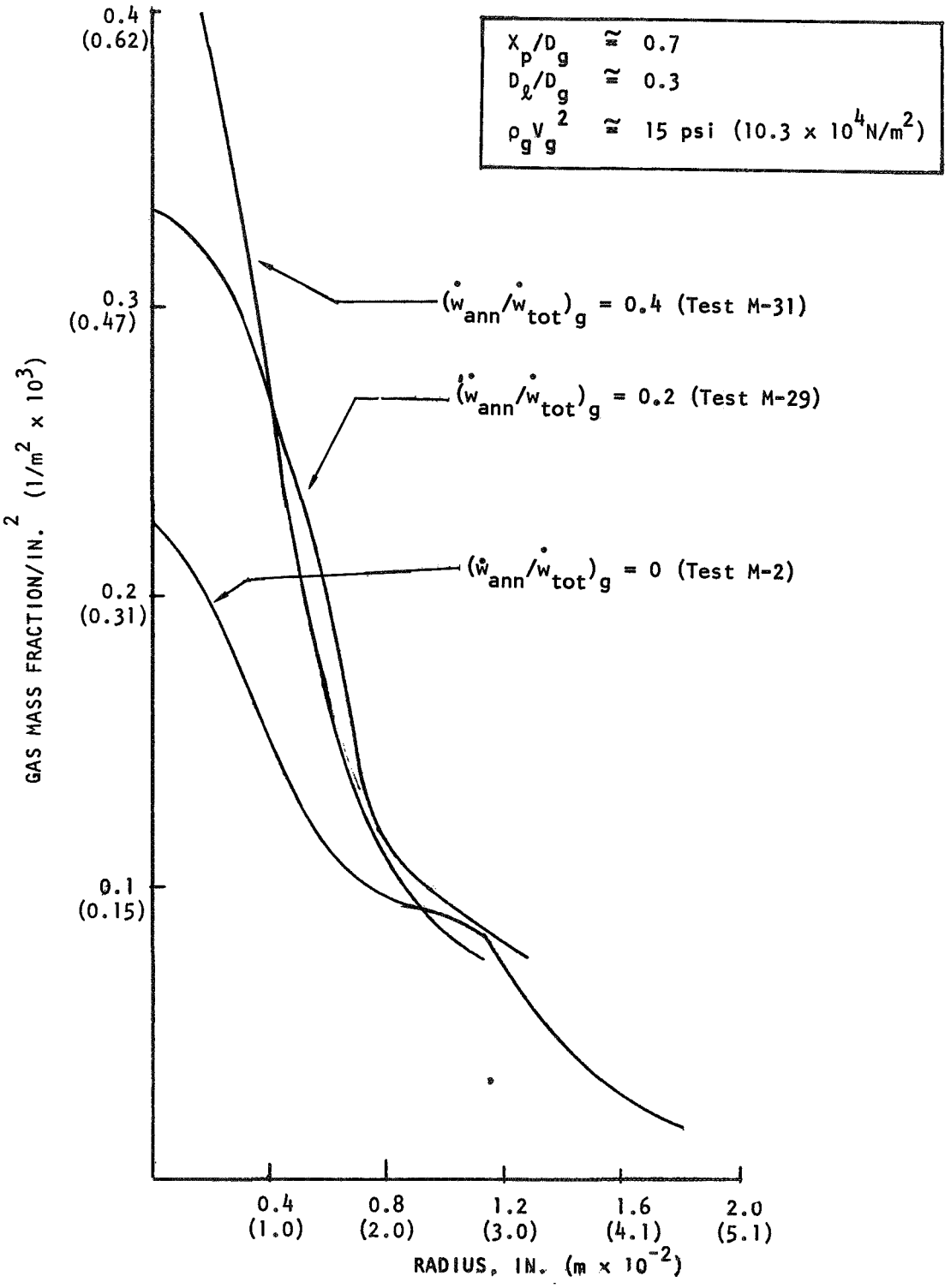

Figure 86. Gas Mass Distribution Profile Versus Annulus Gas: Impinging Concentric Injector

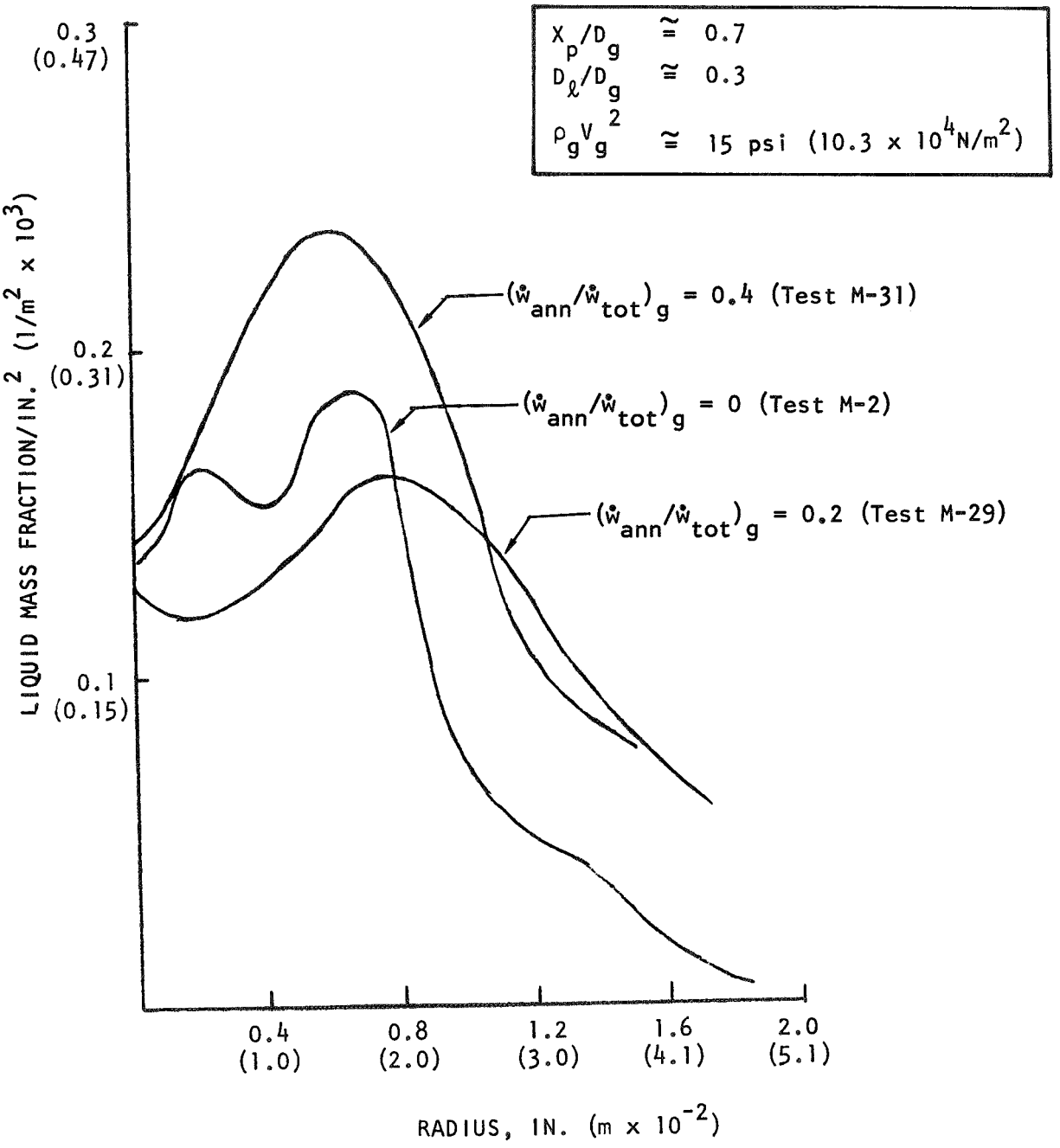

Figure 87. Liquid Mass Distribution Profile Versus Annulus Gas: Impinging Concentric Injector

Performance Calculation

Rational design of rocket engine components using fundamental engineering principles requires a basic understanding of combustion and its relationship to the physical processes which control it. For most bipropellant liquid or gas-liquid systems, c* efficiency is affected by both propellant vaporization and mixing. In this program, overall c* efficiency was predicted by the product of the vaporization limited and the mixing limited combustion efficiencies, $(\eta_{c^*})_{vap}$ and $(\eta_{c^*})_{mix}$, respectively. This approach, which was developed and substantiated in extensive application to liquid-liquid propellants systems, was first applied to gas-liquid systems in Task I of the subject program. The approach itself is discussed in some detail in Ref. 1 and 2. The present section briefly describes the calculation of vaporization and mixing limited performance based on results of the Task II cold-flow investigations. The calculated performances in this section apply to the FLOX/CH_4 propellant combination; however, no liquid property corrections were made to correct the wax mass median dropsize to FLOX mass median dropsize. The trends reported for FLOX/CH_4 would be similar for both LOX/GH_2 and LF_2/GH_2, although the absolute levels and slopes would differ somewhat.

Vaporization Efficiency. The effects of incomplete propellant vaporization on c* efficiency were quantitatively studied by means of an analytical propellant combustion model developed at Rocketdyne several years ago by Lambiris, Combs, and Levine. Current computer programs (Ref. 1 and 2), which have evolved from this model, determine the predicted hot-fire vaporization efficiency as a function of the mass median dropsize and the distribution of dropsizes around a median dropsize value when used with specific geometry and operating conditions. To best understand the practical significance of the Task II atomization data in terms of $(\eta_{c^*})_{vap}$, a series of combustion model computations was conducted for the set of design/operation conditions presented in Table 19.

Mass median dropsize and dropsize distribution were the variable parameters for the calculations. The distributions used were those actually measured in atomization tests of the various injector types as presented in a preceding section of this report.

TABLE 19

COMBUSTION MODEL INPUT PARAMETERS

Propellant System:	FLOX (82% F_2)/CH_4 (g)
Mixture Ratio:	5.75
Nominal P_c:	500 psia (345 x 10^4 N/m^2)
Injection Velocity:	V_{ox} = 100 ft/sec (30.5 m/s)
Chamber Geometry:	L* = 30 inches, ε_c = 2 (0.76 m)

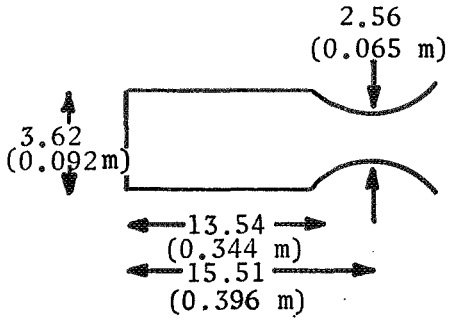

The effects of variations in the dropsize distribution about the mass median ($\bar{D}$) on computed vaporization-limited combustion efficiencies are shown in Fig. 88 for two different mass median dropsizes; 150 and 200 μ (150 and 200 x 10^{-6} m). Consider first the spread due to possible differences in dropsize distribution about $\bar{D}$ for individual element types. The vaporization efficiency is seen to vary up to about 4 percent (in this dropsize range) between the least and the most monodispersed distributions for the basic concentric and impinging concentric concepts. For the other three injector concepts $(\eta_{c*})_{vap}$ varies (individually) only by a maximum of 2 percent. The variation due to dropsize distributions between different injector types reached a maximum of about 5 percent for $\bar{D}$ of 200 μ (200 x 10^{-6} m) and decreased for smaller $\bar{D}$ values.

The combustion model data are replotted in Fig. 89 as a function of the mass median dropsize and the average dropsize distributions for the impinging concentric and the basic concentric injector concepts, respectively. Only $\bar{D}$ values less than 200 μ (200 x 10^{-6} m) provide efficiencies high enough to be of practical interest for the system used in the combustion efficiency calculations. Further, values of $\bar{D} \leq 100$ μ (100 x 10^{-6} m) will provide essentially

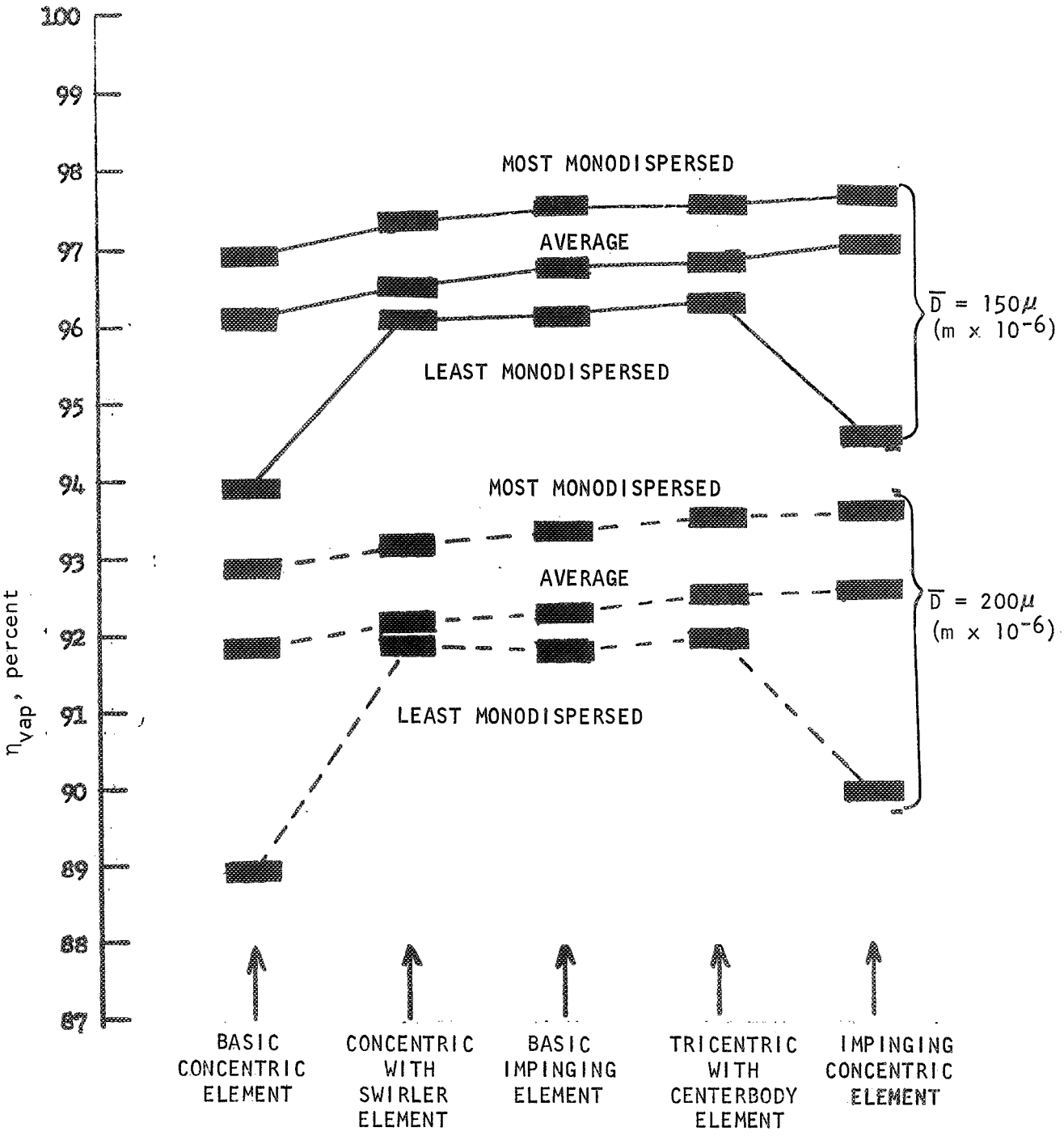

Figure 88. Effects on Vaporization Efficiency of Variation on Dropsize Distribution About the Mass Median Dropsize

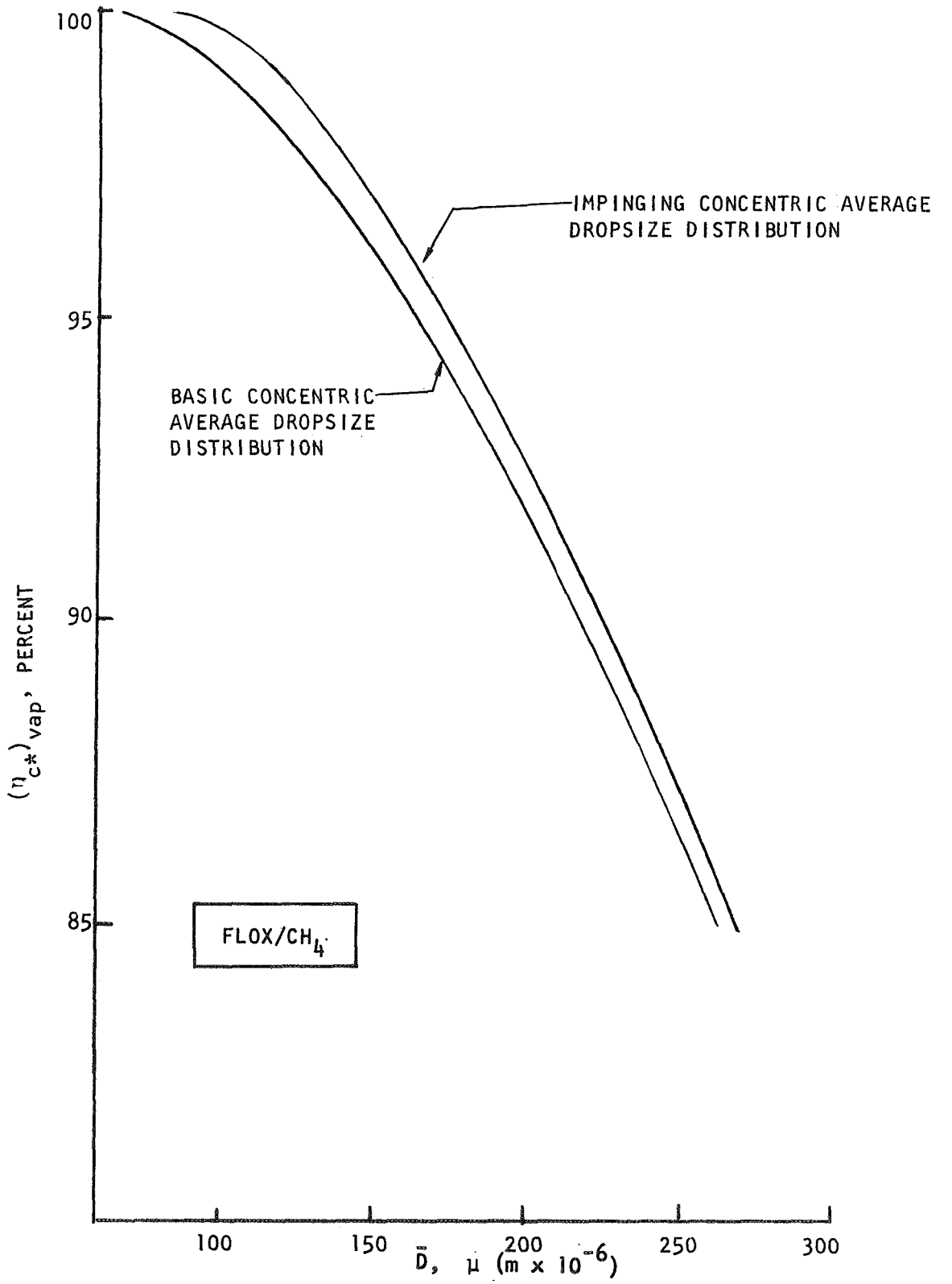

Figure 89. Vaporization Efficiency Versus Mass Median Dropsize and Average Dropsize Distributions

complete vaporization. It may be concluded from these two figures (88 and 89) that the dropsize distribution about $\bar{D}$ must be considered to predict the exact value of vaporization efficiencies. However, the dropsize distribution is clearly a secondary parameter to $\bar{D}$ itself.

Complete sets of curves of $(\eta_{c^*})_{vap}$ were generated for essentially all Task II atomization tests for each injector type. These were used for element concept optimization and rating (see the Injector Rating Section), but are omitted here for the sake of brevity. The vaporization efficiency trends are the same (inversely related) as the dropsize trends previously reported.

Mixing Efficiency. Uniform mixing is a prerequisite for high combustion efficiency regardless of injector type. For this study, the analysis was based on a simplified stream tube model in combination with cold-flow experiments to determine distribution of propellants. The c* efficiency due to mixing $(\eta_{c^*})_{mix}$ is determined by summation of individual mass weighted c* contributions of each individual stream tube and comparing the total to that theoretically attainable at the injected mixture ratio. This calculation has been further explained in the description of the data reduction procedure.

FLOX/CH_4 mixing efficiencies, based on Task II cold-flow data, were generated for each of the injector concepts. Comparing these efficiencies with the mixing factors (E_m) attained, illustrates that the trends observed with the mixing factor are, in general, the same as trends with the predicted mixing efficiency $(\eta_{c^*})_{mix}$. However, the steepness of predicted mixing efficiency trends may differ. In addition, the relative levels of the predicted mixing efficiencies for FLOX/CH_4, LOX/GH_2, LF_2/GH_2, etc., propellant systems might be significantly different. As in the case of $(\eta_{c^*})_{vap}$, the $(\eta_{c^*})_{mix}$ curves for the FLOX/CH_4 (MR = 5.75) system are omitted for brevity. These curves were used, however, in support of the injector concept optimization and rating analysis.

For convenience, a correlation between E_m and $(\eta_{c^*})_{mix}$ for FLOX/CH_4 (at a nominal P_c of 500 psia; 345 x 10^4 N/m^2) is included (Fig. 90), which may be readily used to convert cold-flow E_m curves to approximate values of $(\eta_{c^*})_{mix}$. The relation is approximate because $(\eta_{c^*})_{mix}$ depends to some extent on the actual distribution, even for selected values of E_m, propellant combination, and injected mixture ratio.

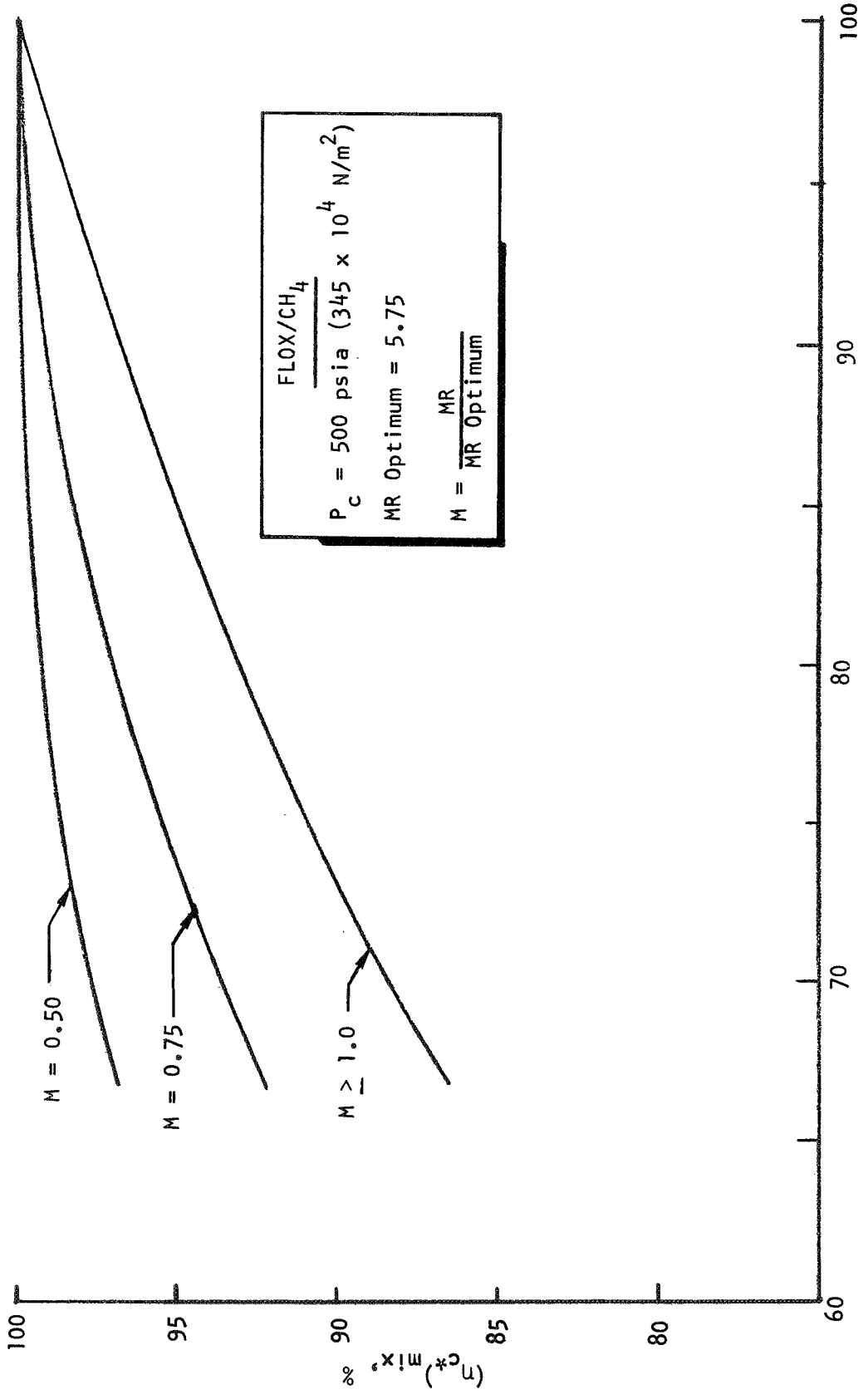

Figure 90. Predicted Mixing Effects on Performance

TASK II INJECTOR RATING

The Task II cold-flow data were used to optimize each of the individual element types investigated for application to a 5000-lb (22,200 N) thrust, 500-psia (345 x 10^4 N/m^2) FLOX/CH_4(g) system and then to rate the optimized designs for selection of those to be further evaluated in Task III. The optimization and rating is described in this section.

The concepts evaluated in Task II included basic impinging, basic concentric tube, concentric tube with swirler, impinging concentric, and tricentric with centerbody elements suitable for use with LOX/GH_2, FLOX/CH_4(g), and LF_2/GH_2 systems. Because the objective of the cold-flow test matrices for these elements was to simulate three propellant systems in which optimum hot-firing operating conditions varied widely (for instance, LOX/GH_2 and LF_2/GH_2 optimum mixture ratios are approximately 5 and 15, respectively), design conditions used in the test matrix represented nominal averages for the three propellant combinations. In addition, physical sizes of the cold-flow injectors (T/E) were limited by anticipated facility limitations. Therefore, several interpolations and extrapolations were required to apply the test results to a specific propellant combination and thrust per element.

The main ground rules (with regard to operating parameters) are listed below which were used for evaluation, optimization, and comparison of the injector concepts.

1. FLOX/CH_4 propellant combination
2. 5.75 mixture ratio
3. 160 R (88.9 K) FLOX injection temperature
4. 1500 ft/sec (457 m/s) gas injection velocity (maximum)
5. 350 psid (241 x 10^4 N/m^2) liquid injection pressure drop (maximum)
6. 5000 lbf (22,200 N) (vacuum) thrust per element

7. 500 psi (345×10^4 N/m^2) chamber pressure

8. 30-in. (0.76 m) chamber characteristic length

9. 2.0 chamber contraction ratio

Design parameters for each injector type were optimized with regard to predicted atomization and mixing under these operating conditions. The optimized concepts were then rated under two categories, i.e., their predicted capacity for (1) propellant atomization, and (2) propellant mixing. In this rating process, the overall confidence level of the cold-flow data and of the extrapolations used were also considered. These rating processes are described as follows.

Rating of Injector Atomization Potential

The Task II atomization experiments were used to predict individual injector atomization characteristics under hot-fire conditions. These data have been previously presented for each individual injector concept. This section reviews the method used to optimize and compare the five gas-augmented injector concepts on the basis of mass median dropsize alone. The FLOX/CH_4 hot-fire conditions and restrictions used as a basis for this comparison have been outlined above. The five injector concepts studied can be divided into two fundamental categories, impinging and concentric. Each category is considered below with its particular set of parameters.

Impinging Concepts. As mentioned in a preceding section, Task II cold-flow tests were designed to simulate a variety of propellant systems. In addition, test facility flowrate, temperature, and pressure restrictions limited the thrust-per-element capabilities for several of the injector concepts. Therefore, the use of cold-flow data to predict hot-fire atomization characteristics involved extrapolation of several critical operating parameters. Among these are scale (element size) and momentum flux. Because of the limited number of tests conducted, some extrapolations were necessary using data trends from closely related injector concepts (such as the basic impinging and impinging concentric).

Task II cold-flow atomization experiments with the basic impinging and impinging concentric injector concepts involved the following parameters:

MR	mixture ratio (impinging coaxial only)
X_p/D_g	liquid/gas penetration parameter
$\rho_g V_g^2$	gas momentum flux
D_ℓ or Dg	scale, as indexed by liquid or gas orifice diameter
D_ℓ/D_g	ratio of liquid orifice diameter to gas orifice diameter
N	number of liquid jets/element
$\left(\frac{\dot{W}_{annulus}}{\dot{W}_{total}}\right)_g$	fraction of annulus gas (impinging concentric only)

Cold-flow tests with the impinging pentad injector indicated that mixture ratio need not be considered if the penetration parameter is accounted for. This was also assumed to hold for impinging triplet and unlike doublet injectors and for the impinging concentric concept. Furthermore, additional cold-flow tests for all of the above mentioned injectors showed that the penetration parameter has little effect for $0.2 \leq X_p/D_g \leq 0.8$. (For higher penetration, dropsize increases significantly, however.) Thus, for the purpose of comparing impinging-type injectors, mixture ratio was not considered and corrections for penetration parameter were made only when it was outside the range indicated above.

For the basic impinging pentad injector, the gas momentum flux parameter $(\rho_g V_g)^2$ was varied. Results indicated the mass median dropsize to be a proportional to $(\rho_g V_g^2)^{-1/5}$. Earlier preliminary gas-augmented injector tests with N=2 (triplet) resulted in a -1/4 power relationship, while recent impinging concentric data over a narrow range of momentum flux suggested a lower $\rho_g V_g^2$ dependence. In the calculations that follow, a -1/5 power exponent has been used for all impinging element types to correct for changes in the momentum flux parameter.

Basic Impinging Pentad. A graph (Fig. 91) of $\overline{D}$ vs D_ℓ was constructed as a function of D_ℓ/D_g using test data for variable D_g and D_ℓ/D_g at constant momentum flux and $0.2 \leq X_p/D_g \leq 0.8$. On this single graph, then, are seen the parametric influences of injection element geometry for the impinging pentad. (Note that the included angle between individual oxidizer streams and the central fuel stream was not a test variable, but was always 45 deg; 0.78 rad).

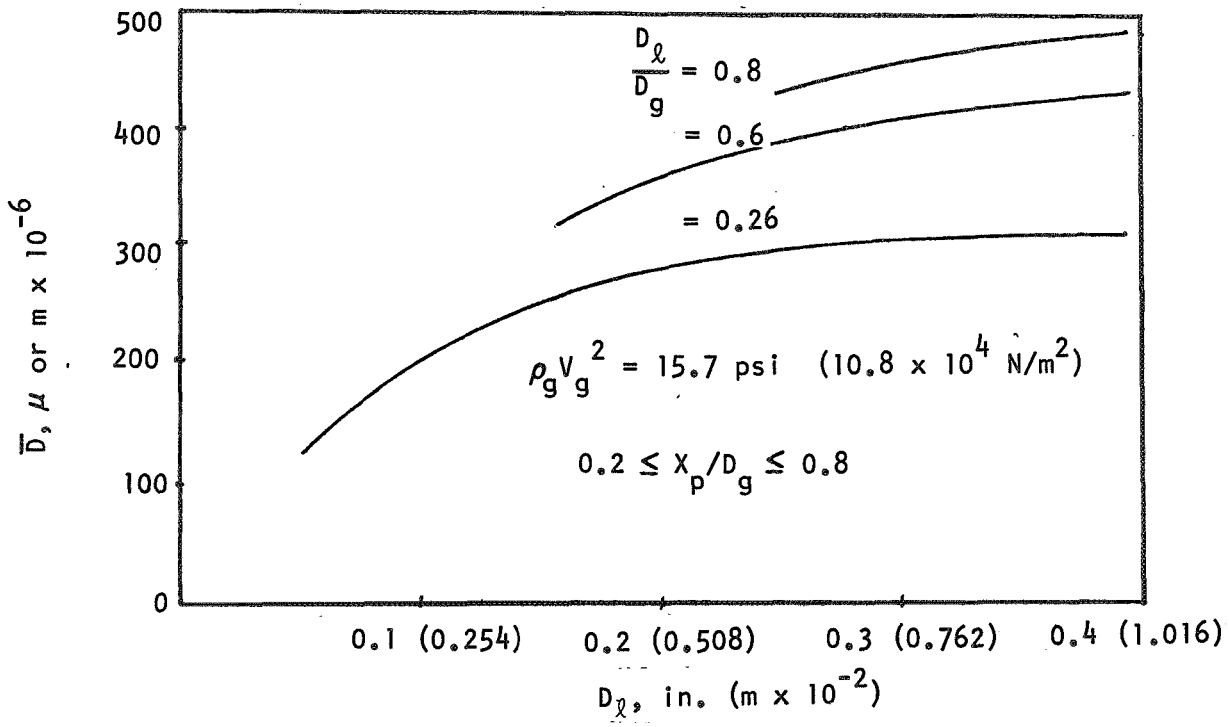

Figure 91. Parametric Influence of Injection Element Geometry for the Basic Impinging Pentad

It is obvious from this graph that $\overline{D}$ can be minimized by using small liquid diameters; however, a fixed flowrate per element requires an increased liquid velocity and is limited by (1) available injection pressure and/or (2) the attendant increase of X_p/D_g into a high range (>0.8) where poor atomization would result. The graph similarly indicates a benefit of using low values of D_ℓ/D_g. Task I effort suggested that D_ℓ/D_g should not be less than about 0.3 based on mixing considerations.

For the conceptual FLOX/methane hot-fire system under consideration, the following operating conditions were selected: D_ℓ = 0.190 in. (0.483×10^{-2} m), D_ℓ/D_g = 0.40, and X_p/D_g = 0.63. The D_ℓ and D_ℓ/D_g values can be used with Fig. 91 to uniquely determine a mass median dropsize of 315 μ (315×10^{-6} m) for $\rho_g V_g^2$ = 16 psi (11.0×10^4 N/m^2). Extrapolating to hot-firing gas momentum flux according to $\overline{D} \propto (\rho_g V_g^2)^{-0.2}$ yields a predicted dropsize of $\overline{D}$ = 155 μ (155×10^{-6} m).

Basic Impinging Triplet and Doublet. For the triplet (N=2) and unlike doublet (N=1) injectors, an evaluation was used similar to that for the pentad. However, because only two cold-flow test data points were obtained with each of these injectors, the basic impinging pentad data had to be used for geometry corrections. These geometry corrections were required because the unlike doublet and triplet cold-flow geometry did not correspond exactly to the previously described FLOX/CH_4 system used for concept optimization and rating.

The method of predicting dropsizes for the triplet and unlike doublet can be illustrated by consideration of Fig. 92. The lower curve in this figure (D_ℓ/D_g = 0.35, D_ℓ = 0.21; 0.53×10^{-2} m) was obtained experimentally. The other curves were derived by combining this experimentally observed influence of N at fixed D_ℓ/D_g and D_ℓ with trends of $\overline{D}$ versus both D_ℓ and D_ℓ/D_g obtained from the pentad (fixed N) data in Fig. 91.

Each injector type (the triplet and the doublet) was optimized for atomization with regard to an X_p/D_g versus D_ℓ/D_g tradeoff to obtain the orifice sizes. In cases where the design geometry yielded a penetration parameter, X_p/D_g, outside of the 0.2 to 0.8 range, the dropsizes were corrected to the proper X_p/D_g by the cold-flow data trends presented in Fig. 93. Selected design liquid diameters for the triplet and unlike doublet were 0.27 in. (0.69×10^{-2} m) and 0.38 in. (0.97×10^{-2} m), respectively, while the respective diameter ratios chosen were 0.58 and 0.79. The resulting X_p/D_g values were 0.89 and 1.25. The design conditions yielded an appropriate dropsize from Fig. 93 for each of the respective concepts.

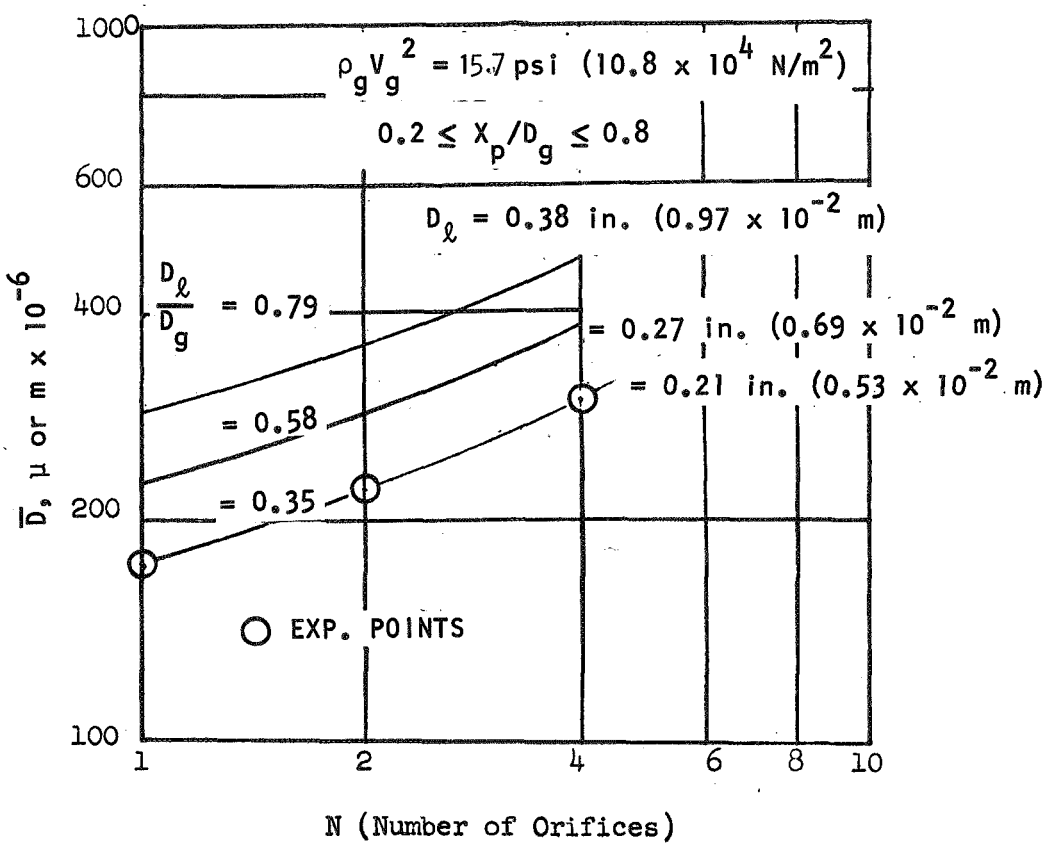

Figure 92. Parametric Influence of the Number of Liquid Orifices on Dropsize for Constant Geometries

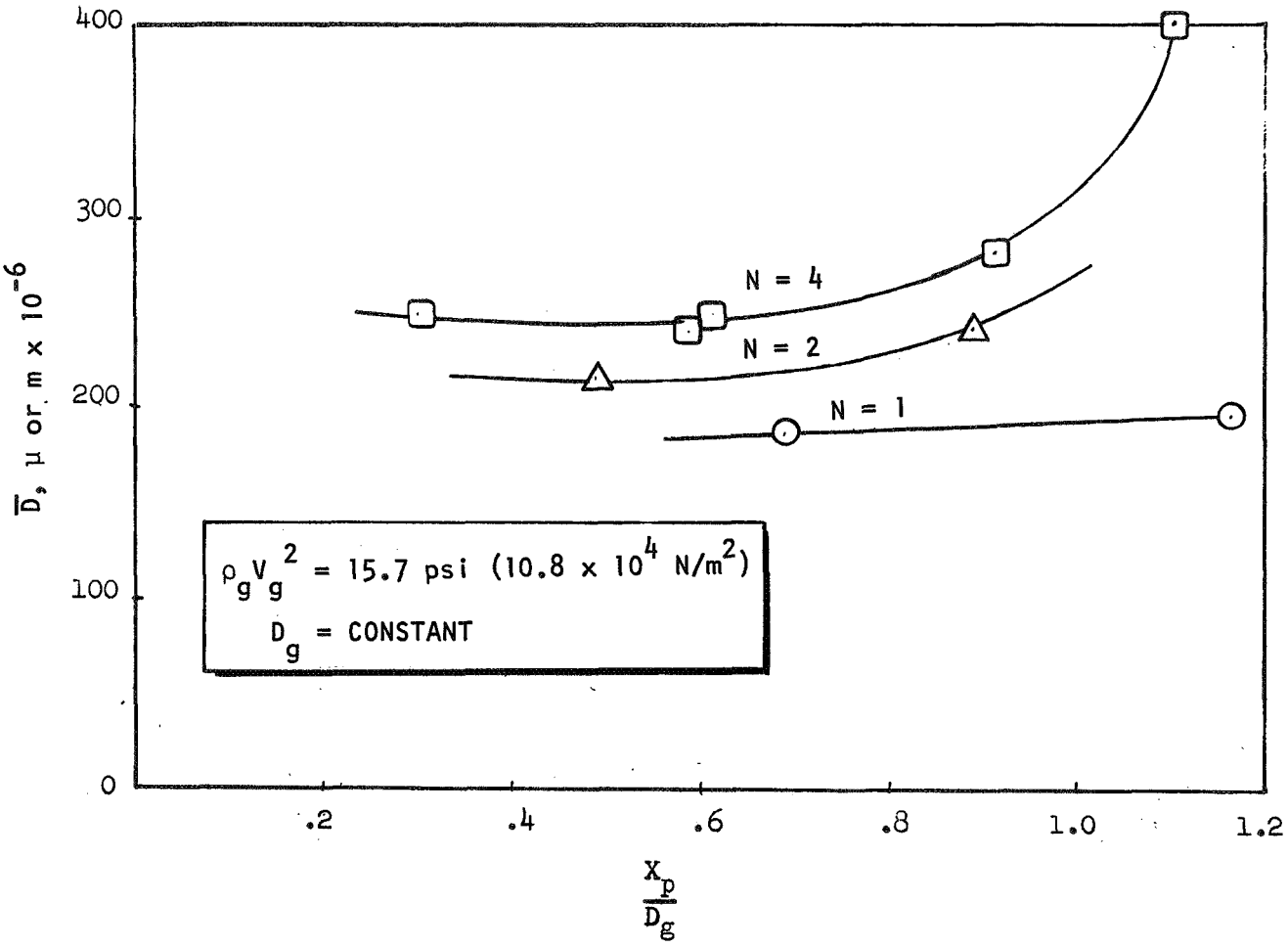

Figure 93. Parametric Influence of the Number of Liquid Orifices and X_p/D_g on Mass Median Dropsize (Basic Impinging Injector Concept)

Finally, corrections were made for the momentum flux parameter using the -1/5 power dependence. The calculations resulted in mass median dropsize of 155 μ (155×10^{-6} m) for the triplet and 150 μ (150×10^{-6} m) for the unlike doublet injector concept. In retrospect, it is seen that the comparatively better atomization indicated in Fig. 93 for the doublet and triplet is counterbalanced by the necessarily larger D_ℓ for a given flowrate per element so that the optimized dropsizes for the pentad, triplet, and doublet are essentially equal.

Impinging Concentric. Impinging concentric tests were conducted using four liquid orifices (i.e., N=4). Only three atomization tests with variable injector geometry were made with this concept. Therefore, it was necessary to make supplementary use of the basic impinging test data to fully develop the shape of a curve illustrating the geometric parameter effects for the impinging concentric injector (similar to Fig. 91). A plot of $\overline{D}$ versus D_g as a function of D_ℓ/D_g was obtained from these data and is shown in Fig. 94.

Initial mass median dropsizes were estimated directly from Fig. 94 using FLOX/CH_4 system design conditions of D_ℓ = 0.2 (0.508×10^{-2} m), D_ℓ/D_g = 0.45, and X_p/D_g = 0.7. This initial dropsize was then corrected to the hot-fire momentum flux using the -1/5 power dependence. The $\overline{D}$ resulting from this process is 150 μ (150×10^{-6} m). Noting that the cold-flow injector liquid tubes were not recessed, it is probable that the impinging concentric injector concept could perform better in a recessed configuration, but it was not possible at this time to account for the potential effects of post recess for the impinging concentric element type.

Concentric Concepts. The main parameters found to influence atomization of the concentric element types include the following*:

MR = mixture ratio

$(V_g - V_\ell)$ = relative velocity

*It should be noted that liquid injection velocity (V_ℓ), while not experimentally investigated in Task II, would be expected to influence atomization based on theoretical considerations.

D_ℓ = liquid orifice (post) ID

recess = post recess/D_ℓ

Y = annulus gaps

V_s = swirl velocity (concentric with swirl only)

D_{cb} = centerbody diameter (tricentric with centerbody only)

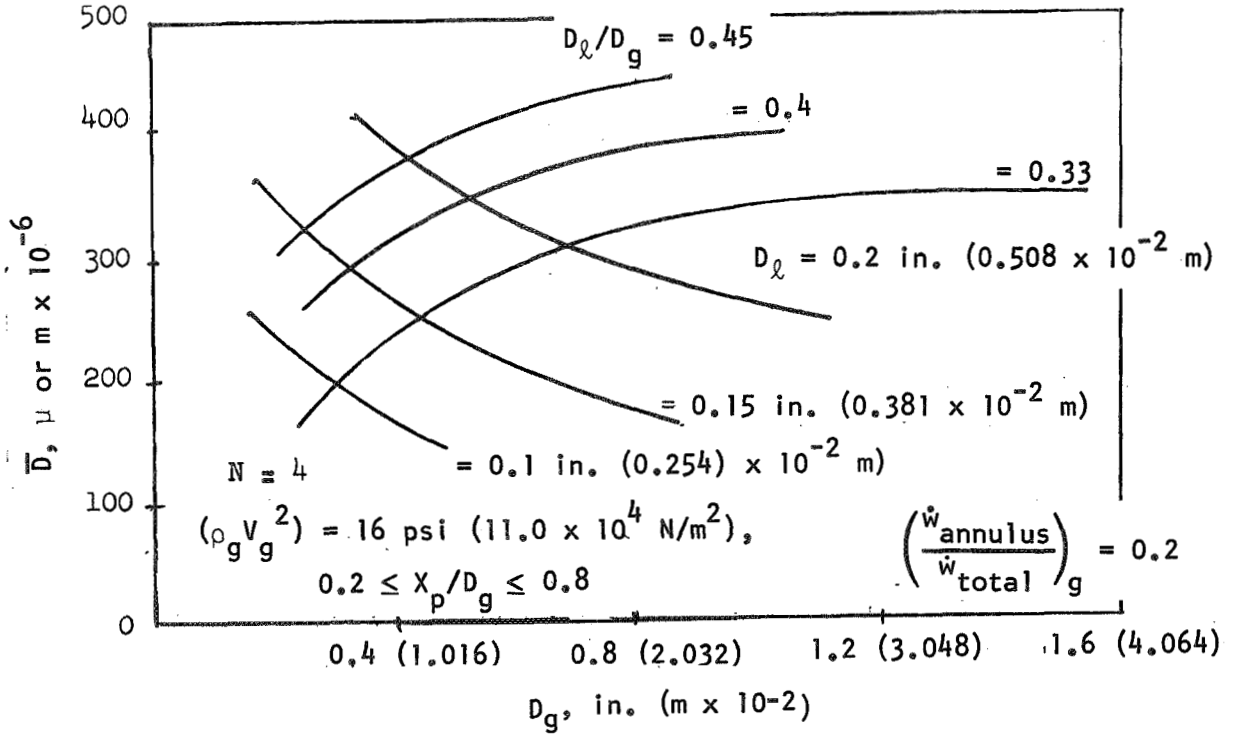

Figure 94. Parametric Influence of D_ℓ/D_g and D_ℓ on Mass Median Dropsize (Basic Impinging and Impinging Concentric Coaxial Concepts)

Interpolation procedures for each injector concept are discussed below.

Basic Concentric. For the basic concentric element, the swirl velocity and centerbody diameter do not apply, and annulus gap effects have not been investigated. The cold-flow test data allow $\bar{D}$ to be determined as a function of $(V_g - V_\ell)$ and post recess (MR = constant). These data are presented in Fig. 95 for a 5.85 mixture ratio.

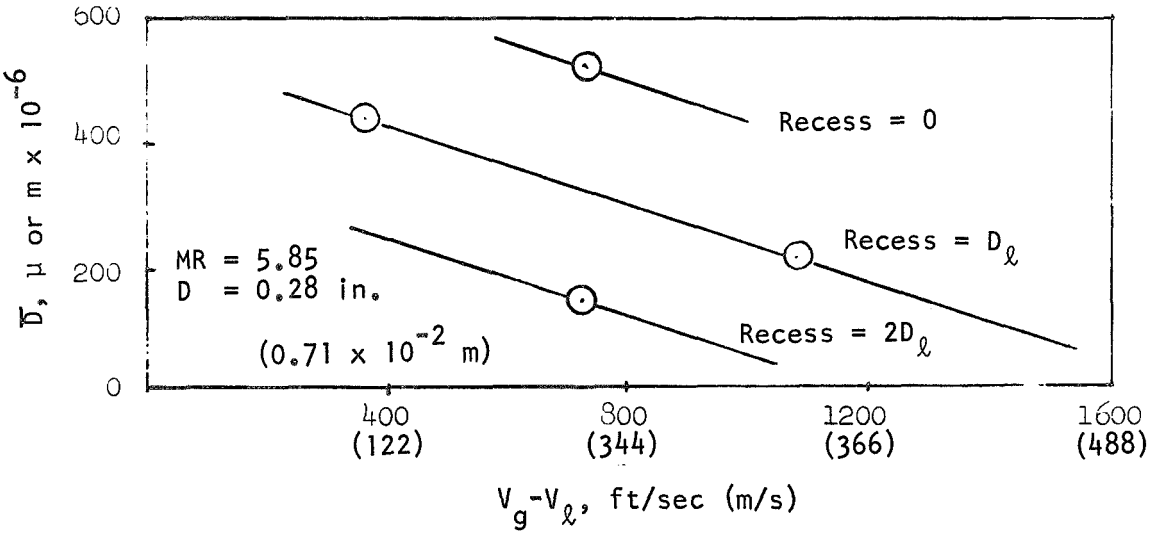

Figure 95. Parametric Effect of V_g-V_ℓ (Basic Concentric Injector)

Initial dropsize values for the reference FLOX/CH_4 system are obtained from this figure with (V_g-V_ℓ) = 1400 ft/sec (427 m/s). This leaves a dropsize correction for scale as the remaining correction to be applied. The Task II cold-flow data suggest* a linear correction factor of $\Delta\bar{D}/\Delta D_\ell$ = 1000 /in. (394 x 10^4 m/m), independent of (V_g-V_ℓ). The reference hot-fire liquid diameter is 0.45 in. (1.14 x 10^{-2} m) while the cold-flow liquid diameter, from which Fig. 95 was generated, was only 0.28 in. (0.71 x 10^{-2} m). This implies a $\bar{D}$ correction of +170 μ (170 x 10^{-6} m). Correcting the mass mean dropsize obtained from Fig. 95 yields $\bar{D}$'s of 270 μ (270 x 10^{-6} m) and 110 μ (110 x 10^{-6} m)** for recess/D_ℓ values of 1 and 2, respectively. Thus, the atomization potential for basic coaxial injectors is determined predominantly by the maximum recess compatible with heat transfer considerations. At some recess between 1.0 and 2.0 D_ℓ, the coaxial element dropsize would match that predicted for the impinging-type elements (i.e., ~ 150 μ; 150 x 10^{-6} m).

*It will be recalled that data from the set of five small-scale coaxial element tests is questionable as a result of difficulty in controlling the small gas and liquid flowrates. Thus, the scale correction was made with a lower degree of confidence than were the other interpolations.

**As is obvious from Fig. 95 it was necessary to extrapolate a two-point curve from V_g-V_ℓ of about 1100 ft/sec (335 m/s) to the hot fire design point of 1400 ft/sec (427 m/s). Additional data may show the dropsize to asymptotically approach zero.

Concentric With Swirler. Of the seven concentric element primary variables mentioned above, only swirl velocity and (V_g-V_ℓ) were varied for the concentric swirler injector concept. Because mixture ratio, relative velocity, and liquid orifice diameter effects must also be considered, the following assumptions were made to aid interpolation and extrapolation of the cold-flow data to the reference FLOX/CH_4 system design considerations:

1. Basic concentric element data may be used to determine concentric swirler atomization trends for the limiting case of zero swirl velocity.
2. The addition of 20 ft/sec (6.1 m/s) swirl velocity reduces mass median dropsizes by approximately 50 percent as seen in the cold-flow data with V_g-V_ℓ = 1080 ft/sec (329 m/s) (Fig. 58). That is, the $\overline{D}$ reduction with V_s is assumed to be independent of other parameters for V_g-V_ℓ = 1080 ft/sec (329 m/s).
3. The effect of a further increase in the swirl velocity from 20 ft/sec to 80 ft/sec (6.1 to 24.4 m/s), reduces $\overline{D}$ by an addition of 20 percent which is also seen in the cold-flow data for (V_g-V_ℓ) = 1080 ft/sec (329 m/s) in Fig. 58.

Following the first assumption, a plot (Fig. 96) of mass median dropsize versus (V_g-V_ℓ) was constructed from the basic concentric cold-flow data for a mixture ratio of 5.75 and at zero post recess.

For the hot-fire relative velocity, this yields a mass median dropsize of approximately 250 μ (250 x 10^{-6} m) before any scale correlations have been made. Using the basic concentric tube scale factor of $\Delta\overline{D}/\Delta D_\ell$ = 1000 μ/in. (394 x 10^4 m/m), the correction for the required hot-fire liquid diameter yields an approximate mass median dropsize of 415 μ (415 x 10^{-6} m). Correcting this value for the addition of a swirl velocity leads to a predicted mass median dropsize of 208 μ (208 x 10^{-6} m) for a 20 ft/sec (6.1 m/s) swirl velocity and of 170 μ (170 x 10^{-6} m) for an 80 ft/sec (24.4 m/s) swirl velocity.

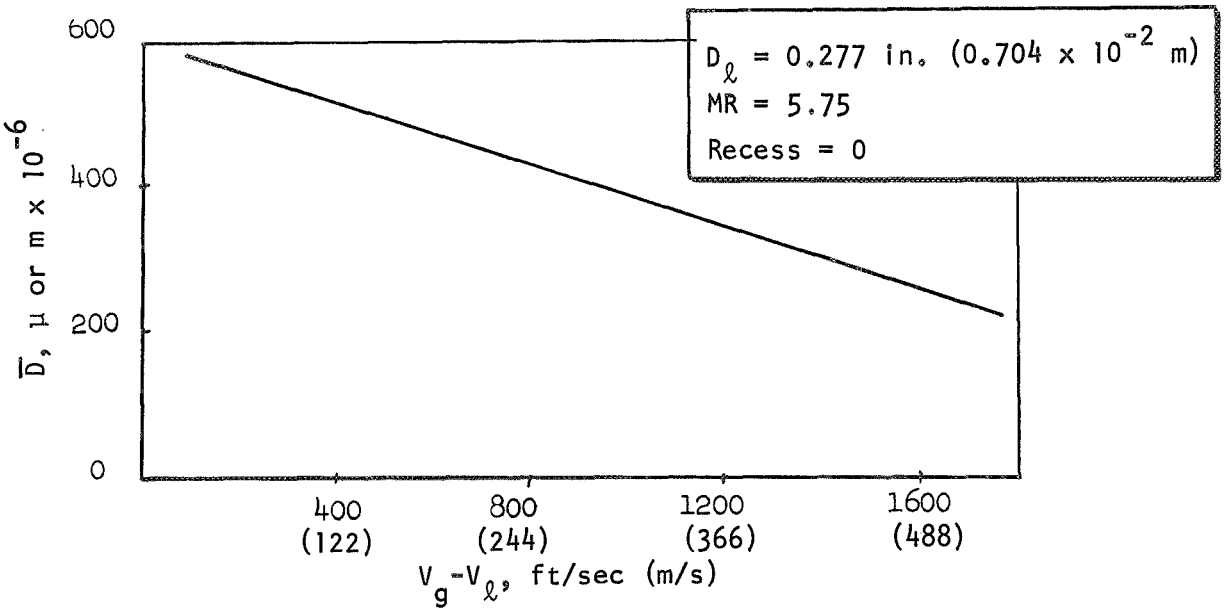

Figure 96. Parametric Effect of Gas Injection Velocity Difference on Mass Median Dropsize (Basic Concentric Injector)

Tricentric With Centerbody. Among the concentric tube primary variables mentioned above, only the swirl velocity does not apply to the tricentric with centerbody concept. However, only three of these parameters (scale, injection velocity difference, and mixture ratio) were investigated experimentally with this element type. Results from these tests yield a 280 μ (280 x 10^{-6} m) mass median dropsize for the appropriate mixture ratio and thrust per element levels of the reference FLOX/CH_4 system. Extrapolations to the hot-fire V_g-V_ℓ can be made from the cold-flow data, yielding a 185 μ (185 x 10^{-6} m) mass median dropsize. The various annulus gap dimensions are also considered important but, because they were not varied independently, no attempt was made to optimize the concept with regard to the gap dimensions*. The addition of liquid post recess in the hot-fire model should also yield a dramatic reduction in $\bar{D}$ if cold-flow trends from related injector concepts are assumed. Thus, the tricentric with centerbody concept is expected to yield extremely good atomization potential for the FLOX/CH_4 system.

Atomization Rating Summary. Five gas augmented injector concepts have been compared on the basis of their hot-fire atomization capability as predicted

*This was done later in Task III and found to have considerable importance.

from their cold-flow mean dropsize curves. The basic concentric and concentric with swirler concept designs were restricted by anticipated limits in recess and V_s because of injector face heat transfer and chamber compatibility, respectively. Considering the atomization characteristics alone, the injectors are listed below in order of decreasing predicted performance.

1. Impinging concentric
2. Basic impinging
3. Tricentric with centerbody
4. Basic concentric (post recess = D_ℓ)
5. Concentric with swirler (V_s = 20 ft/sec; 6.1 m/s)

The atomization potential variations between different injector types with each optimized from cold-flow experimental data is not great, although at off-optimum design conditions, extreme variations in atomization potential were observed for all concepts tested. In rating the injector types, some consideration has been given to potential dropsize reductions resulting from introducing liquid tube recess to the impinging concentric and tricentric with centerbody injectors. This reasoning was used to place the impinging concentric injector above the basic impinging and concentric types, and to rate the tricentric concept above both the basic concentric and concentric swirler designs. Task I hot-fire data for both of the impinging elements indicate good atomization for large thrust/element injectors. In addition, uncertainty of the scale factor for the basic concentric and concentric swirler and lack of mixture ratio data for the concentric swirler partially influenced low ratings for these element types.

Rating of Injector Mixing Potential

Because the cold flow propellant mixing facility has a higher thrust-per-element test limitation, many of the scale extrapolations made in the atomization analysis were not needed. However, several interpolations and

extrapolations are still necessary to determine the optimized mixing performance at the reference hot-fire operating conditions. These procedures are described below for each of the individual injector concepts.

Impinging Concepts. Test results for all impinging type (i.e., basic impinging and impinging concentric elements) injector concepts were presented in a previous section. Resultant mixing efficiencies have shown mixing to be a function of the liquid penetration parameter, D_ℓ/D_g, the gas momentum flux, scale, and the ratio of annulus to total gas flowrate. However, several of these parameters (e.g., X_p/D_g, D_ℓ/D_g, and $\rho_g V_g^2$) exert little or no influence on FLOX/CH_4 mixing efficiency when they are maintained within a given range. The predicted mixing efficiencies for the FLOX/CH_4 propellant system described above are given in the following section.

Basic Impinging. Selection of a penetration parameter in the range as high as possible without increasing $\overline{D}$ (0.9) and a FLOX injection velocity of approximately 100 ft/sec (30.5 m/s) yields liquid and gas orifice diameters of 0.23 (0.58×10^{-2} m) and 0.59 in. (1.50×10^{-2} m); $D_\ell/D_g = 0.39$. From the Task II data showing the influence of X_p/D_g, D_ℓ/D_g, and scale on mixing efficiency, a mixing efficiency of approximately 97 percent may be predicted. This high level is substantiated by the 99-percent combustion efficiency attained with this concept in the first hot-fire test in Task I.

Impinging Concentric. The main difference between the basic impinging and impinging concentric concepts is the presence of the annulus fuel flowrate in the latter. The amount of annulus fuel was varied experimentally, keeping the other flowrates and hardware constant. Results from these tests showed mixing potential to decrease with increasing annulus flowrate. Therefore, a relatively low percentage (20 percent) of the total fuel will be assumed for the annulus flowrate. With this assumption, the same procedure for η_{c^*mix} prediction may be followed with this concept as was followed with the basic impinging. Again, the momentum flux in the center orifice exhibited little influence on mixing in Task II cold-flow tests. To obtain the same X_p/D_g range (0.9) as selected for the basic impinging element performance prediction,

the D_ℓ/D_g must be increased significantly above the Task II test range (0.45 versus 0.33). However, extremely good mixing was obtained for LOX/GH_2 with this injector concept at a D_ℓ/D_g = 0.4 in Task I. Thus, extrapolation of the Task II results (with Task I hot firing in mind) yields no significant decrease in mixing efficiency at 0.45 D_ℓ/D_g. Selection of 100 ft/sec (30.5 m/s) FLOX injection velocities and a 0.9 penetration parameter leads to liquid and gas orifice diameters of 0.23 and 0.51 (0.58 and 1.30 x 10^{-2} m). Under these conditions, a 99-percent mixing efficiency is predicted according to Task II cold-flow data. Similar values of $(\eta_{c^*})_{mix}$ were obtained in long L* hot-fire tests made with LOX/GH_2 in Task I with a larger-scale injector.

Concentric Tube Concepts. Cold flow test results for all concentric tube concepts were presented in a previous section. Resultant mixing efficiencies have shown mixing to be a strong function of mixture ratio and post recess and to vary also with the gas-liquid injection velocity differences, and scale in the ranges tested. The methods used in the mixing analyses for each of the concentric tube concepts are described below.

Basic Concentric Injector. To predict a mixing efficiency for the basic concentric injector, the mixing efficiency must be extrapolated with regard to the injection velocity difference (V_g-V_ℓ) and the element scale. The actual data points and extrapolated (dashed) curves are shown in Fig. 97.

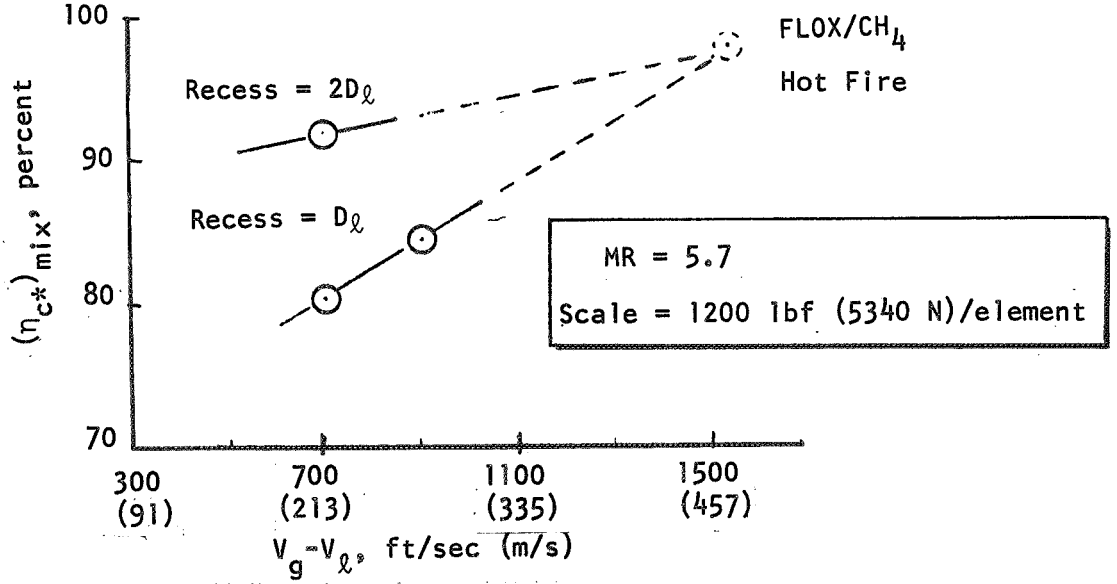

Figure 97. Gas Velocity Influence on Mixing Efficiency; Basic Concentric Injector

Obviously the limited number of data make the extrapolation with V_g-V_ℓ rather difficult. As a best estimate, the predicted hot-fire mixing efficiency for V_g-V_ℓ = 1400 ft/sec (427 m/s) would be on the order of 98 percent for a recess equal to one or two liquid diameters. Task II cold-flow test results in which the scale was varied indicate that, for recess/D_ℓ = 1.0, E_m would decrease on the order of 5 percent from the cold-flow element size used to obtain the above curve (D_ℓ = 0.21 in.; 0.53 x 10^{-2} m) to the hot-firing element size (D_ℓ = 0.45 in.; 1.14 x 10^{-2} m, T/E = 5000 lbf; 22,200 N). The corresponding decline in $(\eta_{c*})_{mix}$ would be $\approx$ 2 percent, but should be somewhat less for a deeper post recess (recess/D_ℓ = 2.0). The estimated $(\eta_{c*})_{mix}$ for the reference design case with post recess equal to D_ℓ is about 98 percent.

Concentric Tube With Swirler. Only three cold-flow tests were made in Task II with this concept. Relatively good mixing ($(\eta_{c*})_{mix} \cong 95$ percent) was obtained in these tests. However, to predict a mixing efficiency for the reference FLOX/CH_4 system, extrapolations are needed with respect to injection velocity difference, scale, and mixture ratio. These extrapolations had to be made from the basic concentric tube data with subsequent application of the observed influence of swirl velocity. Because the concentric tube with swirler has zero recess, these extrapolations should also be made from basic concentric tube data at zero recess. However, there is only one data point with these qualifications, which limits the confidence level. The cold-flow data reflects mixing efficiencies on the order of 95 percent with a liquid orifice diameter of 0.21 in. (0.53 x 10^{-2} m), V_g-V_ℓ = 875 ft/sec (267 m/s) and a 10.0 mixture ratio. However, the lack of data available for extrapolation to the hot-fire operating parameters with regard to mixture ratio, V_g-V_ℓ, and scale requires the assignment of a low mixing rating to this injector concept.

Tricentric With Centerbody. Five cold-flow mixing tests were made in Task II with this concept. Extrapolations were needed with respect to the injection velocity difference (V_g-V_ℓ) and the mixture ratio to predict mixing efficiencies for the FLOX/CH_4 system. The V_g-V_ℓ extrapolation can be made

directly from the cold-flow test data. No significant change in predicted mixing efficiencies are seen when $V_g - V_\ell$ varies from 600 to 950 ft/sec (183 to 290 m/s). Assuming no further change in mixing efficiency occurs when this velocity difference is increased to 1500 ft/sec (457 m/s) yields a predicted mixing efficiency of 95 percent with a mixture ratio of 10.0. No data were taken in Task II with varying mixture ratio, so no direct extrapolation to the FLOX/CH_4 5.75 mixture ratio may be made. However, the trend of the effect of mixture ratio on mixing efficiency for the basic concentric indicates a significant efficiency increase with decreasing mixture ratio. Thus, the predicted mixing efficiency for the FLOX/CH_4 system would be greater than 95 percent.

Mixing Analysis Summary. The injector concepts were rated in terms of mixing potential based on analysis discussed in the preceding sections. In this rating process, the overall confidence level in obtaining the mixing efficiency prediction was also taken into account. The injector concepts were rated with regard to mixing in the following order:

1. Impinging Concentric
2. Basic Concentric (Recess/$D_\ell \geq 1.0$)
3. Basic Impinging Pentad
4. Tricentric With Centerbody
5. Concentric With Swirler

TASK III, APPLICATION TO SPACE-STORABLE PROPELLANTS

Analyses and additional cold-flow simulation experiments were conducted in Task III employing the element types chosen based on the Task II cold-flow test results and analysis. These selected injection elements included the basic (recessed) concentric, the tricentric with centerbody, and two thrust-per-element sizes of the impinging concentric concept. Whereas the Task II results were designed to characterize injector elements for general applicability to gas/liquid propellant systems (e.g., LO_2/GH_2, $FLOX/CH_{4(g)}$, and LF_2/GH_2), under Task III the interest narrowed to the specific application to $FLOX/CH_{4(g)}$ at a nominal 500-psi (345×10^4 N/m^2) chamber pressure. The Task III test matrices were designed (1) to permit more direct interpolation of the cold-flow data to the nominal $FLOX/CH_{4(g)}$ operating conditions (MR = 5.25 to 5.75, ρ_g of $CH_{4(g)}$, P_c at 500 psi; 345×10^4 N/m^2, etc.) and (2) to examine significant parameters omitted or insufficiently tested in Task II. These data, when combined with applicable Task II results, were intended to provide for further optimization of the injector design concepts and to guide the selection of the two most promising high thrust/element designs for Task IV hot-fire evaluation.

In accord with the performance analysis concepts presented in the Task I discussion, the injectors' influence on performance was considered to depend upon their ability to atomize and uniformly mix the propellants. The cold-flow experiments, with inert fluids, were used to simulate the atomization and mixing characteristics of the selected injector concepts. As in Task II, the atomization experiments were conducted using the molten wax technique and the mixing experiments through the use of liquid and gas mass flux distribution measurements.

DESIGN OF COLD-FLOW INJECTORS

The cold-flow injectors were single element models designed to have the same orifice dimensions as the hot-firing elements they modeled. Principal injector design parameters for the respective injector types are discussed below. Where feasible, existing Task II hardware was utilized.

Basic Concentric Injector Model

A nominal 5000-lbf (22,200 N)-thrust-per-element basic concentric injector was designed with a 120 ft/sec (36.6 m/s) liquid injection velocity and a 1500 ft/sec (457 m/s) gas injection velocity. These hot-fire injection velocities were assumed because of limitations enforced by the cold-flow simulation fluids. A lower more desirable hot-fire liquid injection velocity would require relatively low cold-flow liquid velocities for the desired simulation, while a higher hot-fire gas velocity would require cold-flow injection Mach numbers greater than sonic. Thus, a 0.43-in. (1.09×10^{-2}m) liquid post inside diameter, a 0.11-in. (0.28×10^{-2}m) gas annulus gap and a post (wall) thickness of 0.035 (0.089×10^{-2}m) was selected. This yielded liquid and gas injection areas of 0.15 and 0.21 $in.^2$ (0.97 and $1.35 \times 10^{-4} m^2$), respectively. The primary variables investigated with the recessed basic concentric concept were post recess and gas density. Post recess was adjusted by varying the length of the liquid injection tube. The overall concentric element injector assembly was the same as used in Task II (Fig. 35).

Impinging Concentric Injector Model

Two different element sizes were used for the impinging concentric injector (four gas/liquid concentric jets impinging on a control gas jet) cold-flow tests. Basically, element size was scaled according to the liquid post (inside) diameter, D_L, with 0.19 and 0.40 in. (0.48 and 1.02×10^{-2}m) used, thereby simulating thrust-per-element sizes of 1250 and 5000 lbf (5550 and 22,200 N) at a nominal FLOX injection velocity. The central gas orifice

size, concentric gas annulus gap, and post thickness were always scaled accordinto to D_ℓ and were not varied otherwise. Another primary geometric variable was the liquid to central gas orifice diameter ratio, D_ℓ/D_g. The cold-flow injectors were designed to accommodate variation in D_ℓ/D_g by using a series of central gas orifice diameters while maintaining constant geometry in the four concentric tubes. The collet chuck assembly applied in Task II was utilized to facilitate changes in the orifices with these models as shown in Fig. 37. The primary dimensions for the impinging concentric injectors are given in Table 20. Not shown on the table is the fact that the liquid orifice posts in the concentric tubes were recessed by one post ID for all Task III cold-flow tests with this injector.

Tricentric With Centerbody Injector Model

The variables investigated using the selected 5000-lb (22,200 N)-thrust-per-element tricentric with centerbody injector concept included the annulus gaps, recess, and gas density. To accomplish this, both the annulus gap dimensions and the centerbody diameter were varied. Again the basic Task II injector design was used (see Fig. 38). The primary injector orifice dimensions for the cold-flow tests with this concept are given below in Table 21.

EXPERIMENTAL APPARATUS, TEST PROCEDURES AND DATA REDUCTION

The Task III cold-flow distribution tests were conducted in the Propulsion Research Area (PRA) and the molten wax atomization (dropsize) tests were made at the Combustion and Heat Transfer Laboratory (CHTL) at Rocketdyne's Santa Susana Field Laboratory. These facilities were previously described in the Task II section of this report along with the procedures used for both types of tests. As mentioned in the Task I, the performance analysis approach used requires evaluation of two principal modes of performance losses: incomplete propellant spray vaporization, and imperfect mixing of fuel and oxidizer. The

TABLE 20

IMPINGING CONCENTRIC TUBE INJECTOR DIMENSIONS

D_ℓ		$(D_g)_{center}$		Annulus Gap		Post Thickness		D_ℓ/D_g	$(A_\ell)_{tot}$		$(A_g)_{center}$		$(A_g)_{annulus}$	
in.	m x 10^{-2}	in.	m x 10^{-2}	in.	m x 10^{-2}	in.	m x 10^{-2}		$in.^2$	m^2 x 10^{-4}	$in.^2$	m^2 x 10^{-4}	$in.^2$	m^2 x 10^{-4}
0.19	0.48	0.62	1.57	0.06	0.15	0.028	0.071	0.33	0.12	0.77	0.30	1.94	0.23	1.48
0.19	0.48	0.46	1.17	0.06	0.15	0.028	0.071	0.42	0.12	0.77	0.17	1.10	0.23	1.48
0.19	0.48	0.33	0.84	0.06	0.15	0.028	0.071	0.58	0.12	0.77	0.09	0.58	0.23	1.48
0.40	1.02	0.90	2.29	0.12	0.30	0.049	0.124	0.44	0.51	3.29	0.64	4.13	0.96	6.19
0.40	1.02	0.69	1.75	0.12	0.30	0.049	0.124	0.58	0.51	3.29	0.38	2.45	0.96	6.19

TABLE 21

TRICENTRIC WITH CENTERBODY INJECTOR DIMENSIONS

Inner Gas Annulus								Liquid Annulus								Outer Gas Annulus							
ID		OD		Y_g (gap)		Area		ID		OD		Y_ℓ (gap)		Area		ID		OD		Y_g (gap)		Area	
in.	$mx10^{-2}$	in.	$mx10^{-2}$	in.	$mx10^{-2}$	$in.^2$	m^2x10^{-4}	in.	$mx10^{-2}$	in.	$mx10^{-2}$	in.	$mx10^{-2}$	$in.^2$	m^2x10^{-4}	in.	$mx10^{-2}$	in.	$mx10^{-2}$	in.	$mx10^{-2}$	$in.^2$	m^2x10^{-4}
0.25	0.64	0.46	1.17	0.11	0.28	0.12	0.77	0.53	1.35	0.75	1.91	0.11	0.28	0.21	1.35	0.81	2.06	0.90	2.29	0.05	0.13	0.12	0.77
0.12	0.30	0.46	1.17	0.17	0.43	0.16	1.03	0.53	1.35	0.75	1.91	0.11	0.28	0.21	1.35	0.81	2.06	0.90	2.29	0.05	0.13	0.12	0.77
0.25	0.64	0.46	1.17	0.11	0.28	0.12	0.77	0.53	1.35	0.75	1.91	0.11	0.28	0.21	1.35	0.81	2.06	1.03	2.62	0.11	0.28	0.31	2.00
0.25	0.64	0.46	1.17	0.11	0.28	0.12	0.77	0.53	1.35	0.83	2.11	0.15	0.38	0.32	2.06	0.90	2.29	0.99	2.51	0.05	0.13	0.13	0.84
0.12	0.30	0.46	1.17	0.17	0.43	0.16	1.03	0.53	1.35	0.75	1.91	0.11	0.28	0.21	1.35	0.81	2.06	0.96	2.44	0.07	0.18	0.20	1.29
0.35	0.89	0.46	1.17	0.06	0.15	0.07	0.45	0.53	1.35	0.75	1.91	0.11	0.28	0.21	1.35	0.81	2.06	0.86	2.18	0.02	0.05	0.06	0.39

cold-flow tests characterizing these processes will be described in a subsequent section. The applicable data reduction procedures were described in the Task II section of this report.

COLD-FLOW TESTS AND RESULTS

A series of 42 cold-flow tests (23 atomization and 19 mixing tests) were conducted under Task III using the molten wax and gas/liquid mass distribution facilities. The following discussion details the cold-flow test matrices for each of the selected Task III cold-flow models.

Basic Concentric Injector

Performance predictions based on Task II data showed η_{c*} to be very sensitive to the post recess of the large thrust-per-element basic concentric injector. The main Task III concentric injector test objective was to determine the amount of recess necessary to obtain the 96-percent combustion efficiency goal with the nominal hot-firing system at the 5000-lbf (22,200 N)-thrust-per-element level. In Task II, both the cold-flow gas injection velocity and thrust per element were lower than anticipated for the FLOX/CH_4 hot-fire system. In the Task III cold-flow tests, the gas injection velocities and the element size were adjusted to simulate these hot-fire conditions. The gas density was another variable which was investigated. This allowed the extrapolation to hot-fire densities which was required because the cold-flow tests were made at ambient pressures (lower densities).

Six atomization and three mixing cold-flow tests were conducted with the recessed basic concentric injector element. Primary variables for these tests were the amount of post recess and the gas density, with all other operating conditions held constant. The gas density was varied only in atomization tests because of experimental limitations existing at that time on the mixing facility. A summary of the test operating conditions along with the mass median dropsize and E_m attained is presented in Table 22.

TABLE 22

SUMMARY OF BASIC CONCENTRIC INJECTOR TESTS

Test No.	D_ℓ		Annulus Gap		A_ℓ		A_g		Post Recess $\frac{}{D_\ell}$	MR	$V_g - V_\ell$		V_ℓ		$\bar{D}$, μ or	E_m,
	in.	$mx10^{-2}$	in.	$mx10^{-2}$	$in.^2$	m^2x10^{-4}	$in.^2$	m^2x10^{-4}			ft/sec	m/s	ft/sec	m/s	$mx10^{-6}$	percent
A-71	0.43	1.09	0.11	0.28	0.15	0.98	0.21	1.35	3	5.8	1075	328	12.0	3.66	148	--
A-72									3	5.4	1080	329	1.4	0.43	158	--
A-73a									3	6.7	1530	466	2.5	0.76	190	--
A-73b									3	6.2	1535	468	2.4	0.73	195	--
A-74									1	5.7	1553	473	2.3	0.70	347	--
A-75									5	5.5	1515	462	2.1	0.64	153	--
M-41									5	6.1	914	279	10.4	3.17	-	88.1
M-42									3	5.8	913	278	10.1	3.08	-	83.0
M-43									1	6.3	912	278	10.8	3.29	-	50.7

The first two atomization tests were designed to investigate the influence of gas density on the mass median dropsize. A post recess of three liquid diameters was used in these open air tests with (essentially) constant mixture ratio and constant $V_g - V_\ell$. Because of the minor experimental variations in the test mixture ratios, the values of $\bar{D}$ listed in Table 22 were corrected to a mixture ratio of 5.75 (using Task II correlations) and are plotted in Fig. 98 . As expected, increasing gas density descreased the mass median dropsize. For comparison, the methane injection density at a chamber pressure of 500 psi (345×10^4 N/m^2) and injection temperature of 800 R (44.4 K) is approximately 0.9 lbm/ft^3 (14.4 kg/m^3).

The amount of post recess was varied in the remaining atomization tests. These data also were corrected by means of Task II results to account for any deviations in mixture ratio from the nominal value of 5.75. The resultant mass median dropsizes are plotted in Fig. 99. Note that the effect of increasing post recess lessens considerably for this element at post recesses greater than three liquid diameters. An analogous result was seen in the investigation of the post recess influence on mixing efficiency. These data, plotted in Fig. 100, show a 20-percent increase in η_{mix} as the amount of post recess increases from one to three liquid diameters, but only a 2 percent further increase as the post recess was changed from three to five liquid diameters.

Impinging Concentric Injector

Eight atomization tests and seven propellant mixing cold-flow tests were conducted with the impinging concentric injector concept. A summary of the operating conditions for all Task III impinging concentric injector tests is given in Table 23. Primary variables for these tests included overall mixture ratio, annulus mixture ratio, center gas momentum flux, the liquid-to-center gas orifice diameter ratio (D_ℓ/D_g), and scale*. Note that for all

*The liquid penetration parameter, X_p/D_g, which is another significant parameter, was not further investigated under Task III. For these tests, X_p/D_g was maintained within a range of values where it should not influence the test data.

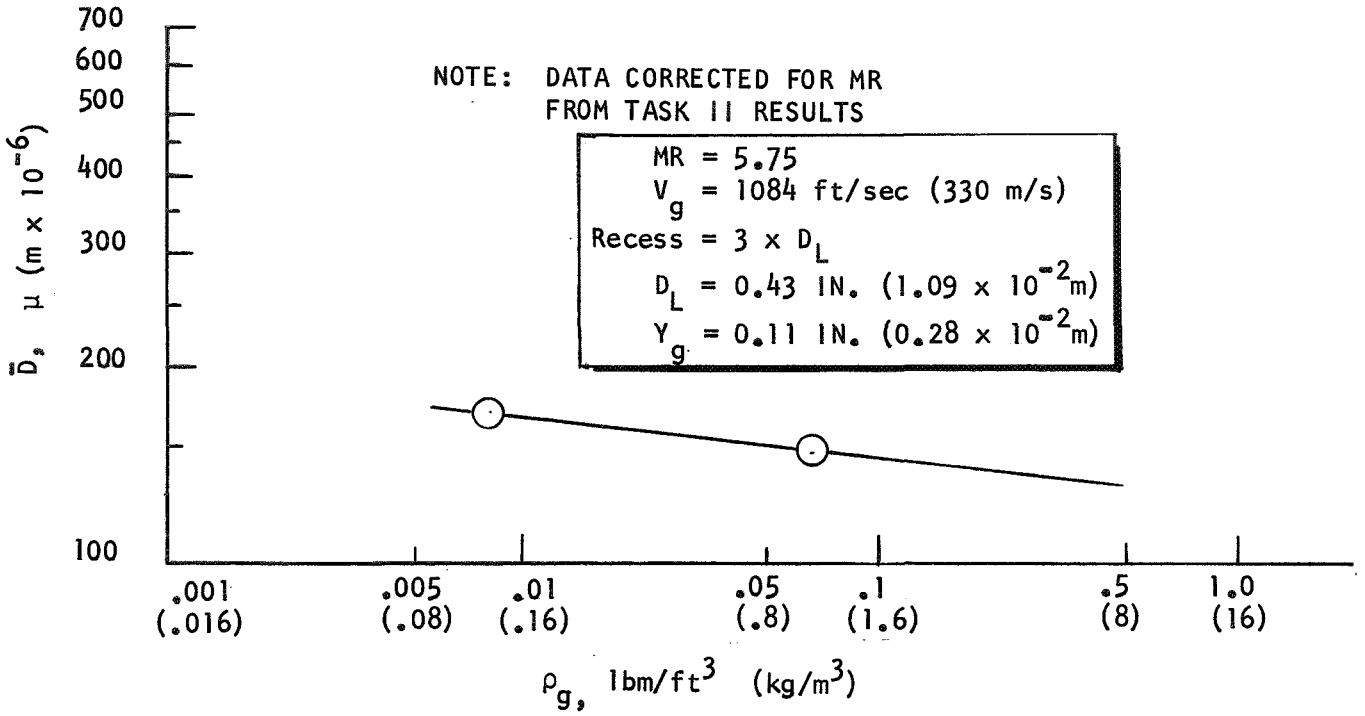

Figure 98. The Effect of Injected Gas Density on Mass Median Dropsize: Recessed Basic Concentric Element

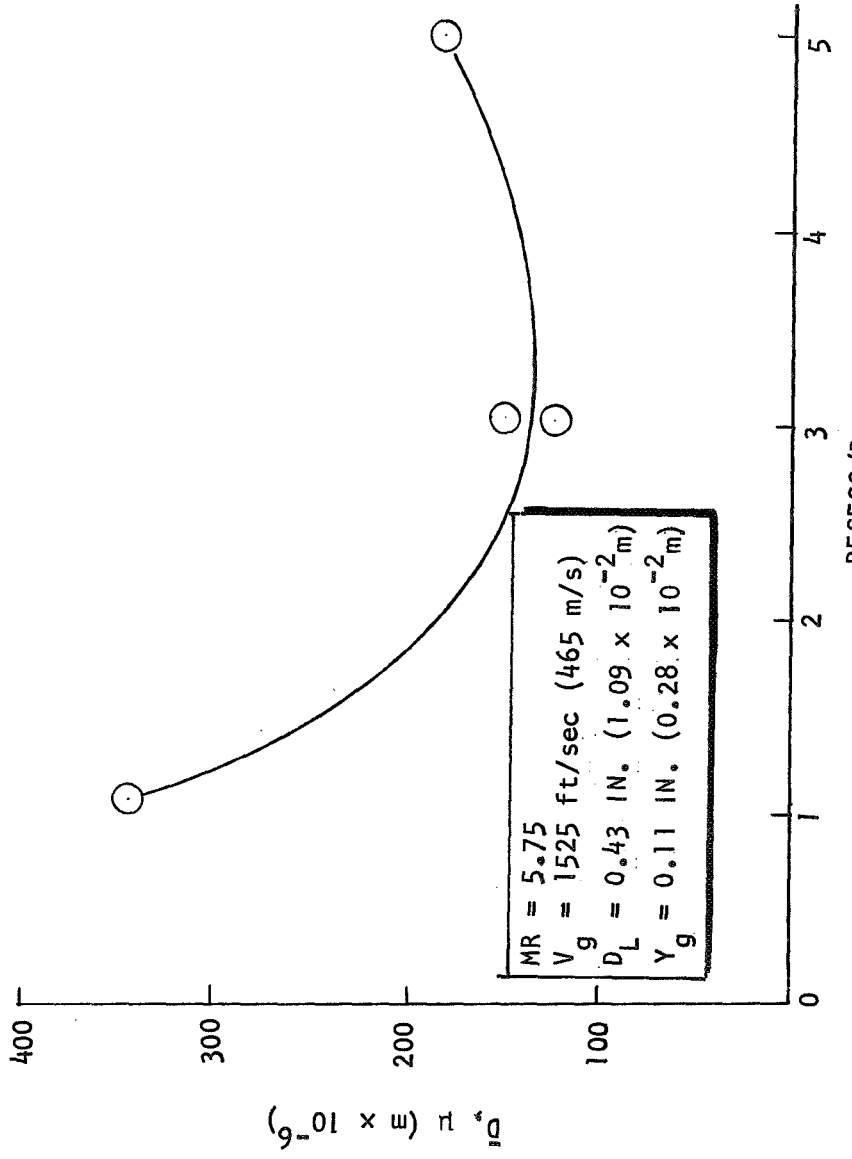

Figure 99. The Effect of Post Recess on Mass Median Dropsize: Recessed Basic Concentric Element

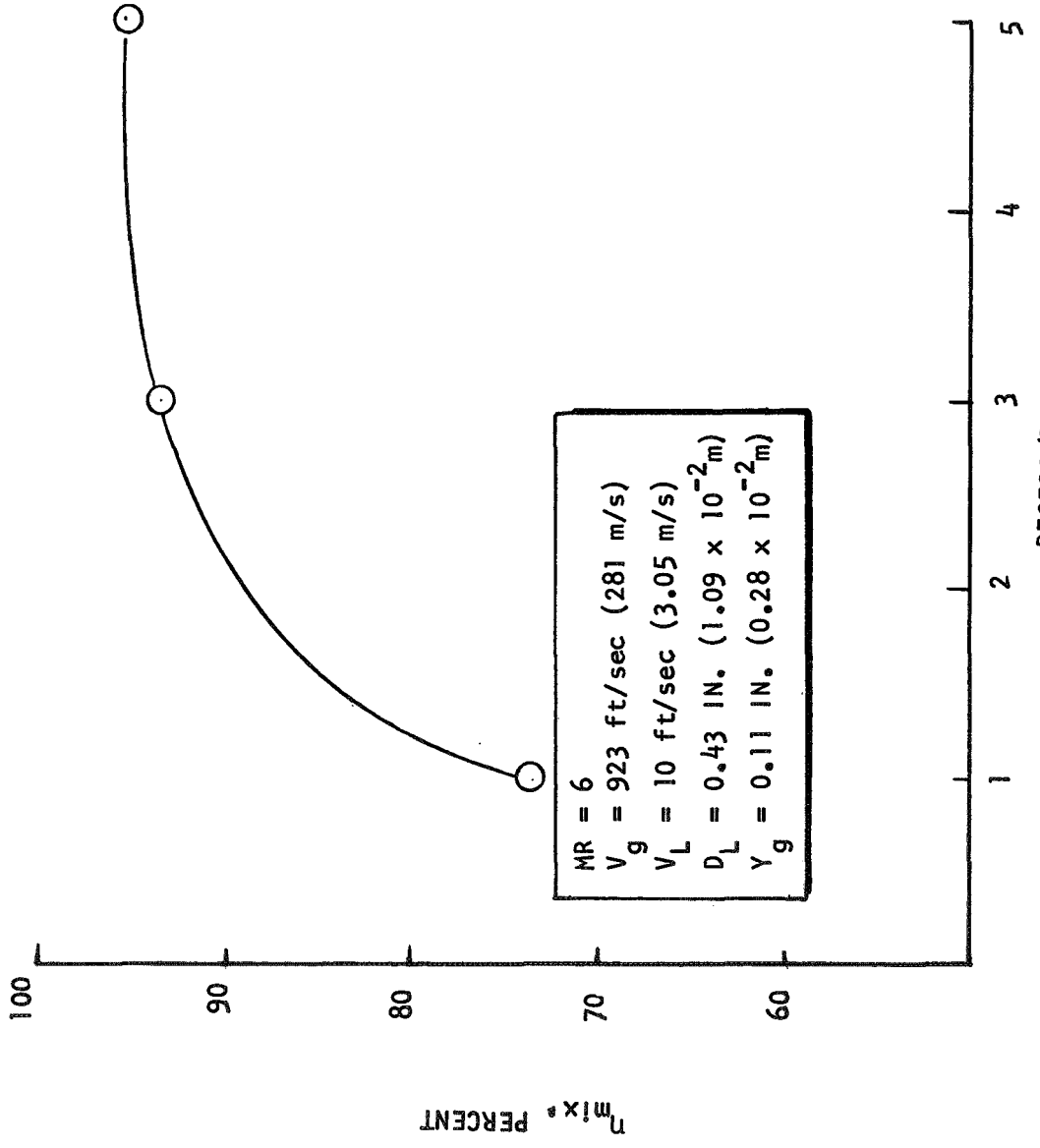

Figure 100. The Effect of Post Recess on Mixing Efficiency: Recess Basic Concentric Element

TABLE 23

SUMMARY OF IMPINGING CONCENTRIC INJECTOR TESTS

Test No.	D_ℓ		D_g		Annulus Gap		$\left(\frac{\dot{W}_{ann}}{\dot{W}_{tot}}\right)_g$	V_g (center)		V_g (ann)		MR	D_ℓ/D_g	X_p/D_g	$\rho_g V_g^2$ (center)		MR (ann)	$\bar{D}$, μ or	E_m,
	in.	$mx10^{-2}$	in.	$mx10^{-2}$	in.	$mx10^{-2}$		ft/sec	m/s	ft/sec	m/s				psi	N/m^2x10^4		$mx10^{-6}$	percent
A-82	0.19	0.48	0.62	1.57	0.06	0.15	0.20	2714	827	1041	317	11.6	0.31	0.30	15.8	10.9	59	300	--
A-83	0.19	0.48	0.62	1.57	0.06	0.15	0.20	1015	309	369	112	5.8	0.31	0.38	14.7	10.1	29	319	--
A-84	0.19	0.48	0.46	0.17	0.06	0.15	0.29	1086	331	365	111	5.8	0.42	0.31	16.1	11.1	20	339	--
A-85	0.19	0.48	0.33	0.84	0.06	0.15	0.45	1074	327	383	117	5.8	0.58	0.30	15.7	10.8	13	411	--
A-86	0.40	1.02	0.69	1.75	0.12	0.30	0.43	955	291	317	97	5.7	0.58	0.30	14.1	9.7	13	540	--
A-87	0.40	1.02	0.90	2.29	0.12	0.30	0.31	1001	305	337	103	6.2	0.45	0.34	14.9	10.3	20	495	--
A-88	0.19	0.48	0.46	1.17	0.06	0.15	0.45	622	190	380	116	8.7	0.42	0.58	4.8	3.3	19	421	--
A-89	0.19	0.48	0.46	1.17	0.06	0.15	0.29	1086	331	366	112	3.8	0.42	0.21	16.2	11.2	13	310	--
M-44	0.19	0.48	0.62	1.57	0.06	0.15	0.20	920	280	334	102	7.9	0.31	0.50	14.7	10.1	39	-	67.9
M-45	0.19	0.48	0.46	1.17	0.06	0.15	0.29	970	296	327	100	9.2	0.42	0.48	16.1	11.1	32	-	69.0
M-46	0.19	0.48	0.33	0.84	0.06	0.15	0.45	947	289	335	102	9.8	0.58	0.48	15.3	10.5	22	-	62.7
M-47	0.40	1.02	0.69	1.75	0.12	0.30	0.43	962	293	324	99	10.1	0.58	0.48	15.9	11.0	24	-	37.9
M-48	0.40	1.02	0.90	2.29	0.12	0.30	0.32	930	283	331	101	9.6	0.45	0.51	14.9	10.3	30	-	36.9
M-49	0.19	0.48	0.46	1.17	0.06	0.15	0.38	944	288	316	96	10.5	0.42	0.62	9.1	6.3	36	-	70.6
M-50	0.19	0.48	0.46	1.17	0.06	0.15	0.29	746	227	351	107	6.6	0.42	0.35	15.5	10.7	23	-	69.3

these tests the concentric orifice oxidizer posts were recessed by a length of one post (inside) diameter.

The initial parameter investigated was the overall mixture ratio. Overall mixture ratio previously appeared to exert no effects on basic impinging injectors independent of the other parameters described in the preceding paragraph. The impinging concentric is a hybrid concept, however, and based on the basic concentric results there was concern that changing mixture ratio might influence the contribution of the annular gas streams toward atomization of the liquid. The center gas momentum flux, percent annulus gas (D_ℓ/D_g), annulus gap, and scale were maintained constant. The mixture ratio changes were accomplished at constant X_p/D_g by simultaneously varying the gaseous simulant density (GN_2 or GHe) and liquid injection velocity. Results plotted in Fig. 101, suggest that the mass median dropsize is independent of overall mixture ratio for the conditions tested. This is in accord with results obtained with the basic impinging injector concept in Task II.

In Task II, impinging concentric injector characterization changes in D_ℓ/D_g were accompanied by a variation in the concentric tube mixture ratio*. A series of atomization and propellant mixing tests was run to distinguish separate influences of these parameters. For both mixing and atomization tests, D_ℓ/D_g was varied both with and without concentric tube mixture ratio changes while holding all other parameters in ranges where no variance in $(\eta_{c*})_{mix}$ or $\overline{D}$ had been observed in previous tests. The combination of these two procedures yielded in the independent effects of both D_ℓ/D_g and concentric tube mixture ratio changes. Results for both propellant mixing and atomization tests simulating FLOX/CH_4 are shown in Fig. 102. Mixing efficiency decreased from approximately 96 to 91 percent as D_ℓ/D_g increased from 0.42 to 0.58 at constant coaxial tube mixture ratio (MR_{tube}). Also, mixing efficiency decreased

*The concentric tube mixture ratio, or $\dot{w}_\ell/(\dot{w}_g)_{ann}$, can be considered an alternate to "percent annulus gas" as an operating parameter.

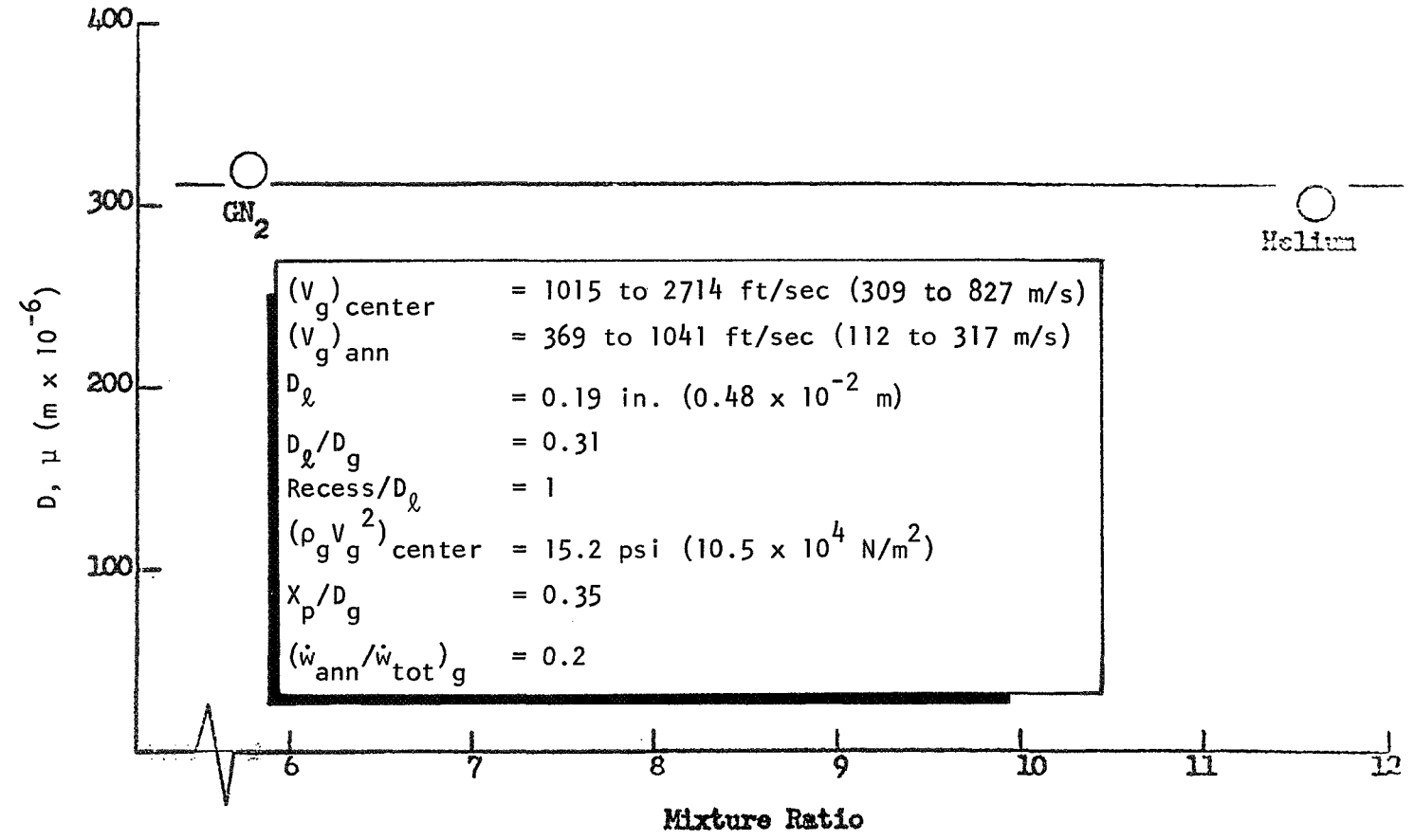

Figure 101. Effect of Overall Mixture Ratio on Propellant Dropsize: Impinging Concentric Injector Concept

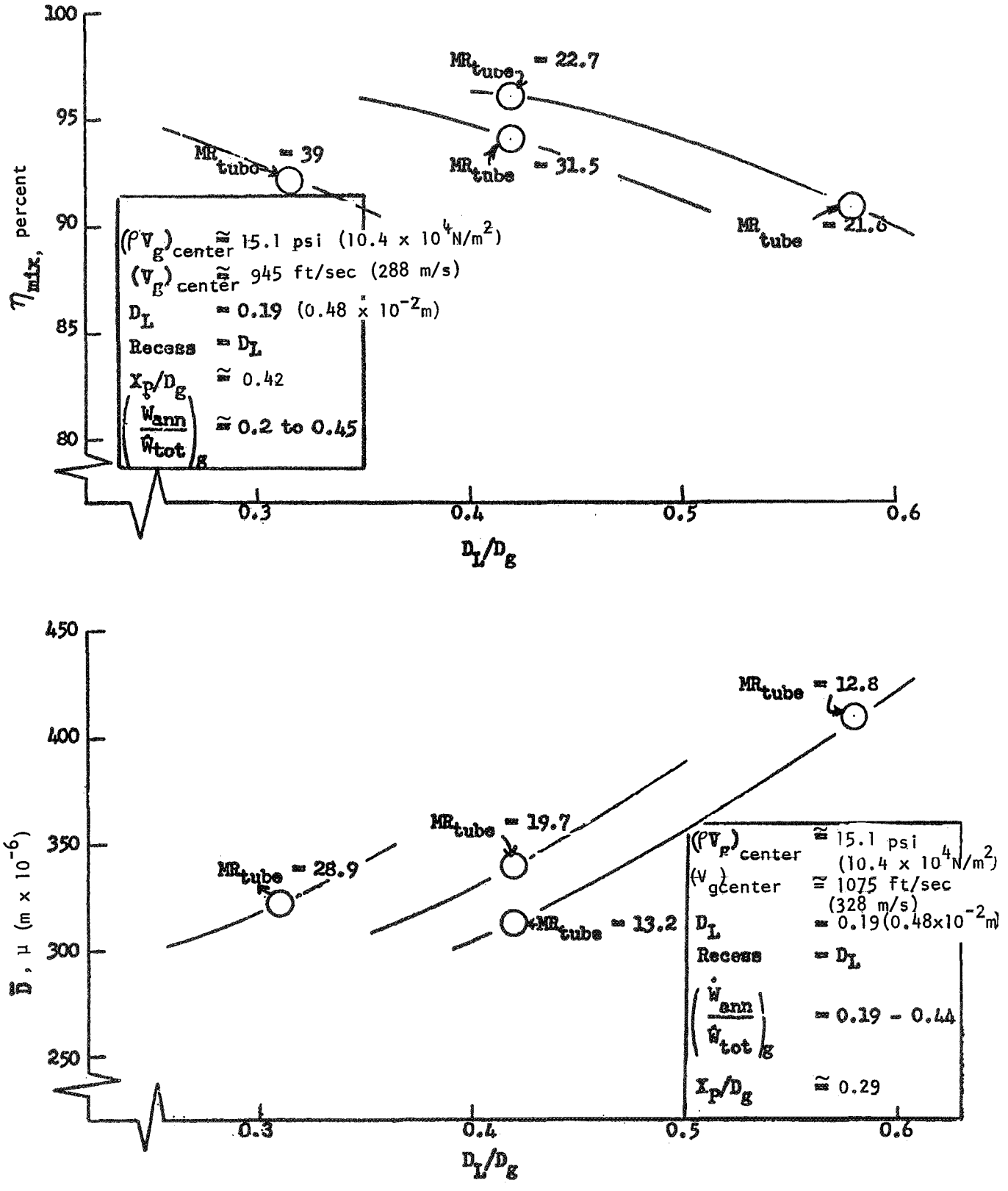

Figure 102. The Effect of Coaxial Tube Mixture Ratio and D_ℓ/D_g on Mixing and Atomization: Impinging Concentric Injector Concept

from approximately 96 to 94.3 percent as the concentric tube mixture ratio increased from 22.7 to 31.5 at constant D_ℓ/D_g. The median dropsize, $\bar{D}$, increased (decreased vaporization efficiency) with increasing D_ℓ/D_g and also increased with the concentric tube mixture ratio, as expected. The effect of concentric tube mixture ratio is in qualitative accord with the mixture ratio effects observed in the Task II basic concentric injector tests, while the effects of D_ℓ/D_g are similar to the Task II basic impinging element test results. This illustrated the hybrid nature of the impinging concentric injector concepts. In summary, D_ℓ/D_g and MR_{tube} (or alternatively the percent annulus gas) exert independent effects on both atomization and mixing. Increasing D_ℓ/D_g beyond about 0.45 appears to adversely influence both $(\eta_{c^*})_{vap}$ and $(\eta_{c^*})_{mix}$ potential as would any increases in MR_{tube} within the range tested.

The D_ℓ/D_g and scale effects on both propellant mixing and dropsize are illustrated in Fig. 103. The D_ℓ/D_g test data were described in the preceding paragraph. Increasing scale (e.g., as indexed by D_ℓ or D_g) yields a large decrease in both mixing and atomization (vaporization) efficiencies at constant D_ℓ/D_g. As D_ℓ was increased from 0.19 to 0.40 in. (0.48 to 1.02×10^{-2}m), mixing efficiencies dropped from approximately 95 to 67.5 percent while the mass median dropsize almost doubled. Note that for both levels of scale (D_ℓ), the D_ℓ/D_g effects were similar.

The remaining parameter investigated in Task III with this injector concept was the center gas momentum flux $(\rho_g V_g^2)_{center}$. Results of varying this parameter (over the range feasible under atmospheric pressure test conditions) are presented in Fig. 104. As expected, the mixing efficiency increased and the mass median dropsize decreased with increasing center gas momentum flux. Because the center gas momentum flux for the FLOX/CH_4 hot-fire system would be 10 to 30 times the largest $(\rho_g V_g^2)_{center}$ in these cold-flow tests, the predicted performance for the hot-fire conditions would be considerably higher than attained under cold-flow conditions.

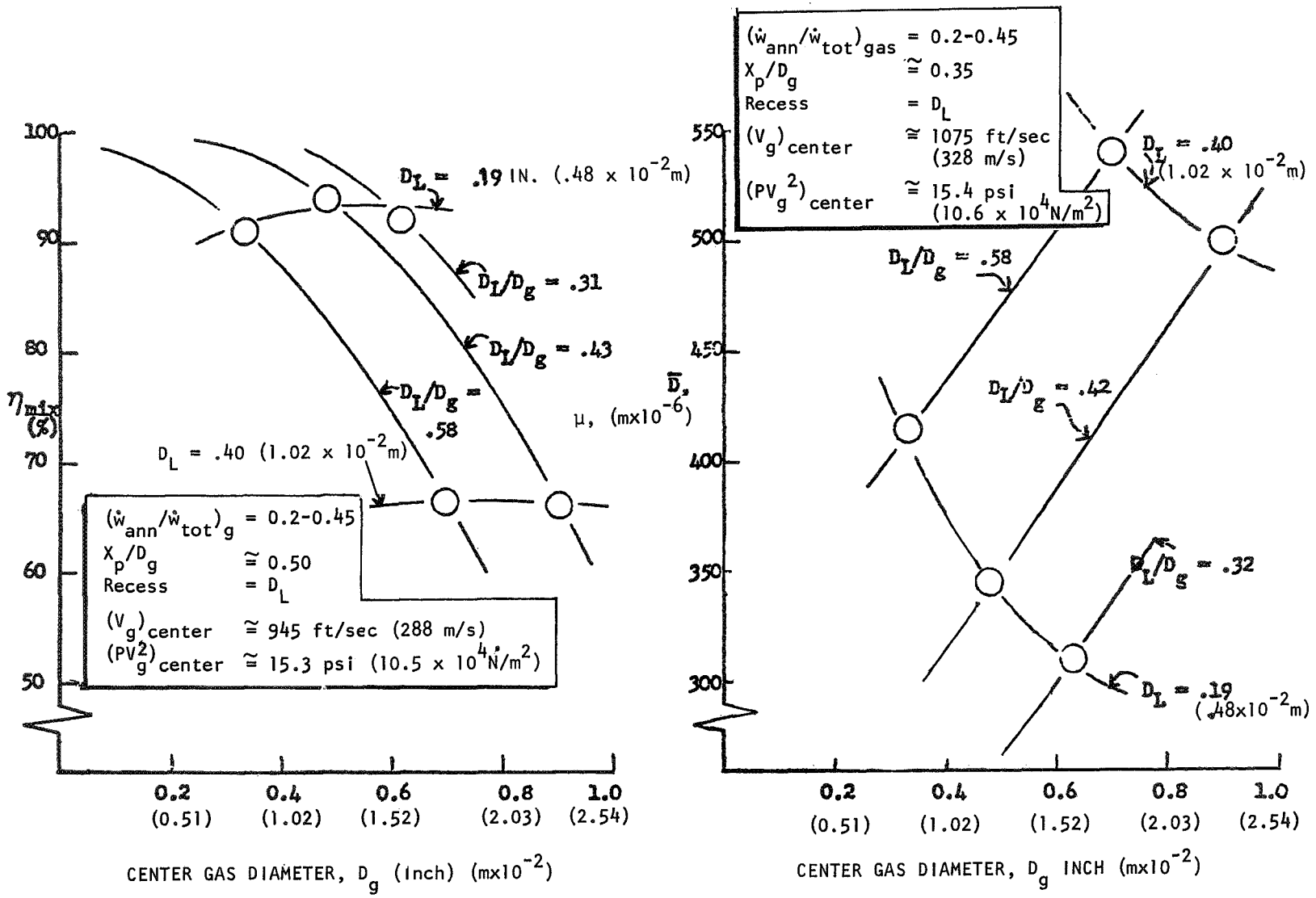

Figure 103. The Effect of Geometry on Mixing and Atomization: Impinging Concentric Injector Concept

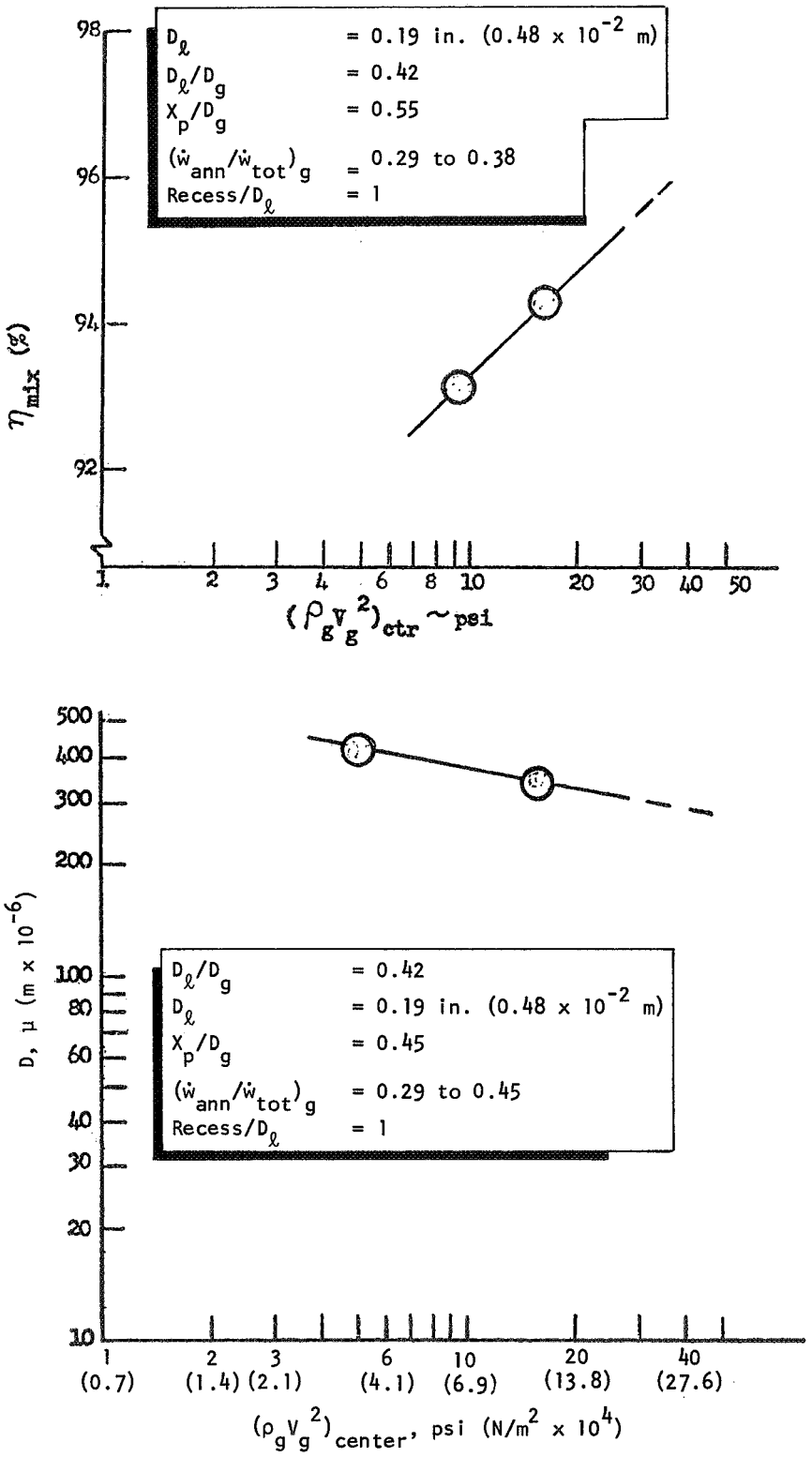

Figure 104. Effect of Center Gas Momentum Flux on Mixing and Atomization: Impinging Concentric Concept

Tricentric With Centerbody Injector

Nine atomization and nine mixing tests were conducted in Task III with the tricentric with centerbody injector concept. Operating conditions for these tests are given in Table 24. The parameters investigated include plug diameter, annulus, liquid annulus recess, V_g-V_ℓ, and gas density. In all tests the inner and outer annulus gas velocities were equal. The liquid injection velocity (V_ℓ) was allowed to vary to achieve the selected mixture ratio.

The initial tests with this injector concept were designed to investigate the effect of varying each of three annulus gaps independently*. The mixture ratio and gas velocities were held constant for these tests but V_ℓ was allowed to vary. The results are plotted in Fig. 105 and 106 for mixing and atomization tests, respectively. Mixing efficiency increased in the range tested with decreasing inner or outer gas gaps or with an increasing liquid gap while the mass median dropsize was decreased by increasing the inner gas gap or decreasing the outer gas and liquid gaps. However, examination of the data indicated the results may be more readily interpreted by expressing the geometric changes in terms of (1) the inner to outer gas gap ratio, and (2) the inner to outer gas injection area ratio. This area ratio parameter is equivalent to the inner to outer gas flowrate ratio because both the inner and the outer gas velocities were held constant. The data from Fig. 105 and 106 were therefore replotted against the gas injection area ratio in Fig. 107 with the gas gap ratios noted. This leaves some question as to which of these two parameters are the most significant. However, one set of relative optimum conditions can be picked from this plot for the hot-fire model. Note that the mixing efficiency varied considerably more over the range of $(A_{in}/A_{out})_g$ while the mass median dropsize doesn't; i.e., specifically $(\eta_{c*})_{vap}$ based on combustion model calculations

*For the tricentric concept, two additional degrees of freedom become available compared to most conventional injector element types. Thus, even for fixed total flowrates, mixture ratio, and injection velocities, a pair of geometric parameters may be varied.

TABLE 24

SUMMARY OF TRICENTRIC WITH CENTERBODY INJECTOR TESTS

Test No.	Inner Gap $(Y_{in})_g$		Liquid Gap Y_ℓ		Outer Gap $(Y_{out})_g$		D_{plug}		$\left(\frac{Y_{in}}{Y_{out}}\right)_g$	$\left(\frac{A_{in}}{A_{out}}\right)_g$	MR	V_g		V_ℓ		Recess $\frac{}{Y_\ell}$	$\bar{D}$, μ or $mx10^{-6}$	E_m, percent
	in.	$mx10^{-2}$	in.	$mx10^{-2}$	in.	$mx10^{-2}$	in.	$mx10^{-2}$				ft/sec	m/s	ft/sec	m/s			
A-91	0.11	0.28	0.11	0.28	0.05	0.13	0.25	0.64	2.4	1.0	5.9	1518	463	1.8	0.55	0	167	--
A-92	0.17	0.43	0.11	0.28	0.05	0.13	0.12	0.30	3.8	1.3	5.6	1544	471	2.0	0.61	0	177	--
A-93	0.11	0.28	0.11	0.28	0.11	0.28	0.25	0.64	1.0	0.4	5.7	1505	459	3.0	0.91	0	151	--
A-94	0.17	0.43	0.11	0.28	0.07	0.18	0.12	0.30	2.4	0.8	5.7	1515	462	2.5	0.76	0	166	--
A-95	0.06	0.15	0.11	0.28	0.02	0.05	0.35	0.89	2.4	1.2	5.8	1545	471	1.0	0.30	0	164	--
A-96	0.11	0.28	0.15	0.38	0.05	0.13	0.25	0.64	2.4	0.9	5.4	1576	480	1.2	0.37	0	133	--
A-97	0.06	0.15	0.11	0.28	0.02	0.05	0.35	0.89	2.4	1.2	6.0	1553	473	1.0	0.30	3	156	--
A-98	0.06	0.15	0.11	0.28	0.02	0.05	0.35	0.89	2.4	1.2	5.3	1087	331	0.6	0.18	3	167	--
A-99	0.06	0.15	0.11	0.28	0.02	0.05	0.35	0.89	2.4	1.2	6.1	1029	314	5.1	1.55	3	231	--
M-51	0.11	0.28	0.11	0.28	0.05	0.13	0.25	0.64	2.4	1.0	5.7	899	274	7.5	2.29	0	-	89.0
M-52	0.17	0.43	0.11	0.28	0.05	0.13	0.12	0.30	3.8	1.3	5.7	936	285	8.9	2.71	0	-	77.6
M-53	0.11	0.28	0.11	0.28	0.11	0.28	0.25	0.64	1.0	0.4	6.0	898	274	13.8	4.21	0	-	71.5
M-54	0.17	0.43	0.11	0.28	0.07	0.18	0.12	0.30	2.4	0.8	5.7	935	285	11.3	3.44	0	-	91.5
M-55	0.06	0.15	0.11	0.28	0.02	0.05	0.35	0.89	2.4	1.2	6.1	910	277	4.3	1.31	0	-	90.8
M-56	0.11	0.28	0.15	0.38	0.05	0.13	0.25	0.64	2.4	0.9	5.8	896	273	5.3	1.62	0	-	91.3
M-57	0.11	0.28	0.11	0.28	0.05	0.13	0.25	0.64	2.4	1.0	5.8	919	280	7.6	2.32	3	-	94.2
M-58	0.11	0.28	0.11	0.28	0.05	0.13	0.25	0.64	2.4	1.0	5.8	708	216	5.5	1.68	3	-	95.0
M-59	0.11	0.28	0.11	0.28	0.05	0.13	0.25	0.64	2.4	1.0	7.6	939	286	6.9	2.10	3	-	91.8

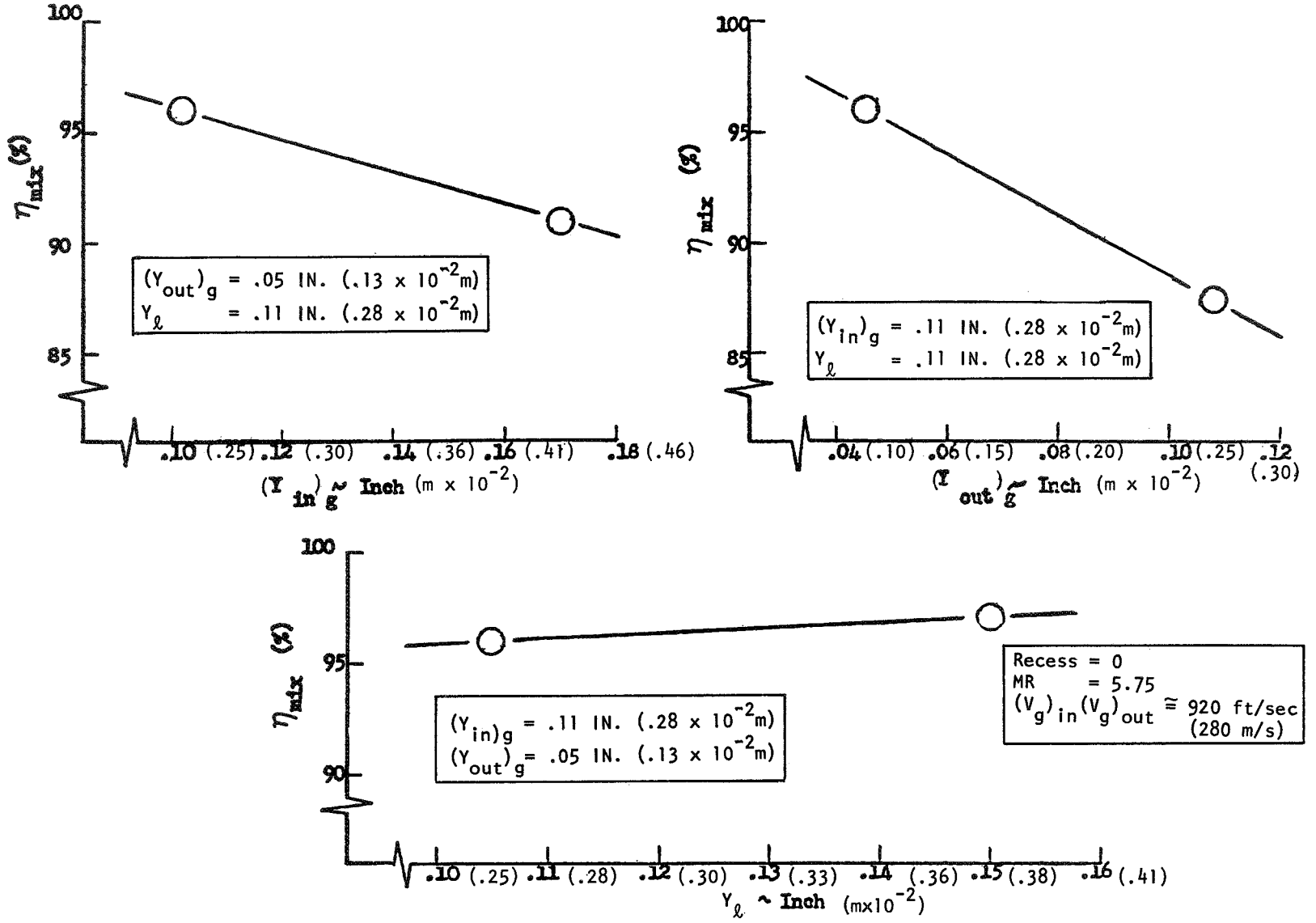

Figure 105. Effect of Annulus Gaps on Mixing Efficiency: Tricentric With Centerbody Injector

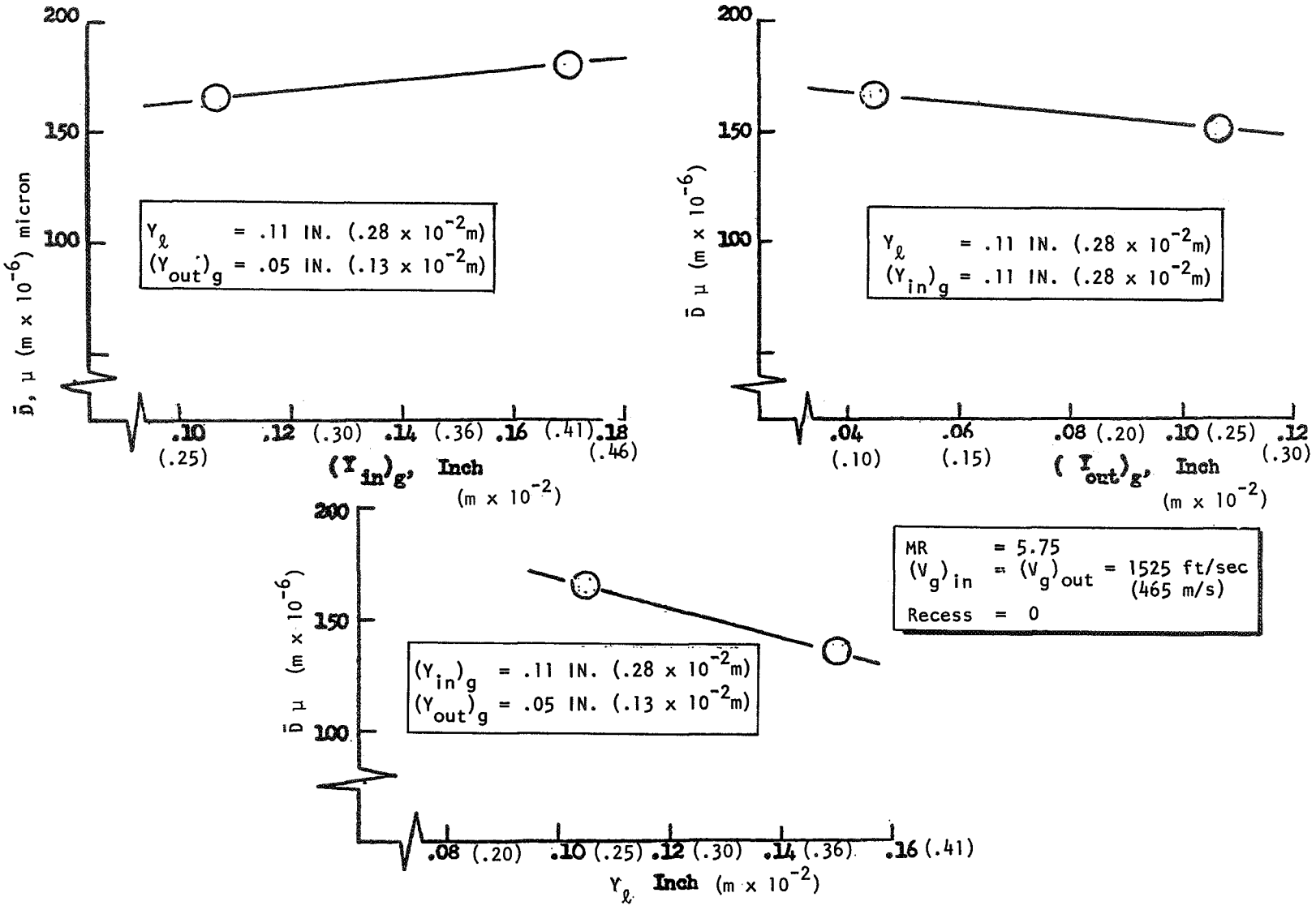

Figure 106. Effect of Annulus Gaps on Mass Median Dropsize: Tricentric With Centerbody Injector

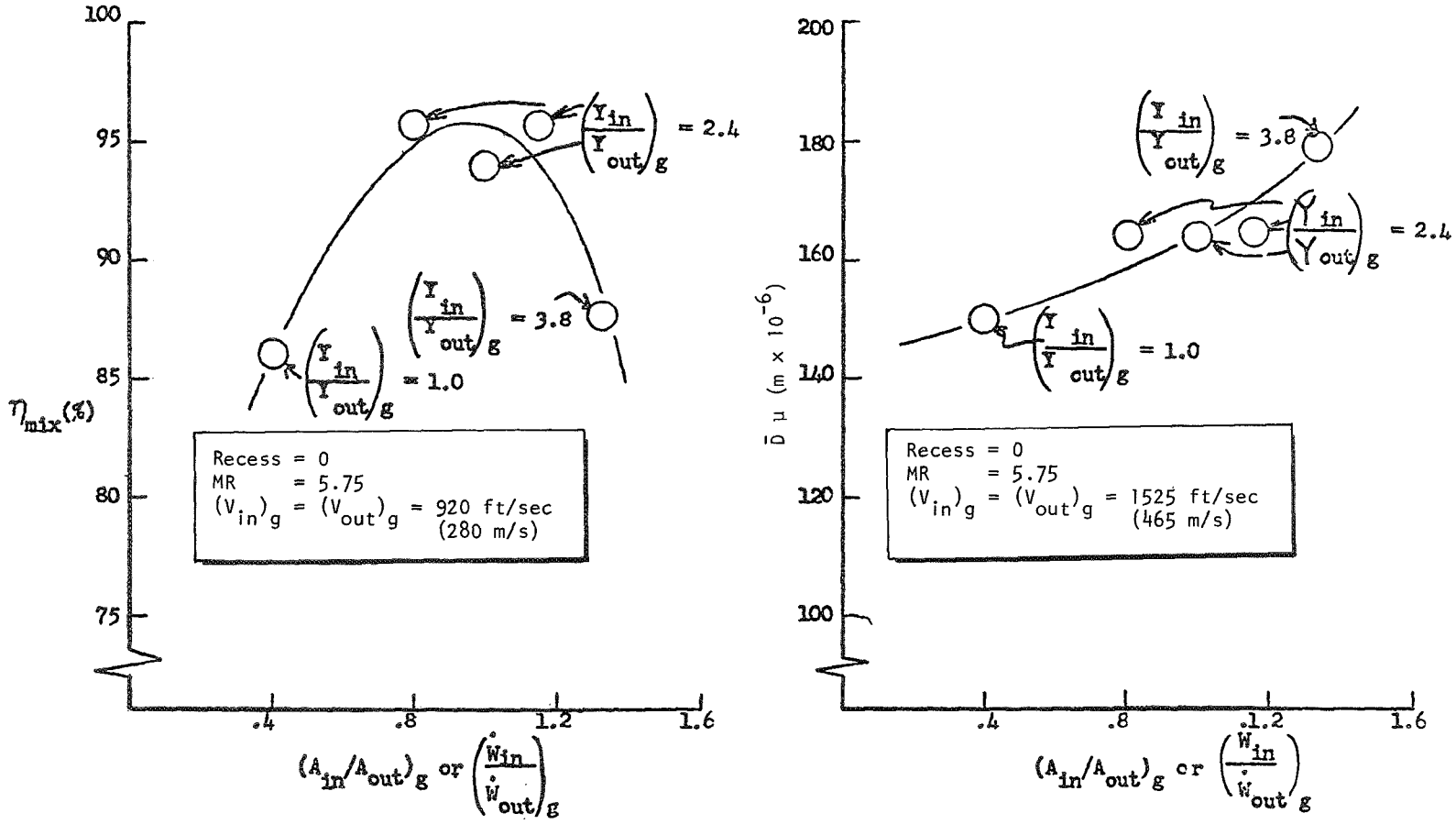

Figure 107. The effect of Inner to Outer Gas Injector Area on Mixing and Atomization: Tricentric With Centerbody Injector

varied from approximately 97 to 94 percent with the changes in $\bar{D}$, while $(\eta_{c^*})_{mix}$ (Fig. 107) ranged from about 86 to 96 percent. Therefore, a set of relatively optimum hot-fire conditions would be taken from the peak of the mixing curve, i.e., $(Y_{in}/Y_{out})_g \cong 2.4$ and $(A_{in}/A_{out})_g \cong 1.0$.

The effect of recessing the liquid jet annulus is illustrated in Fig. 108 for both mixing and atomization. Note that recessing the liquid annulus a distance of three liquid gaps had a favorable effect on both mixing and atomization. This amount of recess increased the mixing efficiency from 96 to 98 percent while decreasing the mass median dropsize attainable from 165μ to 150μ (165 to 150 x 10^{-6}m), which would increase vaporization efficiency from approximately 95.5 to 97 percent. It should be noted that the actual depth for this concept, three liquid gaps or about 0.3 in. (0.76 x 10^{-2}m) was much less than that required (1.2 in. 3.05 x 10^{-2}m or greater) for good atomization and mixing with the basic concentric concept presented earlier.

In Fig. 109, results are presented whereby V_g-V_ℓ was varied from 700 to 900 ft/sec (213 to 274 m/s) in mixing tests and from 1100 to 1600 ft/sec (335 to 488 m/s) in atomization tests. The predicted mixing efficiency remained almost constant with ΔV; however, the mass median dropsize was decreased from 170μ to 150μ (170 to 150 x 10^{-6}m) An additional data point, in which the gas density was varied, is shown on the mass median dropsize curve in Fig. 109. This point represents an anomaly in the data in that the gas density was increased at constant operating conditions resulting in an increase rather than a decrease in mass median dropsize. The operating parameter believed responsible for this anomaly is the liquid injection velocity which increased by a factor of 8 when the gas density was increased. The effects of this variation could negate any effects of the gas density variance.

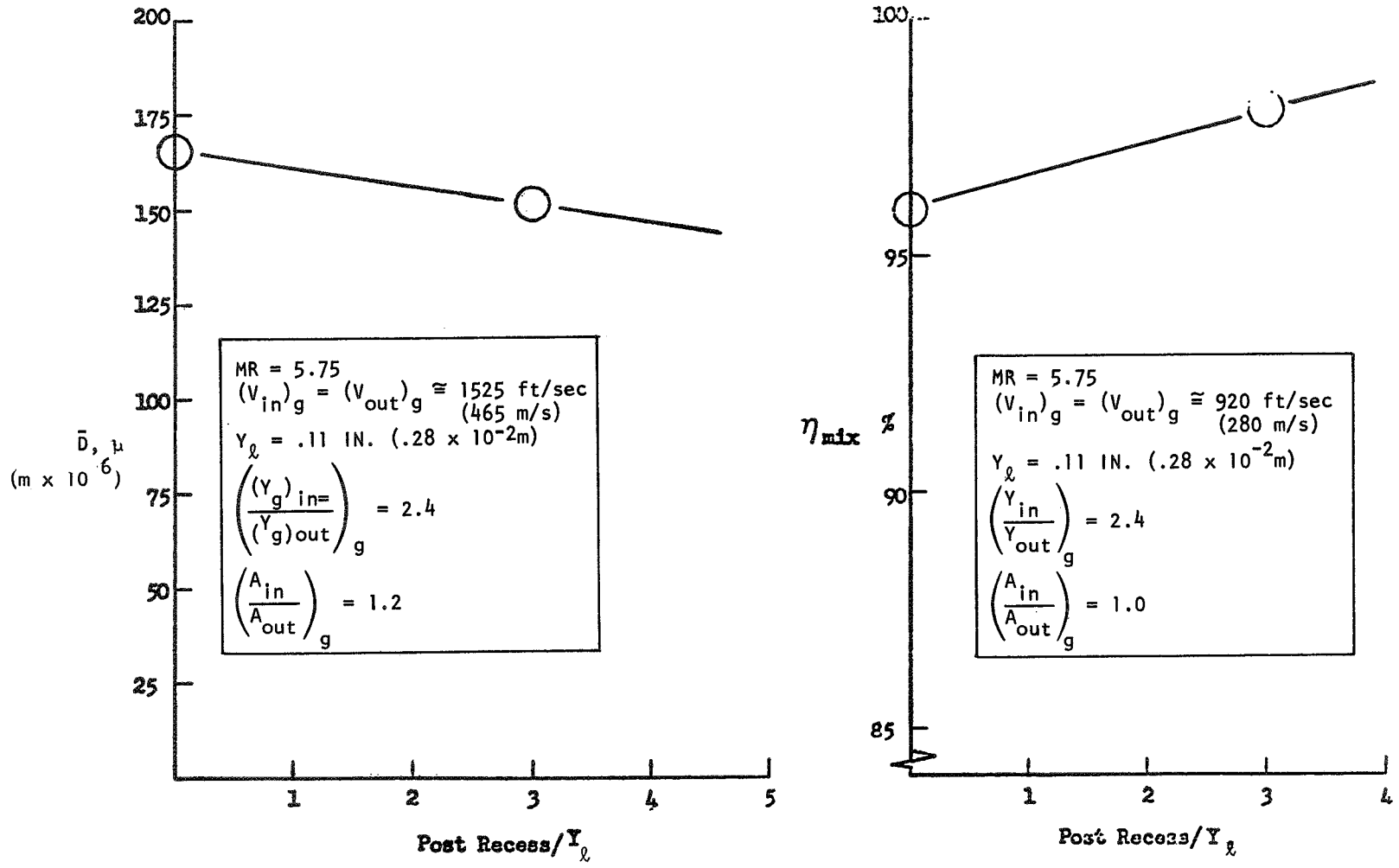

Figure 108. The Effect of Post Recess on Mixing and Atomization: Tricentric With Centerbody Injector

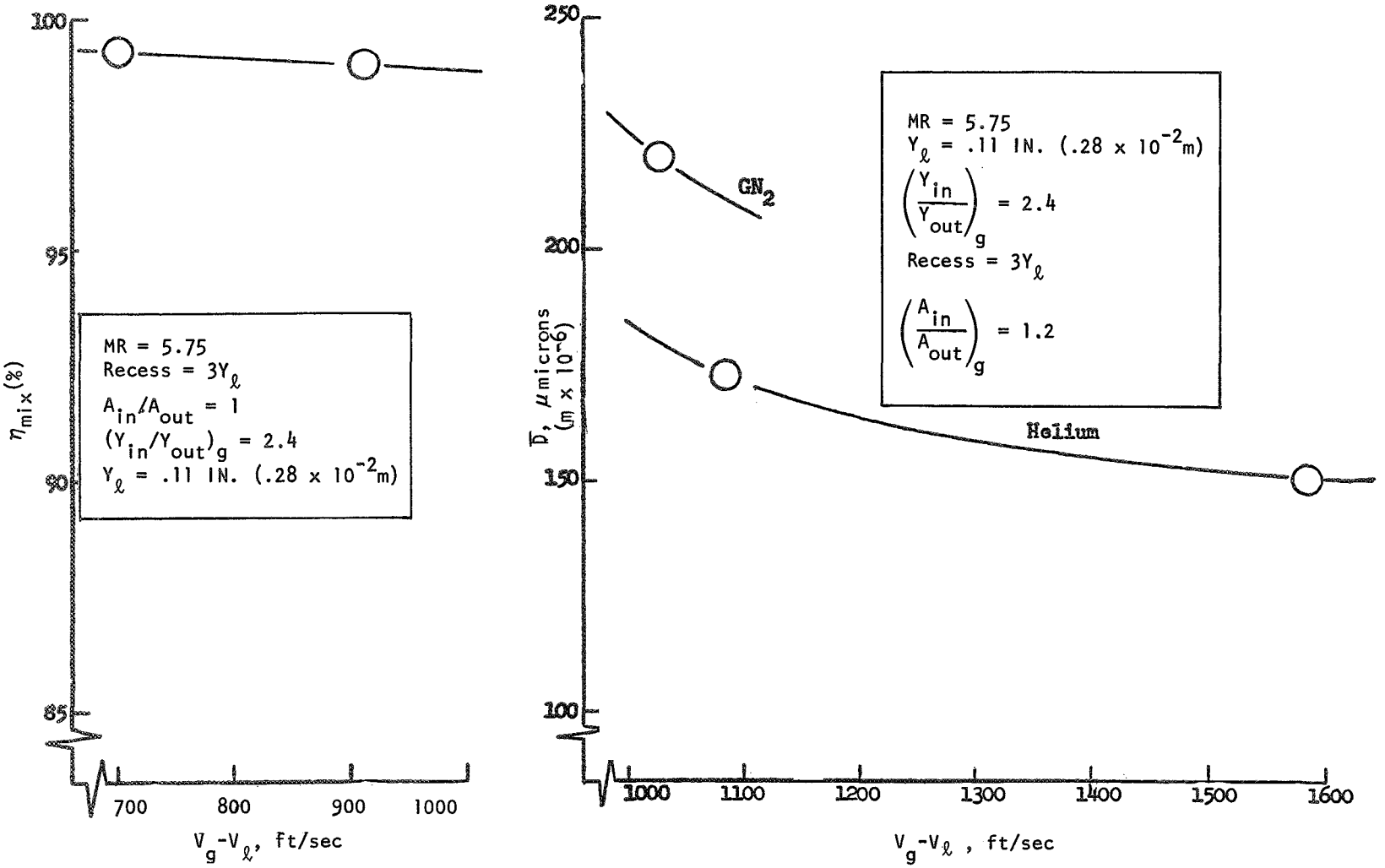

Figure 109. The Effect of V_g-V_ℓ on Mising and Atomization: Tricentric With Centerbody Injector

COMPARISON OF TASK II AND III DATA

One of the objectives of Task III was to supplement the data taken in Task II, thereby providing more cold-flow definitive curves for application to the FLOX/CH_4 propellant combination. Selected Task II data were replotted with appropriate Task III data and are discussed below according to injector type. Only those parameters are discussed which were investigated in both Task II and III.

Basic Concentric Injector Concept

As reported in the preceding section, the basic concentric tube injector operating parameters investigated in Task III were the gas density, the amount of post recess, and the relative gas velocity. Combined Task II and III test results with this injector concept are presented in Fig.110 and 111 . In Fig.110, the atomization results are compared for several cases as a function of the gas-to-liquid velocity difference. Although each curve presented in this figure differs in mixture ratio or the amount of post recess, the general slope of all curves is constant. The expected improvement in atomization with lower mixture ratios and higher gas velocities is evident in this figure. With a recess of three post diameters, the larger-scale (D_ℓ= 0.43 in. 1.09 x 10^{-2}m) element seemed to provide slightly better atomization than the one used in Task II (D_ℓ= 0.28 in.; 0.71 x 10^{-2}m) with a recess of 1.0 x D_ℓ . In addition, the asymptotic nature of these curves as V_g-V_ℓ increases above 1000 ft/sec (305 m/s) is illustrated in this figure, thus indicating an insignificant effect at V_g-V_ℓ = 1500 to 2000 ft/sec (457 to 610 m/s).

The effect of scale (indexed by D_ℓ) for constant operating conditions on both atomization and mixing is illustrated by combining Task II and III data in Fig. 111. Note the change in slope in the atomization curve as the liquid diameter (scale) decreases below approximately 0.25 in. (0.64 x 10^{-2}m). At liquid diameters larger than 0.25 in. (0.64 x 10^{-2}m), the slope of the atomization curve is approximately 960μ /in.-D_ℓ (378 x 10^{-4}m/m-D_ℓ). However, this

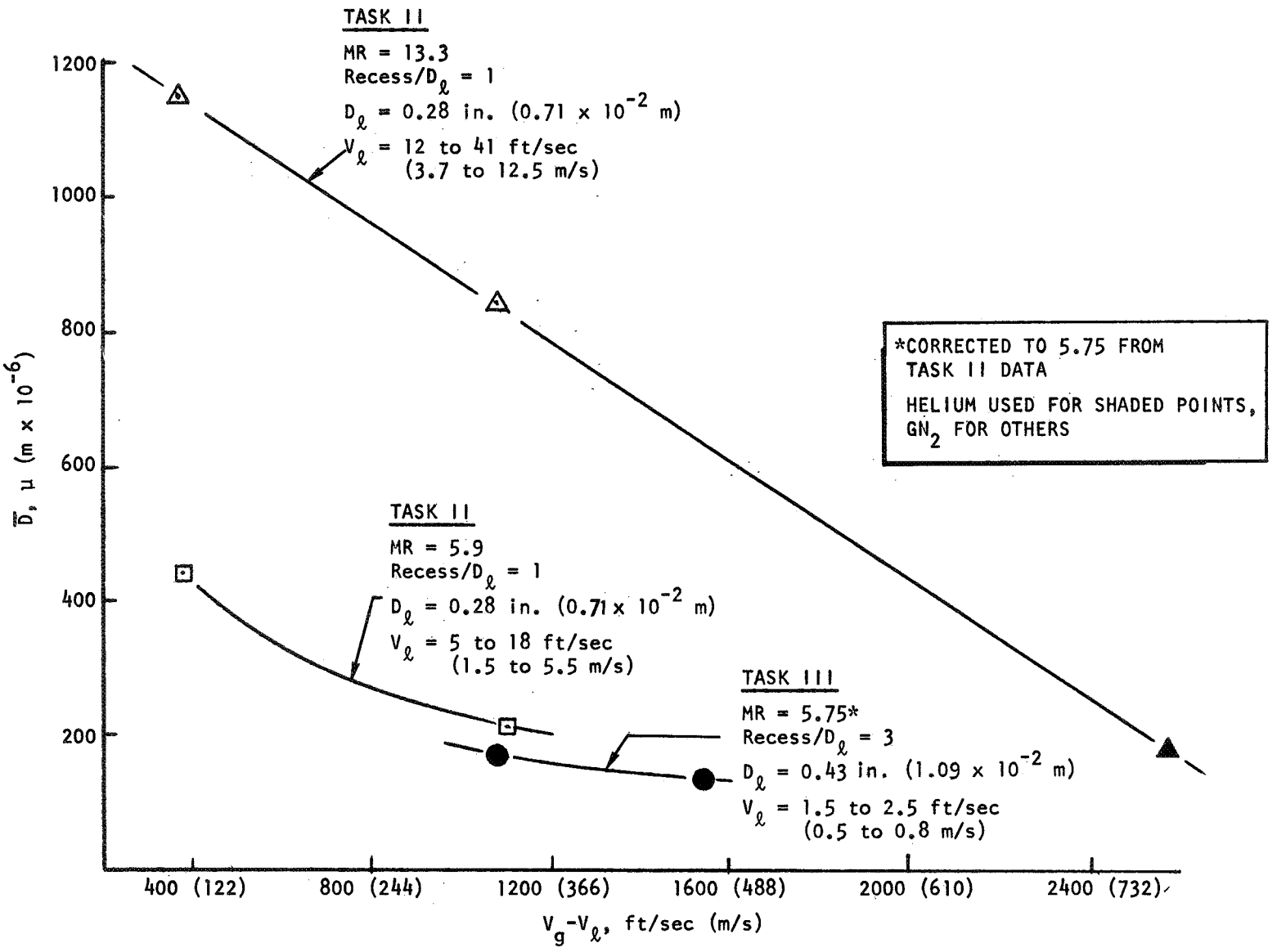

Figure 110. Tasks II and III Dropsize Data Comparison: Basic Concentric Injector

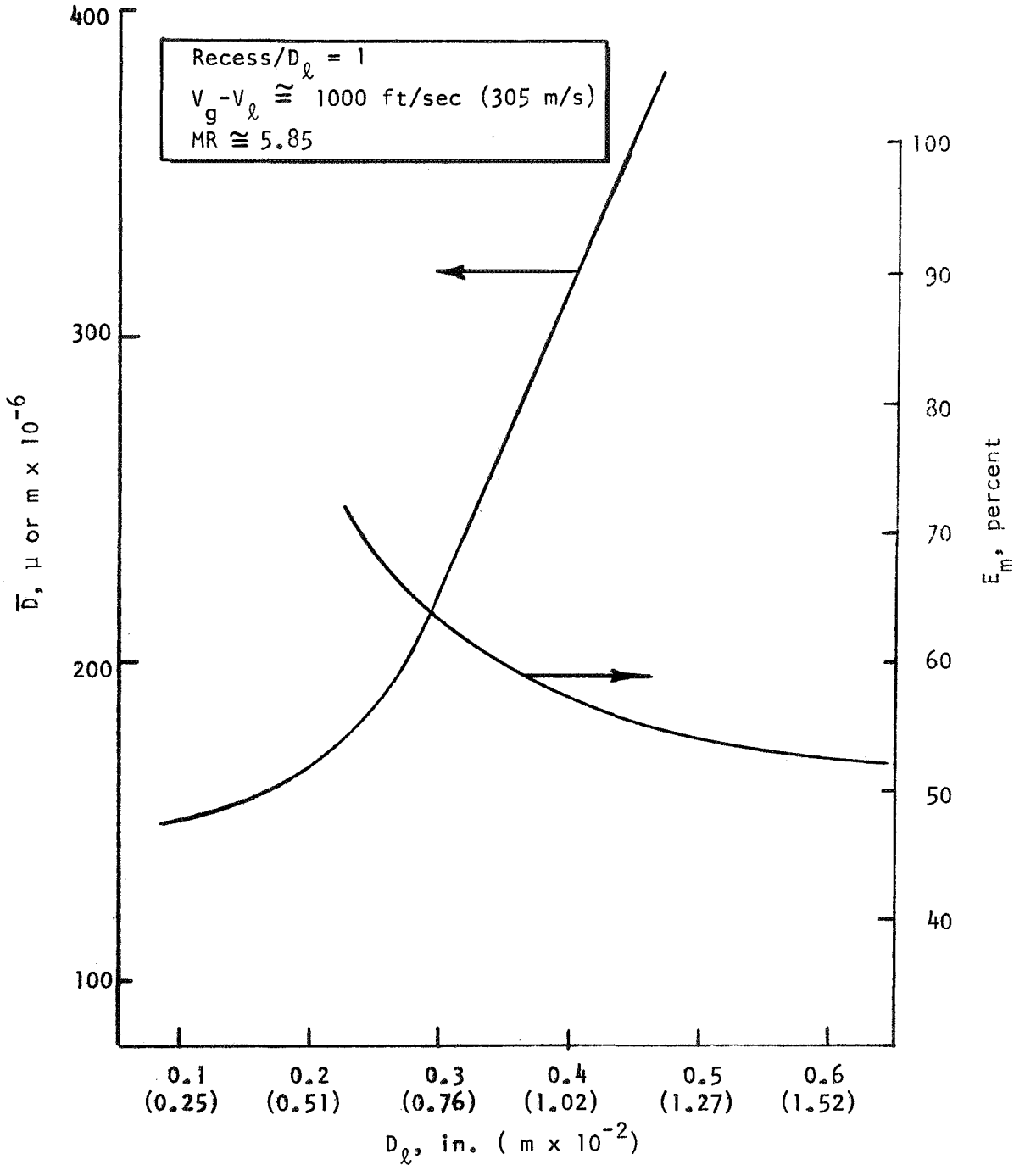

Figure 111. Scale Effects on Mixing and Dropsize: Basic Concentric Injector

slope is drastically reduced at smaller liquid diameters, i.e., to approximately 90μ/in.-D_ℓ (35 x 10^4m/m-D_ℓ) at 0.1 in. (0.25 x 10^{-2}m) liquid diameter. Increasing the scale has a similar effect on E_m; i.e., E_m is decreased by approximately 40 percent as D_ℓ (scale) increased from 0.21 to 0.62 in. (0.53 to 1.57 x 10^{-2}m).

Impinging Concentric Injector Concept

Several differing impinging concentric injector geometries were tested in Task II and III. These data are plotted together in Fig.112 and 113. As indicated in the figures, some other parameters of the Task II and III data differ, notably X_p/D_g and annulus gas velocity; however, it was concluded that this effect would be secondary (in the range over which they were varied) compared with those of D_ℓ and D_ℓ/D_g*. Rather consistent trends are indicated as a function to the geometric parameters, and, in addition, conditions conducive to good atomization (low $\bar{D}$) tend to produce good mixing (high E_m).

Tricentric With Centerbody Injector Concept

Tricentric element cold-flow atomization data from Tasks II and III are plotted together in Fig. 114. The mixture ratio was approximately 5.75 (minor variations) for these tests. If the difference in gas density between Task II and Task III data is ignored, the combined data in Fig. 114provides a curve of $\bar{D}$ versus V_g-V_ℓ from 300 to 1500 ft/sec (91 to 457 m/s) for fixed orifice geometry, i.e., $(A_{in}/A_{out})_g$ = 1.0 and $(Y_{in}/Y_{out})_g$ = 2.1 to 2.4 (the obvious influences of different $(A_{in}/A_{out})_g$ and liquid annulus recess have been described previously.) A big improvement in $\bar{D}$ occurs as V_g-V_ℓ goes from 300 to about 900 ft/sec (91 to about 274 m/s); subsequently , $\bar{D}$ decreases at a lower rate.

*Further correction to account for differences in X_p/D_g is feasible, but was not done in plotting Fig. 113 .

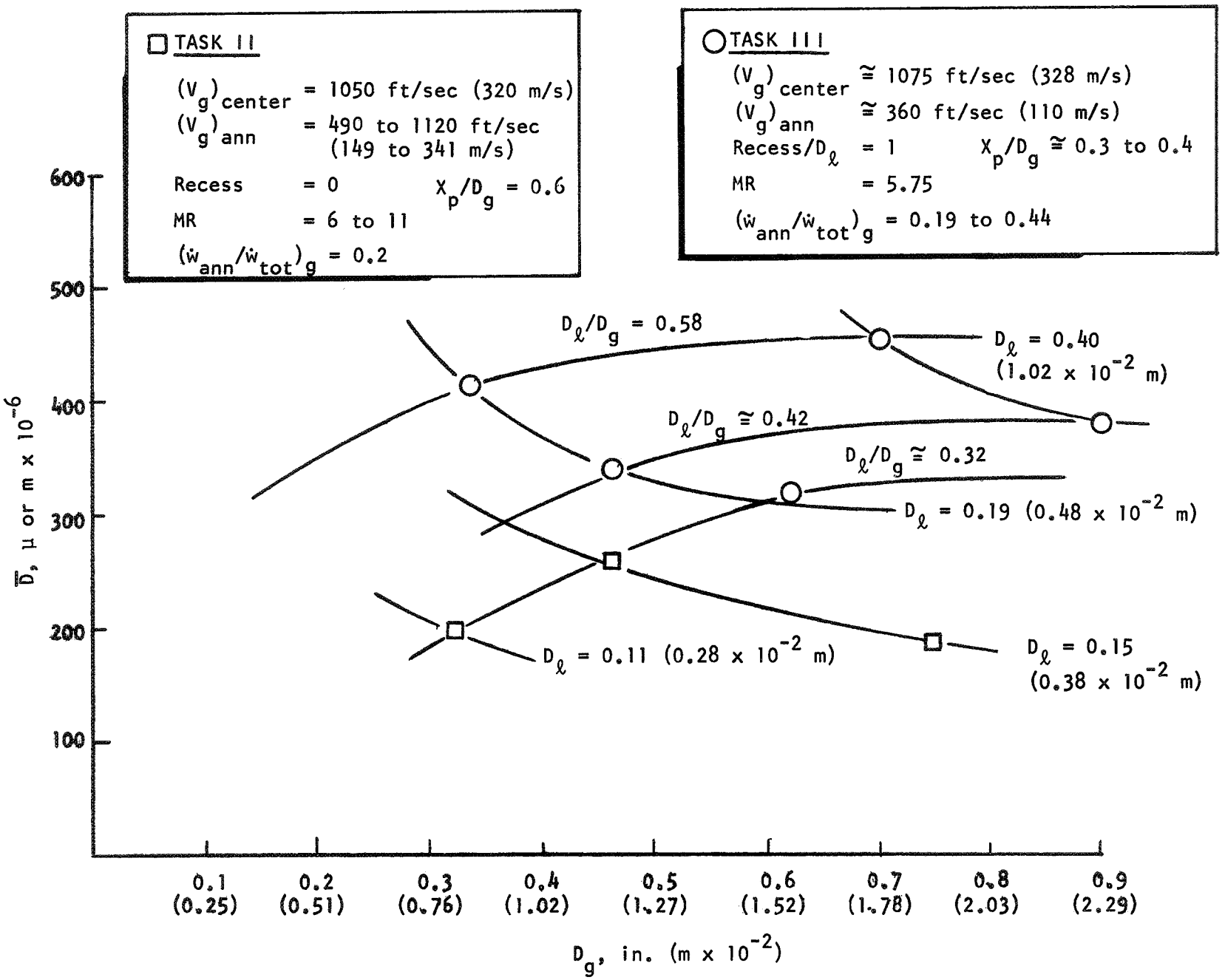

Figure 112. Comparison of Tasks II and III Atomization Data: Impinging Concentric Injector

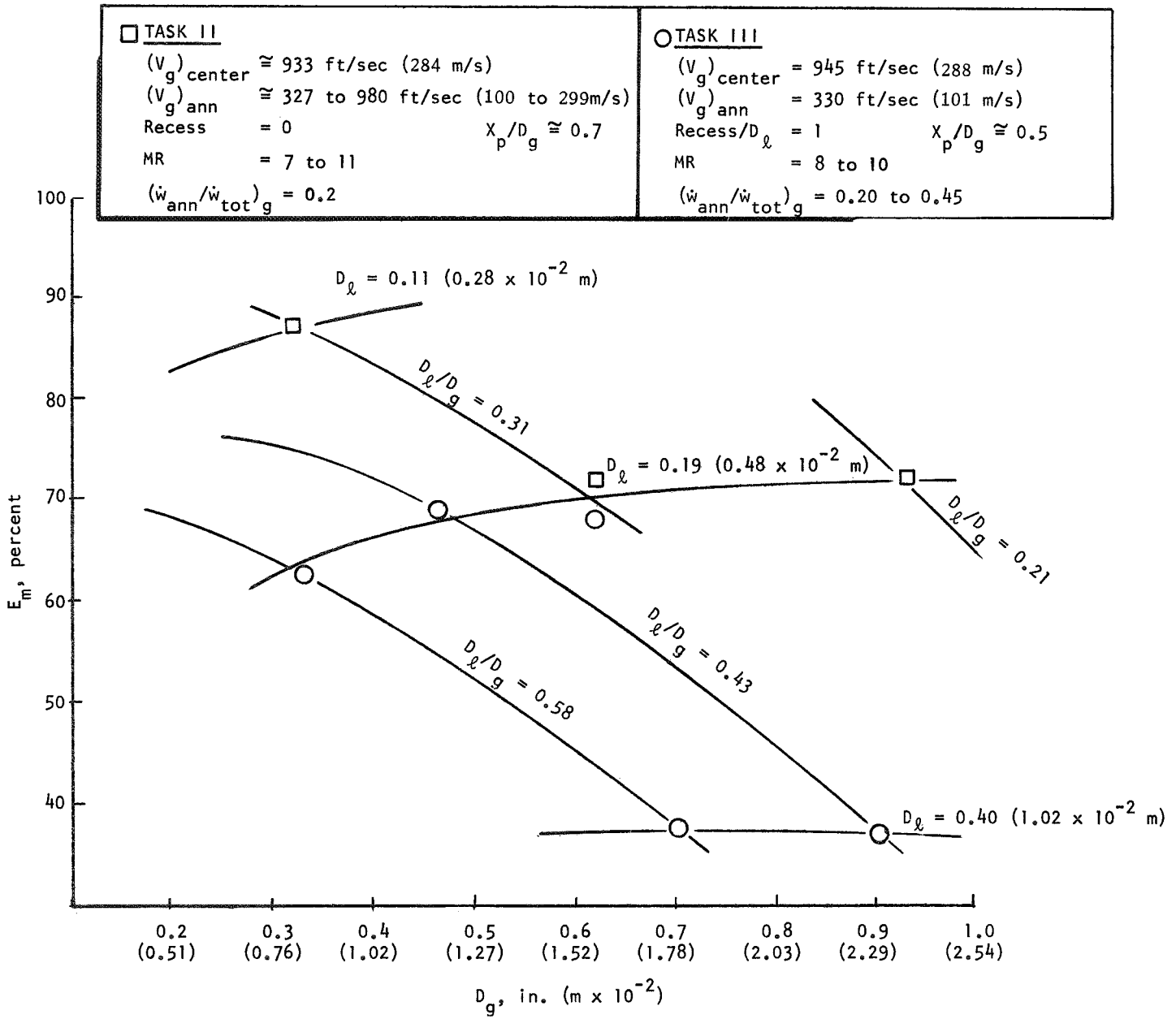

Figure 113. Comparison of Tasks II and III Mixing Data: Impinging Concentric Injector

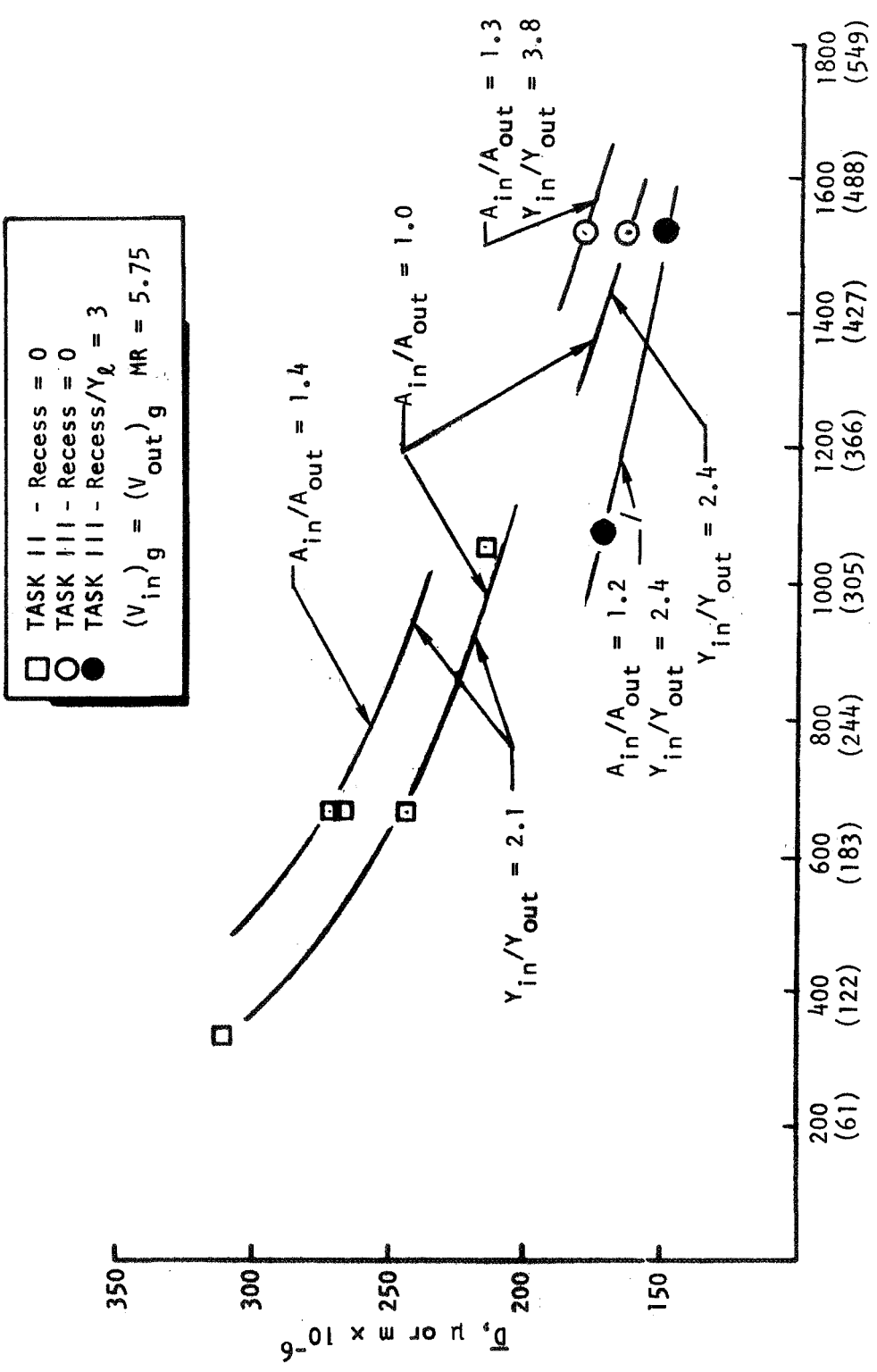

Figure 114. Comparison of Tasks II and III Atomization Data: Tricentric With Centerbody Injector

HOT-FIRE INJECTOR RATING AND SELECTION

The cold-flow atomization and mixing experiments completed under Task III were designed to simulate a selected FLOX/CH_4(g) propellant system. The application of these data to predict performance capabilities of the Task III injector concepts is described below leading to partial design optimizations, an overall rating of the three injector concepts, and a selection of the injectors to be evaluated in Task IV hot-firing tests.

The nominal design requirements used for evaluation and comparison of the injector concepts in Task III are listed as follows:

1. FLOX/CH_4(g) propellant combination
2. 5.75 mixture ratio
3. 160 R (88.9 K) FLOX injection temperature
4. 1700 ft/sec (518 m/s) gas injection velocity (maximum)
5. 420-psid (289 x $10^4 N/m^2$) liquid injection pressure loss (maximum)
6. 10-psid (6.9 x $10^4 N/m^2$) liquid injection pressure loss (minimum)
7. 5000-lbf (22,200N) (vacuum) thrust per element
8. 500-psi (345 x $10^4 N/m^2$) chamber pressure
9. 30-in. (0.76m) chamber characteristic length
10. 2.0 chamber contraction ratio

With the exception of the gas injection velocity and the liquid injection pressure drop, all of the above parameters were fixed for the performance rating. These two design parameters along with the orifice geometry were optimized with regard to predicted atomization and mixing for each injector type. The optimized concepts were then compared under three categories, i.e., their predicted capacity for (1) propellant atomization, (2) propellant mixing, and (3) chamber

compatibility. In this rating process, the overall confidence level of the cold-flow data and of necessary extrapolations from cold-flow to hot-firing test parameters was also considered. The relative ratings of each injector in the atomization, mixing, and chamber compatibility (heat transfer) categories determined the overall injector rating from which the most promising concepts were selected for use in the Task IV hot-fire tests. These rating processing are described in the following sections.

Atomizing Rating Process

The Task II and III atomization experiments were used to predict individual injector atomization characteristics under hot-fire conditions. These data have been previously presented for each individual injector concept. This section reviews the method used to optimize and compare the three injector concepts on the basis of atomization alone. The injectors are rated using the mass median dropsizes attained in cold-flow tests with wax as the liquid propellant simulant. Several liquid property corrections for differences in the liquid density, surface tension, and viscosity have been used in past investigations to yield the droplet distribution that would be obtained with the hot-fire liquid propellant. However, there remains uncertainty as to the validity of such corrections. In any case, the corrections would uniformly affect mean dropsizes of all injector concepts being rated and so they were not applied in this study.

Basic Concentric Injector. Task II and III cold-flow tests with the recessed basic concentric injector concept indicate: the post recess-to-liquid diameter ratio should be 3.0 or greater, the maximum available gas injection velocity (1700 lb/sec; 518 m/s) should be employed, and the liquid orifice size should be minimized. The latter conclusion is dependent upon Task III test data which indicates an improvement in atomization as the scale is decreased. However, the effect of liquid injection velocity was not determined experimentally because of the limited number of tests. The improvement seen by reducing the

liquid diameter could be negated by a deterioration caused by the liquid velocity increase (at constant liquid flowrate). However, no liquid velocity correction is available at the present time, and the available data do not permit an accurate analysis of the specific tradeoff between D_ℓ and V_ℓ.

Task III cold-flow tests with this concept simulated a 275-psi ($189 \times 10^4 N/m^2$) FLOX injection pressure drop. Selecting a post recess-to-liquid diameter ratio of three and V_g = 1700 lb/sec (518 m/s) yields a mass median dropsize of 140μ (140×10^{-6}m) from Task III results (Fig.110) at a mixture ratio of 5.75. With this injection ΔP, the liquid orifice diameter (D_ℓ) for the required thrust level would be 0.43-in. (1.09×10^{-2}m). Correcting this dropsize to the hot-fire gas densities according to the Task III data yields a mass median dropsize of 130μ (130×10^{-6}m) for the propellant simulant. This number is contingent upon the ability to recess the post by three liquid diameters without incurring injector overheating. In addition, as stated above, no correction was available for the increased liquid injection velocity.

Impinging Concentric Injector. Cold-flow results with the impinging concentric injector concept have isolated specified ranges for several individual operating parameters for attainment of of optimum performance. However, hot-fire operating conditions don't permit simultaneous employement of all these optimized parameters. As a result, several significant design tradeoffs are necessary, the most notable of which are: (1) $\rho_g V_g^2$ versus X_p/D_g, (2) D_ℓ/D_g versus T_g*, and (3) percent annulus gas versus X_p/D_g.

In determining the optimum performance with this injector concept, atomization and mixing must be considered together because the operating conditions in which the best atomization potential is attained will not necessarily have the best mixing potential. Therefore, the overall performance was calculated for each of the design tradeoffs described above and was used to determine the

*With all other parameters constant, the fuel injection temperature describes the fuel injected momentum flux with a gaseous propellant.

optimum design conditions for the FLOX/CH_4 propellant system. These optimum operating conditions were found to be D_ℓ = 0.194 in. (0.493 x 10^{-2}m), D_ℓ/D_g = 0.3, X_p/D_g = 0.95, 20 percent of the fuel in the concentric tube annuli, and an injected fuel temperature of 1100 R (611 K) ($\rho_g V_g$ = 410 psi; 282 x $10^4 N/m^2$).

In calculating the mean dropsize, the initial value was taken from the Task III curve (Fig. 103) at D_ℓ = 0.194 in. (0.493 x 10^{-2}m) (this is the necessary orifice diameter to meet the required FLOX injection flowrate at the maximum $(\Delta P)_{inj}$ of 420 psi; 289 x $10^4 N/m^2$) and the appropriate D_ℓ/D_g. Corrections were then made for (1) the appropriate X_p/D_g from Task II data, Fig. 60 , (2) the concentric tube mixture ratio from Task III data, Fig. 102, and (3) the center gas momentus flux from Task III data, Fig. 104. The optimum conditions resulted in a corrected mass median dropsize of approximately 240μ (240 x 10^{-6}m) for the propellant simulant (molten wax). No data were available to correct this value for the higher annulusgas velocities available in hot fire ($(Vann)_{HF}$ = 3 $(Vann)_{CF}$). This correction would lower the above prediction.

Tricentric With Centerbody Injector. Cold-flow tests conducted in Tasks II and III with the tricentric with centerbody injector concept indicated the maximum gas injection velocity (1700 ft/sec; 518 m/s) and the minimum liquid injector pressure drop (i.e., minimum liquid injection velocity, in this case 25 ft/sec or 7.6 m/s) should be employed. Optimizing the annulus gap dimension over the range of conditions tested under Task III yields a nominal inner to outer gas injection area ratio of 1 and an inner-to-outer gas gap ratio of 2.4. In addition, the post recess-to-liquid gap ratio of the hot-fire geometry was arbitrarily limited to three (approximately 0.3 in.; 0.76 x 10^{-2}m). These parameters were used as a design point, together with injection areas, for the mass median dropsize prediction.

Cold-flow tests in Task III (Fig.107 and 108) yield the initial dropsize of 150μ (150 x 10^{-6}m) for the optimum $(A_{in}/A_{out})_g$, $(Y_{in}/Y_{out})_g$, and post recess mentioned above. The above mentioned mass median dropsize was corrected to a 25 ft/sec (7.6 m/s) injection velocity (A_ℓ = 0.7 in.^{2}; 4.5 x 10^{-4}m^2) from the Task III data, but was not corrected for gas density (because no correction is available for this element type). The Task III data yielded a correction for the liquid area change necessary to decrease the velocity; i.e., $\Delta\bar{D}/\Delta A_L$ = 225 μ/in.^{2} (35 x 10^{-2}m/m^2) in the range of liquid areas from 0.21 to 0.32 in.^{2} (1.35 to 2.06 x 10^{-4}m^2). Extrapolating these results to a liquid area of 0.7 in.^{2} (4.5 x 10^{-4}m^2) yielded mass mean dropsize of 40μ (40 x 10^{-6}m). The correction for the gas injection velocity from the cold-flow test conditions of 1525 ft/sec (465 m/s) to the 1700 ft/sec (518 m/s) maximum was made by extrapolating Task II and III test data. This yielded an optimum mass mean dropsize of 35μ (35 x 10^{-6}m) for the propellant simulant.

Atomization Rating Summary. The three gas augmented injector concepts were compared on the basis of their hot-fire atomization potential as predicted from their cold-flow median dropsize curves. Considering these atomization characteristics along, the injectors are ranked below.

1. Tricentric with centerbody ($\bar{D}$ = 35μ; 35 x 10^{-6}m)
2. Recessed basic concentric ($\bar{D}$ = 130μ; 130 X 10^{-6}m)*
3. Impinging concentric ($\bar{D}$ = 240μ; 240 x 10^{-6}m)

Vaporization efficiencies of 100, 99, and 88 percent would be predicted respectively from the mass median dropsizes with no liquid property corrections used.

*This dropsize depends on the feasibility of recessing the LOX post by three post diameters, or approximately 1.2 in. (3.05 x 10^{-2} m). If injector face heat transfer reduces the allowable recess to, for example, 0.4 in. (1.02 x 10^{-2} m), the predicted $\bar{D}$ would rise to 290μ (290 x 10^{-6}m).

Propellant Mixing Rating Process

The Task II and III cold-flow mixing tests were used to predict individual injector mixing characteristics under hot-fire conditions. These data have been previously presented for each individual injector concept. The procedures used to optimize and compare the three injector concepts on the basis of mixing alone are described below.

Basic Concentric Injector. As mentioned in the atomization rating section, cold-flow tests with the recessed basic concentric injector concept indicate the maximum gas injection velocity (1700 ft/sec; 518 m/s) and a minimum scale should be employed along with a post recess-to-liquid diameter ratio of three or greater. These parameters were used as the design point for the prediction of the highest mixing efficiency attainable with this injector concept.

Limiting the post recess to liquid diameter ratio to three, yields a mixing efficiency of 93 percent from Task III cold-flow data in which a 275-psi (189 x $10^4 N/m^2$) FLOX injection pressure drop and a V_g-V_ℓ of 925 ft/sec (282 m/s) was employed. Unlike the case for the atomization rating for this concept, the change in liquid post diameter associated with an increase in FLOX injector pressure drop to the maximum value of 420 psi (289 x $10^4 N/m^2$) has an insignificant effect on the predicted mixing efficiency. In addition, no gas density correction may be made because density was not investigated experimentally. However, a correction was made to increase V_g-V_ℓ to the value specified in the above mentioned FLOX/CH_4 system. This correction was obtained from the Task II data (Fig. 55) assuming the trends with V_g-V_ℓ to be parallel with the larger recess and liquid diameter. Results from this extrapolation yield a 97-percent mixing efficiency for the recessed basic concentric injector concept. This value is contingent upon the ability to recess the post by three liquid diameters without incurring injector overheating.

Impinging Concentric Injector. Several design tradeoffs with this injector concept are described in the atomization rating section. The same tradeoffs were analyzed to determine the optimum mixing potential; (1) ($\rho_g V_g^2$) versus X_p/D_g, (2) D_ℓ/D_g versus T_g, and (3) percent annulus gas versus X_p/D_g. Again the optimum conditions were chosen by comparing the overall performance for these design tradeoffs because optimum atomization and mixing do not occur at the same operating conditions. These optimum operating conditions were found to be D_ℓ= 0.194 in. (0.493×10^{-2}m), $D_\ell;D_g$ = 0.3, X_p/D_g = 0.95, 20 percent of the fuel in the concentric tube annuli, and an injected-fuel temperature of 1100 R; 611 K ($\rho_g V_g^2$ = 410 psi; $282 \times 10^4 N/m^2$).

In all cases, the initial value of mixing efficiency was taken from the Task III geometric curve for D_ℓ = 0.194 in.; 0.493×10^{-2}m (ΔP = 420 psi; $289 \times 10^4 N/m^2$) and the appropriate D_ℓ/D_g. Corrections were then made for the appropriate X_p/D_g (Fig. 61) and the center gas momentum flux (Fig. 104). The optimum conditions listed above yielded a predicted mixing efficiency of 99.5 percent.

Tricentric With Centerbody Injector. As mentioned in the atomization rating section, the cold-flow tests conducted in Task II and III resulted in selecting the maximum gas injection velocity of 1700 ft/sec (518 m/s), a nominal inner-to-outer gas injection area ratio of 1.0, and an inner-to-outer gas gap ratio of 2.4. In addition, the post recess-to-liquid gap ratio of the hot-fire geometry was again limited to three. These parameters were used as the design point for the prediction of the mixing efficiency.

Task III mixing limited performance data yielded an initial predicted mixing efficiency of 98 percent for the optimum inner-to-outer gas area ratio, gas gap ratio, and post recess mentioned above, but at a gas injection velocity and liquid injection velocity of approximately 900 ft/sec (274 m/s) and 75 ft/sec (22.9 m/s), respectively. This initial mixing efficiency was corrected from Task II and III extrapolations to account for an increase in V_g to 1700 ft/sec (518 m/s) and to a decrease in the liquid injection velocity to the 25 ft/sec (7.6 m/s). These corrections resulted in a 99-percent mixing efficiency prediction for the tricentric with centerbody injector concept.

Mixing Rating Summary. The injector concepts were rated in terms of mixing potential from the preceding section as predicted from their cold-flow mixing experiments. Considering these mixing characteristics alone, the injectors are listed below in order of decreasing predicted mixing performance.

1. Impinging concentric, $(\eta_{c*})_{mix}$ = 99.5 percent
2. Tricentric with centerbody, $(\eta_{c*})_{mix}$ = 99 percent
3. Recessed basic concentric $(\eta_{c*})_{mix}$ = 97 percent

Heat Transfer Rating Process

No heat transfer data were obtained in the Task III tests. However, because thrust chamber heat transfer is so largely determined by the combustion environment, considerable qualitative information about injector/chamber compatibility can be obtained by examination of the predicted mass flux and mixture ratio along the injector periphery. Additional guidance was obtained from relevant hot-firing experience with several of the injector element types.

With oxidizers such as fluorine, liquid oxygen, or FLOX, experience has shown high mixture ratio zones are especially prone to produce wall erosion and/or overheating. Therefore, the injectors may be rated to some extent according to their tendency to produce relatively high liquid (oxidizer simulant) fluxes near the edges of the measured spray field. As previously discussed, the impinging concentric elements show a tendency for the oxidizer simulant to move toward the outside more rapidly than the fuel (gas) simulant, although recirculation of fuel-rich gases and some spray turning by axially directed combustion gases may alleviate this condition. In addition, the basic concentric injectors began to show higher mixture ratios near the edges of the spray field as the amount of post recess was increased from one to five liquid diameters. The tricentric with centerbody elements did not show this effect.

Considering next the pertinent hot-firing experience, basic concentric elements have a rather widespread reputation for relatively low heat fluxes. This was shown in work done under NASA Contract NAS3-11191 where concentric element injectors produced heat fluxes about half as high as a basic impinging pentad. However, the basic concentric has never been hot-fired with as much post recess as recommended herein for good performance. The possibility of injector face heat transfer problems becomes higher at the larger values of post recess, especially with hypergolic propellants such as FLOX/CH_4. In contrast, the single element, high-thrust, impinging concentric inject concept tested in Task I has demonstrated satisfactory injector heat transfer characteristics over a wide range of chamber pressures and mixture ratios with LOX/GH_2.

From the above-mentioned considerations, the injector concepts were rated with regard to injector and chamber heat transfer in the following manner:

1. Tricentric with centerbody
2. Impinging concentric
3. Basic concentric

Overall Injector Rating and Selection

As a result of the preceding analysis, the injector concepts tested in Task III were rated according to their applicability to the FLOX/CH_4 propellant system previously specified. The tricentric with centerbody concept was rated first because of its overall high rating in each categroy. The impinging concentric concept had a number one rating in the mixing category and was intermediate in the heat transfer rating because of the hot-fire performance and heat transfer capabilities observed in Task I hot-fire tests. An additional factor in favor of this element type was the Task I hot-firing experience in which it provided good performance with LOX/GH_2 under conditions similar to those required in Task IV tests. Thus, the impinging concentric element was given an overall rating of second. The basic concentric injector concept was rated relatively high

in atomization but last in mixing. In addition, the basic concentric was rated last in the heat transfer category because of possible injector face burning in the recessed liquid post. Thus, this concept received an overall rating of third. In summary, the following ratings were made for the Task III injector concepts:

1. Tricentric with centerbody
2. Impinging concentric
3. Basic concentric

It was predicted that all of the injector concepts in this list would be capable of attaining the performance goal of 96-percent combustion efficiency with the FLOX/CH_4 propellant system. The top two injector element concepts were recommended for the Task IV hot-firing tests.

TASK IV, SPACE-STORABLE TESTS

The Task IV phase of the program was essentially a hot-fire testing phase to demonstrate feasibility of the gas augmentation principle with the FLOX/methane (gas) propellant combination. The objectives of these tests were to investigate performance, stability and throttleability of two injector concepts, the tricentric with centerbody and the impinging concentric, which evolved from Tasks II and III. The performance goal was 96-percent c* efficiency.

HARDWARE DESIGN

Injectors

As mentioned above, the injector concepts selected for hot-firing evaluation were the impinging concentric and the tricentric-with-centerbody types, each designed as a single element (5000 lb; 22,200 N thrust) injector. The selected test matrix, described in a later section of this report, required several orifice size changes. Thus, both the impinging concentric and the tricentric with centerbody injector concepts were designed with individual interchangeable orifice sizes. Each injector was designed to employ Rigimesh injector face coolant using 5 to 9 percent of the main fuel flowrate. However, the Rigimesh was later replaced with a graphite or ablative liner during the test series with each injector because of burning of the uncooled part of the injector face. In addition, both injectors were designed (for heat transfer reasons) with zero liquid orifice recess; however, each injector was altered during the test series to employ recess to increase injector performance. In the impinging concentric injectors, this was accomplished by shortening the liquid (center) posts in the concentric tubes, while for the tricentric-with-centerbody injector the liquid annulus tubes were recessed. The liquid orifice length-to-diameter ratios were always maintained sufficiently large to ensure repeatable turbulent flow characteristics. The injector designs are individually described below in more detail.

Tricentric with Centerbody Injector Design. The shear of the gas surrounding the liquid stream exerts a primary influence on mixing and atomization with the tricentric-with-centerbody injector concept. In this injector concept, a solid center plug is surrounded by a gaseous fuel annulus, a liquid annulus, and another gaseous fuel annulus, respectively, with increasing radius. Cold-flow tests in Task II and III indicated optimum inner-to-outer fuel annulus area ratio and optimum inner-to-outer fuel annulus gaps to be approximately 1.0 to 2.4, respectively. Using these values for the baseline injector design along with (1) a maximum fuel velocity (1770 ft/sec; 539 m/s) within both annuli, (2) a maximum fuel injection temperature (1100 R; 611 K)*, and (3) a 0.035 (0.089×10^{-2}m) wall thickness** results in a tradeoff between two remaining design degrees of freedom, the diameter of the centerbody and the liquid injection velocity. This tradeoff was to be investigated experimentally. For the baseline injector, a nominal V_{ℓ} = 75 ft/sec (23 m/s) and D_{plug} = 0.25 in. (0.64×10^{-2}m) were selected.

A number of injector dimensions were varied to complete the test objectives. Plug diameter variations and individual annulus gap variations were accomplished by use of interchangeable manifold and orifice parts in a manner similar to that used in the cold-flow injector fabrication. The main difference was the added precaution of avoiding intermanifold seals in the hot-fire injector design. The tricentric-with-centerbody injector dimensions are presented in Table 25, and a typical sketch is presented in Fig. 115.

Impinging Concentric Injector Design. This configuration consisted of four liquid-gas concentric elements self-impinging on a central showerhead gas stream. This injection pattern is similar to the recessed impinging concentric injectors hot fired under Contract NAS3-7962 and under Task I of the

*The maximum fuel injection temperature was set by anticipated facility limitations. In order to not exceed a 0.9 Mach number, the maximum fuel injection velocity was therefore set at 1770 ft/sec (539 m/s).

**To eliminate tube tip recirculation and therefore tube burning, the FLOX injection tube ends were chamfered 10 deg (0.17 rad) from the fuel side to yield a tube tip thickness of 0.010 in. (0.025×10^{-2}m) at the exit.

TABLE 25

TRICENTRIC WITH CENTERBODY INJECTOR DIMENSIONS

Inner Fuel Annulus								Oxidizer Annulus								Outer Fuel Annulus							
ID		OD		Y_{in} (gap)		A_{in}		ID		OD		Y_{ℓ} (gap)		A_{ℓ}		ID		OD		Y_{out} (gap)		A_{out}	
in.	$mx10^{-2}$	in.	$mx10^{-2}$	in.	$mx10^{-2}$	$in.^2$	m^2x10^{-4}	in.	$mx10^{-2}$	in.	$mx10^{-2}$	in.	$mx10^{-2}$	$in.^2$	m^2x10^{-4}	in.	$mx10^{-2}$	in.	$mx10^{-2}$	in.	$mx10^{-2}$	$in.^2$	m^2x10^{-4}
0.181	0.460	0.400	1.016	0.110	0.279	0.100	0.645	0.470	1.194	0.609	1.547	0.070	0.178	0.118	0.761	0.679	1.725	0.767	1.948	0.044	0.112	0.100	0.645
0.253	0.643	0.443	1.125	0.095	0.241	0.103	0.664	0.507	1.288	0.746	1.895	0.119	0.302	0.234	1.509	0.821	2.085	0.891	2.263	0.035	0.089	0.098	0.632
0.434	1.102	0.564	1.433	0.065	0.165	0.102	0.658	0.635	1.613	1.136	2.885	0.253	0.643	0.703	4.534	1.212	3.078	1.264	3.211	0.027	0.069	0.105	0.677
0.433	1.100	0.579	1.471	0.072	0.183	0.115	0.742	0.647	1.643	0.848	2.154	0.101	0.257	0.236	1.522	0.918	2.332	0.970	2.464	0.026	0.066	0.077	0.497
0.433	1.100	0.579	1.471	0.072	0.183	0.115	0.742	0.647	1.643	0.848	2.154	0.101	0.257	0.236	1.522	0.918	2.332	0.992	2.520	0.037	0.094	0.115	0.742

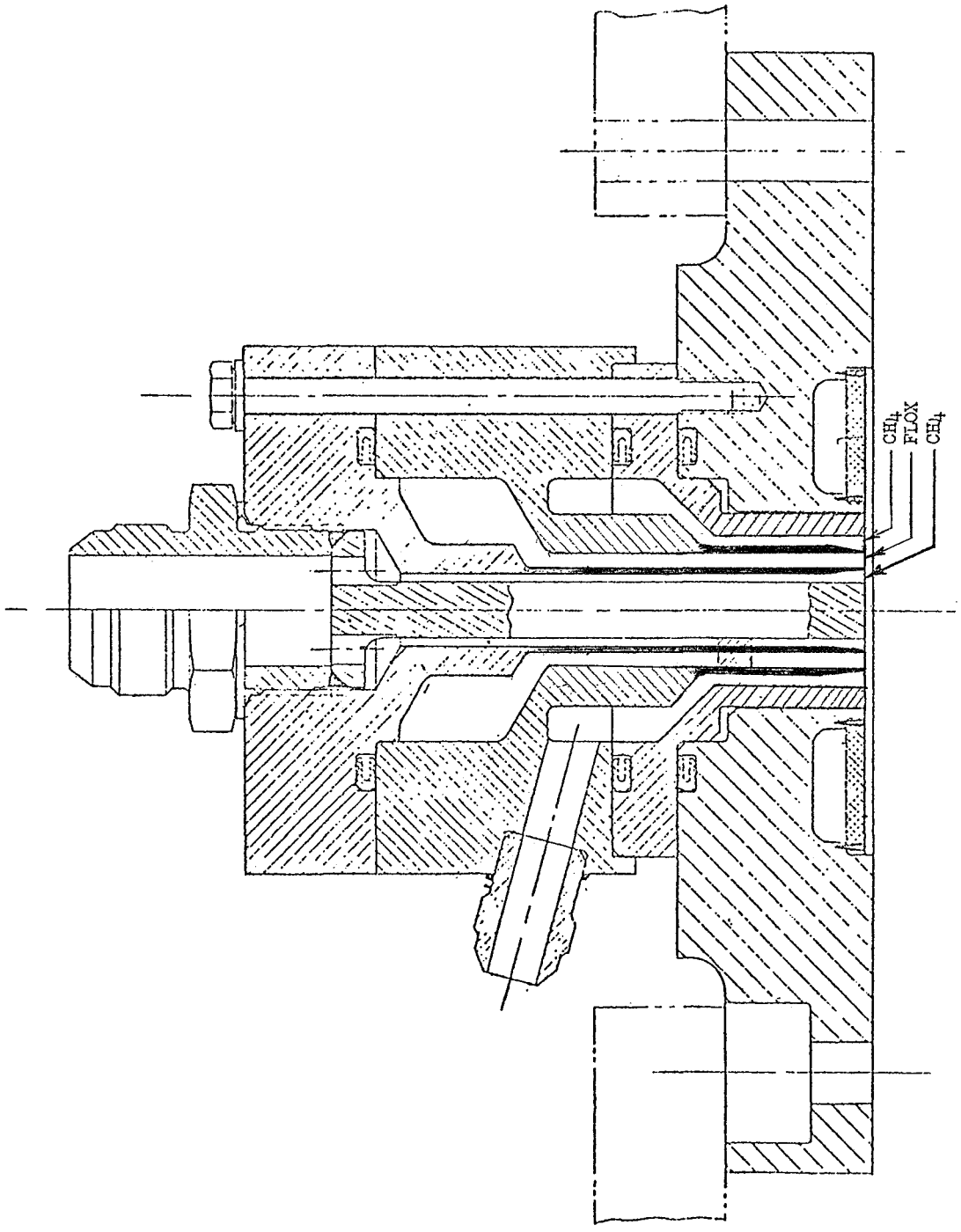

Figure 115. Tricentric With Centerbody Injector

subject program. The main difference is a change in the included angle between the impinging concentric streams from 120 to 90 deg (2.09 to 1.57 rad) to accommodate, with FLOX/CH_4, a range of liquid penetration distances similar to those evaluated with LOX/GH_2. This change altered the shape of the recessed cup, reduced the cup depth and the resultant liquid impingement point moved from the injector face plane to approximately 0.45 in. (1.14 x 10^{-2}m) downstream of the injector face.

Two FLOX injection velocity values, 100 and 150 ft/sec (30.5 and 45.7 m/s), were selected for investigation. This yielded computed FLOX injection pressure drops of 200 and 450 psi (138 and 310 x 10^4 N/m^2), respectively. Requirements for a 500-psi (345 x 10^4 N/m^2) chamber pressure and a 5.75 mixture ratio yielded baseline liquid (FLOX) orifice diameters of 0.238 and 0.190 in. (0.605 and 0.483 x 10^{-2}m). Results from the Task II and III cold-flow tests indicated near optimum design conditions at $D_\ell/D_g \cong 0.30$ for D_ℓ = 0.19 in. (0.48 x 10^{-2}m). However, other parameters were varied during the cold-flow tests which tend to qualify this value. Thus, the hot-fire injector orifice sizes were varied to test this criteria. All injector dimensions used are given in Table 26.

An annulus fuel flowrate of about 25 percent of the total fuel appeared to be optimum in Task II and III. Thus, 25 percent was selected as a baseline, yielding the appropriate annulus fuel injection areas assuming equal annulus and center fuel temperatures and injection velocities. A 0.035 in. (0.089 x 10^{-2}m) liquid post thickness was selected, based on a compromise between a minimum desired for optimum performance and the thickness required for mechanical strength. The orifice ends of the FLOX tubes were chamfered 10 deg (0.17 rad) from the fuel side to a 0.010 in. (0.025 x 10^{-2}m) thickness to eliminate the potential tube-end recirculation and therefore tube burning.

To complete the test objectives, a number of injector dimensions were varied, namely the liquid orifice diameters, the center fuel orifice diameter and the fuel annulus gaps. These variations were facilitated by use of a Swagelok tee and reducer combination for the connection of (replaceable) gas-liquid

TABLE 26

IMPINGING CONCENTRIC INJECTOR DIMENSIONS

D_o		$(D_f)_{center}$		Annulus Gap (Y_f)		D_o/D_f	$(A_o)_{tot}$		$(A_f)_{center}$		$(A_f)_{ann}$	
in.	$mx10^{-2}$	in.	$mx10^{-2}$	in.	$mx10^{-2}$		$in.^2$	m^2x10^{-4}	$in.^2$	m^2x10^{-4}	$in.^2$	m^2x10^{-4}
0.238	0.605	0.553	1.405	0.012	0.030	0.44	0.174	1.122	0.240	1.548	0.050	0.323
0.238	0.605	0.744	1.890	0.027	0.069	0.32	0.174	1.122	0.436	2.812	0.116	0.748
0.238	0.605	0.454	1.153	0.026	0.066	0.54	0.174	1.122	0.162	1.045	0.112	0.722
0.190	0.483	0.603	1.532	0.021	0.053	0.32	0.118	0.761	0.289	1.864	0.076	0.490
0.190	0.483	0.553	1.405	0.021	0.053	0.34	0.118	0.761	0.240	1.548	0.076	0.490
0.190	0.483	0.454	1.153	0.021	0.053	0.42	0.118	0.761	0.162	1.045	0.076	0.490

concentric tubes and a Swagelok fitting to attach the (replaceable) central fuel orifice and concentric tubes to the injector block. A sketch of the injector assembly is presented in Fig. 116.

Thrust Chamber

Three workhorse thrust chamber designs were used during the Task IV hot-fire testing. In one case, the primary chamber assembly components included a steel bomb ring to house pulse guns for stability evaluation, an uncooled copper combustion zone, and a graphite-lined nozzle section. The chamber assembly is presented in Fig. 117. In another case, the chamber assembly components included a stainless-steel, graphite-lined combustion zone and graphite-lined nozzle. This chamber assembly is pictured in Fig. 118 . In the third case, the stainless-steel bomb ring, the copper combustion zone, the stainless-steel combustion zone, and the stainless-steel nozzle section were used, all with graphite liners, to yield an extended 57.6 in. (1.46 m) characteristic length. Relevant chamber dimensions are summarized as follows.

Combustion chamber diameter, in. (m x 10^{-2})	3.700 (9.398)
Nozzle throat diameter, in. (m x 10^{-2})	2.615 (6.642)
Nozzle throat area, $in.^2$ (m^2 x 10^{-2})	5.369 (0.346)
Contraction area ratio, ε_c	2
Expansion area ratio, ε_ℓ	2
L*, in. (m)	30 and 57.6 (0.76 and 1.46)
Injector to throat length, in. (m)	15.4 and 29.2 (0.39 and 0.74)

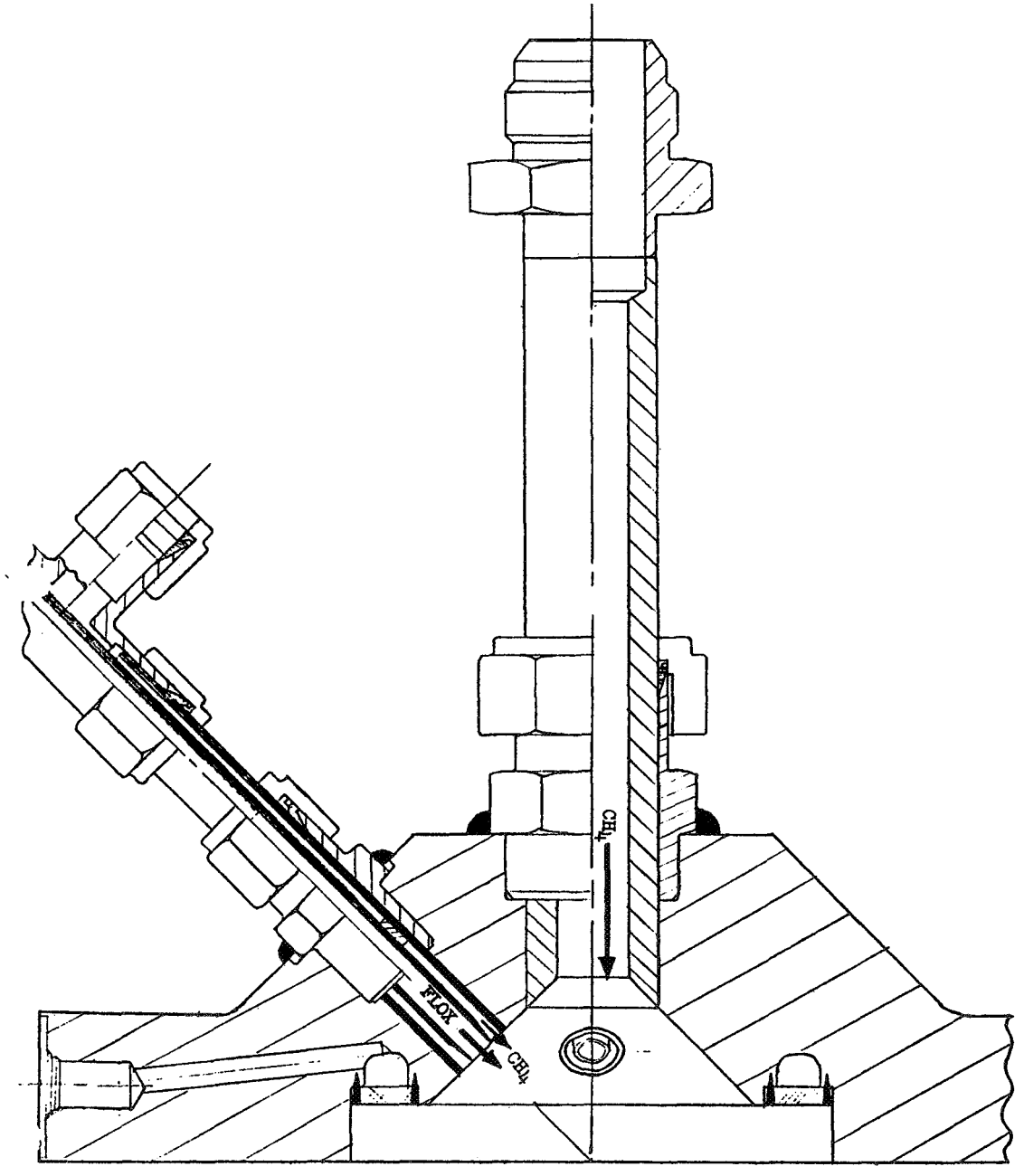

Figure 116. Recessed Impinging Concentric Injector

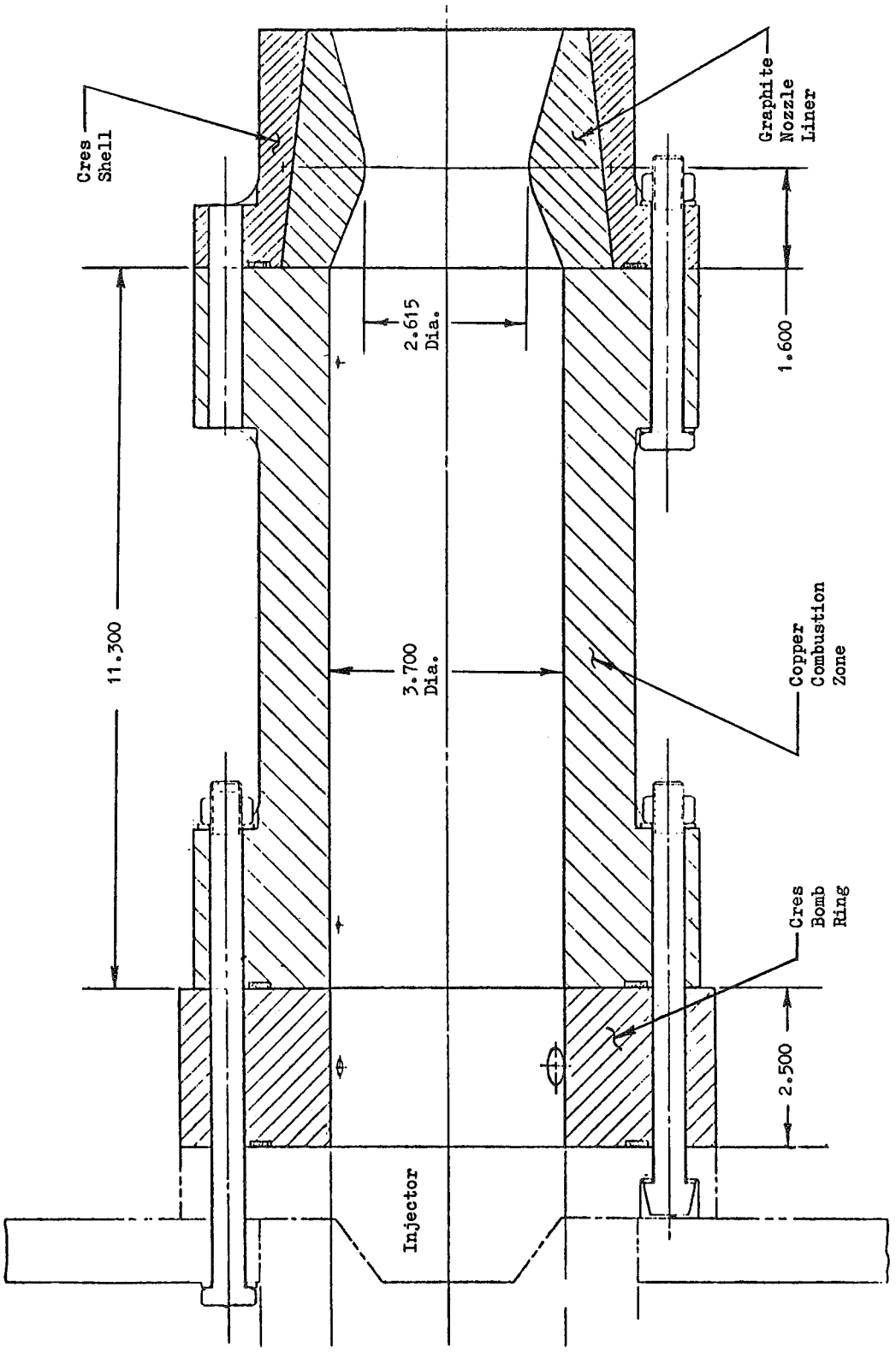

Figure 117. Basic Thrust Chamber Assembly (Tests 24 through 31)

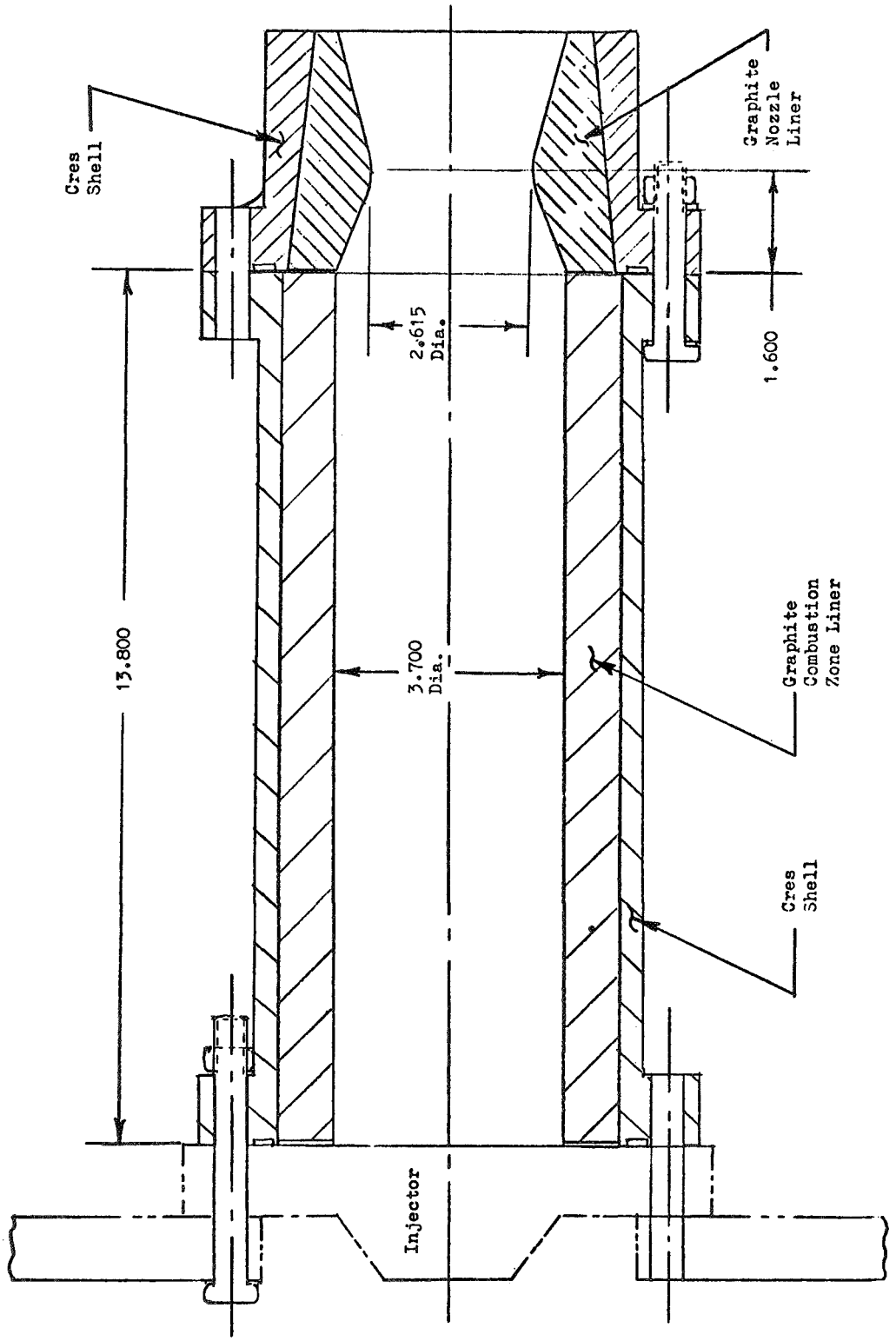

Figure 118. Alternate Thrust Chamber Assembly (Tests 32 through 55 and 59 through 63)

During the hot-firing phase of the program, bomb (pulse gun) pulsing was used to determine the stability characteristics of the injector. A bomb ring was designed to house three pulse guns to generate finite amplitude distriburbances for artificial instability initiation. The bomb ring was 2.5 in. (6.4×10^{-2}m) thick and sandwiched between the chamber and injector as shown in Fig. 117. Three pulse guns were mounted in bosses machined in the ring. All of the gun axes were in a single plane normal to the combustor axis and approximately 1.25 in. (3.2×10^{-2}m) below the injector face. The pulse guns were oriented to give tangential, radial, and chordal disturbances similar to those used in Task I. This orientation was tailored for the single-element (centrally located) injector configuration. Existing gunpowder pulse guns were used which are similar to those used during Task I.

The pulse gun-bomb ring barrels were examined as possible quarter-wave dampers for any induced instability. The simplified approach taken was to assume that the total length of the pulse gun, and its connecting tube through the chamber wall (bomb ring), formed a quarter-wave resonator. The corresponding frequency was then compared with expected instability frequencies. Six cases were considered, two each for radial, chordal, and tangential gun orientations: (1) unfired guns with a 2500 ft/sec (762 m/s) sound speed, and (2) just-fired guns with a 4,000 ft/sec (1219 m/s) sound speed. The computed frequencies ranged from 1300 to 2000 Hz. These frequencies were considerably lower than those of the most likely chamber cross-sectional acoustic resonances (first tangential = 8550 Hz, second tangential = 14,200 Hz and first radial = 17,800 Hz) so that damping of these instabilities by pulse gun cavities appeared unlikely. These pulse gun barrel frequencies were comparable to that of the first longitudinal mode (1825 Hz) which was not expected.

Three chamber pressure Photocons were used initially (with the chamber shown in Fig. 117) to monitor the stability characteristics of the injectors. These Photocons were mounted in the bomb ring about 1.25 in. (3.2×10^{-2}m) downstream from the injector face and from 90 to 180 deg (1.57 to 3.14 rad) apart. These Photocons were recessed approximately 1/2 in. (1.27×10^{-2}m) back from the hot-gas wall of the chamber similar to the mounting used during

Task I. Bomb ring damage subsequently resulted in the Photocon (one used) relocation to the chamber flange downstream of the bomb ring about 1.0 in. (2.54×10^{-2}m) and mounted about 3 in. (7.6×10^{-2}m) from the hot-gas wall. One chamber pressure Photocon was used in conjunction with the chamber assembly pictured in Fig. 118 . This Photocon was mounted about 3 in. (7.6×10^{-2}m) away from the hot-gas wall on the flange adjacent to the injector face. One oxidized injection pressure Photocon was used for all tests.

The initial chamber design (Fig. 117) contained provisions for six chamber pressure and/or temperature pickup ports, three in each of the copper combustion zone flanges. These ports were located 1.0 in. (2.5×10^{-2}m) downstream of the bomb ring and 1.5 in. (3.8×10^{-2}m) upstream of the start of convergence. Four pressure pickup ports, two on each flange, were provided on the alternate chamber assembly shown in Fig. 118.

A transient heat transfer analysis (see Appendix E) was used to predict chamber wall temperature characteristics for the combustion zone and nozzle. This analysis indicated maximum hot-gas side wall temperatures of approximately 1200 F (922 K) in the copper combustion zone (somewhat highter with the graphite combustion zone) and 3200 F (2033 K) at the throat (graphite) after 2.5 seconds of operation at nominal conditions.

SPACE-STORABLE HOT-FIRE TESTS

The Task IV hot-firing tests were directed toward characterizing the 5000-lbf (22,200 N) thrust single-element tricentric with centerbody and the impinging concentric injector configurations with respect to performance and stability. The minimum performance goal was 96-percent c* efficiency. Additional test objectives included:

1. Specific design variable optimization for achievement of high performance

2. Evaluation of injector performance for various percentages of "secondary" GCH_4 flow. For the impinging concentric element, this was the annulus gas flow; for the tricentric element, the term was not truly applicable but was arbitrarily considered to be the inner annulus gas flow.

3. Determination of the effects of varying the methane (gas) injection temperature on performance and stability.

4. Evaulation of the injector operating characteristics at 10-percent thrust.

Liquid FLOX (83.5-percent)/gaseous methane were used as the main propellants with injection of the gaseous methane specifically designed to augment the atomization and mixing processes. The nominal baseline operating conditions were as follows:

Vacuum Thrust based on 60:1 nozzle, lbf	5000 (22,000)
Overall Mixture Ratio*, o/f	5.25 to 5.75
Chamber Pressure, $lbf/in.^2$ ($N/m^2 \times 10^{-4}$)	500 (345)
Chamber Characteristic Length (L*), in. (m)	30 to 57.6 (0.76 to 1.46)
Methane Temperature, R (K)	Amb to 1100 (amb to 611)
Duration, sec	2 to 2.5

The test series were formulated to investigate the effects of fuel injection temperature, liquid and gas injection velocities, ratio of "secondary" fuel to total fuel flowrate, amount of liquid post recess, and chamber pressure (throttle test), first with the tricentric with centerbody and then with the

*This nominal mixture ratio was treated as 5.75 in Tasks II and III, but in more current engine applications (Contract NAS3-11191 and NAS3-12051), a mixture ratio of 5.25 has been selected.

impinging concentric injector concept. Dynamic stability of the hardware was evaluated, aided by artificially induced pulse gun disturbances.

Facilities and Equipment

The test facilities used for Task IV hot-fire tests are located in the Propulsion Research Area (PRA). The PRA is comprised of five multiposition firing pits with a centrally located blockhouse which permits direct observation of the engine firings. Test stand Uncle was employed for the hot-firing tests. A schematic of this test stand is given in Fig. 119. The FLOX was transferred to a run tank (Fig. 119) from a 120 gal (0.45 m^3) FLOX storage tank, while the methane was obtained directly from gaseous K-bottles. These K-bottles were replaced with new bottles when below an acceptable operating pressure level.

The methane was heated with the pebble bed heater (which was heated prior to the tests by hot gaseous nitrogen) and with Cal-rod heaters on the feed lines. Three main fuel valves were used, respectively, for (1) center or inner annulus fuel flowrate, (2) annulus or outer annulus flowrate, and (3) face coolant flowrate. One main oxidizer valve was employed.

Because this facility had been used for previous FLOX/methane tests, little modification was required. The primary facility modification was to the gas heating system which required: (1) installation of a gas heater to be used for convective heating of the pebble-bed heat exchanger, (2) servicing of the valve connecting the GN_2 gas heater and heat exchanger for 1000 F (811 K) use, and (3) the addition of the third fuel main valve.

Instrumentation. Task IV hot-fire instrumentation is listed in Table 27. Redundant measurements were made on the important experimental parameters to increase data reliability. The particular instrumentation used for the various types of measurements are described below.

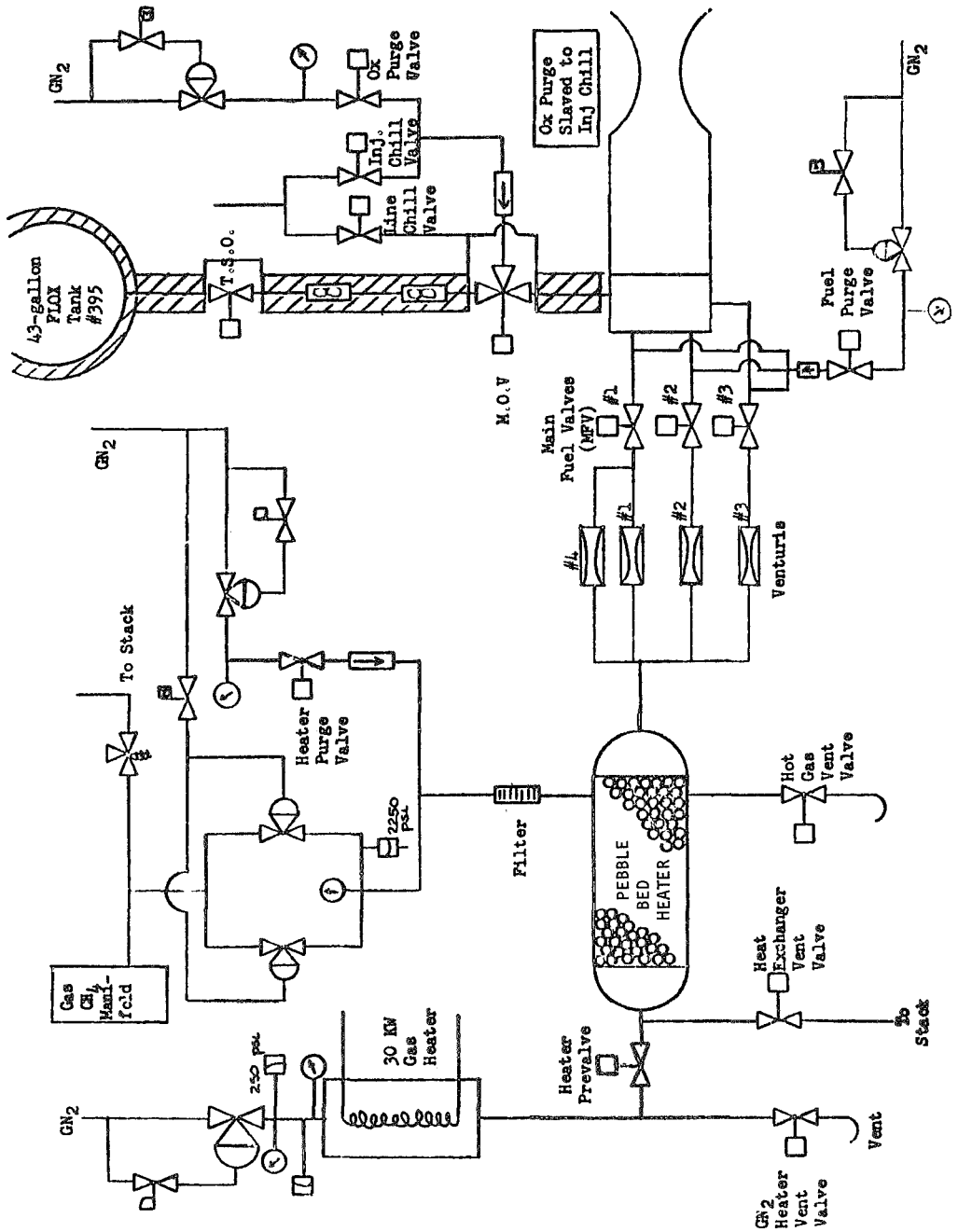

Figure 119. Schematic of Uncle Stand FLOX/Methane Propellant Feed System

TABLE 27

INSTRUMENTATION FOR TASK IV TESTS

Parameter	Range	Transducer	Recorder*
Pressure			
GCH_4 Bottle Bank Manifold	0 to 3000 psi (0-2068 x 10^4 N/m^2)	Taber	G
GCH_4 Regulator Inlet	0 to 3000 psi	Taber	G, B
GCH_4 Venturi Inlet (4)	0 to 3000 psi	Taber	G, B
GCH_4 Venturi Throat (4)	0 to 3000 psi	Taber	G, B
GCH_4 Injection (2)	0 to 2000 psi (0-1379 x 10^4 N/m^2)	Taber	G, B, O
Oxidizer Tank	0 to 2000 psi	Taber	G
Oxidizer Injection	0 to 2000 psi	Taber	G, B, O
Oxidizer Injection	0 to 2000 psi	Photocon	T, O
Chamber Pressure (3)	0 to 1000 psi (0-689 x 10^4 N/m^2)	Taber	G, B, O
Chamber Pressure (3)	0 to 1000 psi (0-689 x 10^4 N/m^2)	Photocon	T, O
Temperature			
Heater Outlet	60 to 1000 F (289-811 K)	C/A	G, B
Heater Bed (2)	60 to 1000 F	C/A	G, B
Venturi Inlet (2)	60 to 1000 F	C/A	G, B
Fuel Injection (2)	60 to 1000 F	C/A	B
FLOX Flowmeter (2)	-290 to -310 F (94 to 83 K)	Rosemount Bulb	G, B
FLOX Injection	-240 to -305 F (122 to 86 K)	I/C	G, B
FLOX Flow	1 to 12 lb/sec (0.45 to 5.44 kg/s)	Fischer-Porter	O, B
Thrust	0-10,000 lbf (0 to 44,400 N)	Baldwin Load Cell	O, B, G
Acceleration	0-300 g	Electra Scientific Model V5	O, T

*G = Graphic; B = Beckman; O = Oscillograph; T - Tape

Thrust. The thrust chamber mount was supported on flexures, which allowed free movement parallel to the engine axis (horizontally), restrained in the thrust direction by a Baldwin dual-bridge load cell which measured the thrust.

Pressures. Pressures were measured with bonded strain-gage transducers (Taber "Teledyne" series 206 or equivalent). Chamber pressure was measured at two circumferential positions in two axial positions: near the start of nozzle convergence and near the injector face.

Flowrates. The oxidizer flowrates were measured by means of Fischer-Porter turbine flowmeters of a type proved suitable for service in FLOX. The oxidizer line had two flowmeters in series to measure the volumetric flowrate. Gaseous fuel flowrates were measured by sonic venturi meters.

Temperatures. Reliable measurement of cryogenic propellant flowrates requires accurate determination of liquid density or temperature as well as the volumetric flowrate. This temperature measurement was done by use of shielded platinum resistance bulbs (Rosemount Model 176) immersed in the liquid stream. Injection and venturi temperature measurements were made with chromel-alumel thermocouples.

Special Instrumentation. Photocon pressure transducers were used to detect high-frequency oscillations in the combustion chamber and in the oxidizer injection pressures. An accelerometer was mounted on the chamber.

Data Recording. All pressure, temperature, and flow measurements were recorded on tape during each firing by means of a Beckman Model 210 Data Acquisition and Recording System. This system acquires analog data from the transducers, which it converts to digital form in binary-coded decimal format. The latter are recorded on tapes which are then used for computer processing.

The Beckman Data Acquisition Unit sequentially samples the input channel at a rate of 5625 samples per second. Programmed computer output consists of tables of time versus the average parameter value over an approximate 200-microsecond (200×10^{-6}s) slice time, printed out at the approximately 200 msec (200×10^{-3}s) intervals during the firing, together with calibration factors, prerun and postrun zero readings, and related data. The instantaneous parameter values are machine-plotted and displayed as CRT outputs on appropriately scaled and labeled grids for simple determination of gradients, establishment of steady-state, etc.

Primary data recording for these firings was on the Beckman 210 system. In addition, the following auxiliary recording system was employed.

1. An 8-channel, Brush, Mark 200 recorder was employed in conjunction with the Beckman unit, primarily to establish time intervals for computer data reduction and, additionally, for "quick-look" information on the most important parameters. This is a direct-inking system, with display high-gloss, graduated paper moving at 20 mm/sec (20×10^{-3}m/s).
2. A CEC, 36-channel direct reading oscillograph was used as backup for the Beckman 210 system and for indication of any oscillatory combustion.
3. Direct-inking graphic recorders (DIGR's), either Dynalog rotary chart or Esterline-Angus strip chart, were used to set prerun propellant supply pressures, for recording of propellant manifold pressures, to provide quick-look information, and as secondary backup to the Beckman and oscillograph recorders.
4. An Esterline-Angus, 20-channel event recorder was used for direct-inking recording of main propellant valve signal and travel, as well as for chart drive and camera actuations.
5. A high-frequency (RIL) tape recorder was used to monitor Photocon and accelerometer responses.

Test Procedure. The overall test procedure used on all tests was as follows:

1. Clean the injector assembly for propellant compatibility and install with the appropriate thrust chamber configuration on the test stand.
2. Connect the required plumbing and instrumentation and leak check the systems.
3. Coordinate the test schedule with Test Operation Control.
4. Preheat the methane pebble bed heater to the desired temperature (1 day before the test).
5. Verify correct operation of the propellant system valves.
6. Verify sequence timing on the Esterline-Angus recorder.
7. Verify adequate supply of methane fuel for the test series.
8. Secure the area.
9. Transfer FLOX from the 120-gal (0.45 m^3) storage tank to the 43-gal (0.16 m^3) run tank.
10. Make the final blockhouse preparations.
11. Sequence start (run the test).
12. Vent the propellant systems to atmospheric pressure.
13. Transfer FLOX from the run tank to the storage tank.
14. Open the test pit and secure all systems.

The test operational sequence used for all tests except test No. 24 and 25 was as follows. This sequence is shown schematically in Fig. 120 .

1. Fuel and oxidizer hardware purges on
2. Oxidizer chill flowing through injector initiated; oxidizer purge slaved off
3. Oxidizer chill off; oxidizer purge slaved on

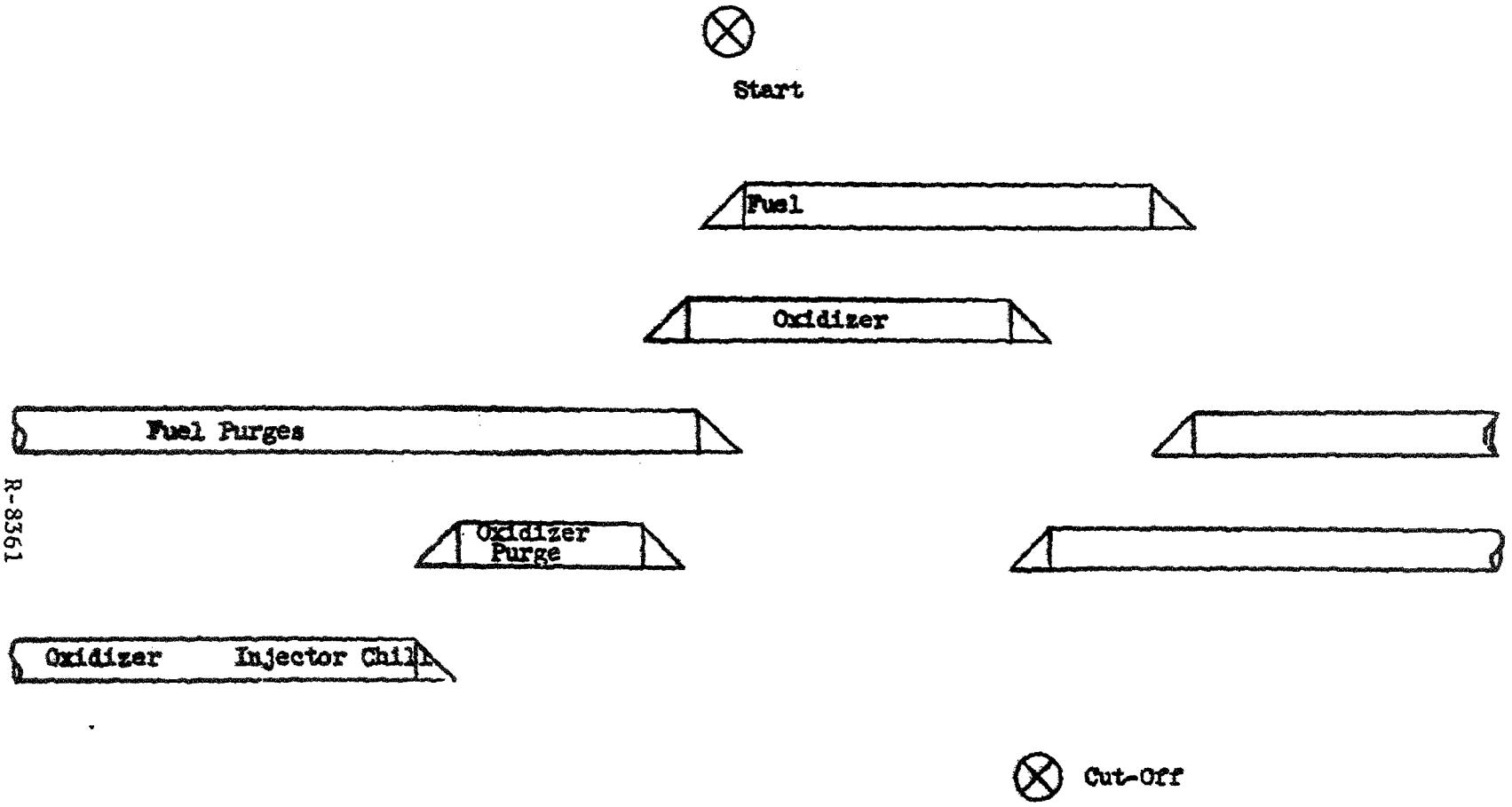

R-8361
282

Figure 120. **Test Operational Sequence**

4. Oxidizer main valves open
5. Oxidizer purge off (at main oxidizer valve opening)
6. Fuel main valves open
7. Injector fuel purge off (at main fuel valve opening)
8. Mainstage
9. Cutoff signal
10. Oxidizer propellant valve closed
11. Oxidizer purge initiated (at main oxidizer valve closed)
12., Fuel main valve closed
13. Fuel purges initiated (at main fuel valve closed)

For test No. 24 and 25 a fuel lead was used as well as the fuel lag. This was changed after test No. 25 because of injector damage which incurred during these tests (discussed in the section on test description).

Testing

Forty hot-fire tests were conducted during Task IV, 29 of the tests being of sufficient duration for reliable performance calculations. Of these 29 tests, 12 were conducted with the tricentric with centerbody injector concept and 17 with the impinging concentric injector. These tests along with a detailed test plan are described in the following sections.

Tricentric with Centerbody Tests. The test plan for this injector was formulated mainly to demonstrate the performance and stability characteristics of this concept. In addition to demonstrating performance (η_c*, 96 percent), the test goals included a parametric performance investigation of mixture ratio, methane temperature, $V_g = V_\ell$, the ratio of inner-to-outer gas annulus injection flowrates (equivalent to $(A_{in}/A_{out})_g$ because gas injection velocities and densities were equal) FLOX injection velocity, and one throttle test. The initial tests (tests No. 24 and 25) were conducted with the

orifice geometry (i.e., the liquid injection area and the ratio of inner-to-outer fuel injection areas and annulus gaps) and operating conditions indicated to be optimum in Task II and III cold-flow tests. Unfortunately, severe injector burning (discussed in the test descriptions) occurred in these tests, negating any performance calculations and inflicting substantial injector damage.

Another configuration with a different fuel injection area ratio $(A_{in}/A_{out})_g$ but with the optimum annulus gap ratios was then tested (tests 26 through 30). Design material and operational changes, incorporated to eliminate injector erosion, were successful but combustion efficiencies were low. Therefore, this configuration was modified to yield the cold-flow optimum area ratio, thereby changing the gas annulus gap ratio (Y_{in}/Y_{out}) from optimum. Although a substantial gain in performance was achieved at constant V_g-V_ℓ, results remained in the low 90's (test No. 31). Another configuration was tested (tests 32 through 35) with an increased liquid injection area (this produced a very low FLOX injection velocity) along with optimum fuel area and gap ratios. Results revealed low performance and significant flow instabilities (i.e., chugging) because of low liquid injection velocities. Subsequent tests (tests 36 to 38) were made with the same configuration as was used for test No. 31 but with varying fuel injection temperature (to vary V_g-V_ℓ) and varying mixture ratio. Results showed a substantial gain in performance, reaching approximately 97 percent with a 4.5 mixture ratio, but still below the level desired at higher mixture ratios.

These encouraging results led to the repair of the configuration damaged on the initial tests No. 24 and 25. However, seal failure in the next test (No. 55) negated these repairs before any steady-state performance could be established. Therefore the remaining tests (tests No. 59 through 63) were conducted with the configuration from which the high performance was obtained at a 4.5 mixture ratio. Based on the cold-flow results, this configuration was modified to include a small amount (0.200 in.; 0.508×10^{-2}m) of liquid post recess in an effort to increase performance at a higher mixture ratio. Results yielded combustion efficiencies on the 97-percent level at a 5.25

mixture ratio which exceeded the program performance goal. Combustion was stable and the hardware was in good condition after the tests. A more detailed description of the individual tests follows.

Test No. 24. The first FLOX/CH_4 hot-firing test was conducted using the nominal tricentric with centerbody injector, which contained a 0.25 in. (0.63 x 10^{-2}m)-diameter centerbody (plug) surrounded by gas, liquid, and gas annulus gaps of 0.095, 0.119, and 0.036 in. (0.241, 0.302, and 0.091 x 10^{-2}m), respectively. The posts (walls) separating the liquid annulus from the two gas annuli were 0.035 in. (0.089 x 10^{-2}m) thick. The outer and inner fuel injection areas were equal (i.e., A_{in}/A_{out} = 1). Approximately 8 percent of the fuel was used as coolant for the injector Rigimesh. The thrust chamber for this test contained a steel pluse gun ring mounted at the injector end, an uncooled copper combustion zone, and a steel nozzle shell with a graphite throat insert. The injector-to-throat length was 15.4 in. (0.39 m) and the resultant L* was 30 in. (0.76 m). The test was programmed for 300 msec (300 x 10^{-3}s) of mainstage at 500-psia (345 x 10^4 N/m^2) chamber pressure and 5.75 mixture ratio with a fuel injection stagnation temperature of 860 R (478 K). During the test, the actual FLOX flowrate was higher than planned (MR = 7.1), although the chamber pressure of 500 psi (345 x 10^4 N/m^2) was as targeted. The actual mainstage portion lasted 250 msec (250 x 10^{-3}s). Pertinent operating conditions and performance numbers for this test and the subsequent tests are listed in Table 28.

Posttest inspection of the hardware revealed damage to the injector tube ends in contact with the FLOX, the pulse gun chamber spacer, and to the three Photocons which were inserted in the chamber spacer. Photographs of the damaged injector tube ends are presented in Fig.121 and 122. By some means the stainless-steel posts were apparently heated to the ignition temperature with FLOX. Conceivably, this post tip heating may have resulted from recirculation of hot combustion gases in the void flow area downstream of the tube ends as depicted below.

TABLE 28

TRICENTRIC WITH CENTERBODY INJECTOR HOT-FIRE TEST RESULTS

Test No.	Duration, seconds	F_{vac}		P_c (nozzle)		$\dot{w}_o$		$\dot{w}_f$ (total)		$(\dot{w}_{in})_f$		$(\dot{w}_{out})_f$		MR	V_ℓ		V_g		T_g		$\left(\frac{\dot{w}_{in}}{\dot{w}_{out}}\right)_f$	$\left(\frac{Y_{in}}{Y_{out}}\right)_f$	$\left(\frac{A_{in}}{A_{out}}\right)_f$	η_c^* from P_c, %	η_c^* from F, %
		lb	N	psia	$N/m^2 \times 10^4$	lb/sec	kg/s	lb/sec	kg/s	lb/sec	kg/s	lb/sec	kg/s		ft/sec	m/s	ft/sec	m/s	R	K					
24	0.28	3867	17,200	502	346	12.57	5.70	1.77	0.80	0.80	0.36	0.82	0.37	7.10	91	27.7	1250	381	855	475	0.98	2.6	1.0	87.4*	88.1*
25	0.22	FLOX Manifold Contamination																				2.7	1.1		
26	0.40	2848	12,670	369	254	8.50	3.86	2.05	0.93	1.17	0.53	0.78	0.35	4.15	59.1	18.0	1257	383	543	302	1.50	2.8	1.5	86.1*	87.3*
27	0.40	3308	14,710	427	294	11.50	5.22	1.80	0.82	1.03	0.48	0.69	0.31	6.38	81.7	24.9	975	297	535	297	1.50	2.8	1.5	78.4*	79.6*
28	2.00	3371	14,990	435	300	10.90	4.94	1.89	0.86	1.08	0.49	0.72	0.33	5.74	76.6	23.3	1004	306	533	296	1.49	2.8	1.5	81.8	83.1
29	0.40	3518	15,650	455	314	10.70	4.85	2.31	1.05	1.27	0.58	0.93	0.42	4.63	74.9	22.8	1570	479	740	411	1.37	2.8	1.5	87.5*	86.9*
30	2.30	3455	15,370	447	308	10.00	4.54	2.08	0.94	1.18	0.54	0.80	0.36	4.83	71.1	21.7	1670	509	860	478	1.48	2.8	1.5	93.2	91.6
31	2.00	3745	16,660	477	329	10.88	4.94	2.07	0.94	0.98	0.44	0.99	0.45	5.26	76.1	23.2	1353	412	835	464	0.99	1.9	1.0	92.3	92.3
32	0.55	3455	15,370	452	312	11.52	5.23	1.97	0.89	0.93	0.42	0.94	0.43	5.83	27.3	8.3	1289	393	745	414	0.99	2.5	1.0	85.4*	82.1*
33	0.38	3495	15,550	455	314	11.66	5.29	1.98	0.90	0.93	0.42	0.95	0.43	5.89	27.0	8.2	1356	413	771	428	0.98	2.7	1.1	85.7*	82.4*
34	2.08	3516	15,640	447	308	11.80	5.35	1.98	0.96	0.94	0.43	0.95	0.43	5.94	27.4	8.4	1567	478	886	492	0.99	2.7	1.1	84.6	82.5
35	2.01	4092	18,200	509	351	13.65	6.19	2.39	1.08	1.13	0.51	1.14	0.52	5.72	32.1	9.8	1083	330	571	317	0.99	2.7	1.1	83.9	82.5
36	2.10	3882	17,270	512	353	11.44	5.19	2.06	0.93	0.97	0.44	0.99	0.45	5.55	78.7	24.0	1369	417	944	524	0.99	1.9	1.0	92.0	90.4
37	2.10	4111	18,290	543	374	12.10	5.49	2.30	1.04	1.06	0.48	1.13	0.51	5.27	83.8	25.5	917	280	599	333	0.94	1.9	1.0	91.8	90.3
38	1.10	3952	17,580	522	360	10.79	4.89	2.35	1.07	1.10	0.50	1.14	0.52	4.59	74.3	22.6	1304	397	808	449	0.96	1.9	1.0	98.4	96.4
55	2.15	Seal Leakage and/or Seal Contamination																				2.6	1.0		
59	2.15	3114	13,850	417	288	8.49	3.85	2.00	0.91	0.98	0.44	1.02	0.47	4.25	60.3	18.4	1800	549	986	548	0.96	1.9	1.0	98.9	97.0
60	2.16	3767	16,760	507	350	10.27	4.66	2.28	1.03	1.12	0.51	1.16	0.53	4.51	73.3	22.3	1632	497	939	522	0.97	1.9	1.0	99.2	97.2
61	2.14	4143	18,430	555	383	11.86	5.38	2.03	0.92	1.01	0.46	1.02	0.46	5.84	83.9	25.6	1194	363	829	461	0.98	1.9	1.0	97.4	95.4
62	2.12	4417	19,650	591	407	12.83	5.82	2.12	0.96	1.05	0.48	1.07	0.48	6.05	90.8	27.7	1053	321	750	417	0.97	1.9	1.0	97.7	95.2
63	4.10	Low P_c (Data Not Stabilized)																				1.9	1.0		

L* = 30 in. (0.76 m)

*The short duration of these tests precludes meaningful performance evaluation.

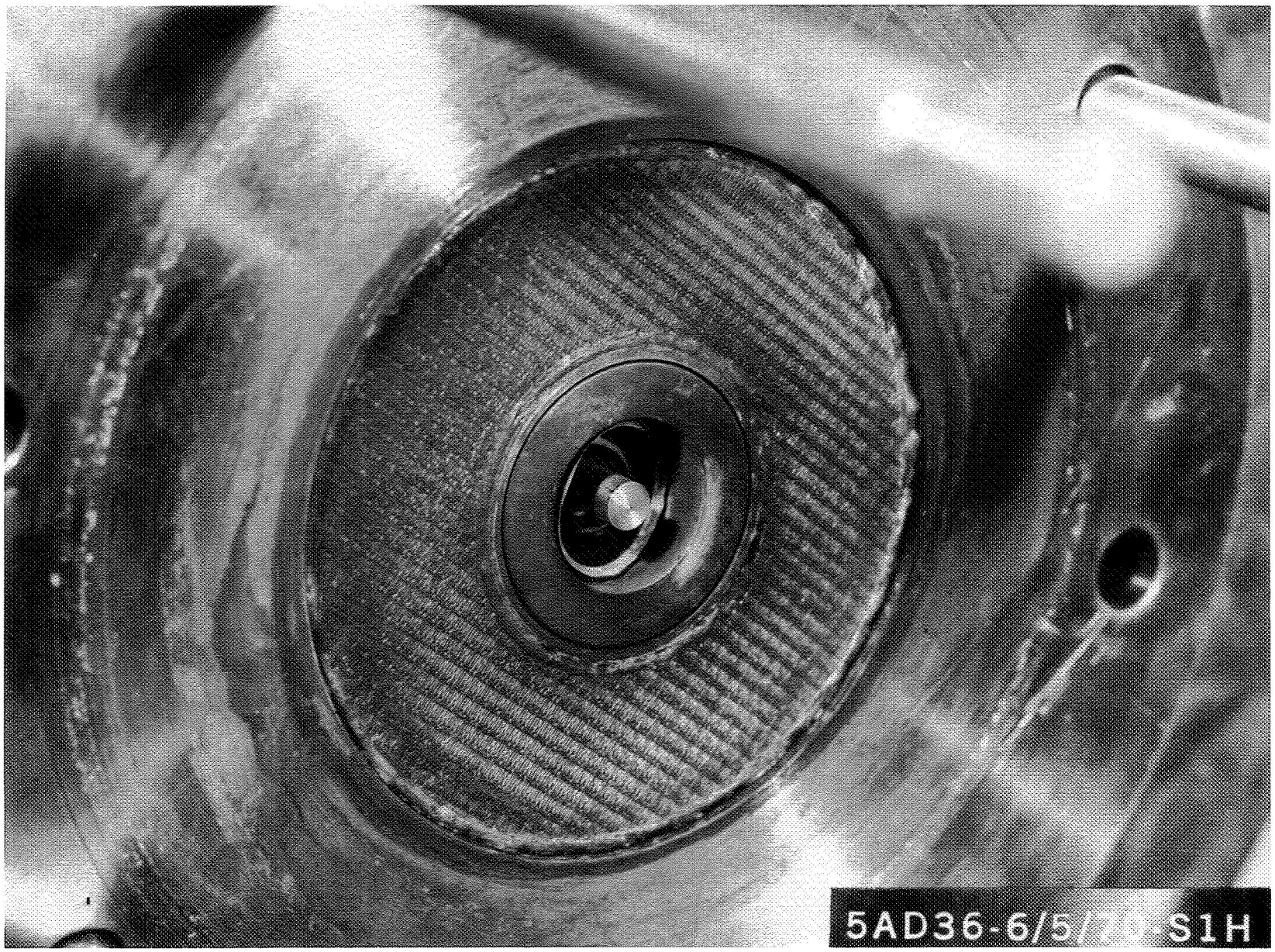

Figure 121. Tricentric With Centerbody Injector, Posttest No. 24

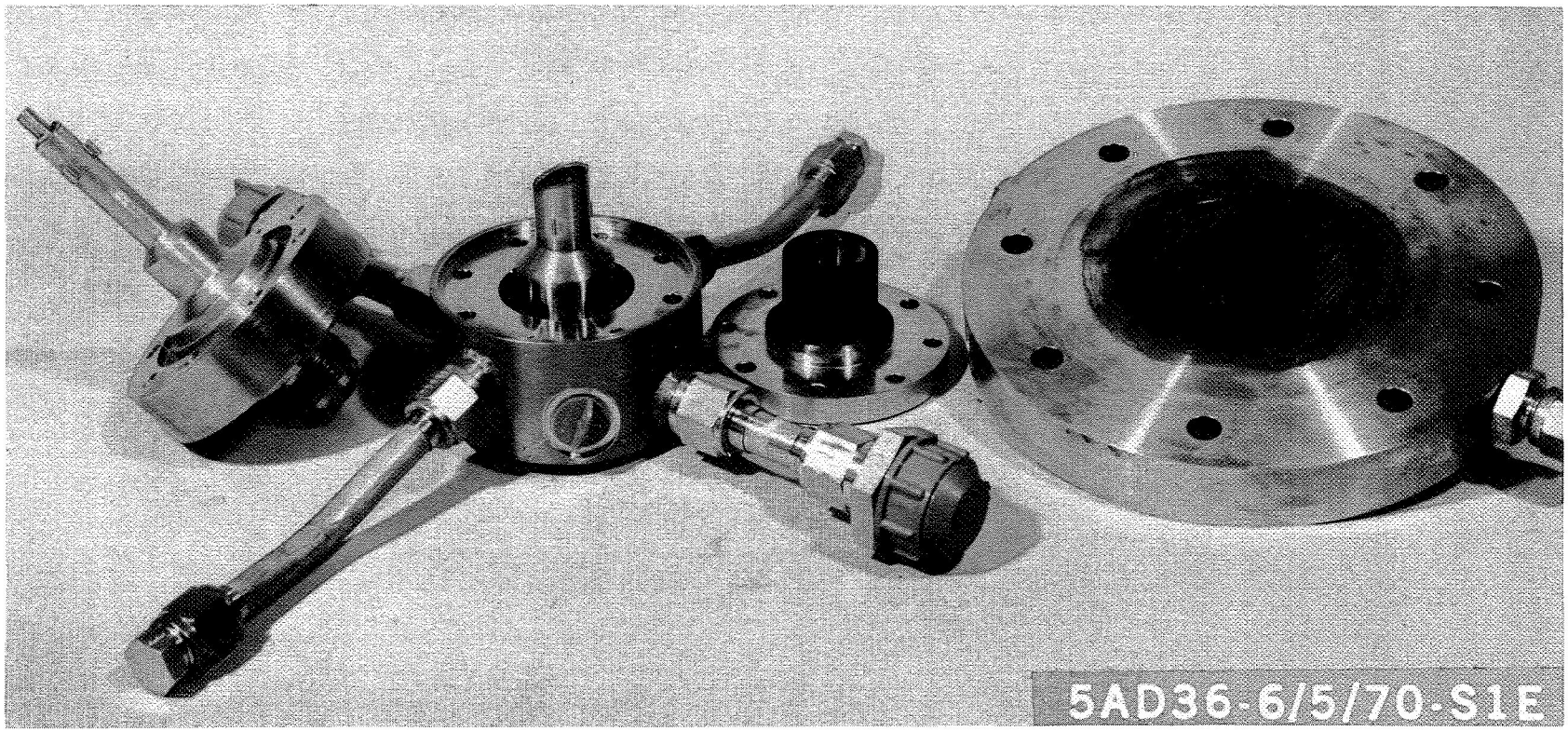

Figure 122. Tricentric With Centerbody Injector Components, Posttest No. 24

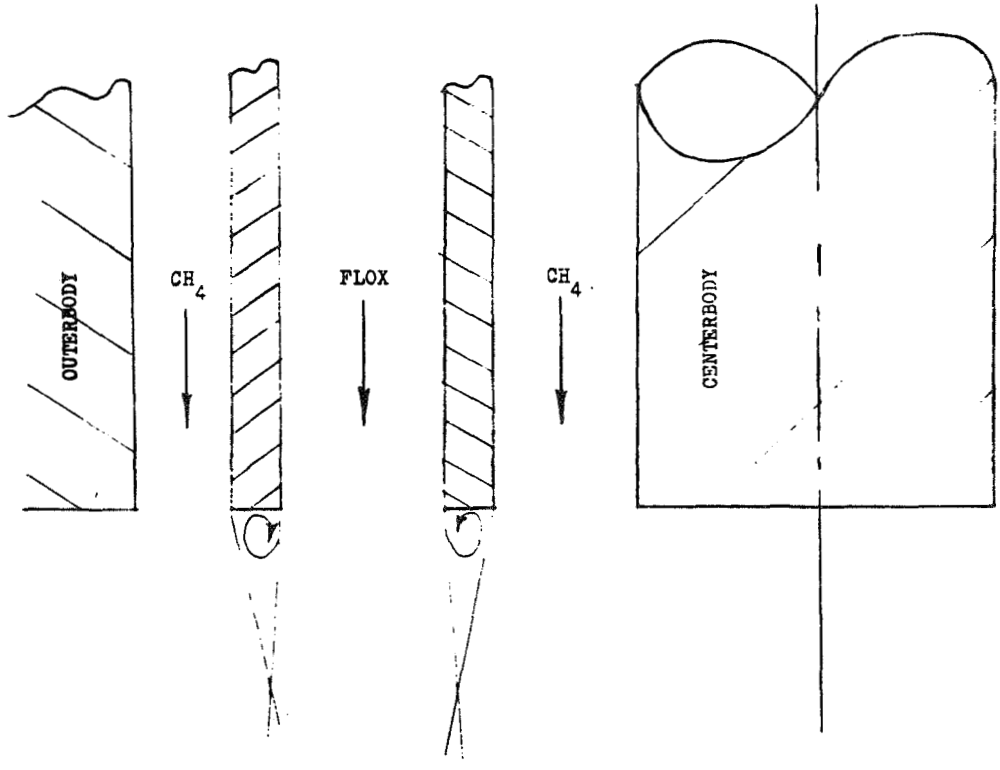

The chamber spacer damage appeared to be due to the boundary layer disturbance caused by the rather large, sharp-edged pulse gun ports (D = 0.5 in.; 1.27 x 10^{-2}m) and the Photocon ports (D = 0.25 in.; 0.64 x 10^{-2}m). These disturbances caused local overheating resulting in chamber erosion and burning of the Photocon diaphragms. Erosion occurred in the area around each pulse gun or Photocon port (approximately 0.5 in.; 1.27 x 10^{-2}m to each side) and was about 1/4 in. (0.64 x 10^{-2}m) deep.

Injector repair procedures included (1) cutting the damaged orifice tubes (Fig. 122) in contact with FLOX about 1 in. (2.54 x 10^{-2}m) shorter than their original length, (2) electron beam welding of 1-in. (2.54 x 10^{-2}m)-long nickel* posts (tips) on the ends of these tubes, (3) machining these ends to the required diameter and wall thickness, and (4) turning a slight radius on each of the tube tip edges. This repair essentially returned the injector to its original geometry. It was hoped that post tip burning might be avoided

*Nickel has a higher ignition temperature with FLOX than stainless steel.

by the change from stainless steel to nickel. The pulse gun chamber spacer adjacent ot the injector was repaired by removing the damaged surface and brazing a 1/2-in. (1.27×10^{-2}m)-thick copper liner inside the steel jacket.

Test No. 25. Test No. 25 was another short test (220 msec, 220×10^{-3}s) with the injector and chamber spacer repaired from the first test. Thus, the injector and chamber assembly was identical to the first test except for the nickel tips on the FLOX tubes and the absence of ports in the chamber spacer. The test was again programmed for about 250 msec (250×10^{-3}s) of mainstage at 500-psia (345×10^{4} N/m^2) chamber pressure and 5.75 mixture ratio with a fuel injection temperature of 860 R (478 K). The actual mainstage portion of the test lasted 220 msec (220×10^{-3}s) and a hard shutdown was observed. Other pertinent operating conditions are presented in Table 28. Posttest inspection of the hardware revealed extensive damage to the injector. Both of the FLOX orifice tubes were eroded back about 1 in. (2.5×10^{-2}m) on one side, the outer body was eroded, and there was significant fire damage evident in the FLOX manifold. Photographs of this damage are presented in Fig. 123 and 124.

Several possible explanations were advanced upon examination of the damage, the instrumentation, and the photographic coverage. The prime possibilities are the following:

1. Contamination in FLOX dome (e.g., ice)
2. Hard start with the CH_4 lead
3. Tip recirculation
4. Cavitating FLOX flow within the injection annulus
5. Shutdown damage because of too short a CH_4 lag

Revisions were made to amend each of the preceding possibilities. These changes are discussed in the following section.

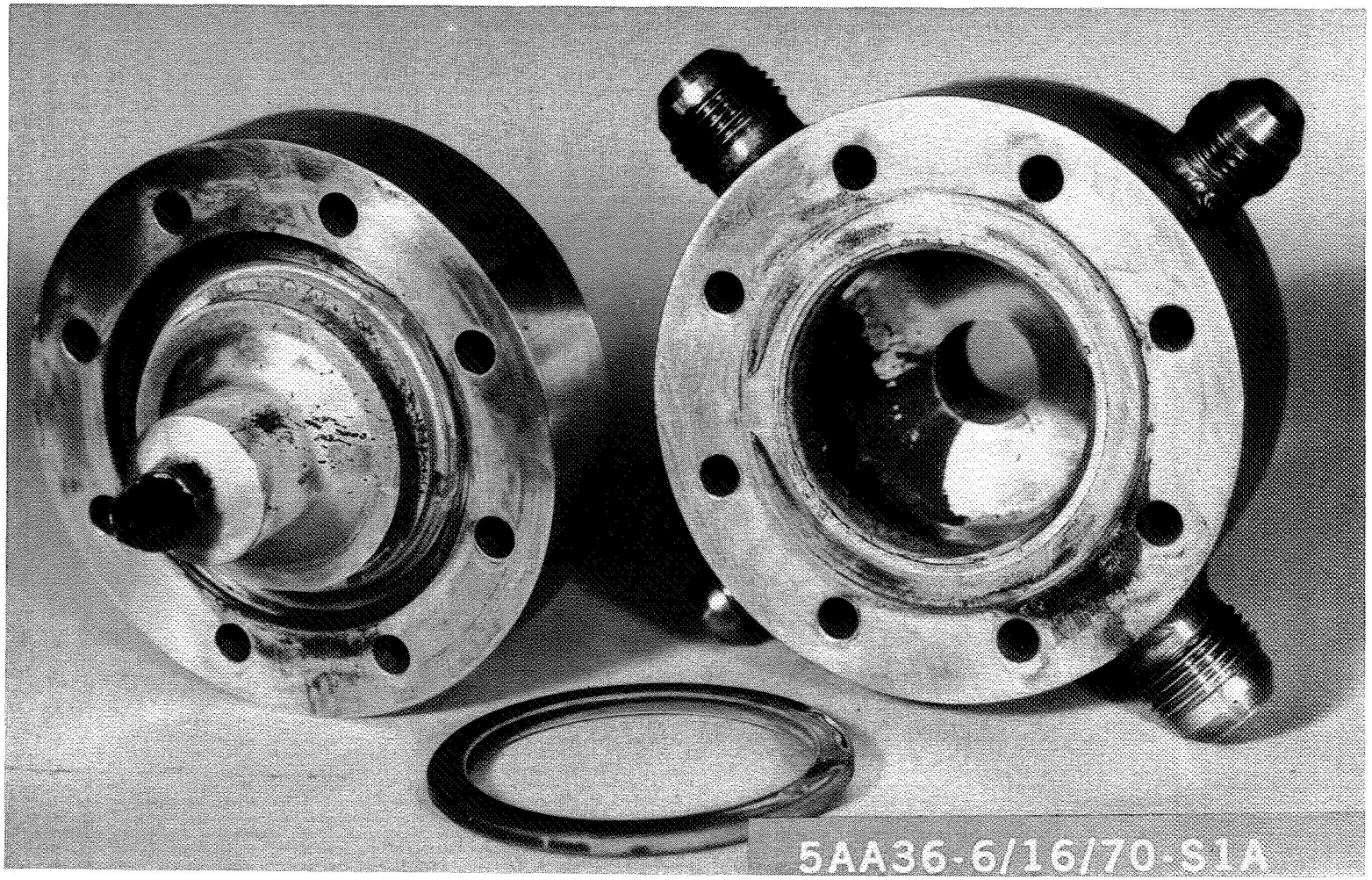

Figure 123. Tricentric With Centerbody Injector FLOX Manifold Damage, Posttest No. 25

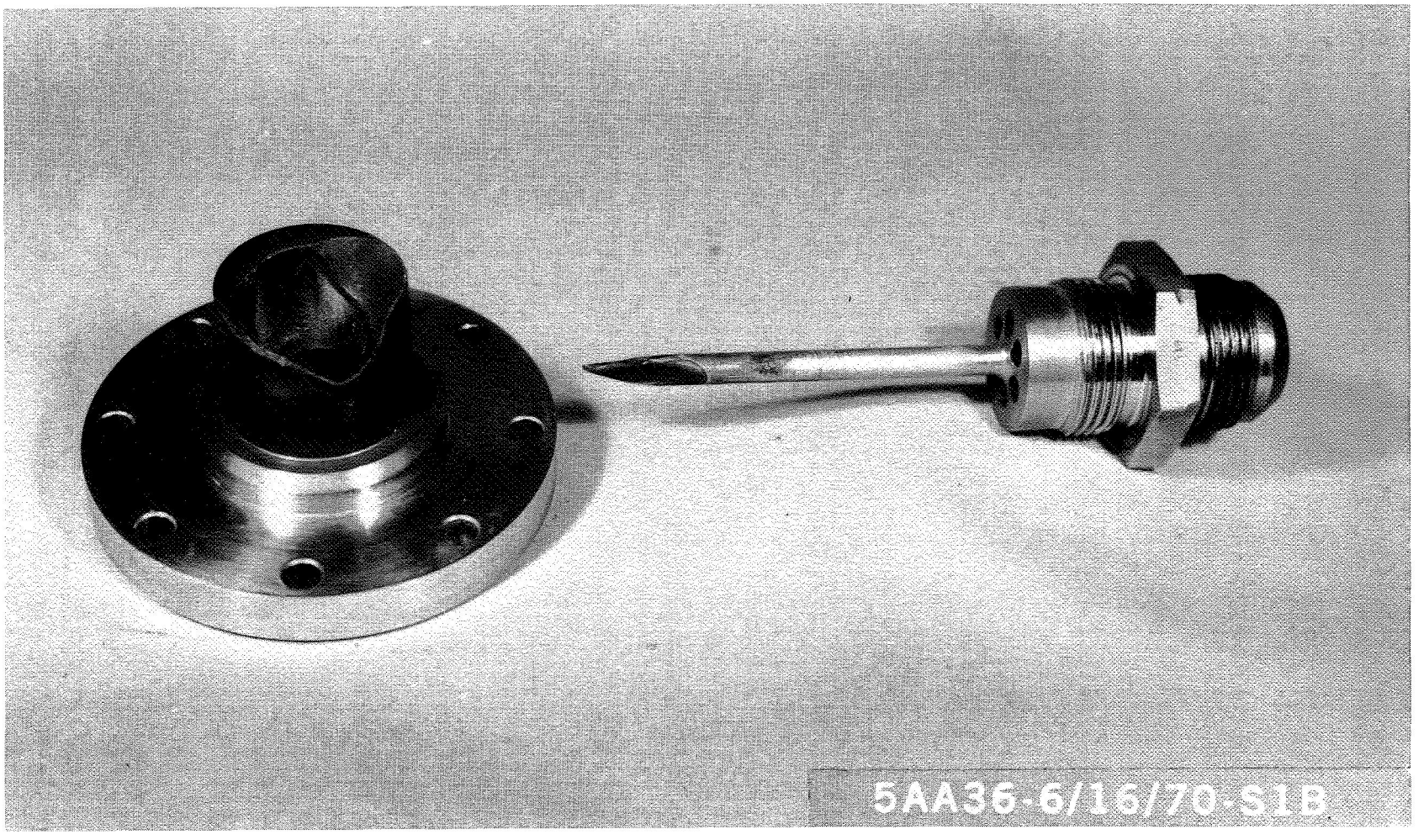

Figure 124. Tricentric With Centerbody Injector Outerbody and Centerbody Damage, Posttest No. 25

Test No. 26. The third FLOX/CH_4 test was conducted with the tricentric with centerbody injector employing an inner-to-outer annulus (methane) injection area ratio of 1.5. This injector contains a 0.43-in. (1.09×10^{-2}m)-diameter post surrounded by gas, liquid, and gas annulus gaps of 0.072, 0.099, and 0.026 in. (0.183, 0.251, and 0.66×10^{-2}m), respectively. By keeping the methane velocity constant, the inner-to-outer methane flowrate ratio was also 1.5. The pretest chilldown sequence was changed to preclude any condensation (in the injector) of moisture from the atmosphere, and the liquid nitrogen tanks, used for the injector chill, were thoroughly dried. The test sequence was also changed to a FLOX lead and a longer methane lag. Tip recirculation was reduced by thinning the exit of the orifice tubes to almost a knife-edge and beveling the tubes 10 deg (0.17 rad) from the gas sides. FLOX flow passages leading into the injection annulus were rounded as much as possible to inhibit flow separation. Finally, the FLOX tube tip material was changed from stainless steel to nickel to lessen the chance of tip burning. A sketch of the injector modifications is shown in Fig. 125.

Approximately 5 percent of the fuel was used as coolant for the injector Rigimesh, and the thrust chamber was the same as used for test No. 25. The test was programmed for 400 msec (400×10^{-3}s) of mainstage at a 400-psia (276×10^4N/m^2) chamber pressure, a 4.0 mixture ratio and an ambient fuel injection temperature. These latter operating conditions were used in a further attempt to lower the heat flux to the orifice tubes.

Test No. 26 was run successfully under these nominal conditions. Posttest inspection of the hardware revealed no injector or chamber damage, indicating revisions made for this test satisfactorily reduced the injector head load.

Tests No. 27 and 28. Test No. 27 was another short test using the same test configuration, chilldown sequence, test sequence, and fuel temperature as test No. 26. The only differences between the two tests were the mixture ratio and the chamber pressure. Test No. 27 was programmed for 400 msec (400×10^{-3}s) of mainstage at a 500-psia (345×10^4 N/m^2) chamber pressure, a 5.75 mixture ratio, and an ambient fuel injection temperature.

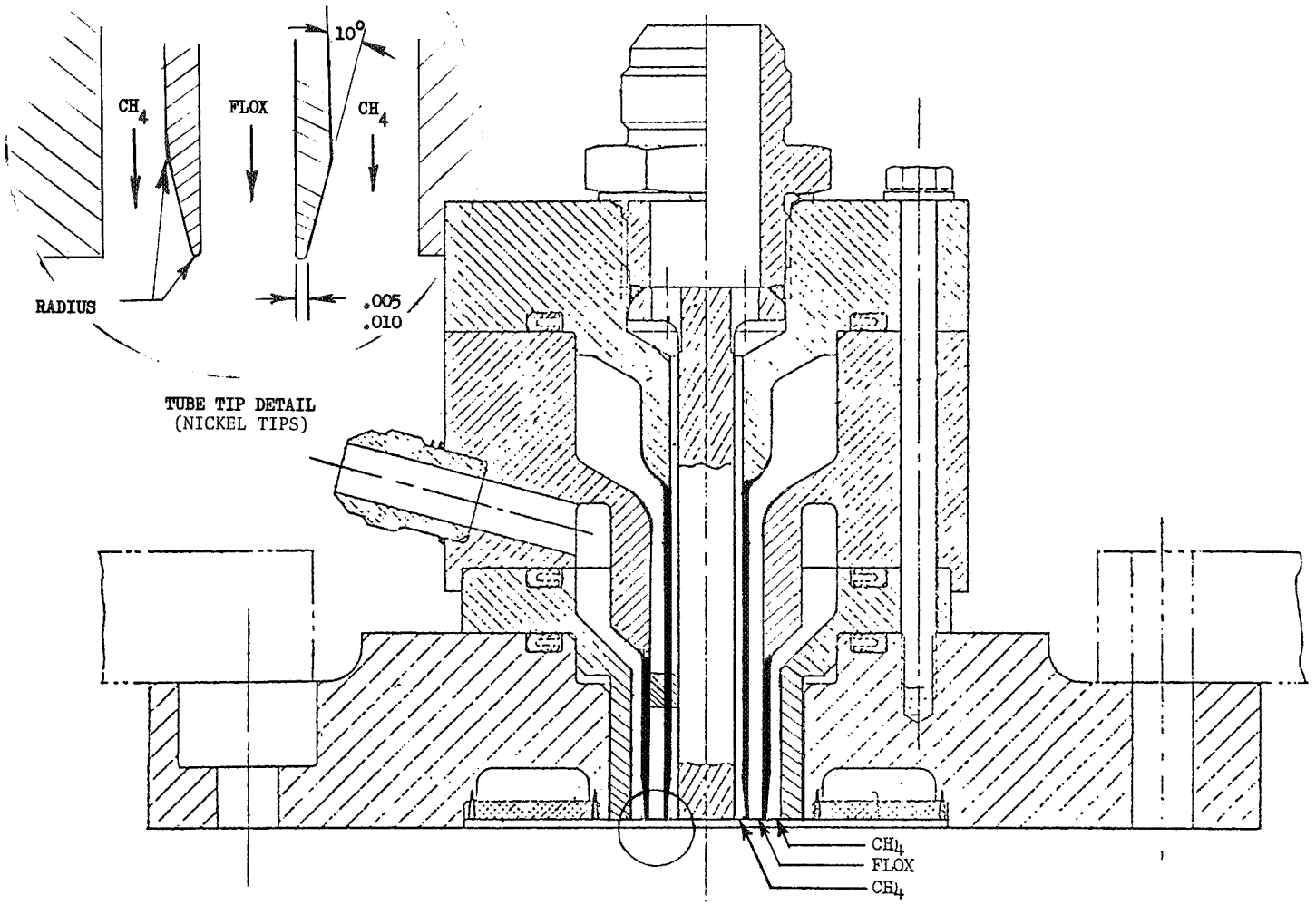

Figure 125 Tricentric With Centerbody Injector Modifications

Posttest inspection again revealed no hardware damage. Therefore, a longer duration test (No. 28) was run with the same operating conditions as the previous test. No hardware damage was encountered and test results were satisfactory. The combustion efficiency for this test was approximately 82.5 percent which is very close to the efficiency predicted from the cold-flow results (η_c*pred = 81 percent) from Task II and III for these design/operating conditions.

Tests No. 29 and 30. Test No. 29 was essentially a repeat of test No. 27 except for increasing the injection temperature of the fuel. The same hardware was used, and a 400-msec (400 x 10^{-3}s) duration was planned as a safety precaution with the increased fuel injection temperature. During the test, the actual fuel flowrate was somewhat higher than planned (MR = 4.6), but no hardware damage occurred.

This test was then repeated for a longer duration, 2.3 seconds in test No. 30. Although an attempt was made to decrease the fuel flowrate from test No. 29, the actual test mixture ratio was 4.8. No injector damage was encountered during this test; however, slight chamber erosion did occur at the downstream edge of the bomb ring and the upstream portion of the combustion chamber. This erosion was most likely perpetrated by discontinuities in the chamber walls at the joint between the bomb ring and chamber and/or by inadequate heat sink capability in the vicinity of the blank pulse gun and Photocon ports. The chamber damage was repaired and the test duration was decreased to approximately 2 seconds for subsequent tests in an effort to minimize chamber erosion.

Test No. 31. In an effort to approach as close as possible to the nominal (i.e., more nearly optimum), geometry (damaged in test No. 25) without fabricating new hardware, the outer fuel annulus used in tests 26 through 30 (A_{in}/A_{out} = 1.5) was machined out to obtain equal inner and outer fuel annulus

injection areas* and a 0.43-in. (1.09×10^{-2}m) centerbody diameter was used surrounded by gas, liquid, and gas annulus gaps of 0.072, 0.101, and 0.039 in. (0.183, 0.257 and 0.099×10^{-2}m), respectively. The posts separating the liquid annulus from the two gas annuli were 0.035 in. (0.089×10^{-2}m) thick but were chamfered (from the gas sides) and rounded at the tips. Approximately 4 percent of the fuel was used as coolant for the injector Rigimesh. The thrust chamber for this test contained a steel pulse gun ring (bomb ring) mounted at the injector end with a copper press fit insert, an uncooled copper combustion zone, and a steel nozzle with a graphite throat insert. The injector-to-throat length was 15.4 in. (0.39 m) and the resultant L* was 30 in. (0.76 m). The test was programmed for 2.0 seconds of mainstage at 500-psia (345×10^4 N/m^2) chamber pressure and 5.75 mixture ratio with a fuel injection stagnation temperature of 860 R (478 K). During the test, the actual FLOX flowrate was lower than planned (MR = 5.3), and the chamber pressure was 474 psi (327×10^4 N/m^2). Pertinent operating conditions and performance numbers for this test and all other tricentric with centerbody tests are listed in Table 28. The c* efficiency for run 31 was 91.8 percent based on P_c and about 0.7 percent lower based on thrust. Examination of the oxidizer injection Photocon and the chamber pressure Photocon indicated that stable combustion was attained.

Posttest inspection of the hardware revealed damage to the thrust chamber and copper chamber spacer insert. A photograph of the damaged pieces is presented in Fig. 126. Scalloped areas (maximum erosion) coincided approximately with ports in the pulse gun ring. Repair procedures resulted in fabrication of a new combustion chamber containing a stainless-steel shell and a graphite insert with a 13.8 in. (0.35 m) length and a 3.7 in. (0.094 m) inner diameter. This maintained the injector-to-throat length of 15.4 in. (0.39 m) and the resultant L* of 30 in. (0.76 m). A schematic of this thrust chamber is presented in Fig. 118.

*The inner-to-outer fuel annulus gap ratio thus became 1.9 with this injector compared to the nominal ("optimum") design value of 2.4.

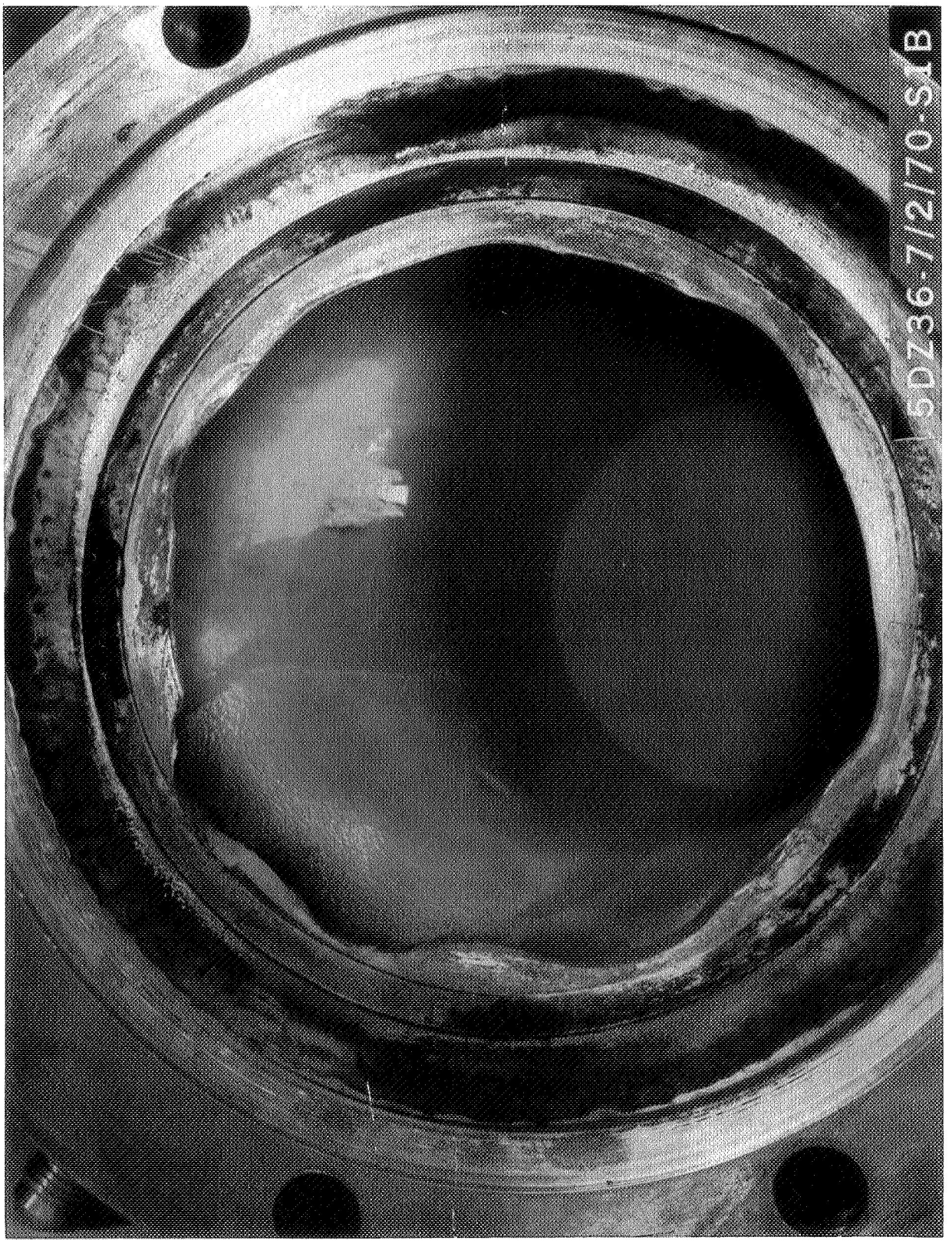

Figure 126. Thrust Chamber Damage Incurred During Test No. 31

Test No. 32 through 35. The low FLOX injection velocity (25 ft/sec; 7.6 m/s) injector model was employed for tests 32 through 35. The injector contains a 0.43-in. (1.09×10^{-2}m) centerbody diameter surrounded by gaps of 0.066, 0.251, and 0.026 in. (0.168, 0.638, and 0.066×10^{-2}m), respectively, with chamfered and rounded tube tips. This yields an inner-to-outer annulus fuel area of 1.0, a fuel annulus gap ratio of 2.5, an oxidizer injection area of 0.70 in.^{2} (4.52×10^{-4}m^2), and a fuel injection area of 0.2 in.^{2} (1.29×10^{-4}m^2).

Stainless steel was used for the injector FLOX tubes in test No. 32. This test was programmed for 2.0 seconds of mainstage at 500-psia (345×10^4 N/m^2) chamber pressure and 5.75 mixture ratio with 860 R (478 K) fuel injection temperature. However, a rough combustion cutoff was encountered approximately 550 msec (550×10^{-3}s) into the test. Analysis of the stability records indicated 200 to 300 psi (138 to 207×10^4 N/m^2) peak-to-peak instabilities at a 500 to 600 Hz frequency. Posttest inspection revealed that the FLOX tubes were burned back approximately 3/4 in. (1.9×10^{-2}m) from the injector face, indicating FLOX ignition with the stainless-steel posts.

The FLOX posts were replaced with nickel-tipped posts for test No. 33, bringing this injector model back to its original condition. This test was programmed for 400-msec (400×10^{-3}s) duration with all other operating conditions the same as with test No. 32. Although rough combustion of approximately the same frequency but 150 psi (103×10^4 N/m^2) peak-to-peak amplitude was observed, no cutoff was encountered and posttest hardware inspection revealed no damage.

Test No. 34 was a repetition of No. 33 with the duration extended to 2.0-seconds of mainstage. The same rough combustion was again observed during mainstage. However, no hardware damage was encountered and the test results were satisfactory, although the combustion efficiency was only 82 percent. The rough combustion, which was of a feed-system-coupled variety, may have influenced the performance attained.

All test conditions except the fuel injection temperature were then held constant for test No. 35. Ambient methane was used for this test with a 2.0-second mainstage duration and a 500-psi (345 x 10^4 N/m^2) chamber pressure. The measured performance was in the low 80's with instabilities similar to those described for tests No. 33 through 35.

Tests No. 36 through 38. In an effort to increase combustion efficiency and eliminate chugging, the injector model used in test No. 31 was again used in tests No. 36 through 38. All three of these tests were programmed for 2.0 seconds of mainstage and a 500-psi (345 x 10^4 N/m^2) chamber pressure. A 5.75 mixture ratio was planned for tests No. 36 and 37, while a mixture ratio perturbation (to 4.5) was planned for No. 38 with all other conditions constant. In addition, hot methane (approximately 900 R; 500 K) was programmed for tests No. 36 and 38 while ambient methane was to be used for test No. 37.

The mainstage duration of test No. 38 was cut after approximately 1 second of mainstage because of the lack of sufficient oxidizer in the propellant tanks. No hardware damage was encountered on any of these tests and test results were satisfactory. Combustion performances were in the 91-percent range for tests No. 36 and 37 but increased to approximately 98 percent during the low mixture ratio test. No instabilities were present in these tests.

Test No. 55. The promising results from test No. 38 led to the repair of the injector configuration damaged in test No. 25. This was the nominal tricentric with centerbody injector with the geometry that was optimum in cold-flow tests. Nickel tips and chamfered tube ends were again used, and the injector dimensions were the same as for tests No. 24 and 25. The test was programmed for a two-second mainstage duration at 500-psia (345 x 10^4 N/m^2) chamber pressure and a 5.25 mixture ratio with a 900 R (500 K) fuel injection temperature.

In the actual test, the Naflex pressure-assisted seal in the oxidizer dome failed (leaked) during chamber pressure buildup resulting in significant damage to the injector and to facility wiring. Photographs of the injector

damage are given in Fig. 127, 128, and 129. The injector orifice element details were considered beyond repair although the face plate (body) was repairable. Face plate repair was accomplished by removing the eroded area, the Rigimesh face, and the inserting of a graphite cloth ablative material to form a new face (Fig. 130). The repaired injector body was used for the subsequent tests (59 through 63).

Tests 59, 60, 61, and 62. In an effort to increase performance with available or easily altered hardware, the configuration used in test No. 38 was modified to incorporate 0.200 in. (0.508×10^{-2} m) FLOX annular recess and used in these tests. All four of these tests were programmed for 2.0 seconds of mainstage at a 500 psia (345×10^4 N/m^2) chamber pressure. The mixture ratio was varied from 4.25 to 6.0.

The actual chamber pressure attained during these tests varied from 417 to 591 psia (288 to 407×10^4 N/m^2) because of higher than anticipated injector pressure losses which were indicative of varying degrees of combustion occurring in the recessed portion of the injector tubes. Combustion performances were high, on the order of 96 to 98 percent, and no instabilities were evident. The hardware was in pre-test condition except for minor erosion of the ablative injector face.

Test No. 63. The injector configuration utilized in the preceding tests was throttled to a 50 psia (34×10^4 N/m^2) chamber pressure in this test. The planned mainstage duration was 4.0 seconds at a 5.25 mixture ratio. Although a chamber pressure of 70 psia (48×10^4 N/m^2) was recorded, reduced data revealed that this did not occur until after the oxidizer main valve had closed, thus indicating steady-state combustion was not attained. Test results were not satisfactory in that no performance data were obtained. Failure to achieve steady-state performance at this throttled condition was attributed to facility propellant feed problems. Programming for an extended run duration would probably permit satisfactory throttle tests. However, further testing was not attempted because of program limitations.

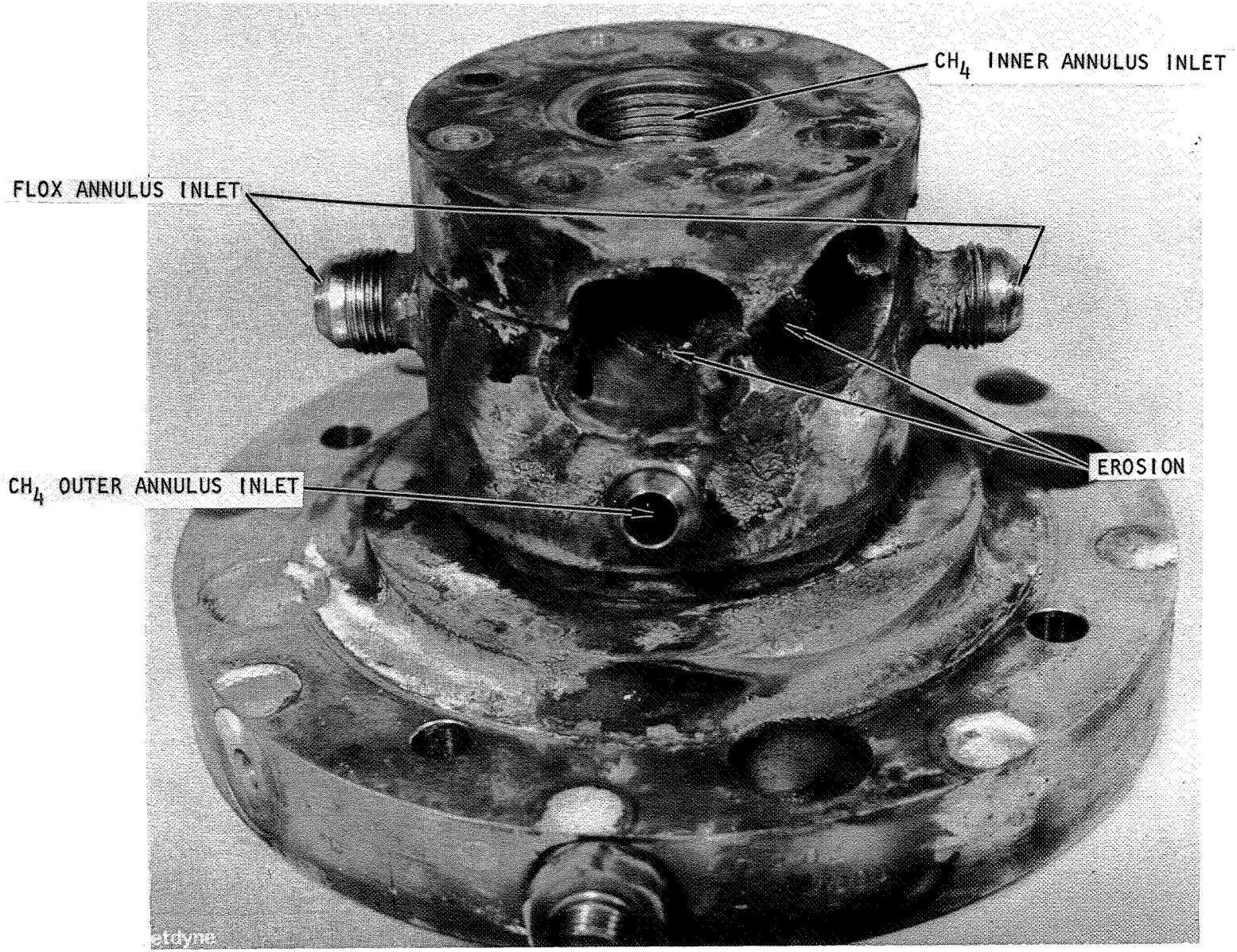

5AA36-8/5/70-S1M

Figure 127. Injector Damage Incurred During Test No. 55 (Upstream Side)

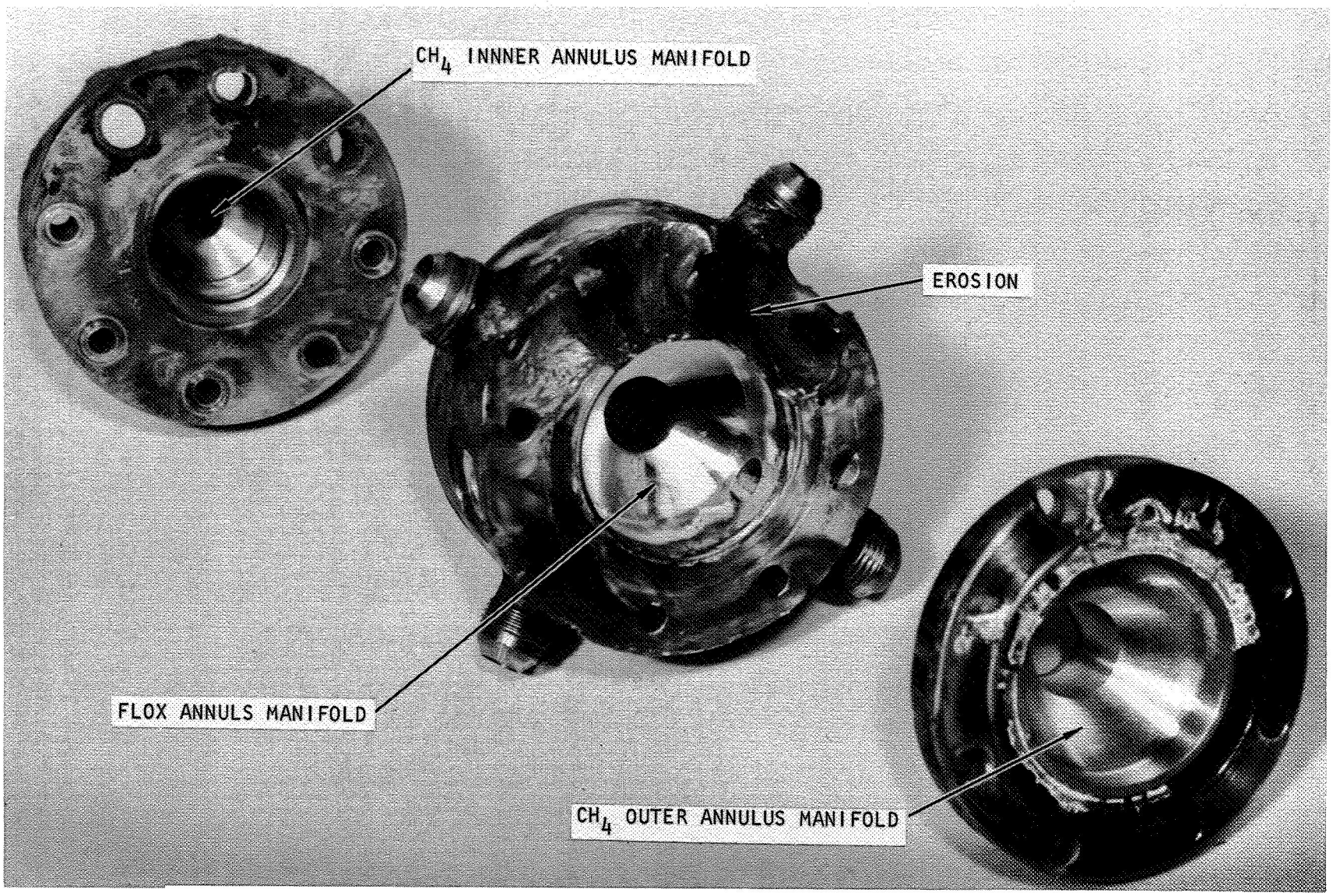

5AA36-8/5/70-S1E

Figure 128 Oxidizer and Fuel Manifold Damage Incurred During Test No. 55

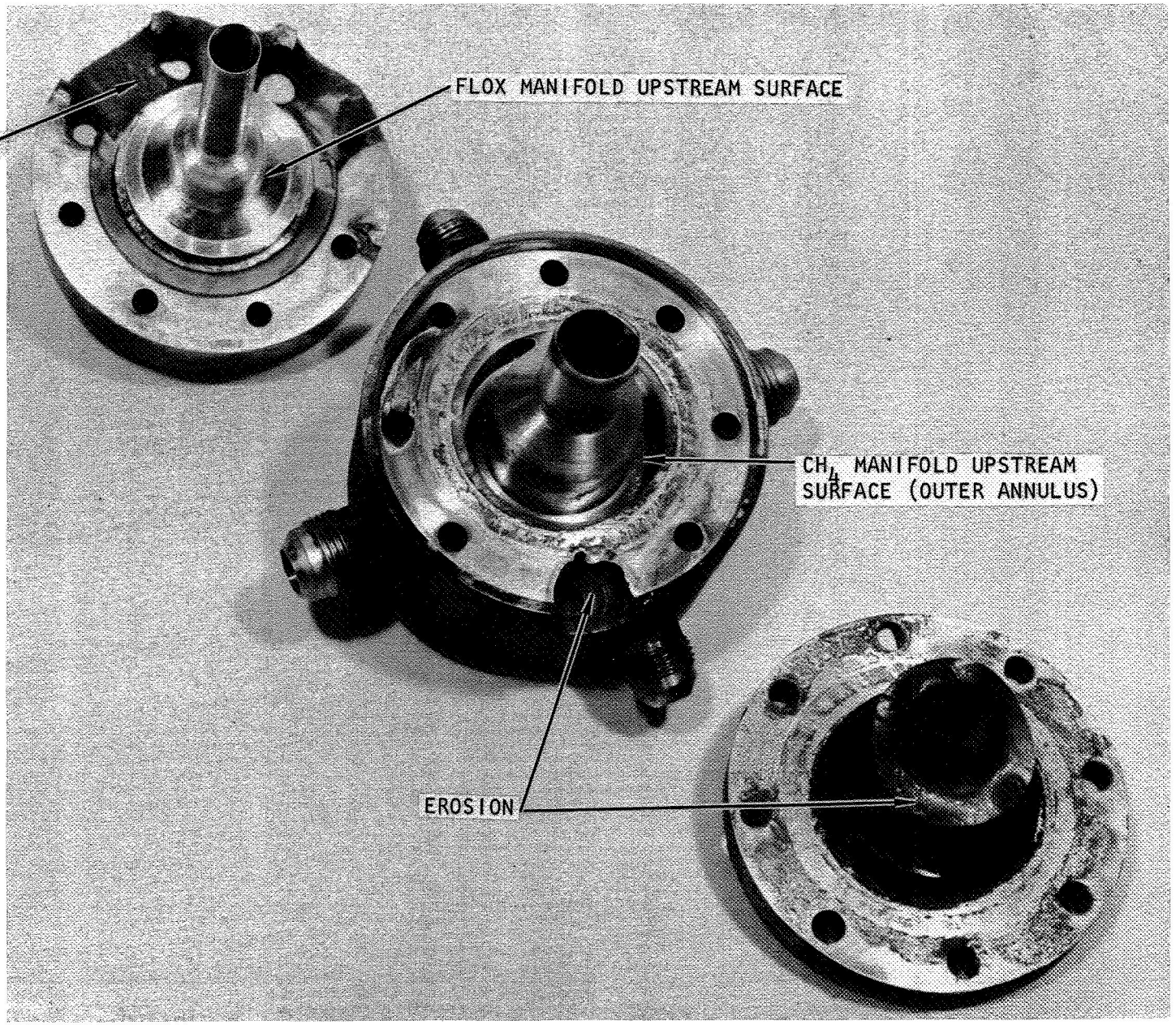

5AA36-8/5/70-S1D

Figure 129. Oxidizer and Fuel Injector Element Damage Incurred During Test No. 55

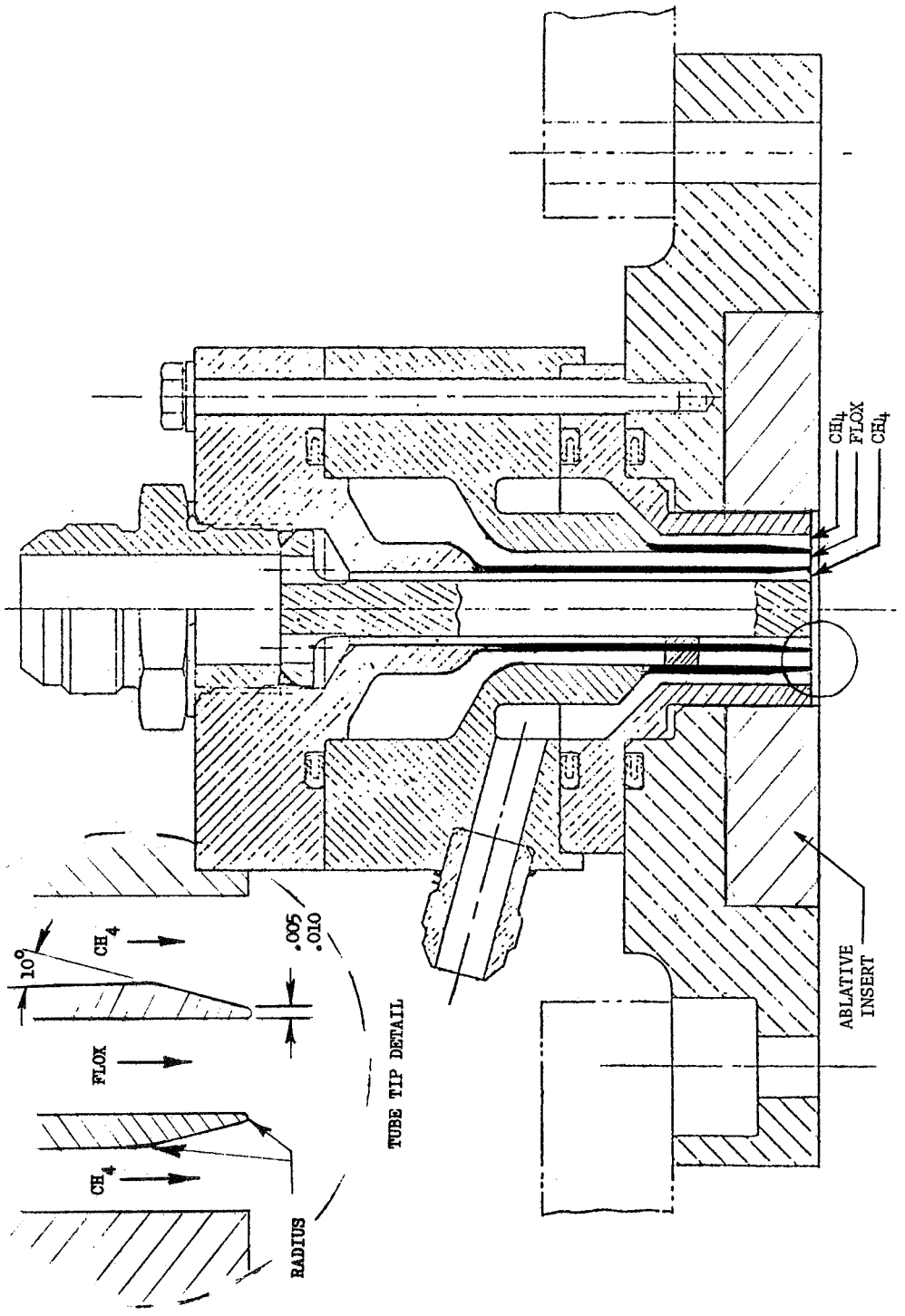

Figure 130. Tricentric With Centerbody Injector With Ablative Face Insert

Impinging Concentric Tests. This test series was formulated to demonstrate performance and stability of the impinging concentric injector concept. Performance goals included demonstration of η_c^* = 96 percent at MR = 5.75 and parametric evaluation of the following parameters: X_p/D_g, $\rho_g V_g^2$, D_ℓ/D_g, scale (indexed by D_ℓ), percent annulus gas, and one throttle test. Although not included in the original test plan, a post recess was also investigated. The initial five tests (tests 39 through 43) with this injector concept were conducted with liquid orifice diameters of approximately 0.24 in. (0.61×10^{-2}m). During these tests, the effects of varying injection velocity ($\rho_g V_g^2$), the center fuel orifice diameter (D_ℓ/D_g), and annulus fuel injection areas (percent annulus gas) were investigated. Performance increased with increasing fuel injection velocity but only to the low 90's while cup recirculation, and therefore erosion of the stainless-steel material, increased substantially with V_g. The latter problem was eliminated by using an ablative cup. A change in the percentage of annulus gas at constant geometric conditions was found to have negligible influence on performance.

The 0.19-in. (0.48×10^{-2}m) liquid diameter (higher injection ΔP) orifice tubes were used next in an attempt to increase performance. This was suggested for increased performance from cold-flow tests. In these tests (tests 44 through 48), the center fuel injection orifice diameter (D_ℓ/D_g) was varied. In addition, the effects of varying the fuel injection temperature and velocity ($\rho_g V_g^2$) was investigated with constant geometric conditions. Combustion performance increased to the 95 percent level. The liquid tubes were recessed slightly (0.200 in.; 0.508×10^{-2}m) for the next tests, while varying the center fuel orifice diameter (D_ℓ/D_g) first and then the injected mixture ratio (X_p/D_g). Results (tests 49 through 54) yielded no significant gain in performance, however. To raise the performance loss in the available remaining tests and to empirically verify the analyses, the chamber characteristic length was increased to 57.6 in. (1.46 m) in the concluding tests (56 through 58) with this injector concept. Results revealed combustion efficiencies in the 98- to 99-percent range. A description of the individual tests is given below.

Tests 39 and 40. The initial test, No. 39, with the impinging concentric injector concept was made with liquid post inside diameters equal to 0.234 in. (0.594×10^{-2}m), thus yielding a FLOX injection velocity of approximately 100 ft/sec (30.5 m/s). The center fuel jet had a 0.744-in. (1.89×10^{-2}m) diameter; thereby making $D_\ell/D_g = 0.32$ and resulting in a center fuel velocity of approximately 600 ft/sec (183 m/s). Seventy-five percent of the fuel was injected through this central showerhead orifice, approximately 5 percent of the fuel was used as face coolant, and the remaining 20 percent was injected through the annulus fuel tubes. The test was programmed for 500 msec (500×10^{-3}s) of mainstage at a 500-psi (345×10^4 N/m^2) chamber pressure, 5.75 mixture ratio, and a fuel injection temperature of 1000 R (556 K).

Operating conditions for this test and all other tests made with the impinging concentric injector concept are presented in Table 29. Posttest inspection revealed that one of the stainless-steel FLOX tubes was slightly eroded at the tip. This tube was replaced with a nickel tube so three stainless and one nickel tube were employed for test No. 40. Test No. 40 was a repetition of test No. 39 except for a longer duration (2 seconds). The performance was low (~89 percent). No indication of any instabilities was observed in this or any subsequent tests with the impinging concentric injector. Posttest inspection again revealed tube tip erosion to one stainless-steel tube and very slight erosion in the stainless-steel cup between two of the FLOX tubes. All stainless tubes were replaced with nickel or nickel-tipped tubes for the remainder of the impinging concentric tests.

Test No. 41. For this test, the same operating conditions and FLOX injection areas were used. However, the center gas and annular fuel injection areas were decreased to obtain higher injection velocities. A 0.553-in. (1.40×10^{-2}m) diameter center tube was employed, making $D_\ell/D_g = 0.44$, and the annulus fuel injection area was reduced to 0.05 in.^{2} (0.32×10^{-4}m^2) (from 0.12 in.^{2}; 0.77×10^{-4}m^2 in test No. 39 and 40). The fuel flowrate was again split approximately 75, 20, and 5 percent in the center jet, annulus jets, and face coolant, respectively. The test was programmed for

TABLE 29

IMPINGING CONCENTRIC INJECTOR HOT-FIRE TEST RESULTS

Test No.	Duration, seconds	D_ℓ		D_g		Annulus Gap (Y_f)		$\frac{D_\ell}{D_g}$	Post Recess D_ℓ	P_c (nozzle)		F_{vac}		T_g		$\dot{w}_o$		$\dot{w}_f$ (total)		$\dot{w}_{f(center)}$		MR	$\left(\frac{\dot{w}_{ann}}{\dot{w}_{tot}}\right)_f$	$(V_g)_{center}$		$(V_g)_{ann}$		V_ℓ		$(\rho_g V_g^2)_{center}$		$\frac{X_p}{D_g}$	η_{c^*} From P_c, %	η_{c^*} From F, %
		in.	m x 10^{-2}	in.	m x 10^{-2}	in.	m x 10^{-2}			psia	N/m^2 x 10^4	lb	N	R	K	lb/sec	kg/s	lb/sec	kg/s	lb/sec	kg/s			ft/sec	m/s	ft/sec	m/s	ft/sec	m/s	psi	N/m^2 x 10^4			
39	0.46	0.234	0.594	0.744	1.890	0.027	0.069	0.32	0	479	330	3634	16,164	865	481	10.75	4.88	1.90	0.86	1.40	0.64	5.65	0.20	559	170	474	144	99	30.2	56	39	1.03	92.3*	90.6*
40	1.96	0.234	0.594	0.744	1.890	0.027	0.069	0.32	0	502	346	3857	17,160	992	551	11.69	5.30	2.04	0.92	1.51	0.68	5.72	0.20	657	200	547	167	111	33.8	71	49	1.01	89.1	88.5
41	2.03	0.243	0.617	0.553	1.405	0.012	0.030	0.44	0	522	360	4011	17,840	1096	609	11.87	5.38	2.01	0.91	1.48	0.67	5.92	0.20	1152	351	1643	501	104	31.7	220	152	0.75	92.7	91.5
42	2.05	0.243	0.617	0.553	1.405	0.026	0.066	0.44	0	513	354	4010	17,840	1091	606	11.76	5.33	2.05	0.93	1.33	0.60	5.73	0.35	1067	325	1212	369	104	31.7	184	127	0.82	92.2	91.9
43	2.05	0.243	0.617	0.454	1.153	0.026	0.066	0.54	0	484	334	3810	16,950	1087	604	11.20	5.08	2.09	0.95	1.36	0.62	5.35	0.35	1644	501	1306	398	99	30.2	427	294	0.62	91.5	91.2
44	2.16	0.189	0.480	0.553	1.405	0.021	0.053	0.34	0	476	328	3780	16,810	1113	618	10.49	4.76	2.22	1.01	1.65	0.75	4.73	0.26	1418	432	1481	451	152	46.3	303	209	0.73	96.1	95.9
45	2.16	↓	↓	0.553	1.405	↓	↓	0.34	0	523	361	4169	18,540	1129	627	11.78	5.34	2.26	1.03	1.69	0.77	5.22	0.25	1337	408	1409	429	171	52.1	292	201	0.84	95.1	95.0
46	2.15			0.454	1.153			0.42	0	487	336	3933	17,490	1085	603	11.28	5.12	2.10	0.95	1.57	0.71	5.36	0.26	1863	568	1336	407	165	50.3	560	386	0.71	93.3	94.1
47	2.12			0.454	1.153			0.42	0	537	370	4334	19,280	578	321	12.60	5.72	2.42	1.10	1.81	0.82	5.21	0.25	1036	316	745	227	187	57.0	360	248	0.99	92.3	93.0
48	2.14			0.553	1.405			0.34	0	507	350	4086	18,170	550	306	13.02	5.91	1.85	0.84	1.31	0.59	7.04	0.29	552	168	669	204	189	57.6	94	65	1.63	94.0**	92.5**
49	2.16			0.553	1.405			0.34	1	486	335	3640	16,190	1087	604	10.14	4.60	2.03	0.92	1.51	0.68	4.99	0.26	1275	389	1234	376	148	45.1	250	172	0.78	96.3	94.3
50	2.14			0.603	1.532			0.32	1	484	334	3663	16,290	1068	593	10.21	4.63	2.03	0.92	1.51	0.68	5.02	0.26	1066	325	1219	372	149	45.4	176	121	0.86	95.3	94.3
51	2.13			0.454	1.153			0.43	1	482	332	3639	16,190	1069	594	10.21	4.63	2.03	0.92	1.51	0.68	5.03	0.26	1889	576	1229	375	151	46.0	571	394	0.65	95.2	93.8
52	2.12			0.553	1.405			0.34	1	515	355	3902	17,360	581	323	10.76	4.88	2.44	1.11	1.82	0.83	4.41	0.26	759	231	792	241	158	48.2	179	123	0.98	96.0	95.0
53	2.14			0.553	1.405			0.34	1	522	360	3939	17,520	565	314	11.56	5.24	2.19	0.99	1.64	0.74	5.28	0.25	664	202	683	208	171	52.1	141	97	1.19	92.2	90.6
54	2.14			0.553	1.405			0.34	1	507	350	3670	16,320	555	308	12.66	5.74	1.94	0.88	1.45	0.66	6.51	0.25	600	183	622	190	186	56.7	113	78	1.45	86.4	81.1***
56	2.17			0.553	1.405			0.34	1	505	348	3749	16,680	887	493	10.29	4.67	2.08	0.94	1.53	0.69	4.93	0.26	1122	342	984	300	153	46.6	223	154	0.84	99.4	97.6
57	2.15			0.454	1.153			0.43	1	511	352	3784	16,830	859	477	10.30	4.67	2.20	1.00	1.64	0.74	4.69	0.25	1559	475	1048	319	154	46.9	490	338	0.70	99.9	98.0
58	2.13	↓	↓	0.553	1.405	↓	↓	0.34	1	514	354	3797	16,890	568	316	10.77	4.89	1.94	0.88	1.45	0.66	5.55	0.25	630	192	643	196	160	48.8	119	82	1.21	98.2	95.8

*Too short duration for performance calculations (0.500 seconds or less)
**Ran out of methane during test
***Lost piece of nozzle exit during test, thereby making thrust measurement unreliable

L* = 57.6 in. (1.46 m) for tests 56-58
L* = 30 in. (0.76 m) for all other tests

2 seconds of mainstage at a 500-psi (345×10^4 N/m^2) chamber pressure and a 5.75 mixture ratio.

A performance gain of about 2.5 percent was realized with the higher gas velocities. However, posttest inspection revealed significant erosion, about 1/8 in. (0.32×10^{-2}m) deep, in the stainless-steel portions of the injector cup between the FLOX orifices. A photograph of the injector damage is presented in Fig. 131. The increased fuel injection velocity apparently significantly increased the cup recirculation resulting in the injector cup erosion.

Injector repair procedures included cleaning up the eroded section of the cup, thereby making a slightly deeper cup, and machining a graphite insert to replace the Rigimesh face coolant. A schematic of the injector assembly is presented in Fig. 132.

Tests No. 42 and 43. Essentially the same geometry and operating conditions were employed in test No. 42 as in 41. The main difference was that the annulus fuel flowrate was increased to approximately 35 percent in an effort to limit the cup recirculation as had been done successfully in Task I, and simultaneously to evaluate the effect of percent annulus gas on performance as required in the test plan. No face coolant fuel was required with the repaired injector.

Posttest inspection revealed minor cup erosion similar in position to the erosion in test No. 41 but not as deep or extensive. However, the combustion efficiency was only approximately 91 percent, so the (center) fuel injection velocity was again increased by decreasing the center jet diameter for test No. 43. All other operating conditions and test hardware remained constant except the targeted mixture ratio. This was decreased to 5.35 in an additional effort to increase performance. A 2-second mainstage duration was again employed.

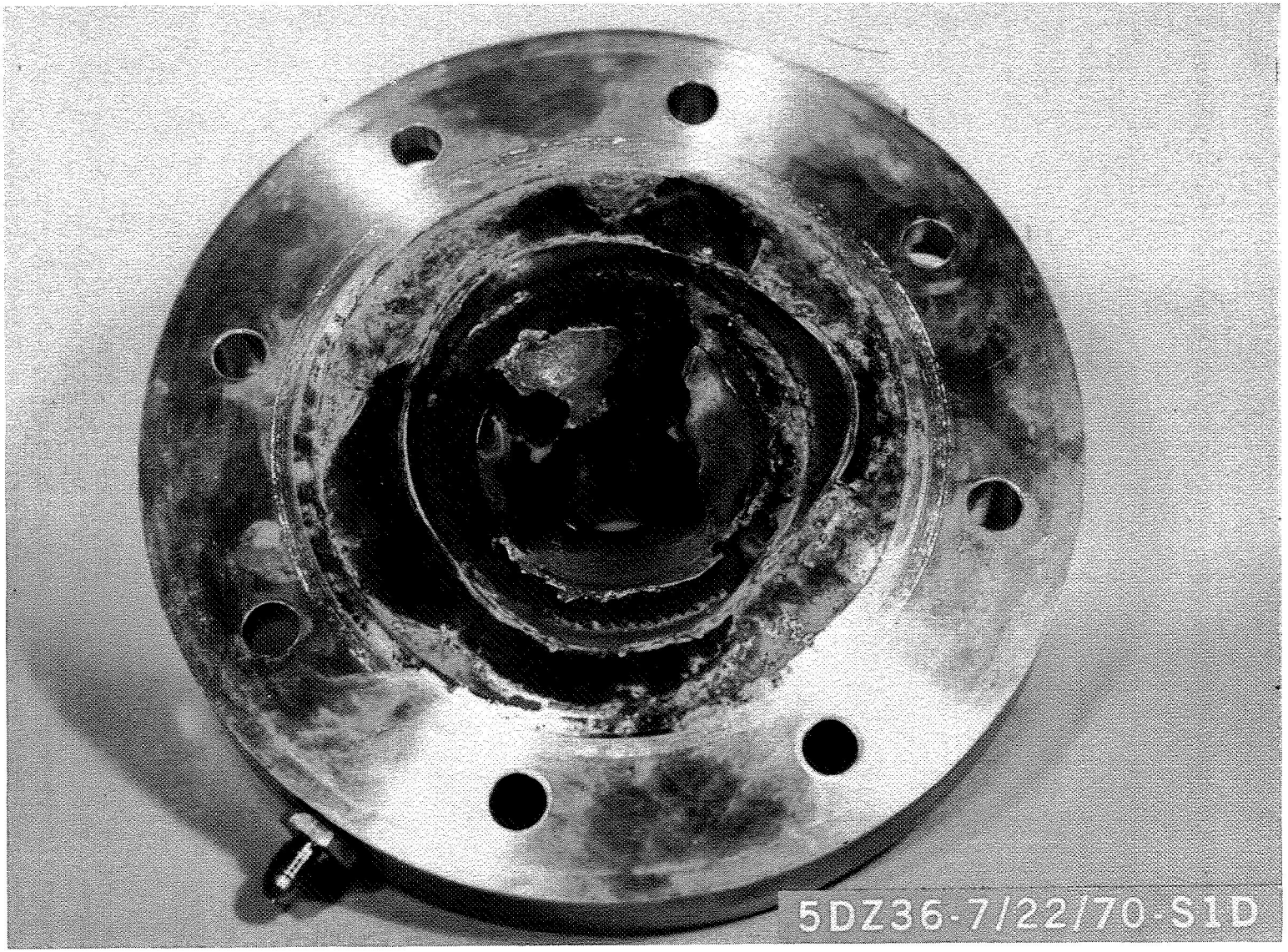

Figure 131. Impinging Concentric Injector Damage Incurred in Test No. 41

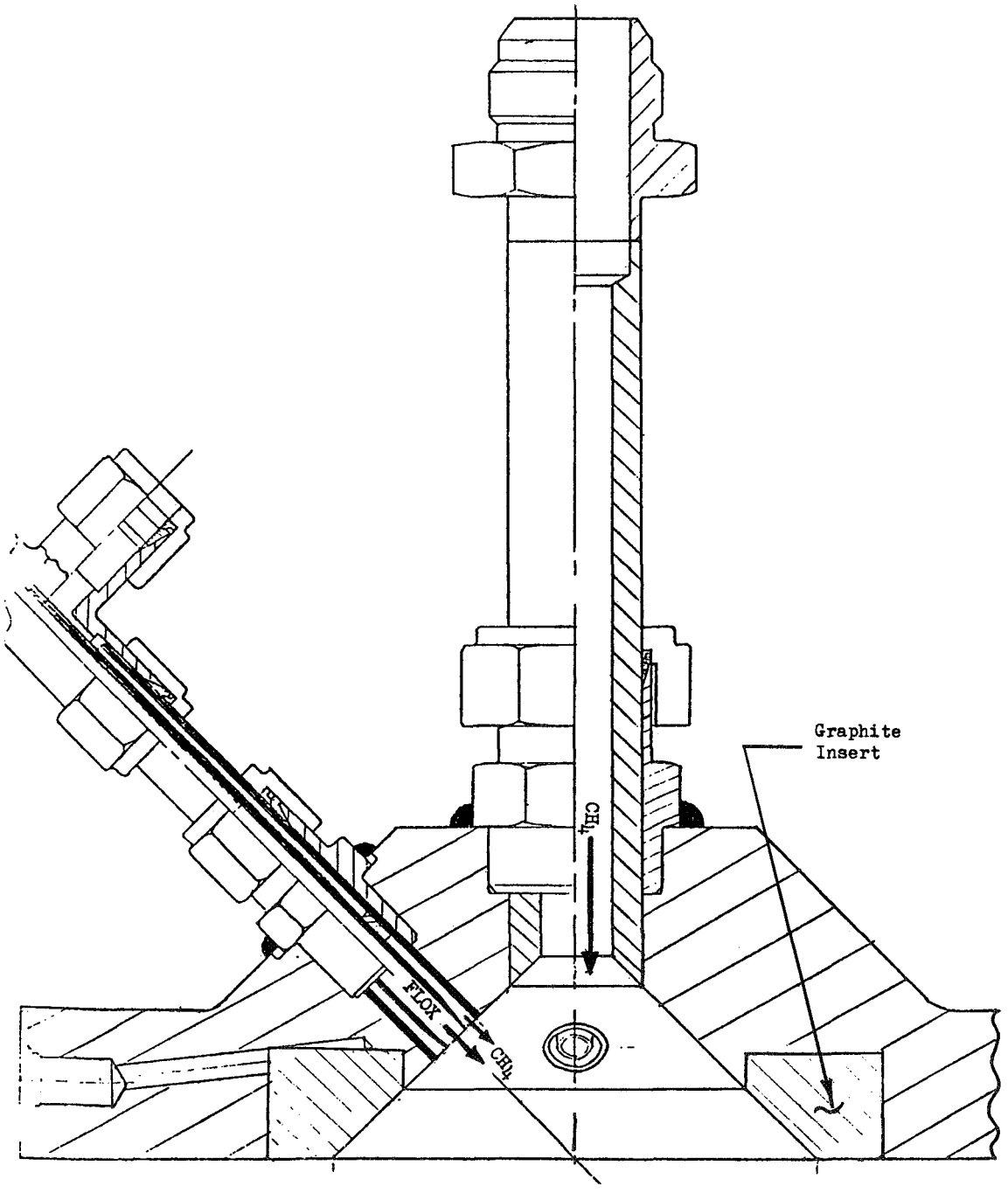

Figure 132. Recessed Impinging Concentric Injector With Steel and Graphite Cup

Posttest inspection revealed hardware damage similar to that occurring in test No. 41. The increased fuel injection velocity induced more recirculation resulting in significant injector erosion, approximately 1/4 in. (0.64 x 10^{-2}m) deep, in the stainless-steel sections between the FLOX tubes and 3/8-in. (0.95 x 10^{-2}m) deep in one of the stainless-steel annulus tubes. However, the graphite section of the cup was still intact. The performance which may have been influenced by erosion of one of the annulus tubes attained in test No. 43 was still in the 91-percent range and no instabilities were observed. Injector repair included machining the cup back approximately 0.7 in. (1.8 x 10^{-2}m) deeper and fabricating a carbon cloth ablative cup insert to replace the eroded stainless steel and the graphite piece used in test No. 43. This essentially returned the cup to its original dimensions. A schematic of the injector repair is presented in Fig. 133.

Tests No. 44 through 48. The liquid tube diameter was decreased to 0.19 in. (0.48 x 10^{-2}m) for tests No. 44 through 48 in an effort suggested by the cold-flow correlations to increase performance. This resulted in increased injector pressure drops (400 to 500 psi; 276 to 345 x 10^4 N/m^2), but the cold-flow data indicated approximately 4-percent gain should be attained in combustion efficiency. The targeted mixture ratio was set at 5.25. Approximately 26 percent of the fuel was employed as annulus fuel. The center fuel orifice diameter (0.533 and 0.445 in.; 1.40 and 1.13 x 10^{-2}m) and the fuel injection temperature (1100 and 570 R; 611 and 317 K) were varied during these tests. A 2.15-second mainstage duration was obtained in each of these five tests at a nominal 500-psi (345 x 10^4 N/m^2) chamber pressure.

Posttest inspection of all five tests revealed only very minor erosion of the ablative cup and of one stainless-steel annulus tube. The actual mixture ratio obtained in the first test was somewhat lower than planned (4.73) because of higher than anticipated system pressure loss. This was corrected in tests No. 45, 46, and 47 and target mixture ratios were obtained. The methane manifold pressure was too low (because of lack of methane in the K-bottle bank) in test No. 48 resulting in an increasing mixture ratio

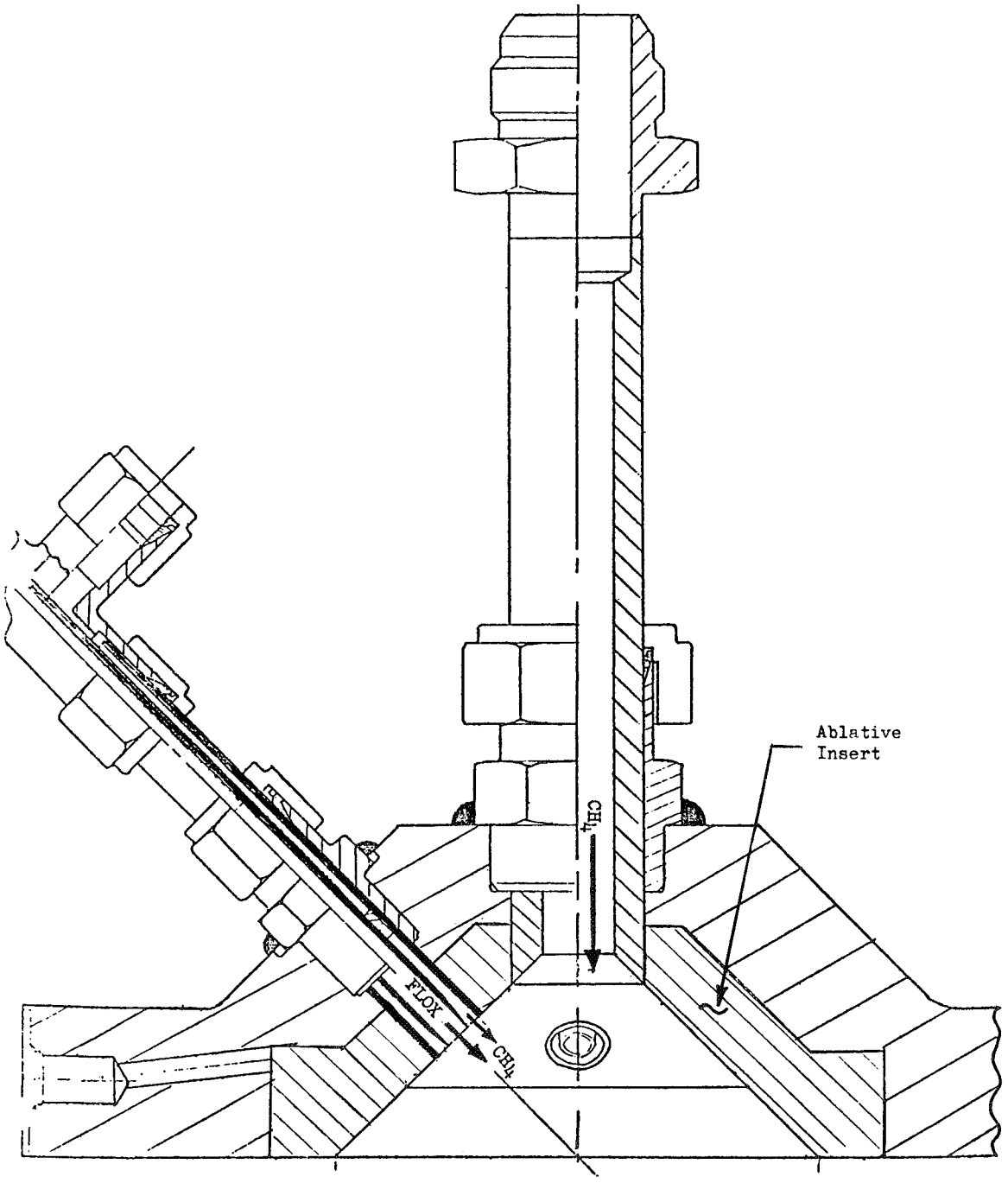

Figure 133. Recessed Impinging Concentric Injector With Ablative Cup

throughout the mainstage duration. However, no hardware damage occurred. Combustion efficiencies increased by approximately 3 percent reaching 95 percent at 5.22 mixture ratio (test No. 45) and 96 percent at a mixture ratio of 4.73 (test No. 44). Combustion was stable during each of these tests.

Tests No. 49 through 51. Tests 49 through 51 were conducted with recessed FLOX tubes. The same FLOX tube diameter and annulus fuel tubes were used for these tests as in tests 44 through 48, but a 0.200-in., 0.508 x 10^{-2}m (one liquid post diameter), recess was employed. These tests were programmed for a 2-second mainstage duration at a 500 psi (345 x 10^4 N/m^2) chamber pressure, a 5.25 mixture ratio, a 1070 R (594 K) fuel injection temperature, and 26 percent of the fuel in the annulus tubes. The center fuel diameter was varied during these tests from 0.445 to 0.553 to 0.603 in. (1.13 to 1.40 to 1.53 x 10^{-2}m) to find the optimum diameter. No hardware damage or instabilities occurred and test results showed an insignificant (less than 0.5 percent) change in combustion efficiency.

Tests No. 52 through 54. In the next test series, a mixture ratio perturbation was made with the same hardware configuration as was used for test No. 49 (D_g = 0.553 in.; 1.40 x 10^{-2}m). Operating conditions were also the same except for the fuel injection temperature (ambient temperature methane was used) and the mixture ratio (4.4 to 6.5). Posttest inspection revealed very minor erosion in the ablative section of the cup and at one annulus fuel tube. Test results were satisfactory with η_c* ranging from approximately 86 to 96 percent. No evidence of instabilities was observed.

Tests No. 56 through 58. The same injector configuration and essentially the same operating conditions were used in these tests as was used in tests No. 49, 51, and 53. However, the chamber characteristic length was increased to 57.6 in. (1.46 m)(29.2-in.; 0.74 m injector-to-throat length) to reduce performance losses caused by incomplete vaporization.

All tests were programmed for 2 seconds of mainstage duration at 500-psia (345×10^4 N/m^2) chamber pressure and 5.25 mixture ratio. The center fuel injection area was varied in test No. 56 and 57 with approximately 860 R (478 K) fuel injection temperature. An ambient fuel injection temperature was used in test No. 58 while the center fuel tube remained constant. In addition, a series of three pulses, from 20, 40, and 80 grain (1.3, 2.6 and 5.2×10^{-3} kg) charges, were programmed to fire at 200-msec (200×10^{-3} s) intervals in test No. 58 after steady-state performance was achieved. These pulses were directed in the radial, chordal, and tangential directions, respectively. Posttest inspection revealed minor erosion in the ablative section of the cup and in the graphite chamber inserts for test No. 56 and 57. After tests No. 58, hardware inspection revealed the pulse gun disturbances had damaged the graphite liner in the chamber spacer, although damage to the chamber spacer was negligible. Test results were satisfactory with no evidence of instabilities and performances were at the 97 to 99 percent level.

Test Results

Performance. Corrected combustion efficiency was the index of injector performance for the experimental program. This parameter was calculated by two independent methods, one based on chamber pressure and the other based on thrust. The procedures for computing the performance are summarized in Appendix B. Efficiencies based on thrust averaged about 1.1 percent (ranging from 1.3 percent more to 2.5 percent less) less than those based on chamber pressure, although the observed trends were always the same. Techniques for obtaining the chamber pressure and thrust parameters are described in Appendix C along with some factors which may explain the thrust and chamber pressure efficiency differences in Task I. A similar discussion would apply to Task IV results.

Efficiencies from both chamber pressure and thrust are presented in Tables 28 and 29 for all tests with the tricentric with centerbody and impinging concentric injector concept. These results are discussed in the following

sections, where for simplicity in presentation the numerical average of the efficiencies calculated from chamber pressure and thrust is plotted and described.

Tricentric with Centerbody Injector. Twelve tests of sufficient duration for steady-state conditions were conducted with this injector concept. The operating conditions and performance data were presented in Table 28. The parameters investigated included mixture ratio (MR), the difference in injection velocities (V_g-V_ℓ) and FLOX injection velocity (V_ℓ) along with several geometric variables, specifically, the ratios of inner-to-outer gas annulus areas (A_{in}/A_{out}), and annulus gaps $(Y_{in}/Y_{out})_g$.

The measured effect of mixture ratio is illustrated in Fig. 134 for constant geometry, V_ℓ, and essentially constant V_g-V_ℓ. The effect is very similar to the cold-flow predicted performance trends previously observed in Task II and III. As the mixture ratio is decreased from 5.5 to 4.5, the combustion efficiency for this particular geometry increases from approximately 91 to 97.4 percent. Thus, the performance of this injector concept is seen to be quite sensitive to injected mixture ratio.

The data presented in Fig. 134, which is for zero FLOX tube recess, were used to correct all tests made with zero recess to a constant mixture ratio for evaluation of other parameters. The data for the zero recess tests were corrected to a 5.25 mixture ratio and plotted in Fig. 135. Note the slight increase in performance as V_g-V_ℓ increases, i.e., as V_g-V_ℓ increased from about 900 to 1600 ft/sec (274 to 488 m/s), η_c* rose on the order of 3 percent. Similar results were seen in cold-flow vaporization data and in the extrapolations of V_g-V_ℓ versus η_{mix} from cold-flow tests over this range of V_g-V_ℓ. However, cold-flow results indicate a higher degree of performance sensitivity as the injected V_g-V_ℓ is decreased into the 300 to 800 ft/sec (91 to 244 m/s) range.

In addition, orifice geometry effects on η_c* are evident in Fig. 135. The top two curves in this figure represent different values of inner-to-outer

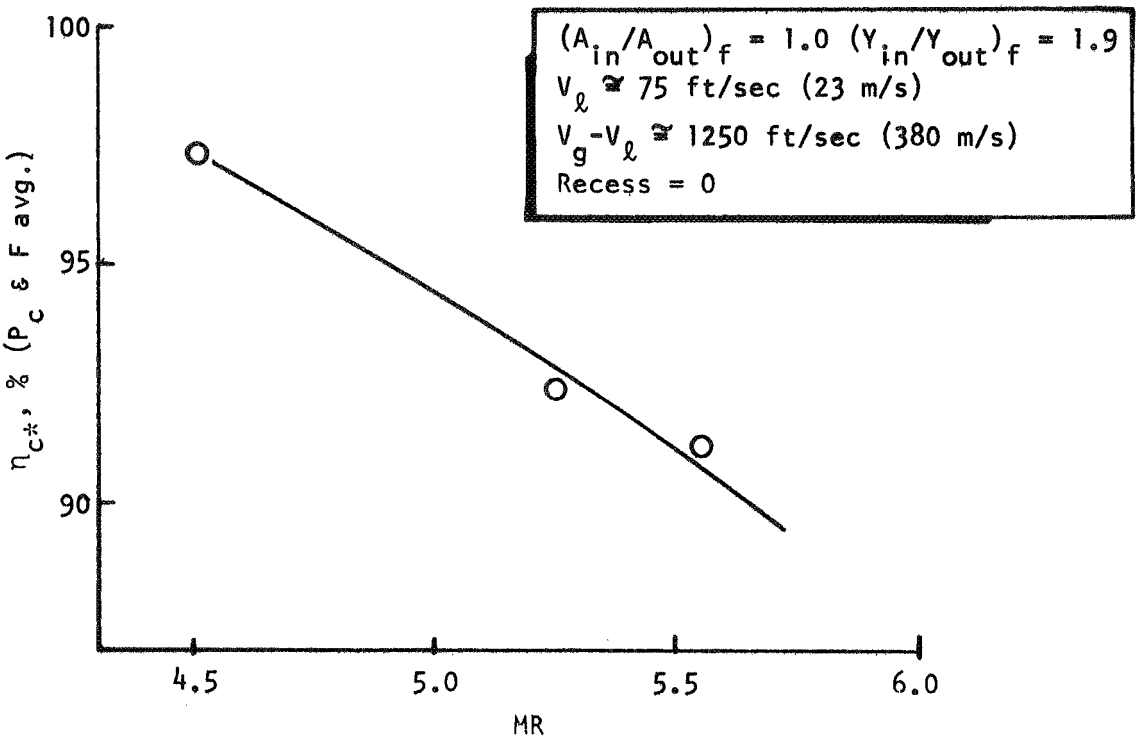

Figure 134. Mixture Ratio Effect on Performance: Tricentric With Centerbody Injector

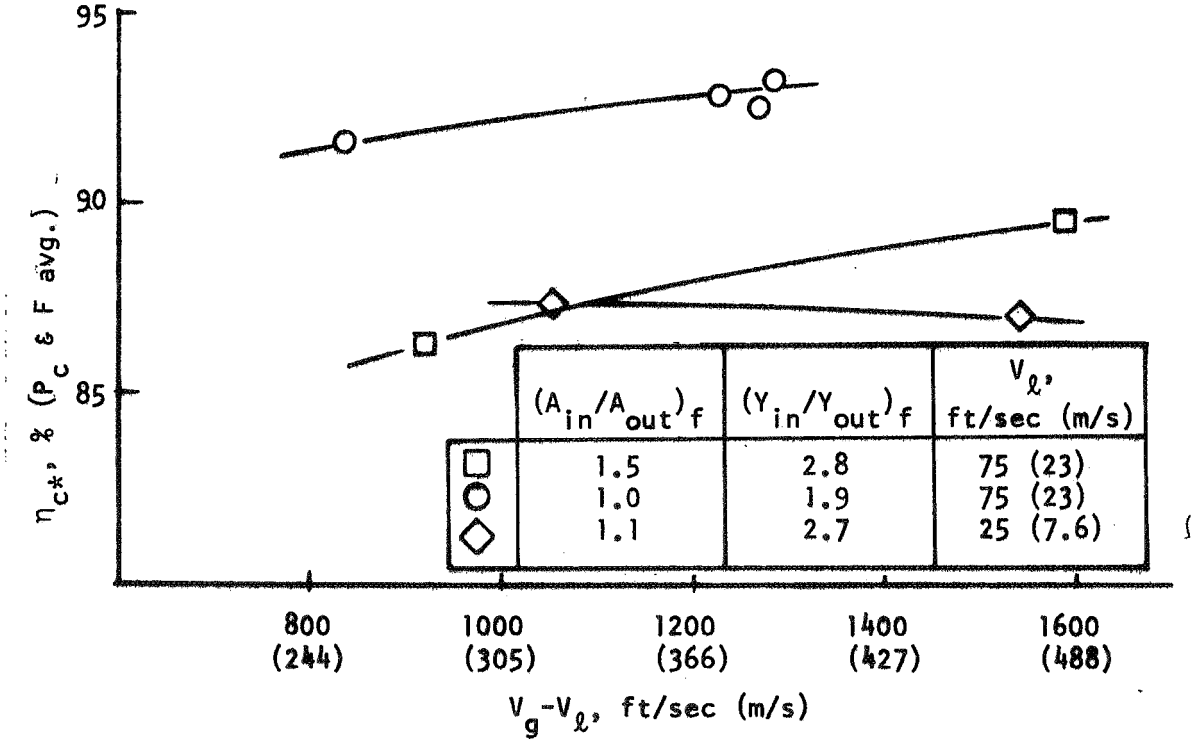

Figure 135. Performance vs V_g-V_ℓ at Constant Mixture RAtio: Tricentric With Centerbody Injector

fuel injection areas $(A_{in}/A_{out})_g$ and annulus gaps $(Y_{in}/Y_{out})_g$ at a constant centerbody diameter and liquid injection velocity. Although there are not sufficient data to distinguish between the individual effects of these two parameters, clearly a 5 percent increase in performance was achieved by changing $(A_{in}/A_{out})_g$ and $(Y_{in}/Y_{out})_g$ from 1.5 and 2.8 to 1.0 and 1.9. This improvement matched very closely that expected on the basis of cold-flow injector modeling data. The improved performance with $(A_{in}/A_{out})_g = 1$ implies the desirability of equally dividing the injected gas flow between the inner and outer annuli. The lower curve in Fig. 135 represents data obtained at a reduced FLOX injection velocity (V_ℓ = 25 ft/sec; 7.6 m/s), indicated by cold flow to be a desirable change. Unfortunately, low-frequency instability (chug) was present in these tests, which undoubtedly influenced the performance. For this reason, the existing hot-firing test data do not define the influence of V_ℓ on performance. No instability of any kind was observed in any of the other tests.

All tricentric injector performances except those for the two low liquid velocity tests which exhibited chugging are shown together in Fig. 136 as a function of mixture ratio. Lines are drawn through data obtained with fixed injector orifice geometry and recess. The only variable not shown explicitly is V_g-V_ℓ which was seen in Fig.135 to be of secondary significance over the range used in these tests relative to MR and injector design. Again the 5 percent improvement with orifice area and gap ratio change is apparent. In addition, the strong performance improvement gained with FLOX annulus recess (0.200 in.; 0.508 x 10^{-2}m) is evident. At MR = 5.25, the gain in η_c* was 5 percent.

As illustrated in Fig. 136, the 5000-lbf (22,220 N) thrust/element recessed tricentric injection with $(A_{in}/A_{out})_g = 1.0$ and $(Y_{in}/Y_{out})_g = 1.9$ achieves a performance of 97.5 percent at the nominal conditions (P_c = 500 psia; 345 x 10^4 N/m^2, MR = 5.25) in the 30-inch (0.76 m) L* chamber, which exceeds the target of 96 percent. In fact, this target performance is reached at mixture ratios up to 6.0. Although not tested at the fuel gap ratio indicated by cold-flow

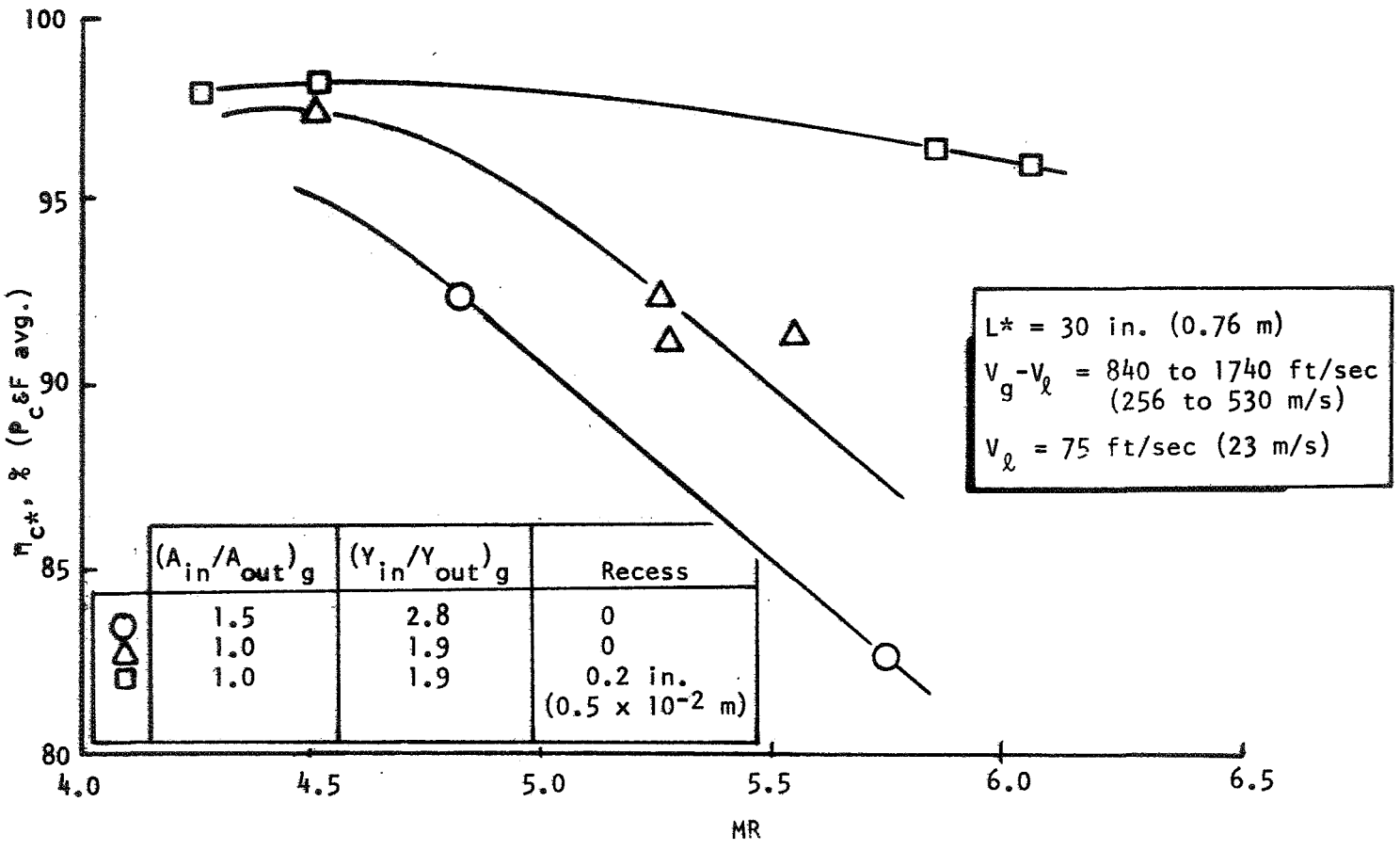

Figure 136. Tricentric With Centerbody Injector Hot Fire Test Results ($FLOX/CH_4$)

tests to be optimum, the zero-recess version of the tricentric injector achieved 96 percent η_c* at mixture ratios just under 5.0.

One of the main objectives of the FLOX/CH_4 hot-fire tests was to empirically verify the performance analysis techniques. This represents the first thorough test with a gas/liquid injection system of these techniques which were previously developed and tested with liquid/liquid propellant. Thus, the cold-flow results were interpolated to the hot-fire operating conditions, to obtain a performance prediction for each hot-fire test. The methods used for these performance predictions have been outlined in a previous section (Task II). Briefly, values of mean dropsize, $\overline{D}$, and $(\eta_c^*)_{mix}$ were obtained from cold-flow curves*, interpolated to the appropriate geometry. These values were corrected (using other cold flow curves) to the appropriate MR, V_g-V_ℓ, and (where applicable) FLOX annulus recess. No physical property corrections were made to $\overline{D}$ because generally accepted dropsize corrections as a function of liquid properties were lacking. The cold-flow values of $\overline{D}$ (and appropriate dropside distributions about $\overline{D}$) were input to standard vaporization-limited combustion models from which values of $(\eta_{c^*})_{vap}$ were then calculated. Predicted values of η_{c^*} were obtained as the product of $(\eta_{c^*})_{vap}$ x $(\eta_{c^*})_{mix}$.

The predicted performance versus actual hot-firing performance attained with this injector concept is presented in Fig. 137. Only the ten 75-ft/sec (23 m/s) liquid injection velocity tests were used in the tricentric with centerbody predictions, discounting the two low V_ℓ tests where chugging instability was encountered. The predicted performances were within a ±3 percent band over a range of actual performance from 82.5 to 98 percent. The correspondance between cold-flow and hot-fire performances was considered extremely successful.

*A more accurate, but somewhat more time consuming approach would involve interpolating to the appropriate value of E_m and then predicting (η_c^*) from generalized curves of $(\eta_c^*)_{mix}$ versus E_m as a function of mixture ratio for the appropriate propellants.

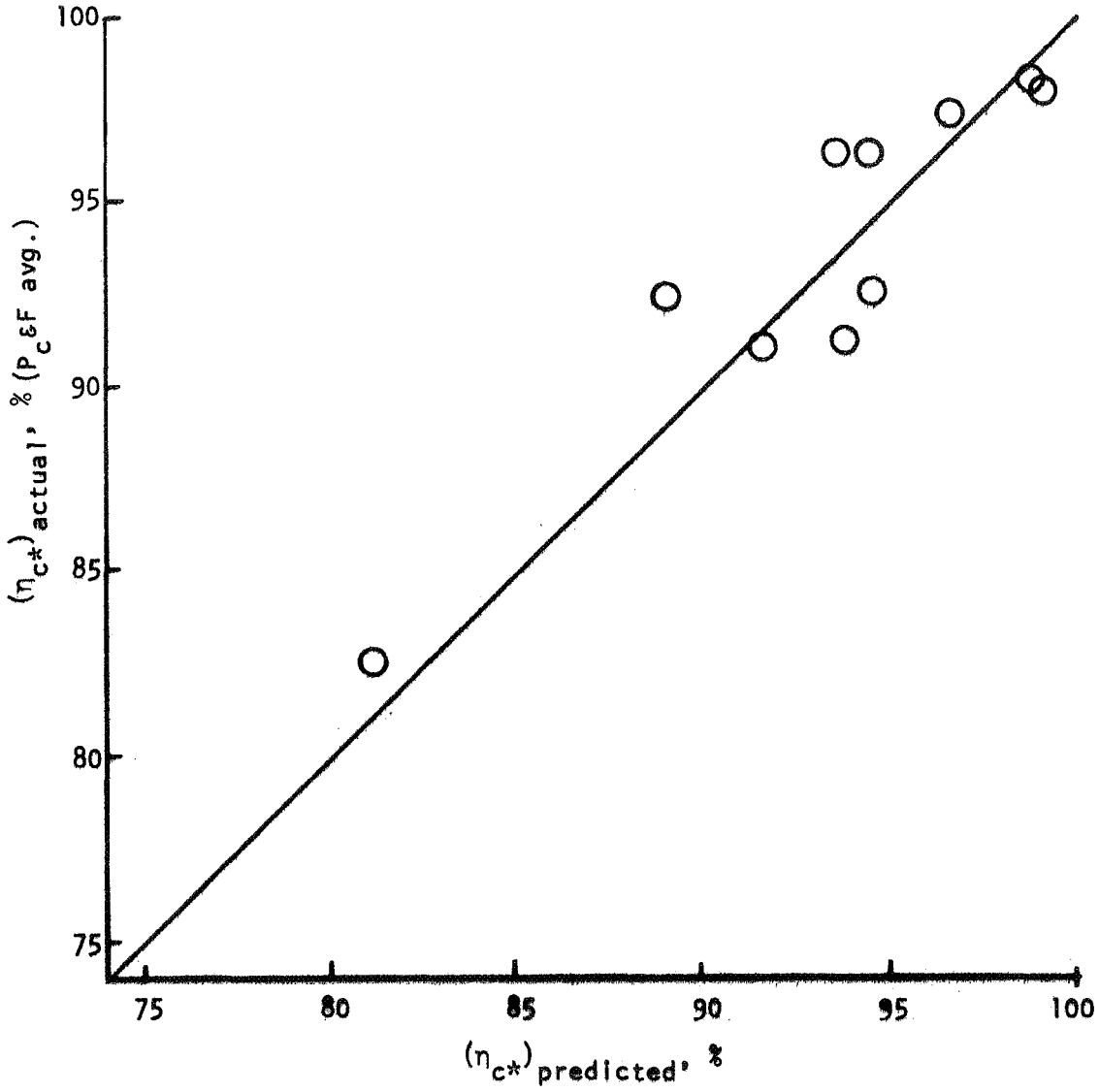

Figure 137. Predicted vs Actual Efficiencies: Tricentric With Centerbody Injector ($FLOX/CH_4$)

It should be pointed out that these performance predictions were made without recourse to any hot firing efficiency data.

Impinging Concentric Injector. Seventeen tests of sufficient duration for steady-state conditions were conducted with this injector concept. The operating conditions and resultant performance numbers are presented in Table 29.

To briefly review the test plan, consider the following. From an analytical standpoint, a most suitable set of independent design/operating variables for this injector is: D_ℓ, D_ℓ/D_g, $\rho_g V_g^2$, X_p/D_g, $\dot{w}_{g,ann}/\dot{w}_{g,tot}$, $V_{g,ann}$ (or annulus gap), and post recess. These variables (except for $V_{g,ann}$) were individually investigated in Tasks II and III. For engine operation at a selected mixture ratio and total flowrate, however, two of the first six variables become dependent. Thus, in the selected hot-firing test plan, based on the nominal mixture ratio and chamber pressure, the chosen set of independent parameters was: D_ℓ, D_ℓ/D_g, X_p/D_g, $(\dot{w}_{ann}/\dot{w}_{tot})_g$*. Under these conditions it is noteworthy that $\rho_g V_g^2$ became a dependent parameter, and, in fact, varied inversely with X_p/D_g. From an operational standpoint the injected methane temperature was varied, permitting changes in X_p/D_g (and $\rho_g V_g^2$) for fixed hardware. Performance results of the hot-fire tests are discussed below.

Cold-flow data and analysis indicated that the percentage of CH_4(g) (up to 40 percent) could be varied with little effect on η_{c^*}. $\dot{w}_{g,ann}/\dot{w}_{g,tot}$ was investigated early in the hot-firing test series with D_ℓ = 0.24 in. (0.61 x 10^{-2}m), D_ℓ/D_g = 0.436, zero recess, a 30-in. (0.76 m) L* chamber and approximately constant X_p/D_g (0.75 to 0.82). The dependent variable $\rho_g V_g^2$ was in the range 184 to 220 psi (127-152 x 10^4 N/m^2). As seen in Fig. 138, variation in $(\dot{w}_{ann}/\dot{w}_{tot})_g$ from 0.20 to 0.35 produced no change in performance under these conditions, as predicted by the cold-flow data. All subsequent tests were made with the percent annulus gas in this range.

In the actual hot-firing tests, two additional parameters were investigated: FLOX post recess and chamber L.

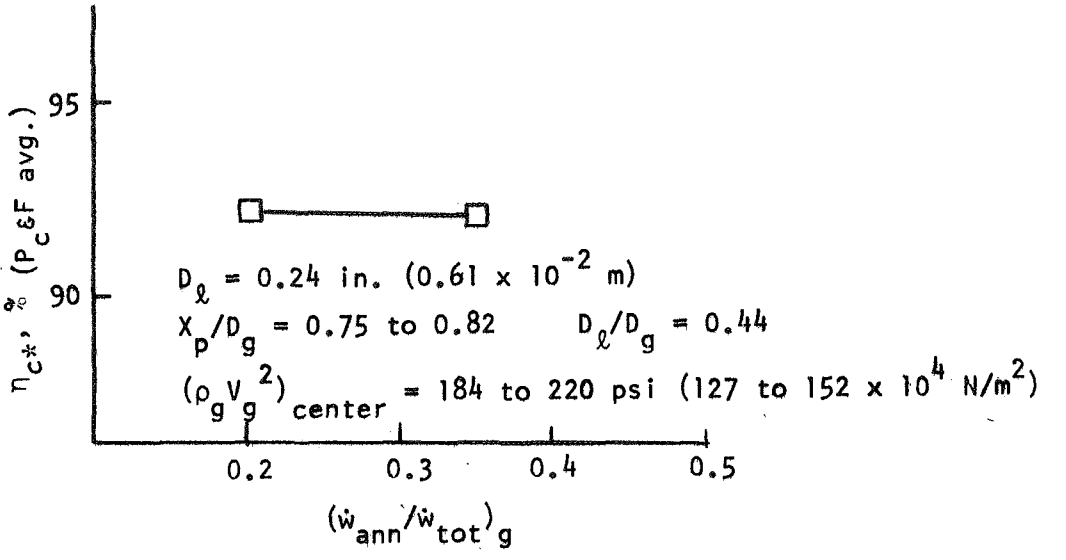

Figure 138. Annulus Gas Effect on Performance: Impinging Concentric Injector

All seventeen impinging concentric injector performance data points are plotted in Fig. 139 as a function of X_p/D_g. As shown, 14 of these were in a 30-inch (0.76 m) L* chamber, the remaining three being obtained in a 57.6-in. (1.46 m) L* chamber. Curves connect the points obtained with fixed orifice dimensions (D_ℓ and D_ℓ/D_g). Tests with flush FLOX posts are represented by open symbols and those with 0.200-in. (0.508 x 10^{-2}m) post recess by closed symbols. In terms of X_p/D_g, an optimum appears to be in the range $0.70 < X_p/D_g < 0.85$ with a substantial decline as X_p/D_g is increased to 1.0 or greater. It must be remembered, however, that $\rho_g V_g^2$, which here is a dependent variable, is decreasing with the larger X_p/D_g and probably is responsible for some of this decline.

To see this effect more clearly, the data are replotted in Fig.140 against the ratio of total gas to total liquid momentum, $M_{g,tot}/M_\ell$. This parameter is essentially analogous to $\rho_g V_g^2$, but was chosen because it reflects contributions of $V_{g,ann}$ as well as $V_{g,center}$ and because it was used to correlate the Task I

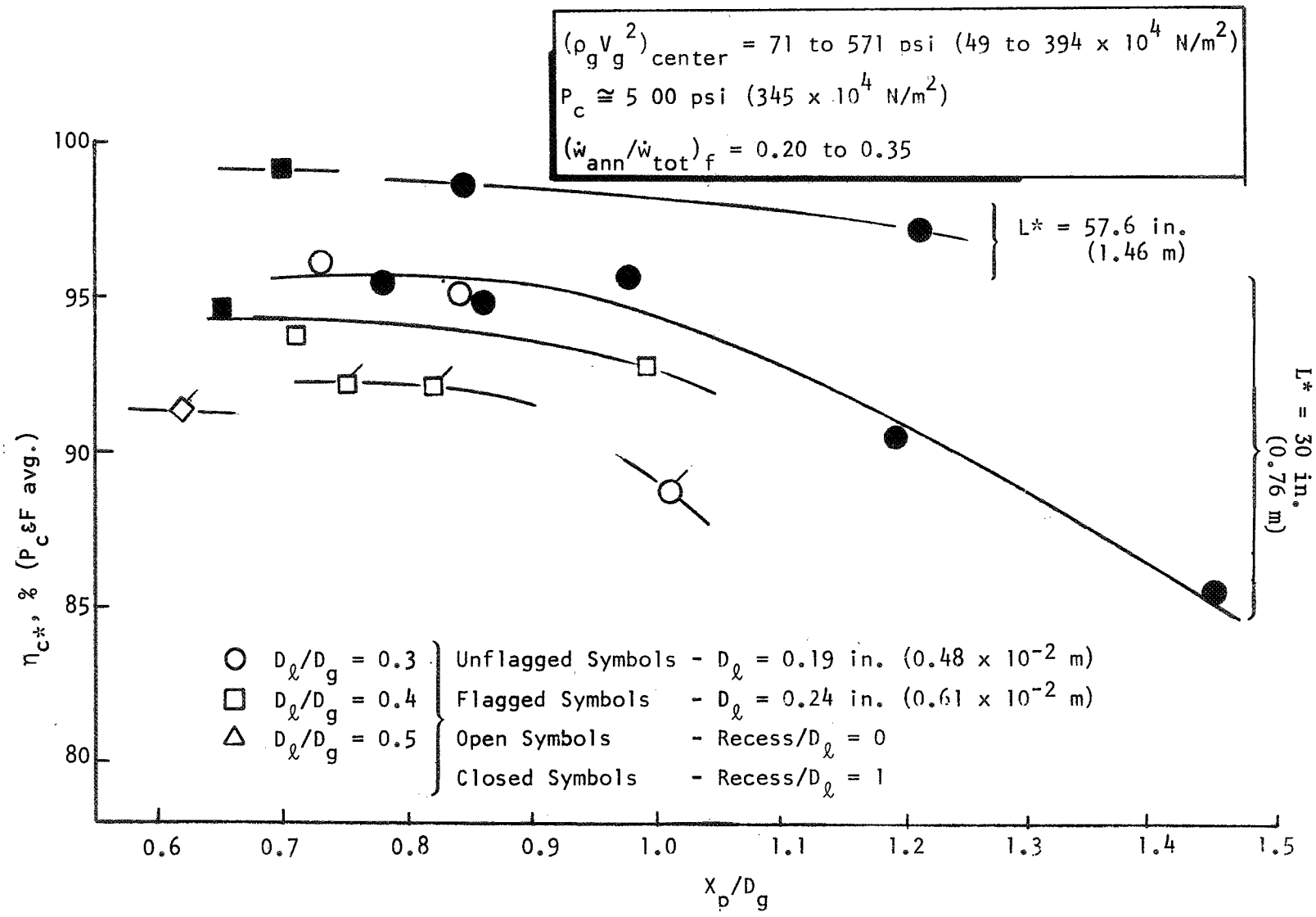

Figure 139. Impinging Concentric Injector Hot-Fire Efficiency vs Penetration Parameter (X_p/D_g)

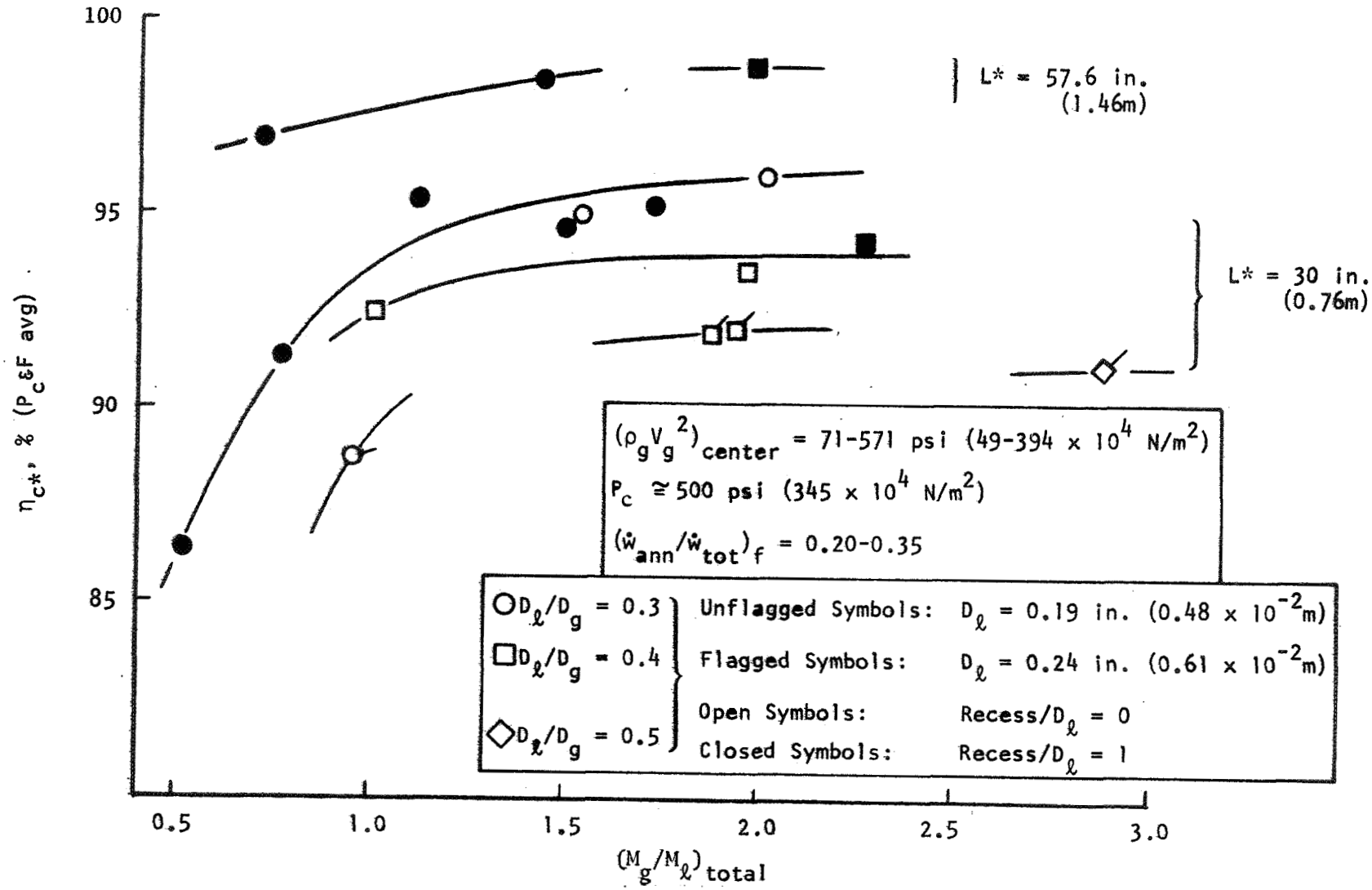

Figure 140. Impinging Concentric Injector Hot-Fire Efficiency vs Momentum Ratio

data. An expected rise in performance is evident as the relative total gas momentum increases from about 0.5 to 1.5. Subsequently, the curves level off, quite likely because of a tradeoff between $\rho_g V_g^2$ and X_p/D_g.

All of the impinging concentric injector performance data are plotted vs mixture ratio in Fig. 141; however, the mixture ratio effects cannot be directly ascertained because other parameters ($\rho_g V_g^2$, X_p/D_g, etc.) were varying at the same time. If the mixture ratio effects are the same as those of the tricentric with centerbody injector (Fig. 134), then the slope of the curves would be nearly identical to that of the 30 in (0.76 m) L* curve (Fig. 141) between mixture ratios of 5.0 and 6.5.

Referring back to Fig. 139, the influence of the geometric parameters is readily apparent and follows the trends predicted from cold-flow analysis. For fixed D_ℓ/D_g, the smaller liquid diameter (D_ℓ = 0.19 in.; 0.48 x 10^{-2}m) injector configuration produced c* efficiencies from 2 to 5 percent higher than those of the design with D_ℓ 0.24 in. (0.61 x 10^{-2}m), depending on the value of X_p/D_g at which they are compared. Similarly, a decrease in D_ℓ/D_g from circa 0.4 to 0.3 raised η_{c*} approximately 2 percent for a given D_ℓ. These effects are shown again in Fig. 142 for a relatively optimum X_p/D_g.

Examination of Fig. 139 for D_ℓ = 0.19 (0.48 x 10^{-2}m), $D_\ell/D_g \cong 0.3$, and L* = 30 in. (0.76 m) shows that recessing the FLOX posts by 0.200 in. (0.508 x 10^{-2}m) had little effect on performance (i.e., the gain was no more than 0.5 percent).

The performance just reached the target of 96 percent for the tests in a 30-in. (0.76 m) L* chamber under the best conditions tested. The long L* (57.6 in.; 1.46 m) chamber tests were performed using the recessed post injector with D_ℓ = 0.19 in. (0.48 x 10^{-2}m) and $D_\ell/D_g \cong 0.3$. These tests were designed (1) to improve performance by reducing $(\eta_{c*})_{vap}$ losses, and (2) to provide hot-firing data which could be used directly to distinguish between incomplete vaporization and imperfect mixing performance losses. As expected, a substantial performance gain was achieved (4 to 6 percent) as can be seen in Fig. 139, resulting in η_{c*} performance from 97 to 99 percent.

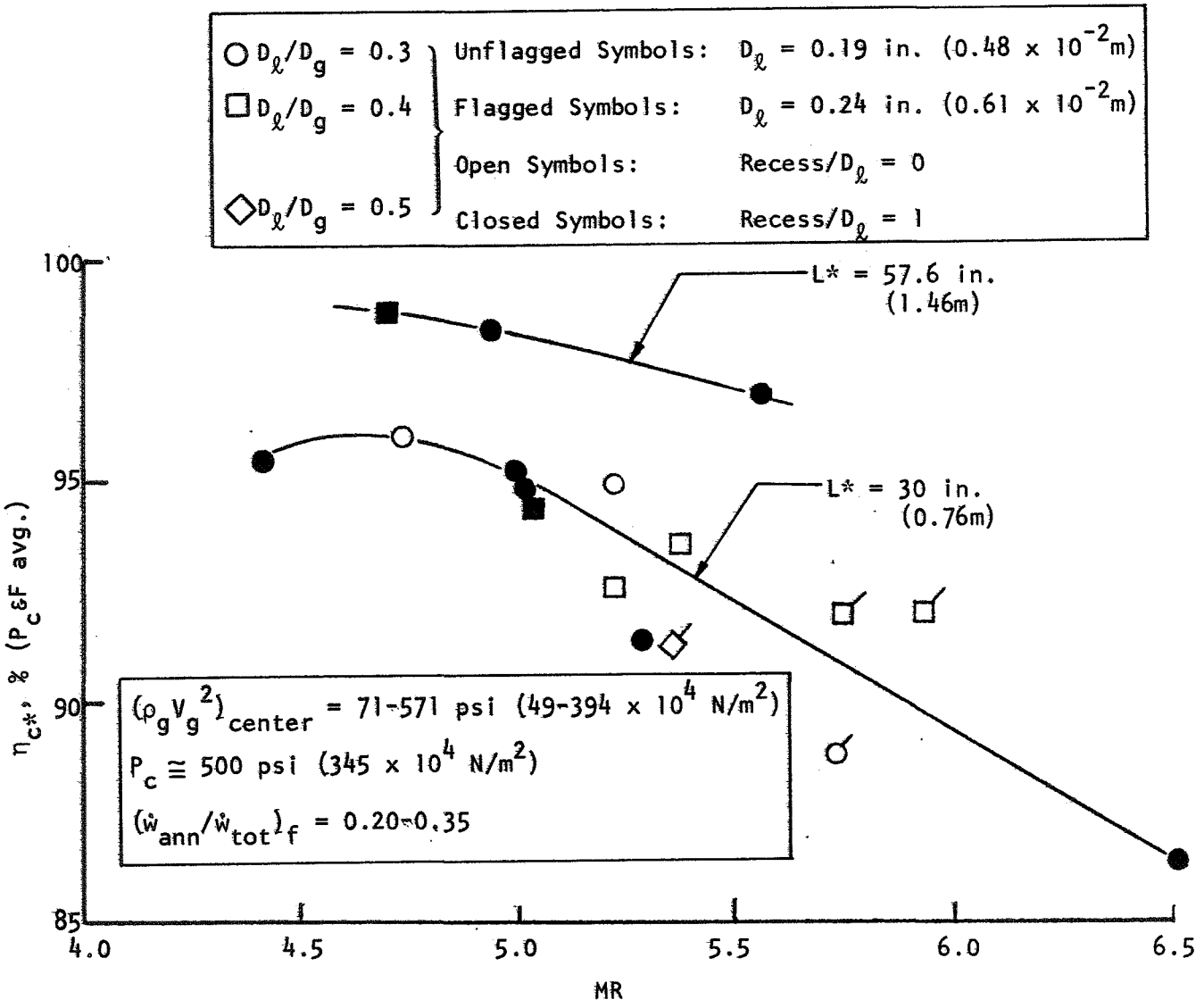

Figure 141. Impinging Concentric Injector Hot-Fire Efficiency vs Mixture Ratio

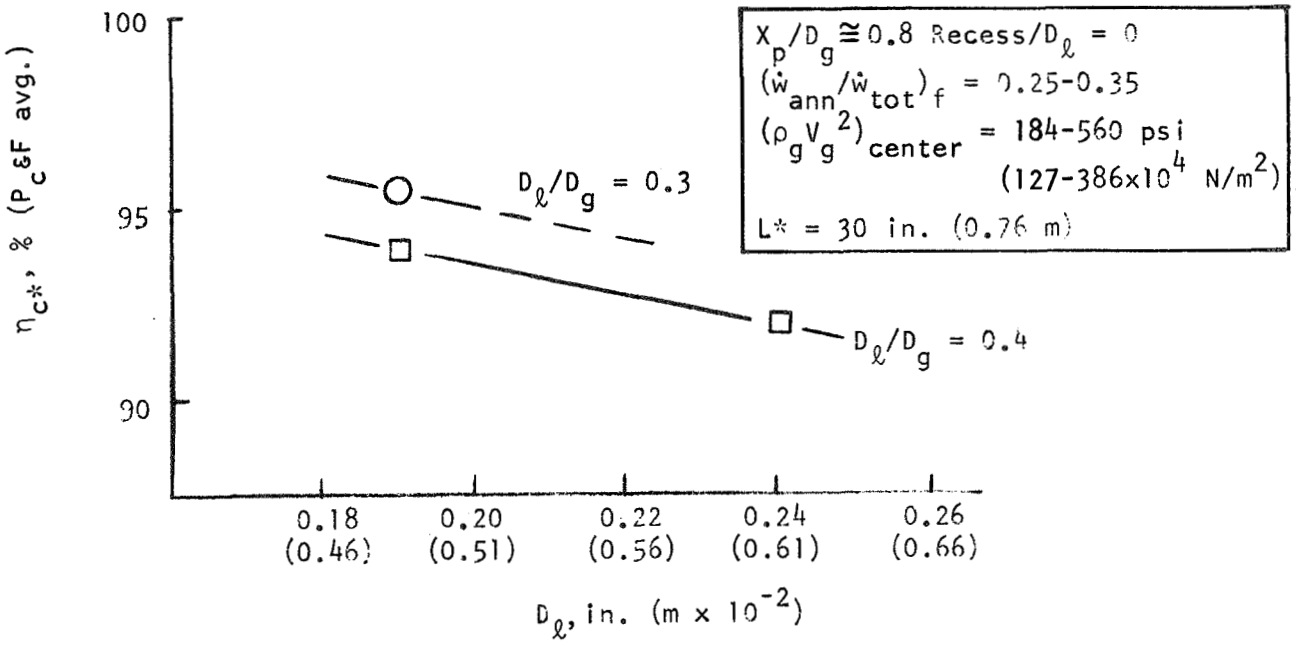

Figure 142. Performance vs D_ℓ: Impinging Concentric Injector

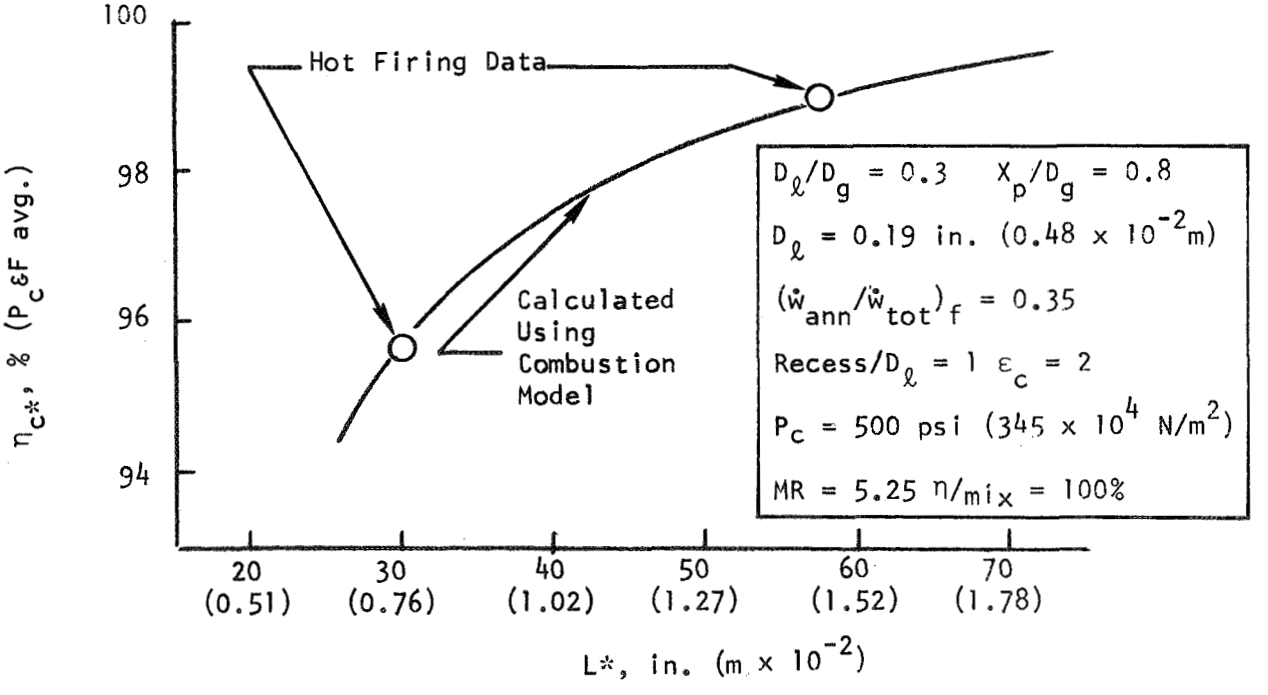

Figure 143. Performance vs L*: Impinging Concentric Injector

An apparent dropsize can be determined by combustion model analysis of performances for tests conducted at 30 in. (0.76 m) and 57.6 in. (1.46 m) L* and at constant operating conditions. This process yielded mass median dropsizes on the order of 150μ (150 x 10^{-6} m) for two of the three* long L* tests, thus indicating vaporization efficiencies to be on the order of 99 percent at the 57.6 in. L*. Therefore, the mixing efficiencies, $(\eta_c^*)_{mix}$, were approximately 100 percent for these two tests (X_p/D_g = 0.7 and 0.84, center $\rho_g V_g^2$ = 223 and 490 psi; 154 and 338 x 10^4 N/m^2). Performance in the 30-in. (0.76 m) L* tests with X_p/D_g in this range (and with D_ℓ = 0.19 in.; 0.48 x 10^{-2}m, $D_\ell/D_g \cong 0.3$) were then almost entirely vaporization limited. Based on the foregoing analysis, η_c^* was calculated from the combustion model as a function of chamber L* for the following injector conditions: $X_p/D_g \cong 0.8$, D_ℓ = 0.19 in.; 0.48 x 10^{-2}m, D_ℓ/D_g = 0.3, recess = 0.2 in. (0.5 x 10^{-2}m). The results provide a continuous curve between the experimental data at L* = 30 and 57.5 in. (0.76 and 1.46 m) as is shown in Fig. 143. Clearly, only small increases in chamber length would be required to exceed 96 percent η_c^*.

As in the case of the tricentric injector, cold-flow data were used to predict η_c^* for each of the hot-firing tests. The steps used in the prediction are systematically described in the Task II section. The approach and assumptions were analogous to those used with the tricentric injector performance predictions. Predicted results are plotted versus the measured η_{c^*} values in Fig.144 . The 13 data points obtained with the D_ℓ = 0.19 in. (0.48 x 10^{-2}m) injector follow a line about 4 percent below the hot-firing values. This difference is attributed primarily to the large extrapolations required in both $\overline{D}$ and $(\eta_c^*)_{mix}$ from cold-flow values of $\rho_g V_g^2$ (5 to 15 psi; 3.4 to 10.3 x 10^4 N/m^2) to hot-firing conditions** ($\rho_g V_g^2 \sim 250$ psi; 172 x 10^4 N/m^2). This extrapolation is illustrated in Fig.145 in terms of $\overline{D}$. For the prediction of η_c^*, the straight line through the two cold-flow data was

The operating conditions on the third long L test were not sufficiently close to any 30 in. (0.76 m) L* test to establish a reliable efficiency gain with increased L*.

**As previously mentioned, 500-psi (345 x 10^4 N/m^2) chamber pressure, hot-firing levels of $\rho_g V_g^2$ are unattainable in atmospheric pressure tests such as used in Tasks II and III due to the large difference in gas density.

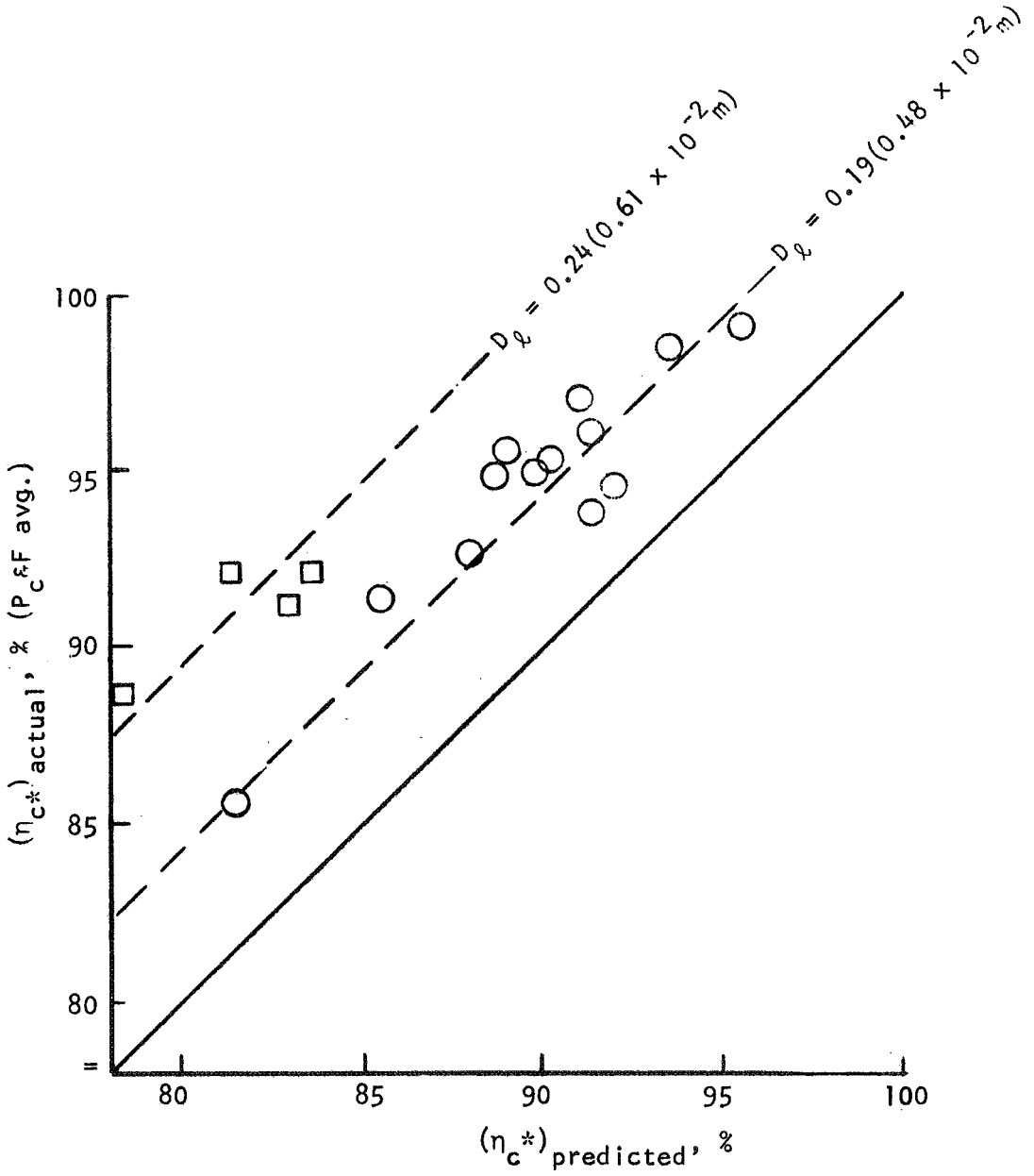

Figure 144. Predicted vs Actual Efficiencies: Impinging Concentric Injector (FLOX/CH_4)

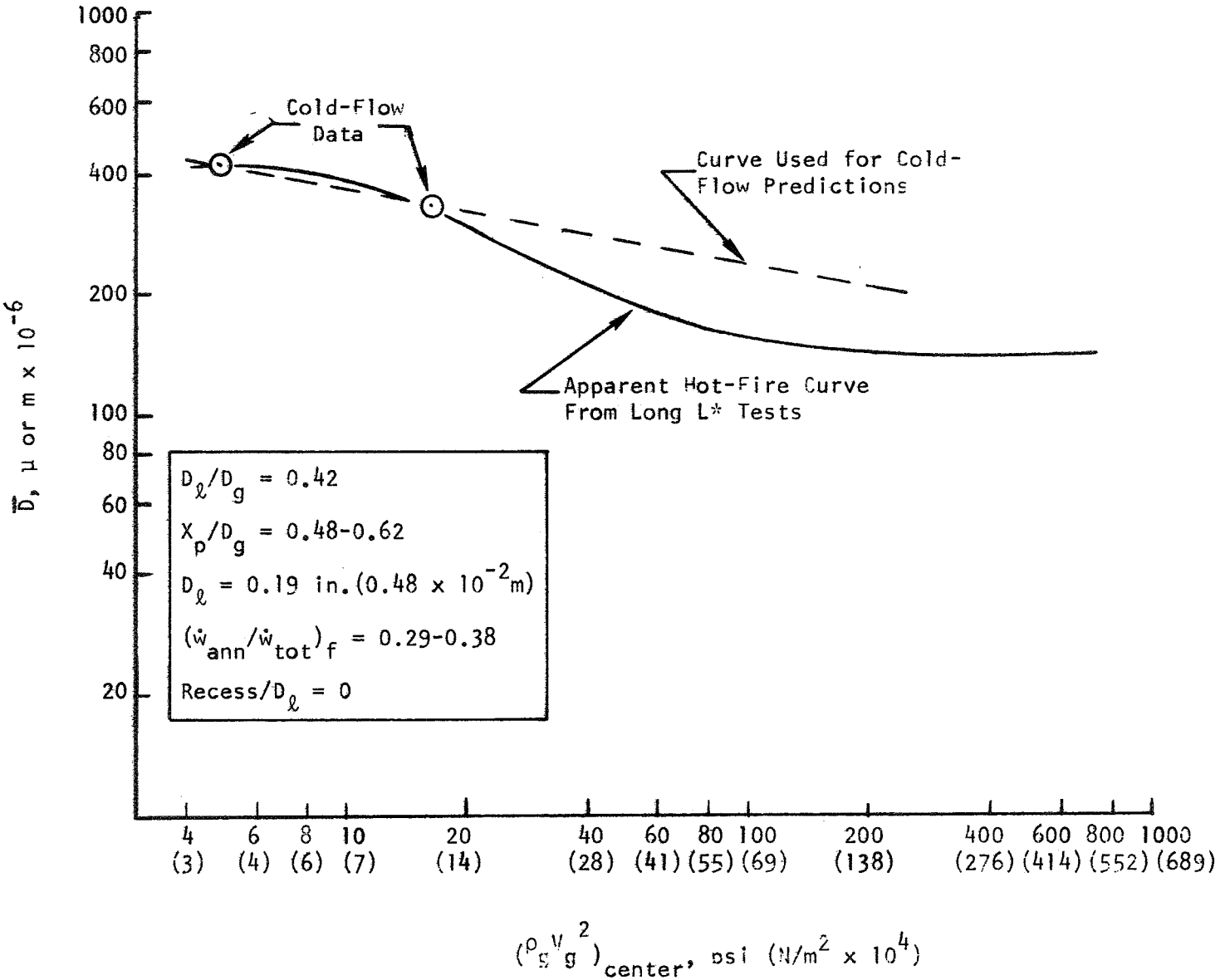

Figure 145. Cold Flow and Hot Fire $(\rho_g V_g^2)_{center}$ Comparisons: Impinging Concentric Injector

used to extrapolate to a value of $\overline{D}$ = 210μ (210 x 10^{-6}m) at $(\rho_g V_g^2)_{center}$ = 200 psi (138 x 10^4 N/m^2). Analysis of the subsequent hot-fire data indicates that $\overline{D}$ was actually about 140μ (140 x 10^{-6}m). Connecting the cold-flow drop-sizes at low $\rho_g V_g^2$ with a few apparent $\overline{D}$ values from hot firing at large $\rho_g V_{g\,c}^2$ as illustrated in Fig. 145 should provide a refined and considerably improved capability for describing parametric effects of $\rho_g V_g^2$ and for performance prediction.

Some additional error was indicated in predicting the influence of X_p/D_g on performance. In particular, the cold-flow curves appear to under-estimate the values of η_c* for $0.5 < X_p/D_g < 0.9$.

For the four tests with D_ℓ = 0.24 in. (0.61 x 10^{-2}m) there were no direct cold-flow data to predict orifice geometry effects on $\overline{D}$ and $(\eta_c^*)_{mix}$ as there had been with D_ℓ = 0.19 in. (0.48 x 10^{-2}m) (Fig. 112 and 113). Instead it was necessary to interpolate between the line D_ℓ = 0.19 in. (0.48 x 10^{-2}m) and the other cold-flow data line at D_ℓ = 0.40 in. (1.02 x 10^{-2}m). Between these two values there was a difference of 30 percent in $(\eta_{c^*})_{mix}$. An attempt was made to graphically interpolate between these curves. Obviously this attempt was not too successful. The predictions for the four tests with D_ℓ = 0.24 in. (0.61 x 10^{-2}m) fell on a line about 5 percent further below the measured η_c* line than did the 13 data points at D_ℓ = 0.19 in. (0.48 x 10^{-2}m), where this interpolation was unnecessary.

Stability. Stability characteristics of the injector were of primary concern throughout the hot-fire testing. Wide-frequency range, fast-responding instrumentation was used during each test to monitor the stability characteristics. The instrumentation consisted of one axial accelerometer, one oxidizer injection pressure Photocon, and from one to three chamber pressure Photocons depending on the thrust chamber used. The chamber pressure Photocons were mounted from 1.25 to 3 inches (0.032 to 0.076 m) downstream of the injector face. Output from this instrumentation was recorded on tape, transcribed on oscillogram type recorders, and for some tests transcribed on expanded-scale Brush recorders.

Dynamic stability characteristics were observed during test 58. For this test, three pulse guns were fired, each with different size charges, i.e., 20, 40, and 80 grains (13.0, 25.9, and 51.8 x 10^{-4} kg). The charges were sequenced to fired in order of ascending weight from the radial, chordal, and tangential pulse guns, respectively. About 200 msec (200 x 10^{-3}s) were allowed between the pulse gun firings, which were sequenced after approximately 1.6, 1.8, and 2.0 seconds of mainstage.

A typical expanded Brush record is presented in Fig. 146 showing the 80-grain charge disturbance from the tangential pulse gun (test 58). The trace for the P_c Photocon shows an overpressure of about 1000 psi (690 x 10^4 N/m^2) above the nominal chamber pressure. As shown, each of the traces indicate that the disturbance damps in less than 5 msec (5 x 10^{-3} s). The magnitude of the P_c overpressures is inconclusive and serves only to show that the disturbances were significant. The pulse gun pulses did not produce a FLOX injection pressure overpressure, possibly because of its location upstream of the injector.

Generally, the stability records indicate that the injector/thrust chamber was statically stable. However, tests 032 to 034, with the low liquid (FLOX) velocity tricentric with centerbody injector, did exhibit 500 to 600 Hz oscillations at peak-to-peak amplitudes of 200 to 300 psi (137 to 206 x 10^4 N/m^2) during mainstage. These oscillations were apparently feed system coupled, possibly related to the low FLOX injection ΔP. All other tests with the tricentric injector and with the recessed impinging concentric injected were characterized by mainstage peak-to-peak pressure amplitudes less than ±5 percent of the operating pressures. A typical case is illustrated in Fig. 146, before and after the pulse gun disturbance.

The observed stability characteristics are briefly summarized as follows:

1. Each of the three pulse gun disturbances in test 58 damped in less than 5 msec (5 x 10^{-3} s), suggesting that the impinging concentric injector is dynamically stable.

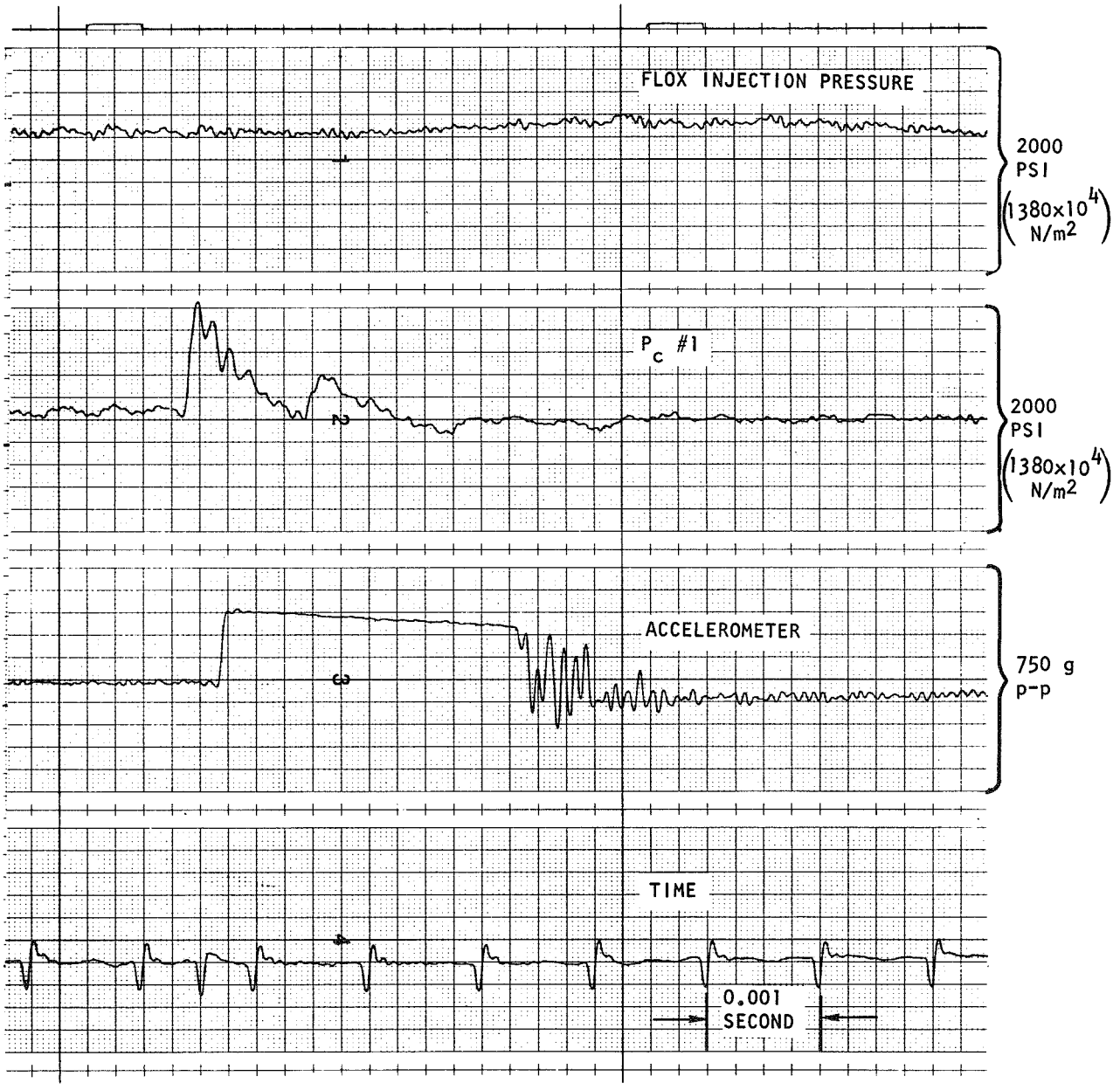

Figure 146. Brush Record of 80 Grain (51.8×10^{-4}kg) Pulse Gun Disturbance - FLOX/CH_4 Test 058

2. The low FLOX velocity tricentric injector was moderately unstable, characterized by 200 to 300 psi (137 to 206 x 10^4 N/m^2) oscillations (peak-to-peak) at 500 to 600 Hz.

3. All other tests were stable with oscillations less than ±5 percent of the operating pressure.

4. No acoustic type instabilities were observed, and if present, were very weak.

5. Low-frequency (50 to 500 Hz) chugging was observed at the start and cutoff during some of the tests, dissipating in a short time.

6. The accelerometer activity was very low and often swamped by instrumentation noise.

7. Overall stability characteristics were very good.

DISCUSSION OF RESULTS

In reviewing results of the four major program tasks, several items bear a need for further discussion. First of all, it is interesting to compare results of Tasks I and IV, in which different propellants were fired using the novel impinging concentric injector. It is also appropriate at this point to critique the cold-flow analytical procedure, as the Task IV tests represent a milestone in empirical verification of these methods as applied to gas-liquid injectors. Next, the performance capabilities are discussed relative to large thrust/element impinging concentric and tricentric injectors applied to LOX/GH_2 as well as FLOX/$CH_{4(g)}$. Finally, performance prediction procedures are outlined using the cold-flow data and the correlations generated through the program.

COMPARISON OF LOX/H_2 AND FLOX/CH_4 PERFORMANCES WITH IMPINGING CONCENTRIC INJECTORS

The impinging concentric injector concept was first developed and applied to the LOX/hot gas/H_2 system under the Two-Stage Injector program, Contract NAS3-7962, where it proved to be quite successful in terms of both performance and stability. This concept, previously illustrated in Fig. 3, is truly a hybrid between basic impinging and concentric types of injectors. It was subsequently tested in Task I of the subject program using LOX/$H_{2(g)}$ propellants, where it again provided high performance and stability. Finally, it was chosen as one of the two concepts that were evaluated in Task IV with FLOX/$CH_{4(g)}$. Table 30 compares some of the pertinent test conditions under which this injector type has been tested.

It is informative to plot together some of the performance data versus key parameters obtained with this injector concept during the different hot-firing efforts. Although, the curves would certainly not be expected to merge, their trends are interesting to compare. The Task I and Two-Stage data were correlated (Fig. 27 and 29) in terms of: (1) the mixing efficiency, $(\eta_{c^*})_{mix}$,

TABLE 30

TEST CONDITIONS FOR THE IMPINGING CONCENTRIC INJECTORS

	Contract NAS3-7962	Task I	Task IV
Propellant	LOX/hot gas/H_2	LOX/GH_2	FLOX/CH_4
Mixture Ratio (nominal)	5.0	5.0	5.25 to 5.75
Thrust/Element, lbf (N)	5,000 , 20,000 (22,200) (88,900)	20,000 (88,900)	5,000 (22,200)
Chamber Pressure (nominal), psi ($N/m^2 \times 10^4$)	500 (345)	500 (345)	500 (345)
Impinging Concentric Orifice Included Angle, degree (rad.)	120 (2.1)	120 (2.1)	90 (1.6)

as a function of the liquid-gas penetration parameters, X_p/D_g; and (2) the vaporization efficiency, $(\eta_{c*})_{vap}$, as a function of the gas-liquid momentum ratio, M_g/M_ℓ. Under Task I, a series of (six) long chamber tests (L^* = 75 in.; 1.9 m) permitted an easy distinction between $(\eta_{c*})_{mix}$ and $(\eta_{c*})_{vap}$ losses. For the Task IV FLOX/$CH_{4(g)}$ data, three moderately long chamber tests (L^* = 57.6 in.; 1.46 m) were made. To discern between $(\eta_{c*})_{vap}$ and $(\eta_{c*})_{mix}$ for all the Task IV data, however, it was necessary to use analytical calculations. For this purpose, the correlations were utilized that produced the $(\eta_{c*})_{pred}/(\eta_{c*})_{actual}$ correspondence illustrated in Fig.144, refined for a "best fit" with the hot-fire data.

The comparisons are shown in Fig.147 . The propellant mixing, based on Task I data, rose continually as X_p/D_g increased from about 0.4 to 0.8. With all the Task IV data included as well, an apparent optimum is seen for $0.7 \leq X_p/D_g \leq 0.9$. The Task IV data plotted in this manner indicate the improved performance with smaller liquid orifices (D_ℓ = 0.19 in.; 0.48 x 10^{-2} m) is due to an improvement in $(\eta_{c*})_{mix}$. The $(\eta_{c*})_{mix}$ data for different D_ℓ/D_g (0.33 and 0.43) tend to merge. For the Task I tests, D_ℓ and D_ℓ/D_g were not varied.

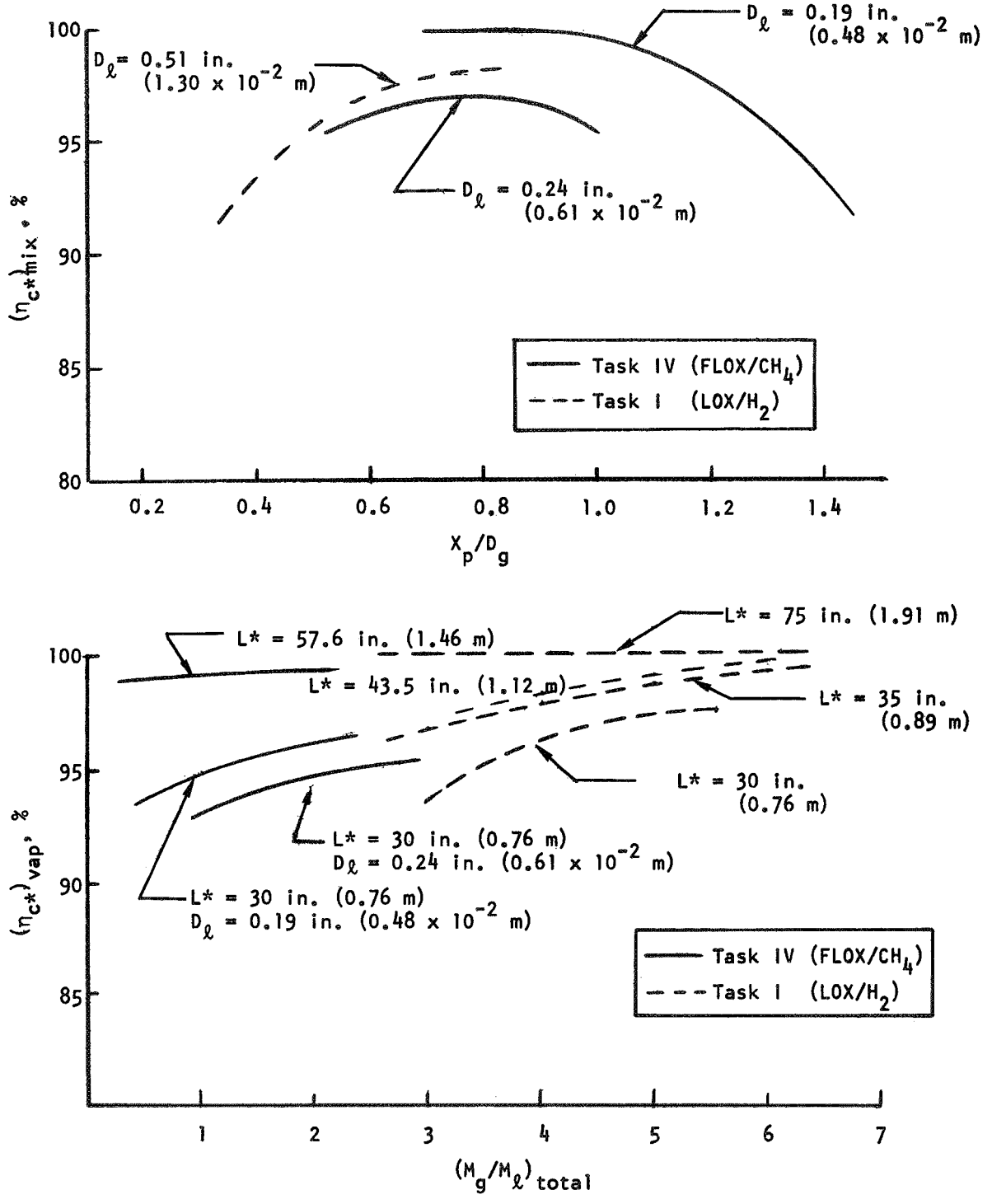

Figure 147. Impinging Concentric Injector Performance Correlations

Vaporization-limited combustion efficiencies are plotted in Fig. 147. Again, overall trends of the Task IV data (with M_g/M_ℓ) show a distinct similarity to those generated under Task I, i.e., a continuous rise in $(\eta_{c^*})_{vap}$ with increasing M_g/M_ℓ. For the short chamber tests (L* = 30 in.; 0.76 m), the FLOX/$CH_{4(g)}$ $(\eta_{c^*})_{vap}$ levels (Task IV) were a couple of percent lower than those obtained in Task I and Contract NAS3-7962. Figure 147 shows this to be due to the relatively low levels of M_g/M_ℓ (0.5 to 2.5) employed in Task IV as compared to those used with the O_2/H_2 systems (2.5 to 9)*. Strong chamber L* influence is seen in the figure as expected based on the analysis. Another notable parametric effect is that of D_ℓ/D_g, whereby the lower values led to better atomization and thus improved $(\eta_{c^*})_{vap}$ for the Task IV tests.

In summary, the Two-Stage (LOX/hot gas/H_2) and Task I (LOX/$H_{2(g)}$) results can be compared directly with Task IV (FLOX/$CH_{4(g)}$) data in terms of the observed influences of X_p/D_g on $(\eta_{c^*})_{mix}$ and of M_g/M_ℓ on $(\eta_{c^*})_{vap}$. Qualitatively, the respective trends observed with these variables appear to be identical for the different propellant systems. For 30-in. (0.76 m) L* chamber tests, slightly better vaporization was achieved with O_2/H_2 systems, possibly due to the higher M_g/M_ℓ attainable with these propellants. On the other hand, at "optimum" X_p/D_g essentially 100 percent $(\eta_{c^*})_{mix}$ was accomplished with the (5000 lbf; 22,200 N thrust per element) FLOX/$CH_{4(g)}$ system, compared to about 98 percent for the (20,000 lbf; 88,900 N thrust per element) LOX/$H_{2(g)}$ system. The implication is that with D_ℓ smaller than the 0.509 in. (1.29×10^{-2} m) used in Task I, an improvement in $(\eta_{c^*})_{mix}$ may have been possible.

EVALUATION OF COLD-FLOW/ANALYTICAL METHOD

The hot-fire data obtained in Task IV provides the first opportunity for a quantitative empirical test of the use of cold-flow injector modeling techniques for performance analysis of gas-liquid injectors. These methods have

*With the FLOX/$CH_{4(g)}$ system it is more difficult to obtain high M_g/M_ℓ. For the Task IV tests, this level was further limited by the $CH_{4(g)}$ heater capabilities.

proved quite useful in application to liquid-liquid systems but prior test of their use for gas-liquid propellant injector has been limited to confirming that parametric trends predicted for the concentric injector corresponded to those observed in hot-fire testing.

Some words seem appropriate at this point to establish what might be expected of the correlations. Task II (where most of the cold-flow testing was done) was by intention of a survey nature, broad in scope of investigation rather than intensive. This was appropriate for a first systematic evaluation of performance characteristic of diverse gas-liquid injectors to clearly establish the parameters of principal importance and to gain some idea of how to optimize them. Seven distinct injector element types were characterized, and for most of these elements, size was varied. Five to seven parameters must be specified for each injector type to define the conditions of operation. Thus, many of the correlations obtained were limited to "two point curves" and in other cases it was necessary to assume that parametric influence on one injector type was the same as that of a similar concept for which there were more data. Most test matrices were set up to evaluate a single parameter at a time with other variables maintained at nominal or baseline values. Thus, interactions or nonlinear influence of two or more variables were, in general, not evaluated. This was obvious in the performance correlation procedures described in the preceding sections. Therefore, it was understood a priori that a precise prediction of hot-firing performances would be somewhat fortuitous, until some hot-firing data became available for upgrading the correlations. Nevertheless, it was expected that parametric trends would be accurately forecast.

Cold-flow predictions made for the Task IV tests were truly "pre-predictions." In the case of the large tricentric element injector, there was no priori hot-firing experience at all, and the impinging concentric injector had never before been used with FLOX/$CH_{4(g)}$. The η_{c^*} predictions for the tricentric injector were presented in Fig. 137, where it was seen that the maximum difference between predicted and measured η_{c^*} was 3 percent over a wide η_{c^*} range, from about 80 to 100 percent. The average deviation was only 1.6 percent.

Thus, the results were very gratifying. A single qualification is that no liquid property corrections were applied to the measured spray dropsizes.

As expected, since the overall predictions for the tricentric injector were this successful, parametric trends forecast by the cold-flow tests agreed well with hot-firing test data. Minor differences included a slightly more gradual decline of mixing efficiency with increasing mixture ratio than predicted. The other cause for the slight (±1.6 percent) difference between $(\eta_{c*})_{pred}$ and $(\eta_{c*})_{hot\ fire}$ resulted from the necessity of interpolating $(\eta_{c*})_{mix}$ and $\overline{D}$ between values of (Y_{in}/Y_{out}) for which there was available cold-flow data (Fig. 107). In effect, the hot-fire results provide an additional point that permits drawing a refined curve, still passing through the existing cold-flow points.

For the impinging concentric injector, the predictions primarily fell along a line (Fig. 144) about 4 percent below the experimental η_{c*}. This was due mainly to inaccurate extrapolation of $\overline{D}$ and $(\eta_{c*})_{mix}$ from cold-flow levels of $\rho_g V_g^2$ (10 to 15 psi; 7 to 10 x 10^4 N/m^2) to hot-firing levels (e.g., 250 psi; 172 x 10^4 N/m^2). A major conclusion resulting from comparison with the hot-firing data is that $\overline{D}$ declines more rapidly with large increases in $\rho_g V_g^2$ than suggested by the (limited range) cold-flow tests.* These conclusions in no way contradict cold-flow data, however, but rather serve to again indicate the need either to: (1) extend the range of cold-flow test parameters or (2) use some hot-firing data to extend the curves. The one area in which some disagreement was noted was in the correlation of $(\eta_{c*})_{mix}$ (or E_m) versus X_p/D_g, where the cold-flow data underpredicted $(\eta_{c*})_{mix}$ by several percent for $0.5 \leq X_p/D_g \leq 0.9$. This points out the need for further improvement of the recirculation model used in reduction of the raw cold-flow data.

Performance for the four tests with a larger FLOX post (D_ℓ = 0.24 in.; 0.61 x 10^{-2} m) were underpredicted by an amount larger than the average 4 percent

*Very roughly, $\overline{D}$ is indicated to decline with $(\rho_g V_g^2)^{0.3}$ rather than with $(\rho_g V_g^2)^{0.2}$ within the 10 to 250 psi (7 to 172 x 10^4 N/m^2) range.

error in predictions for the other 13 tests. This also appears to be an interpolation problem, i.e., the linear interpolation between cold-flow predictions of mixing efficiencies obtained at D_ℓ = 0.19 in. (0.48×10^{-2} m) and D_ℓ = 0.40 in. (1.02×10^{-2} m) was not correct. The remedy for this error is illustrated in Fig. 148 in which the curve for D_ℓ = 0.24 in.; 0.61×10^{-2} m (backed out of the hot-firing results) has been plotted between the existing cold-flow curves for D_ℓ = 0.19 in. (0.48×10^{-2} m) and D_ℓ = 0.40 in. (1.02×10^{-2} m).

PERFORMANCE CAPABILITY OF LARGE THRUST/ELEMENT INJECTORS

The tricentric with centerbody injector, using a 0.20 in. (0.51×10^{-2} m) liquid annulus recess has already demonstrated 97 percent η_{c^*} with FLOX/$CH_{4(g)}$ at a mixture ratio of 5.25 and a 500 psi (345×10^4 N/m^2) chamber pressure in a 30 in. (0.76 m) L* thrust chamber. Analysis indicates that this could be increased to 99 percent η_{c^*} with identical injection conditions in a 50 in. (1.27 m) L* chamber. Several alternate paths are available for further performance increase in a 30 in. (0.76 m) L* chamber. One approach would be to use further FLOX annulus recess. The 0.20 in. (0.51×10^{-2} m) recesses increased η_{c^*} by 5 percent and further recess may yield further gains. However, the recess led to a higher injection ΔP.

A more attractive approach would be to optimize the (annular) orifice exit geometry in terms of $(A_{in}/A_{out})_f$, $(Y_{in}/Y_{out})_f$, and D_{plug}. Adjustment of these parameters has already shown (in Task IV hot-firing tests) performance improvement on the order of 5 percent. The best combination tested included $(A_{in}/A_{out})_f = 1.0$, $(Y_{in}/Y_{out})_f = 1.9$, but the cold-flow data show that about 2 percent improvement should be possible with $(A_{in}/A_{out})_f = 1.0$ and $(Y_{in}/Y_{out})_f = 2.4$. This would permit acquisition of 99 percent η_{c^*} with the present 0.20 in. (0.51×10^{-2}m) recess. Even this latter combination of gas area and gap ratios may not be the best, for the combination of these two variables along with D_{plug} has yet to be systematically optimized, even in cold-flow testing.

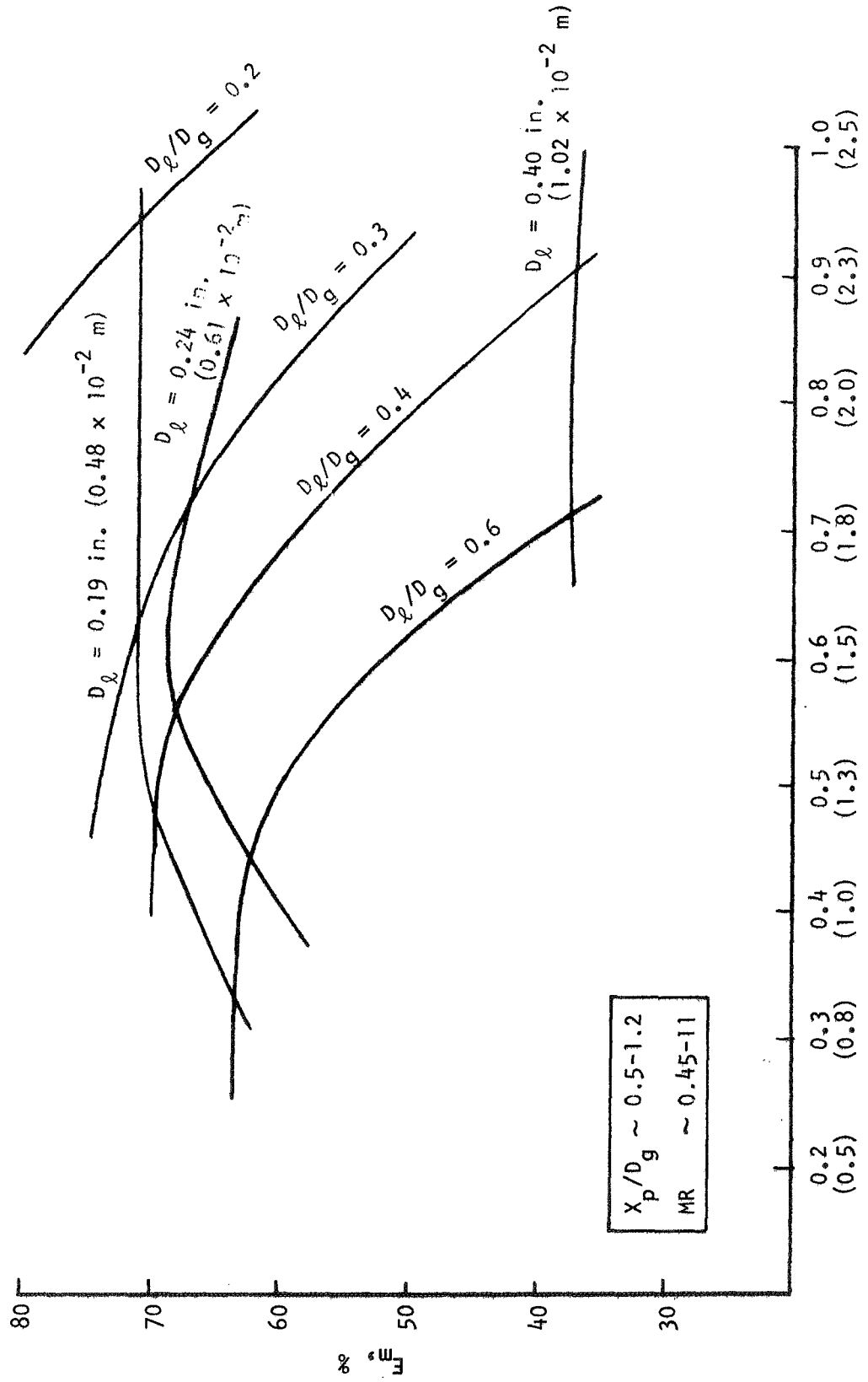

Figure 148. Refined Impinging Concentric Injector Mixing Correlations

In summary, performance capabilities of the 5000-lb (22,200 N)-thrust per element tricentric with centerbody injector appear competitive with the best conventional thrust per element FLOX/$CH_{4(g)}$ injectors. Its inherent stability and design/manufacturing simplicity make this an attractive candidate for FLOX/$CH_{4(g)}$. This injector should also be suitable for LOX/$H_{2(g)}$ application where high performance may be still easier to obtain. For O_2/H_2, $(\eta_{c*})_{mix}$ is less sensitive to maldistribution than FLOX/CH_4 and in addition higher values of $(V_g - V_\ell)$ would be feasible, which should permit a further enhancement of both mixing and atomization.

Figure 143 illustrates the performance of the impinging concentric injector, tested in Task IV, as a function of chamber L*. A 96-percent η_{c*} is shown at a 33 in. (0.84 m) L*. A very promising means of improving the capabilities of this injector (for any given chamber size) would be to increase the included angle between impinging liquid streams from 90 to 120 deg; 1.6 to 2.1 rad (120 deg; 2.1 rad used in Task I). This would tend to increase X_p/D_g for otherwise constant flow conditions, thus permitting operation with a higher $(\rho_g V_g^2)_{center}$ (and higher M_g/M_ℓ) while maintaining X_p/D_g in the range for optimum propellant mixing. Under operational conditions $(\rho_g V_g^2)_{center}$ was limited so that X_p/D_g could be in range of 0.8 to 0.9. The increase in $(\rho_g V_g^2)_{center}$ and (M_g/M_ℓ) should decrease the mean dropsize, improving $(\eta_{c*})_{vap}$ and, according to analysis, should raise η_{c*} to about 97 percent in a 30-in. (0.76 m) L* chamber. Another possible means of increasing performance might be to further decrease D_ℓ/D_g. Both hot-fire and cold-flow data showed that a decrease of D_ℓ/D_g to 0.3 was advantageous. Although early cold-flow work in Task I indicated liquid spray fluxes to be less uniform for $D_\ell/D_g < 0.3$, it is possible that $(\eta_{c*})_{mix}$ may continue to improve for lower diameter ratios. Still another possibility would be to optimize the recessed cup geometry to improve performance. Cup geometry effects were not investigated during the subject program.

Summarizing the capabilities of the impinging concentric injector, it is also predicted to be capable of high (98 to 99 percent) c* efficiencies in short chambers at the 5000-lbf (22,200 N)-thrust per element level with FLOX/$CH_{4(g)}$

(MR = 5.25). It has not yet demonstrated as good a performance as the tricentric injector concept with FLOX/$CH_{4(g)}$, however, and some design changes such as suggested above would be required to make it competitive with the other injector type. With LOX/$H_{2(g)}$ very high performance was demonstrated as well as dynamic stability, even with a thrust per element of 20,000 lbf (88,900 N) with GH_2 at ambient temperatures or lower. Hotter fuel (gas) would still further augment its performance with LOX/$H_{2(g)}$.

PERFORMANCE CORRELATIONS

This section summarizes the recommended procedure for predicting gas-liquid injector performance using the extensive cold-flow data and correlations generated under the subject contract. Injector types included are basic impinging (pentad, triplet, unlike doublet), basic concentric (with or without liquid post recess), concentric with liquid swirl, impinging concentric (four concentric gas-liquid orifices impinging on a central showerhead gas stream), and a tricentric with centerbody (gas-liquid-gas) concept. The scope of this investigation is such that many of the predictions are based on "two point curves" or even on analogy with similar but different element types. The correlations best apply to relatively large elements, e.g., 2000 to 20,000 lb (8890 to 88,900 N) thrust/element, although most of the trends indicated are probably applicable to smaller scale injector elements as well. The following correlations can be applied to LOX/$H_{2(g)}$, $F_{2(\ell)}/H_{2(g)}$, FLOX/$CH_{4(g)}$, etc. Hot-firing verification of the correlations has been accomplished with the tricentric injector injector (Task IV) and with the impinging concentric injector concepts (Contract NAS3-7962, Task I and IV). In all of these tests, cylindrical thrust chambers of contraction ratio 2.0 were used.

For the tricentric injector, the initial vaporization and mixing efficiency correlations, based on cold-flow tests, provided a sufficiently accurate estimate of the hot-firing results (Fig. 137) so that no adjustment in the curves or η_{c^*} prediction procedure is recommended. Thus, the following stepwise procedure duplicates that used in Task IV for performance estimation. On the other hand, hot-firing data from the impinging concentric injector provided

a necessary improvement in the extrapolation of median dropsize and mixing efficiency from cold-flow values of $(\rho_g V_g^2)_{center}$ to hot-firing test levels (Fig. 145 and 149). The dependence of mixing efficiency on X_p/D_g was also refined and Fig. 150 is recommended for use with both 4-on-1 and impinging concentric injector concepts. Finally, Fig. 148 represents an improved correlation of mixing efficiency as a function of liquid orifice diameters. The Task IV FLOX/$CH_{4(g)}$ hot-fire data points were within ±0.1 of the predicted values over the range from 85 to 100 percent (Fig. 151) using the improved curves and performance prediction procedures described below.

Generally, the performance prediction procedure followed is to obtain a base prediction of E_m and $\overline{D}$ from the injector size and orifice geometry data available and to correct this prediction from baseline to planned hot-firing operating conditions. This requires an interpolation of E_m and $\overline{D}$ as a function of such parameters as $(V_g - V_\ell)$, X_p/D_g, etc. Then the mean dropsize, the propellant combination and mixture ratio, injection velocities (and total flowrate), and thrust chamber dimensions are applied as input to a standard combustion model computer program (see page 195 through 199), which calculates $(\eta_{c^*})_{vap}$. The appropriate value of E_m, propellant combination and overall mixture ratio permit evaluation of $(\eta_{c^*})_{mix}$ from curves similar to Fig. 90 for the appropriate propellant combination. This figure was established by simultaneous computation of E_m and $(\eta_{c^*})_{mix}$ for various degrees of propellant maldistribution. Finally the predicted η_{c^*} is obtained as a product of $(\eta_{c^*})_{vap}$ and $(\eta_{c^*})_{mix}$. The methods for obtaining the predicted mixing factor (E_m) and mass median dropsize are outlined below for each injector concept.

Basic Impinging Pentad

1. Obtain E_m and $\overline{D}$ from Fig. 54 and 52, respectively, for the correct element size and orifice geometry (i.e., D_g, D_ℓ/D_g).
2. Correct this base E_m and $\overline{D}$ to the appropriate penetration parameter using Fig. 53 and 50, respectively, assuming that the X_p/D_g trend is independent of D_ℓ and D_ℓ/D_g.

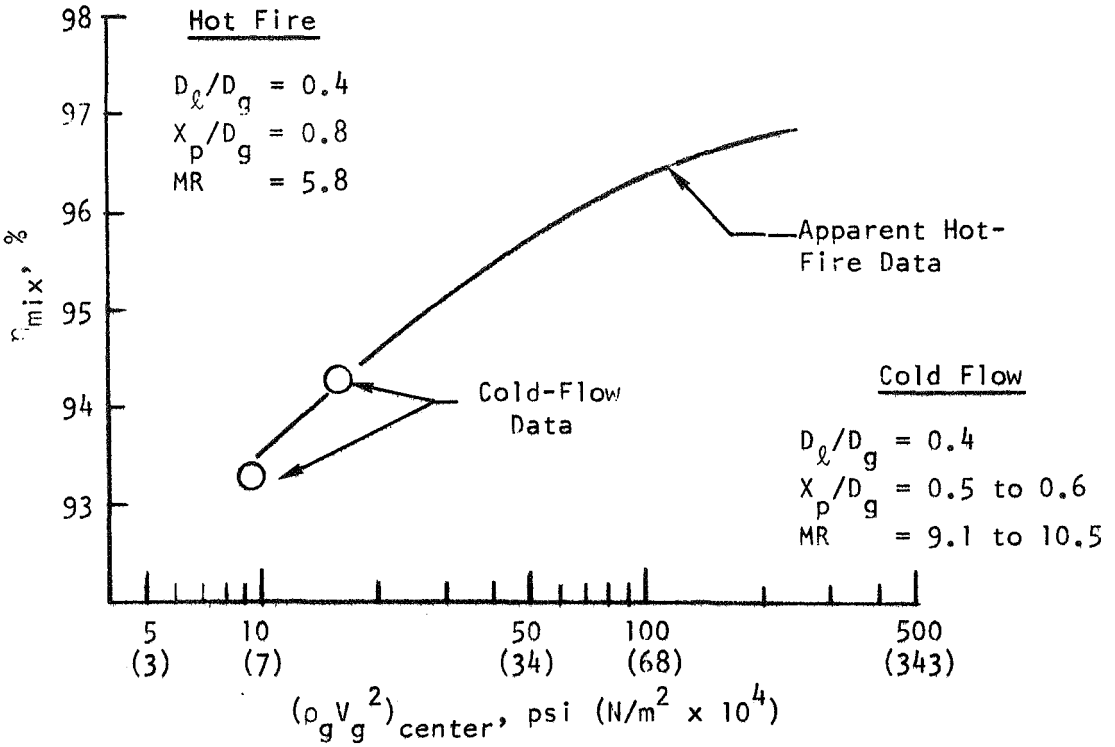

Figure 149. Refined Correlation of $(\rho_g V_g^2)_{center}$ vs Mixing Efficiency: Impinging Concentric Injector

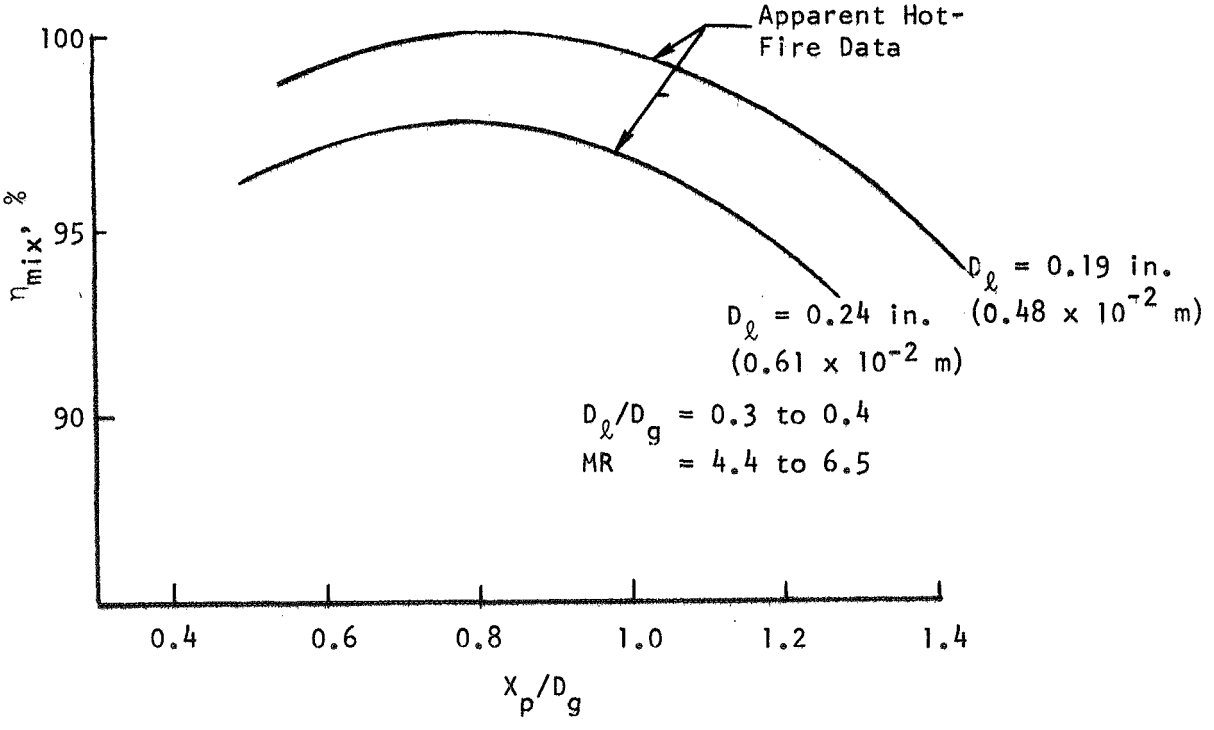

Figure 150. Refined Correlation of X_p/D_g vs Mixing Efficiency: Impinging Concentric Injector

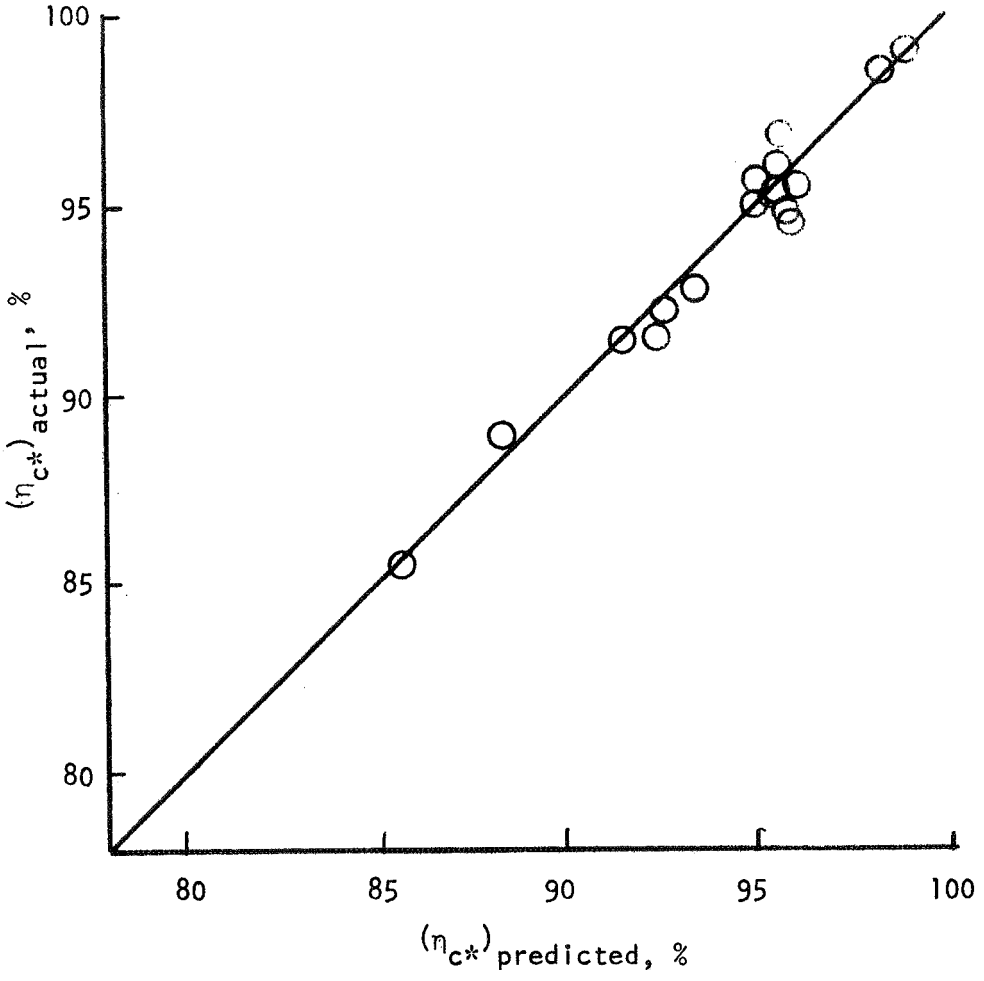

Figure 151. Predicted vs Actual Efficiencies Refined by Hot-Fire Data: Impinging Concentric Injector

3. Using the impinging concentric element curves in Fig. 149 and 145, correct these predictions to the correct center gas momentum flux $\rho_g V_g^2$. Again it is assumed that the $\rho_g V_g^2$ trend is independent of the preceeding variables.

Basic Impinging Triplet and Unlike Doublet

1. Follow steps 1 through 3 for the basic impinging pentad performance prediction procedure.
2. Correct the $\overline{D}$ so obtained for the appropriate number of liquid orifices (i.e., from the 4-on-1 element dropsize to that expected with a triplet or doublet) by use of Fig. 92.
3. No mixing data were obtained for the triplet injector. However, two data points obtained for the unlike doublet suggest that E_m is essentially the same as a pentad for equal X_p/D_g in the range 0.7 to 1.1. In this case, the pentad value can be used.

Basic Concentric Tube

1. Obtain E_m and $\overline{D}$ from Fig. 111 for the appropriate liquid orifice diameter.
2. Correct this E_m and $\overline{D}$ to the appropriate V_g-V_ℓ from Fig. 57 and 110, respectively, assuming no interaction between the parameters D_ℓ and (V_g-V_ℓ).
3. Correct this E_m and $\overline{D}$ to the appropriate mixture ratio from Fig. 57 and 56.
4. Correct E_m and $\overline{D}$ to the appropriate amount of post recess (Fig. 100 and 99).
5. No data were available to correct for the liquid injection velocity and gas density, although these parameters may be quite important. It is recommended that such correlations be added to the procedure in the near future.

Concentric Tube With Swirler

1. Follow steps 1 through 5 for the basic concentric tube performance prediction procedure.
2. Correct the resultant E_m and $\overline{D}$ for the appropriate liquid swirl velocity from Fig. 59 and 58, respectively. This, of course, assumes the swirl velocity trend to be independent of other parameters as necessary assumption because of the limited amount of available cold-flow data.

Impinging Concentric

1. Obtain E_m and $\overline{D}$ from Fig. 148 and 112, respectively, for the correct element size and orifice geometry (D_ℓ, D_ℓ/D_g).
2. Correct this base E_m and $\overline{D}$ to the appropriate penetration parameter, X_p/D_g, using Fig. 150 and 60, respectively.
3. Using Fig. 149 and 145, correct these predictions to the appropriate center gas momentum flux, $\rho_g V_g^2$.
4. No correction is recommended for the percentage fuel injected in the annulus provided that it is in the 20- to 35-percent range.
5. The above estimates are based on a liquid post recess of one liquid post inside diameter. It is recommended that the η_{c^*} estimate be reduced 0.5 percent if the posts are flushed.
6. No correction is available for the annulus gas injection velocity or the injected fuel (gas) density. Curves describing these parametric effects would represent a desirable addition to the calculation procedure.

Tricentric With Centerbody $(V_g)_{in} = (V_g)_{out}$

1. Obtain E_m and $\overline{D}$ from Fig. 107 for the appropriate element geometry.

2. Correct this E_m and $\overline{D}$ to the appropriate mixture ratio from Fig. 57 (concentric injector) and 62.

3. Correct the resultant E_m and $\overline{D}$ to the appropriate value of V_g-V_ℓ from Fig. 64 and 114, respectively.

4. No data are available to account for liquid injection velocity (different from approximately 75 ft/sec) or injected gas density.

5. With this resultant E_m and $\overline{D}$, obtain the performance prediction in the manner outlined previously. Then assuming a straight-line variation, correct prediction for the amount of liquid post recess from the hot-fire data presented in Fig. 136 using the top two curves and the appropriate mixture ratio.

Examples of Performance Prediction Procedure

As an aid to the preceding section, typical engine operating conditions are assumed in this section for each injector type and the performance prediction procedure is exemplified. These sample calculations follow the step-by-step methods outlined by the performance prediction procedure. No attempt has been made to use the optimum operating and design conditions for each injector type. However, this optimum design is easily attainable for specialized engine systems by using these procedures in an iterative fashion.

Several baseline conditions, such as propellant type, thrust level, etc., may be assumed as constant for all of the injector types. These assumptions used for the sample calculations are listed below.

1.	Propellant Combination	FLOX/CH_4(g)
2.	Mixture Ratio	5.75
3.	FLOX Injection Temperature	160 R (89K)
4.	Methane Injection Temperature	1000 R (555K)
5.	Thrust (vacuum) per Element	5000 lbf (22,200 N)

6.	Chamber Pressure	500 psi (345 x 10^4 N/m^2)
7.	Chamber Characteristic Length	30 in (0.76m)
8.	Chamber Contraction Ratio	2.0
9.	FLOX Injection Velocity	150 ft/sec (46m/s)
10.	Methane Injection Velocity	1100 ft/sec (336 m/s)

The sample calculations for each injector type are given below in a step-by-step fashion with the step numbers corresponding to the same numbers in the previous performance correlation procedure section. The procedure followed is to obtaine a base prediction of E_m and $\overline{D}$ (step 1) from the above assumptions and then adjust this value as necessary to fit the planned operating conditions. Unless otherwise noted, the adjustments are differentials made by "adding to" or "subtracting from" the base prediction.

Basic Impinging Pentad. For this element type, the assumed injection velocities and densities and the continuity equation yield FLOX and methane orifice diameters of 0.215 and 0.825 inch (0.546 and 2.096 x 10^{-2} m), respectively, when the constant operating parameters previously stated are considered. From these parameters, a penetration parameter of 0.86 (with a 45 deg; 0.79 rad included angle between oxidizer and fuel streams) and a fuel momentum flux of 260 psi (179 x 10^4 N/m^2) may be calculated. The method of predicting E_m and $\overline{D}$ is shown below:

1. From Fig. 54 and 52, E_m and $\overline{D}$ for this geometry are 80% and 260 μ (260 x 10^{-6} m), respectively.
2. Corrections for the penetration parameter (which may differ from those of Fig. 54 and 52) yield E_m and $\overline{D}$ of 82% and 260 μ (260 x 10^{-6}m), respectively, from Fig. 53 and 50. (The differential is added to or subtracted from the base values determined in step 1.)
3. Using Fig. 90 and 149 together plus Fig.145 to correct to the appropriate $\rho_g V_g^2$ yields a final E_m and $\overline{D}$ of 92% and 110 μ (110 x 10^{-6}m), respectively.

These predicted values of $\overline{D}$ and E_m can then be used to determine vaporization and mixing efficiencies of 99.5 and 97 percent from combustion model data shown in Fig. 89 and 90. Thus, the predicted combustion efficiency for this injector element is the product of η_{vap} and η_{mix} or 96.5 percent.

Basic Impinging Triplet and Unlike Doublet. Using the assumed injection velocities (150 ft/sec; 46 m/s and 1100 ft/sec; 336 m/s), FLOX orifice diameters of 0.322 and 0.430 in. (0.818 and 1.092×10^{-2}m) are required for the triplet and unlike doublet, respectively, while the methane orifice diameter remains 0.825 in. (2.096×10^{-2}m). Penetration parameters are therefore 1.15 and 1.72 for the triplet and unlike doublet (with a 45 deg; 0.79 rad included angle between oxidizer and fuel streams) while the fuel momentum flux remains 260 psi (179×10^4 N/m^2). The performance prediction method is outlined below for the triplet. Similar procedures would be used for the unlike doublet.

1. From Fig. 54 and 52, E_m and $\overline{D}$ for this geometry are 78 percent and 350 μ (350×10^{-6}m), respectively.
2. Penetration parameter corrections from Fig. 53 and 50 yield 98 percent and 430 μ (430×10^{-6}m).
3. Using Fig. 90, 149, and 145 to correct to the appropriate $P_g V_g^2$ yields E_m and $\overline{D}$ of 100 percent and 230 μ (230×10^{-6}m).
4. Correction to the appropriate number of liquid orifices yields 150 μ (150×10^{-6}m) from Fig. 92 (dropsize only). The mixing parameter is assumed to remain at 100 percent.

These values of E_m and $\overline{D}$ yield a vaporization efficiency of 97 percent from Fig. 89 and a mixing efficiency of 100 percent from Fig. 90, thereby obtaining 97 percent combustion efficiency prediction.

Basic Concentric Tube. The assumed injection velocities and propellant densities yield a liquid diameter of 0.430 in. (1.092×10^{-2}m) and a $V_g - V_\ell$

of 950 ft/sec (290 m/s). A post recess will be assumed equal to twice the liquid orifice diameter. The prediction procedure is shown below:

1. An E_m and D of 56 percent and 340 μ (340 x 10^{-6}m), respectively, is attained for the given liquid diameter from Fig. 111.
2. Correcting these values to the appropriate $V_g - V_\ell$ from Fig. 57 and 110 yield 55 percent and 350 μ (350 x 10^{-6}m).
3. The mixture ratio correction from Fig. 57 and 56 yield no change in E_m and $\overline{D}$ for this case since the initial value was 5.85 (step 1) vs 5.75 for the assumed operation.
4. The correction for the amount of post recess from Fig. 100 and 99 yield E_m and $\overline{D}$ of 72 percent and 190 μ (190 x 10^{-6}m), respectively.

These values of $\overline{D}$ and E_m yield η_{vap} and η_{mix} of 92.5 and 89 percent, respectively, (from Fig. 89 and 90), thereby producing a 82.3 percent combustion efficiency prediction.

Concentric Tube With Swirler. The assumptions and calculations made for the basic concentric tube are directly applicable to this injector type, except for the degree of post recess (0.0). In addition, a 60 ft/sec (18 m/s) swirl inlet velocity will be assumed. The sample performance prediction is given below:

1. From the basic concentric tube sample calculations, and E_m and $\overline{D}$ of 55 percent and 350 μ (350 x 10^{-6}m), respectively is attained (same as steps 1 - 3 for the basic concentric).
2. Using the appropriate swirl velocity correction yields 93 percent and 165 μ (165 x 10^{-6}m), respectively, from Fig. 59 and 58. The correction from Fig. 58 is taken as a percentage change and adjusted for $V_g - V_\ell$ differences.

These predicted values of $\overline{D}$ and E_m can then be used to determine vaporization and mixing efficiencies of 95 and 98 percent from combustion model data shown

in Fig. 89 and 90. Thus, the predicted combustion efficiency for this injector element would be 93.1 percent.

Impinging Concentric. The liquid orifice diameter for this element is 0.215 in. (0.546×10^{-2}m) from the assumed conditions. Assuming 80 percent of the fuel flow in the center orifice, a fuel orifice diameter of 0.740 in. (1.880×10^{-2}m) is required to obtain an 1100 ft/sec (336 m/s) fuel injection velocity. These values yield a penetration parameter (with a 45 deg; 0.79 rad included angle between oxidizer and fuel impinging streams) of 0.975 and a fuel momentum flux of 260 psi (179×10^{4} N/m^2). The procedure for predicting performance for this element is described below:

1. The appropriate element geometry yields E_m and $\overline{D}$ of 68 percent and 320 μ (320×10^{-6}m), respectively, from Fig. 148 and 112.
2. Correction to the appropriate penetration parameter from Fig. 150 and 60 yields an E_m and $\overline{D}$ of 68 percent and 360 μ (360×10^{-6}m).
3. From Fig. 90, 149, and 145, correction to the appropriate center fuel momentum flux yields 74 percent and 130 μ (130×10^{-6}m).
4. No correction is applied for the percentage fuel in the annulus in the 20 to 35 percent range.
5. Assuming a liquid post recess of one liquid orifice inside diameter means no correction is applicable.

The final predicted values of E_m and $\overline{D}$ yield η_{mix} and η_{vap} of 91 and 98.5 percent respectively, from Fig. 90 and 89. Thus an 89.6 percent combustion efficiency is predicted with this element.

Tricentric With Centerbody. Assuming equal inner and outer fuel annulus areas with the injection velocities previously described, and an inner to outer annulus gap ratio of 2.4 yields a centerbody diameter of approximately 0.2 in. (0.5×10^{-2}m). The sample calculation for this injector type is giben below:

1. From the element geometry and Fig. 90 and 107, a baseline E_m and $\overline{D}$ of 85 percent and 165 μ (165×10^{-6}m) is obtained.

2. No correction is applicable for the appropriate mixture ratio since the engine and coldflow mixture ratios were 5.75.

3. Correcting to the appropriate values of $V_g - V_\ell$ from Fig. 64 and 114 yield 85 percent and 210 μ (210×10^{-6}m).

4. No correction is available for the higher liquid injection velocity.

5. Obtaining a performance prediction from Fig. 89 and 90 yields a predicted combustion efficiency of 86.5 percent (91 percent for $\overline{D}$ and 95 for E_m) for a zero recess injector element. Assuming an oxidizer annulus recess of 0.1 in. (0.25×10^{-2}m) and using Fig. 136, results in a combustion efficiency of 91.5 percent.

APPENDIX A

DEVELOPMENT OF TWO-PHASE IMPACT PROBES

To determine the mass and mixture ratio distributions produced by the various gas/liquid injectors, it was necessary to develop a measurement system that would be capable of defining local values of both the liquid and gas mass fluxes. At the inception of the subject program, a technique existed for the experimental determination of the liquid mass flux distributions. This technique involves the use of a streamtube collection facility wherein liquid distributions are determined by collecting the liquid spray in a grid of collection tubes. The liquid collection system consists of a 10 by 10 matrix of 100 individual square-ended (1 in. by 1 in.; 2.54×10^{-2}m) collection tubes. This technique of liquid distribution had been used successfully by a number of liquid/liquid propellant programs (Ref. 1).

A special probe was required for determining local values of gas velocity from which local values of gas phase mass flux could be determined. Conventional gas phase stagnation probes (pitot, etc) were not applicable in dense two-phase sprayfields because of the interaction of the liquid droplets and gas near and within a conventional stagnation probe. The gas/liquid droplet interaction phenomenon is discussed further in subsequent paragraphs.

DUSSOURD AND SHAPIRO IMPACT PROBE

A literature search was conducted to determine available means for measuring gas phase velocity in gas/liquid sprayfields. The most applicable work which was found was that of Dussourd and Shapiro who developed a two-phase flow impact probe for the measurement of the gas phase stagnation pressure, and from this the determination of the gas phase velocity (Ref. 6). The reference probe was operated successfully by the referenced authors at ambient pressures in low liquid-to-gas mass flow ratio (MR < 0.2) sprayfields.

Description of Probe

A schematic of the Dussourd/Shapiro probe is presented in Fig. A-1. The probe consists of a tube with appropriate pressure taps and an orifice to vent the water captured by the probe.

The operating principle of the probe is based on the separate deceleration of the gas and particulate phases of the two-phase sprayfield. The droplets and gas (each at their own velocity) encounter the probe tip, but the gas phase is brought to near stagnation conditions at the probe tip and the pressure is measured near the probe tip before the droplets can impart an appreciable amount of their momentum to the gas stagnation pressure.

Analytical Considerations

Dussourd and Shapiro conducted an analytical study to determine the dynamic interactions between the liquid droplets, the gas, and the probe. Near the probe tip a complex three-dimensional flowfield exists. When a droplet crosses the gas streamlines, it is subjected to a drag force because of the velocity difference between the droplet and the gas. In addition, the droplet is subjected to a buoyancy force as a result of the unfavorable pressure gradient created by the deceleration of the gas phase near the probe tip. Thus, the droplet is subjected to both an axial retarding force and a force directed radially outward. The effects if these dynamic forces near the probe tip result in the following: (1) the relative amount of water which is captured is less than the water that would be captured without these forces, and (2) the gas phase stagnation pressure, as measured within the probe, is higher than the true gas phase stagnation pressure because of momentum exchange from the droplets to the gas upstream of the pressure measurement location.

To analytically describe the phenomenon which occurs at the probe tip, Dussourd and Shapiro assumed the following:

1. The gas flow is incompressible, nonviscous, and irrotational.

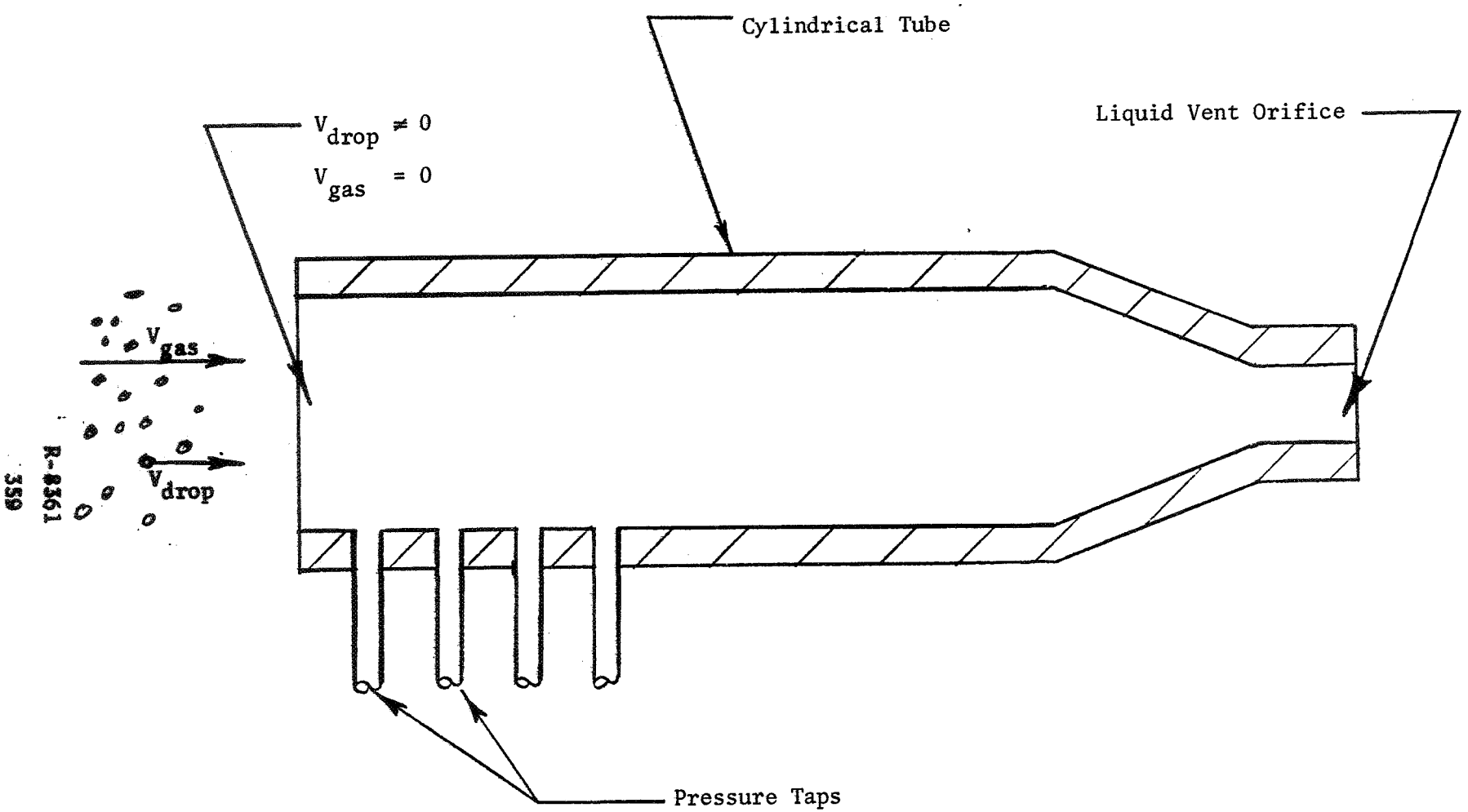

Figure A-1. Schematic of Dussourd and Shapiro Probe

2. The gas phase flow pattern is unaffected by the presence of the droplets.

3. The droplets behave like solid spheres with no mutual interaction.

4. The droplets are small compared to the probe dimension and are monodispersed.

5. The drag coefficient of the droplets is a function of the droplet Reynolds number based on the relative droplet-gas velocity difference.

6. The drag forces are the only significant forces acting on the droplet. Other forces, such as gravity and buoyancy, are small.

7. The droplets and gas are in dynamic equilibrium far upstream from the probe tip.

From the Dussourd analytical study two dependent probe parameters evolved: (1) the probe droplet capture efficiency, and (2) the probe overpressure ratio which is a measure of the gas droplet interaction near the probe tip. The capture efficiency was defined as:

$$e \equiv \frac{\text{Actual Capture Rate of Droplets}}{\text{Capture Rate of Droplet With No Gas/Droplet Interactions}} \qquad \text{(A-1)}$$

The overpressure ratio (OPR) was defined as:

$$\text{OPR} \equiv \frac{P_{meas} - P_o}{1/2\ \rho_g V_{g,\infty}^2 \left(\frac{\dot{w}_\ell}{\dot{w}_g}\right)} \geq 1 \qquad \text{(A-2)}$$

where P_{meas} = the gas phase stagnation pressure as measured by the probe

P_o = the true gas phase stagnation pressure

ρ_g = the gas phase density

$V_{g,\infty}$ = the gas phase velocity far upstream of the probe

$\dot{w}_\ell$ = local liquid droplet mass flow

$\dot{w}_g$ = local gas mass flow

From the Dussourd analytical study, it evolves that the droplet capture efficiency and overpressure are functions of two-dimensionless parameters: (1) the obedience number, which is an index of the relative effect of the gas phase potential field on the droplets, and (2) the droplet Reynolds number, which is an index of the droplet drag.

The obedience number (ON) was defined as:

$$ON \equiv 3/4 \frac{\rho_{g,\infty} D}{\rho_{\ell} d} \tag{A-3}$$

where D = the probe tip diameter

d = diameter of the droplets

$\rho_{g,\infty}$ = the gas phase density far upstream of the probe

ρ_{ℓ} = the liquid phase density

The droplet Reynolds number was defined as:

$$Re_{\infty} \equiv \frac{\rho_{g,\infty} V_{\ell,\infty} d}{\mu g} \tag{A-4}$$

The relationship between the probe capture efficiency and the obedience number is shown in Fig. A-2 as a function of droplet Reynolds number. The dependency of the probe overpressure ratio on the obedience number and the droplet Reynold's number is presented in Fig. A-3.

Dussourd and Shapiro conducted experimental studies which indicated that the theoretical predictions of Fig. A-2 and A-3 were in general agreement with the test results. Their experimental studies were conducted employing the following range of pertinent flowfield variables:

Freestream gas phase Mach number, 0.47 to 0.75

Local liquid to gas flowrate ratio ($\dot{w}_{\ell}/\dot{w}_{g}$), 0.13 to 0.20

Monodispersed spray, droplet diameter, 8 to 18 μ (8 to 18 x 10^{-6} m)

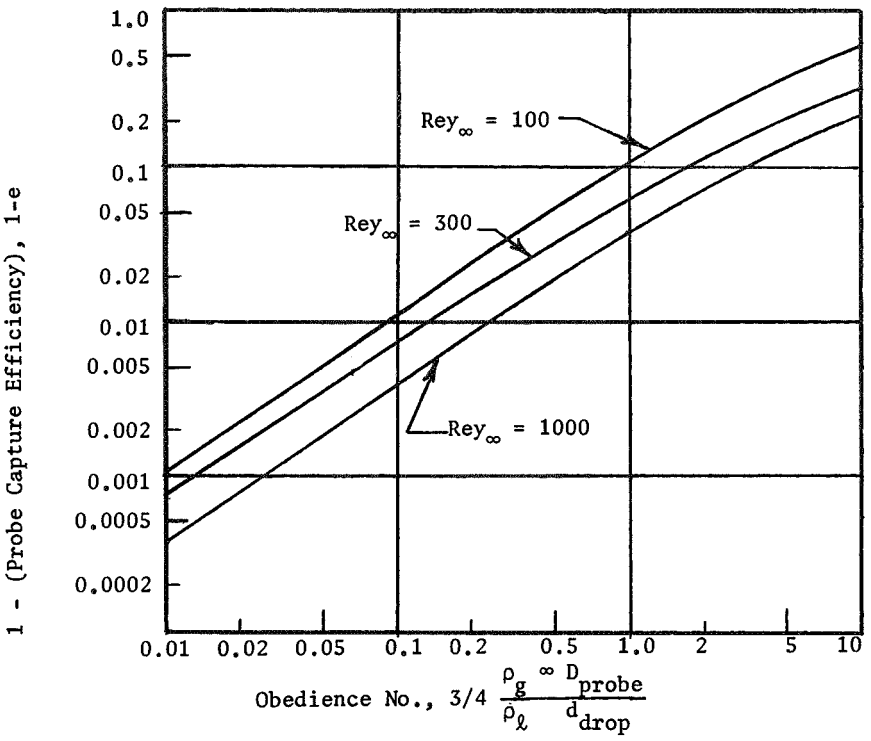

Figure A-2. Dussourd and Shapiro Capture Efficiency vs Obedience Number and Reynolds Number

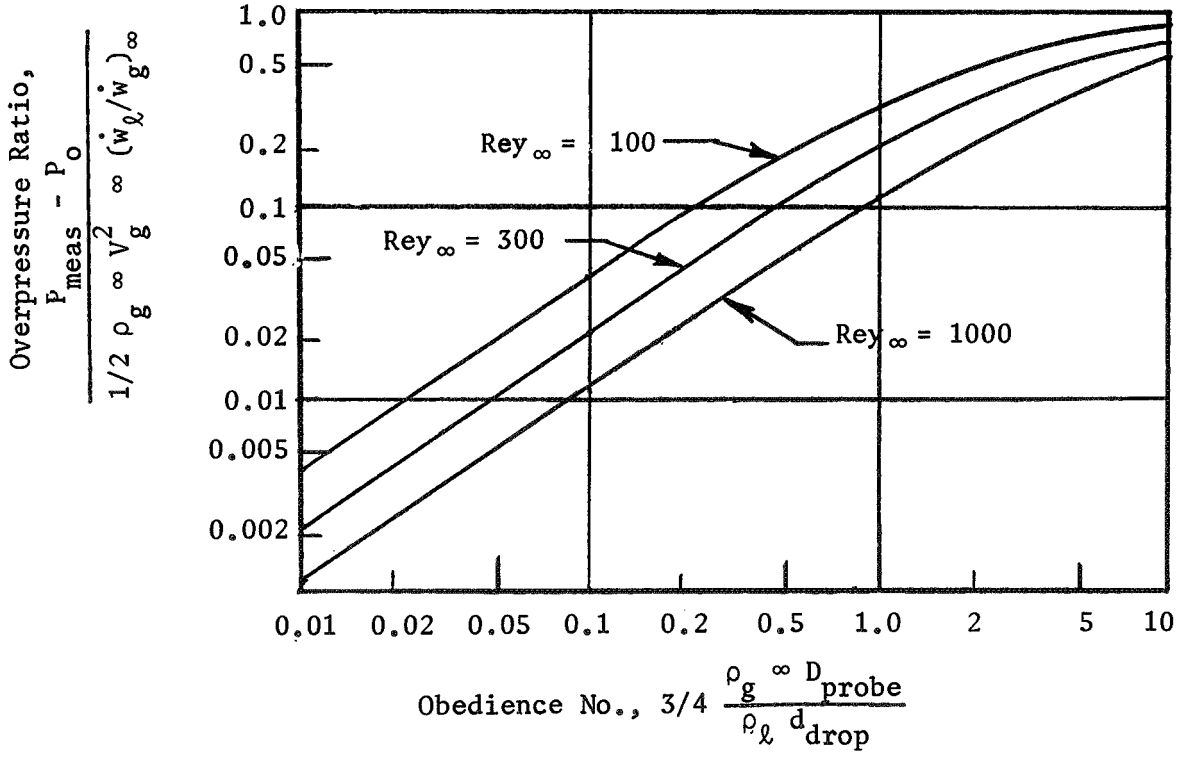

Figure A-3. Dussourd and Shapiro Overpressure Ratio vs Obedience Number and Reynolds Number

For the subject study, the expected two-phase flowfield variables differ significantly from those listed above. Consequently, it was deemed necessary to conduct a feasibility analysis to determine the applicability of the two-phase impact probe for the gas/liquid mixing studies.

Probe Feasibility Studies

The primary purpose of the probe feasibility studies was to determine analytically whether or not a Dussourd-type probe was capable of producing reliable data in the anticipated two-phase flowfields. Thus, considerations were given to the probe overpressure ratio and capture efficiency for the two-phase flowfields of interest.

The principal difference between the Dussourd study and the flowfields of interest in the subject program can be seen by comparing the aforementioned list of the Dussourd and Shapiro operating parameters with those following:

1. Local freestream Mach number, 0.02 to 0.40
2. Local liquid to gas flowrate ratios, 0.25 to 15
3. Polydispersed droplet spray diameters, 25 to 500 μ (25 to 500 x 10^{-6} m)
4. Nonequilibrium (unequal) velocities between droplets and gas upstream of probe tip

Overpressure Ratio. It will be recalled that "overpressure ratio" (over-unity) measures the difference between the probe pressure data and the true gas stagnation pressure which results from a partial transfer of spray momenta to the declerated gas stream. This overpressure ratio must be either negligible or small enough to be accurately described analytically or by calibrations to permit accurate probe application. To determine the feasibility of employing a Dussourd-type impact probe for the subject studies, the Dussourd-Shapiro data reduction method was extended analytically to

include polydispersed sprays with a nonuniform dropsize distribution function* (Nukiyama-Tanasawa) and two different velocity "distribution functions". One velocity distribution function was simply a uniform velocity for all dropsize groups while the other resulted from the application of droplet drag equations to a polydispersed liquid sprayfield. The gas velocity profile used in the droplet drag equation approximated the analytical far field solution for a free jet. Several cases were run to compare the effects of uniform droplet velocities with various initial gas velocities, volume mean dropsizes, mixture ratios, mass average liquid velocities, and distance in which the droplets are subjected to drag. Typical results of this comparison are given in Table A-1 in terms of percent overpressure. Note that, as defined in the table, this term differs from Dussourd's "overpressure data" by the mixture ratio factor. Note that the difference in the percent overpressure coefficient calculated with these two droplet velocity distribution functions is approximately 1 percent. Thus the influence of droplet velocity distribution on any data corrections for overpressure would be negligible. This, of course, does not imply that the average spray velocity level is inconsequential. In fact, comparison of cases 3 and 4 indicates a substantial decrease in overpressure with increasing average liquid velocity.

Comparisons were also obtained between the percent overpressure calculated for both a monodispersed and a Nukiyama-Tanasawa dropsize distribution where the volume mean dropsize of the latter was equal to the monodispersed dropsize. Using the Nukiyama-Tanasawa distribution, the contribution of each dropsize group to the overpressure was found and summed to yield a total percent overpressure. The comparison is illustrated in terms of "percent overpressure" in Fig. A-4 through A-6 for several constant volume mean dropsizes, average liquid velocities and local ratios of liquid to gas flowrate and for a probe inlet diameter of 0.3 inch (0.76×10^{-2} m).**

---

* The polydisperse sprays were represented by a series of discrete dropsize groups in these computations.

**Theoretical analysis predicts that decreasing the probe inlet diameter would decrease the overpressure ratios presented in Fig. A-2 and A-3.

TABLE A-1

EFFECT OF VELOCITY DISTRIBUTION ON OVERPRESSURE

Case No.	D_{30}, μ or m x 10^{-6}	MR	V_ℓ (mass avg.)		Drag Dist.		V_g (initial)		Overpressure Coefficient	
			ft/sec	m/s	in.	m	ft/sec	m/s	Case (1)*	Case (2)*
1	30	6	100	30	5	0.13	900	274	68	67.4
2	30	6	100	30	2	0.05	900	274	68	69.9
3	100	6	100	30	5	0.13	900	274	11.4	11.8
4	100	6	30	9	5	0.13	900	274	29.3	29.6
5	250	15	100	30	5	0.13	900	274	7.3	7.8
6	250	6	100	30	5	0.13	900	274	2.9	3.1
7	100	1	100	30	5	0.13	900	274	1.9	2.0
8	100	1	100	30	5	0.13	600	183	1.9	2.0
9	250	1	100	30	5	0.13	600	183	0.5	0.5

$P_{o,\ gas}$ = 0.4 psi (0.28 x 10^4 N/m^2)

*Case (1) - Based on Uniform Liquid Velocity
Case (2) - Liquid Velocity Determined by Gas Drag on Various Dropsizes

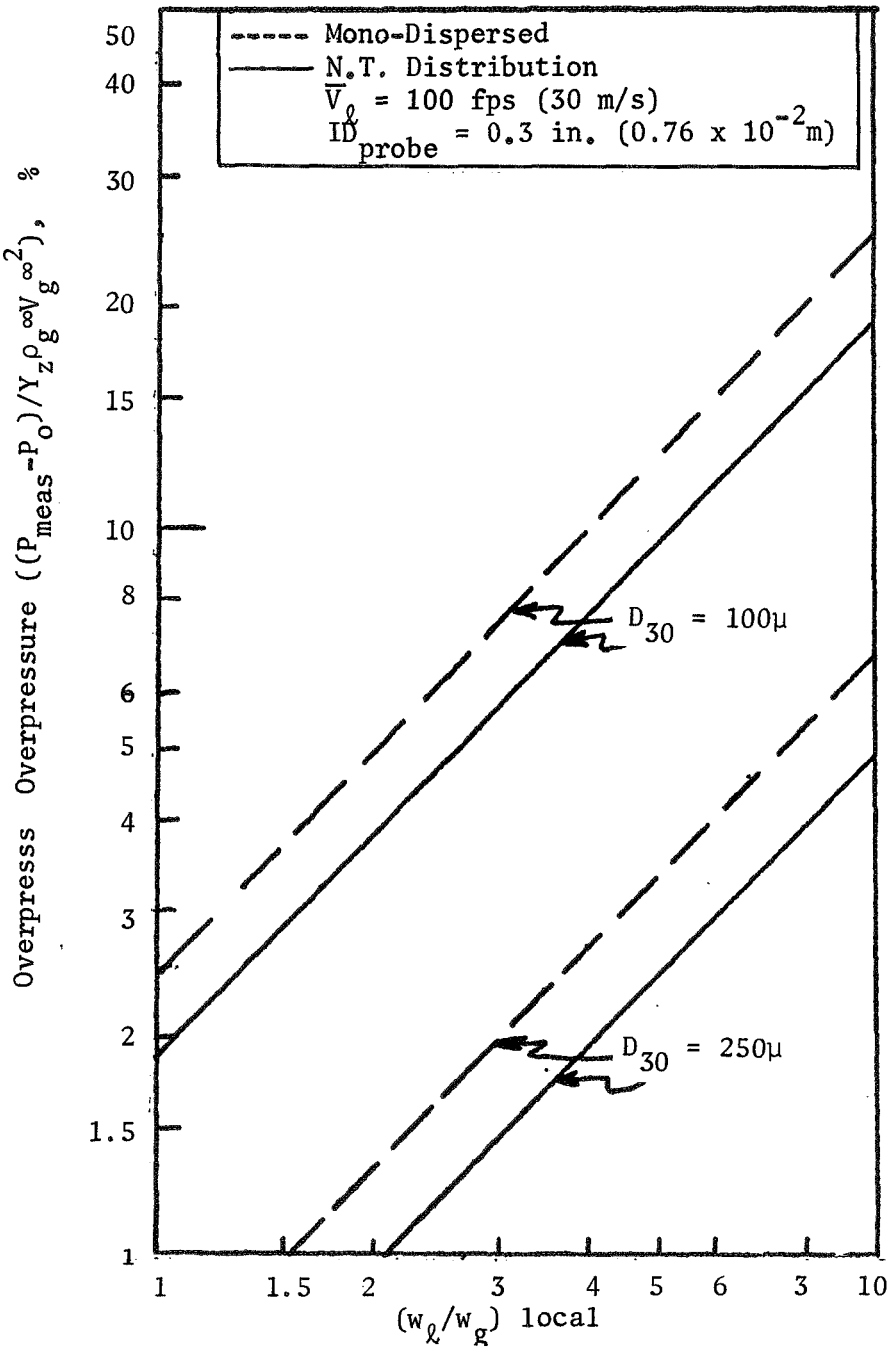

Figure A-4. Percent Overpressure as a Function of D_{30} and $(\dot{w}_\ell/\dot{w}_g)_{Local}$

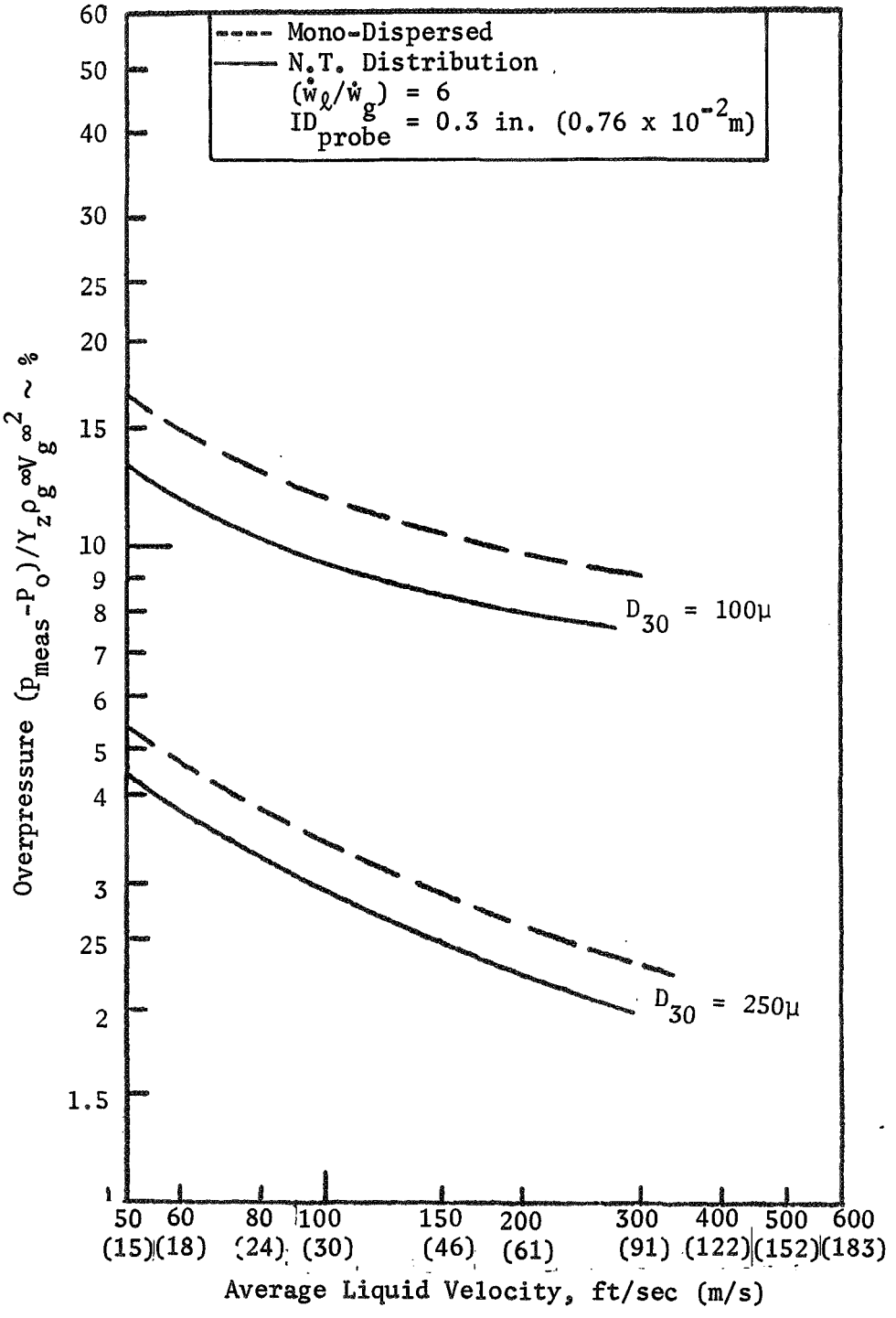

Figure A-5. Percent Overpressure as a Function of Average Velocity and Average Dropsize

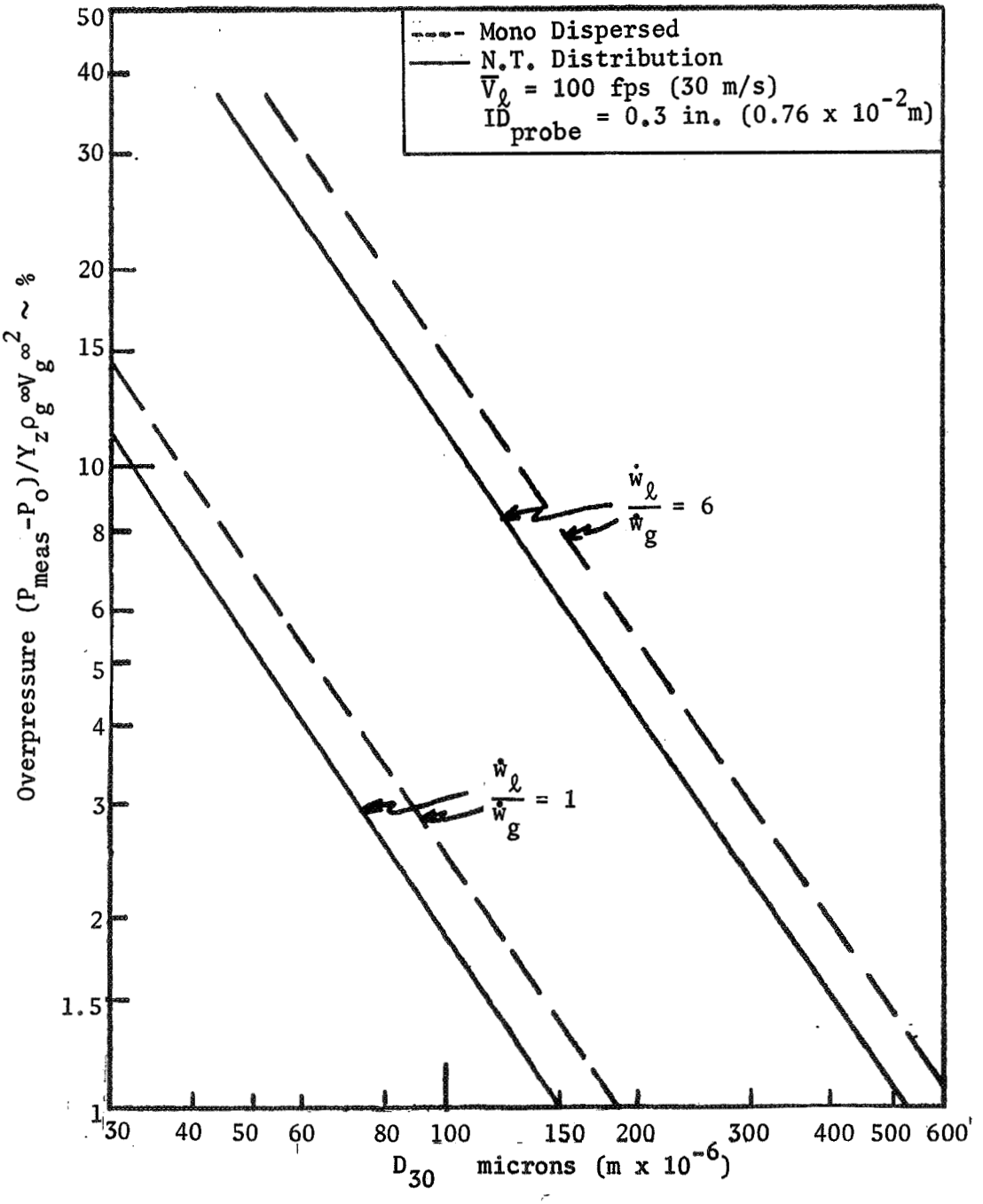

Figure A-6. Percent Overpressure as a Function of Average Dropsize $(\dot{w}_\ell/\dot{w}_g)_{Local}$

Note that the percent overpressure is appreciably less (e.g., 50 percent) for the Nukiyama-Tanasawa distribution than for the monodispersed spray. For a given D_{30}, the polydispersed spray overpressure was found to be smaller by a constant factor than that of the uniform sized drops for any local mixture ratio. Thus, the size distribution of the droplets upstream of the probe does influence the data reduction technique.

The curves generated in this analysis were applied to determine the feasibility of the anticipated cold-flow probe tests. To analytically calculate the overpressure coefficient for pressure measurements under typical anticipated cold-flow test conditions, the average dropsize, the dropsize distribution, the average liquid velocity, and the local ratio of liquid to gas flowrate must be known. In Task I, the hot-fire dropsize was in the 100 μ (100 x 10^{-6}m) range. However, in the simulation of hot-fire conditions at atmospheric pressure, the cold-flow gas momentum is somewhat lower than the hot fire. Thus, the average dropsize resulting from the cold-flow tests will be larger than the hot-fire dropsize. Assuming a cold-flow volume mean dropsize of between 100 and 200 μ (100 and 200 x 10^{-6}m), a Nukiyama-Tanasawa distribution, a liquid average velocity of 50 (15.2 m/s), and a mixture ratio of 5 yields only an 8-percent overpressure coefficient. Thus, it was concluded that overpressures for the subject application would be small enough to permit effective use of a two-phase probe, although overpressure correction should be applied to the data.

Probe Capture Efficiency. Consideration of the probe capture efficiency was necessary to predict the flowfield distortion caused by the presence of the probe. Based on the anticipated (previously listed) flowfield parameters, an expected range of the probe obedience number was approximately 0.05 to 1.0 and the droplet Reynolds number range should be 10^2 to 10^3. Referring to Fig. A-2 the lowest anticipated value of probe capture efficiency is approximately 96 percent. Thus, theoretically, it was concluded that the Dussourd-type probe would not produce any significant distortions in the flowfields of interest.

Discussion of Results. It was concluded that under the contemplated test conditions the overpressure and capture efficiency would not be prohibitive and that the Dussourd-type impact probe could be used as an effective tool for the characterization of the two-phase injector sprayfield of the subject study. However, it was noted that probe flooding (filling of the probe stagnation tube with water) could be a potential problem due to the local mass flow ratios ($\dot{w}_\ell/\dot{w}_g$) being much higher than those used by Dussourd.

TASK I, PROBE DEVELOPMENT

Description of Probe

A modified version of the Dussourd probe was fabricated for the Task I cold-flow distribution studies. The Task I probe with its water accumulation tapoff is shown schematically in Fig. A-7. The choice of a 0.3 in. (0.76×10^{-2}m) probe tip diameter was based on preliminary tests in injector sprayfield which indicated that this size was necessary to prevent flooding of the probe. Under steady-state flow conditions, the probe and water accumulator are filled with stagnant gas and the pressure which is measured at the 0.15-in. (0.38×10^{-2}m)-diameter pressure port, taken as the gas phase stagnation pressure. The pressure tap was located near the probe tip to minimize spray momentum exchange effects on the measured gas stagnation pressure. The liquid droplets which enter the probe tip are collected in the 0.30 in. (0.76×10^{-2}m) diameter tube and are then drained to the liquid accumulator. The probe holding tube was designed so that it could be attached to the 10 times 10 liquid collection grid. Movement of the probe within the sprayfield was manual. Probe stagnation pressures were measured by a bank of single and two-fluid manometers.

Analytical Considerations for Task I Probe Configuration

Theoretical predictions of probe capture efficiency were made for the actual Task I probe as designed. For the 0.30-in. (0.76×10^{-2}m)-diameter probe, a

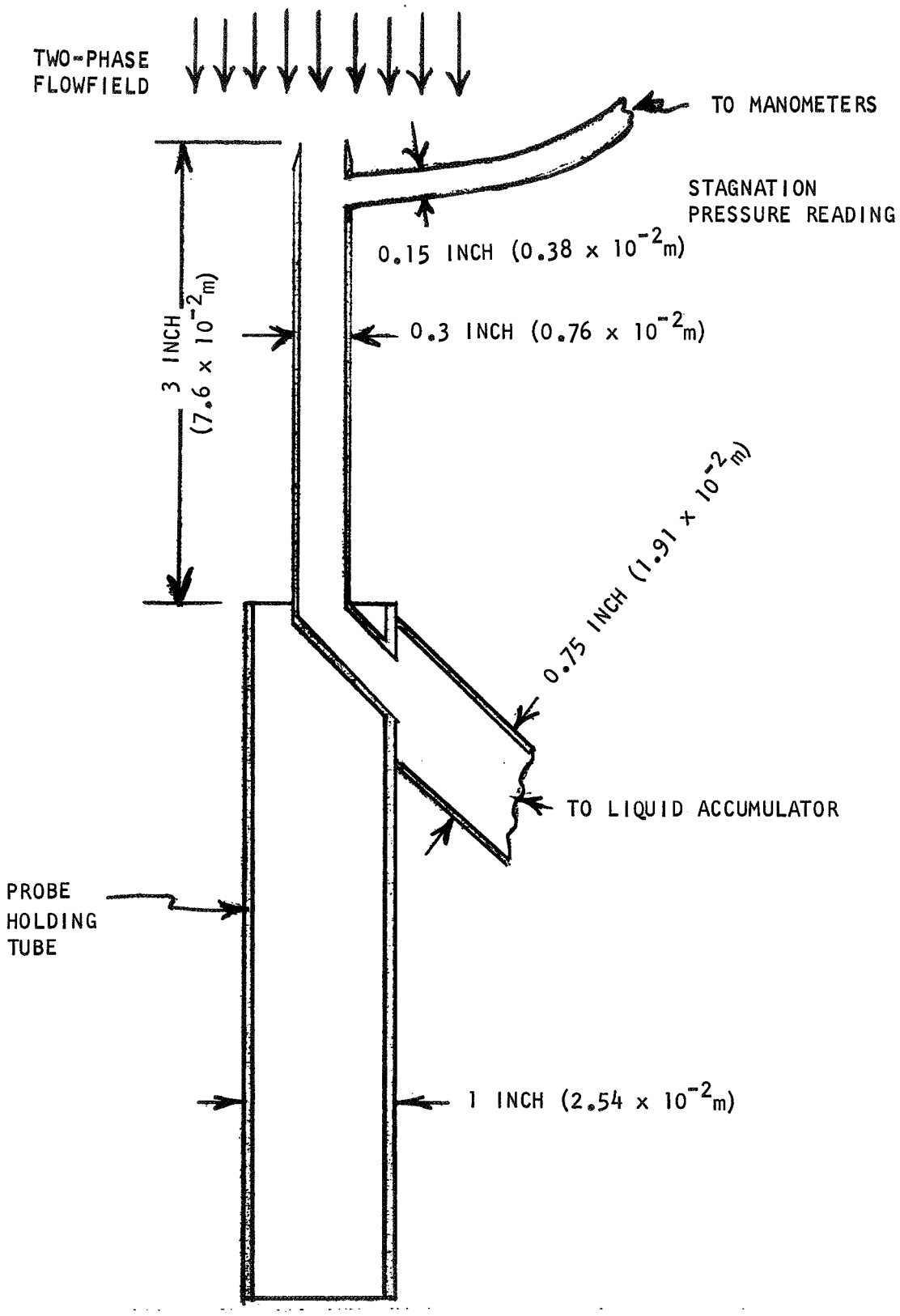

Figure A-7. Schematic of Stagnation Pressure Probe

gas velocity of 400 ft/sec (122 m/s), and droplet diameters of 100 and 10 μ (100 and 10 x 10^{-6}m), the calculated capture efficiency is 99.3 and 96 percent, respectively, thus indicating no significant flowfield distortion by the probe.

Comparisons were also obtained of the percent overpressure calculated for both a monodispersed and Nukiyama-Tanasawa dropsize distribution. Using the latter distribution, the contribution of each dropsize group to the overpressure was found and summed to yield a total percent overpressure. An 8-percent overpressure coefficient was calculated at typical operating conditions.

Probe Checkout Tests

Probe Tests in Gaseous Flowfield. Three preliminary checkout tests were conducted with the probe in a gaseous flowfield. In these tests, both the injected gas (GN_2) flowrate and the gas jet orifice diameter were varied independently. Stagnation pressure measurements made across the flowfield and combined with the appropriate area and gas density yielded velocity, mass flux, and momentum (flux) profiles for the jet. In the free-jet system it was not possible to use continuity to verify the probe measurements because of the gas (air) which was ingested from the surroundings. However, because the static pressure in each cross section of a free submerged jet (a free jet flowing into stagnant surrounding gas) is essentially uniform and equal in the pressure in the surrounding space, the total momentum flux of injected plus entrained gas should not vary with axial location. In other words, momentum is conserved and the injected gas momentum is conserved and the injected gas momentum flowrate should equal the measured gas momentum flowrates summed over each collection plane. In each test, the calculated momentum flow (based on probe pressure measurements) was within 5 percent of the momentum flow injected, which was considered satisfactory. Also, the measured velocity profile was quite similar to a theoretical submerged velocity profile. Subsequent tests were performed to evaluate the probe in an actual two-phase flowfield.

Probe Tests in Gas/Liquid Flowfield. The total (two-phase) momentum flow was measured in the first tests* to compare the total momentum flow at the plane of measurement with that injected. This was accomplished by filling the accumulator and probe with water (to stagnate both gas and spray) and measuring the pressure in the side pressure tap which was also filled with water. Measurements were then made across the flowfield. These measurements, along with the appropriate areas, yielded the two-phase momentum flux at each measuring point. The total collected momentum flow was about 21-percent greater than the axial component of the injected momentum flow from the gas and liquid jets, which was considered reasonably close.

Although (at that time) it was not possible to separate the ingested air from the injected simulant flowrates, qualitative evaluation of the measurement technique was accomplished by measurement of the total gas momentum flow and velocity profiles. The injected gas momentum flow was equivalent to 6.4 lbf (28 N) and the total gas momentum flow measured was 5 lbf (22 N). This indicates that about 1.4 lbf (6 N) was transferred from the gas to the liquid, which seems plausible. Measured gas velocity profiles through the center of the flowfield are plotted in Fig. A-8 for tests with a single-phase gas flow and for a two-phase flow test. The injected gas velocity was the same for both of these tests. Note that the presence of the liquid reduces the centerline gas velocity to about one-half that of the single-phase flow velocity while spreading out the gas from a 3-in. (7.6×10^{-2}m) to a 5-in. (12.7×10^{-2}m)-diameter jet. Again, these trends are quite reasonable and support the validity of the two-phase probe data.

Discussion of Results. A major limitation on the probe technique was the inability to distinguish between injected gas and entrained air flowrates. Additionally, the probe configuration of Task I possessed two measurement problems which deserved further study. As the droplets passed through the probe tip, temporal radial pressure gradients were established. These local pressure

*The cold-flow model of the Task I recessed impinging jet injector was used in these tests.

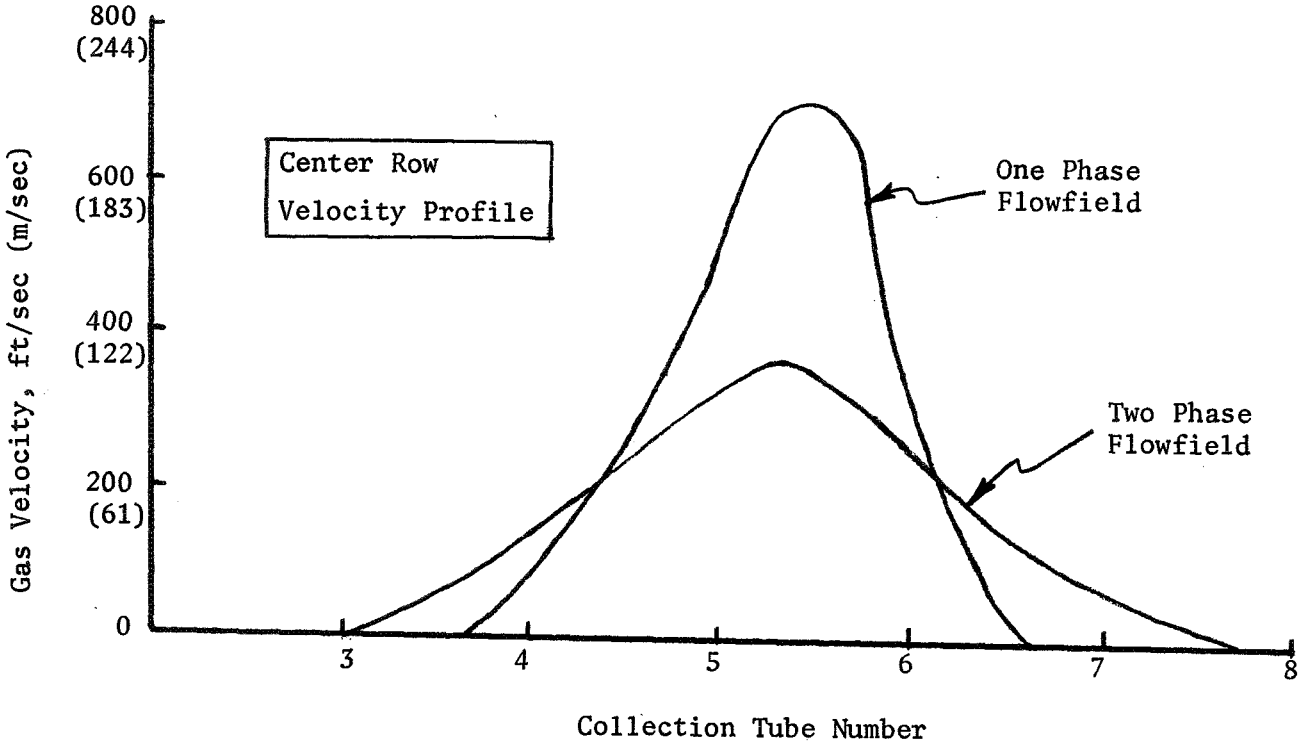

Figure A-8. Recessed Impinging Jet Injector Gas Velocity Profiles

gradients resulted in oscillations in the pressure readings made at the single pressure tap. Also, under high local mixture ratio, low-dynamic-pressure flowfield conditions, water tended to flood the single circular pressure tap. Further probe development was conducted under Task II to minimize the aforementioned problem areas.

TASK II, PROBE DEVELOPMENT

Description of Probe

A schematic of the two-phase impact which was developed under Task II* is presented in Fig. A-9. The probe was constructed of two concentric tubes with a specially designed tip attached to the outer tube. The tip was designed to prevent the passage of water (termed flooding) into the annulus formed by the tubes when the probe was utilized in high liquid/gas flowrate ratio flowfields. In addition, the gas phase stagnation pressure was measured in a 360 deg (6.28 rad) annulus at the probe tip rather than at a single point as in the Task I probe. Tests conducted with both the Task I probe configuration and the concentric tube probe demonstrated that the latter design eliminates the pressure oscillation encountered with the Task I configuration. In addition, the concentric tube probe design avoids the need for an external pressure line at the probe tip, which could create flowfield disturbances.

The gas phase stagnation pressure in the probe annulus was measured with an MKS Baratron-Type 77 Electronic Pressure Meter. The MKS Baratron system possesses accuracy of 0.02 percent of full-scale range (±0.02 mm Hg; 2.66 N/m^2). In addition, an oxygen sampling system was used in conjunction with the concentric tube probe in the Task II studies. This made possible a distinction between injected GN_2 and entrained air flow at each measurement point. The oxygen measurement system is discussed in detail under the Task II Experimental Apparatus Section of this report.

*The probe system development was a joint effort of the subject contract and NAS3-12051.

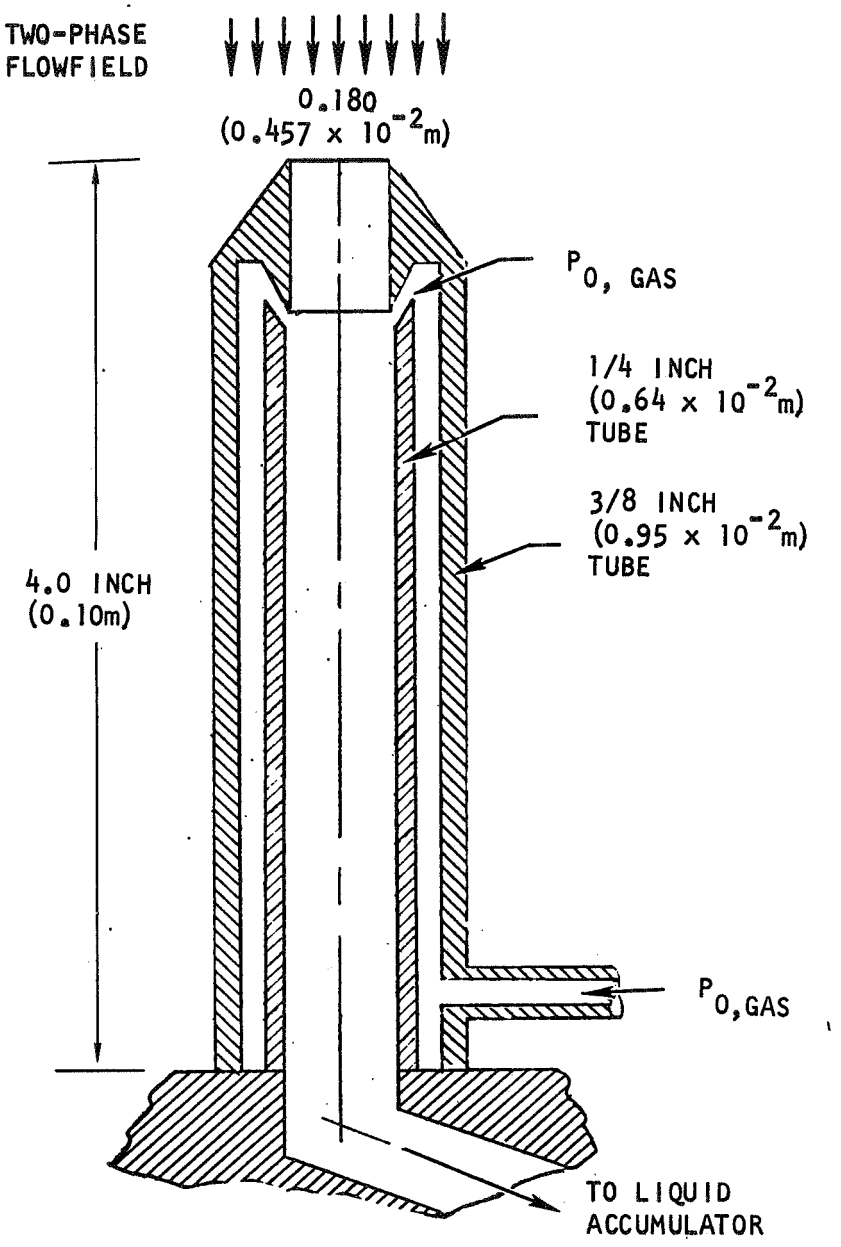

Figure A-9. Schematic of Task II Two-Phase Impact Probe

Probe Calibration

To raise the probe data precision level, it was deemed necessary to calibrate the Task II probe in a liquid droplet/gas flowfield where the pertinent variables such as mass flowrate and mean dropsize were known. A calibration tunnel was designed and fabricated to provide this reference gas-liquid droplet flowfield. A schematic of the tunnel is shown in Fig. A-10. Calibration of the probe was accomplished by measuring the gas velocity profile at the exit of the calibration tunnel. The measured velocity profile was then integrated to determine a measured total gas mass flow, which was compared to the known injected gas flow to obtain the necessary calibration factors.

Preliminary flow experiments indicated that the tunnel provided a relatively uniform (±10 percent of injected mixture ratio) two-phase flowfield at the exit of the tunnel. Calibration of several candidate impact probes was then accomplished including the probes previously described. Probe calibration tests using the probe shown in Fig. A-9 were performed at nominal mixture ratios of 2 and 5 and the results are shown in Fig. A-11. This figure presents the ratio of measured-to-injected gas mass flow as a function of injected mixture ratio. To analyze the data in Fig. A-11, it was necessary to determine the mean dropsize in the two-phase flow. These data were generated by testing a single element from the calibration tunnel injector on the molten wax test facility. However, as indicated in Fig. A-11, overpressure ratio (as implied by $(\dot{w}_{g,\ meas}/\dot{w}_{g,\ inj})$ did not appear to be influenced by dropsize in the range of volume mean dropsizes from 110 to 210 μ (110 to 210 x 10^{-6}m).

Comparison of Probe Calibration Data With Theory

The probe calibrations of Fig. A-11 were analyzed to compare the observed overpressure ratios of the Task II probe with the theory of Dussourd and Shapiro. To compare the probe data and theory it was necessary to correct the probe pressure data for the pressure rise within the probe tip. The

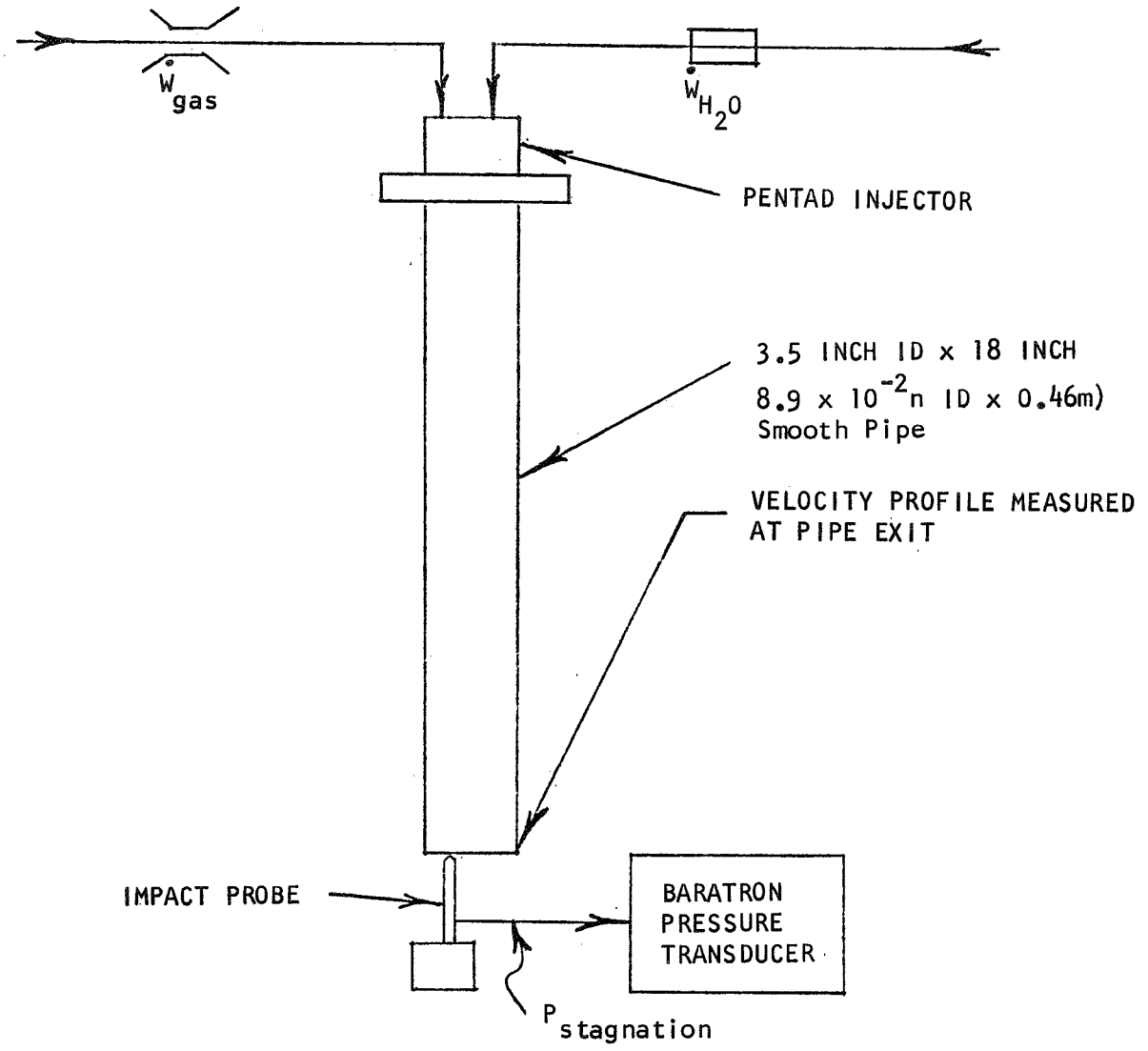

Figure A-10. Schematic of Two-Phase Flow Calibration Tunnel

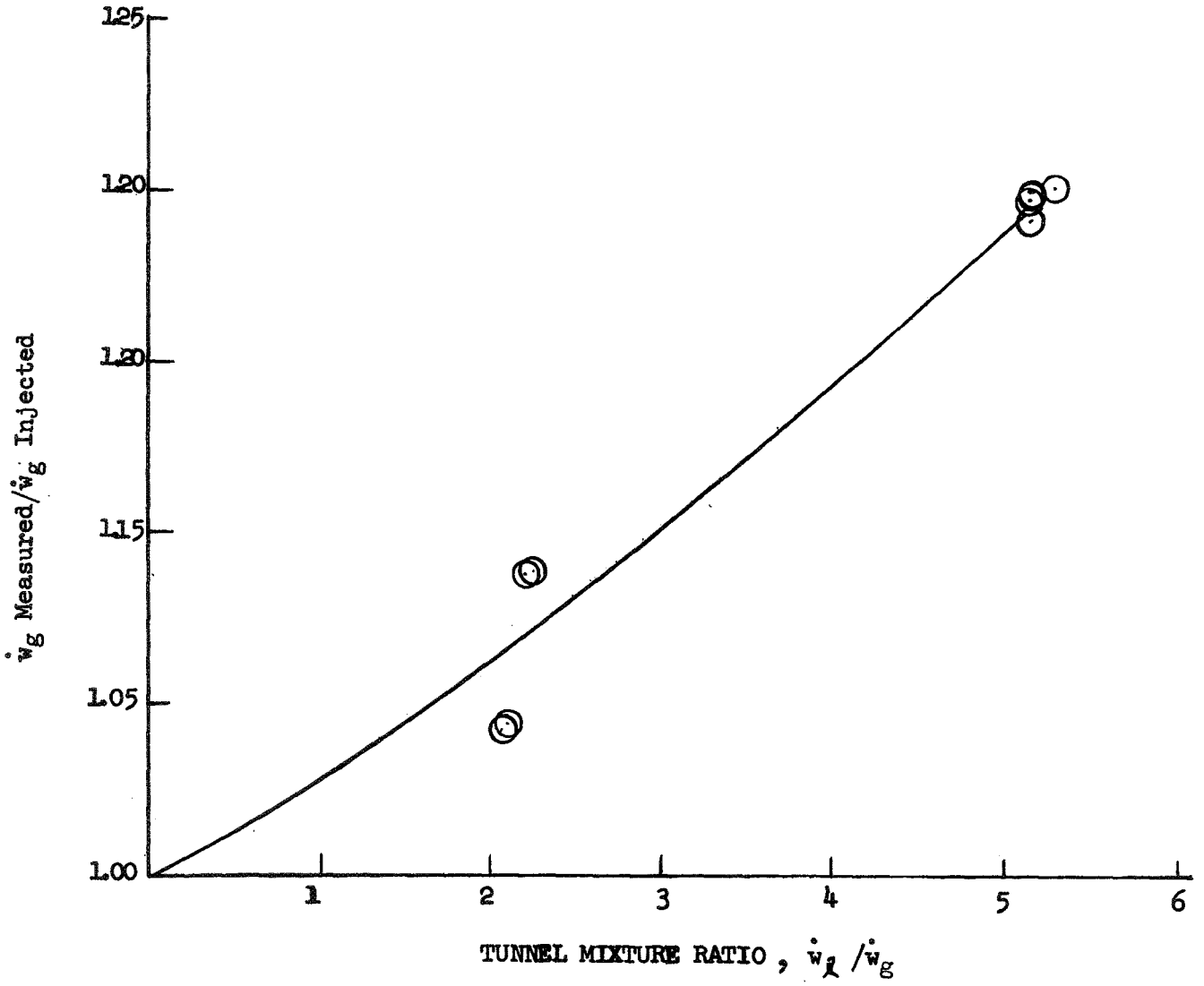

Figure A-11. Impact Probe Calibration Data from Two-Phase Calibration Tunnel

pressure gradient within the probe tip was estimated by a simple one-dimensional analysis of momentum exchange between the droplets and the gas phase within the probe tip. The simplified analysis yielded the following expression for the pressure rise in the probe tip:

$$\frac{dp}{d_{(x/D)}} = \left[\frac{3}{4} \frac{C_D}{g_c} \frac{\rho_g}{\rho_\ell} \frac{D}{D_o}\right] V_\ell \, (MR)_\infty \, \rho_g \, V_g \qquad \text{(A-5)}$$

where C_D = the droplet drag coefficient

x = The distance from the probe tip to the pressure measurement location

D = the internal diameter of the probe

D_o = the droplet diameter

$(MR)_\infty$ = mixture ratio upstream of the probe

The foregoing equation was employed to correct the data of the calibration tests. Using the corrected data, an apparent overpressure ratio at the probe tip was calculated for each test point as a function of obedience number and Reynolds number.

Discussion of Results

Examination of the calibration data (corrected by Eq. A-5) shows that three of the four data points are in agreement with the theory of Dussourd and Shapiro; i.e., the calculated probe tip overpressure based on the experimental data was 3 to 7 percent, compared to the Dussourd-Shapiro prediction of 1/2 to 2 percent. However, for one test a negative overpressure ratio was predicted, which is not physically plausible.

Lack of exact agreement between the four calibration tests and the Dussourd theory can be attributed to the significant deviations of the Task II probe and flowfield from that of the Dussourd theoretical study. The most noteworthy differences are:

1. The Dussourd theory considers low mass flow ratio (MR < 0.2) flowfields. For the Task II studies the local mass flow ratios are an order of magnitude greater.
2. The Dussourd work employed a sharp-edged tube as a probe, whereas the tip of the Task II probe is configured as a truncated cone. This configuration could lead to higher gas/droplet interaction upstream of the tip with resulting increased overpressure ratios.

Further work would be required to resolve the differences between the calibration test data and the theory of Dussourd and Shapiro. However, in all cases the observed overpressure was 7 percent or less which was considered to be acceptable. It was concluded that the impact probe could be employed as an effective technique for the prediction of injector mixing efficiency with the actual calibration data used to correct for overpressure.

APPENDIX B

HOT-FIRE PERFORMANCE CALCULATION PROCEDURES

The index of injector performance used in this experimental program was corrected c* efficiency. This parameter was calculated by two independent methods, one based on measurement of chamber pressure and the other on measurement of thrust. Details of the computational procedures and of the corrections applied are given in this appendix. A numerical example is included.

CALCULATIONS BASED ON CHAMBER PRESSURE

Characteristic velocity efficiency based on chamber pressure is defined by the following equation:

$$(\eta_{c^*})_{P_c} = \frac{(P_c)_o \ (A_t)_{eff} \ g_c}{(\dot{w}_T) \ (c^*)_{theo}} \tag{B-1}$$

where

$(P_c)_o$ = stagnation pressure at the throat, psia

$(A_t)_{eff}$ = effective thermodynamic throat area, $in.^2$

g_c = conversion factor (32.174 lbm-ft/lbf-sec^2; 9.807 m/s^2)

$\dot{w}_T$ = total propellant weight flowrate, lbm/sec

$(c^*)_{theo}$ = theoretical characteristic velocity based on shifting equilibrium, ft/sec

Values calculated from Eq. B-1 are referred to as "corrected" c* efficiencies, because the factors involved are not measured directly, but are obtained by application of suitable corrections to measured parameters. Thus, stagnation pressure at the throat was obtained from measured static pressure near the start of nozzle convergence by assumption of isentropic expansion; effective throat area was estimated from measured geometric area by allowing for radius changes during firing

(Task I only) and for nonunity discharge coefficient; and chamber pressure was corrected to allow for energy losses from the combustion gases to the chamber wall by heat transfer and friction. Equation B-1 may therefore be written as follows:

$$(\eta_{c^*})_{P_c} = \frac{P_c A_t g_c f_p f_{TR} f_{DIS} f_{FR} f_{HL} F_{IMP}}{(\dot{w}_o + \dot{w}_f)(c^*)_{theo}} \qquad \text{(B-2)}$$

where

P_c = measured static pressure near the start of nozzle convergence, psia

A_t = measured geometric throat area, $in.^2$

$\dot{w}_o$ = oxidizer weight flowrate, lbm/sec

$\dot{w}_f$ = fuel weight flowrate, lbm/sec

f_p = factor correcting observed static pressure to throat stagnation pressure

f_{TR} = factor correcting for change in throat radius during firing

f_{DIS} = factor correcting throat area for effective discharge coefficient

f_{FR} = factor correcting measured chamber pressure for frictional drag of combustion gases at chamber wall

f_{HL} = factor correcting measured chamber pressure for heat losses from combustion gases to chamber wall

f_{IMP} = factor correcting theoretical characteristic velocity for propellant impurities or deviations from the standard

Methods of determining the various correction factors are described in the following paragraphs.

Pressure Correction (f_p)

Measured static pressure near the start of convergence was converted to stagnation pressure at the throat by assumption of no combustion in the nozzle and application of the isentropic flow equations.

For calculation of a "valid" performance value, care must be taken to ensure measurement of a "valid" static chamber pressure near the start of nozzle convergence. Experience gained on related programs (Ref. 2) at Rocketdyne indicates that definite increase in static pressure can occur near the start of convergence. This increase in pressure appears to be caused by the subsonic decelerating effects associated with the turning of the combustion gases by the converging walls prior to acceleration in the nozzle. The magnitude of this increase is dependent on the geometric configuration of the nozzle. Measurement of the static chamber pressure must be taken sufficiently upstream of the start of convergence so that its value is not affected by the subsonic decelerating effects discussed above. Furthermore, chamber pressure must be measured where combustion is nearly complete. During this program, procedures were followed to produce valid static pressure measurements for calculation of performance. These procedures were to locate the static chamber pressure measurements approximately 15 inches (0.38 m) downstream of the injector and (1) 0.5 inch (1.27×10^{-2} m) upstream of the start of convergence during Task I 35 inch (0.89 m) L* tests and (2) 0.5 and 1.5 inches (1.27 and 3.81×10^{-2} m) during Task IV testing. Data taken from another program (Ref. 2) indicated little or no errors in the range with similar sized chambers (L* = 30 inches; 0.76 m and $\varepsilon_c = 2$).

The values of f_p, the stagnation-to-static pressure ratios, were calculated to be 1.0538 and 1.0591 for the LOX/H_2 and $FLOX/CH_4$ 2-to-1 contraction ratio chambers, respectively. Variations in the shifting equilibrium specific heat ratio were minor over the range of test conditions (chamber pressure, mixture ratio, and propellant temperature) employed. These same pressure ratio factors were therefore considered applicable over the entire test matrix, although modified when necessary for contraction ratios other than the nominal 2-to-1.

Throat Radius Correction (f_{TR})

Task I. Temperature changes produced in a water-cooled nozzle wall by radiative and convective heat transfer from the hot combustion gases result in thermal stresses which affect the throat radius. Consequently, the geometric throat diameter measured in an ambient-temperature nozzle is not necessarily the same as that

which exists during firing. Throat diameter during firing would be a function of time, of the physical properties of the throat material, the temperature and pressure of the combustion gases, the nozzle geometry, wall thickness, etc.

A throat radius correction factor, f_{TR}, was used for all Task I tests and is defined as:

$$f_{TR} = \frac{A_{t\ hot}}{A_{t\ cold}}$$

During the Task I hot-firing tests, the thrust chamber throat diameter and area would increase (compared to the ambient dimensions) as a function of the wall temperature. The "hot" throat area was computed for each test as follows:

$$A_{t\ hot} = \left[(\alpha\ \Delta T_{avg} + 1)\ D_{t\ cold}\right]^2 \pi/4 \qquad \text{(B-3)}$$

where

α = thermal expansion coefficient (copper)

ΔT_{avg} = change in average throat wall temperature during the test

$D_{t\ cold}$ = cold throat diameter (pretest)

During the course of the testing, the "cold" throat diameter D_t was measured four times--before test No. 1, 2, and 6 and after test No. 9. The corresponding cold throat areas were 28.883, 28.883, 28.995, and 29.119 $in.^2$ (1.863, 1.863, 1.870, and 1.878 x 10^{-2} m^2). A linear throat area change was assumed for the tests where no throat area (diameter) measurements were taken. The change in the average throat wall temperature was computed from:

$$\Delta T_{avg} = (T_{avg})_{hot} - (T_{avg})_{cold} \qquad \text{(B-4)}$$

$$(T_{avg})_{hot} = T_{wc} + \frac{T_{wg} - T_{wc}}{2} \qquad \text{(B-5)}$$

$$(T_{wg} - T_{wc})_{exp} = (T_{wg} - T_{wc})_{theo} \times \frac{\Delta T_{B\ exp}}{\Delta T_{B\ theo}} \qquad \text{(B-6)}$$

where

$(T_{avg})_{cold}$ = pretest wall temperature (ambient temperature)

ΔT_B = water coolant bulk temperature change

$T_{wg} - T_{wc}$ = gas to coolant wall temperature difference at the throat

The ΔT_{avg} term, then, is the change in the wall temperature (cold to hot) at the midpoint between the gas and coolant throat walls, computed for each test and based on the measured water coolant bulk temperature data. These data were stabilized within 1 second. The resultant correction factors ranged from 1.011 to 1.015 (1.1 to 1.5 percent).

Task IV. A throat radius correction factor was not used for the Task IV testing because (1) a first approximation predicted small changes in the graphite throat area due to heating, (2) material properties and material temperature profiles versus time were uncertain, and (3) the graphite throat material was prone to erosion during the hot-fire testing that would complicate the predicted thermally induced changes. Throat diameter (area) measurements were obtained before and after each Task IV test. The posttest throat area averaged 0.47 percent greater than the pretest area for all data-producing tests (~2 seconds duration). This posttest throat area was used for performance data reduction since the data slice was taken near the end of each test, potentially after most of the erosion.

Throat Discharge Coefficient (f_{DIS})

The discharge coefficient is defined as the ratio of actual flowrate through the throat to the theoretical maximum based on geometric throat area and ideal, uniform, one-dimensional flow with no boundary layer. Values of the discharge coefficient may be estimated either analytically or from correlations of the results of experimental studies of gas flow through nozzles. Its value is sensitive to the ratio of the upstream wall radius of curvature at the throat-to-the throat radius (R_c/R_t) for values of $R_c/R_t \leq 1.0$. In this program, R_c/R_t was 2.0 for the Task I chamber and 1.0 for the Task IV hardware.

The available analytical and experimental techniques were investigated to determine the discharge coefficients for the nozzles and test conditions employed during the program. The Task I nozzle discharge coefficients (f_{DIS}) ranged from 0.9922 to 0.9902, varying mainly with chamber length (L*) and essentially independent of mixture ratio and propellant temperature. The Task IV nozzle discharge coefficients ranged from 0.9893 to 0.9883 for the 30-in. (0.76-m) and 57.6-in. (1.46-m) L* chambers, respectively. Chamber pressure, mixture ratio, and propellant temperature effects were negligible.

Frictional Drag Correction (f_{FR}) and Heat Loss Correction (f_{HL})

Calculation of c* efficiency based on chamber pressure is concerned with chamber phenomena up to the nozzle throat. Drag forces to this point are generally small. Details of the method of estimation of f_{FR} are presented below. This discussion is general and applies to frictional losses for performance based on thrust as well as chamber pressure. Differences between the values of frictional losses for thrust and chamber pressure calculated performance are associated with the different regions over which the frictional losses are integrated.

Heat transfer from the combustion gases to the walls of an uncooled thrust chamber results in loss of enthalpy and thus decreases chamber pressure and thrust. To obtain a true indication of performance efficiency in an uncooled chamber, measured chamber pressure must be corrected by a factor which accounts for heat loss to the walls. Heat transfer to the injector was neglected in this correction because the injector surface area was small relative to that of the chamber and because a major portion of injector heat flux is absorbed by the injected propellants.

The friction factor (f_{FR}) corrects for the energy losses caused by drag forces resulting from the viscous action of the combustion gases on the thrust chamber walls. Its magnitude, which is the integral of the local friction forces over the chamber inside wall, was estimated by a boundary layer analysis utilizing the integral momentum equation for turbulent flow. This analysis accounts for boundary layer effects from the injector to the nozzle exit by suitable description of the boundary layer profile and local skin friction coefficient. A computer

program was used to carry out a numerical integration of the equation, including effects of pressure gradient, heat transfer, and surface roughness. The heat loss factor (f_{HL}) is also determined by the computer program in combination with the friction factor. This combined factor then was used to correct the c* efficiency during the Task IV testing and as a cross check for an alternate method used during the Task I testing. The heat transfer profiles generated relative to these loss corrections are given in Appendix E.

Task IV. During Task IV, the combined friction and heat loss factor f_{FR} and f_{HL} ranged from 1.0040 to 1.0062 for the 30-in. (0.76-m) and 57.6-in. (1.46-m) L* chambers, respectively. These factors do not change significantly within the chamber pressure, mixture ratio, and propellant temperature ranges tested and consequently these effects were neglected.

Task I. Heat loss correction factors were computed for each Task I test by the following equation (Ref. 3):

$$f_{HL} = 1 + 1/2 \left[\frac{\sum_i (q/A_i) A_i}{\dot{w}} \right] \left[\frac{1 - (T_t/T_c)}{h_c - h_t} \right] \qquad \text{(B-7)}$$

where

q/A = heat flux

A_i = area through which heat is transferred

$\dot{w}$ = total propellant flowrate

T_t = theoretical nozzle throat temperature

T_c = theoretical chamber temperature

h_c = theoretical chamber enthalpy

h_t = theoretical nozzle throat enthalpy

The heat transfer losses (q) were computed for each test based on the quantity of heat transferred to the water-cooled nozzle section. The water coolant bulk temperature rise, ΔT, was measured for each test and used to compute the nozzle heat losses as follows:

$$q_{noz} = \dot{w} C_p \Delta T \qquad \text{(B-8)}$$

The q_{noz} experimental was assumed directly proportioned to the q_{noz} ideal at each station in the nozzle, thus:

$$\text{experimental } \sum_i (q/A_i) A_i = \text{theoretical } \sum_i (q/A_i) A_i \times \frac{q_{noz\ exp}}{q_{noz\ ideal}} \qquad \text{(B-9)}$$

This same ratio, $q_{noz\ exp}/q_{noz\ ideal}$, was used to compute the uncooled combustion zone heat transfer, assuming again that the combustion zone heat transfer was proportional to the theoretical heat transfer at each station. The q_{ideal} was taken from the profile given in Appendix E.

The computed correction factors ranged from 1.0044 (test 8) to 1.0151 (test 6), mainly varying with chamber L* from 35 to 75 in. (0.89 to 1.91 m). These factors were assumed to include the small friction loss effects.

The boundary layer analysis computer-calculated losses (f_{FR} and f_{HL}) were determined for a potential (nominal) Task I test case and then compared with the factors calculated from Eq. B-7. The computer-calculated factor was 1.0035 and the comparable factor from the equation was 1.0044 determined for test 8 (i.e., about 0.1 percent difference). The close agreement suggested either method could be used; however, those factors calculated from the equation (B-7) were used in Task I because of greater flexibility in handling the wide range of pressures, propellant temperatures, mixture ratios, and L* explored.

Propellant Impurity Correction (f_{IMP})

During Task I, the LOX was sampled twice during the hot-firing test program and each time the purity was about 99 percent by volume. Most of the impurity was

nitrogen. These oxidizer samples were taken from the LOX storage tanks under low-pressure static conditions and, as such, do not reflect the additional quantities of nitrogen (used as the pressurant) which are normally entrained in the oxygen during transfer to the run tank and during the high-pressure dynamic conditions of a test.

A 1-percent nitrogen impurity was used as the basis for determining the impurity correction factor. Theoretical thermochemical performance calculations were employed (with and without nitrogen) to compute the impurity corrections. The resultant change in the characteristic velocity was approximately 0.2 percent, giving a correction factor $f_{IMP} = 1.002$. This factor varies slightly with chamber pressure and mixture ratio; however, it was assumed constant for all Task I tests.

LOX flowrates as measured were also adjusted for impurities. This adjustment was for the density change due to the impurities and the corrected flowrates were computed as:

$$\dot{w}_{corrected} = \dot{w}_{measured} \frac{\rho_{impure}}{\rho_{pure}} \tag{B-10}$$

where

ρ = density

The approach taken was based on 1-percent nitrogen impurity by volume for each test. The net result was

$$\frac{\rho_{corrected}}{\rho_{pure}} = 0.9965$$

or an 0.35-percent adjustment which was applied to all oxidizer flowrates. Table 4 shows the adjusted flowrates.

During Task IV hot-fire testing, the FLOX was sampled several times with no significant impurities detected. Also, the methane impurities were insignificant. Thus, no impurity corrections were used during Task IV.

CALCULATIONS BASED ON THRUST

An alternate determination of corrected c* efficiency is based upon the following defining equation:

$$(\eta_{c^*})_F = \frac{F_{vac}\, g_c}{(C_F)_{vac}\, \dot{w}_T\, (c^*)_{theo}} \qquad \text{(B-11)}$$

where

F_{vac} = measured thrust corrected to vacuum conditions by the equation: $F_{vac} = F + P_a A_e$, lbf

F = measured thrust, lbf

P_a = ambient pressure, psia

A_e = area of nozzle exit, $in.^2$

g_c = conversion factor (32.174 lbm-ft/lbf-sec^2; 9.807 m/s^2)

$(C_F)_{vac}$ = theoretical shifting thrust coefficient (vacuum)

$\dot{w}_T$ = total propellant flowrate, lbm/sec

$(c^*)_{theo}$ = theoretical shifting equilibrium characteristic velocity, ft/sec

Corrected values of vacuum thrust may be obtained by application of suitable corrections to measurements of thrust made at sea level (site). With these values, which include allowances for all important departures from ideality, theoretical thrust coefficients may be used for calculation of c*. That is, the C_F coefficient is 100 percent if there is no combustion in the nozzle, if chemical equilibrium is maintained in the nozzle expansion process, and if energy losses from the combustion gases are taken into account.

Applicable corrections to measured thrust are specified in the following equation:

$$(\eta_{c^*})_F = \frac{(F + P_a A_e)\, g_c\, \phi_{FR}\, \phi_{DIV}\, \phi_{HL}\, \phi_{IMP}}{(C_F)_{vac}\, (\dot{w}_o + \dot{w}_f)\, (c^*)_{theo}} \qquad \text{(B-12)}$$

where

$(C_F)_{vac}$ = theoretical shifting thrust coefficient (vacuum)

$\dot{w}_o$ = oxidizer weight flowrate, lbm/sec

$\dot{w}_f$ = fuel weight flowrate, lbm/sec

ϕ_{FR} = correction for frictional losses

ϕ_{DIV} = correction for nozzle divergence

ϕ_{HL} = correction for heat losses to chamber and nozzle walls

ϕ_{IMP} = correction for propellant impurities or deviations from the standard

The correction factors in Eq. B-12 were applied to vacuum thrust ($F + P_a A_e$) instead of to measured site thrust (F) because, for convenience, the correction factors were calculated as changes in efficiency based on theoretical vacuum parameters, so that the total correction was of the form $\Delta F/F_{vac}$.

Although they do not appear explicitly in Eq. B-12, corrections to geometric throat area and to measured static chamber pressure at start of nozzle convergence are implicit in the use of theoretical C_F values. Thus, calculation of corrected c* efficiency from thrust measurement includes all the corrections described above for calculations from chamber pressure measurement plus an additional one to account for nonparallel nozzle exit flow. However, because $(C_F)_{vac}$ is essentially independent of the very small changes in chamber pressure and contraction ratio which are involved in corrections to P_c and A_t, these corrections are of no practical significance in calculation of c* from thrust measurements.

Corrections for Frictional Drag (ϕ_{FR}) and Heat Loss (ϕ_{HL})

The basis for and method of calculation of this factor were discussed under calculation of performance based on chamber pressure. Again, the boundary layer analysis was used to calculate the combined friction and heat loss factors during Task IV. These values ranged from 1.0077 to 1.0119 for the 30-in. (0.76-m) and 57.6-in. (1.46-m) L* chambers, respectively.

The Task I friction and heat loss thrust correction factors were calculated for each test by an equation similar to that used for the chamber pressure friction and heat loss correction; i.e.:

$$\phi_{HL} = 1 + 1/2 \left[\frac{\sum_i (q/A_i)A_i}{\dot{w}} \right] \left[\frac{1 - (T_e/T_c)}{h_c - h_e} \right] \qquad \text{(B-12)}$$

where

T_e = theoretical nozzle exit temperature

h_e = theoretical nozzle exit enthalpy

The heat transfer losses (q) for the thrust corrections were computed in the same manner as those used for the chamber pressure except the complete chamber losses were applicable. The resultant correction factors ranged from 1.0074 (test 8) to 1.0202 (test 6), varying mainly with chamber length (i.e., varying with the 35-in. (0.89-m) and 75-in. (1.91-m) L* chambers, respectively).

Correction for Nozzle Divergence (ϕ_{DIV})

The one-dimensional theoretical performance calculations assume that flow at the nozzle exit is uniform and parallel to the nozzle axis. The correction factor, ϕ_{DIV}, allows for nozzle divergence (i.e., for nonaxial flow) and for nonuniformity across the nozzle exit plane. It was calculated by a computer program which utilized the axisymmetric method of characteristics for a variable-property gas.

The nozzle divergence factor was essentially independent of chamber pressure mixtuer ratio and propellant temperature for the entire test matrix. Its value was 1.015 for the Task I and 1.017 for Task IV.

Correction for Propellant Impurities (ϕ_{IMP})

As previously discussed, during the Task I testing, propellant sampling indicated approximately 1 percent by volume nitrogen impurity in the LOX. This 1 percent was used as the basis for the thrust impurity correction. The resultant correction

factors would be slightly above the 1.002 values used for the chamber pressure correction; however, this 1.002 value was used to correct the thrust for each of the tests.

The Task I LOX flowrate was also corrected for impurities as previously mentioned.

No impurity corrections were made during the Task IV testing.

NUMERICAL EXAMPLE

The performance data reduction method and corrections are illustrated by the following numerical example. This example is typical of all Task IV tests, differing only slightly from the Task I method. Data from test No. 61 are analyzed in this example. The subject test was conducted in the 30-in. (0.76-m) L* chamber near nominal design conditions using FLOX/CH_4 propellants. Pertinent steady-state raw data (static chamber pressure, propellant flowrates, measured thrust) from this test are presented in Table B-1. CRT printouts of the pertinent parameters (as a function of time) were used to determine when steady state had been achieved.

TABLE B-1. DATA FROM TEST NO. 61

Parameter	Numerical Value
Static Chamber Pressure[1]	(521.8 + 518.8)/2 = 520.3 psia (359 x 10^4 N/m^2)
Oxidizer Flowrate[2]	(11.967 + 11.748)/2 = 11.858 lbm/sec (5.38 kg/s)
Fuel Flowrate (Inner and Outer Annulus)	(1.007 + 1.024) = 2.031 lbm/sec (0.92 kg/s)
Measured Thrust	3994.7 lbf (17,750 N)
Posttest D_t/A_t	2.633 in./5.445 $in.^2$ (6.68 x 10^{-2} m/3.51 x 10^{-3} m^2)
Mixture Ratio	5.838
c^*_{theo}	7144.5 ft/sec (2180 m/s)

[1] Average value of the static chamber pressure measured at two circumferential locations (120 degrees apart)

[2] Value is average of two flowmeters in series

Beckman traces of static chamber pressure, measured thrust, oxidizer flowrate, fuel venturi temperature and pressure for test No. 61 are shown in Fig. B-1 through B-5. The data slice interval for calculation of performance is noted. Steady-state performance was determined at approximately 1.7 seconds into the 2.1-second test. These traces are representative of the hot-fire tests conducted during the program. Beckman data were used for calculation of performance values.

Performance Based on Chamber Pressure

Corrected c* efficiency based on chamber pressure measurement was calculated using Eq. B-2. Values of the measured parameters ($\dot{w}_o$, $\dot{w}_f$, and A_t) and the theoretical c* used in Eq. B-2 are shown in Table B-1. As was noted previously, to obtain a valid static chamber pressure, the measurement should be taken sufficiently upstream of the start of convergence so it is not affected by subsonic decelerating effects. The static chamber pressure, measured 1/2 inch (1.3×10^{-2} m) from the start of nozzle convergence, was used for calculation of performance in the Task IV chambers.

Methods of determining the various connection factors in Eq. B-2 were outlined previously. Estimation of these correction factors for test No. 61 is described in the following paragraphs.

Pressure Correction (f_p). Measured static pressure was converted to stagnation pressure at the throat by assumption of no combustion in the nozzle and application of the isentropic flow equations. The value of f_p, the stagnation-to-static pressure ratio, was estimated to be 1.0670 for the 1.89 contraction ratio chamber used for test No. 61.

Throat Radius Connection (f_{TR}). No throat radius correction was used for test No. 61. The measured posttest throat area (diameter) was used as shown in Table B-1. The pretest to posttest throat area change was small; i.e., 0.23-percent increase.

Throat Discharge Coefficient (f_{DIS}). For all Task IV 30-in. (0.76-m) L* experiments, the throat discharge coefficient was estimated to be 0.9893.

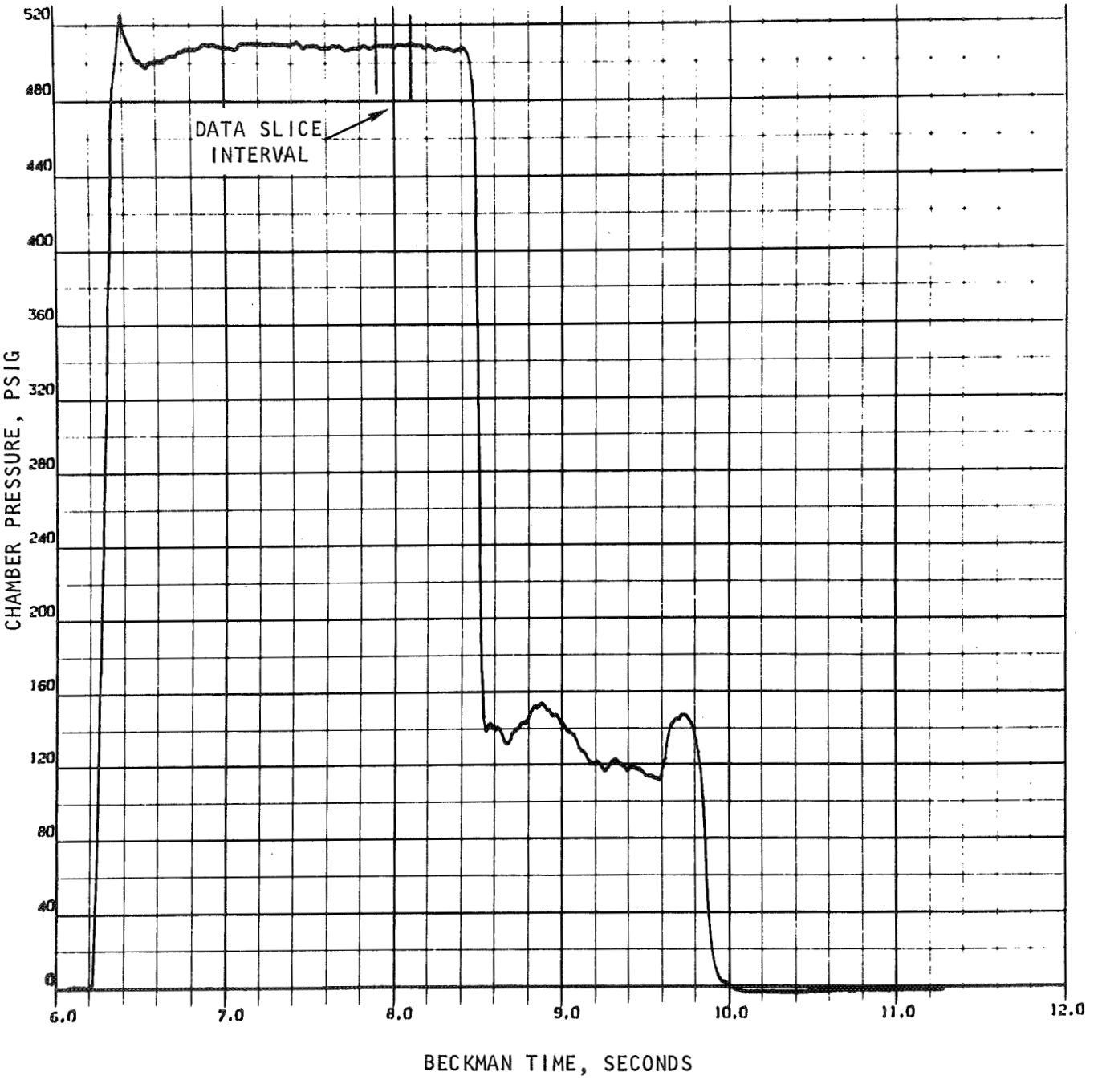

Figure B-1. Static Chamber Pressure vs Time--Test No. 61

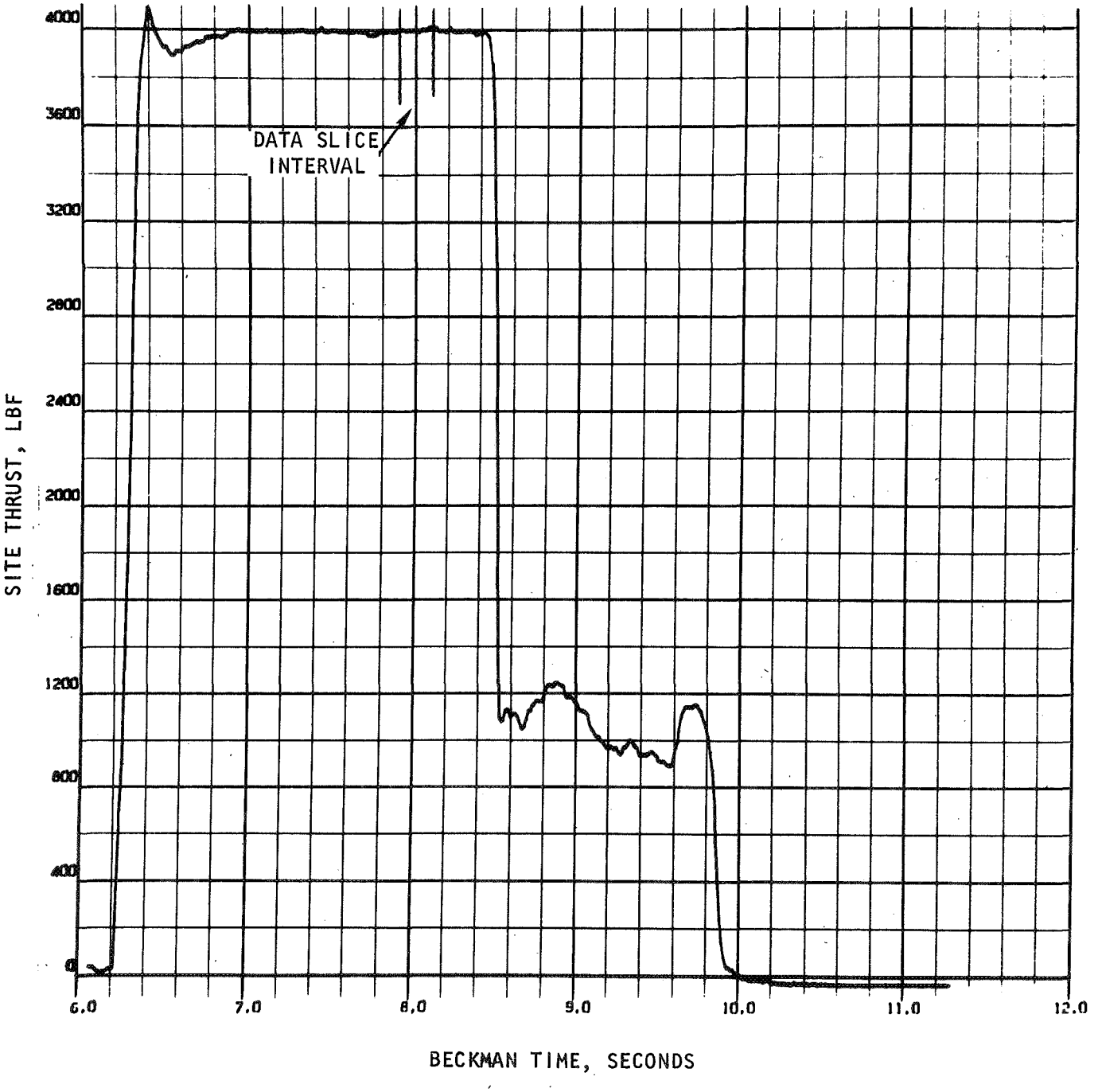

Figure B-2. Site Thrust vs Time--Test No. 61

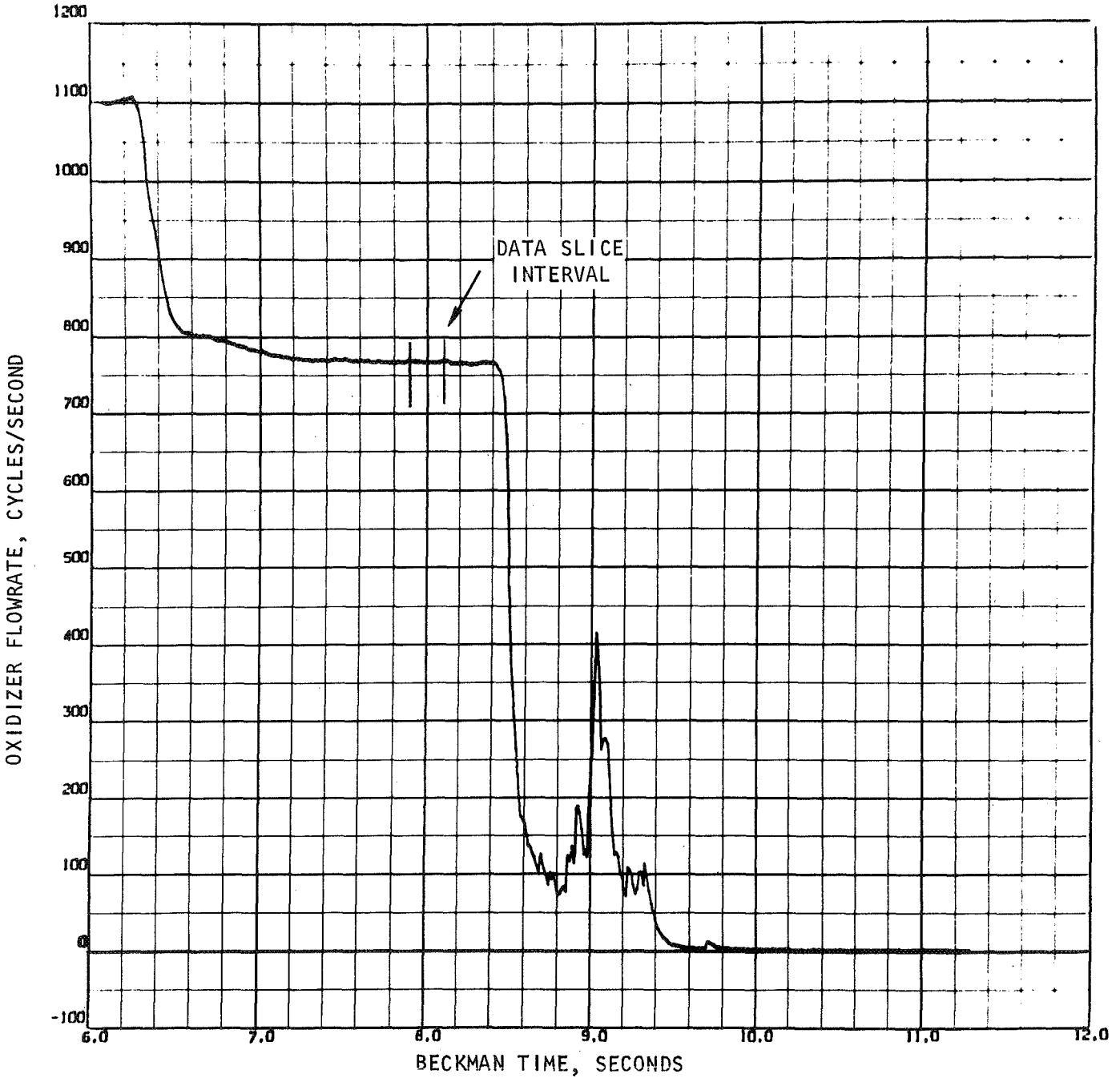

Figure B-3. Oxidizer Flowrate (cps) vs Time From Flowmeter No. 1--Test No. 61

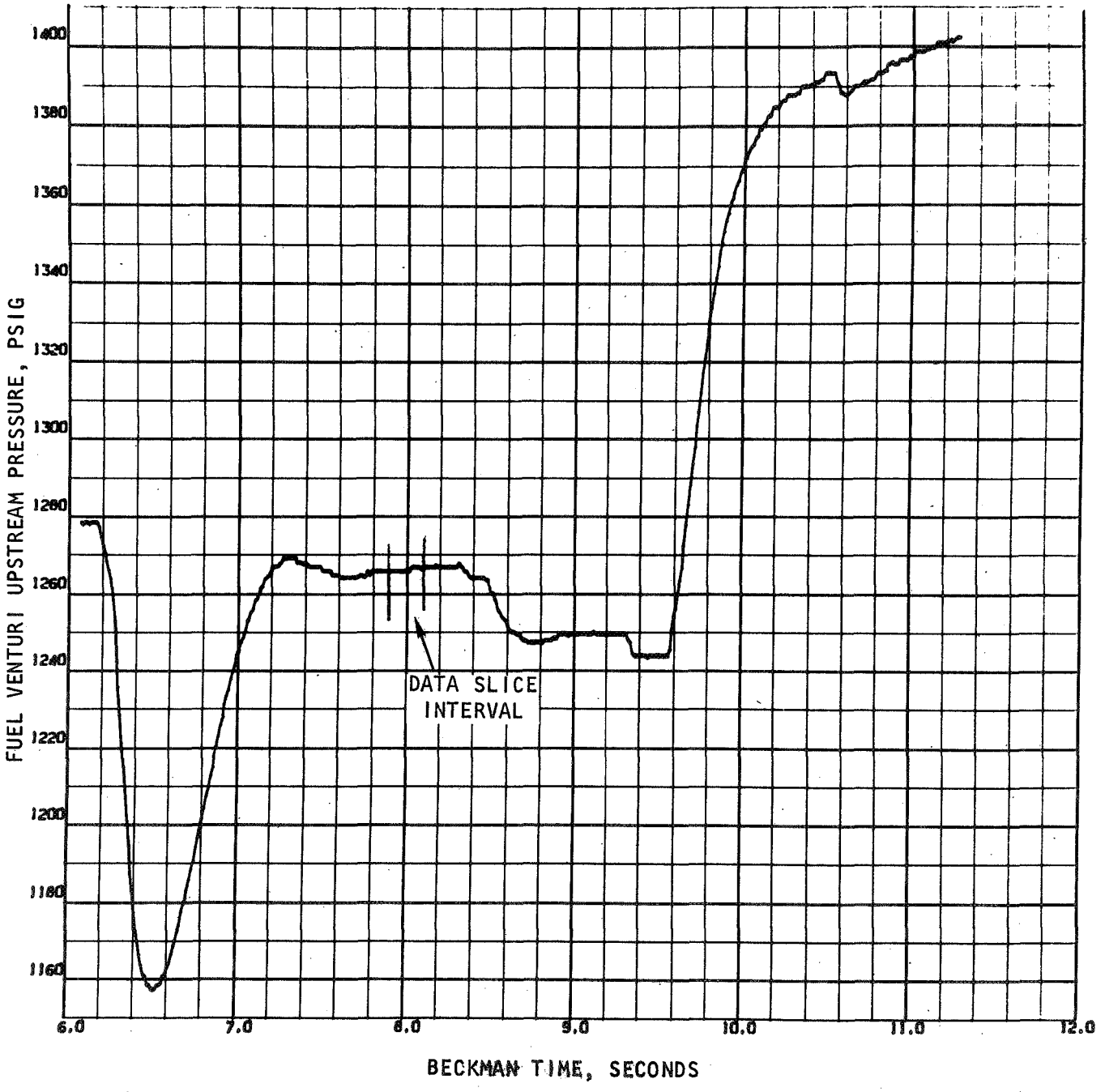

Figure B-4. No. 1 Fuel Venturi Upstream Pressure vs Time--Test No. 61

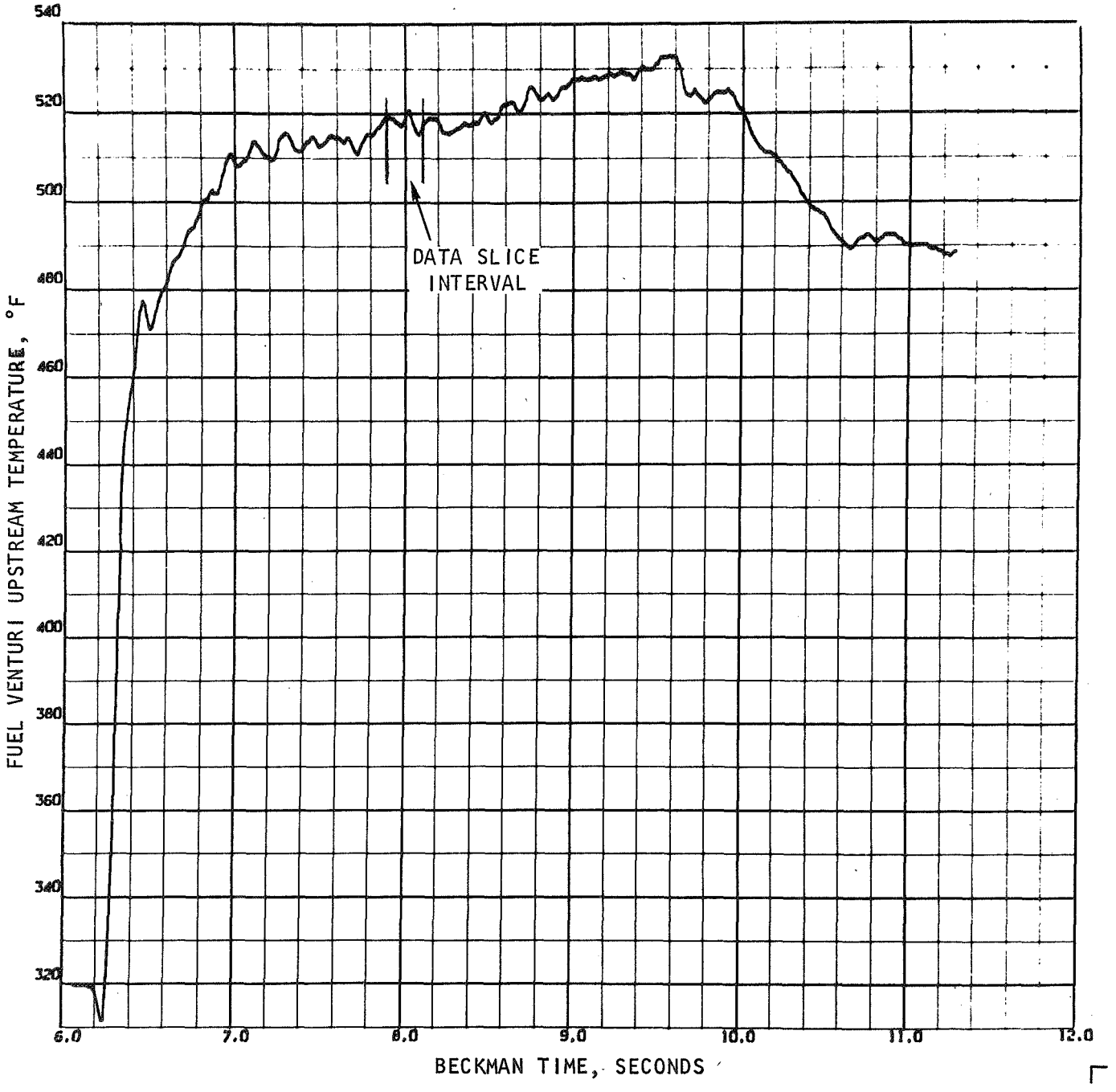

Figure B-5. No. 1 Fuel Venturi Upstream Temperature vs Time--Test No. 61

Frictional Drag and Heat Loss Correction (f_{FR}) and f_{HL}). The combined friction and heat loss for the subject test was calculated to be 1.004.

Propellant Impurity Correction (f_{IMP}). No propellant impurity correction was used for the Task IV tests.

Corrected c* Efficiency From P_c. Corrected c* efficiency (based on chamber pressure) for the test was 97.35 percent.

Equation B-2 with the appropriate numerical values shown is presented below for test No. 61.

$$(\eta_{c^*})_{Pc} = \frac{P_c\ A_t\ g_c\ f_p\ f_{TR}\ f_{DIS}\ f_{FR}\ f_{HL}\ f_{IMP}}{(\dot{w}_o + \dot{w}_f)\ (c^*)_{theo}}$$

$$(\eta_{c^*})_{Pc} = \frac{(520.3)\ (5.445)\ (32.172)\ (1.067)\ (1)\ (0.9893)\ (1.004)\ (1)\ (1)}{(11.858 + 2.031)\ (7144.5)}$$

$$(\eta_{c^*})_{Pc} = 97.35 \text{ percent}$$

Performance Based on Thrust

Corrected c* efficiency based on thrust measurement was calculated using Eq. B-12. Initially, vacuum thrust was calculated from the measured thrust, ambient pressure, and nozzle exit area as follows:

$$F_{vac} = F_{meas} + P_a\ A_e = 3994.7 + (13.7)\ (10.80) = 4142 \text{ lbf } (18{,}430 \text{ N})$$

This was desired because the corrections to be applied were calculated as changes in efficiency based on theoretical vacuum parameters.

Methods of determining the correction factors to be applied to the vacuum thrust in the calculation of c* efficiency were presented previously.

Estimation of the values used for test No. 61 are described below in the following paragraphs.

Corrections for Frictional Drag and Heat Loss (ϕ_{FR} and ϕ_{HL}). These losses were calculated for the subject test conditions and the combined ϕ_{FR} and ϕ_{HL} was determined to be 1.0077.

Nozzle Divergence Correction (ϕ_{DIV}). For all Task IV experiments, the nozzle divergence factor was calculated to be 1.017.

Propellant Impurity Correction (ϕ_{IMP}). No propellant impurity correction was used for the Task IV tests.

Corrected c* Efficiency From F. Corrected c* efficiency (based on thrust) for this test was 95.48 percent. Equation B-12 with the appropriate numerical values shown is presented below for test No. 61:

$$(\eta_{c^*})_F = \frac{(F + P_a A_e)\, g_c\, \phi_{FR}\, \phi_{DIV}\, \phi_{HL}\, \phi_{IMP}}{(C_F)_{vac}\, (\dot{w}_o + \dot{w}_f)\, (c^*)_{theo}}$$

$$(\eta_{c^*})_F = \frac{(4142.6)\ (32.174)\ (1.0077)\ (1.017)\ (1)\ (1)}{(1.4416)\ (11.858 + 2.031)\ (7144.5)}$$

$$(\eta_{c^*})_F = 95.48 \text{ percent}$$

APPENDIX C

EFFICIENCIES FROM CHAMBER PRESSURE AND THRUST - TASK I

Characteristic velocity (c*) or injector efficiency was of primary concern during the hot-firing phase of the program. This efficiency was determined in two ways: from the chamber pressure and flowrate data, and from thrust and flowrate data. Efficiencies based on thrust averaged about 2.2 percent (0.6 to 3.6 percent) less than those based on chamber pressure, although the trends were the same for both efficiencies. Techniques for obtaining the chamber pressure and thrust parameters used are prescribed herein along with some factors which could potentially contribute to the thrust and chamber pressure efficiency differences.

CHAMBER PRESSURE

The static chamber pressure was measured during each test at two locations in the cylindrical portion of the chamber; i.e., upstream of the nozzle contraction section. These pressure pickups were about 15 in. (0.38 m) downstream from the injector face for both the 35- and 75-in. (0.89 and 1.9 m) L* chambers. The two static pressure measurements were recorded by both the oscillograph and DIGR recorders, although the more accurate DIGR values were almost always used. These DIGR pressure measurements were within ±1.5 psi (10×10^3 N/m^2), (0.4 percent) of the average which was used to give a single value for each test.

The perfect gas relationship was employed to obtain the stagnation pressure from the static pressure as follows:

$$P_c = P_s \left[1 + \frac{\gamma - 1}{2} M^2_s\right]^{\frac{\gamma}{\gamma-1}}$$

where P_s is the measured static chamber pressure and M_s is the corresponding Mach number. This approach assumes that the reaction process is basically completed and the gas velocity is near maximum at the pressure pickup point. For the contraction ratio and chamber conditions of interest, $P_c = 1.0538\ P_s$. This relationship was essentially true for the entire pressure and temperature range experienced during the testing.

As previously mentioned, the chamber pressure pickup points were located about 15 in. (0.38 m) downstream of the injector face. For the 75-in. (1.91 m) L* chamber, the pressure pickup points are 1/2 in. (0.015 m) upstream of the joint between the two combustion zone spool pieces; i.e., where a potential discontinuity exists which could disturb the flow and affect the static pressure readings. Also, for the 35-in. (0.89 m) L* chamber, the pressure pickup points were 1/2 in. (0.015 m) above the start of convergence which could potentially change the flow pattern and affect the pressure readings.

THRUST

The thrust was measured during each test by a dual-bridge load cell with the output recorded on both the oscillograph and the DIGR. Again the more accurate DIGR value was used for the performance calculations. The measured thrust than was converted to vacuum thrust for all tests by the following relationship:

$$F_{vac} = F_{site} + P_a A_e$$

where P_s is the ambient pressure and A_e is the chamber exit area. For this test program, the $P_a A_e$ was very nearly constant and equal to 800 lb (3560 N).

The main propellant lines to the test hardware and other stand equipment were mounted so as to minimize interference (resistance) with the thrust measurements; however, some interference was obvious. Therefore, an "in position" calibration was required. Before the first test and following the last test, a thrust calibration fixture was installed in front (at the exit end) of the thrust chamber assembly with a calibration load cell and a hydraulic loading device attached. The thrust system was calibrated and the resultant calibration factor was used to determine each of the thrust values during the testing. The accuracy of these thrust values may be subject to some error because the calibration took place under static, ambient-temperature conditions. During actual testing, the main propellant and water coolant lines were flowing full and the line temperatures, particularly the oxidizer temperatures were cold, rather than ambient. Thus, the dynamic cold lines may offer a different resistance than that of the "as-calibrated" system.

PERFORMANCE EFFICIENCIES

The characteristic velocity efficiencies based on chamber pressure were higher (about 2.2 percent average) than those based on thrust as shown by the tabulated performance data. The first approach is to investigate factors which would tend to bring the two efficiencies closer together. Thrust and chamber pressure appear to be the most suspect, so the more significant factors were singled out which could potentially lower the chamber pressure or raise the thrust and consequently change (lower or raise) their respective efficiencies. These factors are summarized as follows:

1. Measured static pressures and subsequent efficiencies from chamber pressure would be slightly higher than actual if the presumed combustion gas velocities were significantly higher than the actual velocities at the pressure pickup point. Thus, if the combustion process was far from complete and if additional reaction takes place between the pickup point and the nozzle, the static (measured)-to-stagnation pressure corrections would not be valid and the computed stagnation pressure would be slightly higher than actual.
2. Disturbance in the flowfield caused by potential discontinuities in the chamber wall or possible flowfield disturbance at the start of nozzle convergence could result in an erroneously high static (not truly static) pressure reading at the pressure pickup points. Thus, the static-to-stagnation pressure calculations and efficiencies would be slightly higher than actual.
3. Pressurized, full-flowing, and low-temperature propellant and water coolant lines could offer greater resistance to thrust than the static ambient temperature lines as calibrated. Thus, the actual thrust and efficiency from thrust potentially could be higher than measured.

Additional factors could potentially contribute to the differences between the thrust and chamber efficiencies; however, they were deemed less likely and/or less significant.

APPENDIX D

IMPINGING STREAM RECIRCULATION MODEL

Unlike the case with the coaxial injectors, large gas/liquid impinging elements in open-air cold-flow tests normally produce liquid spray fields which expand beyond the accompanying gas flow patterns. Based on such flow behavior, relatively low values of E_m and mixing efficiency would be predicted. Hot-firing tests, however (e.g., those under Task I of the subject contract) have shown large-scale impinging and impinging concentric injectors capable of producing good propellant mixing with $(\eta_{c*})_{mix}$ as high as 95 to 99 percent. The principal reason for this improvement in mixing under hot-firing conditions is believed to be recirculation of fuel-rich gases out of central low mixture ratio zones of high gas flowrate and into the outer spray-rich zones. The ability of the injected streams to induce recirculation has been shown by the strong ingesion of air in the atmospheric tests*. Other evidence of recirculation in hot-fire tests includes the injector face heating and wall hot spots seen in the first test in Task I.

As a result, a simple recirculation model has been formulated. This model was applied to partially redistribute the gas flows measured in open-air cold-flow tests of impinging-type injectors to more nearly match the hot-firing environment being modeled, thereby permitting a calculation of E_m and $(\eta_{c*})_{mix}$.

Basically, gas from the inner (core) region where the local gas velocity exceeds a fraction of the centerline V_g (e.g., V_g, centerline/3) is redistributed into an outer (peripheral) region. Local (cold-flow) measurements of ingestion are used to apportion and distribute the gas recirculation. Other factors used in the model to influence the recirculation patterns are proximity between the core and peripheral regions and local spray fluxes.

*This ingestion has been directly measured by the oxygen analyzer. At 3 to 5 in. (0.076 to 0.127 m) downstream of the injector, the flowrate of ingested air may be twice that of the injected GN_2. This was also observed when GN_2 only (without liquid) is injected into the atmosphere. In this latter case, the flow data were in excellent agreement with available analytical predictions.

This model was empirically developed by matching the Task I impinging concentric injector hot-fire data with the Task II impinging concentric cold-flow data. Although a certain number of parameters were not equal (i.e., scale and the presence of the recessed cup), the trends observed in the hot-fire tests should be simulated in cold flow. In addition, the relative levels of the measured and predicted mixing efficiencies should be approximately equal. Model parameters which were determined empirically include: (1) the boundary which separates the core and peripheral regions, and (2) a coefficient applied to the total amount of recirculation. In the following paragraphs, the model is defined in more detail and the determination of the empirical coefficients is described.

The recirculation model is illustrated schematically in Fig. D-1. The boundary separating the core and peripheral regions was reasoned to be a function of the relative local gas velocities. These measured values were used to determine the relative location of the recirculation boundary; thus, the recirculation boundary will vary with each cold-flow tests, depending on the overall gas velocity level. This can be illustrated by the following equation:

$$V_{rec} = V_{max}/K_1 \qquad \text{(D-1)}$$

where

V_{rec} = velocity at recirculation boundary
V_{max} = maximum gas velocity measured
K_1 = empirical constant

Gas was recirculated out of all streamtubes in which the gas velocity was higher than V_{rec} and into streamtubes in which the gas velocity was lower than V_{rec}.

The hot-fire recirculation processes and the cold-flow ingestion processes both are driven by the momenta of the injected streams and both involve the redistribution of gas mass flowrates. In cold-flow open-air tests, surrounding air is

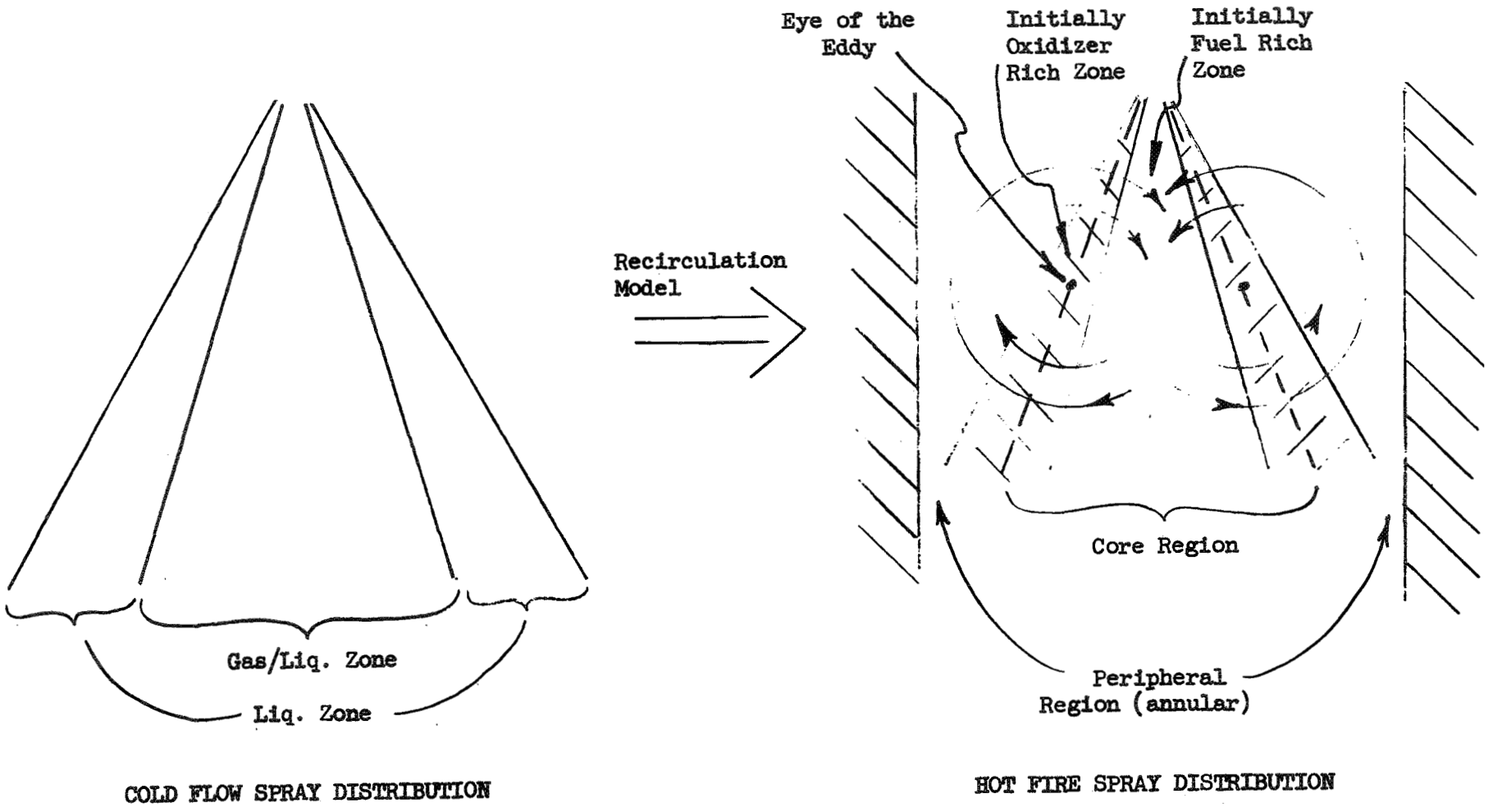

Figure D-1. Comparison of Cold-Flow and Hot-Fire Gas/Liquid Mixing Processes (Impinging Elements)

ingested from an infinite supply by the high-velocity gas and liquid propellant streams. The hot-fire propellant streams will also tend to accelerate mass from the surrounding medium, even though the chamber walls limit the ingestion boundary. The initiation of ingestion within a hot-fire chamber will create a region relatively void of mass flux, thereby setting up lateral pressure gradients and initiating recirculation eddies. Since essentially the same mechanisms which drive the hot-fire recirculation are also present to drive the cold-flow ingestion of gases from the surrounding medium, the ingestion profile measured in each cold-flow test was used as a basis for determining the amount and the distribution of gas flowrates to be recirculated from the gas-liquid core. Mathematically,

$$\dot{w}_{rec} = (K_2) \left(\dot{w}_{ingest}\right)_{i,j} \qquad \text{(D-2)}$$

where

$\dot{w}_{rec}$ = flowrate recirculated

$\dot{w}_{ingest}$ = measured ingestion flowrate

K_2 = empirical constant

i,j = streamtube notation

Because the cold-flow ingestion flowrate was measured with the aid of the oxygen analyzer, the amount of propellant that was recirculated from each core region streamtube can be determined from Eq. D-2 above. The mixture ratio of the propellant recirculated out of each core region streamtube is set by assuming that a small amount of droplet vaporization can occur.

This leaves the redistribution of recirculated gas into the peripheral zone as the only unknown. Attempts to match the Task I impinging coaxial hot-fire data with the Task II impinging coaxial cold-flow data were made using several different distribution functions. This was based on the physical reasoning that the peripheral streamtubes close to the high-gas-flow core region would be more accessible to recirculating flow than the more distant streamtubes. However, distribution functions based solely on radius, such as straight line or parabolic

functions, failed to give an empirical fit with the hot-fire data. It was therefore reasoned that streamtubes in which the liquid flux was very high would tend to ingest more of the recirculated gases than streamtubes with low liquid flux. Thus, the distribution function in the peripheral zone was based on a combination of the liquid and the radius of each individual streamtube as in the following expression:

$$f(\text{dist})_{i,j} = (\dot{w}_\ell/A)_{i,j}/R_{i,j} \qquad \text{(D-3)}$$

where

$f(\text{dist})$ = redistribution function

$(\dot{w}_\ell/A)$ = liquid flux

$R_{i,j}$ = radius

i,j = streamtube notation

The empirical fit between the mixing limited hot-fire tests in Task I and the Task II cold-flow tests is illustrated in Fig. D-2. Note that in spite of differences in scale and the presence of a recessed cup in the hot-fire tests, excellent agreement ($\Delta\eta_{mix}$ < 1 percent) was obtained for two of the three tests Further refinement of the model could bring about a more accurate prediction of the third point ($\Delta\eta_{mix}$ = 3 percent). However, this would involve the addition of one or two more constants to the model. Thus, refinement of the model will be deferred until more hot-fire and cold-flow data are obtained. This recirculation model was used to calculate mixing efficiencies for all Task II impinging injector tests.

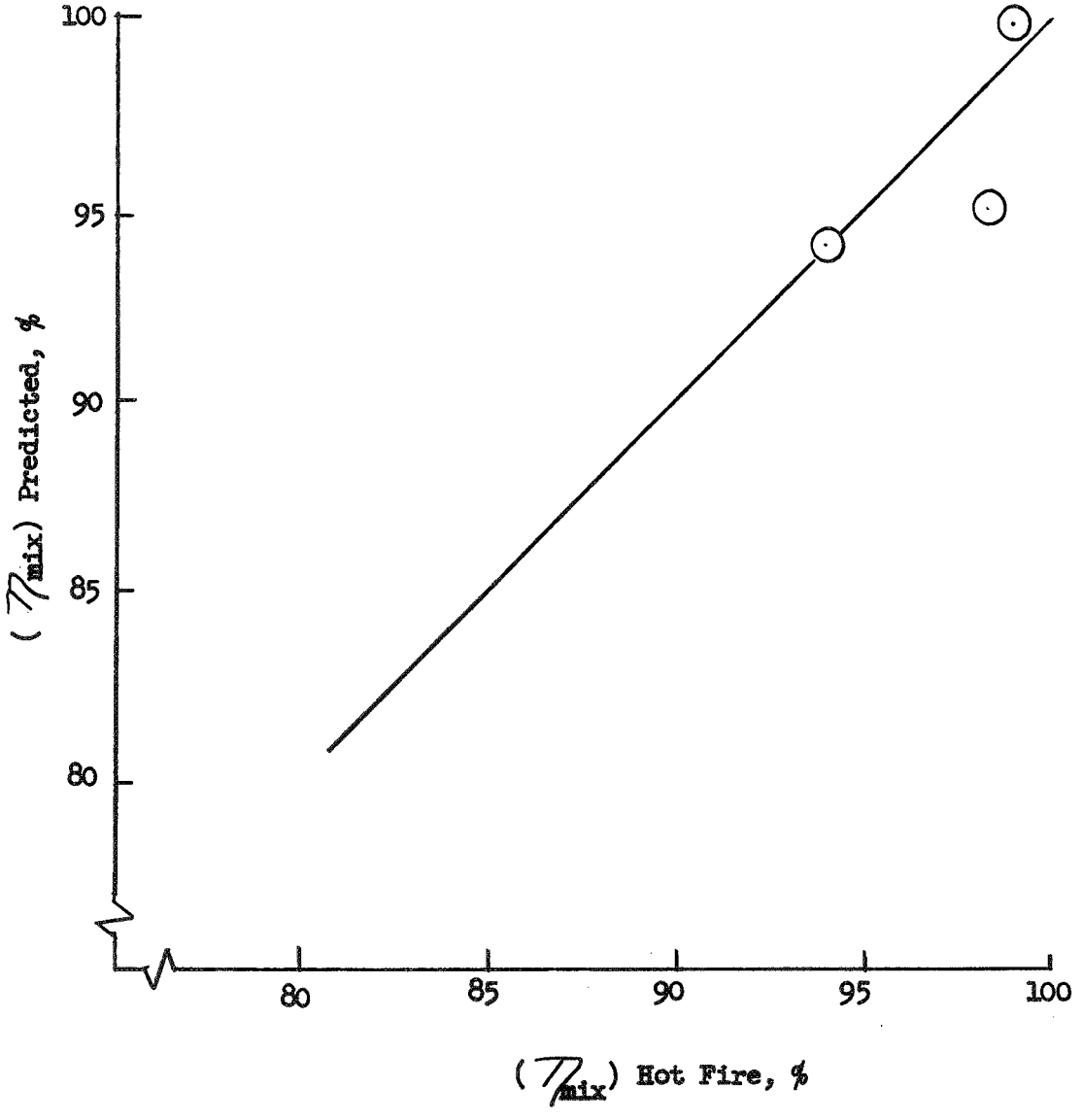

Figure D-2. Predicted vs Observed Mixing Efficiencies for Impinging Concentric Injector Element

APPENDIX E

HEAT TRANSFER

TASK I

The Task I thrust chamber nozzle section contained a water-cooled copper liner adjacent to the hot gas, and a steel jacket as the outside wall. The initial step in the design of the thrust chamber cooling system was to evaluate the hot-gas film coefficient. These coefficients were computed (Eq. E-1), and the resulting maximum values for the throat and combustion zone (ε_c = 2) are listed in Table E-1 along with the nominal design conditions. Virtually the same throat film coefficient was obtained when available experimental data were adjusted to expected conditions. The calculated nozzle heat flux profile is shown in Fig. E-1 and the estimated combustion zone profile is also shown.

The heat fluxes in the throat and the convergence and expansion sections require water cooling to allow for a reasonable test duration, while the combustion zone was constructed as a copper heat sink. The necessary wall thickness at the throat was determined by considering the heat flux capability of the wall and the material strength. The design heat transfer equation is listed as Eq. E-2. The point selected for the nominal design conditions was a wall thickness of 0.2 inch (0.5 x 10^{-2}m) which provides for a 50-percent margin in the heat flux before the melting point is reached. The design wall temperature at the throat of the chamber was computed to be 1350 F (1010 K), which corresponds with a heat flux of approximately 21 Btu/in.^{2}-sec (34.3 x 10^6 W/m^2).

The minimum coolant velocity required to avoid the film boiling regime of water was determined to be 50 ft/sec (15.2 m/s). The saturation temperature of water at 250 psia (172 x 10^4 N/m^2) is 400 F (478 K), which provides subcooling (T_{wc} = T_B) of about 300 F (422 K) at the throat of the cooling system. The resulting water mass flowrate to the nozzle with a 0.1 inch (0.25 x 10^{-2}m) annulus is 45 lb/sec (20 kg/s), and the bulk temperature rise, as computed with Eq. E-3, was

TABLE E-1

O_2/H_2 CHAMBER HEAT TRANSFER OPERATING CONDITIONS, PROPERTIES AND EQUATIONS

NOMINAL CHAMBER CONDITIONS USED FOR THERMAL DESIGN

P_c = 500 psia (345×10^4 N/m^2)

MR = 5.0

T_{aw} = 5420 F (3267 K)

h_g = 0.0052 Btu/in.^{2}-sec-F (0.472×10^4 W/m^2-K) (throat)

h_g = 0.00299 Btu/in.^{2}-sec-F (0.271×10^4 W/m^2-K) (combustion zone)

PROPERTIES FOR COPPER

α = 0.1565 in.^{2}/sec (1.01×10^{-4} m^2/sec)

ρ = 0.323 lbm/in.^{3} (0.895×10^4 kg/m^3)

k = 4.63×10^{-3} Btu/in.-sec-F (346 J/m-sec-K)

T_{melt} = 1980 F (1356 K)

T_{wi} = 80 F (300 K) (combustion zone)

EQUATIONS

Hot-Gas Film Coefficient, Bartz Simplified Equation

$$h_g = \frac{0.026}{d^{0.2}} \frac{\mu^{0.2} C_p}{Pr^{0.6}} G^{0.8} \sigma \qquad \text{(E-1)}$$

where

$$\sigma = \left\{ \frac{T_{wg}}{2\,T_{aw}} \left(1 + \frac{\gamma-1}{2} M^2\right) + 1/2 \right\}^{0.68} \left\{ 1 + \left(\frac{\gamma-1}{2}\right) M^2 \right\}^{-0.12}$$

TABLE E-1

(Concluded)

Heat Conduction Through The Wall

$$Q/A = \frac{k}{\Delta x} \left(T_{wg} - T_{wc}\right) \tag{E-2}$$

$$T_{wc} = T_{sat} + 20 \text{ degrees (nucleate boiling)}$$

Coolant Bulk Temperature

$$Q/A = \frac{\dot{w}_c}{A_S} C_p \Delta T_B \tag{E-3}$$

Transient Heat Conduction in a Slab, Combustion Zone

$$\frac{T_w - T_{aw}}{T_{wi} - T_{aw}} = \sum_{n=1}^{\sigma} \frac{e^{-\delta_n^2 (\alpha t/L^2)} \; 2 \sin \delta_n \cos (\delta_n X/L)}{\delta_n + \sin \delta_n \cos \delta_n} \tag{E-4}$$

where

$$\delta_n \tan \delta_n = (h_g L/k)$$

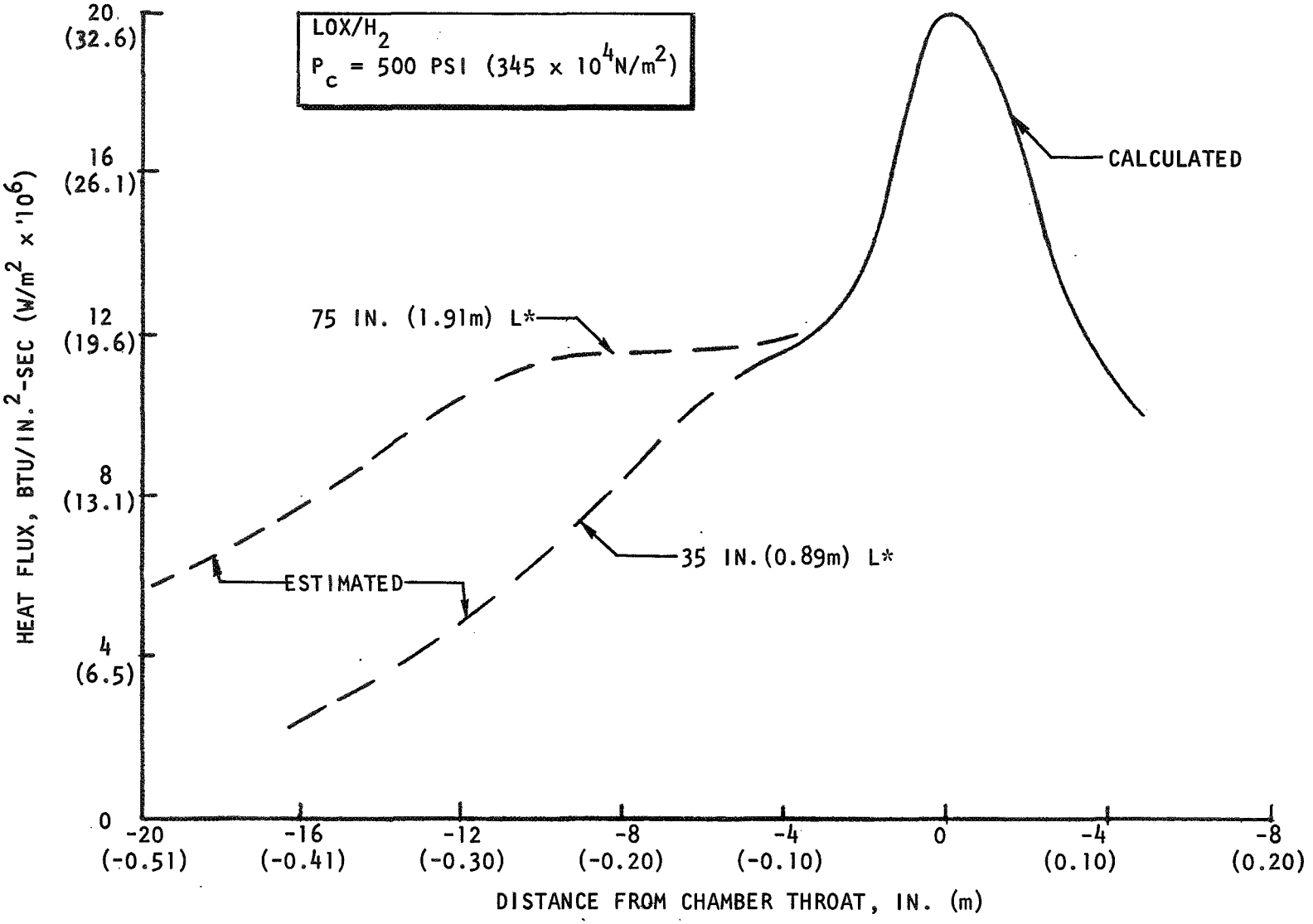

Figure E-1. Axial Heat Flux Profile: LOX/H_2

approximately 56 F (287 K). Therefore, the subcooling at the exit of the nozzle was still approximately 300 F (422 K). During hot-firing tests the coolant velocity was increased to about 67 ft/sec (20.4 m/s) to provide for an additional cooling margin. Correspondingly, the water coolant flowrate increased to about 60 lb/sec (27 kg/s) and the bulk temperature rise was reduced to 42 F (279 K). An increase in the coolant pressure would also increase the cooling margin; however, material strength considerations limited this pressure to about 250 psi (172 x 10^4 N/m^2) at the throat.

A transient analysis was utilized to yield parametric wall temperature curves (Fig. E-2) for the combustion zone. The analysis assumes a step function rise in adiabatic wall temperature at time zero, a uniform initial wall-temperature distribution, and an insulated back wall. The design equation is Eq. E-4. The maximum allowable duration was 3 seconds at the most severe heat transfer condition before melting of the wall would occur at the hot-gas surface. A wall thickness of 1 inch (2.5 x 10^{-2} m) was selected to maintain a somewhat cooler region at the back wall for structural support.

During the Task I testing, Nanmec heat flux probes were used to measure the uncooled combustion zone wall temperature transients. Four temperature probes were used during the first test and two probes on each of the subsequent tests. One probe was located approximately 3 in. (0.076 m) downstream of the injector for each test and the others were located in a plane approximately 15 in. (0.38 m) downstream.

The operating characteristics of the heat flux probes were influenced by the type of tests conducted, the test duration and the proble location. Also, the probe behavior appeared to be very sensitive to immersion depth and the service life was limited to only a few tests before rework was required. Further, the probe behavior was erratic at the high temperatures. Because of these unstabilizing factors, only gross qualitative results were obtained from the probes. The only significant conclusion to be drawn from the heat flux probe data was that the wall temperature transients vs time were almost always above the T_{wg} curve shown in Fig. E-2.

COMBUSTION ZONE (O_2/H_2 PROPELLANTS)

h_g = 0.003 Btu/in.^{2}-sec-F (0.271 x 10^4 W/m^2-K)

T_{aw} = 5420 F (3267 K)

P_c = 500 psia (345 x 10^4 N/m^2)

MR = 5.0

ε_c = 2.0

α = 0.1565 in.^{2}/sec (1.01 x 10^{-4} m^2/sec)

k = 4.63 x 10^{-3} Btu/in.-sec-F (346 J/m-sec-K)

ρ = 0.323 lbm/in.^{3} (0.895 x 10^4 kg/m^3)

T_{wi} = 80 F (300 K)

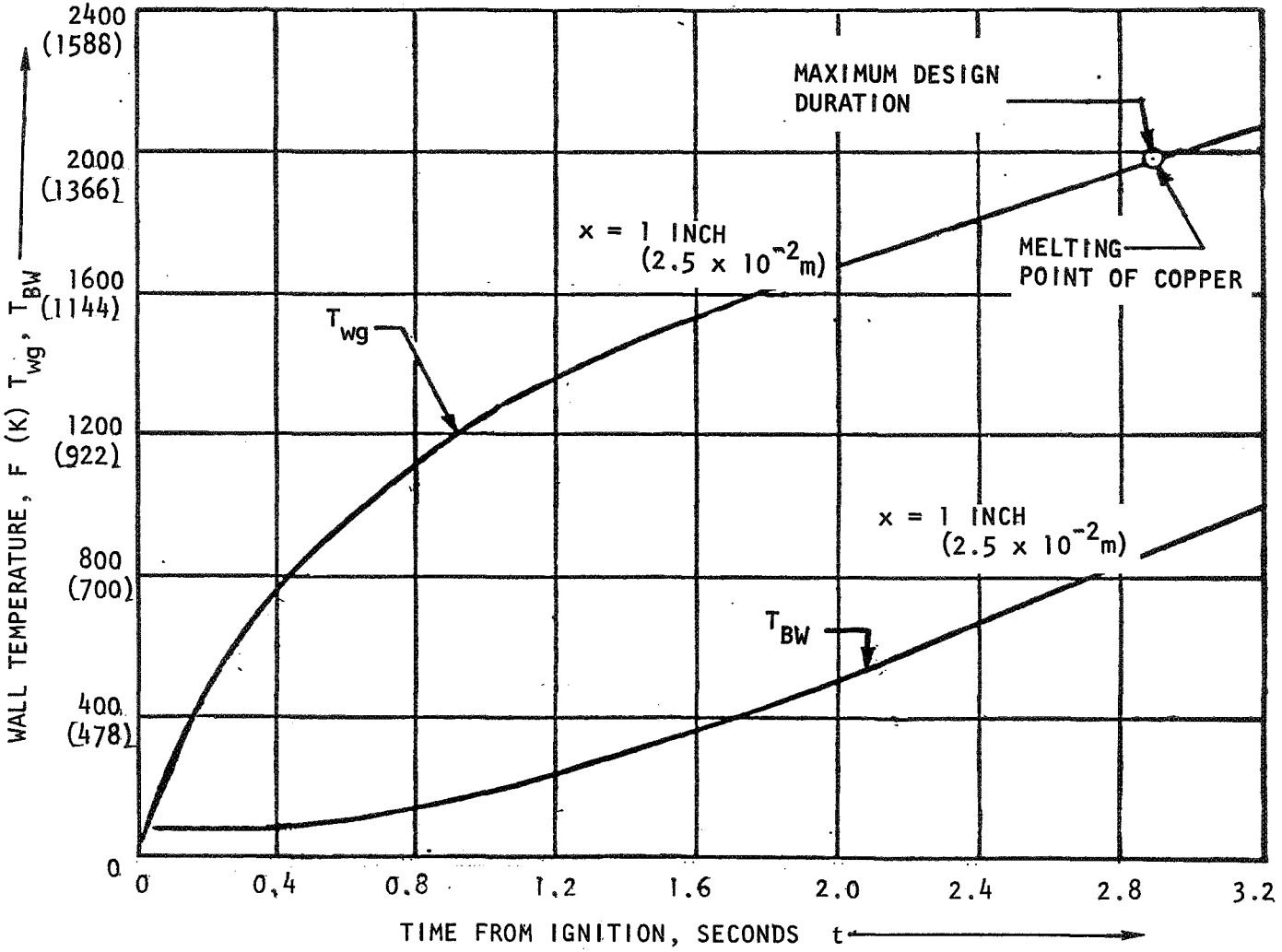

Figure E-2. Transient Heating of a Solid Copper Wall Without Convective Cooling

The water cooled nozzle bulk temperature rise measurements were taken for each Task I test and the results were used to approximate the nozzle heat flux. As previously mentioned, a bulk temperature rise of 42 F (279 K) was prediced for 60 lb/sec (27 kg/s) of water based on the profile shown in Fig. E-1 (based on a nominal chamber pressure and 100 percent c* efficiency). Good agreement was obtained between experimental results and the predicted values as illustrated by test No. 4; operating at close to nominal conditions. During this test the bulk temperature rise was 42 F (279 K), the coolant flowrate was 57.5 lb/sec (26 kg/s) and the c* efficiency was 97 percent (i.e., the total nozzle heat input was within 5 percent of the predicted value (Eq. E-3), independent of the combustion efficiency). Combustion efficiency and nozzle heat transfer varied in the same direction as expected. Also as expected, the heat transfer varied with chamber pressure during the Task I testing.

TASK IV

The Task IV thrust chambers condtained a graphite nozzle section and two different types of combustion zones, one of copper and the other graphite lined. The gas side seat transfer coefficients were computed for this chamber at several potential operating chamber pressures, combustion efficiencies and boundary layer attachment points. A Rocketdyne developed boundary layer heat transfer analysis was used to calculate these gas side heat transfer coefficients. The maximum (nozzle) heat transfer coefficient was 0.00205 Btu/in.^{2}-sec-F (0.186 x 10^4 W/m^2-K) for the nominal 500 psia (345 x 10^4 N/m^2) chamber pressure, 100 percent c* efficiency and the boundary layer assumed to start ~7 in. (0.18 m) downstream of the injector. The maximum combustion zone coefficient was 0.00125 Btu/in.^{2}-sec-F (0.112 x 10^4 W/m^2-K).

A heat flux profile was computed and plotted in Fig. E-3 for the subject chamber with the above mentioned coefficients and an assumed constant hot gas side wall temperature of 1000 R (555 K). This calculated profile is compared (in Fig. E-3) with experimental results from Contract NAS 3-11191 where the chamber length

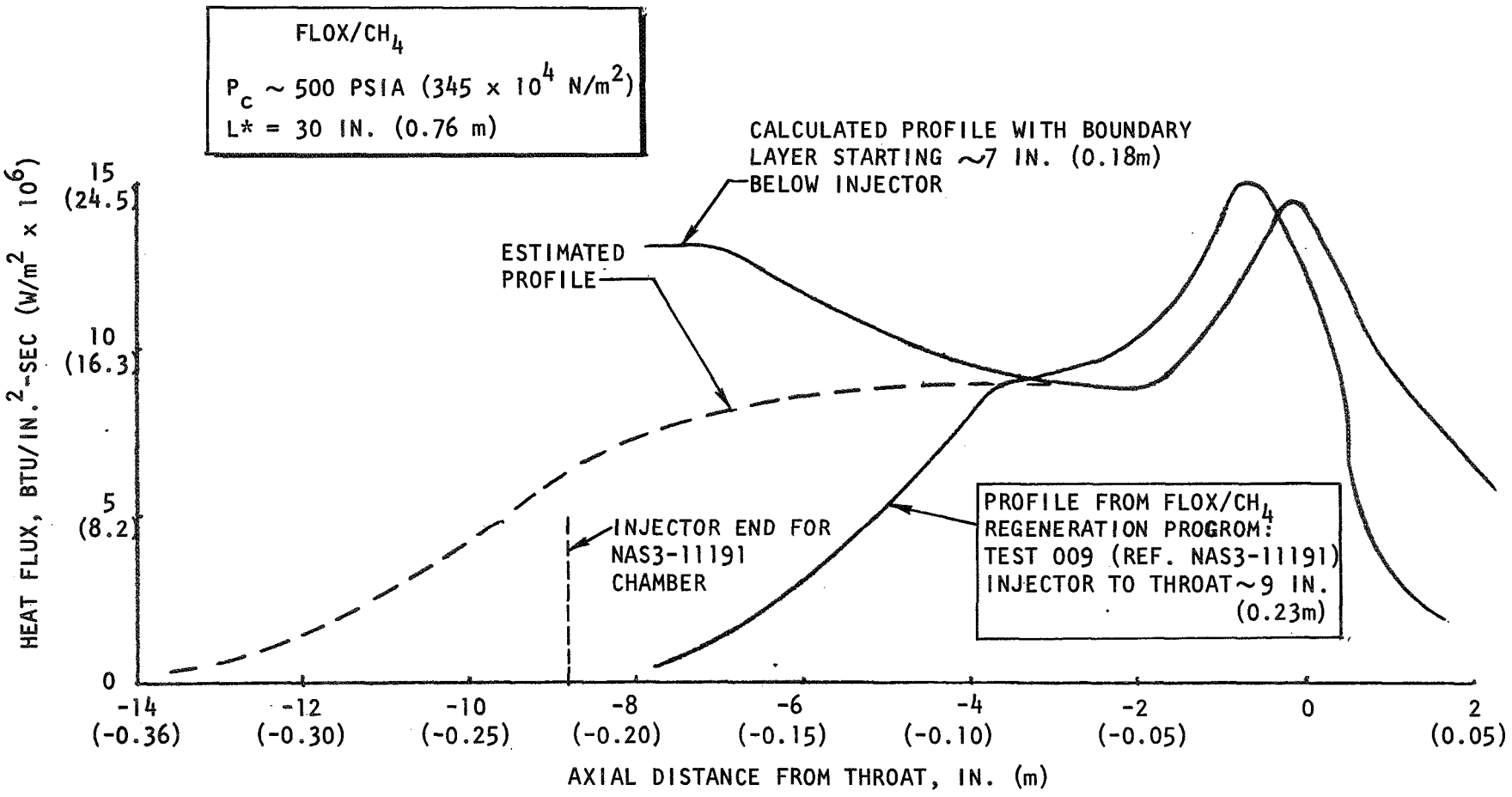

Figure E-3. Axial Heat Flux Profiles: $FLOX/CH_4$

from injector to throat was about 9 in. (0.23 m) compared to 15.4 in. (0.39 m) for the chamber used here. The comparison shows good agreement in the nozzle section but deviates in the combustion zone primarily because of the boundary layer assumptions made in the calculations. The erroneous calculated combustion zone profile was adjusted as shown by the estimated profile in Fig. E-3.

A transient heat transfer analysis was used to predict the chamber wall temperature characteristics for both combustion zone and nozzle conditions. The above mentioned coefficients were used for these calculations. The results indicated a maximum hot gas side wall temperature of approximately 1200 F (922 K) in the copper combustion zone (higher with the graphite combustion zone) and 3200 F (2033 K) at the graphite nozzle throat area after 2.5 seconds of nominal operation.

Heat flux measurements were planned and the probes were to be installed in the copper combustion zone during the Task IV testing. However, these plans were discarded because of damage to the copper combustion zone and the subsequent change to graphite early in the test program. Thus, no Task IV heat flux measurements were obtained.

APPENDIX F

REFERENCES

1. Dickerson, Tate, and Barsic: Correlation of Spray Injector Parameters With Rocket Engine Performance, AFRPL-TR-68-147, Rocketdyne, a division of North American Rockwell Corporation, Canoga Park, California, June 1968.

2. Falk, Clapp, and Nagai: Space Storable Propellant Performance Study, NASA CR-72487 (R-7677), Rocketdyne, a division of North American Rockwell Corporation, Canoga Park, California, 24 November 1968.

3. R-7199, Two-Stage Bipropellant Injection System Studies, Rocketdyne, a division of North American Rockwell Corporation, Canoga Park, California, August 1967.

4. Rupe, J.: A Correlation Between the Dynamic Properties of a Pair of Impinging Streams and the Uniformity of Mixture Ratio Distribution in the Resulting Spray, Progress Report No. 20-209, Jet Propulsion Laboratory, Pasadena, California, 28 March 1956.

5. Nukijama, S. and Y. Tanasawa: "An Experiment on the Atomization of Liquid (5th Report, The Atomization Pattern of Liquid by Means of Air Stream);" Summary Section, Trans. SME Japan, February 1940, Vol. 6 No. 22.

6. Dussourd, J. L. and A. H. Shapiro: "A Deceleration Probe for Measuring Stagnation Pressure and Velocity of a Particle-Laden Gas Stream," 1955 Heat Transfer and Fluid Mechanics Institute, University of California, June 1955.

APPENDIX G

NOMENCLATURE

$\bar{A}_{in}$	=	inner annulus area
A_{out}	=	outer annulus area
A_e	=	area of nozzle exit
A_f	=	fuel injection area
A_ℓ	=	liquid injection area
A_g	=	gas injection area
A_t	=	measured geometric throat area
A_o	=	oxidizer orifice area
$(A_t)_{eff}$	-	effective thermodynamic throat area
$(c^*)_{theo}$	=	theoretical characteristic velocity based on shifting equilibrium
$(C_F)_{theo}$	=	theoretical shifting thrust coefficient (vacuum)
D_{plug}	=	plug or centerbody diameter
D_g	=	diameter of gas jet
D_ℓ, D_L	=	liquid jet diameter
D_o	=	oxidizer orifice diameter
D_s	=	swirl inlet diameter
D_{30}	=	volume mean drop diameter
$\bar{D}$	=	mass median drop diameter
E_m	=	Rupe mixing factor
F	=	thrust
F_{vac}	=	measured thrust corrected to vacuum conditions by the equation: $F_{vac} = F + P_a A_e$

g_c = gravitational constant

L^* = characteristic length

M_g = gas momentum

M = Mach number

M_ℓ = liquid momentum

MR = mixture ratio, flowrate oxidizer (liquid)/flowrate fuel (gas)

P = static pressure

P_a = ambient pressure

P_c, $(P_c)_o$ = nozzle stagnation pressure

P_o = stagnation or total pressure

T = static temperature

T_g = gas temperature

T_o = stagnation temperature

V_s = liquid swirl (inlet) velocity

V_f = fuel velocity

V_ℓ = liquid velocity

V_g = gas velocity

V_j = gas velocity

$\dot{W}_g$, $\dot{w}_g$ = gas flowrate

$\dot{w}_{g,c}$ = gas flowrate through central orifice

$\dot{W}_f$, $\dot{w}_f$ = fuel flowrate

$\dot{W}_\ell$, $\dot{w}_\ell$ = liquid flowrate

$\dot{W}_o$, $\dot{w}_o$ = oxidizer flowrate

$\dot{w}_t$ = total propellant weight flowrate

$(\dot{w}_{ann}/\dot{w}_{tot})_g$ = annulus gas to total gas fraction

X_p/D_g = penetration parameter: $2.5 \left[\frac{M_\ell}{M_g} \cos^2 \theta\right]^{1/2}$

ρ = density

ρ_g = gas density

ρ_ℓ = liquid density

ε_c = contraction area ratio

ε_e = expansion area ratio

θ = complement of impingement angle between liquid and gas jets

γ = specific heat ratio

Y_g = gas annulus gap

Y_ℓ = liquid annulus gap

Y_{in} = inner annulus gap

Y_{out} = outer annulus gap

η_{c*} = characteristic velocity efficiency

$(\eta_{c*})_{vap}$, η_{vap} = vaporization efficiency

$(\eta_{c*})_{mix}$, η_{mix} = mixing efficiency

APPENDIX H

DISTRIBUTION LIST (CONTRACT NAS3-12001)

Report Copies	Recipient	Designee
	National Aeronautics & Space Administration Lewis Research Center 21000 Brookpark Road Cleveland, Ohio 44135 Attn:	
1	Contracting Officer, MS 500-313	
5	Liquid Rocket Technology Branch, MS 500-209	
1	Technical Report Control Office, MS 5-5	
1	Technology Utilization Office, MS 3-16	
2	AFSC Liaison Office, 501-3	
2	Library	
1	Office of Reliability & Quality Assurance, MS 500-111	
1	D. L. Nored, Chief, LRTB, MS 500-209	
6	L. H. Gordon	Project Manager, MS 500-209
1	E. W. Conrad, MS 500-204	
1	R. H. Kemp, MS 49-1	
1	R. H. Knoll, MS 501-2	
1	H. H. Valentine, MS 501-2	
1	C. Aukerman, MS 500-204	
1	J. W. Gregory, MS 500-209	
2	Chief, Liquid Experimental Engineering, RPX Office of Advanced Research & Technology NASA Headquarters Washington, D. C. 20546	
2	Chief, Liquid Propulsion Technology, RPL Office of Advanced Research & Technology NASA Headquarters Washington, D. C. 20546	
1	Director, Launch Vehicles & Propulsion, SV Office of Space Science & Applications NASA Headquarters Washington, D. C. 20546	
1	Chief, Environmental Factors & Aerodynamics Code RV-1 Office of Advanced Research & Technology NASA Headquarters Washington, D. C. 20546	

Report Copies	Recipient	Designee
1	Chief, Space Vehicles Structures Office of Advanced Research & Technology NASA Headquarters Washington, D. C. 20546	
1	Director, Advanced Manned Missions, MT Office of Manned Space Flight NASA Headquarters Washington, D. C. 20546	
6	NASA Scientific & Technical Information Facility P. O. Box 33 College Park, Maryland 20740	
1	Director, Technology Utilization Division Office of Technology Utilization NASA Headquarters Washington, D. C. 20546	
1	National Aeronautics & Space Administration Ames Research Center Moffett Field, California 94035 Attn: Library	Hans M. Mark Mission Analysis Division
1	National Aeronautics & Space Administration Flight Research Center P. O. Box 273 Edwards, California 93523 Attn: Library	
1	National Aeronautics & Space Administration Goddard Space Flight Center Greenbelt, Maryland 20771 Attn: Library	Merland L. Moseson, Code 620
1	National Aeronautics & Space Administration John F. Kennedy Space Center Cocoa Beach, Florida 32931 Attn: Library	Dr. Kurt H. Debus
1	National Aeronautics & Space Administration Langley Research Center Langley Station Hampton, Virginia 23365 Attn: Library	E. Cortwright Director
1	National Aeronautics & Space Administration Manned Spacecraft Center Houston, Texas 77001 Attn: Library	J. G. Thiobodaux, Jr., Chief Propulsion & Power Division

Report Copies	Recipient	Designee
1	National Aeronautics & Space Administration George C. Marshall Space Flight Center Huntsville, Alabama 35812 Attn: Library	Hans G. Paul Leon J. Hastings James Thomas Dale Burrows I. G. Yates Clyde Nevins J. Blumrich
1	Jet Propulsion Laboratory 4800 Oak Grove Drive Pasadena, California 91103 Attn: Library	Henry Burlage, Jr. Duane Dipprey
1	Defense Documentation Center Cameron Station Building 5 5010 Duke Street Alexandria, Virginia 22314 Attn: TISIA	
1	Office of the Director of Defense Research & Engineering Washington, D. C. 20301 Attn: Office of Asst. Dir. (Chem. Technology)	
1	RTD (RTNP) Bolling Air Force Base Washington, D. C. 20332	
1	Arnold Engineering Development Air Force Systems Command Tullahoma, Tennessee 37389 Attn: Library	Dr. H. K. Doetsch
1	Advanced Research Projects Agency Washington, D. C. 20525 Attn: Library	
1	Aeronautical Systems Division Air Force Systems Command Wright-Patterson Air Force Base, Dayton, Ohio Attn: Library	D. L. Schmidt Code ARSCNC-2
1	Air Force Missile Test Center Patrick Air Force Base, Florida Attn: Library	L. J. Ullian

Report Copies	Recipient	Designee
1	Air Force Systems Command Andrews Air Force Base Washington, D. C. 20332 Attn: Library	Capt. S. W. Bowen SCLT
1	Air Force Rocket Propulsion Laboratory (RPR) Edwards, California 93523 Attn: Library	
1	Air Force Rocket Propulsion Laboratory (RPM) Edwards, California 93523 Attn: Library	
1	Air Force FTC (FTAT-2) Edwards Air Force Base, California 93523 Attn: Library	Donald Ross
1	Air Force Office of Scientific Research Washington, D. C. 20333 Attn: Library	SREP, Dr. J. F. Masi
1	Space & Missile Systems Organization Air Force Unit Post Office Los Angeles, California 90045 Attn: Technical Data Center	
1	Office of Research Analyses (OAD) Holloman Air Force Base, New Mexico 88330 Attn: Library RRRD	
1	U. S. Air Force Washington, D. C. Attn: Library	Col. C. K. Stambaugh, Code AFRST
1	Commanding Officer U. S. Army Research Office (Durham) Box CM, Duke Station Durham, North Carolina 27706 Attn: Library	
1	U. S. Army Missile Command Redstone Scientific Information Center Redstone Arsenal, Alabama 35808 Attn: Document Section	Dr. W. Wharton
1	Bureau of Naval Weapons Department of the Navy Washington, D. C. Attn: Library	J. Kay, Code RTMS-41

Report Copies	Recipient	Designee
1	Commander U. S. Naval MIssile Center Point Mugu, California 93041 Attn: Technical Library	
1	Commander U. S. Naval Weapons Center China Lake, California 93557 Attn: Library	
1	Commanding Officer Naval Research Branch Office 1030 E. Green Street Pasadena, California 91101 Attn: Library	
1	Director (Code 6180) U. S. Naval Research Laboratory Washington, D. C. 20390 Attn: Library	H. W. Carhart J. M. Krafft
1	Picatinny Arsenal Dover, New Jersey 07801 Attn: Library	I. Forsten
1	Air Force Aero Propulsion Laboratory Research & Technology Division Air Force Systems Command United States Air Force Wright-Patterson AFB, Ohio 45433 Attn: APRP (Library)	R. Quigley C. M. Donaldson
1	Electronics Division Aerojet-General Corporation P. O. Box 296 Azusa, California 91703 Attn: Library	G. G. Whipple
1	Aerojet Ordnance and Manufacturing Company 601 S. Placentia Street Fullerton, California 92631	P. R. Holmes
1	Aerojet Liquid Rocket Company P. O. Box 13222 Sacramento, California 95813 Attn: Technical Library 2484-2015A	D. Kors R. Stiff C. E. Tedmon

Report Copies	Recipient	Designee
1	Aeronutronic Division of Philco Ford Corp. Ford Road Newport Beach, California 92663 Attn: Technical Information Department	Dr. L. H. Linder
1	Aerospace Corporation 2400 E. El Segundo Blvd. Los Angeles, California 90045 Attn: Library-Documents	J. G. Wilder
1	Arthur D. Little, Inc. 20 Acorn Park Cambridge, Massachusetts 02140 Attn: Library	A. C. Tobey
1	Astropower Laboratory McDonnell-Douglas Aircraft Company 2121 Paularino Newport Beach, California 92163 Attn: Library	
1	ARO, Incorporated Arnold Engineering Development Center Arnold AF Station, Tennessee 37389 Attn: Library	
1	Susquehanna Corporation Atlantic Research Division Shirley Highway & Edsall Road Alexandria, Virginia 22314 Attn: Library	
1	Battelle Memoria Institute 505 King Avenue Columbus, Ohio 43201 Attn: Report Library, Room 6A	
1	Beech Aircraft Corporation Boulder Facility Box 631 Boulder, Colorado Attn: Library	Douglas Pope
1	Bell Aerosystems, Inc. Box 1 Buffalo, New York 14240 Attn: Library	T. Reinhardt W. M. Smith

Report Copies	Recipient	Designee
1	Bendix Systems Division Bendix Corporation 3300 Plymouth Street Ann Arbor, Michigan Attn: Library	John M. Bruege
1	Bellcomm 955 L'Enfant Plaza, S. W. Washington, D. C. Attn: Library	H. S. London
1	Boeing Company Space Division P. O. Box 868 Seatle, Washington 98124 Attn: Library	J. D. Alexander C. F. Tiffany
1	Chemical Propulsion Information Agency Applied Physics Laboratory 8621 Georgia Avenue Silver Spring, Maryland 20910	Tom Reedy
1	Chrysler Corporation Missile Division P. O. Box 2628 Detroit, Michigan Attn: Library	John Gates
1	Chrysler Corporation Space Division P. O. Box 29200 New Orleans, Louisiana 70129 Attn: Librarian	
1	Curtiss-Wright Corporation Wright Aeronautical Division Woodridge, New Jersey Attn: Library	G. Kelley
1	University of Denver Denver Research Institute P. O. Box 10127 Denver, Colorado 80210 Attn: Security Office	
1	Fairchild Stratos Corporation Aircraft Missiles Division Hagerstown, Maryland Attention: Library	

Report Copies	Recipient	Designee
1	Research Center Fairchild Hiller Corporation Germantown, Maryland Attn: Library	Ralph Hall
1	Republic Aviation Fairchild Hiller Corporation Farmington, Long Island New York	
1	General Dynamics/Convair P. O. Box 1128 San Diego, California 92112 Attn: Library	Frank Dore
1	Missiles and Space Systems Center General Electric Company Valley Forge Space Technology Center P. O. Box 8555 Philadelphia, Pa. 19101 Attn: Library	A. Cohen F. Schultz
1	General Electric Company Flight Propulsion Lab. Department Cincinnati, Ohio Attn: Library	D. Suichu Leroy Smith
1	Grumman Aircraft Engineering Corporation Bethpage, Long Island, New York Attn: Library	Joseph Gavin
1	Hercules Powder Company Allegheny Ballistics Laboratory P. O. Box 210 Cumberland, Maryland 21501 Attn: Library	
1	Honeywell Inc. Aerospace Division 2600 Ridgeway Road Minneapollis, Minnesota Attn: Library	
1	IIT Research Institute Technology Center Chicago, Illinois 60616 Attn: Library	C. K. Hersh

Report Copies	Recipient	Designee
1	Kidde Aer-Space Division Walter Kidde & Company, Inc. 567 Main Street	R. J. Henville
1	Ling-Temco-Vought Corporation P. O. Box 5907 Dallas, Texas 75222 Attn: Library	
1	Lockheed Missiles and Space Company P. O. Box 504 Sunnyvale, California 94087 Attn: Library	
1	Lockheed Propulsion Company P. O. Box 111 Redlands, California 92374 Attn: Library, Thackwell	H. L. Thackwell
1	Marquardt Corporation 16555 Saticoy Street Box 2013 - South Annex Van Nuys, California 91409	L. R. Bell Jr. T. Hudson
1	Martin-Marietta Corporation (Baltimore Division) Baltimore, Maryland 21203 Attn: Library	
1	Denver Division Martin-Marietta Corporation P. O. Box 179 Denver, Colorado 80201 Attn: Library	Dr. Morganthaler F. R. Schwartzberg
1	Orlando Division Martin-Marietta Corporation Box 5827 Orlando, Florida Attn: Library	J. Fern
1	Western Division McDonnell Douglas Astronautics 5301 Bolsa Ave Huntington Beach, California 92647 Attn: Library	R. W. Hallett G. W. Burge P. Klevatt
1	McDonnell Douglas Aircraft Corporation P. O. Box 516 Lambert Field, Missouri 63166 Attn: Library	R. A. Herzmark

Report Copies	Recipient	Designee
1	Rocketdyne Division North American Rockwell Inc. 6633 Canoga Avenue Canoga Park, California 91304 Attn: Library, Department 596-306	Dr. J. J. Thompson S. F. Iacobellis
1	Space & Information Systems Division North American Rockwell 12214 Lakewood Blvd. Downey, California Attn: Library	
1	Northrop Space Laboratories 3401 West Broadway Hawthorne, California Attn: Library	Dr. Willian Howard
1	Purdue University Lafayette, Indiana 47907 Attn: Library (Technical)	Dr. Bruce Reese
1	Radio Corporation of America Astro-Electronics Products Princeton, New Jersey Attn: Library	
1	Rocket Research Corporation Willow Road at 116th Street Redmond, Washington 98052 Attn: Library	F. McCullough, Jr.
1	Stanford Research Institute 333 Ravenswood Avenue Menlo Park, California 94025 Attn: Library	Dr. Geral Marksman
1	Thiokol Chemical Corporation Redstone Division Huntsville, Alabama Attn: Library	John Goodloe
1	TRW Systems Inc. 1 Space Park Redondo Beach, California 90278 Attn: Techn. Lib. Doc. Acquisitions	D. H. Lee H. Burge

Report Copies	Recipient	Designee
1	TRW Incorporation TAPCO Division 23555 Euclid Avenue Cleveland, Ohio 44117	P. T. Angell
1	United Aircraft Corporation Corporation Library 4000 Main Street East Hartford, Connecticut 06108 Attn: Library	Dr. David Rix Erle Martin Frank Owen Wm. E. Taylor
1	United Aircraft Corporation Pratt & Whitney Division Florida Research & Development Center P. O. Box 2691 West Palm Beach, Florida 33402 Attn: Library	R. J. Coar Dr. Schmitke T. E. Bailey
1	United Aircraft Corporation United Technology Center P. O. Box 358 Sunnyvale, California 94038	Dr. David Altman
1	Vickers Incorporated Box 302 Troy, Michigan	
1	Vought Astronautics Box 5907 Dallas, Texas Attn: Library	

UNCLASSIFIED

Security Classification

DOCUMENT CONTROL DATA - R & D

(Security classification of title, body of abstract and indexing annotation must be entered when the overall report is classified)

1. ORIGINATING ACTIVITY (Corporate author)	2a. REPORT SECURITY CLASSIFICATION
Rocketdyne, a Division of North American Rockwell Corporation, 6633 Canoga Avenue, Canoga Park, California 91304	UNCLASSIFIED
	2b. GROUP

3. REPORT TITLE

INVESTIGATION OF GAS-AUGMENTED INJECTORS

4. DESCRIPTIVE NOTES (Type of report and inclusive dates)

FINAL REPORT

5. AUTHOR(S) (First name, middle initial, last name)

P. F. Mehegan; D. T. Campbell; C. H. Scheuerman

6. REPORT DATE	7a. TOTAL NO. OF PAGES	7b. NO. OF REFS
31 May 1971	458	6

8a. CONTRACT OR GRANT NO.	9a. ORIGINATOR'S REPORT NUMBER(S)
NAS3-12001	R-8361
b. PROJECT NO.	
c.	9b. OTHER REPORT NO(S) (Any other numbers that may be assigned this report)
d.	NASA CR-72703

10. DISTRIBUTION STATEMENT

11. SUPPLEMENTARY NOTES	12. SPONSORING MILITARY ACTIVITY
	NASA Lewis Research Center Cleveland, Ohio

13. ABSTRACT

The gas-augmented injector program was initiated to investigate the use of high-energy gas to enhance atomization and mixing and to generally improve gas-liquid injector concepts. Performance analyses, cold-flow experiments, and hot-firing tests were systematically conducted to produce stable operation with combustion efficiencies to 99 percent using large thrust-per-element injectors; i.e., 20,000-lb (88,900 N)-thrust per element with LOX/H_2 propellants and 5000-lb (22,200 N)-thrust per element with FLOX/CH_4 propellants. Also, promising analytical/cold-flow/hot-fire performance correlation techniques were developed that may be used to guide future injector designs.

DD FORM 1 NOV 65 1473

UNCLASSIFIED

Security Classification

14. KEY WORDS	LINK A		LINK B		LINK C	
	ROLE	WT	ROLE	WT	ROLE	WT
Gas-Augmented Injectors						
Oxygen/Hydrogen						
FLOX/Methane						
Atomization						
Vaporization						
Mixing						
Distribution						
Performance Analysis						
Cold-Flow Studies						
Hot-Fire Testing						
Impinging Concentric Injector						
Tricentric With Centerbody Injector						
Performance						
Stability						
Design Criteria						
Injector Characterization						
Performance Correlating Parameters						